Determination of Degassing Patterns in Volcanic Systems

Amy Sarah Diana Collinson

Submitted in accordance with the requirements for the degree of
Doctor of Philosophy

The University of Leeds
School of Earth and Environment
May 2014

The candidate confirms that the work submitted is her own, except where work which has formed part of jointly authored publications has been included. The contribution of the candidate and the other authors to this work has been explicitly indicated below. The candidate confirms that appropriate credit has been given within the thesis where reference has been made to the work of others.

Chapters 3 - 7 contain work significantly expanded from the publication:

Collinson, A. S. D., and J. W. Neuberg (2012), Gas storage, transport and pressure changes in an evolving permeable volcanic edifice, *Journal of Volcanology and Geothermal Research*, *243–244*, 1–13, doi:10.1016/j.jvolgeores.2012.06.027

Chapter 10 contains work included in the pending publication:

Collinson, A. S. D., and J. W. Neuberg (in prep.), Modelling gas transfer, storage and resulting displacement in a 3D permeable volcanic edifice.

Both papers have been prepared in their entirety by A. S. D. Collinson, with comments from the co-author, J. W. Neuberg.

To my Family for their love, patience, understanding and unwavering support.

But, most importantly, for the hugs when I needed them most.

and to Hope.

Acknowledgements

Thank you to Locko firstly for accepting me to do an MRes with him before seeing some small potential in me and secondly, for encouraging me to apply for a PhD. It has been a long, eventful but thrilling and exciting few years and I am exceedingly grateful for being given this amazing opportunity. Thank you also for the assistance of my Research Support Group of one, Ivan Savov. I extend this gratitude to all the members of the Volcano group at the University of Leeds, who have all offered suggestions and advice on the research at various stages in its development.

I also acknowledge the mutual help between Mark Thomas and myself with regards to solving our numerous problems with the program, Comsol Multiphysics. Additionally, I acknowledge the support team at Comsol for answering my queries and in particular, David Lin for supplying many weeks worth of trials for the Earth Science Module, without which the method employed could not have been used. Thank you to Richard Rigby for always going above and beyond and solving all my IT related problems.

I am indebted to the staff at both Aberdeen Royal Infirmary and St James's Hospital, Leeds, in addition to the staff at Baxter medical care, and the numerous supply drivers. Of course Twitch, Wiggle and Pickles also played an instrumental, if somewhat annoying and frustrating role without which I would never have completed this work as it stands.

Finally, to my dear friends, Kerry, Tai and Hannah-Bea for their support, encouragement and for reminding me to be optimistic.

Abstract

The volume of gas contained within a silicic magma, dissolved and subsequently exsolved, greatly influences the behaviour of a volcano. There is a marked contrast between the behaviour of a volcano "open" to degassing, compared to one which is "closed". It is, therefore, essential to understand the entire degassing process of gas transport, storage and loss.

The particular focus of this study is the effect different permeabilities and pressure gradients within a volcanic edifice have on the degree and pattern of the gas velocity. Gas loss is modelled numerically in two- and three-dimensions using a finite element approach. By combining the time-dependent continuity equation and Darcy's law, a partial differential equation is derived and solved for the pressure. The associated pressure gradient is used in Darcy's law to determine the corresponding gas velocity distribution. The momentum equation is also used to determine the surface displacement pattern resulting from the movement and storage of gas within the system.

The model framework is applied to numerous volcanic scenarios including cracks and sealing within the dome structure and shear fractures at the margin between the conduit and country rock. Two case studies are investigated: Ash venting at Soufrière Hills volcano in March 2012, and persistent, repetitive ring-shaped degassing at Santiaguito. Quantitative estimates regarding gas emissions and deformation provide the link to constraining observations.

The results show the country rock and dome are important and it is the relative permeabilities, rather than the actual values which determine the pressurisation. A decrease of just two orders of magnitude in the surrounding permeability could switch behaviour from effusive to explosive. For efficient gas storage within a volcano, a high permeability is required to hold the gas, whilst a low permeability is necessary to trap it. From the modelled surface displacement patterns and gas emissions at the surface, it may be possible to track the migration of large volumes of gas, particularly if used in conjunction with real-time monitoring of active volcanoes.

Notation and Abbreviations

Nomenclature for the modelling

A	m^2	Surface area
x, y	m	Horizontal spatial coordinate
z	m	Vertical spatial coordinate
ρ	kgm^{-3}	Gas density
ρ_S	kgm^{-3}	Gas density at start
ρ_E	kgm^{-3}	Gas density at end
ρ_r	2500 kgm^{-3}	Rock density
$\boldsymbol{V}$	m	Total displacement
u, v, w	m	Directional components of the displacement
C		Elasticity tensor
n_ex	wt.%	Exsolved gas
n_tot	wt.%	Total gas
g	9.81 ms^{-2}	Acceleration due to gravity
$\mathbf{F}_v$	N	Vector force
R	8.314 $\mathrm{m}^3\mathrm{PaK}^{-1}\mathrm{mol}^{-1}$	Ideal gas constant
$\boldsymbol{I}$		Identity matrix
l	m	Length
Q_m	$\mathrm{kgm}^{-3}\mathrm{s}$	Mass source term
M	0.018 kgmol^{-1}	Molecular mass
k	m^2	Permeability
ϕ		Porosity
P	Pa	Gas pressure
P_atm	0.1×10^6 Pa	Atmospheric pressure
P_lith	Pa	Lithostatic pressure
ΔP	Pa	Pressure change
∇P	Pam^{-1}	Pressure gradient
ν	0.25	Poisson's ratio
K	4.1×10^{-6} $\mathrm{Pa}^{-\frac{1}{2}}$	Solubility constant (H_2O in silicic magma)
ϵ		Strain tensor
ϵ_x, ϵ_{xy}, ϵ_{xz}...		Components of strain tensor
σ	Pa	Stress tensor

σ_x, σ_y, σ_z	Pa	Components of normal stress
τ_{xy}, τ_{xz}, τ_{yx}...	Pa	Components of shear stress
T	1123 K	Temperature
t	s	Time
$\boldsymbol{u}$	ms^{-1}	Gas velocity
μ	1.5×10^{-5} Pas	Gas viscosity
V	m^3	Volume
w	m	Width
E	10 GPa	Young's modulus

Glossary

Closed System Degassing	Exsolution occurs, but exsolved gas is trapped within the melt.
Open System Degassing	Exsolved gas is lost shortly after exsolution.
Equilibrium State	The point where all domains within the model have reached stability and no further changes to the results will be observed unless an additional change in the conditions is imposed, assuming a constant supply of gas from depth.
Permeability (Darcian)	A measure of the ease at which fluid is transmitted through a material. Often calculated using Darcy's law.
Poisson's Ratio	The ratio (between -1 and 0.5) of the strain in the applied direction to that perpendicular. An incompressible material has a Poisson's ratio of 0.5.
Porosity	The percentage of void spaces vs. bulk volume of a porous media.
Strain	A measure of the deformation in response to an applied stress.
Stress	The force per unit area applied to an object which may experience strain.
Normal Stress	Component of stress perpendicular to the plane.
Shear Stress	Component of stress parallel to the plane.
Young's Modulus	Indicates the stiffness of an elastic material (ratio of stress to strain).

Abbreviations

CAD	Computer Aided Design

COSPEC	Correlation Spectroscopy
DEM	Digital Elevation Model
EDM	Electronic Distance Meter
FDM	Finite Difference Method
FEM	Finite Element Method
FTIR	Fourier Transform InfraRed
FVM	Finite Volume Method
FZ	Fracture Zone
GPS	Global Positioning System
IDOAS	Imaging Differential Optical Absorption Spectroscopy
InSAR	Interferometric Synthetic Aperture Radar
m.a.s.l.	Metres Above Sea Level
MultiGAS	Multisensor Gas Analyzer System
MVO	Montserrat Volcano Observatory
SHV	Soufrière Hills volcano
TOMS	Total Ozone Mapping Spectrometer
(V)LP	(Very) Long Period earthquakes
VT	Volcano-Tectonic earthquakes

Contents

Notation and Abbreviations **viii**

List of Figures **xvi**

List of Tables **xxvi**

1 Introduction **1**

1.1 Degassing pathways 1

1.1.1 Permeable foam model 2

1.1.2 Degassing through the conduit walls 3

1.1.3 Surface gas emissions 5

1.1.4 Sealing degassing pathways 7

1.2 Physical Properties 9

1.2.1 Darcian permeability and porosity measurements 9

1.2.2 Rock mechanics and the failure criterion 14

1.2.3 Volatile contents of magmas 15

1.3 Volcanic monitoring 16

1.3.1 Measuring gas emissions 17

1.3.2 Volcano deformation 20

1.3.3 Volcanic seismicity 21

1.4 Key aims of the research 23

1.5 Overview of the Thesis 23

2 Method **25**

2.1 Darcy's law and its use in Volcanology 25

2.2 Equations 26

2.2.1 Modelling the gas loss 27

2.2.2 Modelling the displacement 28

2.2.3 Coupling the equations for fluid flow and displacement 29

2.3 Model assumptions 29

2.4 Solving using the finite element method 30

2.4.1 Problem formulation 32
2.4.2 Geometry creation 32
2.4.3 Meshing 32
2.4.4 Specifying the constraints 33
2.4.5 Boundary and domain conditions 34
2.4.6 Solving the problem 38
2.4.7 Study types and solver settings 41
2.4.8 Postprocessing of results 42
2.5 Summary 44

3 The Conceptual Basic Model 46
3.1 The principal block model 46
3.2 Conduit gas velocity and pressure development 53
3.3 Summary 57

4 A Time-Dependent Example - "Dome Collapse" 59
4.1 An unloading event 60
4.2 Summary 64

5 Gas Escape Through Fracture Zones 66
5.1 Fracturing of the conduit-wall boundary 66
5.1.1 Instantaneous fracturing 68
5.1.2 Propagating shear fractures 69
5.1.3 Resealing the fractures 75
5.1.4 Fractures propagating downwards 79
5.2 Brittle failure and resulting surface displacement 81
5.3 Summary 88

6 Sealing the Volcano 89
6.1 Decreasing the permeability 89
6.2 Summary 93

7 Cracked Dome 95
7.1 Crack formation 97
7.2 Deforming the cracks 105
7.3 Summary 113

8 Gas Storage and Release in 3D 115
8.1 Model Setup 115
8.2 Permeability variation and implications 117

8.2.1 Pressure . . . 118
8.2.2 Pressure change . . . 122
8.2.3 Gas velocity . . . 125
8.2.4 Displacement . . . 126
8.3 Groups with similar displacement behaviour . . . 131
8.4 Example Models . . . 131
8.4.1 Example Models: Pressure . . . 134
8.4.2 Example Models: Pressure Change . . . 139
8.4.3 Example Models: Surface gas emissions . . . 141
8.4.4 Example Models: Surface displacement . . . 145
8.5 Summary . . . 150

9 Further Model Variations of Gas Storage and Release in 3D 152
9.1 Altering the fracture zone . . . 153
9.1.1 Implications of fracture zone size . . . 160
9.2 Permeability Variation . . . 161
9.2.1 Model description . . . 161
9.2.2 Pressure . . . 163
9.2.3 Displacement and gas velocity . . . 167
9.2.4 Changing the minimum conduit permeability . . . 170
9.2.5 Implications of permeability variability . . . 175
9.3 Effects of Topography . . . 177
9.3.1 Pressure . . . 177
9.3.2 Pressure change . . . 178
9.3.3 Displacement . . . 183
9.3.4 Groups . . . 187
9.3.5 Example Models . . . 191
9.3.6 Model **19** comparison . . . 199
9.3.7 Implications of topography . . . 199
9.4 Summary . . . 203

10 Case Studies 205
10.1 Model framework . . . 205
10.1.1 Boundary conditions . . . 205
10.1.2 Permeability . . . 205
10.1.3 Porosity . . . 206
10.1.4 Volcanic gas . . . 207
10.1.5 Rheology . . . 209
10.1.6 Topography . . . 210

10.1.7 Summary of results . . . 211
10.1.8 Implications . . . 212
10.2 Ash-Venting at Soufrière Hills volcano . . . 213
10.2.1 Model scenario . . . 216
10.2.2 Results: Pressure . . . 216
10.2.3 Results: Surface gas emissions . . . 222
10.2.4 Results: Surface displacement . . . 224
10.2.5 Summary of the March 2012 ash-venting event . . . 225
10.3 Ring-shaped degassing at Santiaguito . . . 228
10.3.1 Trigger mechanism . . . 230
10.3.2 Model scenario . . . 231
10.3.3 Results: Pressure . . . 234
10.3.4 Results: Surface gas emissions . . . 239
10.3.5 Results: Surface displacement . . . 241
10.3.6 Conduit permeability gradient . . . 243
10.3.7 Summary of ring-shaped degassing at Santiaguito . . . 248
10.4 Summary . . . 251

11 Discussion and Conclusions 252
11.1 Implications from the modelling . . . 252
11.1.1 Sealing the volcano . . . 252
11.1.2 Dome cracks and fracturing . . . 253
11.1.3 Permeability variations . . . 254
11.1.4 Country rock and dome . . . 255
11.1.5 Switches in volcanic behaviour . . . 256
11.1.6 Event equilibrium times and cyclicity . . . 257
11.2 Suggestions for further work . . . 258
11.2.1 Reynolds number and applicability of Darcy's law . . . 258
11.2.2 Gas species . . . 259
11.2.3 Crystallisation . . . 259
11.2.4 Permeability . . . 259
11.2.5 Geological structure . . . 260
11.2.6 An optimal model . . . 260
11.3 Conclusions . . . 264

12 References 266

A Analytical Solutions **284**
A.1 1D homogeneous model . . . 284
A.1.1 Analysis of Results . . . 285
A.2 1D layered model . . . 286
A.2.1 Analysis of Results . . . 287
A.3 2D circular flow . . . 289
A.3.1 Analysis of results . . . 290
A.3.2 Layered circular flow . . . 291
A.3.3 Analysis of results . . . 291
A.4 Radial flow . . . 294
A.4.1 Analysis of results . . . 296
A.5 Spherical flow . . . 298
A.5.1 Analysis of results . . . 299
A.6 Implications for the modelling . . . 301

B The validity of Darcy's law **302**
B.1 Reynolds number . . . 302
B.2 Darcy's law versus Forchheimer equation . . . 304
B.2.1 Analysis of results . . . 305
B.3 Implications for the modelling . . . 307

C Gas density and viscosity **308**
C.1 Gas density . . . 308
C.1.1 Temperature . . . 308
C.1.2 Ideality . . . 312
C.2 Gas viscosity . . . 313
C.3 Implications for the modelling . . . 314

D De-coupling along the conduit-wall margin **316**
D.1 Modelling de-coupling . . . 316
D.2 Implications for the modelling . . . 319

List of Figures

1 Introduction

1.1 Compilation of published Darcian permeabilities and porosities for a variety of volcanic rocks. 9

1.2 Darcian permeabilities and porosities measured for volcanic and experimental materials ordered according to volcano. 10

1.3 A comparison between the dissolved H_2O content as calculated by Henry's law (Equation 1.3) to that by VolatileCalc for three different temperatures 17

2 Method

2.1 Simple example showing a triangular mesh element with three numbered nodes. 33

2.2 Examples of different 2D mesh types. 34

2.3 Examples of different triangular mesh resolutions. 34

2.4 General model configuration showing the different domains and boundary types. 35

2.5 Comparison of the number of nodes allocated to each triangular mesh element dependent upon the discretisation order. 40

3 The Conceptual Basic Model

3.1 Setup for the principal block model with a central conduit surrounded by wall-rocks and topped by an overburden. 46

3.2 Average pressure and gas velocity for the conduit, dome and wall-rocks in each model. 48

3.3 Examples from the six groups identified from the pressure pattern results. 50

3.4 Gas overpressure derived, by subtracting the lithostatic pressure, for the 6 examples in Figure 3.3. 50

3.5 Permeability criteria determining pressurisation pattern. 52
3.6 Vertical pressure profiles for the models in Figures 3.3 and 3.4. 54
3.7 Average conduit gas velocity (a), conduit pressure (b), and edifice (wall-rocks and dome) pressure (c) against wall-rock/dome permeability for different conduit permeabilities. 55
3.8 Pressure plots where the conduit has a permeability of 10^{-10} m^2 for different edifice (wall-rock and dome) permeabilities. 56
3.9 Gas velocity plots, on a logarithmic scale, where the conduit has a permeability of 10^{-10} m^2 for different edifice permeabilities. 57

4 A Time-Dependent Example - "Dome Collapse"

4.1 Photographs showing the Soufrière Hills volcano lava dome, taken from Windy Hill, before and after the July 2003 dome collapse (Mattioli et al., 2004). 60
4.2 Before and after the 2010 dome collapse of Merapi lava dome (Surono et al., 2012). 60
4.3 Setup for the unloading event with a central conduit surrounded by wall-rocks and topped by an overburden. 61
4.4 Dome collapse model where the conduit has a permeability of 10^{-10} m^2, wall-rocks and dome of 10^{-16} m^2. 62
4.5 Time sequence for the dome collapse model. 63
4.6 The difference in average pressure for each domain with the source term compared to without. The total gas content used is 7 wt.%. . . 64

5 Gas Escape Through Fracture Zones

5.1 Setup for the brittle failure model showing the location of the conduit, wall-rocks and fracture zones. 67
5.2 Initial equilibrium pressure and gas overpressure for the model. 68
5.3 Pressure, pressure change and gas overpressure for instantaneous fracture of the conduit-wall margin. 69
5.4 Brittle failure model, where a system of fractures propagates up the margin from 1500 m depth to the surface. 70
5.5 Close up images of Figure 5.4a, when the fractures are located between 1500 and 700 m depth, showing the relationship between the top of the fracture, the pressure, gas overpressure and change in pressure. 71

5.6 Pressure and pressure change, with respect to the state of the system at time 9700 seconds, for the brittle failure model where the failure is halted and held. 73
5.7 (a) Average pressure for the three domains and (b) the change in average pressure relative to time 9700 s, when the fractures have been halted. 74
5.8 (a) Pressure for three points in the model and (b) the change in average pressure relative to time 9700 s, when the fractures have halted. 74
5.9 Brittle failure model similar to Figure 5.4, but fractures begin at 1200 m, propagate upwards and are progressively resealed. 76
5.10 Maximum gas overpressure against fracture length and time for the fractures, conduit and wall-rocks for different fracture permeabilities. 77
5.11 Maximum gas overpressure against fracture length and time for the fractures, conduit and wall-rocks for different maximum fracture lengths. 78
5.12 Brittle failure model where the fractures propagate downwards. . . . 80
5.13 Setup for modelling brittle failure with surface displacement. 81
5.14 The pressure, pressure change and gas overpressure within the system at different times representing different fracture extents. 82
5.15 The displacement change in response to brittle failure along the conduit-wall margin. 83
5.16 Pressure change graphs for each domain for different start and end fracture permeabilities 85
5.17 Displacement change for three points within the model: (0, 0) top of the conduit; (500, 0) top right wall-rock; (980, -430) mid right wall-rock, for different start and end fracture permeabilities. 86
5.18 Displacement change graphs for the top of the spine (0,0), top corner (500, 0) and the middle of the right wall-rock edge (980, -430), for the model with fracture permeability increasing from 10^{-14} to 10^{-8} m^2. 87

6 Sealing the Volcano

6.1 Setup for model investigating sealing within the dome. 90
6.2 Model to investigate sealing of the system. 91
6.3 Pressure change in response to sealing the dome. 91
6.4 The start and end gas overpressure results. 92
6.5 Maximum overpressure versus thickness of the sealed layers. 92
6.6 Initial and end equilibrium displacement. 93

7 Cracked Dome

7.1 Examples of fumaroles from active volcanoes. 96
7.2 Setup for the two cracked dome models. 98
7.3 Pressure for two temporal cracked dome models, showing the initial crack-free systems and the dome with cracks after 18 hrs and the end equilibrium. 99
7.4 Pressure change for the two models in response to crack development. 100
7.5 Gas Overpressure for the two models in response to crack development. 101
7.6 Average pressure change within the domains in each model. 102
7.7 Gas velocity, on a logarithmic scale, for the two cracked dome models. 103
7.8 The approximate equilibrium times for the four domains in each model dependent upon edifice (wall-rocks and dome) permeability and assuming a conduit permeability of 10^{-10} m^2. 104
7.9 Pressure at the start and pressure change at the end, relative to the start equilibrium, for each domain in the two models. 104
7.10 Geometry for the model with a central conduit surrounded by wall-rocks and overlain by a cracked dome. 106
7.11 Start and end equilibrium pressure for the two models. 106
7.12 The end-equilibrium pressure change for the two models. 107
7.13 Gas overpressure for the start and end equilibrium positions of each model. 108
7.14 The gas velocity patterns for the two models are very similar, with the greatest gas velocities within the high permeability conduit, and around the crack margins. 109
7.15 Total displacement at the start (top) and the displacement change at the end (bottom). 110
7.16 Change in width of the nine cracks in (a) the original model (Model **3**), (b) the model run without crack *8* (Model **4**) and (c) the difference between the two models. 111
7.17 Arrows illustrating the magnitude and direction of displacement relative to the starting displacement for the cracks. 112

8 Gas Storage and Release in 3D

8.1 The model setup. 116
8.2 The average gas pressure within each domains for the initial state of the models. 119
8.3 The difference between the end and start gas pressure results for each model for the different FZ permeabilities (10^{-10}, 10^{-12} and 10^{-14} m^2). 123

8.4 Maximum surface gas velocity at the start and surface gas velocity change at the end for each model with the three different FZ permeabilities. . . . 127
8.5 The maximum initial surface displacement and the displacement change in terms of uplift and subsidence for each model at the three FZ permeabilities. . . . 129
8.6 Permeability criteria determining which model displays which displacement behaviour due to the FZ. . . . 132
8.7 The differences between Groups `2A`, `4C` and `4D` are subtle, but are due to the relative distributions of subsidence and uplift. . . . 134
8.8 Permeability conditions for the two cross sections at the start, and through the failure at the end (x = 1100m). . . . 135
8.9 The initial gas pressure, with the permeability conditions from Figure 8.8 shown for reference. . . . 137
8.10 The end gas pressure change relative to the initial pressurisation shown in Figure 8.9. . . . 138
8.11 The average pressure change within each domain for all the example models. . . . 140
8.12 Pressure change in the FZ for each example model. . . . 141
8.13 Surface gas velocity at the start and end. . . . 142
8.14 Graph showing the maximum surface gas velocity within the scar. . . . 143
8.15 Gas loss estimates for the conduit and core domains in metric tonnes (t). . . . 144
8.16 Comparison between the initial surface displacement (top) and the average pressure across all domains in the eight example models (bottom). 145
8.17 The pressure (at x = 850m) and the total surface displacement at the start for the eight example models. . . . 147
8.18 Displacement change at three time-steps and the final equilibrium displacement change for each example model. . . . 148
8.19 The displacement change for the maximum inflation, maximum deflation and average surface displacement for each example model. . . . 149
8.20 Average change in surface displacement for all the models (left) and for models **58**, **2**, **26**, **12** and **47** only (right). . . . 150

9 Further Model Variations of Gas Storage and Release in 3D

9.1 The initial permeability conditions (left) and zoomed images of the different end FZ sizes. . . . 153

9.2 The start pressure (top) and the pressure change results for the four model runs. . . . 155
9.3 The initial gas velocity and the associated surface gas velocity. Also, cross-sections for the end gas velocity increase and the end surface gas velocity. . . . 156
9.4 Approximate gas loss from the domains of the conduit and core. . . . 157
9.5 The displacement change at different times and the end equilibrium displacement change. . . . 158
9.6 Change in average pressures, maximum surface gas velocity and maximum and average surface displacement for each model. . . . 159
9.7 The initial permeability conditions for the different permeability variations. . . . 162
9.8 Start pressure and the end pressure change for two cross sections through the model. . . . 164
9.9 Start pressure and end pressure change for the models when the country rock has the higher permeability of 10^{-12} m^2. . . . 166
9.10 Start surface displacement, end surface displacement change and the end surface gas velocity for models **U1** and **Gz_** for the two different country rock permeabilities. . . . 168
9.11 Estimates for the gas lost (t) from each of the conduit and core domains and the maximum surface gas emission rate (t/day) for the models with the different country rock permeabilities. . . . 169
9.12 The initial results for the three model runs for the eight models. . . . 171
9.13 The change in average pressure for each domain, maximum gas velocity in the top of the scar and maximum and average surface displacement for each model in response to FZ. . . . 172
9.14 The topography for the two model configurations (a) the original model from Chapter 8 with the scar, and (b) the model without the scar. . . . 177
9.15 The average pressure in each domain at the start. . . . 179
9.16 The difference in initial average pressure for the models without and with a scar, plotted in pascal and as a percentage. . . . 180
9.17 Change in average pressure at the end of each model without the scar. 181
9.18 Difference in end pressure change between the models without the scar compared to the original models. . . . 182
9.19 Initial maximum surface displacement and change, for the models without the scar, in response to the FZ. . . . 185

9.20 Difference in initial maximum surface displacement, and displacement change in response to the FZ, in terms of inflation and deflation, between the two sets of models. 186
9.21 Permeability criteria determining which model displays which displacement behaviour due to the FZ. 189
9.22 The differences between groups `T2`, `T3` and `T4` showing dominant inflation, and groups `T5` and `T6` with both deflation and inflation. . . . 191
9.23 End pressure change for the example models without the scar. 193
9.24 The end pressure change, for the models with the scar, relative to the initial pressurisation as shown in Figure 8.9. 194
9.25 Gas velocity change at time 10000 seconds with respect to the initial, for models **t47**, **t1**, **t39** and **t19**. 195
9.26 There are large uncertainties in the calculation of the maximum surface gas emission due to the large surface area the emissions cover. . . 195
9.27 The initial total surface displacement and the end displacement change patterns for the models with and without the scar. 197
9.28 Displacement change at three time-steps and the final equilibrium displacement change. 198
9.29 Progression showing the relationship between the changing pressure, displacement and gas velocity for the original Model **19** with the imposed scar. 201
9.30 Progression showing the relationship between the changing pressure, displacement and gas velocity for Model **t19** without the scar. 202

10 Case Studies

10.1 Map of Montserrat showing key locations, adapted from MVO (2012a).213
10.2 Timeline for the March 2012 degassing event. 214
10.3 Photographs of the eruption event and the vents. 215
10.4 Plan view showing the location of the imposed "2010 collapse scar" and the new vent. 217
10.5 Cross-section through the model showing the different domains. . . . 217
10.6 Pressure at the start of the model. 218
10.7 The pressure change with time. 219
10.8 Pressure change with time for longer fracture zones. 220
10.9 Pressure change at different depths with time for the conduit and fractures. 221

10.10Detail of the dome region showing the gas velocity, on a logarithmic scale, for the new vent and the top of the dome when the fractures have reached the surface (after 7000 seconds). 222
10.11Average velocity for the vent in the 2010 scar for the two different fracture lengths modelled. 223
10.12Displacement change for the shorter (top) and longer (bottom) length fractures. 224
10.13Displacement change images for the shorter length fractures. 225
10.14The hypothesis is the VT seismicity triggered the reactivation of shear fractures along the margin between the conduit and country rock. . . 226
10.15Suggested permeability relationships for the event at Soufrière Hills volcano in March 2012. 227
10.16Topographic map for Santa Maria volcano and Santiaguito. 228
10.17View of Santiaguito from Santa Maria volcano 229
10.18Audio, visible and seismic signals associated with an event as described by Johnson et al. (2009). 230
10.19Cross section through the 3D model geometry showing the separate regions. 233
10.20(a) Average permeability in the fracture zones with time for the seven events. (b) Detail for event 1 showing the duration and repose period. 234
10.21The initial pressure for the model prior to any vulcanian emissions. . 235
10.22Average pressure change for the five domains in the model. 235
10.23Pressure change at different depths within the conduit/plug (x = 0 m), fractures (x = 23 m) and edifice margin (x = 50 m) for events `E1` and `E4`. 236
10.24Pressure change at different times (s) for events `E1` and `E4`. 238
10.25Average surface gas velocity in the ring fractures and the interior dome in response to the seven ring-shaped degassing events. 239
10.26Gas velocity at different times (s) on a logarithmic scale for events `E1` and `E4`, showing the gas ring and the progressive gas velocity increase within the interior dome. 240
10.27After the development of the ring, the region of the dome emitting gas propagates inwards. 240
10.28Maximum and average dome surface displacement in response to 7 ring-shaped degassing events. 241
10.29Displacement change at different times (s) for events `E1` and `E4`. . . . 242
10.30The conduit permeability and the initial pressure before any vulcanian explosions. 243

10.31 Pressure change at different times (s) for events `E1` and `E4` for a gradient permeability in the conduit and deeper plug. 245
10.32 Pressure change at different times (s) for events `E1` and `E4` for a gradient permeability in the conduit and shallow plug. 246
10.33 Surface displacement change for the volcano flank with depth (z) for events `E1` and `E4` for two different plug extents. 247
10.34 For Figure 10.33, the surface displacement change is taken for a line along the surface of the flank. 248
10.35 Details of the processes hypothesised to occur to generate ring-shaped degassing at Santiaguito. 249
10.36 The suggested permeability relationships for the gas ring events at Santiaguito. 250

11 Discussion and Conclusions

11.1 An optimal degassing model incorporating the most important processes occurring inside volcanic systems. 262
11.2 An optimal half-conduit model, to be incorporated with Figure 11.1. . 263

A Analytical Solutions

A.1 Model setup for a one-dimensional homogeneous system. 285
A.2 Comparison between the analytical and numerical solutions for 3 different meshes. 285
A.3 Model setup showing a one-dimensional system with N layers. 286
A.4 The analytical and numerical pressure results for each model run. . . 288
A.5 Setup for two-dimensional circular flow. 289
A.6 Pressure along the circle with radius 90 m and the velocity at $y = 0$. . 290
A.7 Pressure along the circle with radius 90 m and gas velocity at $x = 0$ for Model **1** with 2 layers. 293
A.8 Pressure along the circle with radius 90 m and gas velocity at $x = 0$ for Model **2** with 5 layers. 293
A.9 Scenario modelling radial gas flow. 294
A.10 Pressure and gas velocity for the radial flow scenario, Model **2**. 296
A.11 Comparison between the analytical and numerical results for three different meshes. 297
A.12 Comparison between the analytical and numerical results for spherical model with three different meshes. 300
A.13 Pressure and gas velocity for the 3D radial flow model, Scenario **2**. . . 301

B The validity of Darcy's law

B.1 The Reynolds number for different gas velocities and pathway sizes. . 303
B.2 A comparison between Inertial and Darcian permeabilities for volcanic rocks. 304
B.3 A comparison between Darcy's law and the Forchheimer equation for different Darcian permeabilities and a gas density of 0.19 kg/m^3. . . . 306
B.4 A comparison between Darcy's law and the Forchheimer equation for different Darcian permeabilities and a gas density of 96.39 kg/m^3. . . 307

C Gas density and viscosity

C.1 Gas densities at different temperatures (°C) and pressures (MPa) according to the ideal gas law. 309
C.2 (a) The maximum overpressure at different constant temperatures for the six example models. (b) The change relative to a temperature of 0°C. 309
C.3 Temperature distribution with a conduit temperature of 850 °C decreasing to 200 °C at the overburden surface (1) or at all exterior boundaries (2). 310
C.4 The difference between the results for the Gradient 1 compared to a constant temperature. 311
C.5 The difference between the results for Gradient 2 compared to a constant temperature. 311
C.6 A comparison between the gas density as calculated by the ideal gas law and from steam tables. 312
C.7 The difference between the pressure when the density is calculated by the ideal gas law to that from steam tables with a temperature of 850 °C. 313
C.8 The velocity at different permeabilities and viscosities against the pressure gradient. 314

D De-coupling along the conduit-wall margin

D.1 The two models used to investigate de-coupling the conduit region from the surrounding wall-rocks. 317
D.2 The average pressure for each domain and the maximum surface displacement above the spine for the coupled and de-coupled scenarios. . 318

List of Tables

2 Method

2.1 Settings for the domain and boundaries for calculating gas flow and the resulting displacement. 36

2.2 A description of the most important solver settings provided by Comsol Multiphysics®. 43

3 The Conceptual Basic Model

3.1 Permeability conditions for the six example models shown in Figures 3.3 and 3.4. 49

3.2 Permeability (k) criteria for the six groups. 51

4 A Time-Dependent Example - "Dome Collapse"

4.1 Permeability and porosity conditions for the Unloading Model. 61

5 Gas Escape Through Fracture Zones

5.1 Permeability and porosity values for the gas escape through fracture zones model. 67

5.2 Permeability and porosity values for the brittle model with surface displacement. 81

6 Sealing the Volcano

6.1 Permeability and porosity conditions for the Sealing Gas Escape Routes Model. 90

7 Cracked Dome

7.1 Permeability and porosity values for the cracked dome model. 97

7.2 Permeability and porosity values for the crack widening models. . . . 105

8 Gas Storage and Release in 3D

8.1 Permeability values chosen for each domain in the model. 118
8.2 Explanation for the main points of interest in Figure 8.2. 120
8.3 Explanation for the main features of interest in the pressure change results relating to Figure 8.3 124
8.4 Explanation for points labelled in Figure 8.4 regarding the surface gas velocity at the start and end of each model. 128
8.5 Explanation for features shown in Figure 8.5 for the initial surface displacement and final displacement change. 130
8.6 Permeability criteria determining which model displays which displacement behaviour due to the FZ. 133

9 Further Model Variations of Gas Storage and Release in 3D

9.1 Permeability conditions for model **19**. 152
9.2 Quantification of the FZ sizes in the four models. 154
9.3 Permeability conditions for the models with each conduit permeability variation type. 170
9.4 Permeability criteria determining which model displays which displacement behaviour due to the FZ. 190

10 Case Studies

10.1 Permeability conditions for the ash-venting event at Soufrière Hills model. 218
10.2 Permeability and porosity values for the ring-shaped degassing model. 233

A Analytical Solutions

A.1 The thickness and permeability for the layers in each of the four models. 287
A.2 The number of mesh elements used and the gas velocity through the one-dimensional layered system. 287
A.3 The sector angle and permeability for the layers in the two circular models. 292
A.4 The number of elements in each mesh used in the two models for circular flow. 292
A.5 The inner (r_1) and outer (r_2) radii for each radial flow model. 296
A.6 The inner (r_1) and outer (r_2) radii for each spherical flow model. . . . 299

Chapter 1

Introduction

The total volume of gas in a magma, dissolved and subsequently exsolved, greatly influences the degree of explosiveness of a given volcano (e.g. Sparks, 2003a, Gonnermann and Manga, 2007). There are marked switches in behaviour of silicic volcanic systems between an open system where gas is free to escape, and a closed system in which the gas is confined. Consequently this results in changes in eruption style from generally effusive dome building type to explosive type (e.g. Eichelberger et al., 1986, Sparks, 2003a, Gonnermann and Manga, 2007, Cashman and Sparks, 2013). It is therefore essential to understand degassing to determine how gas may be stored and subsequently lost and where. Integral to this is the variation in permeability within the volcanic system and how this relates to the pressurisation (e.g. Eichelberger et al., 1986, Bernard et al., 2007, Bouvet de Maisonneuve et al., 2009).
As stated by Jaupart and Allègre (1991) the ability for a silicic volcanic system to degas is directly tied to the availability of degassing pathways and the existence of a driving pressure. Such conditions have been investigated by a number of studies, many of which have derived models incorporating Darcy's law, including the permeable foam model of Taylor et al. (1983) and Eichelberger et al. (1986), expanded further by the addition of horizontal degassing through the conduit walls (Jaupart and Allègre, 1991).

1.1 Degassing pathways

Degassing pathways have previously been investigated and researchers have identified the existence of a number of degassing routes. These include vertically through the conduit (e.g. Eichelberger et al., 1986) or along the conduit-wall margin (e.g. Tuffen et al., 2003), and horizontally through the conduit wall (e.g. Jaupart and Allègre, 1991). In addition, gas exits the volcano in different ways from violent plinian or vulcanian eruptions to high velocity fumaroles and less obvious diffuse

gas emissions.

1.1.1 Permeable foam model

Taylor et al. (1983) noted a marked depletion in volatile contents between pumices (3.1 wt.%) and lava obsidians (0.1 - 0.3 wt.%) in samples taken from various Western USA volcanoes. They hypothesised the reduced volatile content within the obsidian samples was a result of open-system degassing permitting the volatiles to freely exit the magma via degassing pathways. In contrast, the higher volatile contents evident within the pumice represented a more closed system behaviour where the gas is confined and unable to escape. Moreover, in the case of the pumice deposits from explosive eruptions, Taylor et al. (1983) suggested that the bulk of the degassing occurred during the eruption sequence itself, because they showed the magma erupted from the vent was successively depleted in volatiles. They further concluded this volatile loss must have occurred prior to ejection from the conduit and was therefore not a consequence of explosive fragmentation. Due to the limited time scales available for degassing to occur in this situation, they suggested the only viable mechanism was that the magma had developed the state of a permeable magmatic foam.

This permeable foam model was further expanded by Eichelberger et al. (1986) via an investigation of rocks from the Obsidian Dome (Inyo Dome Chain, California). They again found evidence for decreased volatile content in the lava flow deposits compared to the postulated content of the host magma, thereby supporting unhindered degassing on ascent. The calculated initial water content by Eichelberger et al. (1986) was partially based on the presence of the hydrous mineral hornblende and its stability conditions, suggesting an initial content of $2 - 3$ wt.% decreasing to around 0.1 wt.% upon extrusion. They postulated the degassing process began with exsolution of volatiles, forming bubbles. Sufficient volumes of these interacting bubbles would generate permeability and permit volatile transfer and thus allow a large gas loss. Eichelberger et al. (1986) further suggest that once gas flow is achieved, volatiles may be lost through fracturing and a tephra-filled funnel structure which, in the case of the Obsidian Dome, is believed to extend from 500 m depth, and thought to have been created during the initial explosive phase of an eruption. Eichelberger et al. (1986) determined that if this tephra-filled funnel was generated during an explosive eruption, this would create the required high permeability to permit later effusive lava emission. However, they also state that given enough time, this permeable tephra would solidify, thus reverting back to a more "closed" system behaviour, therefore triggering more violent activity to resume. Eichelberger et al. (1986) suggests a magma may become a foam when the volume of gas present reaches 60 %,

whilst $70 - 75$ % is normally attributed to magma fragmentation (Woods, 1995). Eichelberger et al. (1986) used Darcy's law to model the gas loss through this permeable foam and showed that if degassing occurs freely within the system, the magma expansion seen in explosive deposits cannot be attained.
Friedman (1989) believes the initial water content for Obsidian Dome was no greater than 0.3 wt.% rather than the $2 - 3$ wt.% quoted by Eichelberger et al. (1986). Friedman (1989) suggests the evidence supporting a more hydrous melt is actually a consequence of melt contamination through interaction with groundwater. A further objection made by Friedman (1989) is that no textural evidence has been found supporting the permeable foam model. This has been countered by Westrich and Eichelberger (1994) whose laboratory experiments clarify that no field evidence remains of the permeable foam hypothesis due to the lithostatic pressure overbearing the bubble internal pressure, leading to bubble collapse. However, Stasiuk et al. (1996) have since found possible permeable foam structures in their examination of Mule Creek (New Mexico). Thirdly, the main objection of Friedman (1989) is that degassing acts to increase the magma viscosity, thus the degree of gas loss proposed would increase the viscosity thereby seriously affecting eruption behaviour and consequently result in the permeable foam erupting as a spine.
Fink et al. (1992) suggest an alternative to the permeable foam model, whereby degassing occurs in three stages: initially, degassing within the magma chamber as a closed system, where exsolution and bubble growth occurs; secondly, degassing on ascent, although there is some doubt as to the mechanism; and thirdly movement away from the vent promoting vesiculation resulting in further degassing post eruption. The main point of contention between the two models is in the permeable foam model, Westrich and Eichelberger (1994) believe the extruded magma is significantly degassed prior to eruption, whilst the model of Fink et al. (1992) suggests further degassing occurs after magma extrusion, suggesting there is insufficient time during the eruption for full degassing to occur. However, the velocity of magma decreases next to the wall rocks, potentially providing a mechanism, within the time frame, for degassing to occur (Rust et al., 2004).
Currently, there is no conclusive evidence to discount either theory, and it may be possible for both to be applicable, but under different circumstances.

1.1.2 Degassing through the conduit walls

Jaupart and Allègre (1991) developed the ideas for the permeable foam model and added that gas may be lost laterally through permeable conduit walls. They proposed the permeable foam may move the gas from the centre of the conduit towards the walls allowing escape through the country rock. The volume of gas lost to the

country rock is thought to be a function of chamber and wall rock pressure. Decreasing eruption rate with time reduces the pressure and correspondingly increases the volume of gas which may be lost. However, silicic volcanic eruptions commonly begin a phase of activity with explosive behaviour, later becoming effusive. Jaupart and Allègre (1991) disagree with the assumption made in the model of Eichelberger et al. (1986) that a horizontal driving pressure of 10 MPa is required to move the gas to the conduit walls.

For degassing through the conduit walls to occur, a viable pathway must exist. Heiken et al. (1988) drilled into the conduit of the Obsidian Dome and encountered near horizontal fractures infilled with pyroclastic material (tuffisite veins) juxtaposed with the conduit and rhyolitic dykes. These tuffisite veins have been encountered elsewhere, including Soufrière Hills (Montserrat) and Lascar (Chile) volcanoes (Sparks, 1997). The generation of these fractures has been attributed to hydrofracturing resulting from high fluid pressures (Heiken et al., 1988, Sparks, 1997). The presence of radial dykes originating from the Inyo Dome volcanic conduit suggest a higher magmatic pressure and thus providing the required driving pressure to force gas from the system (Heiken et al., 1988).

Further evidence for degassing through the conduit walls comes from Mule Creek (New Mexico), a 20-21 Ma fossilised volcanic vent exposed in a 300-350 m high field outcrop (Stasiuk et al., 1996, Ratté, 2004). This volcanic system is believed to have extruded magma of silicic-intermediate composition and provides unhindered observations of inside the shallow conduit and dome. Field evidence has suggested an initial explosive phase (depositing rhyolitic pumice), followed later by more effusive dome building activity, analogous with the 1980 Mount St. Helens (USA) eruption (Stasiuk et al., 1996). The water content of the magma prior to eruption has been estimated from melt inclusions at a minimum of $2.5 - 3$ wt.%. However, there is evidence for variable gas loss within the upper vent, with a higher concentration of vesicles ($20 - 40$ vol.%) decreasing to 0 vol.% at the vent margins. In addition, an increase in vesiculation with decreasing depth is also visible, with 20 vol.% at 300 m rising to 40 vol.% at 200 m depth below the rim, which may be accounted for by bubble growth through decompression and coalescence (Stasiuk et al., 1996). The decrease in bubble content outwards from the centre of the vent has been suggested as proof of open system degassing with volatile loss being most efficient at the conduit walls (Stasiuk et al., 1996). This could be vertically along the margin between the magma conduit and the wall-rocks, or laterally through the walls themselves. Stasiuk et al. (1996) suggested degassing was efficient in this region due to a slow ascent rate coupled with friction-induced shearing resulting in elongated, overlapping pores, that enhance the permeability and thus generate degassing path-

ways. Stasiuk et al. (1996) have also found evidence for areas exhibiting a permeable foam-like appearance, thus potentially supporting the hypothetical permeable foam model of Taylor et al. (1983). However, there is some disagreement whereby the model predicted 60% porosity for permeability to be sufficient for degassing, whilst field evidence suggests the shearing-induced permeability may enhance gas flow and therefore reduce the required porosity (Stasiuk et al., 1996).

Throughout the contact between the conduit and country rock there are a number of tuffisite veins running approximately perpendicular to the conduit, similar to those found by Heiken et al. (1988). Stasiuk et al. (1996) believe these were formed during the actual eruption and may represent a lateral degassing route. There are also a number of potentially syn-eruptive microbreccia-filled veins, breccia pipes and rhyolitic dykes, all of which are believed to represent degassing routes during magma ascent (Stasiuk et al., 1996, Ratté, 2004). By comparing the estimated pre-eruptive volatile contents with field measurements, Stasiuk et al. (1996) have suggested more than 50 % degassing occurred at depths greater than 350 m, although this cannot be corroborated as there is no known field exposure of this depth (Stasiuk et al., 1996, Ratté, 2004).

Tuffisite veins have been found to be common features in a wide range of volcanic environments from basaltic to rhyolitic composition (Tuffen et al., 2003, Noguchi et al., 2008). Tuffisites are ash-filled fractures which may increase both the permeability and porosity of the volcanic edifice in which they are found (Castro et al., 2012, Kolzenburg et al., 2012). The effect of tuffisite veins on permeability is only evident down to approximately 2 km depth, below which the increasing pressure may result in compaction and sealing of the degassing pathways (Kolzenburg et al., 2012). Tuffen et al. (2003) proposed that the tuffisite veins in the rhyolitic conduit of the Torfajökull volcano (Iceland) may represent repeated episodes of magma fracturing and healing. Additionally, they suggest this magma fracturing may be a viable mechanism for the generation of hybrid and long-period earthquakes. This is supported by Neuberg et al. (2006) who show that a non-destructive, repetitive and stationary source is required to explain the low-frequency seismicity at Soufrière Hills volcano (Montserrat). Consequently Neuberg et al. (2006) believe this source is brittle failure located at the point at which the magma changes from a ductile to a brittle state.

1.1.3 Surface gas emissions

Other than during explosive eruptions, there are two main types of surface gas emission: fumarolic and diffuse. Fumaroles are the most studied form of surface gas loss from volcanoes (Berlo et al., 2013), and represent focussed degassing through regions

of high permeability, such as cracks. These cracks are formed due to mechanisms such as cooling and contraction of the dome structure, fluid pressure, weakened regions, shear zones and local tectonics (e.g. Heiken et al., 1988, Sparks, 1997, Giammanco et al., 1998, Edmonds et al., 2003a, Sparks, 2003a). Gas emissions at summit fumaroles are dominated by volatile species such as H_2O, CO_2, SO_2 and HCl (Delmelle and Stix, 2000, Williams-Jones et al., 2000). Fluctuating gas emissions from fumaroles can be important indicators for the state of the volcanic interior. For example, decreased SO_2 emissions have been noted prior to lava extrusion and explosive events at Soufrière Hills volcano (Edmonds et al., 2003b). Such decreases in SO_2 are attributed to sealing of the upper conduit and dome (Edmonds et al., 2003b).

Diffuse emissions represent the gas lost from the volcano flanks. These emissions are often overlooked in preference of the more prominent emissions of the dome and surrounding summit. However, the presence of such emissions provides supporting evidence for gas loss through the conduit walls into the surrounding edifice or country rock. Diffuse emissions tend to be dominated by volatile species such as CO_2, He and Rn (Delmelle and Stix, 2000, Williams-Jones et al., 2000). Significant studies have been performed in an attempt to determine the nature of CO_2 emissions from Mt Etna, Sicily (e.g. Allard et al., 1991, Giammanco et al., 1998, Bonforte et al., 2013). They found the volume of gas emitted from the flanks of Mt Etna was similar to the volume of gas emitted from the main crater plume. Additionally, due to the gas chemistry, they determined that the source of this diffuse flank degassing was magmatic. Many of the anomalously high concentrations of CO_2 measured within the soil of the volcano's flanks were located over fracture zones (Allard et al., 1991). This is corroborated by data from Giammanco et al. (1998) which shows that whilst the majority of faults on Mt Etna diffusively emit anomalously high volumes of CO_2, only around half of eruptive fissures show this elevated CO_2. Giammanco et al. (1998) suggested this is because faults and fractures are created tectonically and may be sites of higher permeability, which provide a degassing route for volatiles exsolved deeper within the system, whilst eruptive fissures may become sealed over time due to crystallising magma.

Similarly, Williams-Jones et al. (2000) have investigated diffuse degassing on the Arenal, Poás (Costa Rica) and Galeras (Colombia) volcanoes. They discovered different volatiles were predominantly emitted from the volcanic vents (SO_2, HCl, CO_2 and H_2O) compared to the diffuse flank emissions (He, Rn and CO_2). Williams-Jones et al. (2000) also comment that the state of the soil on the flanks plays an important role in allowing gas to escape. If the soil is well-developed with large quantities of clays and organic-rich material (usually common near the base of the

volcanic edifice), this permits better storage of volatiles potentially leading to sealing. Contrastingly, soil located at higher levels on the volcano tended to consist of unconsolidated pyroclastic material, providing good drainage and permitting moisture to escape leading to dry material that provides an unrestricted path for escaping gases (Williams-Jones et al., 2000). However, this simplistic view may be complicated by the observation that the upper flanks are more likely impermeable to gas loss due to the deposition of young lavas, whilst lower down the flanks, gases may take advantage of the prevalence of faults and fractures (Williams-Jones et al., 2000). Williams-Jones et al. (2000) suggest diffuse flank degassing is strongly controlled by the presence of faults and fractures, the hydrothermal system, soil quality, the age of lava deposits and the regional tectonic structure. Heiligmann et al. (1997) observed increases in soil diffuse flank degassing on Galeras prior to the onset of tornillos (a type of long-period seismic signal) and suggest the concentration of diffuse flank degassing may be used as an indicator for the pressurisation of the system.

1.1.4 Sealing degassing pathways

The permeability of a system may be hampered by a variety of processes, for example gas loss, foam collapse, melt crystallisation, deposition of hydrothermal minerals and subsidence (which may be a consequence of degassing) resulting in the closure of fractures (e.g. Sparks and Pinkerton, 1978, Matthews et al., 1997, Cashman and Blundy, 2000). In response to an andesitic melt being supersaturated with water and other volatiles, it begins to crystallise. As water exsolves from the melt it raises the temperature required for the magma to remain liquid (liquidus temperature) and induces the crystallisation of mineral phases such as hornblende, plagioclase, magnetite and pyroxene (Cashman and Blundy, 2000). The deposition of minerals resulting in sealing is temperature and pressure dependent. For example, decreased temperatures trigger the deposition of sulphur which aids the sealing process at shallow levels (Harris et al., 2012). The transfer of volatiles through degassing pathways such as fractures is also thought to aid the sealing process due to the redistribution of silica and the formation of silica polymorphs such as cristobalite (Horwell et al., 2013). Horwell et al. (2013) suggest as little at 5−10 wt.% cristobalite has the potential to reduce the permeability by a factor of 2 to 10 within the dome. Cristobalite in volcanic environments can contribute up to 15 wt.% within the pore spaces, fractures and groundmass (Murphy et al., 2000, Horwell et al., 2013). Baxter et al. (1999) has suggested two mechanisms for the formation of cristobalite in volcanic systems: devitrification of the groundmass glass (crystallisation of glass during slow cooling), and vapour-phase crystallisation (elements carried in solution within the vapour phase, which crystallise during cooling) (Baxter et al., 1999).

Sparks (1997) presents results from models for two different mechanisms for degassing induced pressurisation in the upper parts of volcanic systems. The first, is magma viscosity which may be dramatically increased due to degassing and crystallisation (Sparks, 1997). For example a degassed dacitic magma can have a viscosity seven orders of magnitude greater than the same containing 5 wt.% H_2O (Sparks, 1997). Due to the greater resistance to flow, this increase in viscosity leads to pressurisation, which may force gas into the low pressure environment of the surrounding wall-rocks (Sparks, 1997). The second mechanism is microlite crystallisation. As suggested by Sparks and Pinkerton (1978), the process of magma ascending and degassing results in under-cooling of the melt, thus triggering the production of microlites, particularly at the conduit walls, due to the lower temperature. This is thought to be especially effective at depths of less than 2 km representing the upper parts of most volcanic conduits (Sparks, 1997). Under-cooling is essential before microlite crystallisation can occur (Sparks and Pinkerton, 1978, Sparks, 1997). This can lead to a rapid change in permeability - a high permeability due to volatile exsolution is countered by a corresponding decrease in permeability due to microlite crystallisation (Sparks, 1997). Consequently, the associated increase in microlite content may convert a volcanic system to closed behaviour, but with continual exsolution, thus triggering pressurisation and potentially causing increased dome growth or explosive activity (Sparks, 1997). This view is supported by observations made on Lascar volcano, in which a dome building phase switched to explosive behaviour shortly after the flux of gas through fumaroles decreased (Matthews et al., 1997). Observations at Lascar volcano suggest cyclic behaviour, with a dome building phase followed by fracture closure due to dome subsidence and decreased degassing. This allows pressurisation which is subsequently released during an explosive eruption, reopening degassing pathways and triggering a return to the effusive, dome building state and the commencement of a new cycle (Matthews et al., 1997).

In March 2004, a vulcanian explosive event occurred on Soufrière Hills volcano during a period when there was no active magma extrusion (Green and Neuberg, 2005, Linde et al., 2010). This event generated an eruption column which reached approximately 6 km into the atmosphere. It has been suggested that such a high eruption column and other similar gas expulsions post-dome collapse and during eruptions, are evidence for gas storage at shallow depths (approximately 300 m) within the volcanic edifice (Edmonds et al., 2003b, Green and Neuberg, 2005, Herd et al., 2005, Jousset et al., 2013).

Sealing the system by decreasing the permeability within certain regions will induce the gas to switch between degassing pathways. When one degassing pathway is sealed, an alternative, if it exists, will be sought (Harris et al., 2012).

1.2 Physical Properties

1.2.1 Darcian permeability and porosity measurements

A significant requirement for this field of research is the ability to adequately describe the variables involved, one of the most important of which, being the permeability. Currently, there are no real time measurements for permeabilities inside the active conduit and immediate surroundings. However, there are numerous examples of permeability and porosity measurements for quenched post-eruptive and synthetic materials (Figure 1.1). The majority of measurements for volcanic rocks have yielded permeabilities within the range of 10^{-16} to 10^{-10} m^2. Data provided by Eichelberger et al. (1986) show a trend of increasing permeability with increasing porosity. However, Figure 1.2 shows that even for the same volcano, a wide variety

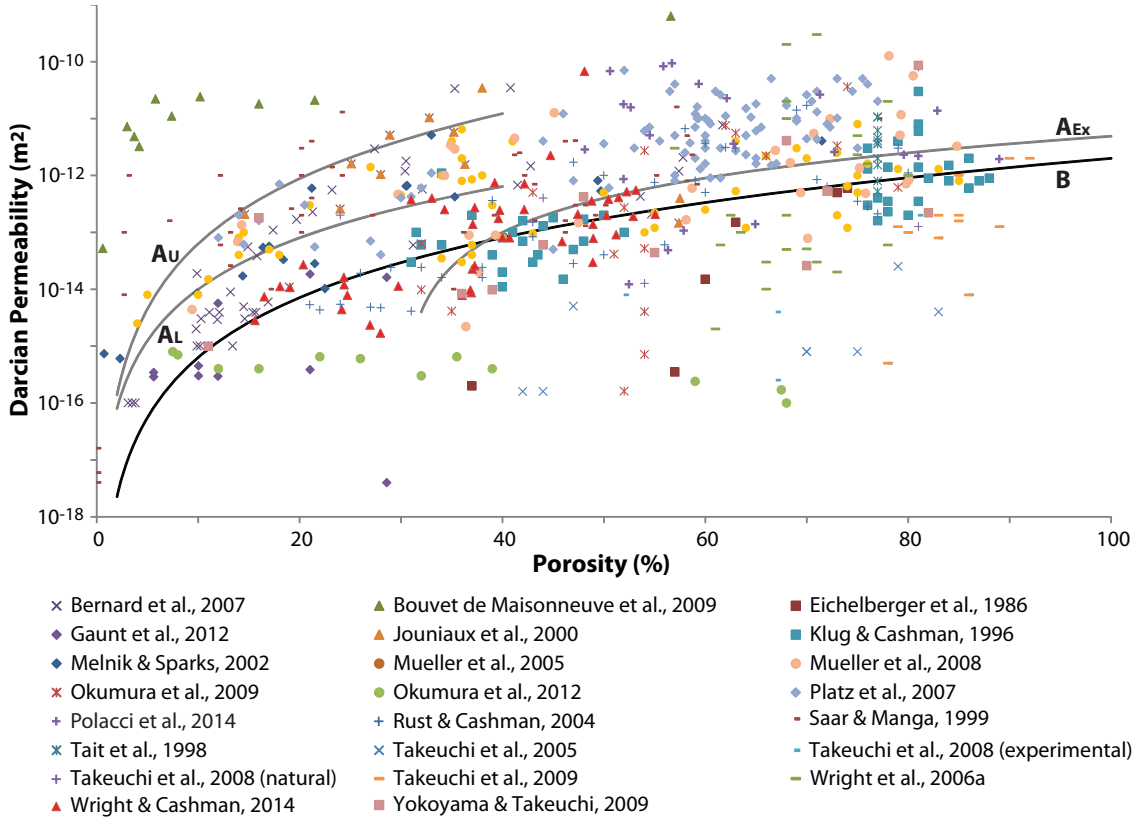

Figure 1.1: Compilation of published Darcian permeabilities and porosities for a variety of volcanic rocks. The plot shows there is not a simple relationship between permeability and porosity. The lines represent example empirical formulae describing the relationship between permeability and porosity as derived by Mueller et al. (2005) for $\mathbf{A_U}$ and $\mathbf{A_L}$ the upper and lower limits for effusive rocks, respectively, and $\mathbf{A_{ex}}$ for explosive rocks; and Klug and Cashman (1996) (**B**). None of these formulae completely fit all the data. The data are subdivided according to volcano in Figure 1.2.

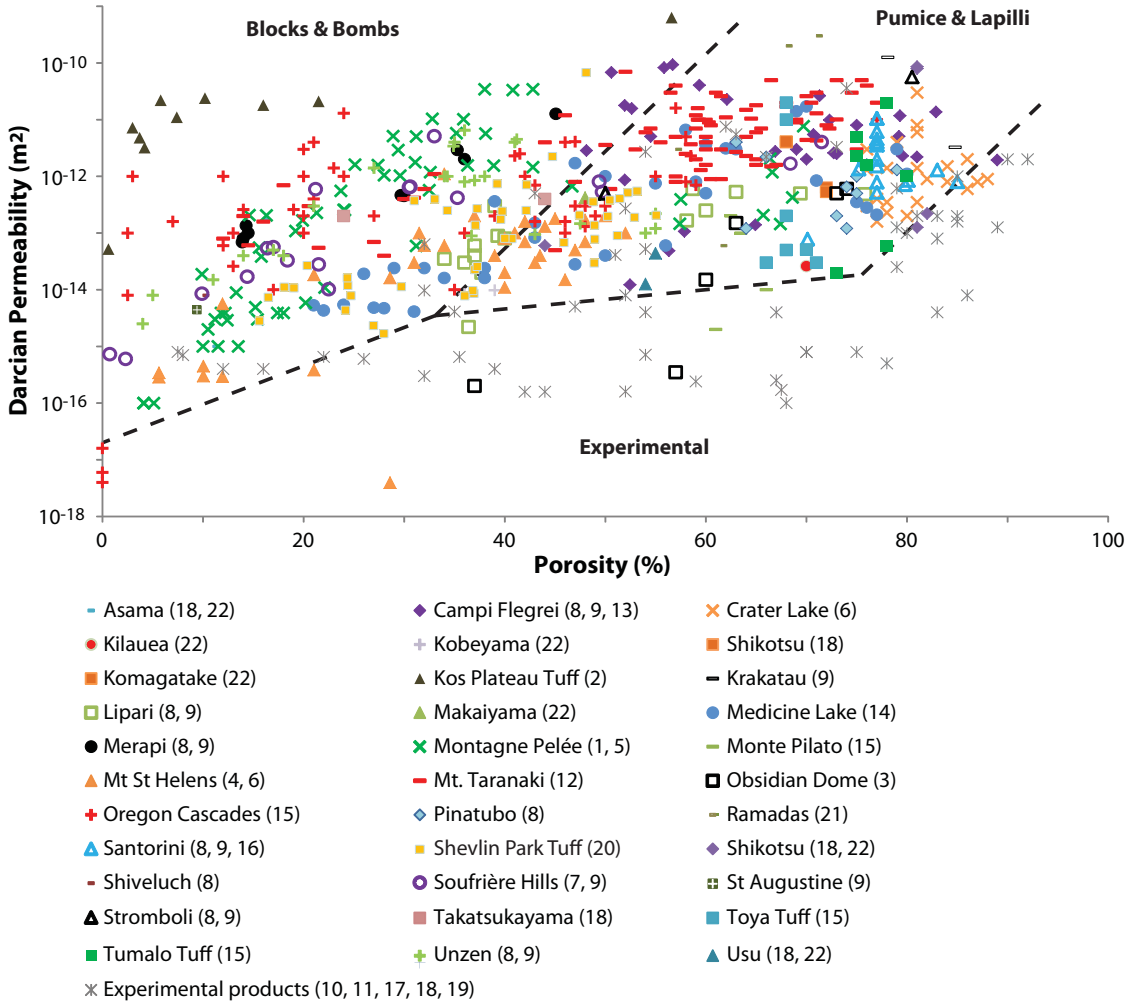

Figure 1.2: Darcian permeabilities and porosities measured for volcanic and experimental materials ordered according to volcano. The graph has been loosely subdivided into three regions representing measurements for blocks and bombs, pumice and lapilli, and experimental products. The data sources for each volcano are indicated: (1) Bernard et al. (2007), (2) Bouvet de Maisonneuve et al. (2009), (3) Eichelberger et al. (1986), (4) Gaunt et al. (2012), (5) Jouniaux et al. (2000), (6) Klug and Cashman (1996), (7) Melnik and Sparks (2002), (8) Mueller et al. (2005), (9) Mueller et al. (2008), (10) Okumura et al. (2009), (11) Okumura et al. (2012), (12) Platz et al. (2007), (13) Polacci et al. (2014), (14) Rust and Cashman (2004), (15) Saar and Manga (1999), (16) Tait et al. (1998), (17) Takeuchi et al. (2005), (18) Takeuchi et al. (2008), (19) Takeuchi et al. (2009), (20) Wright and Cashman (2013), (21) Wright et al. (2006a), (22) Yokoyama and Takeuchi (2009).

of permeabilities are possible for the same porosity. It is generally accepted that degassed obsidian type rocks form in an open system and have a very low permeability, whilst the very high permeability of pumice samples is thought to be formed by rapid ejection from a closed system. The question is how useful is either rock formation for determining the permeability inside the volcano? Obsidian has a low

permeability on formation because all the gas has escaped, suggesting a viable degassing pathway (permeability) must have existed. However, its low permeability on formation would have resulted in sealing, if it formed inside the system. Similarly, pumice has a very high permeability because gas has continued to exsolve in a region of the volcano devoid of efficient degassing pathways. Continued expansion of the bubbles, and consequently the magma, led to fragmentation and explosive eruption.

Many studies have measured the permeability in different orientations within samples and discovered strong anisotropy (e.g. Tait et al., 1998, Wright et al., 2006a, 2009, Bernard et al., 2007, Bouvet de Maisonneuve et al., 2009, Wright and Cashman, 2013). In the case of Bernard et al. (2007), the orientation of the sample produced permeability variations between 28 and 162 %, relative to its mean permeability. Permeability measurements from Mount St Helens have identified five distinct layers within the structure of extruded dome spines which have been classified, from outer to inner, as fault gouge, cataclastic breccia, sheared dacite, flow-banded dacite and massive dacite (Gaunt et al., 2011, 2012). Gaunt et al. (2012) discovered a strong anisotropy within the outer fault gouge where the permeability parallel to spine extrusion was two orders of magnitude greater than that perpendicular. Furthermore, they showed that between December 2004 and December 2005, the permeability of the Mount St Helens dome decreased by approximately two orders of magnitude.

Attempts have been made to apply an empirical power-law relationship between the permeability (k) and porosity (ϕ) (Klug and Cashman, 1996, Rust and Cashman, 2004, Mueller et al., 2005). For example, Equation 1.1,

$$k = c\phi^n \tag{1.1}$$

where c is a constant of proportionality and n is between $3.0 - 3.8$ (Daines, 2000, Mueller et al., 2005). Klug and Cashman (1996) found their data to lie between two curves defined by $n = 3.5$ with $c = 10^{-18}$ (upper) and $c = 4 \times 10^{-20}$ (lower). They also define a mean curve for their data as $c = 2 \times 10^{-19}$ m^2. In contrast, the data for the effusive products of Mueller et al. (2005) is bounded by curves with $c = 1 \times 10^{-17}$ for $n = 3.8$ (upper) and $n = 3$ (lower).

However, Mueller et al. (2005) find their data for explosive products is best described using the percolation theory using equation 1.2 for the porosity ϕ, critical porosity (percolation threshold) $\phi_{cr} = 30$, $\beta = 2$ and empirical constant, $\chi = 1 \times 10^{-16}$ and $\chi = 8 \times 10^{-15}$ for the upper and lower bounds respectively.

$$k = \chi(\phi - \phi_{cr})^\beta \tag{1.2}$$

The percolation theory states that a certain porosity is required before connected

pores span across the entire sample and the sample attains permeability (Sahimi, 1994). The standard theory is based around the randomised placement of equally sized spheres within a sample and according to Sahimi (1994), a porosity of 28.5 % would be required for such a sample to attain permeability. Following this, many magma permeability studies have similarly used a critical porosity value of 30% for both basaltic and silicic magmas (e.g. Candela, 1991, Saar and Manga, 1999, Mueller et al., 2005, Giachetti and Gonnerman, 2013). Whilst the effects of bubble elongation (e.g. Garboczi et al., 1995) and magma crystallisation (e.g Walsh and Saar, 2008) may act to reduce the critical porosity required, it has been suggested that increasing the magma viscosity would require an increased critical porosity (Cashman and Sparks, 2013). Decompression experiments (e.g. Takeuchi et al., 2005, 2008, 2009) have deduced a value of at least 65% porosity is required. This is further corroborated by measurements of silicic pumice which often have porosities exceeding 70 % (e.g Klug and Cashman, 1996, Mueller et al., 2005, Wright et al., 2009). Consequently, Rust and Cashman (2011) suggest a porosity of at least 70 % is required before permeability is attained. However, magma fragmentation is believed to occur at around 70 %, so these samples may be recording this state rather than the point at which permeability is attained. The presence of pumice suggests that volatile exsolution has occurred but the gas has not been permitted to escape due to some region of impermeability within the system. As noted by Rust and Cashman (2011), the discrepancy between the standard percolation theory and measurements of volcanic samples shows that the theory is insufficient in accounting for all the factors affecting the porosity and permeability relationship in volcanic systems. Such factors include magma ascent rate, melt viscosity, crystallisation and shear stresses (Rust and Cashman, 2011).

As the measurements have shown (Figures 1.1 and 1.2), the relationship between permeability and porosity is not simple. Wright et al. (2009) conclude the complex relationship between the permeability and porosity reflects differences in composition and eruption style. Furthermore, sample sizes are small (e.g. 23 - 50 mm cores (Jouniaux et al., 2000, Rust and Cashman, 2004, Platz et al., 2007, Wright et al., 2009, Gaunt et al., 2012)) and isolated, post eruptive samples with often no context as to where they were situated within the system prior to eruption, nor what changes they may have undergone syn- and post-eruption, particularly if the samples were erupted explosively. Furthermore, alterations to the samples may occur between extrusion and collection. For example, Vallance et al. (2008) show significant alteration to the outer gouge surface of a spine extruded from Mount St. Helens. The sample sizes are finite and so provide limited information as to the spatial variation in the permeability and porosity.

The permeability within the volcanic conduit depends on factors such as bubble size and shape, bubble connectivity, magma crystallisation and magma ascent rate. Bubble elongation, due to friction-induced shear at the conduit margins and due to the magma flow, may result in an increase in permeability, particularly in the elongation direction (e.g. Blower, 2001, Okumura et al., 2009, 2013). Okumura et al. (2009) has quantified the shear effects on permeability by calculating that for flowing rhyolitic magma with a water content of 5 wt.%, shear-induced deformation at the conduit-wall margin would generate a permeability greater than 10^{-12} m^2 at depths of several kilometres. Bouvet de Maisonneuve et al. (2009) have presented contrasting styles of elongated porosity development dependent on conditions within the conduit. They show that simple shear, resulting from an ascent rate increase towards the centre of the conduit, results in elongate pores at the conduit margins. In contrast, pure shear, resulting from increasing ascent rate due to the effects of gas bubble expansion, would lead to increasing elongation with decreasing depth and towards the conduit centre (Bouvet de Maisonneuve et al., 2009). These are very different scenarios, dramatically altering the permeability-porosity relationship at the same location within the conduit. It is likely that both simple and pure shear occur within the same volcanic system thus increasing the complexity (Bouvet de Maisonneuve et al., 2009). Contrastingly, when magma ascends slowly and therefore no shear develops, even with high porosity, the permeability may be significantly lower (Sparks, 2003a, Okumura et al., 2012). However, it has been suggested by Llewellin (2007) that the expansion of vesiculating magma coupled with bubble growth may decrease the distance between neighbouring bubbles. This could potentially allow the bubbles to connect and greatly enhance permeability, particularly perpendicular to the magma flow direction - the direction of minimum extension. However, this theory would rely on the bubbles retaining their sphericity implying that little or no shear effects from magma motion would be involved. As the pressure and temperature change, melt begins to crystallise. This is triggered by volatile exsolution and such crystallisation increases the permeability in specific regions, by decreasing the volume of melt in which bubbles may form and move (Blower, 2001, Sparks, 2003a, Clarke et al., 2007, Lensky et al., 2008), provided the crystallinity is sufficiently high (Okumura et al., 2012). However, this is countered by the model of Massol and Jaupart (2009) which shows increased microlite crystallisation increases the magma viscosity, inhibiting bubble growth.

Permeabilities from Geochemistry

Geochemistry can reveal important insights into the gas storage, gas transport and permeability conditions at depth. In particular the proportions of ^{226}Ra and ^{210}Pb in

volcanic products may be measured. ^{226}Ra has a half-life ($t_{\frac{1}{2}}$) of 1599 years, and decays to create ^{222}Rn ($t_{\frac{1}{2}}$ = 3.8 days), which in turn decays to ^{210}Pb ($t_{\frac{1}{2}}$ = 22.6 days) (Berlo et al., 2006, Kayzar et al., 2009). However, ^{222}Rn separates from the melt into the gas phase when the dominant volcanic volatiles (including H_2O) exsolve (Berlo et al., 2006). Consequently, due to the mobilisation of ^{222}Rn with volatiles and its short half-life, the remaining proportions of ^{226}Ra and ^{210}Pb can be used to infer the gas storage/transport conditions. If there is an excess of ^{226}Ra over ^{210}Pb, this suggests gas loss because the ^{222}Rn which creates ^{210}Pb has been lost. In contrast, if there is an excess of ^{210}Pb over ^{226}Ra, this implies gas storage because the ^{222}Rn (along with the gas) has been trapped, or its velocity slowed significantly (Berlo et al., 2006). Consequently, the ratio between these two isotopes can be used to infer the average permeability conditions using Darcy's law by determining the permeability required to allow the gas and ^{222}Rn to escape in less than 3.8 days (Berlo et al., 2006). Berlo et al. (2006) used this calculation on eruption products during the 1980-1986 eruption of Mount St Helens, a period with an excess of ^{226}Ra, to estimate a magma permeability of 10^{-15} - 10^{-10} m^2 is required for the rapid gas loss, dependent upon the distance from source to surface. Similarly, Kayzar et al. (2009) measured the ratio of ^{226}Ra to ^{210}Pb and hypothesised the excess of ^{210}Pb implied a permeable body of volatile-rich melt at depth under Mt. Pinatubo. However, they admit there is no physical evidence for the existence of this.

1.2.2 Rock mechanics and the failure criterion

Rheology describes the manner in which a material deforms in response to an imposed stress, and is controlled by the magma viscosity (Cashman and Sparks, 2013). In turn, this is dependent upon the magma composition, temperature, crystallisation and exsolution (Sparks, 1997, Cashman and Blundy, 2000, Cashman and Sparks, 2013, de' Michieli Vitturi et al., 2010, Schneider et al., 2012). Viscosity increases with crystallisation (Spera, 2000, Cashman and Sparks, 2013), but decreases with temperature (Spera, 2000, Llewellin et al., 2002). The effect of exsolution is dependent upon the nature of the bubbles - small bubbles at low strain rates increases the viscosity, whilst large bubbles at higher strain rates decreases the viscosity of the magma (Llewellin and Manga, 2005, Cashman and Sparks, 2013). In volcanic systems, the viscosity of magma can cover an extremely wide range from 10^0 to 10^{14} Pas (Sparks, 2003b, Cashman and Sparks, 2013), which can result in strong heterogeneity within the volcano.

Deformation behaviour may be described as Newtonian (e.g. water, silicate melts), pseudoplastic (e.g. ice), dilatant (e.g. wet sand) or Bingham (e.g. toothpaste) (Mader et al., 2013). A pure silicate melt will display Newtonian behaviour, but

under high strain rates, this behaviour will become non-Newtonian (Dingwell, 1998). Lavallée et al. (2007) suggests this transition occurs at yield stresses of a few kPa and crystallinity in excess of 30%.

There are three modes of stress: shear, tension and compression. At high strain rates, in response to an imposed shear or tension, materials will deform in a brittle, rather than ductile manner (e.g. Gonnermann and Manga, 2007). However, failure of rocks generally occurs by tension due to the lower tensile strength (Benson et al., 2012). The tensile strength of volcanic rocks has been estimated as up to 10 MPa (e.g. Alidibirov and Dingwell, 1996, Sparks, 1997, Voight et al., 1999, Hale, 2008, Massol and Jaupart, 2009).

In order for failure to occur, the exerted stress must exceed the yield strength of the magma and the wall-rocks (Melnik and Sparks, 1999). Melnik and Sparks (2002) suggest if large overpressures develop at shallow depths within the conduit (up to a few hundred metres depth), this may exceed the tensile strength of the magma resulting in a switch in eruption style between effusive and explosive. The strength of rock varies greatly with depth, such that overpressures up to 20 MPa may be possible within the chamber, but overpressures of only 5 MPa could exceed the yield strength closer to the surface (Sparks, 1997).

Rock failure does not necessarily culminate in an explosive eruption. Evidence for non-explosive brittle failure comes from the presence of tuffisites (Tuffen et al., 2003, Noguchi et al., 2008, Castro et al., 2012, Kolzenburg et al., 2012) (Section 1.1.2), and shear fractures up the conduit-wall margin (Tuffen et al., 2003, Bluth and Rose, 2004, Neuberg et al., 2006, Holland et al., 2011, Pallister et al., 2013) (Section 1.3.3).

1.2.3 Volatile contents of magmas

The most common volatiles in magma are H_2O, CO_2, S-species, Cl and F (e.g. Wallace, 2001). The original volatile contents of a magma may be approximated through petrological and geochemical studies of the eruption products (e.g. Taylor et al., 1983, Cashman and Blundy, 2000, Savov et al., 2008). For example, by the analysis of rhyolitic glass inclusions within erupted andesite, the H_2O content of the Soufrière Hills magma, prior to eruption, has been estimated at $4-5$ wt.% at $5-6$ km depth (Barclay et al., 1998). The point at which gas begins to exsolve from a silicic magma is strongly controlled by the pressure of the system and may be approximated by Henry's solubility laws: Equation 1.3 (for H_2O) and Equation 1.4 (for CO_2) where the pressure, P, is in MPa and n in wt.% of dissolved gas (Burnham, 1975, Sparks, 1978, Lensky et al., 2008, Parfitt and Wilson, 2008).

$$n = 0.4111\sqrt{P} \tag{1.3}$$

$$n = 0.0023P \tag{1.4}$$

An alternative method for calculating the solubility, which also considers the temperature, is VolatileCalc (Newman and Lowenstern, 2002). Figure 1.3 compares the solubility of H_2O as calculated by Henry's law (Equation 1.3) to that derived from VolatileCalc . The solubility of H_2O in rhyolite increases with pressure and decreases with temperature. At pressures of < 50 MPa of the three temperatures plotted, the solubility calculated with Henry's law has the best agreement with VolatileCalc with a temperature of 700 °C. However, at higher pressures, the solubility as calculated by the two methods deviates significantly, with Henry's law predicting a markedly lower solubility than VolatileCalc . Furthermore, neither of these methods account for the interactions occurring with the presence of multiple volatile phases.

A multi-volatile system is very complex and the point at which particular volatiles exsolve is dependent upon their solubility with respect to pressure, temperature, magma composition and the exsolved vapour phase composition (e.g. Papale, 1999, Newman and Lowenstern, 2002, Liu et al., 2005). For example, CO_2 being less soluble than H_2O begins to exsolve at higher pressures deeper within the system (Holloway, 1976, Newman et al., 1988, Dixon et al., 1995, Newman and Lowenstern, 2002). Multi-volatile systems are more complex because the presence of additional volatiles affects the solubility of H_2O. For example, Papale (1999) showed that the presence of CO_2, even in small quantities, results in an increase in the saturation pressure. Therefore H_2O will begin to exsolve at greater depths than if CO_2 was absent. Holloway (1976) showed the solubility of CO_2 increases with H_2O content, but decreases with the addition of other volatiles such as CH_4 or CO. Furthermore, as the least soluble volatile phase begins to exsolve to form bubbles, it forces other volatile phases to diffuse into these bubbles (Holloway, 1976). This occurs even if the saturation point for these other phases has not been reached (Holloway, 1976).

1.3 Volcanic monitoring

It is currently estimated that 600 million people are at direct risk from volcanic eruptions (Sparks et al., 2013). Today, casualties from volcanic activity are generally low compared to other natural disasters. However, there are some notable examples within the last century with significant death tolls. For example: 1902 eruption of Mont Pelée (30,000 fatalities) (Heilprin, 1903); 1985 eruption of Nevado del Ruíz (23,000 fatalities) (Tilling, 1989, Voight, 1990). It is thanks to pioneers such as T. A. Jaggar, Jr and F. Omori who realised that in order to prevent such death tolls

from continuing, permanent observatories were required to study active volcanoes (Tilling, 1989). Consequently the first "tronometer" (seismometer) was designed and deployed on Usu volcano, Japan and Kilauea, Hawaii to detect volcanic seismicity (Tilling, 1989), and monitoring began at observatories such as at Asama volcano (1911) and the Hawaiian Volcano Observatory in 1912 (Jaggar, 1956, Tilling, 1989). Unfortunately, today there are still many active volcanoes that are not monitored or have only basic monitoring equipment installed (Sparks et al., 2012). The success of volcano monitoring was confirmed by the 2010 eruption of Merapi (Indonesia), in which real time monitoring and consequent timely action by the authorities saved up to 20,000 lives (Surono et al., 2012).

Throughout the history of volcanological studies, scientists have strived to develop and utilise different techniques to aid in the monitoring of the contemporary activity of volcanoes, from measuring the volatile output to the interpretation of seismic signals and surface displacement patterns.

1.3.1 Measuring gas emissions

The traditional method for measuring gas emissions is via direct measurements of volcanic fumaroles by means of "Giggenbach bottles", a 1970's Werner Giggenbach invention (Giggenbach, 1975, Stix and Gaonac'h, 2000) based on that used by Robert W. Bunsen in the 1800's. Despite the inherent dangers, logistical problems and the complex process of analysing the samples, this method is still occasionally used,

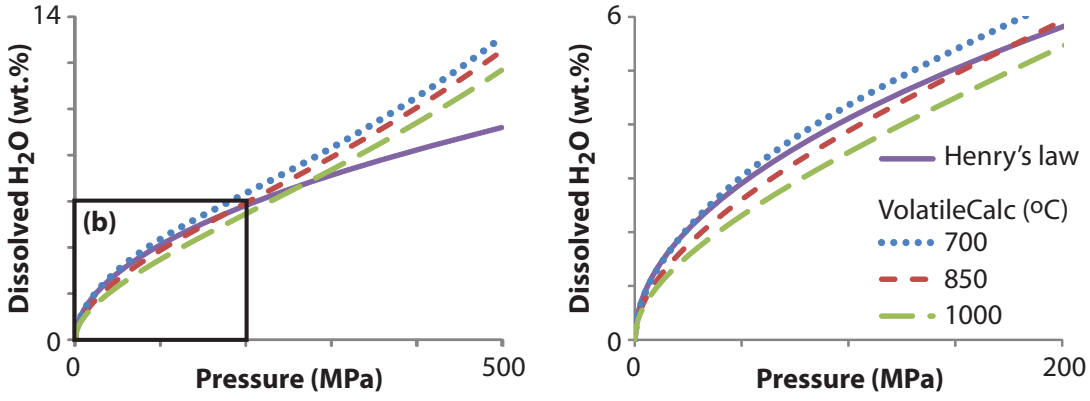

(a) (b)

Figure 1.3: A comparison between the dissolved H_2O content as calculated by Henry's law (Equation 1.3) to that by VolatileCalc for three different temperatures (Newman and Lowenstern, 2002). (b) shows the first 200 MPa from (a) in more detail. Of the three temperatures, the best agreement with Henry's law, at lower pressure (< 50 MPa) is with VolatileCalc at 700°C.

for example at the beginning of the current eruption of Soufrière Hills (Hammouya et al., 1998) and on the Italian volcanoes, Etna, Stromboli and Vulcano (Aiuppa et al., 2005). Other examples of the use of direct sampling techniques include Socorro Island, Mexico (Taran et al., 2010), Erta Ale, Afar, Ethiopia (Zelenski et al., 2013), Volcá de Colima, Mexico (Taran et al., 2002) and Merapi, Indonesia (Surono et al., 2012). However, research has been striving to find alternative, remote methods capable of producing spatially and temporally comprehensive autonomous measurements of degassing at volcanoes. A variety of ground-, air- and satellite-based methods have, and are being used to monitor gas emission from numerous volcanoes around the world.

In the 1960's, COSPEC (Correlation Spectroscopy) was developed, which looks at the absorption of SO_2 by ultra-violet radiation (Casadevall et al., 1984). Although originally created to analyse industrial pollution (Caltabiano et al., 1994), volcanologists were quick to see the potential in such a system for SO_2 monitoring at volcanoes (Stoiber and Jepsen, 1973). Consequently, COSPEC has been used on numerous volcanoes including, but not limited to, Soufrière Hills (Young et al., 1998, Watson et al., 2000, Gardner and White, 2002, Edmonds et al., 2003b), Mount Redoubt (Alaska) (Hobbs et al., 1991), Mount Etna (Sicily) (Allard et al., 1991, Caltabiano et al., 1994), Colima (Mexico) (Casadevall et al., 1984), and Popocatépetl (Mexico) (Delgado-Granados et al., 2001). In the late 1970's, the satellite based Total Ozone Mapping Spectrometer (TOMS) was launched providing measurements of SO_2 in the stratosphere (Stix and Gaonac'h, 2000). The limitation of both COSPEC and TOMS is that they measure the SO_2 absorption of UV radiation and are therefore not capable of detecting other gases such as $H_2O, CO_2, H_2S, HCl, HF$. Hence, since the 1990's many scientists have been investigating the use of infrared techniques such as Open-Path Fourier Transform InfraRed (FTIR) Spectroscopy which has been used to analyse the ratio between SO_2 and HCl (Edmonds et al., 2002, Christopher et al., 2010, Oppenheimer et al., 2002).

Two permanent UV Scanning Spectrometers (Scanspec) have been installed on Montserrat to monitor the SO_2 emission rates autonomously during daylight hours (08:00 to 16:00). This provides a UV spectrum approximately every 5 seconds, supplying data for very short-term variations, and relaying it to the MVO (Montserrat Volcano Observatory) (Edmonds et al., 2003a, Christopher et al., 2010). A further technique is Imaging Differential Optical Absorption Spectroscopy (IDOAS) which was first used on Mount Etna in 2003 and allows two-dimensional measurements of gases and provides a spectrum every 15 minutes (Bobrowski et al., 2006).

The accurate measurement of the two most abundant volcanic volatiles (H_2O and CO_2) is complicated by the concentrations of these two species within the atmo-

sphere. Researchers have attempted to overcome this by decreasing the distance between the sensor and emission source (e.g. Shinohara, 2005, Gerlach et al., 1997). Gerlach et al. (1997) employed a method of cross-sectional profiling by flying through the Popocatépetl volcanic plume with air-based instruments. However this method is very limited both temporally and spatially, and very dependent upon the volcanic activity - it may only be used in ash-free plumes. Shinohara (2005) developed a portable autonomous sensor package (MultiGAS - Multisensor Gas Analyzer System) capable of measuring numerous volatile species including H_2O, CO_2 and SO_2. The system has since been successfully deployed on numerous volcanoes including Tarumae, Tokachi and Meakan (Japan) (Shinohara, 2005); Mt. Etna (Italy) (Aiuppa et al., 2006); Stromboli (Italy) (Aiuppa et al., 2010); Gorely (Kamchatka) (Aiuppa et al., 2012); Soufrière Hills (Montserrat) (Edmonds et al., 2010).

Although considerable progress has been made, weather, volcanic activity and system failures still hamper efforts for reliable, continuous coverage.

The excess sulphur problem

The composition of gas emissions at the surface may vary significantly from that of the magma. Reasons for this include interaction with hydrothermal fluids (Moretti et al., 2013), multiple magma storage chambers (e.g. Edmonds et al., 2001, Moretti et al., 2013) and volatiles exsolving under different conditions at depth and therefore exploiting different escape pathways (e.g. Papale, 1999, Newman and Lowenstern, 2002, Liu et al., 2005).

Through measuring emissions of sulphur-bearing volatiles, it has been determined that more sulphur is emitted from volcanoes (irrespective of magma composition - basaltic to rhyolitic) than the chemistry of the magma suggests. This difference is often in the range of ten times or more (Wallace, 2001). This phenomenon is commonly known as the "excess sulphur problem" (e.g. Delgado-Granados et al., 2001, Sharma et al., 2004, Edmonds, 2008, Edmonds et al., 2010, Surono et al., 2012) and many hypotheses have been proposed to explain it. These include excess vapour before eruption (Wallace and Gerlach, 1994), continuous degassing of unerupted magma (Rose et al., 1982), the breakdown of sulphur-bearing species (anhydrite dissolution) (Devine et al., 1984) and the interaction between mafic magma and the native silicic magma at depth (Barclay et al., 1998, Murphy et al., 2000, Di Muro et al., 2008, Roberge et al., 2009).

1.3.2 Volcano deformation

Changes in surface displacement, potentially inducing cycles of inflation and deflation at volcanic sites, can yield important information regarding the internal workings of an active volcano. There are now many techniques which may be utilised in the monitoring of ground deformation at volcanic sites, including cGPS (continuous Global Positioning System) (e.g. Mattioli et al., 1998, Shepherd et al., 1998, Norton et al., 2002, Wadge et al., 2006, Palano et al., 2012), InSAR (Interferometric Synthetic Aperture Radar) (e.g. Wadge et al., 2006, Bonforte et al., 2011, 2013), Electronic Distance Meter (EDM) measurements (e.g. Jackson et al., 1998, Norton et al., 2002, Ramírez-Ruiz et al., 2002, Surono et al., 2012) and tiltmeters (e.g. Norton et al., 2002, Surono et al., 2012). However, displacement measurements in volcanic environments can be problematic due to vegetation cover (InSAR), atmospheric moisture (InSAR) and volcanic activity destroying equipment (e.g. Wadge et al., 2006). Despite this, displacement measurements at Montserrat have identified different types of vertical and radial ground motion: near- (due to shallow processes within the dome and upper conduit, including pressurisation due to magma or gas, and gravitational collapse (Wadge et al., 2006)) and far-field (several kilometres from the dome) motion and cooling-induced contraction of pyroclastic flow deposits (e.g. Jackson et al., 1998, Shepherd et al., 1998, Norton et al., 2002, Wadge et al., 2006). Bonforte et al. (2011, 2013) investigated the anomalously high levels of CO_2 in the soil on the flanks of Mt. Etna and through the use of InSAR they have proposed a link between diffuse soil emissions, the behaviour of tectonic faults and changes in ground displacement.

At the onset of the ongoing eruption episode of Soufrière Hills in 1995, Gardner and White (2002) observed a link between surface displacement, SO_2 emissions and hybrid earthquakes. Similarly, prior to the 1997 dome collapse of Soufrière Hills, Watson et al. (2000) observed that tilt cycle peaks correlated with increases in both SO_2 emissions and the frequency of hybrid earthquakes.

At volcanic sites, most of the large surface displacements are confined to the near-field. However, measurable surface displacements have been detected 8 km distant from the dome at Soufrière Hills (Norton et al., 2002).

Surface displacement at active volcanoes is often found to be cyclic, with inflation prior to eruption (explosive or effusive) with pressurisation, and deflation as the pressure decreases (e.g. Denlinger and Hoblitt, 1999, Voight et al., 1999, Lensky et al., 2008, Odbert et al., 2014). Surface displacement measurements are generally mm to cm-scale. For example, between January 1998 and December 1999, vertical displacements, measured by cGPS, at Soufrière Hills volcano were up to ± 6 cm at 500 m distance from the dome, coinciding with a period of intermittent explosive

activity but very little dome building Norton et al. (2002). Similarly, up to ≈ 3 cm of subsidence was measured at the volcano by cGPS, accompanying increased volcanic activity during December 2008 - January 2009 (Hautmann et al., 2013). However, $20 - 50$ cm surface uplift in the centre of the dome accompanies repetitive eruption events at Santiaguito (Johnson et al., 2008). 1 cm uplift was detected at Akutan volcano (Alaska) in the early part of 2008, which did not precede an eruption event (Ji and Herring, 2011). Localised subsidence of up to 10 cm at Akutan volcano in 1992-93 and 1996-8 has been attributed to fumarolic degassing and the associated depressurisation (Lu et al., 2000).

1.3.3 Volcanic seismicity

There are different types of seismic events which occur in association with volcanic activity from high freqency Volcano-Tectonic (VT), low frequency long period and hybrid events to surface signals such as rockfalls (e.g. Lahr et al., 1994, Neuberg, 2000, Collier et al., 2006, Collier and Neuberg, 2006). Low frequency volcanic events are defined as having a dominant frequency between 0.2 and 5 Hz (Ferrazzini and Aki, 1987, Chouet, 1988, Jousset et al., 2013) and generally originate at depths of less than 1.5 km below the surface of the dome (Chouet, 1996, Neuberg, 2000). Although they have been proposed as potential precursors to dome collapses and vulcanian explosions (Chouet, 1996, Voight et al., 1999, Neuberg, 2000), the trigger mechanism for these seismic events remains poorly understood. Many studies have proposed that the generation of such events is related to a resonating system of fluid within the solid material of the volcanic edifice (e.g. Ferrazzini and Aki, 1987, Neuberg and O'Gorman, 2002). Two models for the generation of the low frequency resonance of the long period events are the fluid-driven crack model, where gas release results in dome and conduit crack resonance (e.g. Chouet, 1986, 1988, Gil Cruz and Chouet, 1997) and the resonating crack model (due to the interaction between magma and volatiles) (e.g. Neuberg, 2000). In both cases, the low frequencies of these events is attributed to gas-induced attenuation. Gil Cruz and Chouet (1997) have studied the long-period events for Galeras volcano (Colombia) and comment that they appear to be accompanied by bursts of gas emission through cracks in the dome. A third model, magma "wagging", was proposed by Jellinek and Bercovici (2011) and involves the magma oscillating against a surrounding highly porous zone of sheared bubbles. These models only help to explain the frequencies of the seismic events, and not the actual trigger mechanism. More recently, Massol and Jaupart (2009), Thomas and Neuberg (2012) have proposed these events occur due to brittle failure related to changes in the conduit geometry.

VLP (Very Long Period) seismic signals have frequencies less than 0.2 Hz (Jousset

et al., 2013). Jousset et al. (2013) analysed these seismic signals related to the 2010 eruption of Merapi and subdivided them into two classes; firstly, a long signal duration representing the ascent of magma and secondly, a shorter signal duration proposed to represent gas loss. This second type was found to be located on the southern flank of the volcano, which was also the site of maximum surface inflation (up to 10 cm/day (Jousset et al., 2013)). Consequently, these shorter duration signals are thought to represent the migration of gas within the volcanic edifice (Jousset et al., 2013).

Edmonds et al. (2002) have provided evidence of a possible link between surface rockfall events and gas emissions at Soufrière Hills. They observed spikes in the ratios of $HCl : SO_2$ measured using FTIR of up to 6.8 during September 2000 (or approximately SO_2 flux: 2000 td^{-1} and HCl flux: 13000 td^{-1}) coincident with a period of intense rockfall activity possibly linked with magma extrusion (Edmonds et al., 2002). This increase in degassing may in part be related to the release of gas isolated inside pores and fractures. Considering ratios as low as 0.77 had previously been measured (August, 2000), this is a substantial increase reinforcing the idea for different mechanisms that allow the release of different gas species. Young et al. (2003) suggest the cyclic SO_2 flux from Soufrière Hills corresponds to cyclic LP events, confirmed by the 1997-1999 activity. However, Edmonds et al. (2003b) have determined there is no such correlation with the swarms of 2001. Furthermore, hybrid swarms have been detected in the build-up to dome building activity and this has corresponded with a decrease in SO_2 flux (Edmonds et al., 2003b). A large decrease in SO_2 has been detected after dome collapse events. For example, after the dome collapses of 1998 and 2001 at Soufrière Hills, SO_2 peaked immediately after the event and also several days later, which did not coincide with any seismic activity (Edmonds et al., 2003b). This may reflect the renewed openness of the system, or seismic activity releasing trapped gas. During August to October 2001, SO_2 measurements at Soufrière Hills revealed a correlation between gas peaks, rockfall and pyroclastic flow events, but not with long-period and hybrid events (Edmonds et al., 2003b). A hypothetical two-dimensional flow model was proposed by Neuberg et al. (2006) which included consideration of gas loss and friction-controlled slip. The model implies the generation of low frequency events correlates with a zone of brittle failure of the melt. The model also provides a potential mechanism for the generation of fracturing lining the conduit walls, whereby the magma undergoes brittle failure and the resultant fractures are transported up the conduit via magma ascent.

Prior to the 1992 eruption of Galeras, COSPEC measurements observed a significant decrease in the output of SO_2 concurrent with an increase in low-frequency

seismicity. Post-eruption, this seismicity ceased and was consequently attributed to sealing-induced pressurisation of the system (Delmelle and Stix, 2000).

1.4 Key aims of the research

There are various theories of how gas may move through a volcanic system, and numerous surface measurements for gas emissions and surface displacements. This work aims to link the interior of the volcanic system (conduit, wall rocks and dome) with these surface observations. In particular, this research aims to investigate the link between permeability variations, gas behaviour, pressurisation and surface displacement.
Key points of interest in this study include:

- What is the impact of varying permeabilities at shallow levels within the volcano, and how does this affect the gas behaviour and pressurisation?
- How does the gas behaviour change in response to permeability changes with time?
- How do the permeability changes inferred from seismicity change the conditions of gas storage and release?
- Where may volcanic volatiles be stored and how are they released?
- How may the presence of volcanic volatiles affect the surface displacement?
- Can the model results be compared to real observations to further the understanding of internal permeabilities and pressures of silicic volcanoes?

1.5 Overview of the Thesis

Chapter 2 outlines the equations used to model the gas and the resulting displacement, and the method used to solve these equations. Details regarding the development of the geometries and the associated mesh are also included. Chapter 3 describes a simplistic "principal block" model and investigates the influence permeability has on the final results. This model is extended to include time dependency in order to model the effects of unloading on the system (Chapter 4). Chapters 5, 6 and 7 use a combination of fluid flow and displacement modelling to investigate several volcanological phenomena including brittle failure of the magma, sealing the dome and dome cracks.

Chapter 8 shows a more realistic model based upon the topography of Soufrière Hills. The model investigates how different permeability conditions affect a model in which gas is stored at shallow levels within the dome before being released by a fracture zone. The realistic model permits gas emissions and displacement patterns to be plotted on the surface of the topography to give an accurate view of where observations may be expected on a real volcano if the scenario was to occur. Chapter 9 extends this to investigate the implications of altering the fracture zone size, gradient and anisotropic permeability in the conduit, and the effects of a different topography.

In Chapter 10, the modelling assumptions outlined in Chapter 2 are revisited and their impact assessed, before the method is applied to two specific case studies. Namely, an ash venting event at Soufrière Hills volcano during a period of no active extrusion, and ring-shaped degassing at Santiaguito.

Chapter 11 presents the implications of the results and how this may aid our understanding of degassing processes and the role of permeability.

Finally, there are four appendices. Appendix A provides some analytical solutions to aid in the validation of the method used. Appendix B assesses the validity of Darcy's law to determine the range over which the method is valid. The impact of the assumptions of ideality and a constant viscosity are assessed in Appendix C. Finally, Appendix D investigates the potential impact of de-coupling the conduit-wall margin.

Chapter 2

Method

From the literature reviewed in Chapter 1, there are numerous studies on permeability measurements of volcanic materials (e.g. Eichelberger et al., 1986, Klug and Cashman, 1996, Melnik and Sparks, 2002), gas emissions (e.g. Edmonds et al., 2002, 2003a, Shinohara, 2005) and surface displacement (e.g. Norton et al., 2002, Wadge et al., 2006). However, there is a gap with respect to 2D and 3D gas flow within the interior of a volcano with respect to the permeability and how the presence or loss of stored gas affects the pressurisation, and in turn, the surface displacement. In particular, the effects of differing permeability are uncertain and the ability to visualise the resulting gas behaviour within the internal volcanic structures would be advantageous. Furthermore, the implications of the temporal evolution of permeability changes is also lacking.

A first step to understanding the interaction between the permeability and gas pressure distribution within a volcanic edifice is based on Darcy's law and is presented in Section 2.1. This method aims to investigate the impact of permeability and pressurisation on the gas flow and surface displacement. In this chapter, the use of Darcy's law in previous volcanological studies is outlined, before deriving the equations and presenting the software used to solve for gas pressure and gas velocity given a certain permeability distribution.

2.1 Darcy's law and its use in Volcanology

Darcy's law (2.1) was derived by Henry Darcy in 1856, for calculating the flow of groundwater through an aquifer, by relating the fluid flow rate to the permeability and pressure,

$$Q = kA\frac{\Delta P}{l} \tag{2.1}$$

for the flow rate (Q), permeability (k), cross-sectional area (A), pressure loss (ΔP) and distance over which the pressure changes (l). An adapted version of Darcy's law (2.2) was used by Eichelberger et al. (1986) to model gas escape from a permeable foam in direction x,

$$\phi \boldsymbol{u} = -\frac{k}{\mu}\frac{dP}{dx} \tag{2.2}$$

for the porosity (ϕ), pore velocity (velocity divided by porosity) ($\boldsymbol{u}$), permeability (k), gas viscosity (μ) and pressure gradient $\left(\frac{dP}{dx}\right)$ in the x direction.
Despite its origin in hydrogeology, Darcy's law has become a useful relationship for calculating the permeability of volcanic samples (e.g. Eichelberger et al., 1986, Rust and Cashman, 2004, Takeuchi et al., 2005, 2008, 2009, Okumura et al., 2009, 2012, Yokoyama and Takeuchi, 2009) and also modelling the movement of gas through a volcanic system (e.g. Eichelberger et al., 1986, Candela, 1991, Jaupart and Allègre, 1991, Woods and Koyaguchi, 1994, Klug and Cashman, 1996, Melnik and Sparks, 1999, Edmonds et al., 2003b, Gonnermann and Manga, 2005, Ida, 2007, Lensky et al., 2008, Collombet, 2009, Hicks et al., 2009, de' Michieli Vitturi et al., 2010, 2013, Kozono and Koyaguchi, 2010, Matsushima, 2011, Rust and Cashman, 2011, Scharff et al., 2014, Schneider et al., 2012). Some of these studies used the modified form, the Forchheimer equation (2.3) which accounts for a non-linear relationship between the gas flux and pressure gradient (e.g. Rust and Cashman, 2004, Wright et al., 2006a,b, Takeuchi et al., 2008, Bouvet de Maisonneuve et al., 2009, Okumura et al., 2009, 2012, Takeuchi et al., 2009),

$$\nabla P = -\frac{\mu}{k}\boldsymbol{u} - \frac{\rho}{k_f}\boldsymbol{u}^2 \tag{2.3}$$

for the pressure gradient (∇P), gas viscosity (μ), gas density (ρ), Darcian permeability (k) and inertial permeability (k_f) (e.g. Takeuchi et al., 2009).
Darcy's law is used within this study, due to the limited data available for inertial permeabilities and because turbulence would act to decrease velocities. Darcy's law, therefore, provides an upper limit. However, a comparison between Darcy's law and the Forchheimer equation is presented in Appendix B.

2.2 Equations

Gas pressure, gas velocity and the resulting displacement are modelled numerically in two and three dimensions using a finite element approach. The modelling will be performed for a stationary system (with results showing the equilibrium state) or

time dependent to show the systems reaction to change.

2.2.1 Modelling the gas loss

Darcy's law relates the fluid velocity ($\boldsymbol{u}$) to the permeability (k) of the material and the pressure (P). The permeability is a measure of the ease with which a material (e.g. volcanic rock/magma) may transmit fluids (e.g. volcanic gas (H_2O)). In order to describe the gas loss from a static magma, the equations for Darcy's law (2.4)

$$\boldsymbol{u} = -\frac{k}{\mu}(\nabla P + \rho g \nabla z) \tag{2.4}$$

and the continuity equation (2.5)

$$\frac{\partial}{\partial t}(\rho\phi) + \nabla \cdot (\rho \boldsymbol{u}) = Q_{\mathrm{m}} \tag{2.5}$$

are amalgamated to derive a partial differential equation (PDE) (2.6) which is solved for the pressure (P).

$$\frac{\partial}{\partial t}(\rho\phi) + \nabla \cdot \rho \left[-\frac{k}{\mu}(\nabla P + \rho g \nabla z) \right] = Q_{\mathrm{m}} \tag{2.6}$$

The associated pressure gradient (∇P) is used within Darcy's law (Equation 2.4) to obtain the gas velocity ($\boldsymbol{u}$). The ideal gas law (Equation 2.7) is used to calculate the gas density (ρ),

$$\rho = \frac{M}{RT} P \tag{2.7}$$

for the molecular mass (M), ideal gas constant (R), temperature (T) and pressure (P). From the ideal gas law, the gas density varies with pressure, hence the gas is compressible. In most cases in this modelling, the mass source term (Q_{m}) from the continuity equation (2.5) is set to 0, i.e. mass is conserved (mass in the system is always constant so the rate of loss equals the rate of gain). One exception to this is for the inclusion of added mass due to exsolved gas during a dome collapse in Chapter 4.

The porosity (ϕ) and permeability (k) are tensors describing the ability for a material to transmit fluid in different directions, whilst the density (ρ) and the dynamic viscosity (μ) describe the properties of the exsolved volcanic gas. The resulting pressure (P) and gas velocity ($\boldsymbol{u}$) describe the pressure and motion of this volcanic gas.

2.2.2 Modelling the displacement

Modelling the displacement resulting from the presence of gas within the volcano is achieved through the Momentum Equation (2.8), based on Newton's second law of motion ($\boldsymbol{F} = m\boldsymbol{a}$), which is solved for the displacement ($\boldsymbol{V}$).

$$\rho_r \frac{\partial^2 \boldsymbol{V}}{\partial t^2} - \nabla \cdot \sigma = \mathbf{F}_V \tag{2.8}$$

where ρ_r is the rock density, t is time, σ the stress tensor and $\mathbf{F}_V$ a vector force. When a force (stress) is applied to a material it responds through deformation (strain). This strain can be either brittle or ductile dependent upon the material and environmental properties. The Cauchy stress tensor (σ) consists of a sequence of normal (σ_x, σ_y, σ_z) and shear (τ_{xy}, τ_{yx}, τ_{xz}, τ_{zx}, τ_{yz}, τ_{zy}) stresses as shown in Equation 2.9. The Cauchy stress tensor links the strain tensor (ϵ) and the volcanic gas pressure obtained from Equation 2.6 (P) according to Equation 2.10,

$$\sigma = \begin{bmatrix} \sigma_x & \tau_{xy} & \tau_{xz} \\ \tau_{yx} & \sigma_y & \tau_{yz} \\ \tau_{zx} & \tau_{zy} & \sigma_z \end{bmatrix} \tag{2.9}$$

$$\sigma = C\epsilon - P\boldsymbol{I} \tag{2.10}$$

where $\boldsymbol{I}$ is the identity matrix, and C is the elasticity tensor which is a function of the elastic moduli: Young's modulus (E) and Poisson's ratio (ν) (2.11). Young's modulus represents the stiffness of an elastic medium (ratio of stress to strain), whilst Poisson's ratio is the ratio of the strain in the applied direction to that perpendicular.

$$C = \frac{E}{(1+\nu)(1-2\nu)} \begin{bmatrix} 1-\nu & \nu & \nu & 0 & 0 & 0 \\ \nu & 1-\nu & \nu & 0 & 0 & 0 \\ \nu & \nu & 1-\nu & 0 & 0 & 0 \\ 0 & 0 & 0 & \frac{1-2\nu}{2} & 0 & 0 \\ 0 & 0 & 0 & 0 & \frac{1-2\nu}{2} & 0 \\ 0 & 0 & 0 & 0 & 0 & \frac{1-2\nu}{2} \end{bmatrix} \tag{2.11}$$

The strain tensor (ϵ) is dependent upon the displacement vector ($\boldsymbol{V}$) and may be expressed as Equation 2.12 where the displacement gradient is calculated with respect to the material coordinates according to Equation 2.13. In these equations, u, v and w are the directional components of the displacement vector ($\boldsymbol{V}$).

$$\epsilon = \frac{1}{2}\left(\nabla \boldsymbol{V} + \nabla \boldsymbol{V}^T\right) \tag{2.12}$$

$$\nabla \boldsymbol{V} = \begin{bmatrix} \frac{\partial u}{\partial X} & \frac{\partial u}{\partial Y} & \frac{\partial u}{\partial Z} \\ \frac{\partial v}{\partial X} & \frac{\partial v}{\partial Y} & \frac{\partial v}{\partial Z} \\ \frac{\partial w}{\partial X} & \frac{\partial w}{\partial Y} & \frac{\partial w}{\partial Z} \end{bmatrix} \tag{2.13}$$

Alternatively, the strain tensor may be expressed as individual components (2.14) constituting the strain tensor (2.15).

$$\begin{gathered} \epsilon_x = \frac{\partial u}{\partial x}, \qquad \epsilon_y = \frac{\partial v}{\partial y}, \qquad \epsilon_z = \frac{\partial w}{\partial z}, \\ \epsilon_{xy} = \frac{1}{2}\left(\frac{\partial u}{\partial y} + \frac{\partial v}{\partial x}\right), \quad \epsilon_{yz} = \frac{1}{2}\left(\frac{\partial v}{\partial z} + \frac{\partial w}{\partial y}\right), \quad \epsilon_{zx} = \frac{1}{2}\left(\frac{\partial w}{\partial x} + \frac{\partial u}{\partial z}\right). \\ \epsilon_{yx} = \epsilon_{xy} \qquad \epsilon_{zy} = \epsilon_{yz} \qquad \epsilon_{xz} = \epsilon_{zx} \end{gathered} \tag{2.14}$$

$$\epsilon = \begin{bmatrix} \epsilon_x & \epsilon_{xy} & \epsilon_{xz} \\ \epsilon_{xy} & \epsilon_y & \epsilon_{yz} \\ \epsilon_{xz} & \epsilon_{yz} & \epsilon_z \end{bmatrix} \tag{2.15}$$

2.2.3 Coupling the equations for fluid flow and displacement

In order to model both the gas flow and the resulting displacement, the equations for both are coupled and solved together such that for every time-step the result from each equation is linked to the other.

2.3 Model assumptions

The modelling focuses on the role of permeability and how changes to the permeability may affect the state of the volcanic system based upon internal pressurisation and surface gas loss and displacement. Following Section 2.2, pressurisation and gas behaviour are calculated using Darcy's law and the resulting surface displacement is derived from the momentum equation. However, a number of restrictions are applied to the modelling which are itemized here. Further discussions relating to the choice of the parameters are discussed in the relevant parts of section 2.4.

- Only one gas is modelled - therefore, H_2O is simulated because it is the most abundant volatile in volcanic systems
- Usually, each domain is set to a single "bulk" permeability, representing the average for that region. Hence smaller scale structures either enhancing or inhibiting degassing are generally ignored, unless they are the subject of a

particular model investigation, e.g. fracture zones (Chapter 5), sealing (Chapter 6) and cracks (Chapter 7). However, models with permeability anisotropy or gradients in the conduit are discussed in Chapter 9.

- The magma is static, therefore the models represent a volcano in a state of quiescence which has ceased erupting material, but still has the potential to degas.
- The method assumes gas saturation within all the domains, i.e. all empty pore spaces are filled with volcanic gas.
- Gas is continuously supplied through the boundary conditions.
- A constant temperature of 850 °C is assumed. However, the implications of varying the temperature are discussed in Appendix C.
- Gas viscosity is set to the constant value of 1.5×10^{-5} Pas (Appendix C).
- The gas density is calculated according to the ideal gas law, rather than the true behaviour of H_2O (Appendix C).
- Only single values for Young's modulus and Poisson's ratio are used.
- The domains in each model are fully coupled. The impact of de-coupling the conduit and wall-rocks is investigated in Appendix D.
- Inertial effects are neglected. The impact of the inertial effects are investigated in Appendix B.

The impact of these assumptions will be explored in Section 10.1.

2.4 Solving using the finite element method

The equations in Section 2.2 are solved for stationary and time dependent problems using Comsol Multiphysics®[1] which utilises a finite element method. Comsol Multiphysics® is a commercial simulation platform providing a variety of comprehensive tools for defining and solving models. The particular forte of the program is the ability to incorporate many different physics equations into a single multiphysical model. This software is particularly useful for this project as it provides the

[1]More details regarding the software and packages used may be found in the Comsol Multiphysics® Reference Manual, Subsurface Flow Module User's Guide and Structural Mechanics Module User's Guide.

interface and tools for solving the model without the requirement of first programming the interface or solver. Consequently this research can focus on the wide range of geometric and physical parameters affecting the simulations.
The finite element method (FEM) is a numerical method of solving a problem. In contrast to analytical models (Appendix A) which solve the exact equations for the entire domain space, the FEM solves the problem for particular points (nodes) within the domain space, determined by a mesh. Between these points, the result is interpolated to derive the solution for the entire domain space. Consequently the FEM provides an approximate solution to a problem. However, it is particularly useful for complex problems where an analytical solution is not possible either due to the geometry or the physics. A number of steps are required in order to derive a solution by FEM:

1. Problem formulation;
2. Design and creation of geometry;
3. Discretising the geometry by means of a mesh;
4. Specifying the constraints of the model in terms of material properties, physics and boundary conditions;
5. Solving the problem;
6. Postprocessing.

Similar numerical techniques for solving PDEs include finite difference (FDM) and finite volume (FVM). The three methods differ in the manner in which the equations are discretised. FDM uses the differential (strong) form, whilst FVM and FEM use the integral (weak) form of the governing equations (Peiró and Sherwin, 2005). FDM is reliant on a structured mesh and is therefore only suitable for simple (block) geometries (Peiró and Sherwin, 2005). Due to the use of the weak form of the governing PDE, FVM and FEM are more suited to more complex geometries in two- or three-dimensions (Peiró and Sherwin, 2005). In FEM, the nodes on which the variables are computed are located at the vertices of each element, whilst in the FVM, the variables are averaged over control volumes which surround each node (Versteeg and Malalasekera, 2007). Consequently, FEM has a greater accuracy than FVM, although it is more computationally intensive. Therefore, FEM is used here over the FDM and FVM methods because it can handle more complex geometries and will provide a better approximation to the solution of a problem. In the following sections, the six steps to deriving a solution using the finite element method are described in detail.

2.4.1 Problem formulation

The first step to any modelling endeavour is to clearly define the problem to be solved. This involves outlining the purpose of that model. In this work, the basic aim is to determine the effect of changing the permeability on the behaviour of volcanic systems. From this basic principle, more complex models can be designed to investigate particular scenarios. Once the scenario is clearly defined, an appropriate geometry may be designed and the relevant constraints defined.

2.4.2 Geometry creation

Comsol Multiphysics® provides a comprehensive set of CAD (Computer-Aided Design) tools for the creation of 2D and 3D geometries from simple blocks to complex geometries representing topography. For the simplest geometries, standard geometric shapes may be combined and modified to derive the required configuration. However, for more complex geometries requiring precise topographic features, parametric surfaces are used which take input from interpolation functions. Interpolation functions construct a curve or surface based upon an input of discrete data points. This is particularly useful when using topographic data which is often in the form of discrete data points described by the spatial coordinates of x, y and z. By importing topographic data as an interpolation function, this data can then be utilised during geometry creation. This key feature enables the incorporation of elevation data for creating more accurate topography for modelling real volcanoes such as Soufrière Hills. Furthermore two sets of data can be incorporated to distinguish between the differing surfaces of the country rock and dome. For example, the models in Chapters 8 and 9 use topography data provided by Wadge et al. (2009) for 12 July 2003 and 1 August 2005 which represent the topographic surfaces before and after the major dome collapse. However, the accuracy of modelling such complex surfaces is dependent upon the mesh quality and resolution.

2.4.3 Meshing

Meshing is integral to the finite element method and involves discretisation of the geometry into smaller entities. This mesh consists of a number of shapes (elements) and vertices (nodes) (Figure 2.1). The nodes are the points in the domain for which the value of the variable is explicitly calculated. At all non-nodal points, the solution is approximated via interpolation functions. For 2D geometries, the domains are discretised into triangular, quadrilateral or mapped elements to create the mesh (Figure 2.2). In the case of 3D geometries, these elements may be tetrahedral, hexahedral, prism or pyramid shaped. Consequently, these simple shapes can only

approximate complex boundaries, and the accuracy increases with decreasing mesh element size (Figure 2.3). However, the greater the number of elements in a finer mesh, the more computing power and time is required to solve the model.
Meshing complex 3D shapes requires a number of considerations. For example which part of the model is most important and therefore requires the highest mesh quality? In this modelling, this will usually be the region of the conduit and dome and their surroundings. The furthest extents are potentially less important and so a lower quality mesh could be used to reduce the size of the model. A simple 2D shape could consist of less than 500-1000 elements, whilst a complex 3D geometry may require more than 50,000 elements. The number of elements also impacts upon the solution time. A stationary 2D model with 500 elements will take seconds to solve, whilst, a more complex 3D model with time dependency and more than 50,000 will take hours to days to solve, dependent upon the time step and the modelled duration.
Mesh quality is dependent upon the size variation. Provided the elements are uniform in size, the greater the number of elements, the higher the mesh quality. However, a large variation in element size leads to a poor quality mesh. The finer the mesh, the more accurately a complex geometry can by discretised.
When meshing, very narrow regions can cause the greatest problems in terms of quality and resolution. One method of reducing the number of elements in this case is to use a swept mesh which replicates the mesh from a source face and extends it through the selected domain.

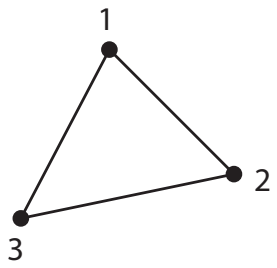

Figure 2.1: Simple example showing a triangular mesh element with three numbered nodes. The variable is calculated explicitly at each node, and interpolated between the nodes. Due to the three nodes, for one dependent variable, there are three degrees-of-freedom which are required to fully describe the variable within this domain of interest. Adapted from Hutton (2004).

2.4.4 Specifying the constraints

The boundary conditions and material properties associated with the governing PDE's provide the constraints allowing the problem to be solved. The boundary

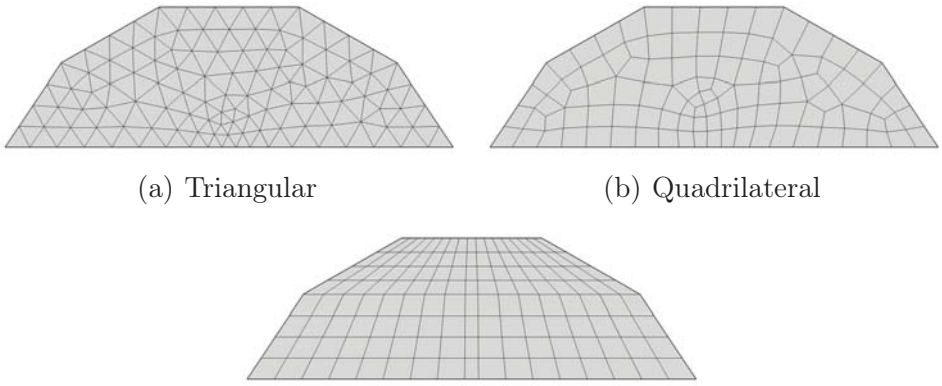

(a) Triangular (b) Quadrilateral

(c) Mapped

Figure 2.2: Examples of different 2D mesh types. The triangular mesh example has more mesh elements (192) than the other 2 examples (quadrilateral: 103, mapped: 136) and for this geometric shape, the mesh quality decreases from triangular to quadrilateral to mapped.

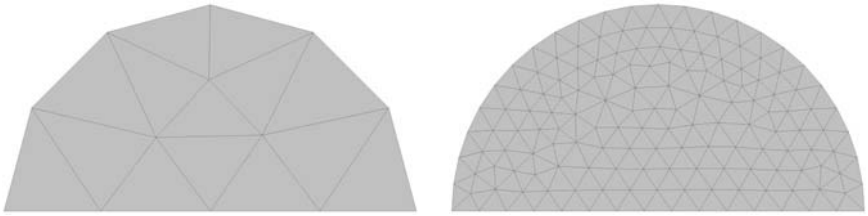

(a) Extremely coarse (b) Moderate

Figure 2.3: Examples of two different triangular mesh resolutions for a circular problem. The extremely coarse mesh provides a very poor representation of the semi-circular shape, whilst a moderate mesh provides a good approximation. Extremely coarse: 14 elements; normal: 265 elements

conditions describe the constraints on the finite geometry to simulate the input from the exterior (unmodelled) regions, whilst the material properties describe the components of the domain.

2.4.5 Boundary and domain conditions

Figure 2.4 illustrates a general configuration for a simplistic 2D model, showing the different domains and the boundaries. Table 2.1 outlines the domain and boundary conditions set for calculating the gas flow and the resulting displacement. For the fluid flow modelling, the boundaries are set to lithostatic pressure ($P_{lith} = P_{atm} + \rho_r g z$), for atmospheric pressure ($P_{atm} = 0.1$ MPa), rock density (ρ_r), acceleration due to gravity (g) and depth (z). Pressure (P) is applied to the exterior boundaries

of the model by simply setting the specified value ($P = P_0$).
Boundary conditions for the displacement modelling are set to either free, fixed ($\boldsymbol{v} = \boldsymbol{0}$) or roller ($\boldsymbol{n} \cdot \boldsymbol{v} = \boldsymbol{0}$). A roller boundary specifies that the normal ($\boldsymbol{n}$) to the direction of maximum displacement is $\boldsymbol{0}$, whilst slip can occur in the other directions. As the models are finite in their extent, this condition approximates a non-finite model, i.e. it simulates the presence of more material beyond the boundary acting to contain the lateral displacement.

Permeability

Measurements of permeability for natural and experimental results have yielded a range of values from 10^{-16} to 10^{-10} m^2 (Section 1.2.1). Hence, the majority of permeability values chosen in the modelling are within this range, with extremes used when necessary. Other models have also been consistent within this range. For example Edmonds et al. (2003b) used a simple form of Darcy's law to model a 1D system with upper conduit and dome permeabilities between 10^{-12} and 10^{-9} m^2. In contrast, Voight and Elsworth (2000) assumed a permeability of 10^{-15} m^2 to model the relationship between gas pressure and dome failure. Furthermore, Melnik and Sparks (2002) use a range between 10^{-16} and 10^{-12} m^2 in their conduit flow model. However, whilst the permeability of materials at the surface is well documented, the permeabilities within the volcanic interior remain uncertain. The choice of permeability values is strongly dependent upon the assumed density of

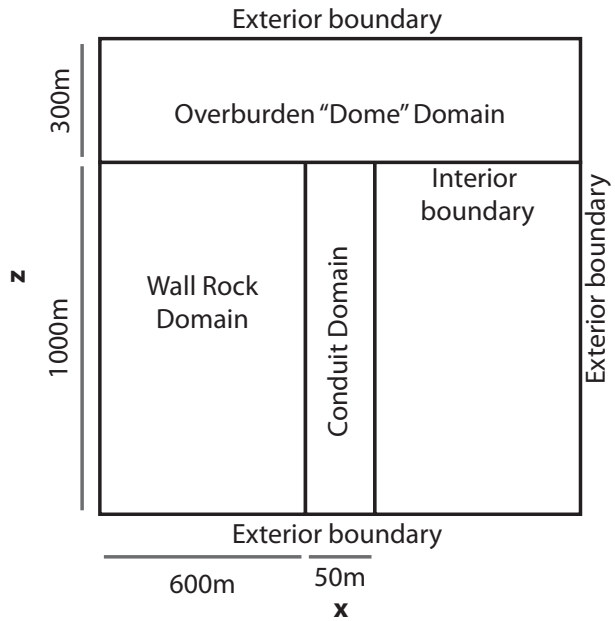

Figure 2.4: General model configuration showing the different domains and boundary types. These are set for the conditions according to Table 2.1.

		Gas Flow	Displacement
Domains (All)		matrix rock permeability (k) matrix rock porosity (ϕ) volcanic gas density (ρ) volcanic gas viscosity (μ)	matrix density (ρ_r) matrix Young's modulus (E) matrix Poisson's ratio (ν) volcanic gas pressure (P)
Boundaries	**Base Exterior**	lithostatic pressure (P_{lith})	fixed
	Lateral Exterior	lithostatic pressure (P_{lith})	roller
	Top Exterior	atmospheric pressure (P_{atm})	free
	Interior	N/A	N/A

Table 2.1: Settings for the domain and boundaries for calculating the gas flow and the resulting displacement. The matrix properties are applied for each of the structural components of the volcano: conduit, wall-rock, dome.

degassing pathways. If a high number of fractures and connected bubble pathways are simulated, a higher average "bulk" permeability will be required.
In the majority of models, particularly for Chapters 4-7, the high permeability of 10^{-10} m^2 is set for the conduit to derive an upper limit. Furthermore, for scenarios where only one model is presented, this is an extreme example where the model shows the maximum effect. Consequently, very low permeabilities are used for sealed regions, and very high permeabilities are used for fractures.
In all models, except Chapter 9, the permeability is set to an isotropic (scalar) value to represent the bulk permeability of a particular domain. However, in Section 9.2, the effect of a gradient or anisotropic permeability in the conduit is investigated. For anisotropy, this means setting the permeability as a tensor according to Equation 2.16.

$$k = \begin{bmatrix} k_x & 0 & 0 \\ 0 & k_y & 0 \\ 0 & 0 & k_z \end{bmatrix} \tag{2.16}$$

To impose a permeability change in time, smoothed step functions are coupled with a single or nested conditional (`if`) statement (Equation 2.17), for example Equation 2.18:

$$k = \texttt{if}\,(location < \texttt{value}, then(\texttt{statement}), else(\texttt{statement})) \tag{2.17}$$

$$k = \texttt{if}\,(z < \texttt{step1}(t), \texttt{step2}(t), k_0) \tag{2.18}$$

where k is the permeability, z depth and k_0 the initial permeability. In this case, $\texttt{step1}(t)$ is a smoothed step function describing the depth over which the change in permeability occurs and at what time this happens, whilst $\texttt{step2}(t)$ describes the change in permeability in terms of the initial value, end value and the duration over which the change occurs. Step functions describe the path of a variable between two values. The step function can be a sharp transition, or may be smoothed.

Porosity

From the equations in Section 2.2, porosity has no effect on the equilibrium result - it only impacts upon the time dependent response. The values used in the time dependency simulate a general value dependent upon the permeability of that domain, e.g. less permeable regions are simulated with a lower porosity. Because the porosity has such a limited effect on the results (when using Darcy's law), processes such as gas storage and loss are described in the text in terms of permeability.

Elastic Moduli

The deformation response of a material is largely dependent upon the elastic moduli, which in this modelling, are Young's modulus and Poisson's ratio. Young's modulus represents the stiffness of an elastic material, whilst Poisson's ratio is the ratio of the strain in the applied direction to that perpendicular. As either value increases, the resulting displacement decreases. A Poisson's ratio of 0.25 has been used often in displacement modelling (e.g. Voight et al., 2010a, Chardot et al., 2010, Hautmann et al., 2013, 2014). The range of values for Young's modulus vary from $3-100$ GPa (e.g. Voight and Elsworth, 2000, Voight et al., 2010a, Chardot et al., 2010, Wadge et al., 2006, Hautmann et al., 2013, 2014, Kendrick et al., 2013). A constant value is used for all domains in the model, therefore, the effect of the Young's modulus is predictable: if 10 GPa gives a displacement of 1 m, 1 GPa and 100 GPa would give displacements of 10 m and 0.1 m, respectively. Therefore, the displacement is inversely proportional to the Young's modulus.
Here, the models are created assuming a static modulus with a Young's modulus of 10 GPa and Poisson's ratio of 0.25.

Additional variables and constants

Additional terms used in the modelling include rock density, temperature, gas density and gas viscosity. The rock density (ρ_r) is used within the calculation for lithostatic pressure for the boundary conditions. Other studies have used a range of densities for intermediate to silicic magma (Andesite - Rhyolite) from $2000-2800$ kgm^{-3}

(e.g. Eichelberger et al., 1986, Wadge et al., 2006, Hale et al., 2009a, Wright and Cashman, 2013). Here, a mid-range value of 2500 kgm^{-3} is chosen. The density is strongly dependent upon the porosity, with the greater the percentage of pore spaces, the lower the density. Decreasing this density in response to an increase in porosity would lead to a corresponding decrease in the pressure pattern and *vice versa*.

The gas density is derived from the ideal gas law (Equation 2.7) using a constant temperature of 1123 K (Melnik and Sparks, 1999, de' Michieli Vitturi et al., 2010). Following conduit flow models (e.g. Melnik and Sparks, 1999, Collombet, 2009, de' Michieli Vitturi et al., 2010, Schneider et al., 2012), the gas viscosity is given a constant value of 1.5×10^{-5} Pas.

Time durations

Throughout this modelling, changes to the state of the volcanic system are imposed over different time durations. These times reflect particular examples which are described in the text related to the specific model. However, the imposed durations can be scaled up or down to suit any scenario.

2.4.6 Solving the problem

What does Comsol Multiphysics® solve?

As with any technique for solving using the FEM, Comsol Multiphysics® solves the weak formulation of the partial differential equations. As an example, here the stationary, one-dimensional, form of Darcy's law (Equation 2.19) is converted into the weak form. The equations solved in this case are as follows:

$$\begin{cases} \nabla \cdot \rho \left(-\dfrac{k}{\mu} \nabla P \right) = Q & \text{in } \Omega \\ -\boldsymbol{n} \cdot \rho \left(\dfrac{k}{\mu} \nabla P \right) = N_0 & \text{on } \Gamma_N \\ P = P_0 & \text{on } \Gamma_R \end{cases} \tag{2.19}$$

where Ω is the domain, and Γ_N and Γ_R are the Neumann and Dirichlet boundary conditions, respectively. Whilst a Dirichlet boundary condition specifies the exact value for the boundary, a Neumann condition specifies the the value of its derivative. In the case of Darcy's law, the Dirichlet boundary condition is used to set boundaries to pressure and the Neumann boundary condition is used to specify the velocity. In this study, all external boundaries are set to pressure, therefore, only Dirichlet boundary conditions are used. However the Neumann condition is documented here

for completeness. The weak formulation may be derived by firstly multiplying the PDE by an arbitrary test function λ and then applying the integral over the domain Ω:

$$\int_{\Omega} \nabla \cdot \rho \left(-\frac{k}{\mu} \nabla P \right) \lambda = \int_{\Omega} Q\lambda \tag{2.20}$$

By applying integration by parts, the left hand side may be rewritten as:

$$\int_{\Omega} \nabla \cdot \rho \left(-\frac{k}{\mu} \nabla P \right) \lambda = \int_{\Omega} \rho \left(-\frac{k}{\mu} \nabla P \right) \cdot \nabla \lambda + \int_{\Gamma_N} -\boldsymbol{n} \cdot \rho \left(-\frac{k}{\mu} \nabla P \right) \lambda \tag{2.21}$$

Therefore, the weak formulation of Darcy's law according to Equation 2.19, may be written in the form:

$$\int_{\Omega} \rho \left(-\frac{k}{\mu} \nabla P \right) \cdot \nabla \lambda - \int_{\Omega} Q\lambda + \int_{\Gamma_N} -\boldsymbol{n} \cdot \rho \left(-\frac{k}{\mu} \nabla P \right) \lambda = 0 \tag{2.22}$$

In Comsol Multiphysics®, this weak form equation, in addition to the Dirichlet boundary condition ($P = P_0$), is solved.

The test function

The test function λ represents a class of functions which are defined by the Lagrange shape functions. These shape functions describe the manner in which the solution is interpolated over each element, between the nodes. The choice of shape function is dependent upon the problem to be solved and the order of accuracy required. For the three nodal example shown in Figure 2.5a, the value of the variable φ for every non-nodal point (x, y) is calculated according to Equation 2.23 (Hutton, 2004).

$$\varphi(x, y) = \vartheta_1(x, y)\varphi_1 + \vartheta_2(x, y)\varphi_2 + \vartheta_3(x, y)\varphi_3 \tag{2.23}$$

$\varphi_1, \varphi_2, \varphi_3$ represent the value of the variable solved for at each node, whilst $\vartheta_1, \vartheta_2, \vartheta_3$ represent the shape functions which interpolate the value at the nodes for every other point (x, y) within the domain (Hutton, 2004). The number of nodes on each element is determined by the discretisation order. The order of the shape function is determined by the number of nodes around each element. For example, a triangle with a linear discretisation order has a node at each vertex of that shape (Figure 2.5). However, a quadratic discretisation adds an extra node midway between each vertex, and cubic two nodes between each vertex and one in the centre (Hutton, 2004).

Following Equation 2.23 for linear elements, for any number of nodes around a

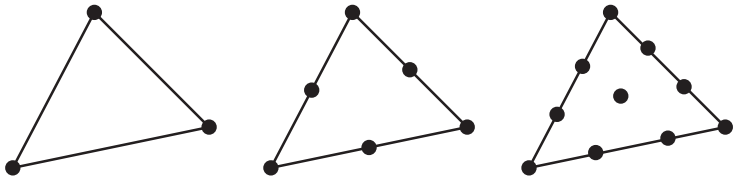

(a) Linear (b) Quadratic (c) Cubic

Figure 2.5: Comparison of the number of nodes allocated to each triangular mesh element dependent upon the discretisation order. A higher order increases the accuracy of the model because it increases the number of actual solutions and decreases the region over which interpolation must be used. However, increasing the number of nodes also increases the solution time. Adapted from Hutton (2004).

triangular element, the polynomial for $\varphi(x, y)$ (Hutton, 2004) is:

$$\varphi(x, y) = \sum_i \vartheta_i(x, y)\varphi_i \tag{2.24}$$

Basis functions represent simple functions which may be added together to derive the form of a curve when the exact characteristics of that curve are unknown. In FEM, basis functions are required to describe the nature of the interpolation between the nodes. For linear triangular mesh elements in FEM, the Lagrange shape functions are used and have the following basis:

$$\begin{aligned}\Phi(0, 0) &= 1 - \zeta_1 - \zeta_2 \\ \Phi(1, 0) &= \zeta_1 \\ \Phi(0, 1) &= \zeta_2\end{aligned}$$

and for quadratic triangular mesh elements:

$$\begin{aligned}
\Phi(0,0) &= (1-\zeta_1-\zeta_2)(1-2\zeta_1-2\zeta_2) \\
\Phi(0.5,0) &= 4\zeta_1(1-\zeta_1-\zeta_2) \\
\Phi(1,0) &= \zeta_1(2\zeta_1-1) \\
\Phi(0,0.5) &= 4\zeta_2(1-\zeta_1-\zeta_2) \\
\Phi(0.5,0.5) &= 4\zeta_1\zeta_2 \\
\Phi(0,1) &= \zeta_2(2\zeta_2-1)
\end{aligned}$$

These Lagrange shape functions are used to define the test function polynomials.

2.4.7 Study types and solver settings

Comsol Multiphysics® provides a comprehensive set of study types and solver settings for deriving the result. The study type determines between stationary or a time dependent solution, whilst the solver settings control the manner in which that study is solved.

Study types

There are three study types which are employed in this method, namely, stationary, time dependent and parametric. Stationary studies generate the equilibrium result for a given set of domain and boundary conditions. An equilibrium result is defined as the point at which all domains within the model have reached stability and no further changes to the results will be observed unless an additional change in the conditions is imposed. In all the modelling scenarios, this is the first study type undertaken as it provides information about a quiescent volcanic system and therefore provides a viable starting point for additional temporal modelling. Time dependent solvers are used to calculate the time dependent progression of the simulated volcanic system in response to a change of state, for example permeability. Parametric studies are invaluable for the calculation of multiple solutions with incremental variations to a parameter. This is used extensively in Chapters 3, 8 and 9 where numerous model runs are generated for one geometry, but for slightly different permeability conditions. In this study, this is particularly useful because the permeability conditions in real-time for volcanic systems is poorly understood. Therefore, this provides data as to how small variations may influence the state. This also provides a quick method for identifying scenarios of particular interest requiring further investigation or models which may be grouped according to similar behaviour.

Solver settings

For each of the study types used within the modelling, there are solver settings which control the manner in which the problem is solved. A number of settings may be adjusted to improve the accuracy of the result and are described in Table 2.2. Careful consideration over the choice in time-step is essential in this modelling. The time-step needs to be small enough to accurately model the changes imposed. A time-step is fine enough when a finer time-step will yield no change to the final results. If the time-step is too large, important detail will be lost, especially if a change is occurring over a short time period (shorter than the time-step) and the results will be inaccurate. However, there is also an important choice between the resolution of the model and the time required to solve the model.

2.4.8 Postprocessing of results

Comsol Multiphysics® provides numerous tools for analysing the results after a model run. In particular results may be plotted in 1D, 2D or 3D dependent upon the dimension of the model and the scope of interest. For example 1D plots may be used to investigate the progression of a variable, such as pressure, through time at a particular geometric point or domain within the model. 2D cross sections allow inspection of the interior conditions of the models, whilst 3D plots allow the representation of surface results depicted on the actual 3D topography to show, for example, the location of surface gas emissions or change in displacement.

Variable change

A useful plot is the change in a particular variable (e.g. pressure or displacement) in response to a change within the system and is created by subtracting the result at a certain point in time (for example at time 0) from subsequent times. Hence, this provides valuable information as to how much that variable has changed and the location over a specified time period. This is especially useful if the change is so small as to be masked by a dominant background state.

Average values

The average value for a particular domain is particularly useful for comparing results for large numbers of models, for example Chapters 3, 8 and 9. It is especially useful as an indicator of pressurisation or gas velocity, permitting easy comparison between models with different permeabilities. In Comsol Multiphysics®, the average value is calculated by integrating the variable of interest over the surface (or domain) and dividing by the total area (or volume) of that surface (or domain).

Setting	Description
Time	The start time, end time and the time step size between them.
Time stepping	Refinement over the time step chosen. Here there are choices between free, intermediate or strict control over the time step chosen.
Physics selection	In a model with multiple physics, for example, Darcy's law and solid mechanics, it can be specified whether the model should be solved for both sets of equations, simultaneously, or for just one. This can be particularly useful to check the result of one physics environment before the second is introduced.
Mesh selection	It is possible to create multiple mesh sequences for a particular geometry. For complex geometries, it can be difficult to create the optimised mesh for the problem. Therefore, it is useful to create different meshes and solve for each to determine the best setup for the problem.
Initial conditions	This provides a starting point from which the final result for the study type can be calculated. For a stationary study, this would be lithostatic pressure, whilst for a time dependent study, an equilibrium solution from a previously solved study would be used.
Solver type	MUMPS, PARDISO or SPOOLES. All solver types use the method, and will result in the same end result. However, they vary in how they utilise the available computational capabilities. MUMPS is used in this study as it is fast and provides facilities for multicore and cluster computing to enable efficient solving of more computationally large simulations.
Results whilst solving	This forces Comsol Multiphysics® to display plots in the required dimension during solving. This is particularly useful for diagnosing problems in time dependent simulations.
Method and termination	Contains a variety of settings which determine the point at which a computation will terminate. The settings may be adjusted to aid with convergence problems arising from the complexity of certain simulations. For example, the Jacobian Update can be changed from "Minimal" to "On every iteration" which increases the stability for nonlinear problems. Other settings to avoid convergence problems are the maximum number of iterations and the tolerance factor.

Table 2.2: A description of the most important solver settings provided by Comsol Multiphysics®.

Gas storage and loss

Pressurisation above lithostatic pressure indicates the presence of gas within the system. This can represent temporal gas storage, where the region always contains gas but it can still be lost at the surface, or permanent storage due to low surrounding permeabilities preventing gas migration. This storage is permanent until a change occurs within the system and the gas is released.
The volume of gas lost from a particular domain is estimated according to Equation 2.25:

$$\begin{array}{ll} \Delta\rho A & \text{in 2D} \\ \Delta\rho V & \text{in 3D} \end{array} \tag{2.25}$$

In 3D models, the surface gas emission rate is approximated by Equation 2.26:

$$\rho_A A \boldsymbol{u} \tag{2.26}$$

Gas is stored within the porosity, therefore it is acknowledged that porosity has an important role in gas storage. However, the permeability controls the migration of gas from one region to another, and this work is primarily concerned with how changing degassing pathways affect the processes of gas storage and loss. Therefore, these processes will be described relative to the permeability, rather than the porosity.

2.5 Summary

In this work, Darcy's law and the continuity equation are combined to investigate the gas flow with respect to changes in permeability and pressure, and the momentum equation is used to model the associated displacement. These equations are coupled and solved using a finite element method within Comsol Multiphysics®. To derive a solution, the method requires a number of steps including, problem formulation; geometry creation and design; meshing; specifying the constraints; solving and post-processing. A variety of tools are utilised in each stage which have been documented in this chapter.
The aim of this modelling is to investigate the impacts of permeability on the behaviour of volcanic systems. Consequently a number of assumptions have been made regarding the additional variables used. The impact of these assumptions of the results will be assessed later in Chapter 10.1.
This method will be used to model a variety of scenarios beginning with a simple 2D stationary model investigating the effect of permeability on the gas pressure and

velocity. This is followed in subsequent chapters by more complex models looking at different volcanological phenomena and how they affect the system. In Chapters 8 and 9 3D models are used in an attempt to simulate surface observations. Finally, in Chapter 10, the method is used to model two specific case studies for Soufrière Hills and Santiaguito.

Chapter 3

The Conceptual Basic Model

This chapter illustrates some of the fundamental patterns in the results which may be obtained using the method described in Chapter 2. In particular, the influence different permeabilities have on a stationary volcanic system is investigated. A stationary system is defined as representing an equilibrium state of the volcanic system dependent upon the current permeability and pressure conditions applied.

3.1 The principal block model

Simple "block-style" models represent a simplified concept of a volcanic system at shallow depths. They encompass a central magma-filled block ("conduit"), surrounded on either side by the "wall-rocks" of the volcanic edifice and topped by an overburden ("lava dome") (Figure 3.1). Each domain is set to a specific permeability, and lithostatic pressure is applied to the exterior boundaries, as shown

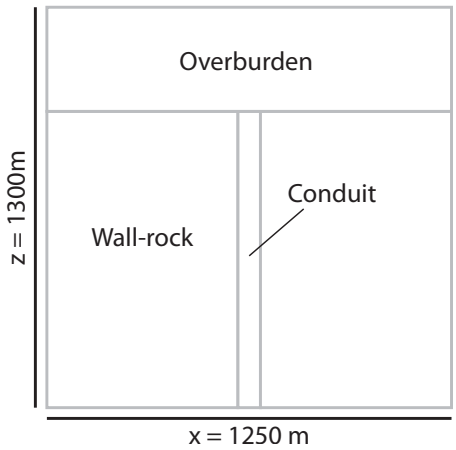

Figure 3.1: Setup for the principal block model with a central conduit surrounded by wall-rocks and topped by an overburden.

previously in Figure 2.4. The 2D models shown here are created using cartesian coordinates, therefore simulating a dyke.

In order to determine how different permeabilities affect the model results, a systematic parameter variation is carried out. Following the results obtained by permeability studies (e.g. Eichelberger et al., 1986, Klug and Cashman, 1996, Melnik and Sparks, 2002, Mueller et al., 2005, 2008), the permeability of each domain is varied within the range 10^{-16} to 10^{-8} m^2 in 10^2 increments, providing a catalogue of 125 stationary models. For each model, the average pressure and average gas velocity are plotted for the three domains comprising the volcanic system (conduit, dome and wall-rocks) (Figure 3.2).

These graphs (Figure 3.2) show significant variation in the pressurisation and gas velocity between the models, and both are extremely sensitive to changes in permeability within each domain. The pressure within the conduit increases with decreasing dome and wall-rock permeability because gas becomes confined. However, as the conduit permeability decreases, the wall-rock and dome have less of an impact in pressurising the conduit. Similarly, the gas velocity within the conduit decreases with decreasing conduit permeability. However, for both properties within the conduit, the dome has a greater influence than the wall-rock. As an example, for a conduit permeability of 10^{-8} m^2 the conduit pressure increases with decreasing dome permeability, but there is little change as the wall-rock permeability decreases. The pressurisation behaviour of the wall-rocks is very similar to that of the volcanic conduit, but lower in magnitude. The pressure in the wall-rocks decreases slightly with decreasing conduit permeability. However, the dome permeability appears to have the largest impact, as a decreasing dome permeability acts to confine the gas within the wall-rocks. For the gas velocity within the wall-rock, only the wall-rock permeability appears to have any effect. The pressurisation within the dome is significantly lower than that in either the conduit or wall-rocks, due to the lower lithostatic load. Decreasing the dome permeability increases the pressure in all domains. The highest dome pressure occurs with a high conduit permeability (10^{-8} to 10^{-12} m^2), a lower wall-rock permeability and a low dome permeability, for example models **23** (conduit: 10^{-8} m^2, wall-rock: 10^{-12} m^2 and dome: 10^{-16} m^2) and **24** (conduit: 10^{-8} m^2, wall-rock: 10^{-14} m^2 and dome: 10^{-16} m^2). For a high conduit permeability, a very high or very low wall-rock permeability results in a decreased dome pressure. If the wall-rock permeability is high, it does not act to confine the gas within the conduit, resulting in an overall lower pressurisation within the entire system. If the wall-rock has a very low permeability it confines the gas within the conduit, resulting in a localised dome pressurisation and therefore a lower overall average dome pressure. The gas velocity within the dome decreases with decreas-

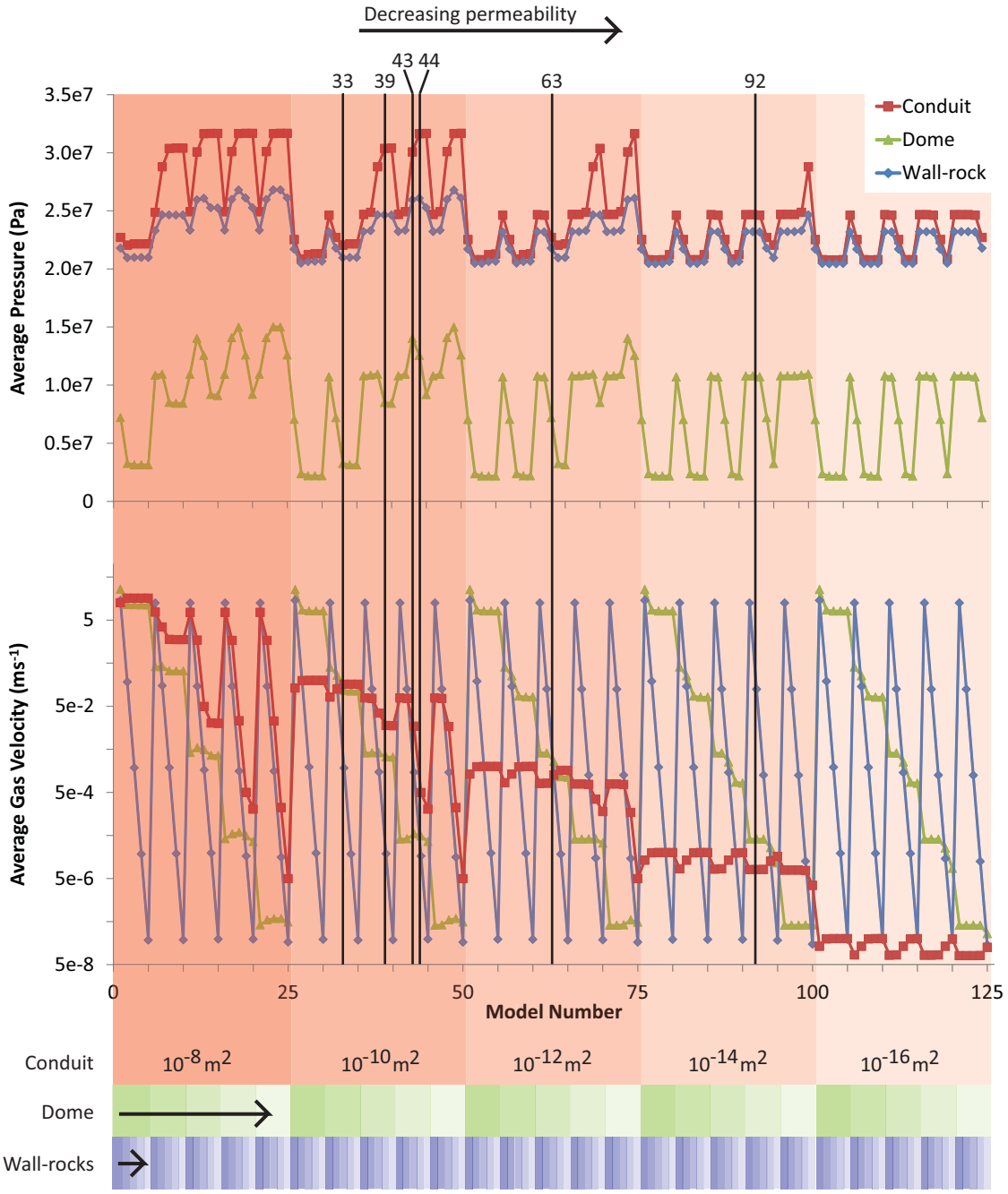

Figure 3.2: Average pressure (top) and gas velocity (bottom) for the conduit, dome and wall-rocks in each model. For each conduit permeability, there are five dome permeabilities and for each dome permeability, there are five wall-rock permeabilities. All permeabilities decrease from left to right by 10^2 decrements from 10^{-8} to 10^{-16}m^2. The numbered models are used as examples to show important features.

ing dome permeability but neither the wall-rock nor the conduit seem to have a significant impact.

With respect to the pressure spatial patterns, the models may be divided into six groupings, examples of which are shown in Figure 3.3[1]. The permeability conditions for each of the six example models is provided in Table 3.1. The changes in pressure are due to the permeability variations between each domain. However, these groupings are very broad and there are changes in the degree of pressurisation within each group dependent upon the permeabilities chosen. Furthermore, they do not take into account variations in gas velocity. Figure 3.4 shows the overpressure imposed by the gas, by subtracting the lithostatic pressure. Similar to the pressure patterns, these gas overpressure plots (Figure 3.4) show distinct variations across the six groupings, and help to identify which model configurations are more prone to pressurisation.

Table 3.2 and Figure 3.5 summarise the permeability conditions which result in the different pressure patterns characteristic of each group. All the models in Groups `1`, `2` and `3` show very little variation in pressure across the model runs, with only a slight variation in Group 1 occurring if the conduit and dome have the same permeability. In this case, there is a slight increase in pressure at the contact between the conduit and dome. However, in the case of Groups `4`, `5` and `6`, there is a marked increase in pressurisation when the conduit is several orders of magnitude more permeable than the surrounding wall-rocks and lava dome.

Model	**Conduit (m^2)**	**Wall-rocks (m^2)**	**Overburden (m^2)**
Group `1` (**33**)	10^{-10}	10^{-12}	10^{-10}
Group `2` (**63**)	10^{-12}	10^{-12}	10^{-12}
Group `3` (**92**)	10^{-14}	10^{-10}	10^{-14}
Group `4` (**44**)	10^{-10}	10^{-14}	10^{-14}
Group `5` (**39**)	10^{-10}	10^{-14}	10^{-12}
Group `6` (**43**)	10^{-10}	10^{-12}	10^{-14}

Table 3.1: Permeability conditions for the six example models shown in Figures 3.3 and 3.4.

[1]The pressure results for all 125 models may be viewed on the accompanying DVD.

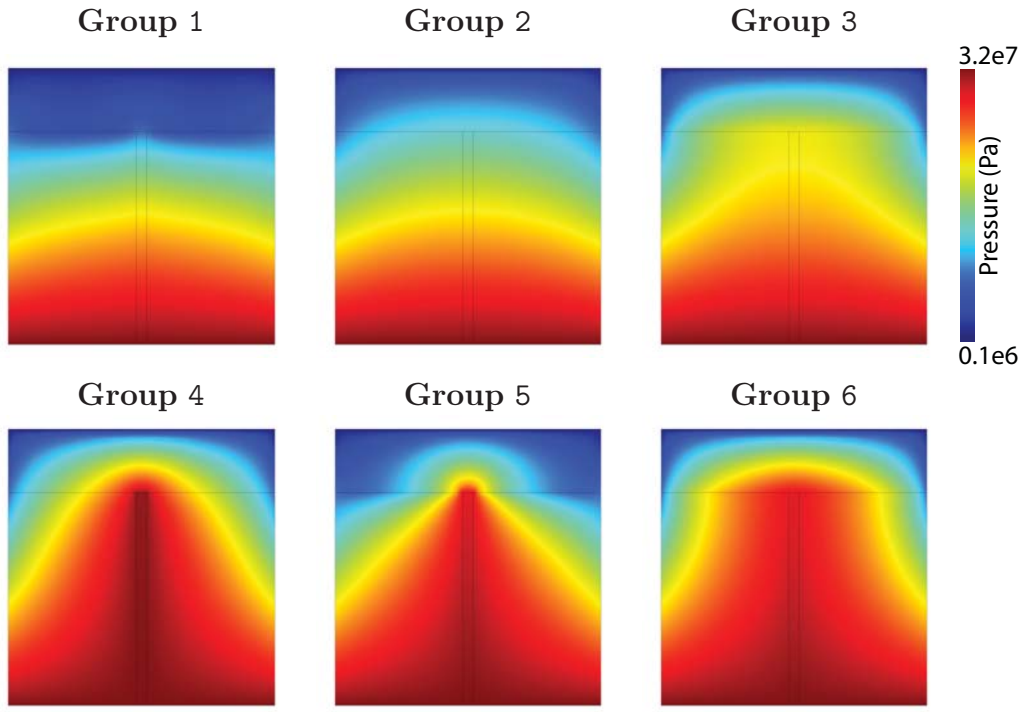

Figure 3.3: Examples from the six groups identified from the pressure pattern results. Models **33**, **63**, **92**, **44**, **39** and **43**, respectively.

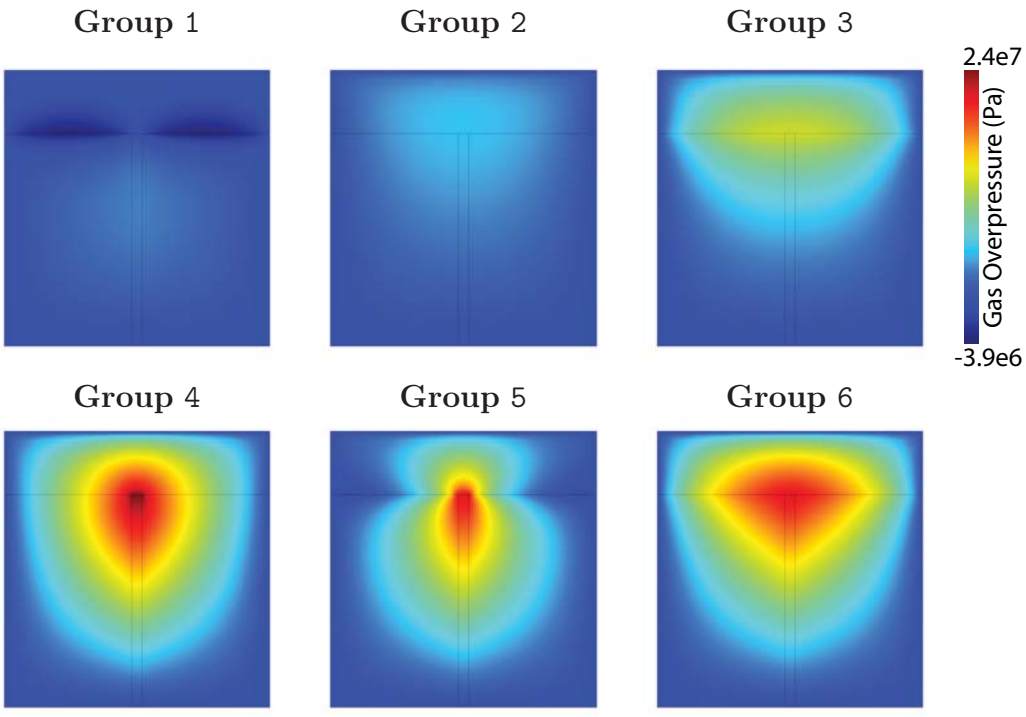

Figure 3.4: Gas overpressure derived, by subtracting the lithostatic pressure, for the 6 examples in Figure 3.3.

Group	Relative Permeability (k)
1	The dome and conduit permeabilities are equal, with a lower wall-rock k, or The conduit and wall-rocks have equal k, with a higher dome k, or Dome $k >$ conduit $k >$ wall-rocks k, or Dome $k >$ wall-rock $k >$ conduit k.
	A high dome permeability
2	All domains have equal k, or The wall-rock and dome have equal k, with a lower k in the conduit.
	No variation or less permeable interior
3	The wall-rock and conduit have equal k, with a lower dome k, or The dome and conduit have equal k, with a higher wall-rock k, or Wall-rock $k >$ conduit $k >$ dome k, or Wall-rock $k >$ dome $k >$ conduit k.
	Higher wall-rock permeability
4	The wall-rock and dome have equal k, with a higher conduit k.
	More permeable conduit
5	Conduit $k >$ dome $k >$ wall-rock k.
	More permeable conduit
6	Conduit $k >$ wall-rock $k >$ dome k.
	More permeable conduit

Table 3.2: Permeability (k) criteria for the six groups. A more permeable conduit is the key parameter for groups 4-6. The main controlling factor determining the group behaviour is shown in italics.

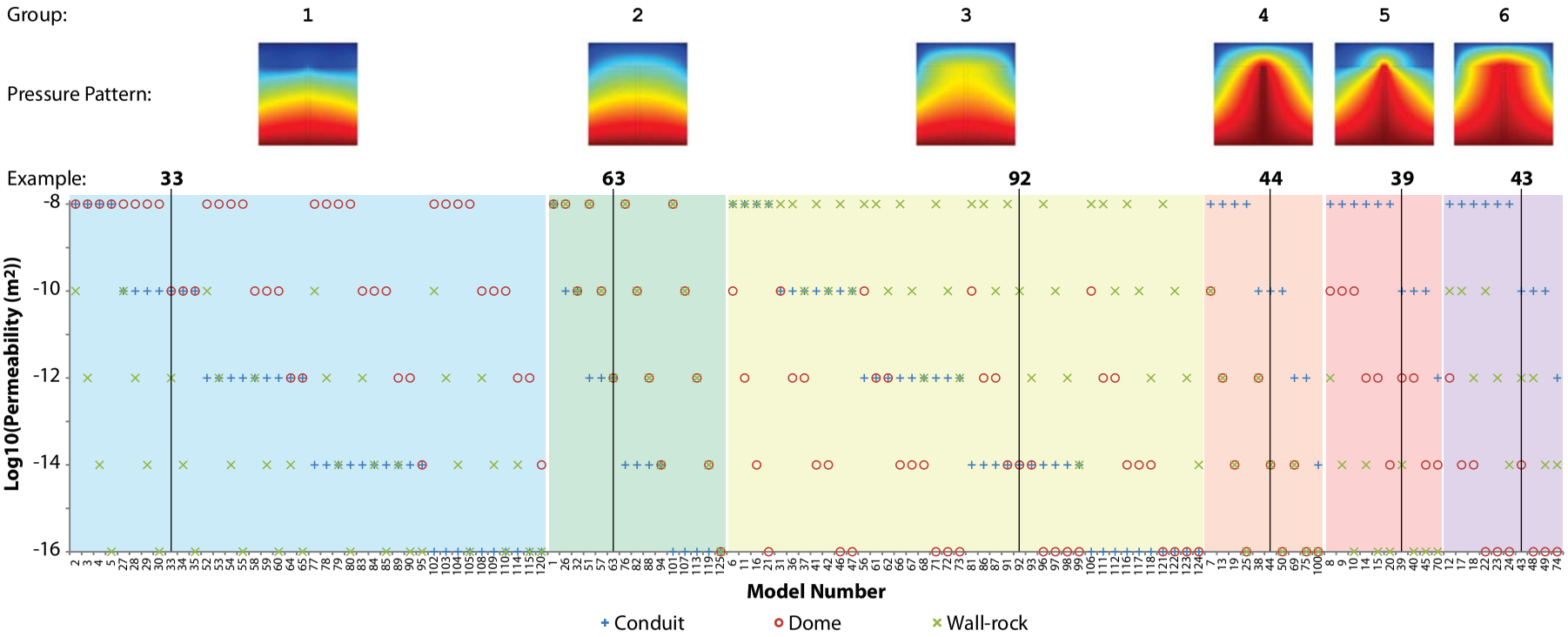

Figure 3.5: Permeability criteria determining pressurisation pattern. See Table 3.2 for details.

The main controlling factor causing the pressure pattern of Group 1 is the higher dome permeability leaving the gas in the underlying domains unconfined, consequently leading to a very low pressurisation. Group 2 shows a low pressurisation which is only slightly higher than that of the background lithostatic pressure. This is derived either when all the domains have the same permeability or else the conduit has a lower permeability, with the wall-rock and dome permeability equal. The important factor controlling Group 3 is the higher wall-rock permeability. Group 4 shows a very high pressurisation because the conduit has the highest permeability, but it is confined by the lower permeabilities of the wall-rock and overlying dome. In both Groups 5 and 6 the conduit is again the most permeable. However, in Group 5 the dome permeability is greater than that of the wall-rocks, consequently leading to a very localised pressure pattern within the dome. In contrast, the permeability of the dome is lower than that of the wall-rocks in Group 6 and acts to confine both the conduit and the wall-rock.

Groups 1 and 2 show only low levels of pressurisation and, in their current states, are unlikely to inhibit gas motion. However, Groups 3 - 6 show more extreme pressurisation patterns and are consequently more likely to result in explosive volcanic eruptions.

Figure 3.6 shows the vertical pressure profiles for the models in Figures 3.3 and 3.4. They highlight the pressure variation present in the selected examples. Groups 1 and 2 show very little change from lithostatic pressure (linear increase from $0.1 - 32$ MPa). Whilst 3 - 6 show increasing pressurisation within the conduit compared to the lithostatic pressure of the far wall-rock. In particular, Groups 4 - 6 show a very little change in pressure with decreasing depth within the conduit and sections of the wall-rocks immediately adjacent. Furthermore, this high pressure within the conduit may drive the gas towards the wall-rock.

3.2 Conduit gas velocity and pressure development

Here, gas velocity and pressurisation changes are investigated when the conduit is surrounded by wall-rocks and a dome having equal permeability. Figure 3.7a shows the sensitivity of the conduit gas velocity to the model permeabilities. The conduit gas velocity decreases with decreasing permeability, regardless of whether the less permeable region is the conduit or the wall-rocks and dome. For high conduit permeabilities, gas velocity is controlled by the wall-rock and dome permeability, whilst for low conduit permeabilities, velocity is controlled by the low-permeability conduit. The conduit permeability appears to be the dominant controller, with the surrounding edifice permeability playing a secondary role.

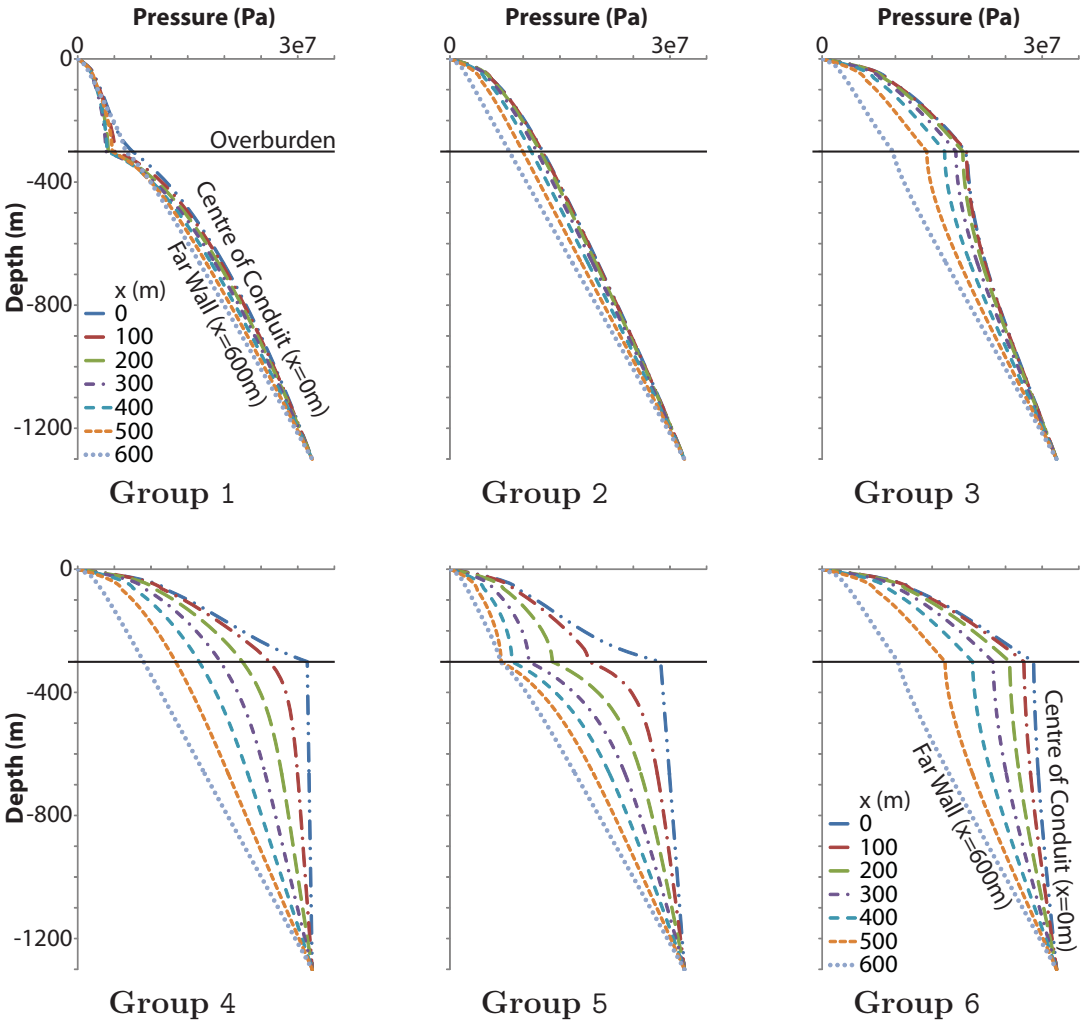

Figure 3.6: Vertical pressure profiles for the models in Figures 3.3 and 3.4. The profiles are taken at 100 m intervals from the centre of the conduit at 0 m. The boundary between the wall-rock and the overburden is marked at 300 m depth. Data plotted for the example models: **33**, **63**, **92**, **44**, **39** and **43**, respectively.

The pressurisation is most strongly controlled by relative, rather than actual, permeabilities within the model (Figure 3.7b and c). The lowest conduit pressurisation occurs when the conduit permeability is lower than or equal to that of the surrounding wall-rocks and dome. However, once the conduit permeability exceeds that of the surroundings, the pressure increases sharply and reaches a maximum once the surrounding permeability is approximately four orders of magnitude lower. Decreasing the wall-rock and dome permeability further, leads to no change in the pressurisation. For example, for a conduit permeability of 10^{-10} m^2 the pressure is lowest with a surrounding permeability of 10^{-8} m^2 with a value of 22.7 MPa, increasing to 31.7 MPa once the surrounding permeability drops to 10^{-14} m^2. The pressure remains at this level even when the wall-rock and dome permeability is de-

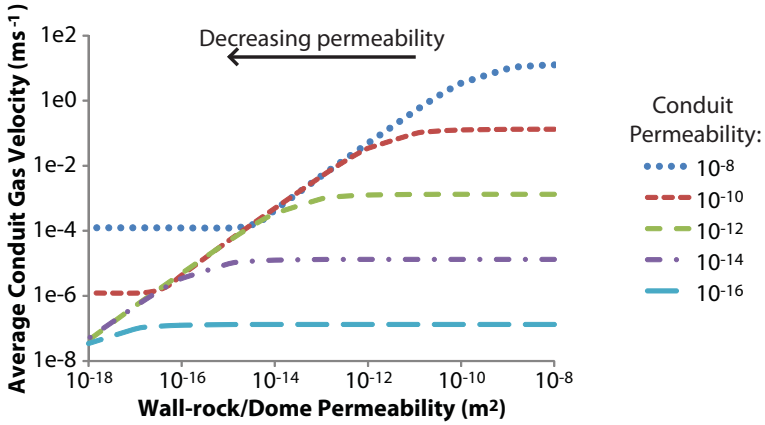

(a) Average conduit gas velocity

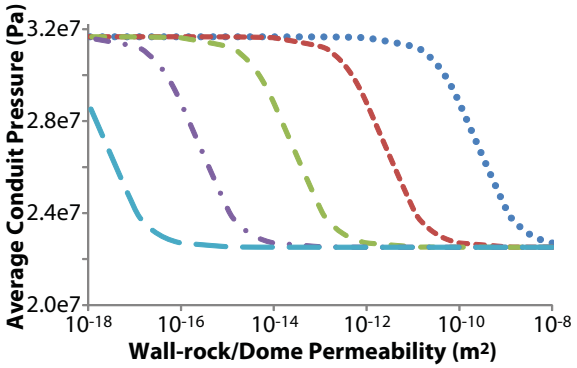

(b) Average conduit pressure

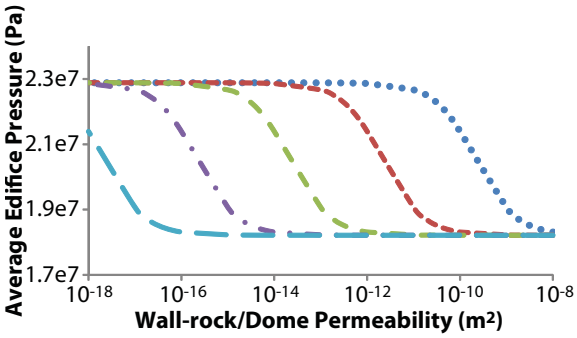

(c) Average edifice pressure

Figure 3.7: Average conduit gas velocity (a), conduit pressure (b), and edifice (wall-rocks and dome) pressure (c) against wall-rock/dome permeability for different conduit permeabilities.

creased to 10^{-18} m^2. Consequently, pressurisation is dependent upon the difference in permeability between the conduit and the surrounding edifice, whilst gas velocity is more strongly controlled by the actual permeability values.

Figures 3.8 and 3.9 show pressures and gas velocities respectively, for the models with a conduit permeability of 10^{-10} m^2 and decreasing wall-rock and dome permeabilities. The decrease in permeability within the wall-rocks and dome could result

from sealing the degassing pathways (Section 1.1.4). The pressure patterns show (a) and (b) are members of Group 2 (from Figure 3.5, Table 3.2), whereas (c) - (f) are from Group 4. The lower surrounding permeabilities in (c) - (f) act to confine the gas within the conduit leading to pressurisation and a maximum gas overpressure of $\approx$ 20 MPa. Such a high gas overpressure will exceed the tensile strength of the magma and wall-rocks at this depth, resulting in failure (Sparks, 1997). This is a stark reminder that a volcanic system, that initially appears harmless in terms of pressurisation, can quite easily become unpredictable and prone to violent eruptive behaviour.

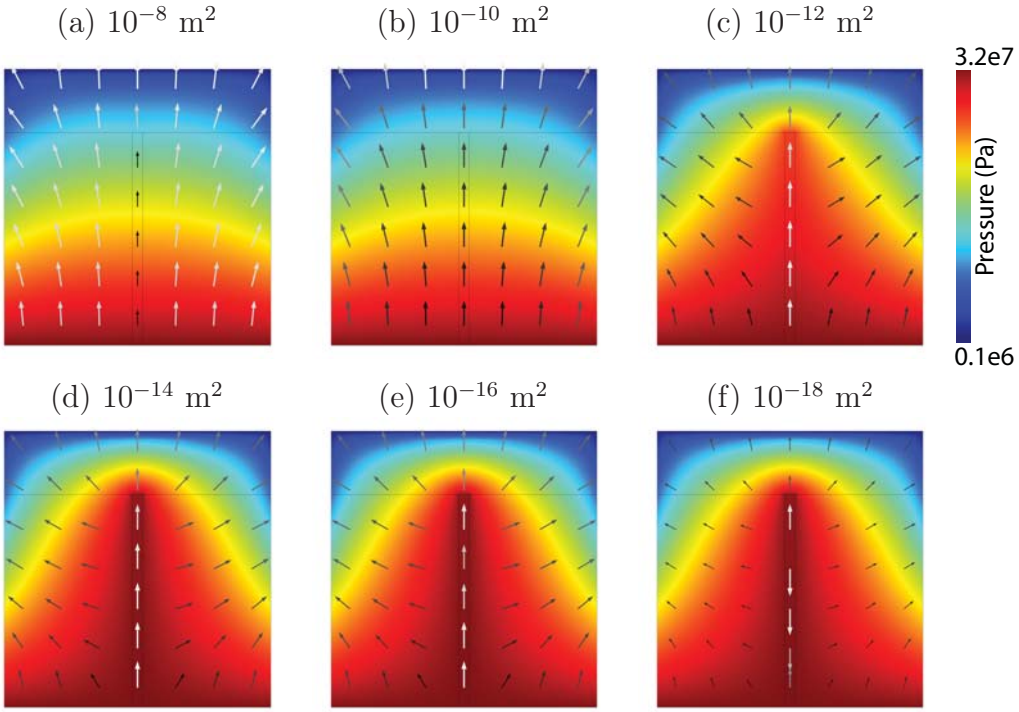

Figure 3.8: Pressure plots where the conduit has a permeability of 10^{-10} m^2 for different edifice (wall-rock and dome) permeabilities. (a) and (b) show patterns consistent with Group 2 (from Figure 3.5, Table 3.2), whereas (c)-(f) represent Group 4. Whilst the edifice permeability is equal to or greater than the conduit permeability, the edifice gas velocity is greater. However, once the edifice is less permeable than the conduit, the conduit is the region of greatest gas velocity. (f) shows downward flow due to the high conduit permeability and pressure, surrounded by a very low permeability preventing gas escape from the conduit. The arrows represent the gas velocity on a logarithmic scale, but due to the large velocity differences between the models, the arrow colouration is on different scales, increasing from black to white.

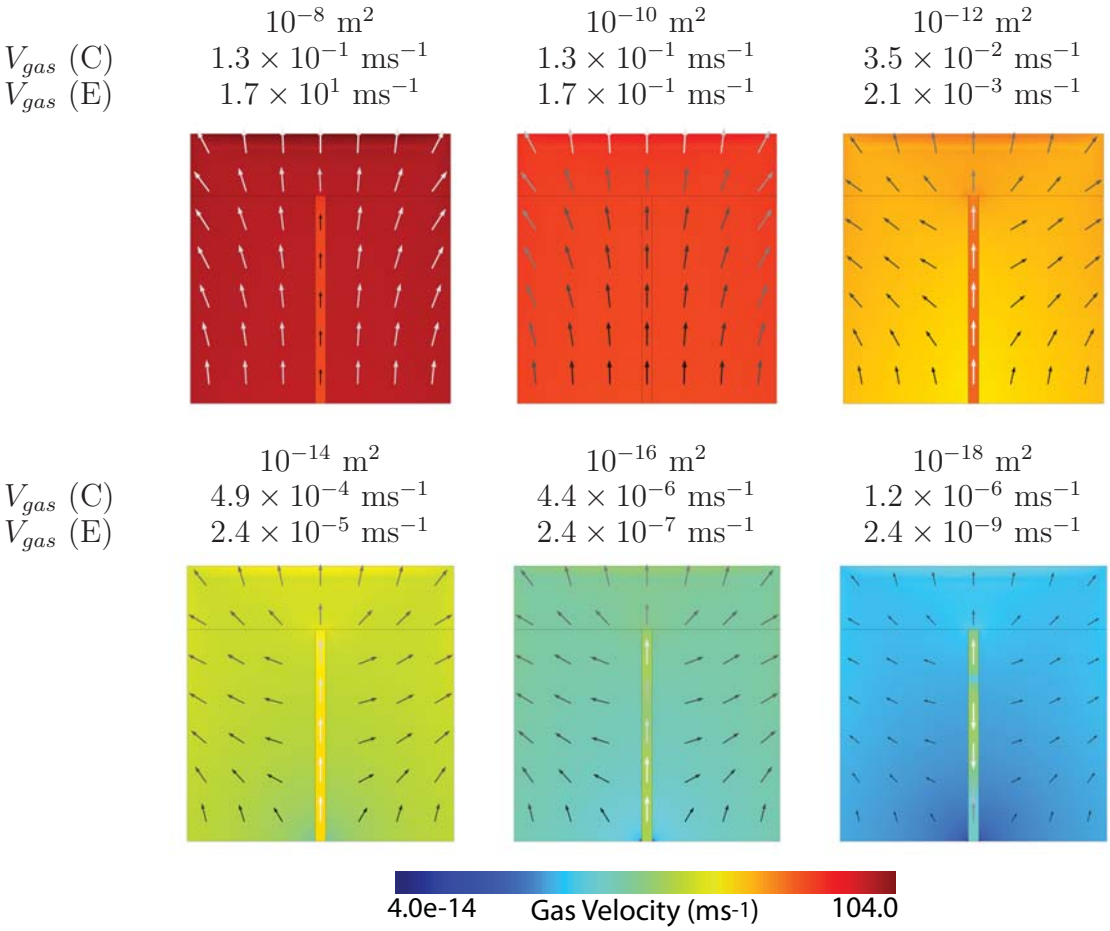

Figure 3.9: Gas velocity plots, on a logarithmic scale, where the conduit has a permeability of 10^{-10} m^2 for different edifice permeabilities. The average gas velocity in the conduit and edifice are quoted as V_{gas} (C) and V_{gas} (E), respectively. The arrows also represent the gas velocity on a logarithmic scale. However, due to the large velocity differences between the models, the arrow colouration is on different scales, increasing from black to white.

3.3 Summary

This simplistic 2D model highlights the action of Darcy's law where permeability, pressurisation and gas velocity are strongly linked. The resulting gas flow and pressure distribution are highly dependent upon the relative permeabilities within the volcanic system and may be extremely sensitive to seemingly small changes. If the conduit has a lower permeability than the surroundings, the gas within is not confined, leading to little or no pressurisation. However, if either the conduit or wall-rock have a higher permeability than the dome, the dome acts to confine the gas leading to pressurisation. The greatest pressurisation is seen when the gas within a highly permeable conduit is confined by very low permeability wall-rock and dome (seal/plug). Furthermore, this pressurisation permits greater gas storage

at shallow depths which could be released after removal of the overburden (dome collapse event).

Groups 1 and 2 represent a volcano which can freely degas and any eruptive activity occurring as effusive dome building because the overpressure is not high enough to trigger an explosive eruption. In contrast Groups 3 - 6 represent volcanic systems which are becoming increasingly sealed leading to decreased degassing at the surface, increasing internal gas overpressures (above the tensile strength of the conduit and wall-rocks), and would likely lead to an explosive eruption. However, as the models have shown, a volcano can easily change behaviour, from unpressurised to pressurised, by decreasing the edifice permeability by as little as two orders of magnitude. Following the experiments of Moore et al. (1994), Edmonds et al. (2003b) suggest a greater permeability decrease of three orders of magnitude could occur over a time period of as little as 2-6 days, giving little warning. This switch in behaviour would be indicated by decreased surface gas emissions in accordance with those measured prior to explosive events at Soufrière Hills (Edmonds et al., 2003b) and Merapi (Surono et al., 2012).

In subsequent chapters, time dependency is used to investigate the response to permeability variations. The effects on surface displacement are also considered in order to model specific scenarios found at different volcanoes.

Chapter 4

A Time-Dependent Example - "Dome Collapse"

Dome collapse events are regular occurrences on active silicic volcanoes and can have profound implications for populations in the vicinity. They involve either partial or complete removal of the lava dome material and a corresponding unloading and decompression of the conduit and surrounding country rock. Examples of trigger mechanisms for dome collapses include seismicity, pressurisation, lava extrusion, instability of the growing dome and heavy rainfall (e.g. Voight and Elsworth, 2000, Watts et al., 2002, Williamson et al., 2010, Wadge et al., 2014).

The largest recorded dome collapse on Soufrière Hills volcano occurred on 12-13 July 2003 and involved the removal of 210×10^6 m^3 (Edmonds and Herd, 2005, Herd et al., 2005, Edmonds et al., 2006, Voight et al., 2006) (Figure 4.1), 80 % of which was removed in about 2.6 hours (Herd et al., 2005). Associated with the dome collapse was a 15km high ash cloud and an emission of 100 ± 30 kt SO_2 (Herd et al., 2005). On 20 May 2006, a similar dome collapse event removed 115×10^6 m^3 of dome material with 85% removed within 35 minutes (Trofimovs et al., 2012). This was a smaller dome collapse than that of the July 2003 event, but the resulting ash cloud reached 17 km into the atmosphere with the volume of SO_2 estimated at 200 kt - twice that of the previous event (MVO, 2006, Loughlin et al., 2010).

Figure 4.2 shows photographs, before and after the large 2010 dome collapse of the Merapi lava dome. The eruption cloud reached elevations of up to 17 km and emitted $\approx$ 440 kt SO_2 (Surono et al., 2012).

It has been suggested that such high eruption clouds and other gas expulsions after dome collapse events are evidence for gas storage at shallow depths of $\approx$ 300m within the volcanic edifice (Edmonds et al., 2003b, Green and Neuberg, 2005, Herd et al., 2005, Jousset et al., 2013).

Dome collapse events are particularly dangerous due to the generation of pyroclas-

(a) 31 May 2003 (Before) (b) 12 August 2003 (After)

Figure 4.1: Photographs showing the Soufrière Hills volcano lava dome, taken from Windy Hill, before and after the July 2003 dome collapse (Mattioli et al., 2004).

(a) September 2010 (Before) (b) June 2011 (After)

Figure 4.2: Before and after the 2010 dome collapse of Merapi lava dome (Surono et al., 2012).

tic flows. The situation at Soufrière Hills is made even more precarious due to the proximity of seawater (Edmonds and Herd, 2005). During the 2003 event, hot pyroclastics interacted with colder sea water to create a base surge which subsequently travelled up to 4 km inland and affected an area of 7 km^2, thereby devastating a much larger area than the original dome collapse (Edmonds and Herd, 2005).
Whilst a dome collapse comprises a large number of complex physical processes, for example changes to the internal stress, fragmentation wave and ejection of volcanic material (Fowler et al., 2010), only the aspect of unloading and decompression on the resident magma is within the scope of this study.

4.1 An unloading event

An unloading event is modelled using a simplistic 2D "block-style" model (Figure 4.3), similar to those in Chapter 3, with the permeability in the conduit ex-

ceeding that of the surrounding wall-rock and overburden (Table 4.1). Following the observations of decreased gas emissions prior to large dome collapse events, implying reducing permeability (Edmonds et al., 2003b, Surono et al., 2012), the overburden is "sealed" with a low permeability. The unloading occurs over a period of 20 minutes with the "removal" of 300 m of dome which is crudely simulated by increasing the permeability of the overburden through time from 10^{-16} to 10^{-6} m[21]. This permeability increase represents the increase in free-space post dome-collapse and is sufficiently high to result in atmospheric pressure throughout the overburden domain. Concurrently, the lithostatic pressure along the boundaries is decreased by 7.46 MPa (equivalent to a load of 300 m) to simulate the diminished load.

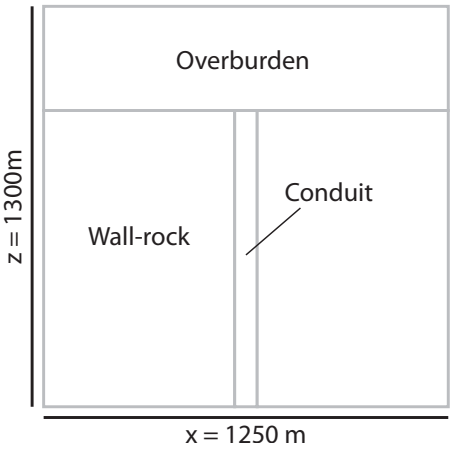

Figure 4.3: Setup for the unloading event with a central conduit surrounded by wall-rocks and topped by an overburden.

Domain	**Permeability (m^2)**		**Porosity**
	t_1	t_2	
Conduit	10^{-10}	-	0.3
Edifice	10^{-12}	-	0.3
Overburden	10^{-16}	10^{-6}	0.3

Table 4.1: Permeability and porosity conditions for the Unloading Model. High permeabilities are set to the conduit and edifice, with a very low permeability overburden. This results in a high initial pressurisation.

[1]Other attempts to simulate a dome collapse include neglecting the dome domain and controlling the base dome pressure boundary condition; or using a moving boundary to decrease the domain thickness. However, the presented method of increasing the permeability is the easiest method and less prone to solution problems.

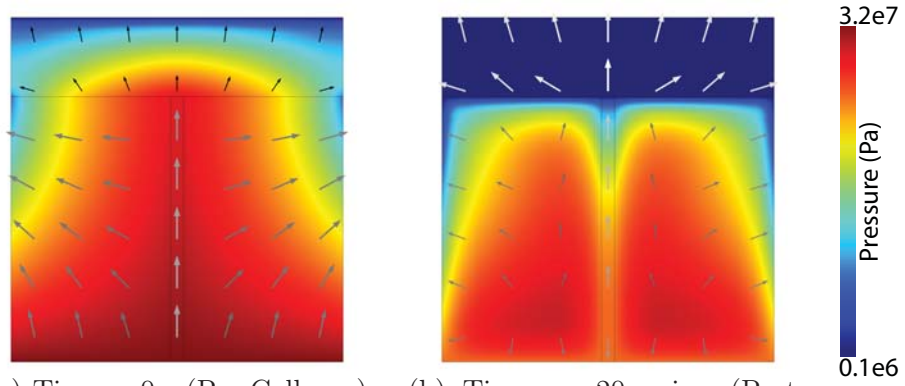

(a) Time = 0 s (Pre-Collapse)

(b) Time = 20 mins (Post-Collapse)

(c) Time = 2 hrs (Post-Collapse)

(d) Time = 14 hrs (Post-Collapse Equilibrium)

Figure 4.4: Dome collapse model where the conduit has a permeability of 10^{-10} m^2, wall-rocks and dome of 10^{-16} m^2. The arrows show the gas velocity direction and magnitude on a logarithmic scale from 3.14×10^{-7} to 15.2 ms^{-1} (black to white).

Figure 4.4a shows the initial pressure, prior to the collapse. This represents a member of Group 6 from Chapter 3. The low permeability overburden induces pressurisation of the system. The dome collapse event results in decompression of the underlying material, most rapidly within the conduit region of highest permeability (Figure 4.4b). Figure 4.4c shows the state of the system after 2 hours. The model predicts a significant time lag for the pressure and gas velocity within the edifice to resume an "equilibrium state" after the dome collapse (Figure 4.4d).

Figure 4.5 shows a time history for the duration of the dome collapse and shortly after. This plot shows data for three points within the model, located at the base of the dome, centre of the conduit and within the edifice. The pressure for the base of the dome is controlled by the decrease in permeability imposed to simulate the collapse. The pressure within the conduit begins to reduce seconds after the onset of the collapse, and continues to decrease sharply. In contrast, it takes several minutes for the pressure within the remaining edifice to respond to the unloading.

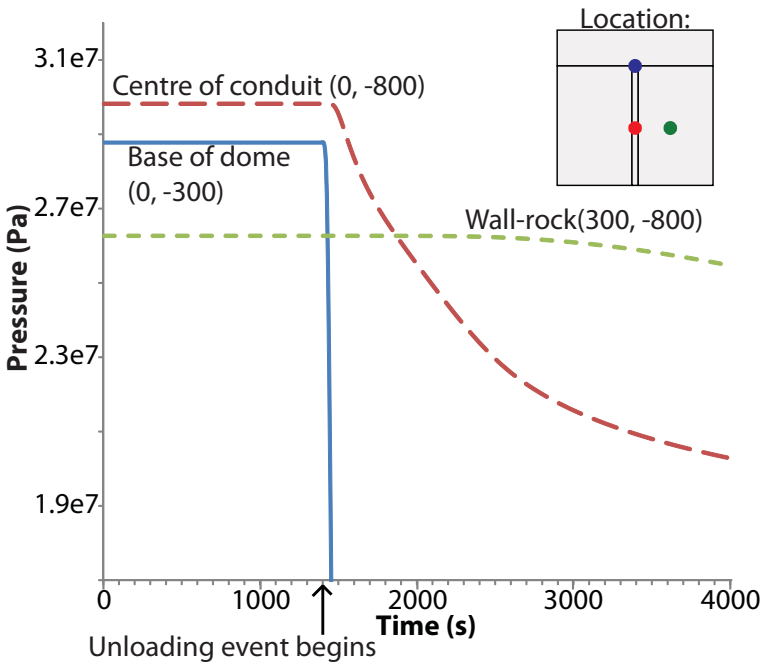

Figure 4.5: Time sequence for the dome collapse model. Data taken for the centre of the conduit, base of the dome and within the edifice, the locations of which are shown (inset). Exsolution of stored gas would occur as soon as the pressure decreases - most rapidly within the domains of the conduit and dome.

Once it commences, the rate of declining pressure within the edifice is slower than in the conduit. Exsolution of stored dissolved gas would commence as soon as depressurisation begins.

The highest gas velocity recorded for this model occurred 10 minutes after the onset of the collapse, with a peak gas velocity of 90 ms^{-1}. After this peak, the gas velocity drops to $8 - 15$ ms^{-1}. Because the degassing pathway in this instance is the entire width of the conduit, such high gas velocities would result in turbulent flow, which is beyond the scope of this model (Appendix B).

Using the solubility law, a decrease in average conduit pressure of 14 MPa in this model during the "dome collapse" event corresponds to an increase of gas (due to exsolution) of 1.5 wt% or ≈ 40 kgm^{-3}. Consequently, a source term (Equations 4.1 and 4.2) is included in this model to account for the additional sources of gas due to exsolution.

$$\frac{\partial}{\partial t}\nabla \cdot (\nabla n_{ex}\rho_r) = Q_m \tag{4.1}$$

$$n_{ex} = n_{tot} - K\sqrt{P} \tag{4.2}$$

Figure 4.6 shows this source term affects the model results, although, the effects

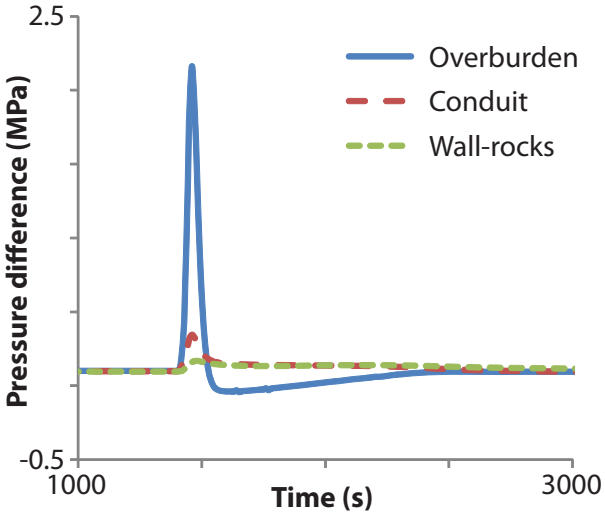

Figure 4.6: The difference in average pressure for each domain with the source term compared to without. The total gas content used is 7 wt.%.

generated by the dome collapse event itself last approximately 1200 seconds, which corresponds to the duration over which the unloading event is modelled. However, the greatest change occurs in just 125 seconds. The difference is relative to the change in pressure across each domain. Consequently, the overburden experiences the greatest change, followed by the conduit.

4.2 Summary

This is a very simplistic approach to modelling an unloading event in 2D and consequently neglects many of the effects which occur during a dome collapse. The "collapse" of the dome is crudely simulated as an increase in the permeability, whilst in reality the material is removed. Furthermore, the change in lithostatic load along the boundary conditions should be calculated based upon the response time of the material and should not be imposed, as it is in this study. However, the model serves as a good example for modelling the gas flow in time and consequently will lead to more complex temporal models in forthcoming chapters. Furthermore, it highlights that the time a region takes to respond is dependent upon its permeability. The greater the permeability, the faster the domain responds to the change. Consequently, events such as dome collapses continue to exert changes even after the dramatic visible effects have ceased. This model also serve to highlight the results must be analysed in conjunction with the validity of Darcy's law (Appendix B). In particular, the high gas velocities generated within the conduit indicate turbulent flow, which is beyond the scope of Darcy's law. However, Darcy's law, modelling

laminar flow, indicates the maximum gas velocity for a given scenario, which is still a useful indicator providing an upper limit for gas emissions.
In Chapter 5 the implications of brittle failure are investigated before looking at sealing gas escape routes at shallow levels in Chapter 6.

Chapter 5

Gas Escape Through Fracture Zones

Several studies link gas escape to fracture zones that are generated by brittle failure of the magma. Tuffen et al. (2003) propose a mechanism whereby stress accumulation in a viscoelastic magma leads to the generation of fractures through which gas can escape. Neuberg et al. (2006) relate the generation of low frequency earthquakes at Soufrière Hills to brittle failure along the conduit-wall boundary as the magma ascends. Lavallée et al. (2008, 2011) show that although the formation of fracture zones do not necessarily lead to accelerated ascent rate, the acceleration of ascent (and strain) rate does result in the formation of fractures. According to these studies, brittle failure in magma as it ascends will produce a system of cracks in a fracture zone along the conduit wall which will act as gas escape routes, resulting in an increase in the permeability within these regions. These shear fractures are thought to be associated with ring-shaped degassing at volcanoes such as Santiaguito (Bluth and Rose, 2004, Holland et al., 2011), and degassing around spines at Mt. St Helens (Gaunt et al., 2011, 2012, Pallister et al., 2013).
The purpose of this chapter is to investigate the effects of these fracture zones on the degassing of active volcanic systems by increasing the permeability at the margin between the conduit and wall-rocks. Finally, deformation modelling is used to show how the presence of fracture zones may impact surface displacement.

5.1 Fracturing of the conduit-wall boundary

A simplistic "block-style" model is used with a central conduit, adjacent to wall-rocks (Figure 5.1) with two 10 m wide domains representing narrow zones on either side of the conduit, where an increasing permeability is modelled due to the development of a propagating fracture zone. The permeability of the conduit is higher than that of the wall-rocks and initially the "fracture zones" have a very low permeability, simulating the case where they may be sealed (Table 5.1). The fractures are modelled

as an increase in permeability from 10^{-16} to 10^{-6} m^2.
In the first part of this chapter several models are run with this configuration, but for different fracture behaviours: instantaneous up the entire conduit-wall boundary; propagating upwards; upward propagating but progressively resealed; and downwards propagating. The starting equilibrium position for each model run is shown in Figure 5.2. Initially, the pressure distribution and gas behaviour are determined by the lithostatic pressure and variation in permeability. The lower permeability of the conduit walls prevents gas from escaping laterally.

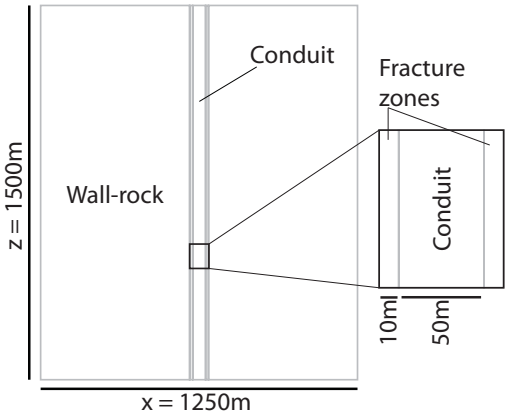

Figure 5.1: Setup for the brittle failure model showing the location of the conduit, wall-rocks and fracture zones. The geometry is very similar to that used previously in Chapters 3 and 4, however it has been modified to include a spine and two fracture zones either side of the conduit.

Domain	**Permeability (m^2)**		**Porosity**
	$\mathbf{t_1}$	$\mathbf{t_2}$	
Conduit	10^{-10}	-	0.5
Wall-rocks	10^{-12}	-	0.1
Fracture zones	10^{-16}	10^{-6}	0.3

Table 5.1: Permeability and porosity values for the gas escape through fracture zones model. The conduit and wall-rocks are simulated with high permeabilities, whilst the fractures zones are initially sealed. A high post-fracturing permeability of 10^{-6} m^2 provides an upper limit for the scenario.

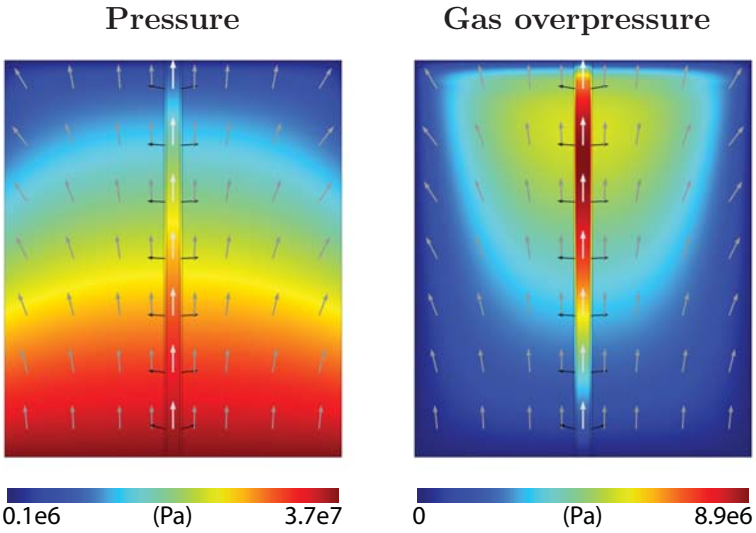

Figure 5.2: Initial equilibrium pressure and gas overpressure for the model. Gas velocity arrows increase logarithmically between 3.9×10^{-7} and 0.3 ms^{-1} from black to white.

5.1.1 Instantaneous fracturing

In this first example, the fracturing is "instantaneous" up the entire length of the conduit-wall margin. Figure 5.3 shows the pressure, pressure change and gas overpressure results for the model at two time-steps: immediately after fracturing and the end equilibrium position. Once the fracturing occurs, there is a small decrease in average pressure within the conduit of 0.5 MPa. However, the conduit rapidly repressurises and returns to a level 0.002 MPa higher than the initial. The average pressure within the wall-rocks rises by 1 MPa as the gas is permitted to escape horizontally through the wall-rocks. Due to the lower wall-rock permeability, the wall-rocks are much slower to respond than the more permeable conduit. The main degassing route has become the fractures which provide an unrestricted escape path to the surface. However, the average pressure within the fractures has also risen by 1.3 MPa due to the surrounding low permeabilities.

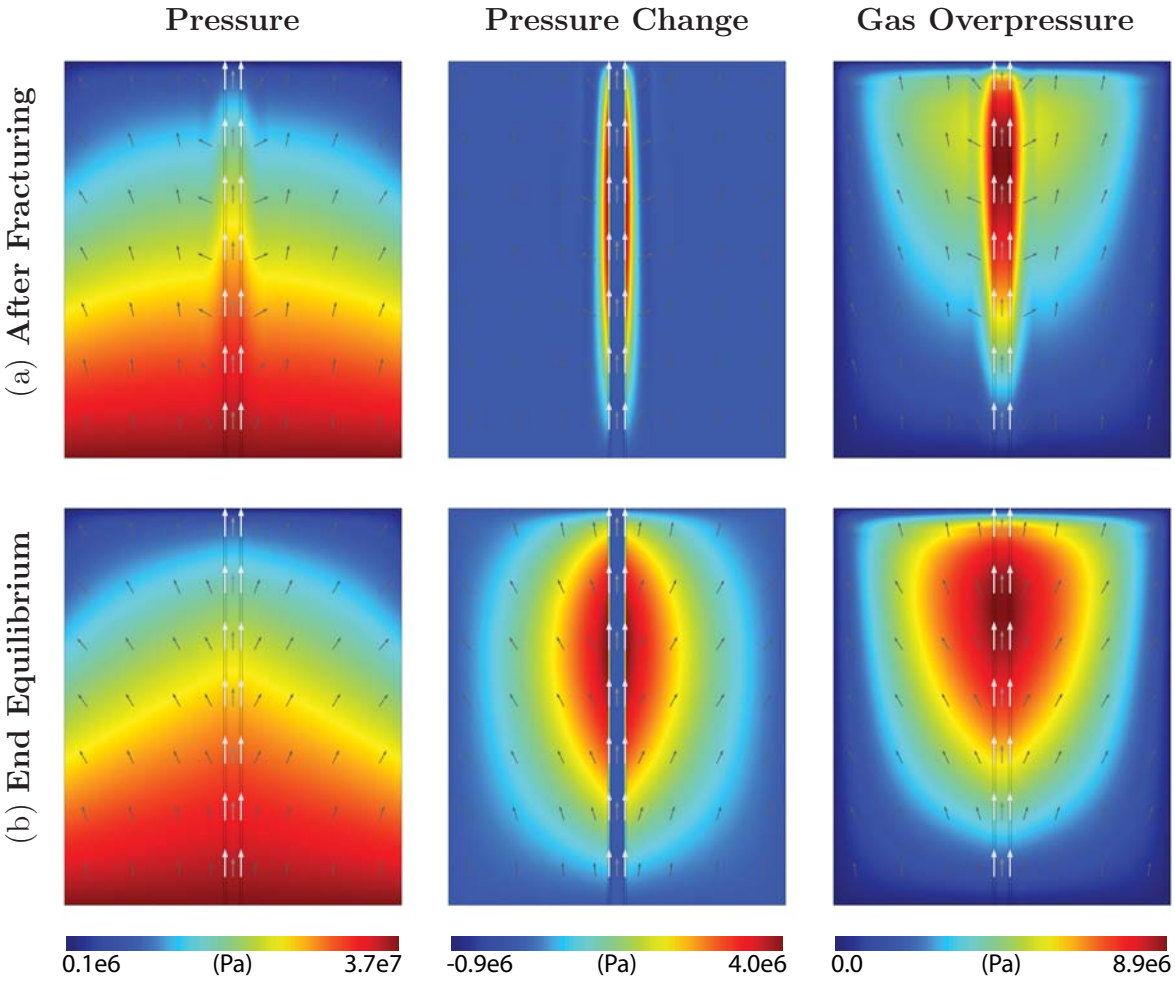

Figure 5.3: Pressure, pressure change and gas overpressure for instantaneous fracture of the conduit-wall margin. The "instantaneous" fracturing is modelled with a duration of 100 seconds, however, it takes the model 13 hours to reach equilibrium. Gas velocity arrows within the conduit and wall-rocks increase on a logarithmic scale between 8.8×10^{-4} and 0.3 ms^{-1} from black to white.

5.1.2 Propagating shear fractures

These fracture zones have been suggested, by Neuberg et al. (2006), as a potential trigger mechanism for low frequency earthquakes. However, fractures which are generated instantaneously up the length of the conduit-wall margin to the surface are unlikely to generate the localised depth signals observed. Consequently, in this second example, the fracturing begins at a depth of 1500 m and propagates vertically to the surface over an arbitrary period of 100 minutes.

The pressure, pressure change and gas overpressure results are shown in Figure 5.4. In Figure 5.4a, fracturing of the conduit-wall margin has begun and the fractures extend to 700 m depth. In response to this brittle failure, the pressure has increased through the conduit and corresponding wall margin where the fractures have devel-

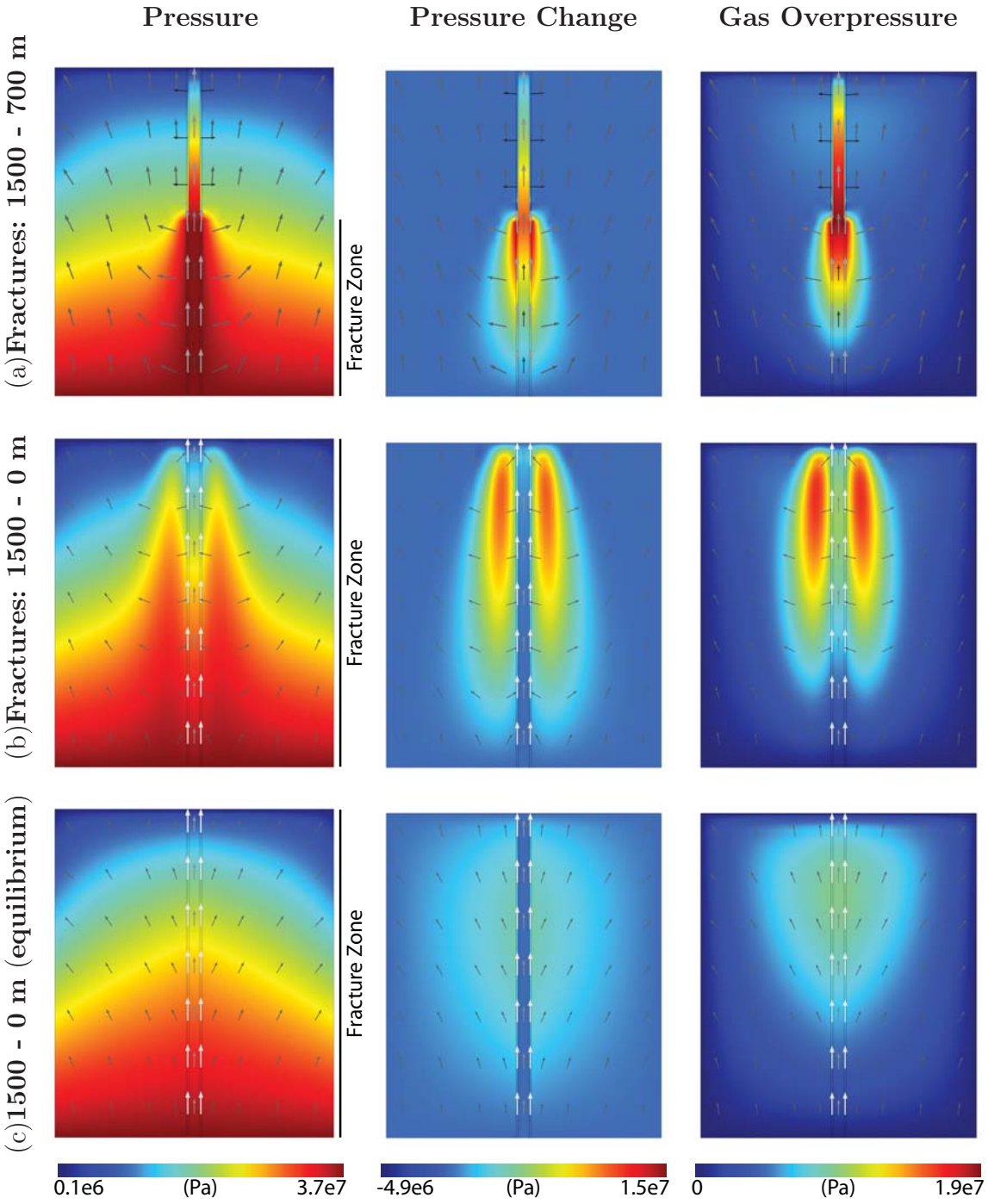

Figure 5.4: Brittle failure model, where a system of fractures propagates up the margin from 1500 m depth to the surface. The conduit has a permeability of 10^{-10} m^2, the wall-rocks of 10^{-12} m^2. The fractures are simulated by increasing the permeability of two narrow zones at the conduit margin from 10^{-16} to 10^{-6} m^2. Three different time-steps are shown from the temporal model: a. where the system of fractures has propagated upwards 800 m to a depth of 700 m; b. the fracture zone has reached the surface; c. the system has resumed equilibrium. There is no change to the pressure along the boundary condition, therefore the equilibrium position is the same as that for Figure 5.3. Gas velocity arrows within the conduit and wall-rocks increase logarithmically from black to white with a range of 8.7×10^{-4} and 0.3 ms^{-1}.

oped. However, the greatest pressure increase is seen within the fractures and the wall-rock immediately adjacent (Figure 5.5). In the conduit, the greatest pressurisation is seen where the top of the fracture is located, and it decreases away from this point, vertically, in both directions. However, in the fractures and wall-rocks, the greatest pressurisation is also seen at the top of the fracture and decreases gradually below. This pressurisation is the result of the highly permeable fractures being capped by unfractured, and therefore lower permeability, material above. Consequently, this could provide a suitable environment for the storage of considerable volumes of gas. There is no pressurisation of the fractures and wall-rocks seen above the fracture's extent. The fracture development prompts a more vigorous horizontal gas flow along the wall margin. Furthermore, the fracturing has resulted in a marked change in the gas velocity pattern within the conduit. The high pressure region of the conduit shows only a very low gas velocity due to the low pressure gradient. In contrast, the higher pressure gradient at shallower depths within the conduit (before fracturing) forces a much higher gas velocity towards the surface.

When the fractures reach the surface (Figure 5.4b), the conduit rapidly depressurises close to lithostatic. This would be accompanied by a rapid expulsion of the stored gas. In contrast, the wall-rocks are much slower to respond due to the lower permeability. Figure 5.4c shows the system once equilibrium has been resumed, approximately 4 hours after the fracture zone reached the surface. Whereas the propagating fracture zone is an effective mechanism for degassing the conduit and wall margins, on attaining equilibrium the system maintains higher pressure at

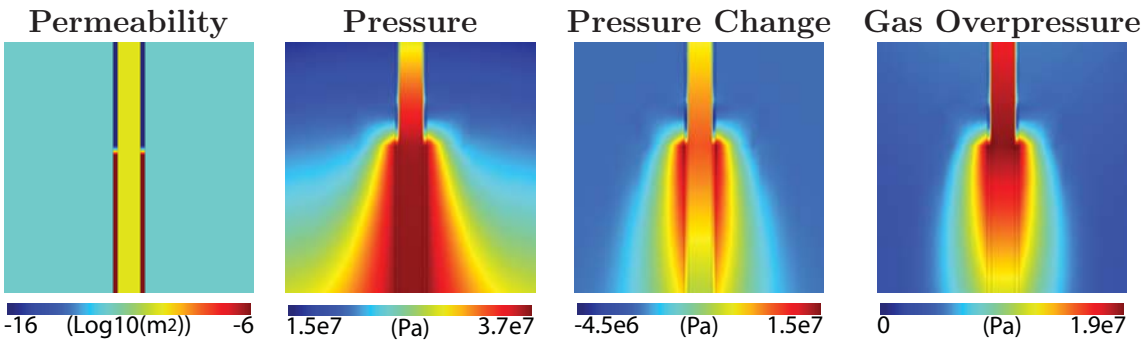

Figure 5.5: Close up images of Figure 5.4a, when the fractures are located between 1500 and 700 m depth, showing the relationship between the top of the fracture, the pressure, gas overpressure and change in pressure. The greatest pressurisation is seen at the top extent of the fractures. Whilst a high pressure is maintained within the conduit, the unfractured conduit-wall margin shows depressurisation. The greatest change in pressure in response to the fracturing occurs within the fractures themselves, due to the high permeability being confined by the surrounding low permeabilities.

shallow depths. This increase in pressure is located within the wall-rocks due to the higher permeability of the fracture zones no longer confining the gas to the conduit, and permits some horizontal gas flow to the wall-rocks. Increasing the pressure within the wall-rocks, increases the capacity for gas storage (compared to the initial state of the system).

Halting the fractures

If the propagation of fractures is halted part-way up the conduit, pressurisation continues and accumulates around the fracture margin (Figure 5.6). Following the model of Neuberg et al. (2006), this does not necessarily increase the potential for further failure, because in their model the formation of shear fractures is triggered by the ascending magma rather than variations in the gas pressure (Holland et al., 2011). However, it may be possible that if a critical gas pressure (exceeding the yield strength of the rock (Section 1.2.2)) is reached, fragmentation could occur.
In Figure 5.6 the fracture tops are located 500 m below the surface and show behaviour in accordance with Figure 5.4a. Figures 5.6b and c show the pressurisation if the fractures cease to propagate and remain at 500 m below the surface. Whilst, the region of greatest pressure is the conduit, in response to the halted fractures, the conduit shows very little change in pressurisation. In contrast, the fractures themselves show the greatest change in pressure over the entire duration of the model (Figure 5.7a). However, the regions of greatest pressure increase, relative to the halted fractures, are the wall-rocks (Figure 5.7b). The location of greatest pressurisation in response to the halted fractures is within the fractures at 450 m below the surface (50 m above the top of the fracture (Figure 5.8)). Pressurisation within the wall-rocks is widespread, whereas the conduit shows only limited response. Overall, halting the fractures results in greater pressurisation than if the fractures continue propagating. This is because, in the latter, the edifice does not have sufficient time to fully equilibrate until the fractures have reached the surface. Whilst the pressure conditions within the conduit respond rapidly to the pause, the edifice takes a further 1.5 hours to react due to the relatively low permeability. Furthermore, the model does not fully reach equilibrium until approximately 14 hours after the fractures are halted.
Brittle failure can occur when the exerted pressure exceeds the yield strength of the rock (Section 1.2.2). Consequently, whether fractures can reasonably halt, as in this scenario, is dependent upon the gas overpressure reached and the yield strength. The modelled scenario, with fractures increasing in permeability from 10^{-16} to 10^{-6} m^2 maintains gas overpressures in excess of 20 MPa. This is significantly higher than the yield strength of 5 MPa suggested by Sparks (1997). This suggests the modelled

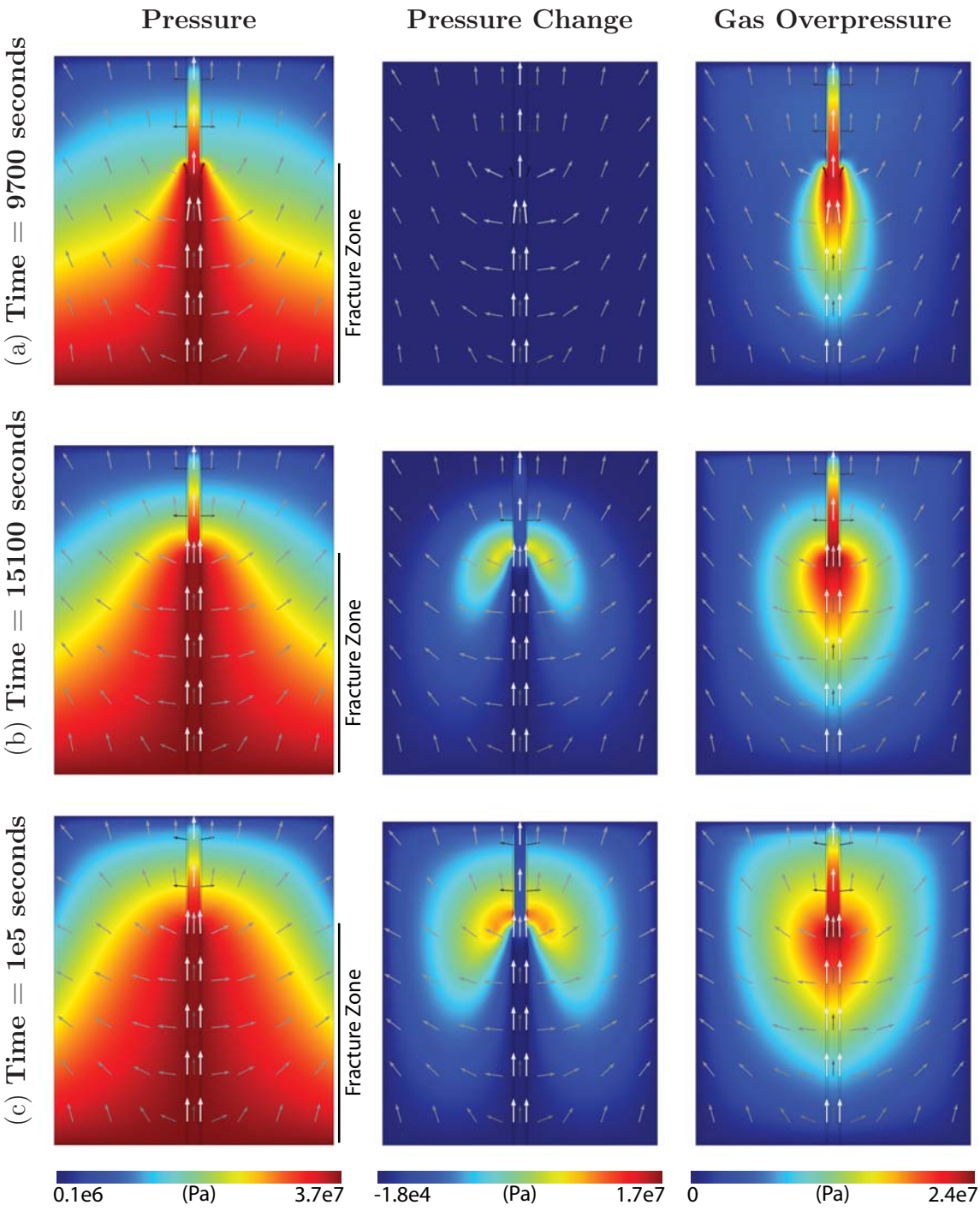

Figure 5.6: Pressure and pressure change with respect to the state of the system at time 9700 seconds for the brittle failure model where the failure is halted and held. Gas velocity arrow range (logarithmic): 2.8×10^{-6} to 0.7 ms^{-1}.

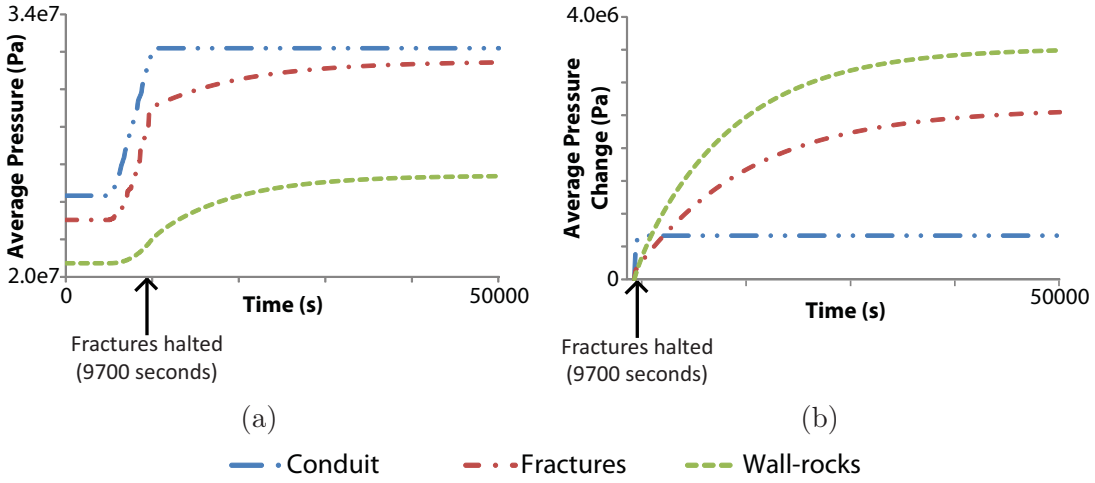

Figure 5.7: (a) Average pressure for the three domains and (b) the change in average pressure relative to time 9700 s, when the fractures have been halted. The fractures show the greatest pressure change across the entire model duration (a). The conduit also shows a significant change, although it shows very little change once the fractures have been halted (b). However, the wall-rocks show the greatest pressure increase after the fractures have halted (b).

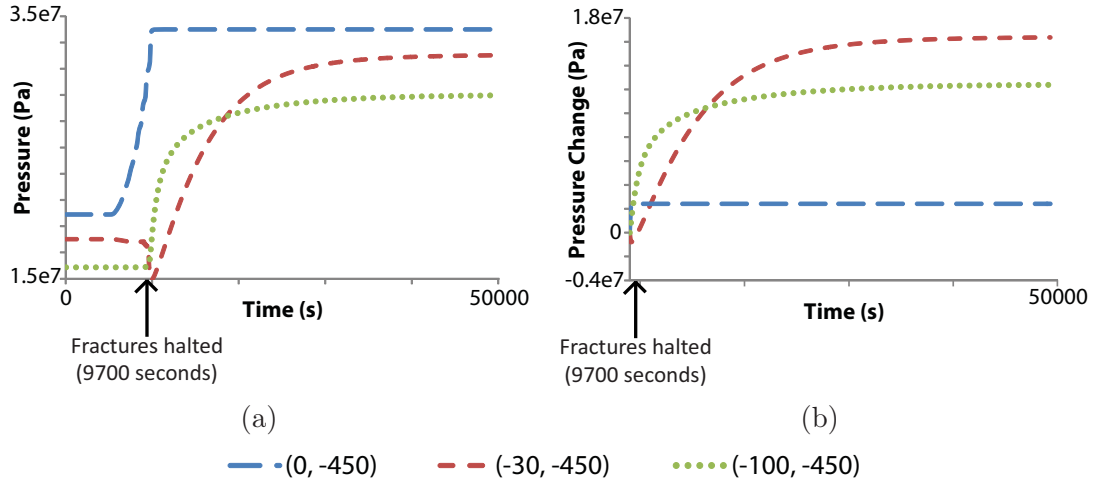

Figure 5.8: (a) Pressure for three points in the model and (b) the change in average pressure relative to time 9700 s, when the fractures have halted. The greatest pressurisation relative to the time when the fractures are halted is 50 m above the top of the fractures.

scenario is too pressurised to permit the fracture zones to halt. However, the gas overpressure could be reduced by decreasing the permeability contrast, and restricting the gas supply. For example, running the same model, but with the fractures modelled as an increase in permeability from 10^{-12} m^2 (wall-rock k) to 10^{-10} m^2 (conduit k), reduces the gas overpressure to less than 10 MPa.

5.1.3 Resealing the fractures

Figure 5.9 shows a similar model to that in Figure 5.4, except the fractures propagate upwards between 1200 m depth and the surface, and are gradually resealed. In Figure 5.9a, the fractures extend between 1200 and 700 m depth. Related to this fracturing, is an increase in the pressure within the conduit and adjacent wall-rocks, but also a slight depressurisation at deeper depths because the gas is no longer confined by the impermeable conduit margin. However, the pressurisation is not as significant as that seen in Figure 5.4a, where the fractures are not resealed. In Figure 5.9b the fracture zone is located between 1200 and 200 m depth. Similar to 5.9a, the pressure gradient is very low within the conduit and consequently, there is depressurisation deeper in the conduit, but pressurisation occurs at shallower levels associated with the fracturing. When the fractures reach the surface (Figure 5.9c) there is instantaneous depressurisation down the conduit and fracture zones. The fractures only extend between 500 m depth to the surface because the fractures have begun to reseal at depth. Figure 5.9d has the fractures extending between 200 m and the surface. Once the fractures have completely resealed, the model resumes its original equilibrium position (Figure 5.2). This model shows that if the low permeability conduit-wall boundary remains unfractured at depth, the conduit, immediately adjacent, depressurises as the gas stored is able to escape via the fractures above. This depressurisation is greatest immediately above the base of the fractures. However, once the fractures begin to reseal at depth, pressurisation occurs at depth, because gas is becoming confined to the conduit again.

Figure 5.10 investigates how changing the fracture permeability affects the gas overpressure. Results are plotted for five different fracture permeabilities ranging from 10^{-6} to 10^{-14} m^2. For a very high fracture permeability (10^{-6} or 10^{-8} m^2) the maximum gas overpressure increases with fracture length. Once the fractures begin to reseal, the pressure remains high before dropping sharply as the fractures reach shallower depths. The decrease in pressure is greater within the fractures and conduit, due to the higher permeability releasing the gas more readily. For a fracture permeability of 10^{-12} m^2 which is the same as that in the wall-rocks, the results show depressurisation within the fractures and conduit, but pressurisation within the wall-rocks as the gas which has been confined to the conduit is permitted to exit into the adjacent wall-rocks. Once the fractures reach the surface, the pressure in all domains gradually returns to the original level. When the fracture permeability is 10^{-14} m^2, the pressure within the fractures and conduit decreases by 0.2 MPa once fracturing begins, before increasing to the original level once the fractures reseal. In contrast, fracturing results in an increase in the wall-rock pressure by 0.3 MPa, which decreases once the fractures reseal.

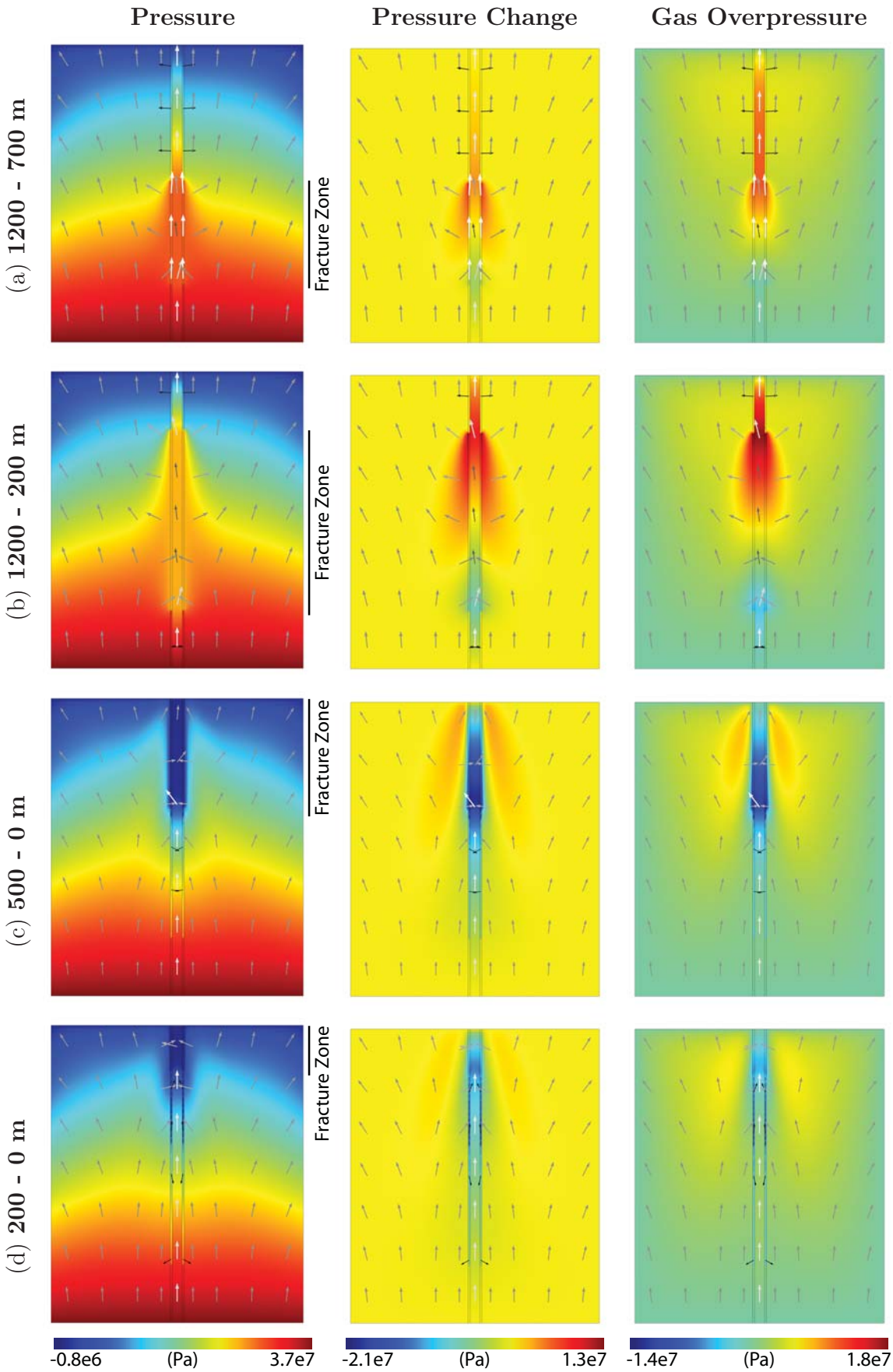

Figure 5.9: Brittle failure model similar to figure 5.4, but fractures begin at 1200 m, propagate upwards and are progressively resealed. The location of the fracture zone is indicated in each plot. Gas velocity arrows are on a logarithmic scale and range within the conduit and wall-rocks: 6.5×10^{-8} - 0.5 ms^{-1} from black to white.

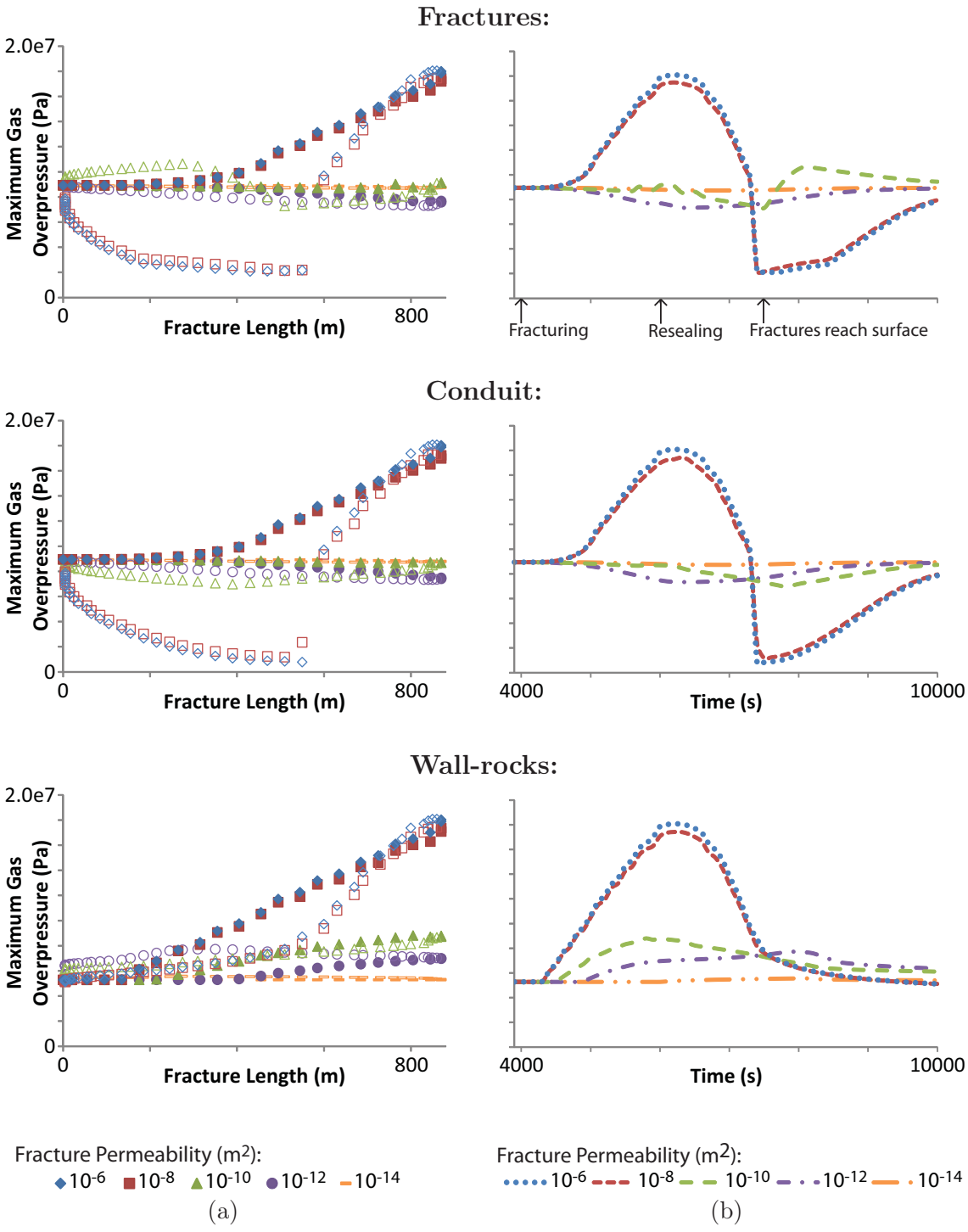

Figure 5.10: Maximum gas overpressure against fracture length (left) and time (right) for the fractures (top), conduit (middle) and wall-rocks (bottom) for different fracture permeabilities (10^{-6} to 10^{-14} m^2). The permeability of the wall-rocks is 10^{-12} m^2. The filled symbols represent when the fractures are increasing in length, whilst the unfilled symbols show the fractures decreasing due to resealing.

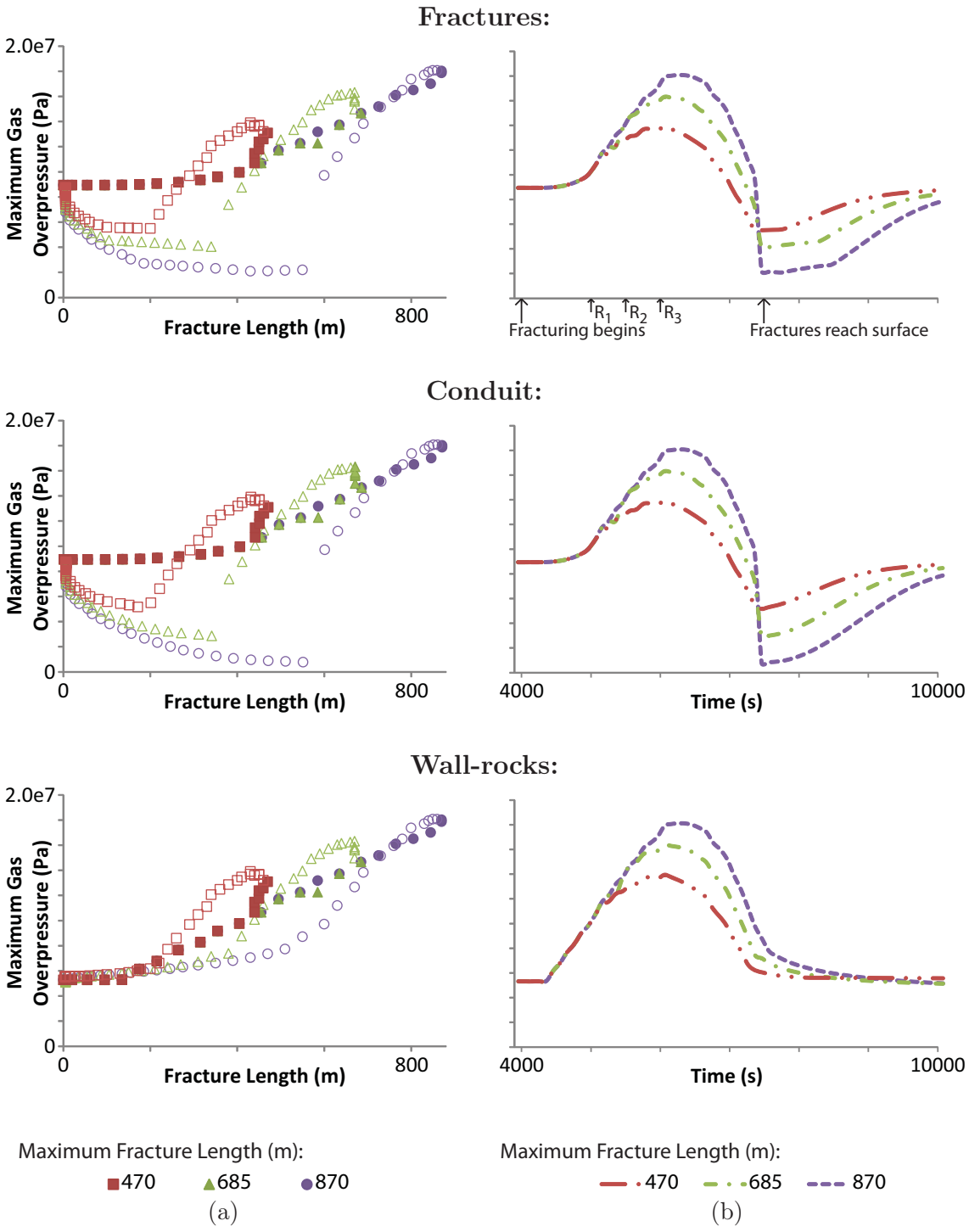

Figure 5.11: Maximum gas overpressure against fracture length (left) and time (right) for the fractures (top), conduit (middle) and wall-rocks (bottom) for different maximum fracture lengths. The filled symbols represent when the fractures are increasing in length, whilst the unfilled symbols show the fractures decreasing due to resealing. R_1, R_2 and R_3 represent the resealing times for 470, 685 and 870 m respectively.

Figure 5.11 shows how changing the time between fracturing and resealing, and therefore the maximum fracture length, affects the maximum gas overpressure reached within the three domains. The results plotted are for models with a fracture permeability of 10^{-6} m^2. In all three domains, the maximum gas overpressure increases with fracture length. Accordingly, once the fractures reach the surface the depressurisation also increases with fracture length. The greater the fracture length, the more gas can be accommodated within the higher permeability, and confined by the lower permeability of the surroundings.

5.1.4 Fractures propagating downwards

In Figure 5.12, the system of fractures propagates downwards from the surface to a depth of 1500 m, simulating an event where fracturing is initiated by cooling and contraction, and continues to depth. Significant depth penetration by this mechanism is unlikely, however, this is the opposite situation to that seen in Figure 5.4 and serves as an end-member comparison. Again, the fractures develop over a time period of 100 minutes, and after 50 minutes the fractures have propagated down to a depth of 800 m (Figure 5.12a). In contrast with Figure 5.4, a rapid depressurisation of the conduit coincident with the fracturing is evident. The wall margins also show depressurisation, but respond at a decreased rate due to a lower permeability. The very high permeability of the fractures permits depressurisation down the conduit and wall margins providing a mechanism for gas exsolution and escape. The high pressure gradient within the conduit results in the highest gas velocity below the fracture zone. Figure 5.12b shows the system after the fractures have reached 1500 m depth, at which point, the lithostatic pressure on the boundaries interacts with the high permeability of the fractures. This results in a dramatic re-pressurisation of the conduit. In contrast, the wall margins retain a lower pressure and take a further 4 hours to resume equilibrium (Figure 5.12c).

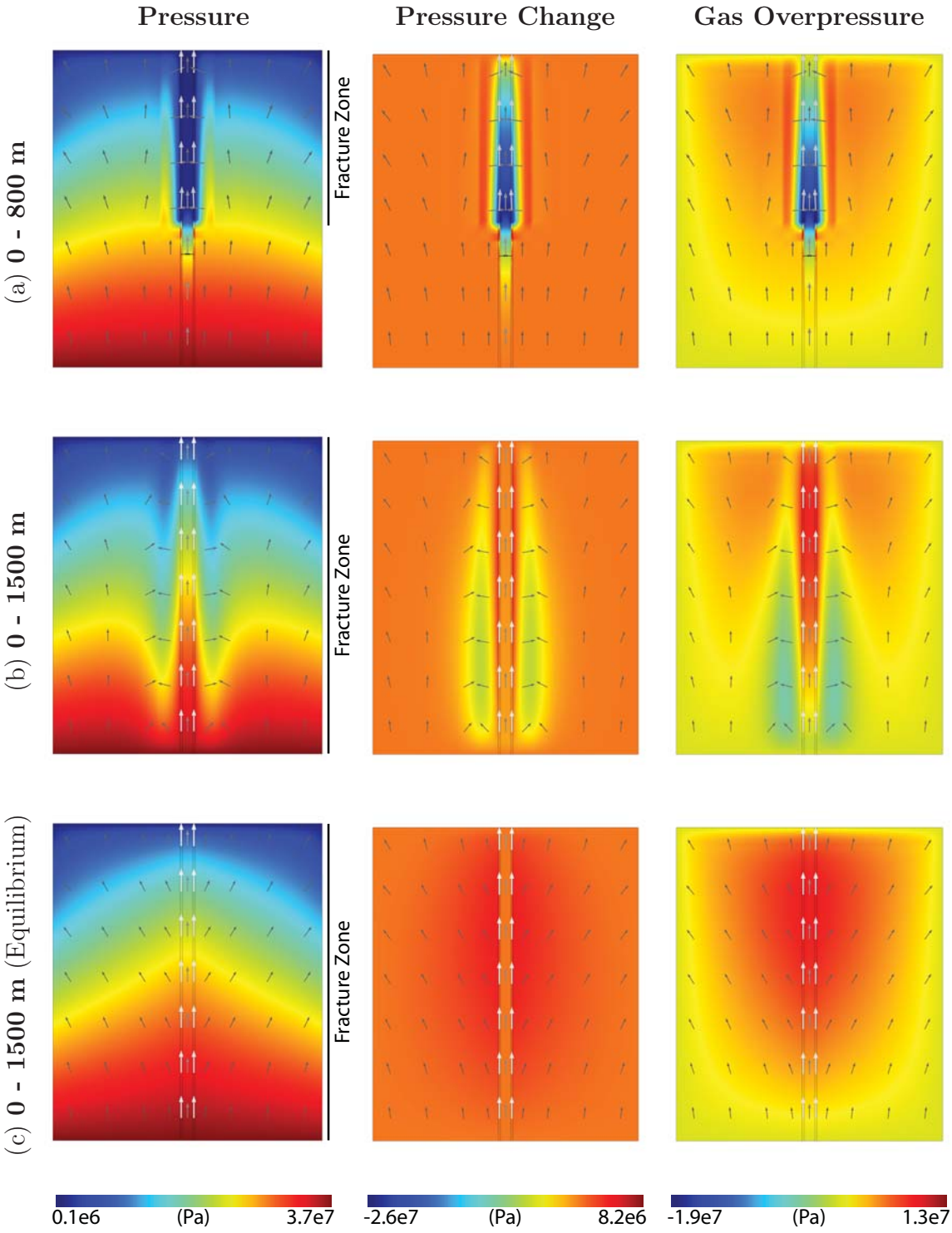

Figure 5.12: Brittle failure model where the fractures propagate downwards. The conduit has a permeability of 10^{-10} m^2, the wall-rocks of 10^{-12} m^2. The fractures are simulated by increasing the permeability of two narrow zones from 10^{-16} to 10^{-6} m^2. The model is represented by three snap-shot images: a. the system of fractures has propagated downwards to a depth of 800 m; b. fractures have reached a depth of 1500 m; c. equilibrium has been re-established. Re-pressurisation occurs in this model due to the unchanged pressure condition on the boundaries. Within the conduit and wall-rocks, the gas velocity arrows increase logarithmically between 8.8×10^{-4} and 0.3 ms^{-1} (black to white).

5.2 Brittle failure and resulting surface displacement

Finally, deformation modelling is incorporated within a model similar to Figure 5.4 (where the fractures propagate vertically but are not resealed), in order to investigate the changes induced by brittle failure at the conduit margin. As before, the model consists of a central conduit, but here it leads to a "spine" (Figure 5.13). Again, there are two "fracture zones" either side, at the conduit-wall boundary, where the permeability is increased from the base to the surface over a time period of 100 minutes (Table 5.2). The results are initially described for increasing the fracture zone permeability from 10^{-14} to 10^{-8} m^2, however, the results for different initial and end fracture zone permeabilities are compared in Figures 5.16 and 5.17.

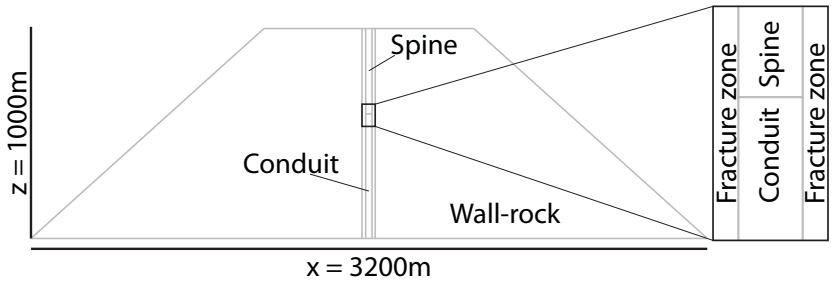

Figure 5.13: Setup for modelling brittle failure with surface displacement. A more realistic geometry representing a volcanic edifice is used to investigate the change in surface displacement with distance from the volcanic summit.

Domain	**Permeability (m^2)**		**Porosity**
	t_1	**t_2**	
Conduit	10^{-10}	-	0.5
Wall-rocks	10^{-12}	-	0.3
Spine	10^{-12}	-	0.3
Fracture zones	10^{-14}	10^{-8}	0.3

Table 5.2: Permeability and porosity values for the brittle model with surface displacement. Additional models are run with different fracture zone permeabilities - initial (t_1) 10^{-12}, 10^{-14}, 10^{-16} m^2; end (t_2) 10^{-6}, 10^{-8}, 10^{-10} m^2. However, the model where the fracture zones increase from 10^{-14} to 10^{-8} m^2 is described in detail because it represents the intermediate model for the set.

Overall, the pressure results (Figure 5.14) agree with those discussed previously in Section 5.1.2, with pressurisation as the fractures ascend, leading to depressurisa-

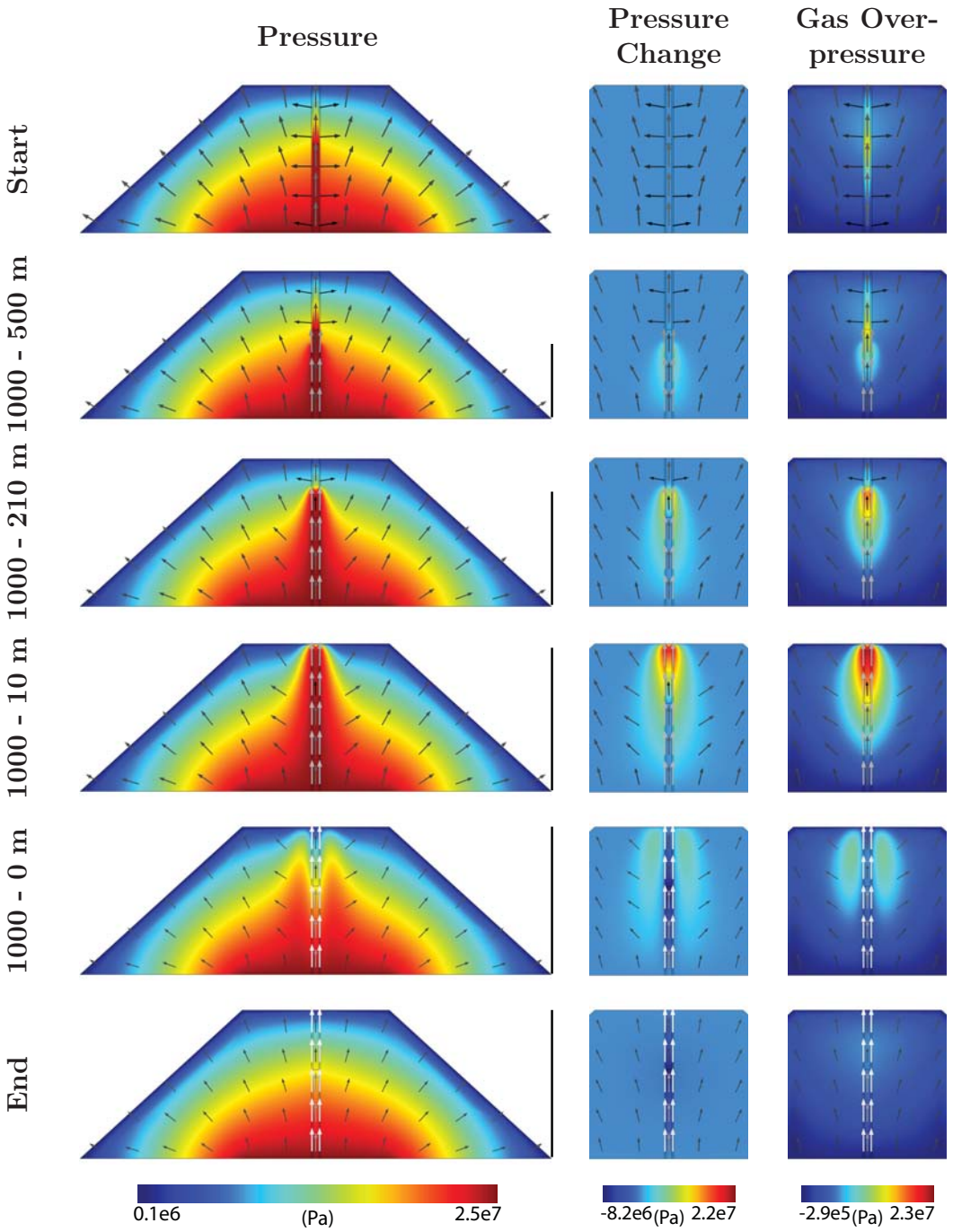

Figure 5.14: The pressure, pressure change and gas overpressure within the system at different times representing different fracture extents (indicated): (a) no fractures, (b) fractures between −1000 and −500 m, (c) −1000 to −210 m, (d) −1000 to −20 m, (e) −1000 to 0 m and (f) end equilibrium with fractures still present.

tion once they reach the surface. Initially, however, the greatest gas overpressure is centred on the base of the spine. This is because the spine, modelled as less permeable, acts to confine gas to the more permeable conduit. This remains the location of the highest gas overpressure, until the fractures have ascended above the base of

the spine. In this case, the greatest gas overpressure is located at the top of the fractures.

Concurrent with the pressurisation, there is a corresponding inflation at the surface, most notable immediately above the conduit and fracture zones, but also evident on the wall-rocks of the volcano (Figure 5.15). The greatest surface displacement is seen directly above the spine and fracture zones. For the current fracture permeability conditions (10^{-14} to 10^{-8} m^2), the model predicts 27 cm surface displacement when the fractures are located just below the surface (Figure 5.15d). This lies within the range of surface uplift (20−50 cm) observed at Santiaguito during repeated vulcanian explosions (Johnson et al., 2008), which are thought to be related to shear fractures along the conduit-wall margin (Bluth and Rose, 2004). Once the fractures reach the surface, there is rapid depressurisation and the surface displacement drops to 3.4 cm below the initial level (Figure 5.15f). The degree of surface displacement seen across the edifice decreases with increasing distance from the centre. However, the model still predicts a maximum inflation of 1.7 cm on the mid wall-rock, which decreases

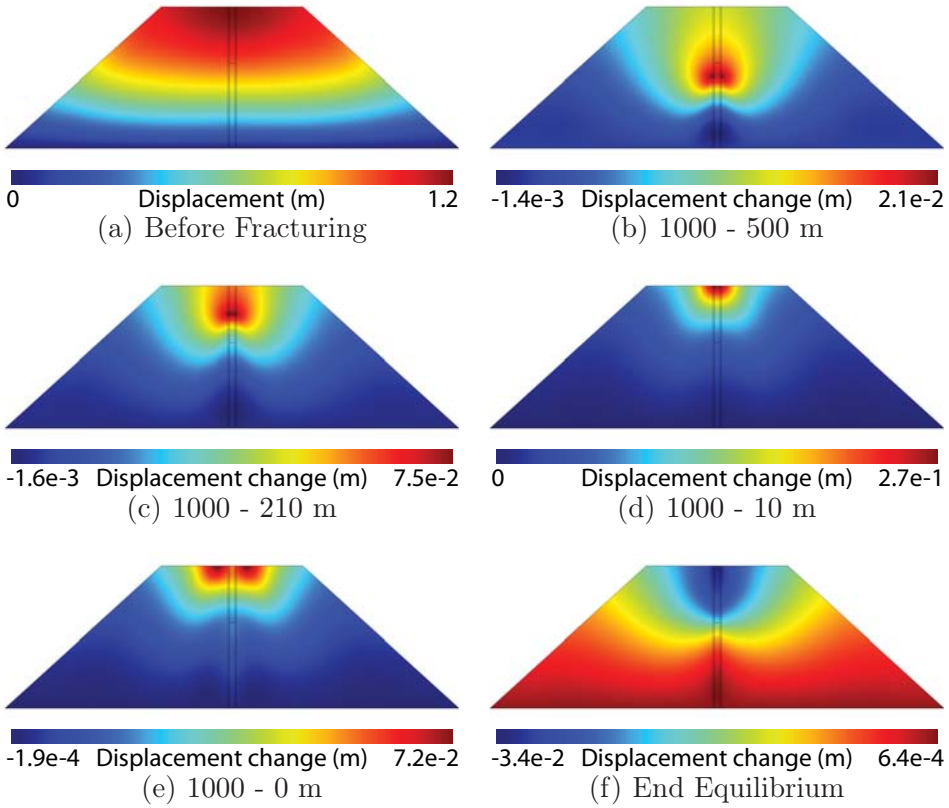

(a) Before Fracturing (b) 1000 - 500 m (c) 1000 - 210 m (d) 1000 - 10 m (e) 1000 - 0 m (f) End Equilibrium

Figure 5.15: The displacement change in response to brittle failure along the conduit-wall margin. (a) shows the total displacement of the initial system in equilibrium, before the fracturing has begun. (b)-(f) show the displacement change with respect to (a).

gradually to approximately 0.7 cm below the initial.

Figures 5.16 and 5.17 show the pressure change and displacement change respectively for 9 models with different start and end fracture permeabilities. The initial fracture permeability ranges from 10^{-12} to 10^{-16} m^2 and the final ranges between 10^{-6} and 10^{-10} m^2.

Figure 5.16 plots the average pressure change for each of the domains in the model runs. In response to fracturing, the conduit is the first domain to experience significant pressurisation. The spine is the domain which sees the greatest pressurisation (almost 1.2 MPa), although pressurisation here only begins once the fractures reach the base of the spine. However, all domains show pressurisation in response to the fracturing and rapid depressurisation once the fractures reach the surface, except when the final fracture permeability is 10^{-10} m^2. These models show significantly different pressurisation patterns because a fracture permeability of 10^{-10} m^2 is the same permeability as the conduit. Hence, the conduit is effectively widened by the fracturing. This results in depressurisation in the conduit concurrent with the fracturing. The other three domains (spine, fractures and wall-rocks) all show pressurisation, although significantly less than the other models, except for 10^{-16} to 10^{-10} m^2 which experiences depressurisation in the spine once the fractures reach the spine base. For starting fracture permeabilities of 10^{-14} and 10^{-16} m^2, the wall-rock experiences pressurisation, which continues, albeit at a slower rate, even once the fractures reach the surface. This suggests that in these models, instead of the gas being lost, much of it is redistributed into the wall-rock structure.

The nature of the pressure change is echoed by the displacement change results. In Figure 5.17, the results are plotted for three points within the model: (0, 0) top of the conduit; (500, 0) top right wall-rock; (980, -430) mid right wall-rock. For all three points, the greatest surface inflation is seen when the fractures increase in permeability from 10^{-16} to 10^{-6} m^2. This is because the low initial fracture permeability leads to the greatest pressurisation and consequently, has the greatest potential for gas storage. As the initial permeability increases, the maximum inflation reached decreases. When the end fracture permeability is 10^{-10} m^2, it is the same as for the conduit and results in a markedly different surface displacement pattern. For an initial fracture permeability of 10^{-12} m^2, there is still deflation seen throughout once the fractures reach the surface. However, when the initial fracture permeability is 10^{-16} or 10^{-14} m^2, the fractures intersecting with the surface result in continued surface inflation in the wall-rocks. This is due to pressurisation of the wall-rock by increasing the permeability of the fracture zones to that of the conduit. This effectively widens the conduit and encourages lateral gas flow towards the wall-rock.

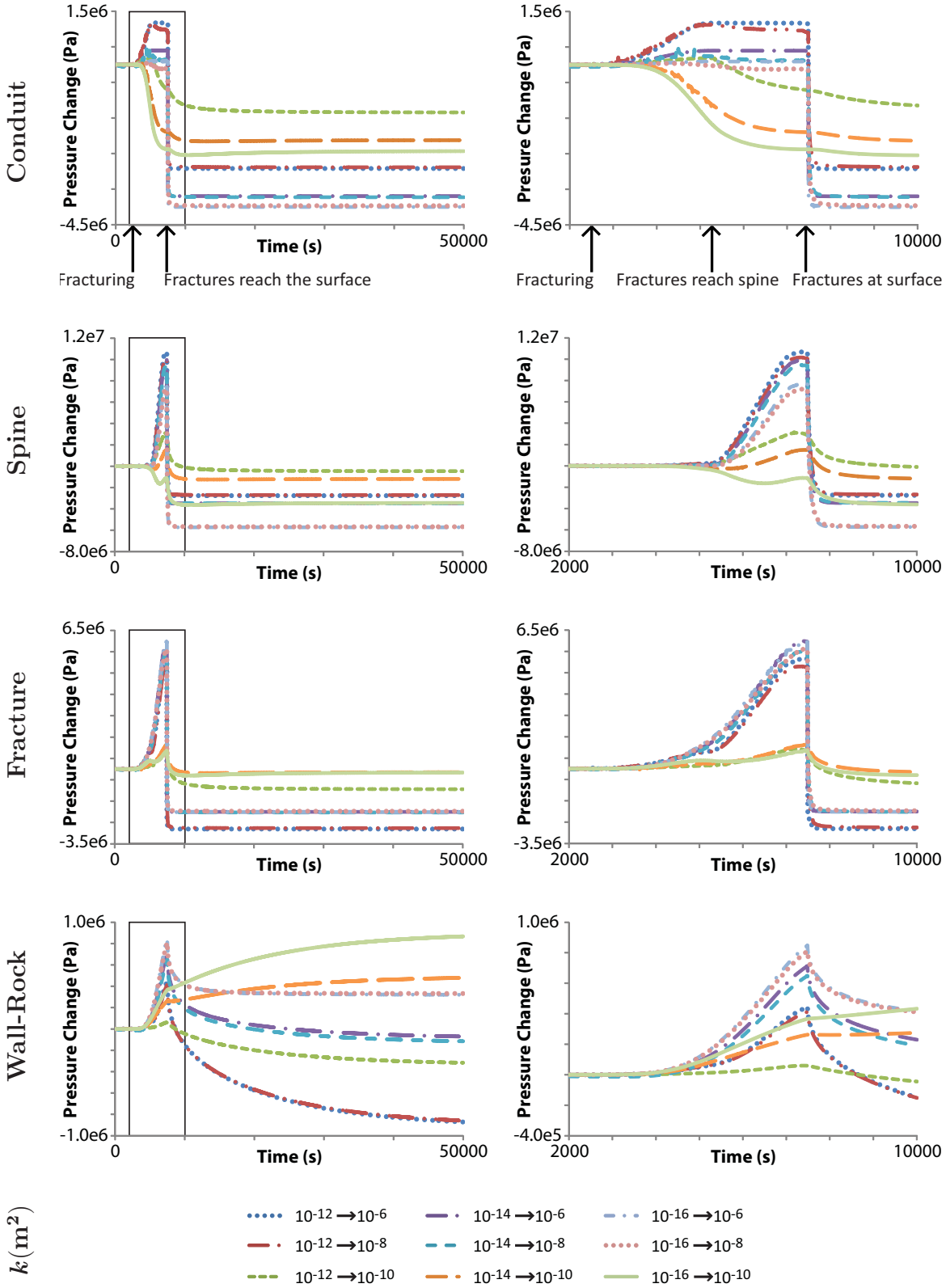

Figure 5.16: Pressure change graphs for each domain for different start and end fracture permeabilities. The conduit is the first domain to experience any pressure change. The region of greatest pressure change is the spine, although this is the last domain to begin pressurising.

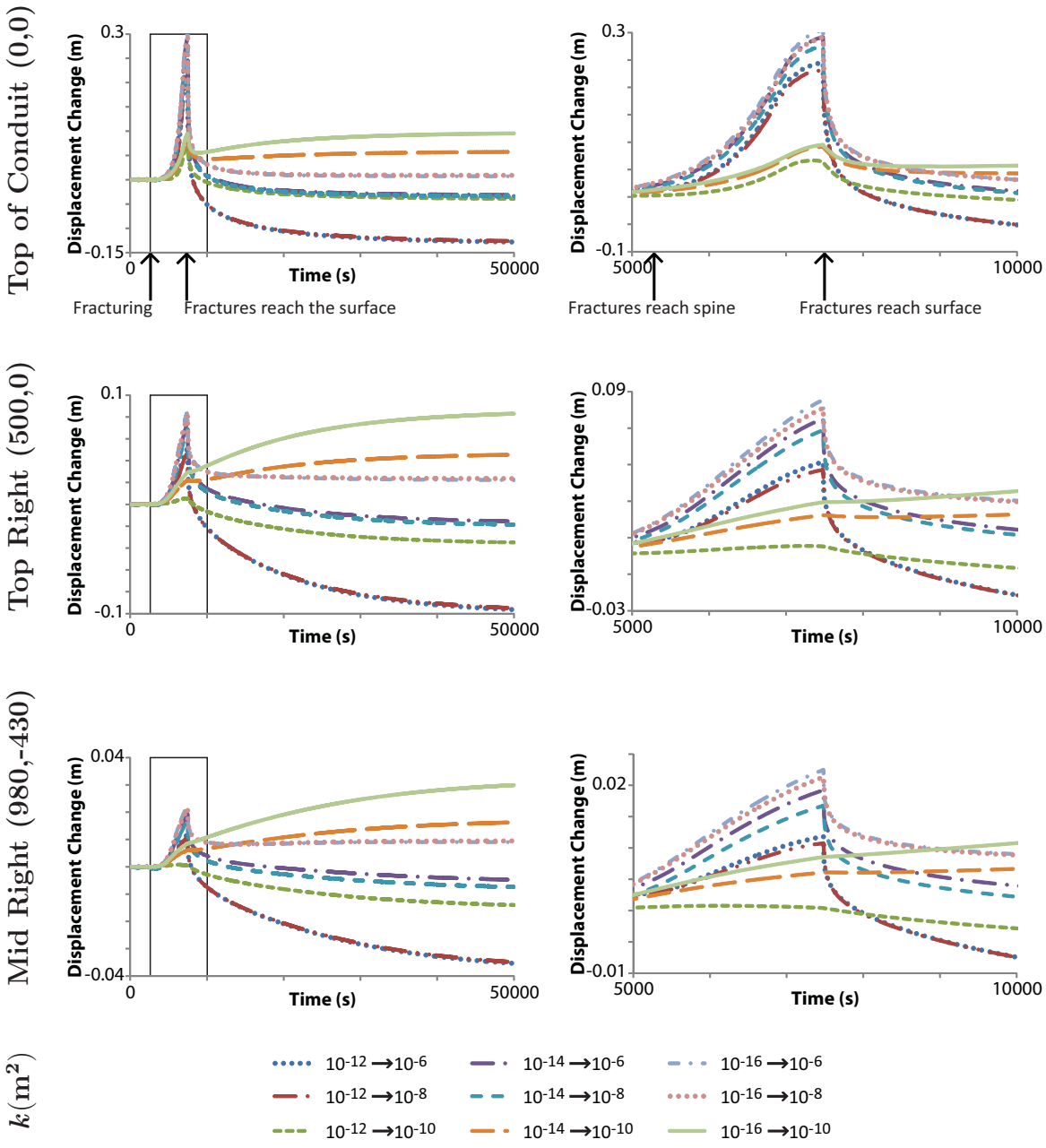

Figure 5.17: Displacement change for three points within the model: (0, 0) top of the conduit; (500, 0) top right wall-rock; (980, -430) mid right wall-rock, for different start and end fracture permeabilities. The graphs on the right concentrate just on the inflation and subsequent deflation seen in each model.

Figure 5.18 shows that the displacement change at the surface is directly related to the depth to which the fractures reach below the surface. The longer the fractures, and therefore the shallower the depth of their extent, the greater the surface uplift. If the fractures do not reach the surface, the uplift continues before levelling off. Subsidence only occurs if the fractures reach all the way to the surface. This variation in displacement pattern with changing fracture depths suggests that this could potentially be used to interpret volcanological observations to determine the presence and nature of fractures, and the redistribution of gas at depth. In all the

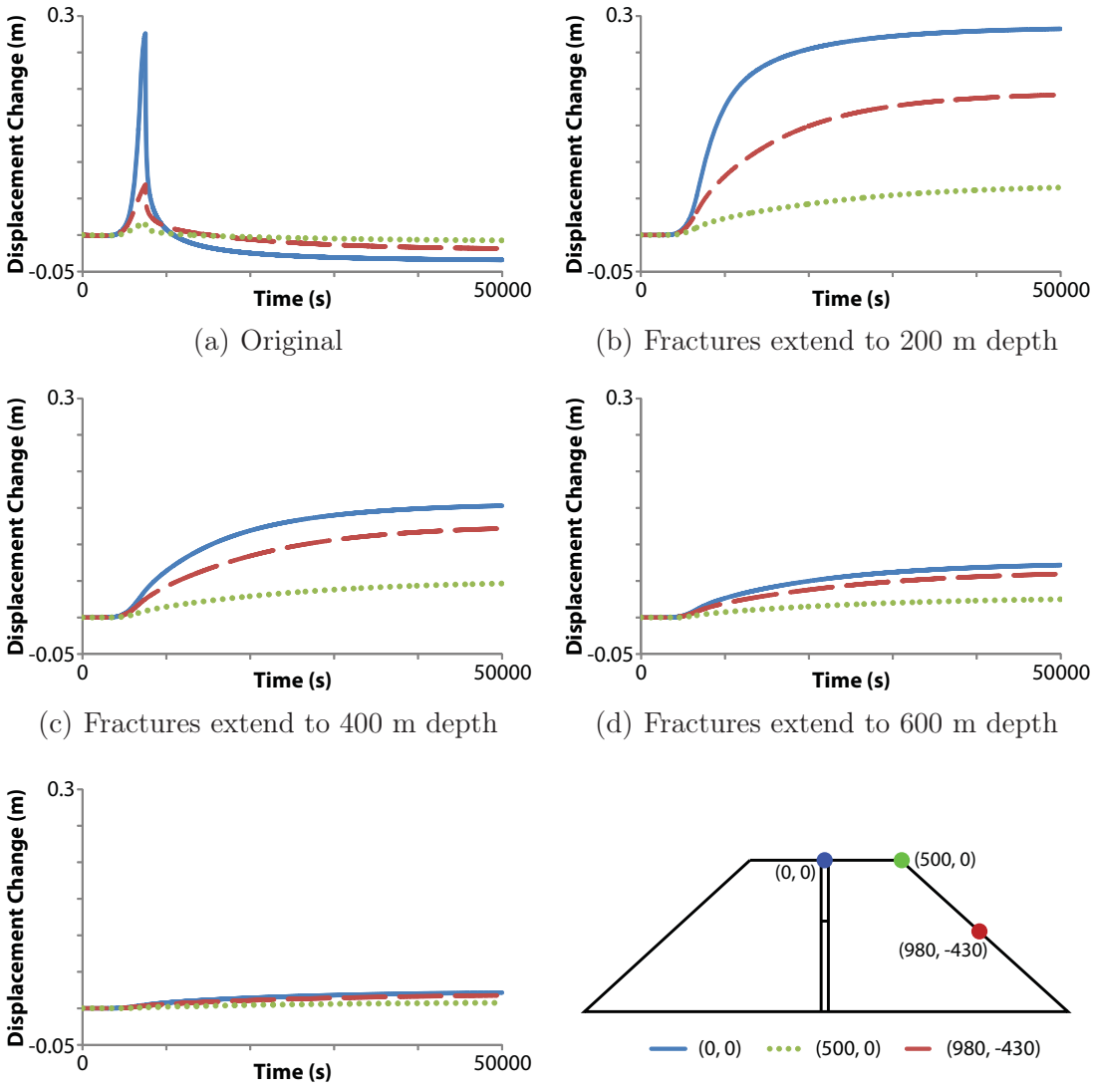

(a) Original

(b) Fractures extend to 200 m depth

(c) Fractures extend to 400 m depth

(d) Fractures extend to 600 m depth

(e) Fractures extend to 800 m depth

(f) Locations of coordinates

Figure 5.18: Displacement change graphs for the top of the spine (0,0), top corner (500, 0) and the middle of the right wall-rock edge (980, -430), for the original model with fracture permeability increasing from 10^{-14} to 10^{-8} m^2. The shallower the fractures reach, the greater the surface displacement.

model runs, the top of the spine experiences significantly more surface displacement than the wall-rocks, although the difference decreases with decreasing fracture length. Longer fractures can accommodate more gas, which is subsequently confined by the surrounding low permeabilities leading to pressurisation. Furthermore, this pressurisation enhances the potential for gas storage.

5.3 Summary

The fracture depths chosen in this chapter range between 1500 and 1000 m depth. However, in reality their location will be determined by the point at which the magma alters from deforming in a ductile, to a brittle manner (glass transition). This is dependent upon magma temperature, viscosity and stress, which is currently beyond the scope of the model. Once the fracture zones reach the surface, gas velocity within the highly permeable fracture zones increases dramatically, (in some cases beyond the validity of Darcy's law - Appendix B). However, the models are useful for showing the pressurisation and gas behaviour prior to the fractures reaching the surface.

The results show that as the fractures develop at depth, the higher permeability results in pressurisation due to the unfractured material above. This contrast in permeabilities and resulting pressurisation provides a suitable environment for gas storage, which is subsequently lost if the fractures reach the surface.

The comparison between the two directions in which fracture zones develop shows very differing behaviour. Ascending magma which triggers shear fractures propagating upward leads to pressurisation of the magma conduit and gas storage prior to explosive release. In contrast, downwards propagation of the fracture zones promotes depressurisation, gas exsolution and gentle degassing. Furthermore, the fracture length is integral in determining the intensity of these opposing behaviours.

The degree of surface displacement seen in response to fracturing is dependent upon the location of the fractures, length and permeability. The shorter and deeper the fractures, the less displacement can be seen at the surface. Similarly, the shorter the fractures and the lower the permeability, the lower the pressurisation resulting in decreased surface displacement. Different regions of the edifice surface respond at different rates to the fracturing. This could be used to infer the permeability conditions within the edifice and the nature of fracture zones at depth.

In the next chapter, storage of gas due to regions of low permeability surrounding high permeability is explored further, in particular for the dome.

Chapter 6

Sealing the Volcano

Processes which decrease the permeability may have a profound impact on a volcanic system. The permeability of the volcanic system may be decreased by a variety of processes including gas loss, foam collapse, melt crystallisation, hydrothermal mineralisation and compaction (e.g. Sparks and Pinkerton, 1978, Matthews et al., 1997, Cashman and Blundy, 2000, Quane et al., 2009). All these processes result in sealing the volcano to gas escape. Consequently, gas is confined and, as discussed previously, this can lead to pressurisation (Chapter 3) and explosive volcanic activity, if the imposed stress exceeds the yield strength (Section 1.2.2).
Here, the impact of sealing within the dome is modelled through the introduction of low permeability regions within the dome structure. The surface displacement due to this sealing is also modelled.

6.1 Decreasing the permeability

The model depicted in Figure 6.1 represents an approximation of a dome with a central magma-filled conduit, surrounded by a layered "talus slope" and overlain by a "spine". Initially all regions of the talus slope and spine have the same permeability, although lower than that of the conduit (Table 6.1). Rapid sealing of the system is simulated using a smoothed step function to decrease the permeability of the spine and embedded talus slope layers from 10^{-12} m^2 to 10^{-16} m^2 over a time period of 20 minutes. Such a short timescale is in accordance with those measured by Quane et al. (2009) for compaction induced sealing in pyroclastic deposits.
The pressure, pressure change and gas overpressure results are shown in Figures 6.2, 6.3 and 6.4, respectively. Initially, Figure 6.2a shows the pressure distribution dominated by the permeability-controlled lithostatic pressure, with the greatest gas overpressure (Figure 6.4a) centred on the base of the spine. This is because the spine has a lower permeability than the more permeable conduit. Sealing the specified

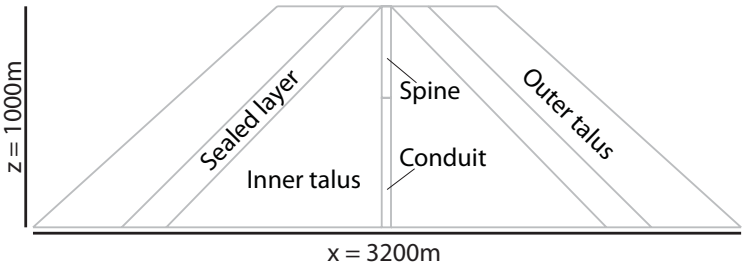

Figure 6.1: Setup for model investigating sealing within the dome. The geometry chosen here represents a general geometry shape which could be applied to both the dome and the volcanic edifice.

Domain	**Permeability (m^2)**		**Porosity**
	$\mathbf{t_1}$	$\mathbf{t_2}$	
Conduit	10^{-10}	-	0.5
Edifice	10^{-12}	-	0.3
Sealed Edifice	10^{-12}	10^{-16}	0.3
Spine	10^{-12}	10^{-16}	0.3

Table 6.1: Permeability and porosity conditions for the Sealing Gas Escape Routes Model. Initially, all domains are highly permeable, although, the conduit is more permeable than the surrounding edifice and spine. Sealing is simulated by decreasing the permeability in the sealed edifice and spine to the very low value of 10^{-16} m^2.

regions (spine and talus sealed layers) results in significant alteration to the pressure pattern (Figure 6.2b). All the regions "below" the talus sealed layers exhibit pressurisation. Furthermore, gas is channelled around the impermeable spine, diverted by the impermeable layers in the talus and drawn towards the margin between the spine and talus slope. The greatest pressurisation is located at the margin between the spine and talus in addition to along the margin between the inner talus and sealed layers (Figure 6.3). In contrast, the outer talus sees significant depressurisation because the sealed regions prevent outwards gas loss. Consequently once sealing has occurred, the outer talus becomes a region void of gas. This model takes approximately 24 hours to respond to the change in permeability and reach an equilibrium state. However, in reality this will depend upon the time taken to seal the gas pathways, which in turn is strongly dependent upon the sealing mechanism. For example, compaction may be rapid (Quane et al., 2009), but mineralisation will take considerably longer than 20 minutes.

Figure 6.5 is a summary of the maximum gas overpressure against the thickness of the sealed layer. Several model runs were computed whereby the spine parameters

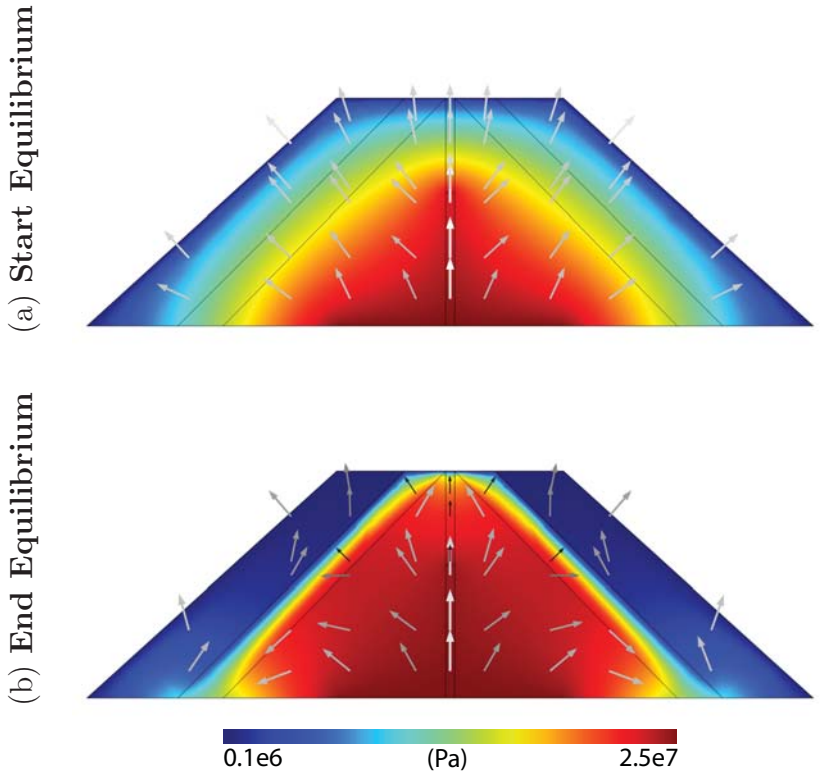

Figure 6.2: Model to investigate sealing of the system. The images present the pressure at two snapshots in equilibrium, (a) before and (b) after sealing. The conduit has a permeability of 10^{-10} m^2 and initially, all other regions are 10^{-12} m^2. After sealing, the spine and sealed talus layers have a permeability of 10^{-16} m^2. The arrows represent the gas velocity and increase logarithmically from black to white between 9.1×10^{-8} and 2.7×10^{-2} ms^{-1}.

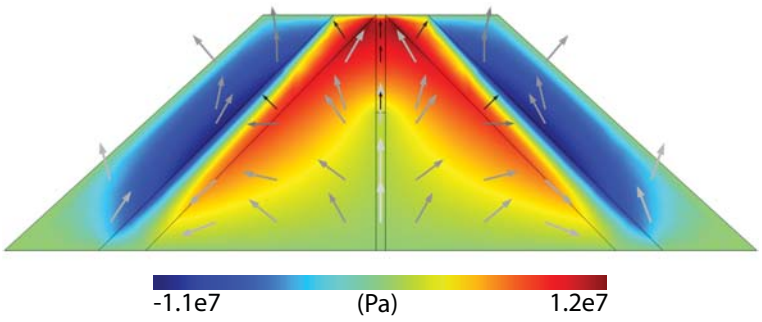

Figure 6.3: Pressure change in response to sealing the dome. The greatest pressurisation is seen at the boundary between the spine and talus as well as at the margin between the inner talus and the sealed region. In contrast, the outer talus is a region of significant depressurisation.

were kept constant, but the thickness of the two sealed layers within the dome were varied between 0.01 and 200 m. The plot shows that the overpressure increases as the thickness of the sealed layers is increased from 0.01 to 10 m. The gas overpressure

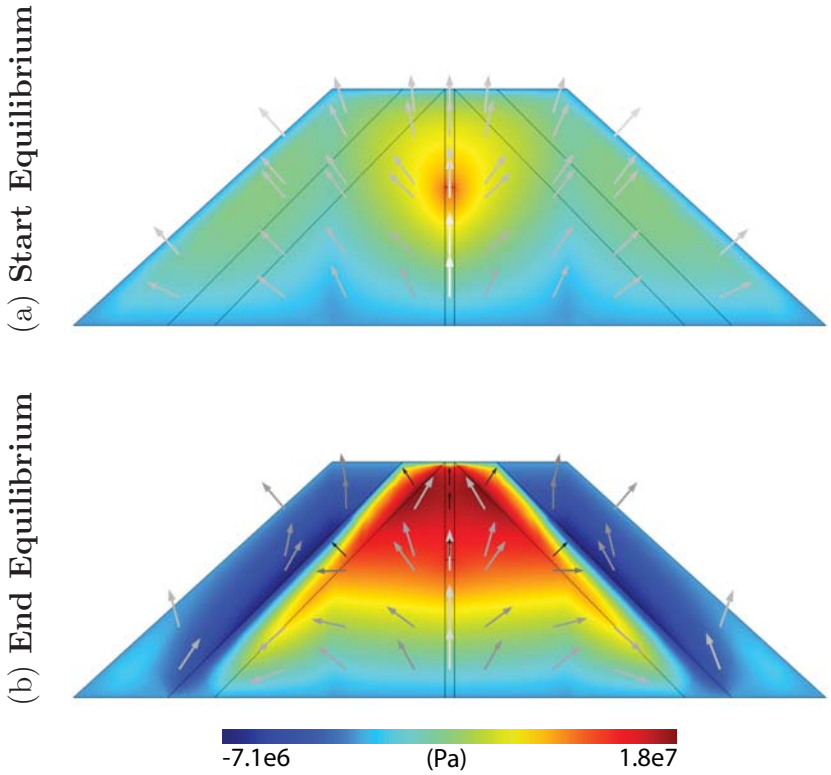

Figure 6.4: The start and end gas overpressure results. Sealing results in a dramatic change in the location and magnitude of the greatest gas overpressure.

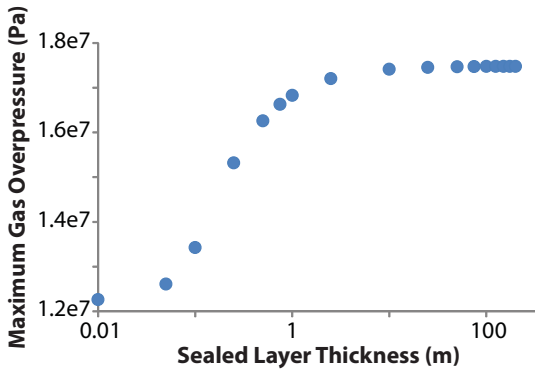

Figure 6.5: Maximum overpressure versus thickness of the sealed layers. The spine thickness remains constant, whilst the thickness of the two sealed layers within the dome are modified, from 0.01 to 200 m.

then stabilises at a value of approximately 17.5 MPa and any further increase in the thickness of the sealed layers has only limited influence on the gas overpressure. However, the ability for a layer of 1 cm thickness to resist such pressurisation ($\approx$ 12 MPa) is questionable.

Figure 6.6 shows the total displacement and displacement change in response to the sealing event. In accordance with the pressure response, sealing results in a

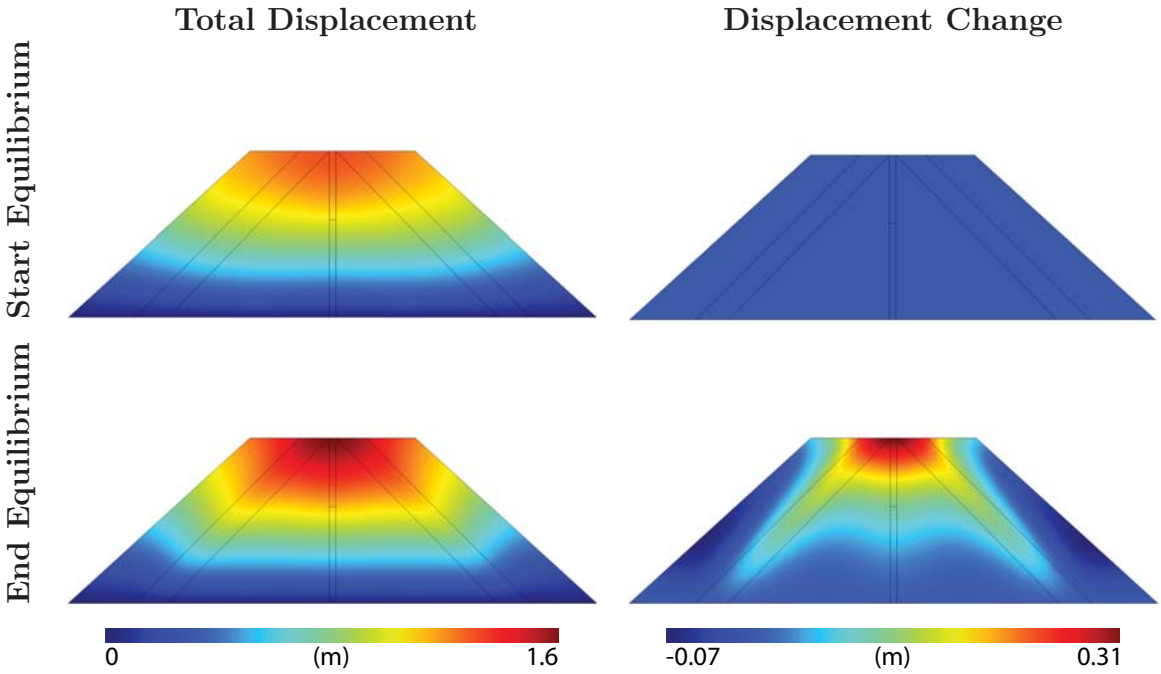

Figure 6.6: Initial and end equilibrium displacement. Displacement change is shown on the right.

maximum surface uplift above the spine of 31 cm. The degree of displacement seen at the surface decreases away from the centre. Furthermore, the model predicts a deflation of 7 cm on the lower flanks.

6.2 Summary

Sealing has a profound impact upon a volcanic system. In particular, sealing results in pressurisation by confining the gas. Furthermore, this pressurisation forces more gas back into solution enhancing the ability to store gas at shallow levels. This is particularly important for explaining the large volumes of gas which are lost following large dome collapse events. This model predicted a pressure increase of 10 MPa at shallow levels which increases the amount of gas which may be dissolved in the melt by up to 1 wt.%. Furthermore, the localised gas overpressure (up to 12 MPa, which exceeds the yield strength of most rocks (Sparks, 1997) (Section 1.2.2)) seen at the margins of the sealed regions shows how pressurisation can build up and culminate in an explosive eruption.

The evidence for sealing at active volcanoes would be decreased gas emissions (Edmonds et al., 2003b, Surono et al., 2012), with potentially localised gas emissions at the boundaries between different permeabilities, such as the margin between the spine and surrounding talus. As seen in Chapter 5, the presence of shear fractures at

the conduit-wall boundary represents an important degassing route. Complete sealing of this pathway may depend upon a complex interplay between upward magma motion and expansion keeping the fractures open, and different sealing processes. The effects of sealing a volcanic system are explored further in Chapter 8. However, the way in which cracks within the dome structure may help to reduce the pressure is investigated in the next chapter.

Chapter 7

Cracked Dome

Cracks within the structure of a volcano are a potential degassing route and are intimately linked to the creation of fumaroles (Figure 7.1). They may vary in size from micro-fractures to large vents or fissures several metres across. Such cracks may be created by a variety of mechanisms including cooling and contraction of the dome structure, fluid pressure, weakened regions, shear zones and local tectonics (e.g. Heiken et al., 1988, Sparks, 1997, Giammanco et al., 1998, Edmonds et al., 2003a, Sparks, 2003a). The location and extent of these fractures may be highly variable and dependent upon the host rock properties and mechanism of fracture creation.

The models in this chapter simulate fractures on the surface of the volcanic dome and investigate how the presence of cracks affect the pressurisation and degassing behaviour. Furthermore, displacement modelling is used to show how cracks may change in response to pressurisation of the volcanic conduit.

(a)

(b)

(c)

Figure 7.1: Examples of fumaroles from active volcanoes. (a) The western flank of Fourpeak volcano, Alaska (Source: Read (2006), Alaska Volcano Observatory (USGS)). (b) Fossa Crater, Vulcano, Aeolian Islands, measuring approximately 10 cm across. Significant sulphur mineralisation is visible, highlighting how cracks/fissures may become progressively sealed over time. (Source: Alean (2007)). (c) Scientists sampling fumarolic gases from Mount Baker, Washington (Source: Chadwick (1981), Cascades Volcano Observatory (USGS)).

7.1 Crack formation

Degassing through the lava dome is investigated by the introduction of "cracks" modelled as narrow zones of high permeability penetrating the volcanic dome structure. Permeabilities within the conduit, wall-rocks and bulk of the dome are constant, with the conduit simulated as the most permeable at 10^{-10} m^2 (Table 7.1). Two cracks are simulated by increasing the permeability from that of the dome (10^{-14} m^2) to 10^{-8} m^2 via a smoothed step function. In this scenario, the cracks are modelled as an increase in permeability rather than with atmospheric pressure in order to account for the presence of debris within the cracks. The aim of this model is to assess the impact of such cracks on the overall pressure and gas flow within a volcanic edifice. Two different models are used to show how varying the depth of crack penetration, relative to a gas storage region, affects the results (Figure 7.2). In both models the smallest crack is "Crack *1*". However, in Model **1**, the largest crack ("Crack *2*") extends through the dome and into the wall-rock. In comparison, this larger crack extends through the wall-rock to intersect the conduit in Model **2**.
Figures 7.3, 7.4 and 7.5 show results for the pressure, pressure change and gas overpressure at different times for the two models. Initially, the pressure is controlled by the lithostatic pressure and the variations in permeability resulting in the highest pressure located within the conduit, where gas is confined by the surrounding lower permeabilities. Figure 7.5 illustrates that the highest gas overpressure is initially at the top of the conduit, where it meets the dome. Once the crack develops, the high permeability cracks become regions of very low pressure and act to draw the gas from the edifice. However, in Model **1**, the influence of the cracks is limited to the immediate area, and the conduit experiences only a very small pressure de-

Domain	**Permeability (m^2)**		**Porosity**
	t_1	**t_2**	
Conduit	10^{-10}	-	0.5
Wall-rocks	10^{-14}	-	0.1
Dome	10^{-14}	-	0.1
Cracks	10^{-14}	10^{-8}	0.8

Table 7.1: Permeability and porosity values for the cracked dome model. A high permeability is set to the conduit, but lower permeabilities in the wall-rocks and dome to simulate pressurisation which could induce crack formation in the dome structure, due to the associated surface displacement. The cracks are simulated by increasing the permeability from 10^{-14} m^2 to 10^{-8} m^2. This is sufficient to provide a viable exit route for gas, but simulates that the cracks may still contain infill.

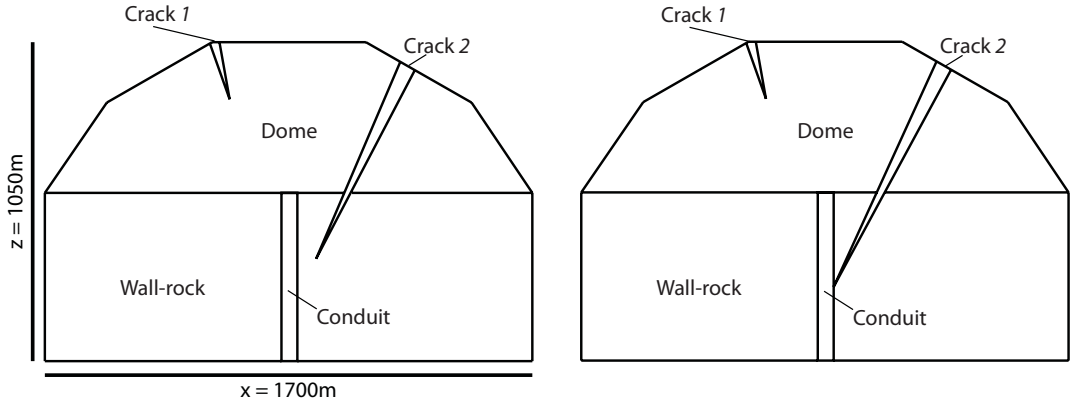

(a) Model **1** (b) Model **2**

Figure 7.2: Setup for the two cracked dome models. The only difference is the depth of Crack *2*.

crease of 1.7×10^4 Pa. In contrast, in Model **2**, all domains experience significant depressurisation in response to the largest crack which reaches the conduit. In this second model, the conduit experiences depressurisation of 9.6 MPa. The influence of the smallest crack in both models is limited to only the crack itself and the area immediately surrounding it.

The area of the volcano affected by the cracks varies between the two scenarios. In Model **2**, depressurisation occurs throughout all domains, whilst in Model **1**, the depressurisation is restricted to the right wall-rock and dome (Figure 7.4). However, whilst Model **2** shows the greatest area affected, Model **1** shows the greatest magnitude of pressure change, located at the base of Crack *2* with a decrease of 24 MPa. Figure 7.5 demonstrates that even after crack development, the region of highest gas overpressure in Model **1** remains largely unchanged, suggesting the cracks in this scenario are ineffective at extracting the stored gas from the system. Furthermore, a very high pressure is maintained around the base of Crack *2* (Figure 7.3), which would likely result in crack closure. Contrastingly, the effect of Crack *2* in Model **2** is so extreme that much of the stored gas is removed.

Figure 7.6 shows the average pressure change for each of the four main domains (left and right wall-rocks, dome and conduit). In Model **1**, the left wall-rock (furthest from Crack *2*) decreases in pressure by only 0.1 MPa. The right wall-rock and dome, however, gradually depressurise by approximately 3.4 MPa. In Model **2**, all domains experience significant depressurisation, but, the wall-rocks and dome are much slower to reach their new equilibrium level, than the more permeable conduit, due to their lower permeability. After the conduit, the dome depressurises the most followed by the right and then the left wall-rocks. In Model **1**, the conduit

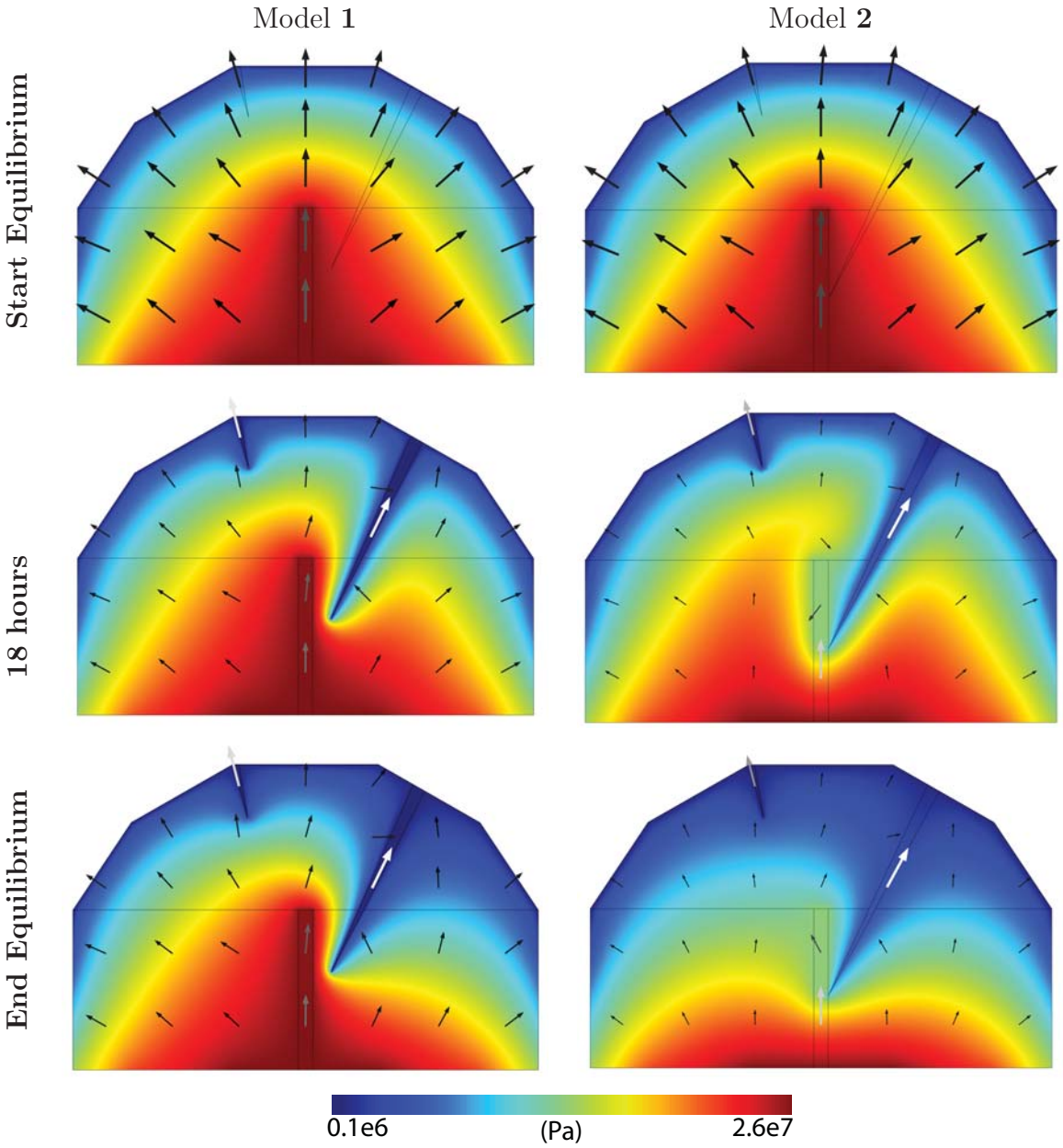

Figure 7.3: Pressure for two temporal cracked dome models, showing the initial crack-free systems and the dome with cracks after 18 hrs and the end equilibrium. Arrows show the gas behaviour on a logarithmic scale increasing from black to white (Model **1**: 9.9×10^{-6} to 0.2 ms^{-1}; Model **2**: 6.7×10^{-6} to 4.1 ms^{-1}).

depressurisation occurs very slowly over approximately 6 days, whilst in Model **2**, the much greater pressure decrease occurs over less than 60 minutes, suggesting not only more complete degassing, but also a more rapid emission, which is demonstrated by the gas velocity plots in Figure 7.7. This contrast in conduit equilibrium times is directly related to the penetration depth of Crack *2*. The crack intersecting the conduit in Model **2** allows the gas to rapidly escape the system, resulting in the

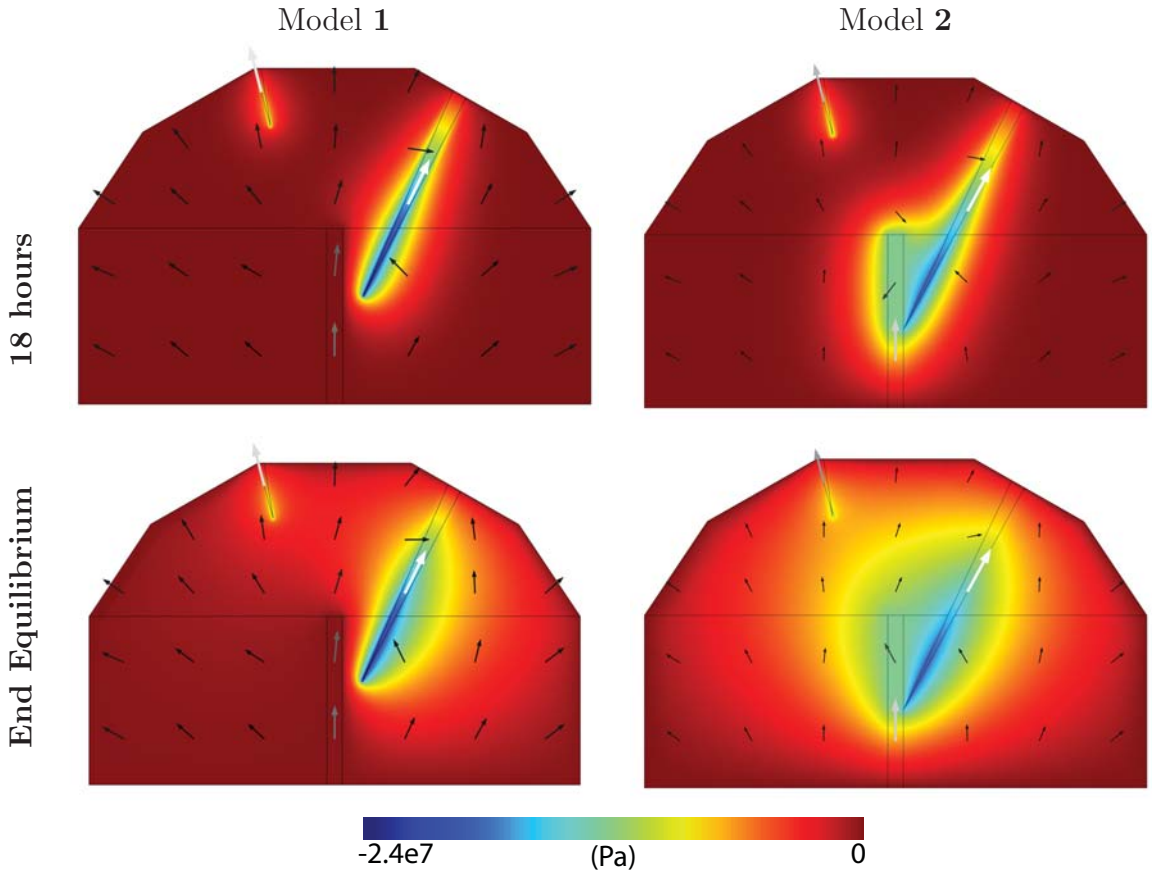

Figure 7.4: Pressure change for the two models in response to crack development. Whilst Model **1** shows the greatest pressure change, Model **2** shows the largest area affected. There is little change to the conduit pressure in Model **1**, whilst Model **2** shows significant depressurisation.

decrease in pressure. However, in Model **1**, the gas is still confined to the conduit by the surrounding low permeability edifice. Consequently, the cracks have only a limited ability to provide an outlet for the gas.

The equilibrium time against edifice permeability for a conduit permeability of 10^{-10} m^2 is shown in Figure 7.8. The main difference between the two models is in Model **2**, the conduit reaches equilibrium very rapidly (less than 3 hours) regardless of the edifice permeability. In contrast, in Model **1**, the conduit equilibrates at a similar rate to the rest of the edifice. With wall-rock and dome permeabilities of 10^{-14} m^2, Model **1** predicts a duration of 28 days to reach equilibrium in all domains. However, with the conduit and cracks unchanged at 10^{-10} and 10^{-8} m^2 respectively, increasing the edifice permeability by two orders of magnitude to 10^{-12} m^2 decreases this time to 12 hours.

Figure 7.9 illustrates there is also variation in the starting pressure and the degree of pressure change dependent upon the edifice permeability. The average pressure, at

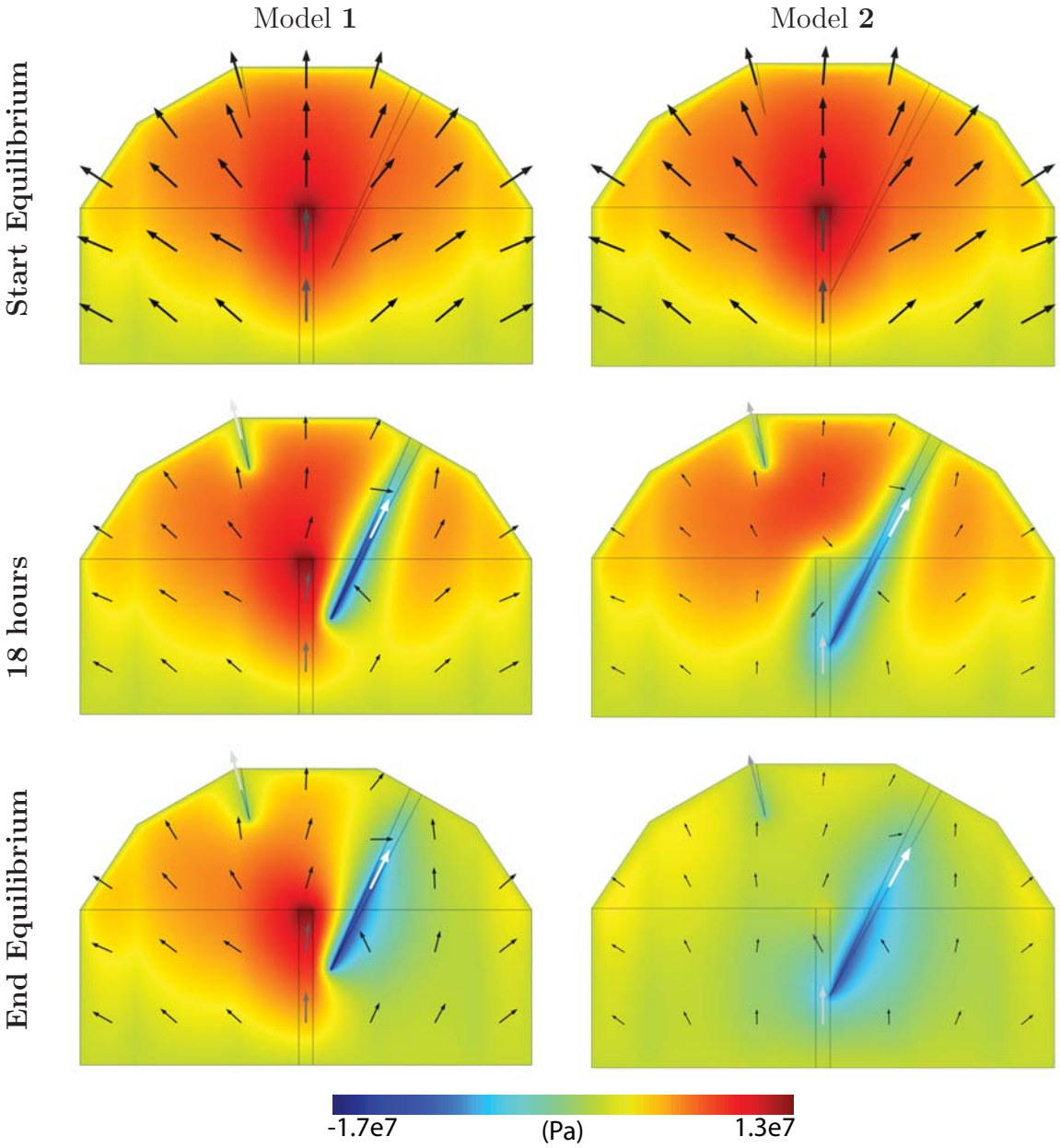

Figure 7.5: Gas Overpressure for the two models in response to crack development. Initially, the greatest gas overpressure is at the top of the conduit in contact with the less permeable dome. Once the fractures have been created, Model **1** maintains this region of high gas overpressure, whereas the depressurisation through the largest crack in Model **2** removes it.

the start, for each domain is the same for the two models, such that the pressure in each domain increases with decreasing edifice permeability. This is because the high permeability conduit is confined by the lower surrounding permeabilities. However, once the edifice permeability reaches three orders of magnitude higher than that of the conduit (10^{-10}m^2), the average pressure in all domains plateaus, and any further

decrease in edifice permeability does not alter the pressure.

In Model **1**, the depressurisation for the conduit and left wall-rock decreases with decreasing edifice permeability, whereas the right wall-rock and dome increase. In Model **2**, the depressurisation increases in all domains with decreasing edifice permeability. The influence of decreasing the edifice permeability is two fold. Firstly, it encourages gas to be stored within the conduit, but also restricts the transfer of gas. Hence, the pressure change is greater for lower edifice permeabilities because the interior pressure is higher and there is more gas available to extract. However, the lower permeability decreases the gas velocity resulting in greater equilibrium times. Additionally, in Model **1** the decreasing edifice permeability particularly affects the pressure change in the conduit and left wall-rock, because the gas is unable to transfer to the cracks. In both cases, there is no further deviation in the pressure change for edifice permeabilities less than 10^{-14} m^2. An edifice permeability of 10^{-10} m^2 represents the special case where the conduit and edifice are equally permeable and in which case there is no contrast in the permeability to aid the storage of gas. Con-

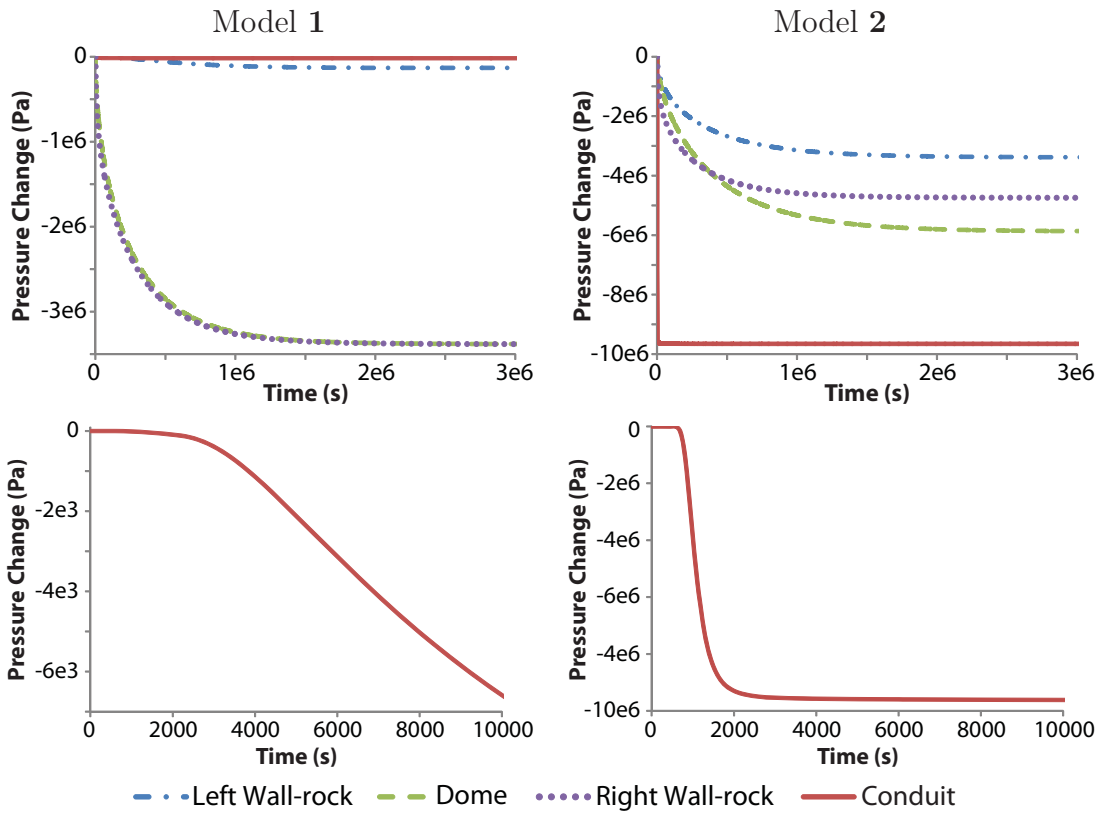

Figure 7.6: Average pressure change within the domains in each model. The first 10000 seconds of the conduit pressure change is also shown (bottom). The conduit in Model **2** undergoes the greater pressure change, and also attains its equilibrium far quicker than in Model **2**.

sequently, the pressure change in these cases, in response to the crack development, is low in all domains.

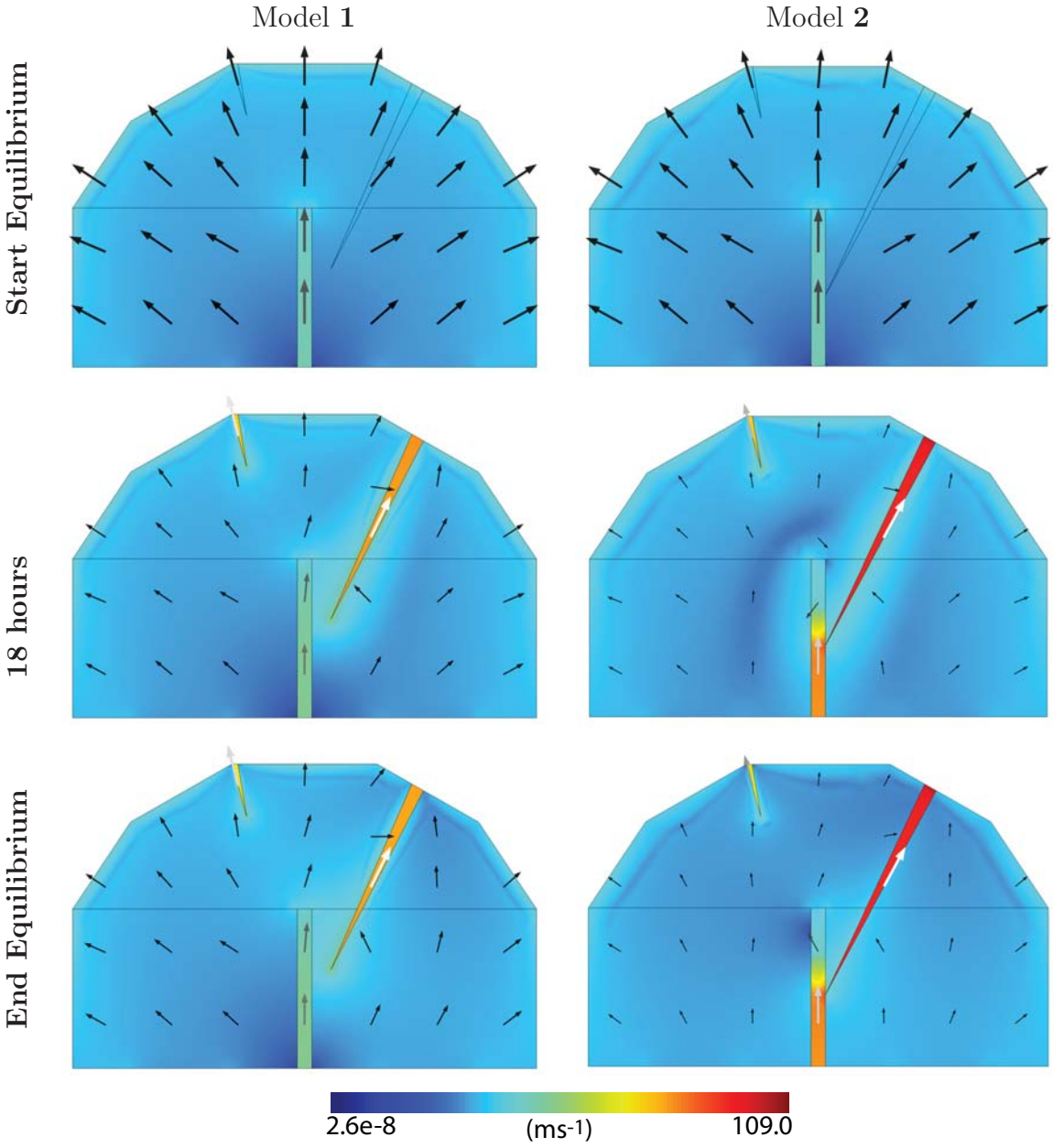

Figure 7.7: Gas velocity, on a logarithmic scale, for the two cracked dome models. Model **2** shows the greatest gas velocity in response to the crack development. There is also a marked contrast in gas velocity within the conduit above and below the point of contact with the crack.

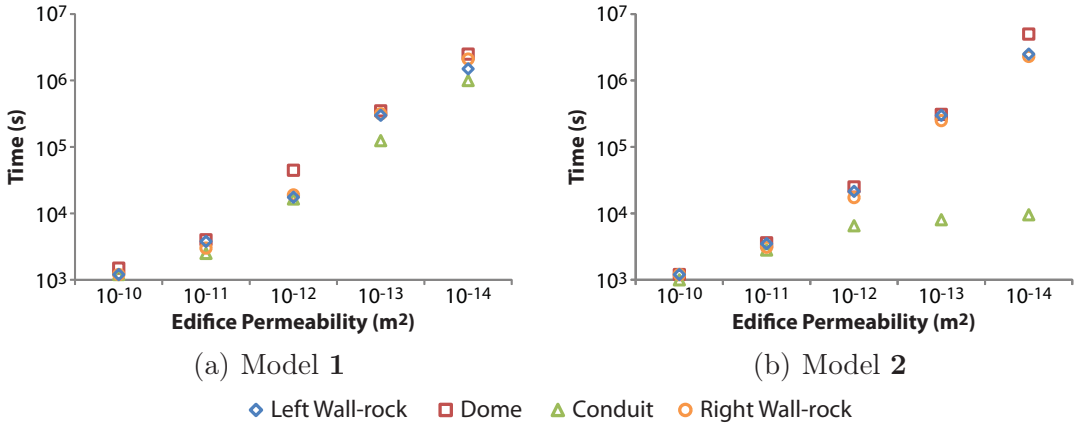

Figure 7.8: The approximate equilibrium times for the four domains in each model dependent upon edifice (wall-rocks and dome) permeability and assuming a conduit permeability of 10^{-10} m^2. The conduit domain takes significantly less time to reach equilibrium in Model **2** due to the depth of Crack *2*.

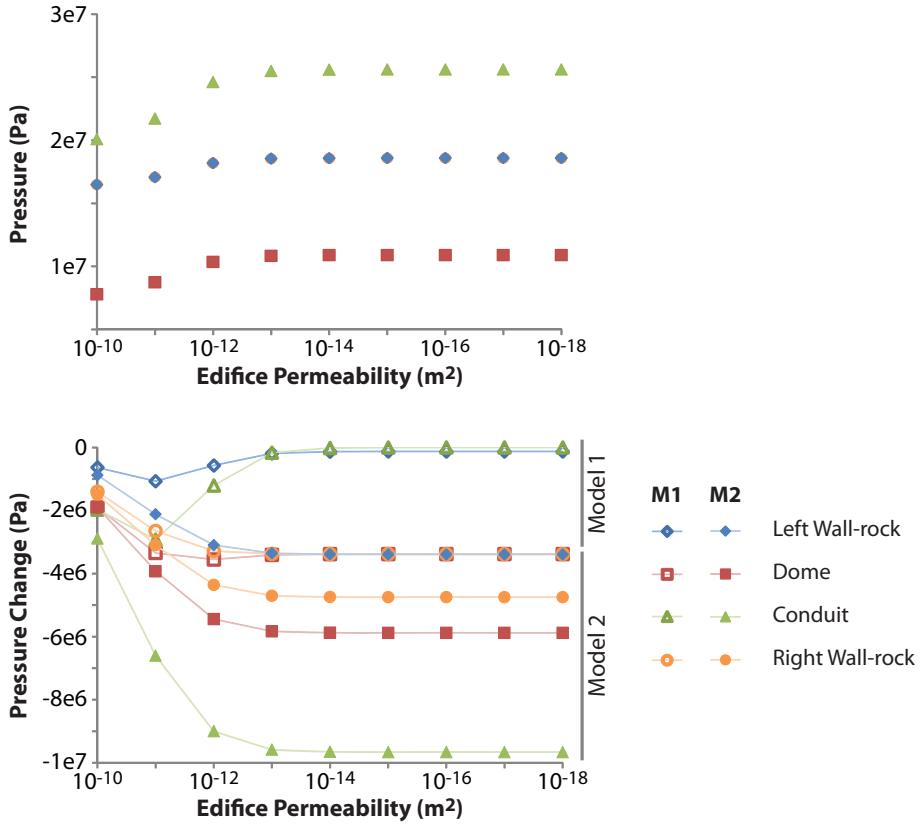

Figure 7.9: Pressure at the start (top) and pressure change at the end (bottom), relative to the start equilibrium, for each domain in the two models. At the start, the pressure in the left and right wall-rocks is equal. In all domains, the cracks result in a decrease in pressure (negative pressure change) regardless of the edifice permeability. The most notable difference is the greater pressure change evident in Model **2**.

7.2 Deforming the cracks

The previous section illustrated how cracks within the dome may be viable degassing routes under the right conditions. In particular, unless the cracks are extensive enough (such as Crack *2* in Model **2**), they may be unable to aid in the complete removal of large volumes of gas from the volcanic interior. Thus, without a viable exit route, gas may continue to accumulate resulting in continued pressurisation. This section investigates how this pressurisation may affect the cracks at the surface.

The previous model is extended to explore the complex interactions that occur within a volcanic system containing multiple cracks, and in particular how these cracks may alter the displacement pattern in response to pressurisation. This pressurisation is induced by increasing the conduit permeability by four orders of magnitude from 10^{-14} to 10^{-10} m^2 (Table 7.2). In reality, this increase in permeability may be achieved due to increased bubble connectivity in response to continued diffusion and coalescence, following the "magma foam" hypothesis of Eichelberger et al. (1986). An alternative method of pressurisation in the model would be to decrease the surrounding permeabilities (wall-rock and dome) to simulate sealing.

Here, the model contains nine cracks of varying width and depth (Figure 7.10). The change in surface crack width is determined by measuring the displacement change of the left and right points where each crack intersects the surface. The new coordinates for those points can then be interpolated using the displacement change in the x and z directions and the difference compared to their initial location of those points determined. The results for two models (**3** and **4**) are shown with the only difference being the presence of Crack *8* in Model **3**.

Figures 7.11 and 7.12 show the pressure and pressure change for the two models. Initially, all the domains have the same permeability (10^{-14} m^2) and therefore, the pressure is controlled by lithostatic pressure and the presence of the cracks. The cracks act to decrease the overall pressurisation within the volcano. Consequently, the shallower regions of Model **3** (dome and upper conduit) are less pressurised than Model **4** due to the addition of Crack *8*. The gas overpressure is initially extremely

Domain	**Permeability (m^2)**		**Porosity**
	t_1	**t_2**	
Conduit	10^{-14}	10^{-10}	0.3
Wall-rocks	10^{-14}	-	0.3
Dome	10^{-14}	-	0.3

Table 7.2: Permeability and porosity values for the crack widening models.

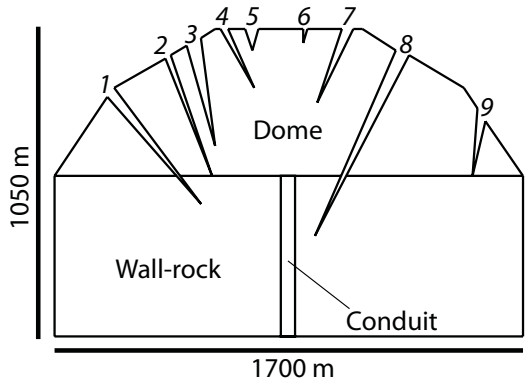

Figure 7.10: Geometry for the model with a central conduit surrounded by wall-rocks and overlain by a cracked dome. The locations of the nine cracks are indicated. Crack *8* is present in Model **3** but absent from Model **4**. The configuration of this model in terms of crack location and extent is arbitrary and represents an extreme example.

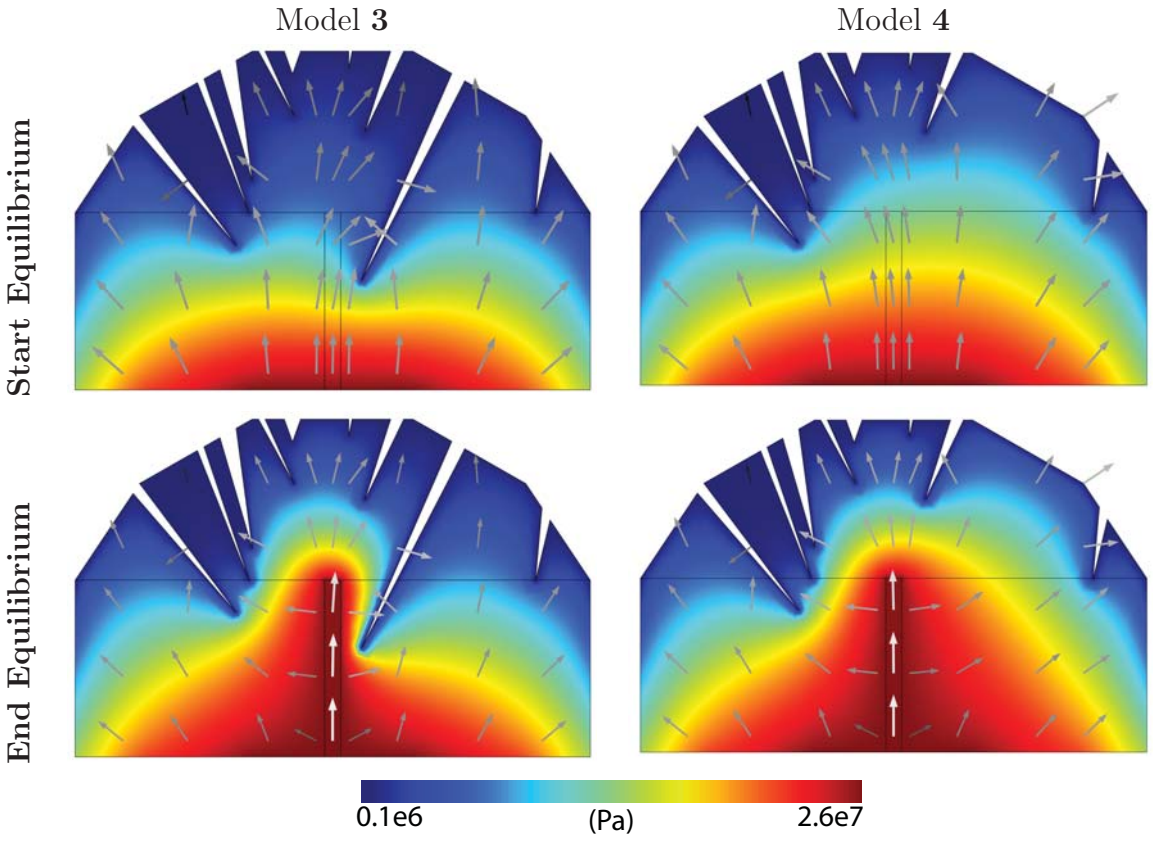

Figure 7.11: Start and end equilibrium pressure for the two models. The presence of Crack *8* in Model **3** has a big impact on the pressure, both at the start and the end. The extent of this crack acts to shield the right-hand portion of the dome from the high pressure of the conduit.

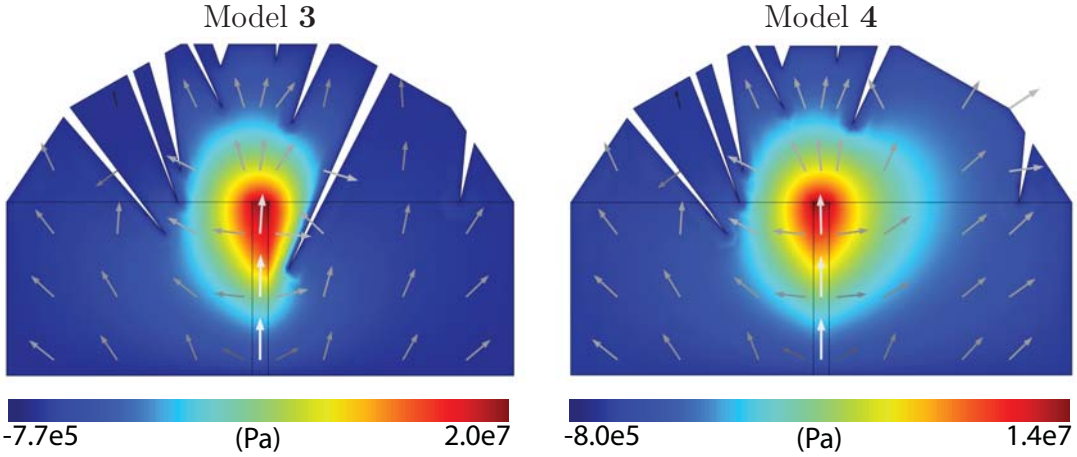

Figure 7.12: The end-equilibrium pressure change for the two models. Both models result in pressurisation, particularly at the top of the conduit due to the increased conduit permeability. The model predicts that Crack *8* acts to restrict the pressure to the conduit and immediate surroundings, whilst in Model **4**, the greatest pressure change is lower, although a greater portion of the dome is affected. However, if this large crack were modelled as in-filled, the pressure would affect a larger region.

low indicating the volcanic systems are in a degassed state and there is no stored gas present (Figure 7.13). However, once the conduit permeability is increased (simulating a "magma foam"), there is marked pressurisation particularly within the conduit. The increased conduit permeability surrounded by the less permeable edifice results in gas storage, despite the presence of the cracks within the dome. This is similar to Model **1** from Section 7.1 where the shallower cracks were unable to prevent gas storage at depth. The lack of Crack *8* and the subsequent increased volume of intact dome in Model **4** provides a greater storage capacity for the gas, and consequently results in a more extensive region of pressurisation. However, the greatest pressure change occurs at the top of the conduit creating the site of greatest gas overpressure.

The gas velocity is presented in Figure 7.14 and, initially, there are very few differences between the two models. The greatest gas velocity in both cases is concentrated around the margins of the cracks, particularly at their deepest extent. However, the surface of the dome where there is a large distance between neighbouring cracks (both at the surface and at depth) also shows a high gas velocity. In contrast, sections of the dome where the distance between the cracks, particularly at the base, is small show very low gas velocities, suggesting the majority of the gas in these instances is lost through the cracks. However, gas may be lost from other, less fractured, regions provided the pressure gradient and permeability are sufficiently high. On increasing the conduit permeability, there is a marked increase

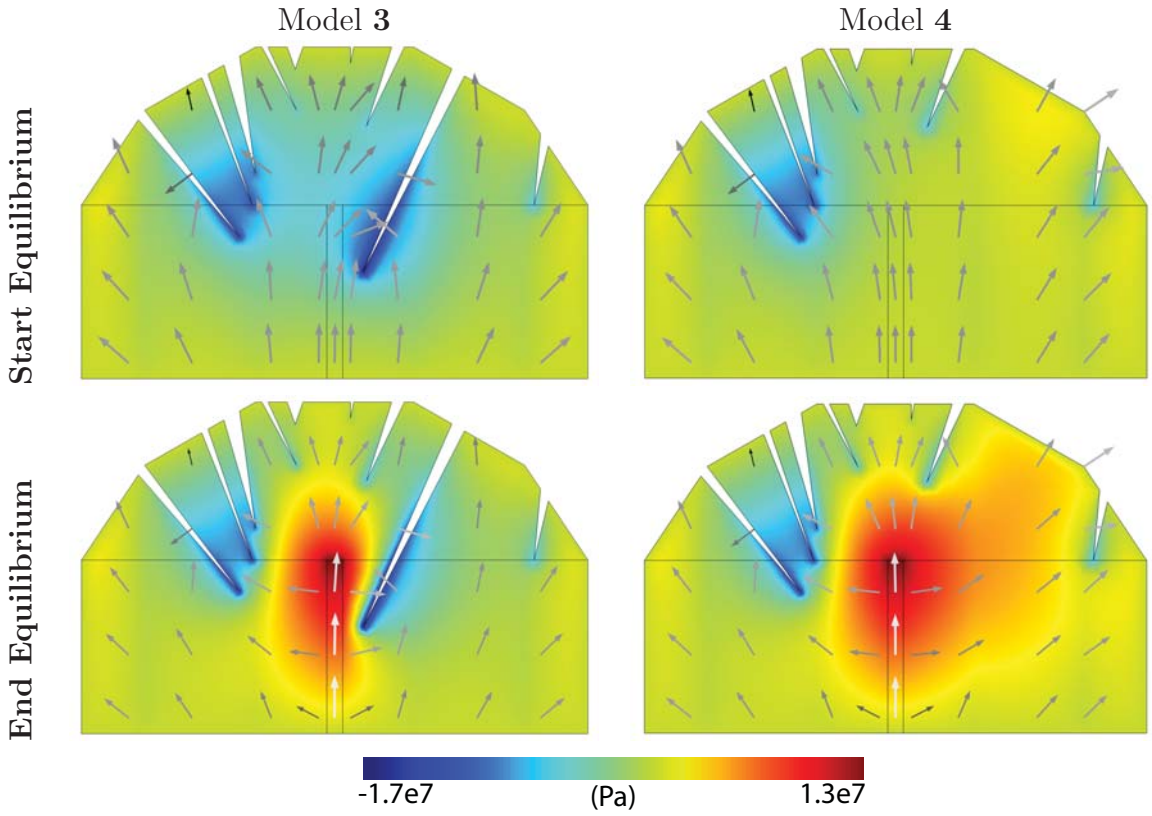

Figure 7.13: Gas overpressure for the start and end equilibrium positions of each model. Initially, the low gas overpressure suggests there is very little gas stored anywhere within the volcanic system. The greatest gas overpressure in response to the increased conduit permeability in each case is located at the top of the conduit. Consequently, this is the region of greatest gas storage. However, in Model **4**, the higher gas overpressure in the right side of the dome also accommodates gas in storage. The deeper the crack, the lower the gas overpressure, showing these cracks are more efficient at extracting the gas, due to the greater pressure gradient.

in gas velocity, particularly within the conduit, but also throughout the dome, especially the region of dome above the conduit. This suggests the gas is being forced predominantly vertically through the dome, rather than horizontally through the country rock.

The greater initial pressurisation in Model **4** results in this model showing the greatest initial surface displacement (Figure 7.15). Furthermore, the lack of Crack *8* in Model **4** results in a different displacement behaviour, both initially and for the temporal response to the influx of gas within the conduit. Initially, the surface of Model **3** has the greatest surface uplift above and to the left of the conduit (around Cracks *2*-*5*). In contrast, in Model **4**, the greatest surface uplift is above and to the right of the conduit (around Cracks *6*-*7*). On pressurisation, the greatest displacement change in Model **3** is located to the left of Crack *8*. In contrast, in Model

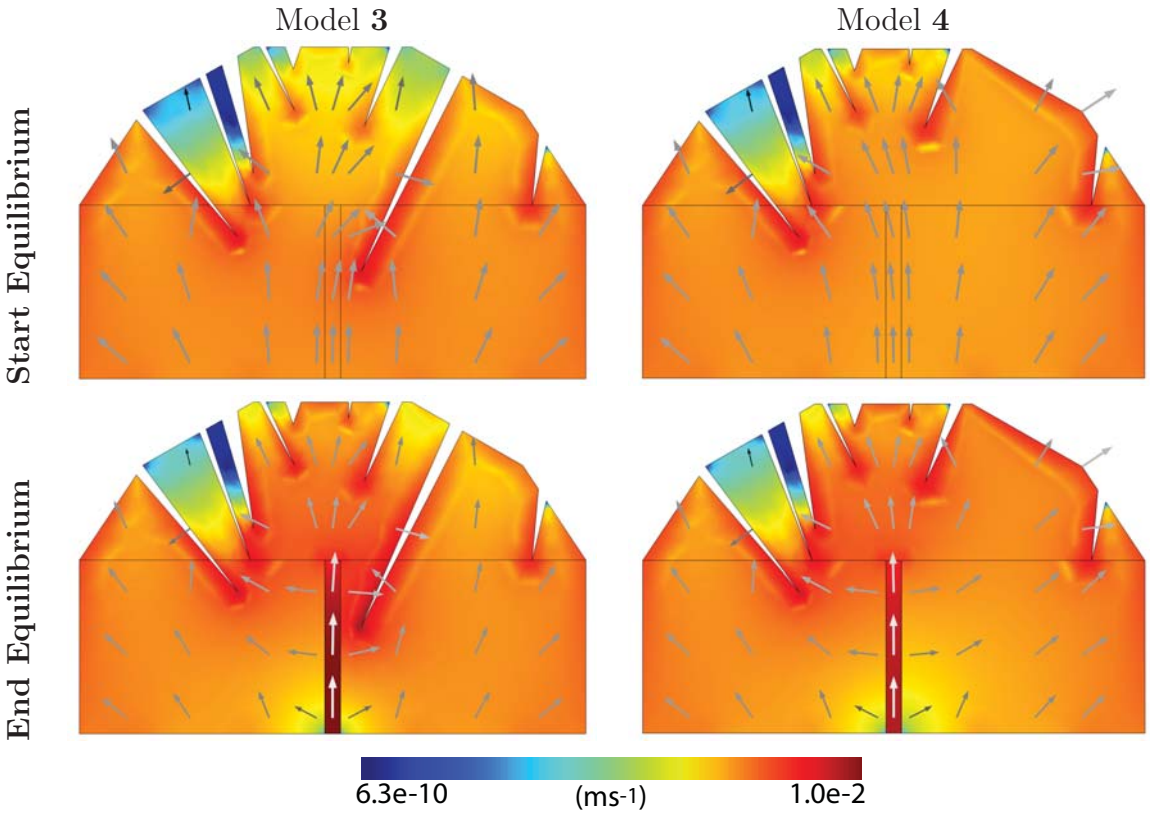

Figure 7.14: The gas velocity patterns for the two models are very similar, with the greatest gas velocities within the high permeability conduit, and around the crack margins. Portions of the dome between cracks which are located close together show much slower gas velocities. This is particularly noticeable between Cracks *1-2* and *2-3*. Gas velocity is shown on a logarithmic scale.

4, the greatest displacement change occurs between Cracks *1* and *2*, with a second, smaller, displacement change to the left of Crack *7*. This differing behaviour is dependent upon the size and extent of the cracks and their proximity to the pressurisation source. Consequently, it may be possible to infer the location and depth of these features particularly if used in conjunction with gas measurements. However, it should be noted, these simulations are restricted to two-dimensions. Extending the problem to 3D may limit the displacement of the cracks, dependent upon their lateral extent.

In response to pressurisation of the volcano, the cracks all show different behaviour - some expand whilst others contract (Figure 7.16). The differences are dependent upon factors such as location relative to the conduit, depth, initial width, and are further complicated by the presence and impact of additional cracks. Cracks *1* and *9* show very similar contraction behaviour between the two models. However, the lack of Crack *8* in Model **4** results in markedly differing crack displacement in response to the pressurisation. Crack *8* in Model **3** shows the greatest crack expansion, followed

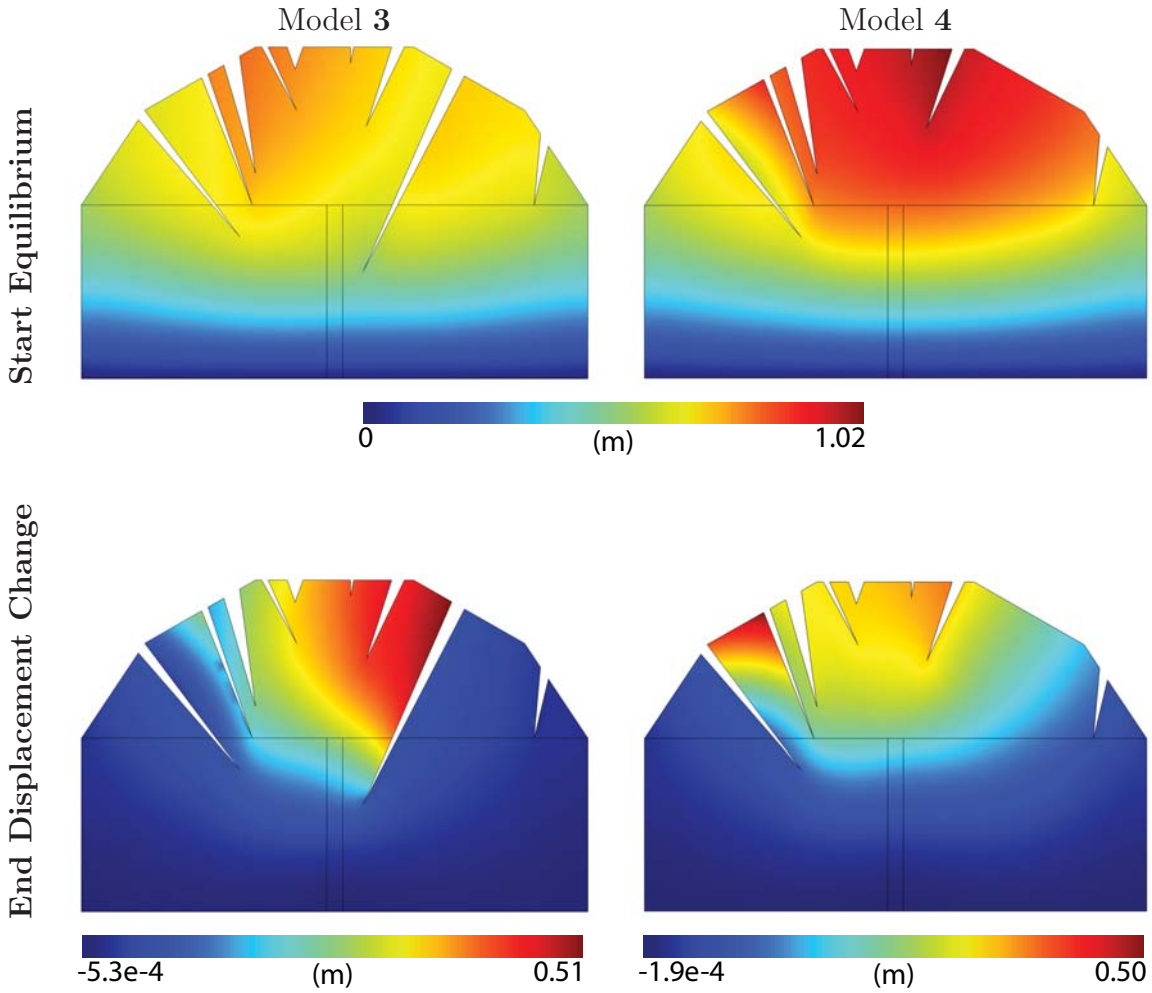

Figure 7.15: Total displacement at the start (top) and the displacement change at the end (bottom). Model **3** initially shows the least displacement, due to the lower initial pressure.

by Crack *2* and *3*. In Model **4**, Crack *2* expands the most, followed by Cracks *3* and *7*. In Model **3**, Cracks *1* and *8* show the greatest change in surface displacement, with *1* narrowing, and *8* widening. However, whilst Crack *1* continues to decrease in width until a new equilibrium width is reached, Crack *8* initially expands, before narrowing slightly. Similarly, Cracks *3* and *7* initially narrow before expanding (rapidly in the case of *3*).

This change in crack width behaviour may be illustrated more clearly in Figure 7.17, where arrows are used to show the magnitude and direction of the displacement. In Model **3** (7.17a), Cracks *2*-*7* show displacement away from Crack *8*, resulting in expansion of this crack. In contrast, in Model **4**, the displacement is away from Cracks *2* and *7* resulting in the opening of these cracks, and the closure of others.

For comparison, four other models are included to show the changing displacement

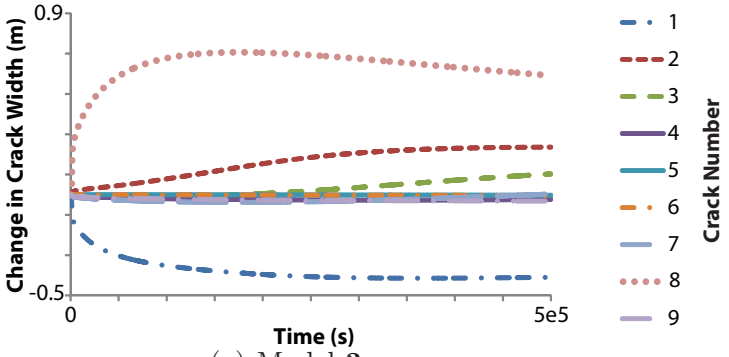

(a) Model **3**

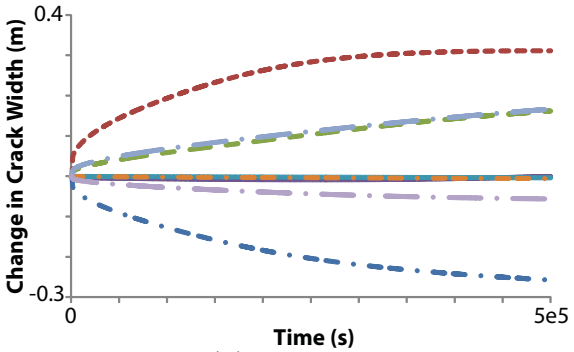

(b) Model **4**

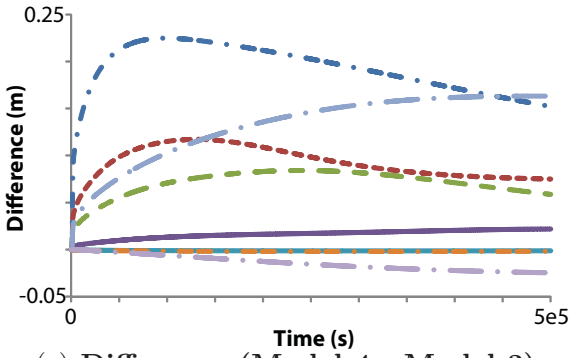

(c) **Difference (Model 4 - Model 3)**

Figure 7.16: Change in width of the nine cracks in (a) the original model (Model **3**), (b) the model run without crack *8* (Model **4**) and (c) the difference between the two models.

patterns dependent upon the cracks present: Model **3** with narrower cracks (Model **3N**), a crack-less dome (Model **5**) and the two models from Section 7.1 (Models **1** and **2**). Model **3N** shows very similar behaviour to that of the original Model **3**, with the overall change in displacement away from Crack *8*. The magnitudes are the same, the only difference is the direction. Model **5** shows the displacement change pattern when there are no cracks present is radial around the conduit, with the displacement change above the conduit being vertical, and getting progressively shallower down the flanks of the dome. The first two-crack model (Model **1**) shows the two cracks

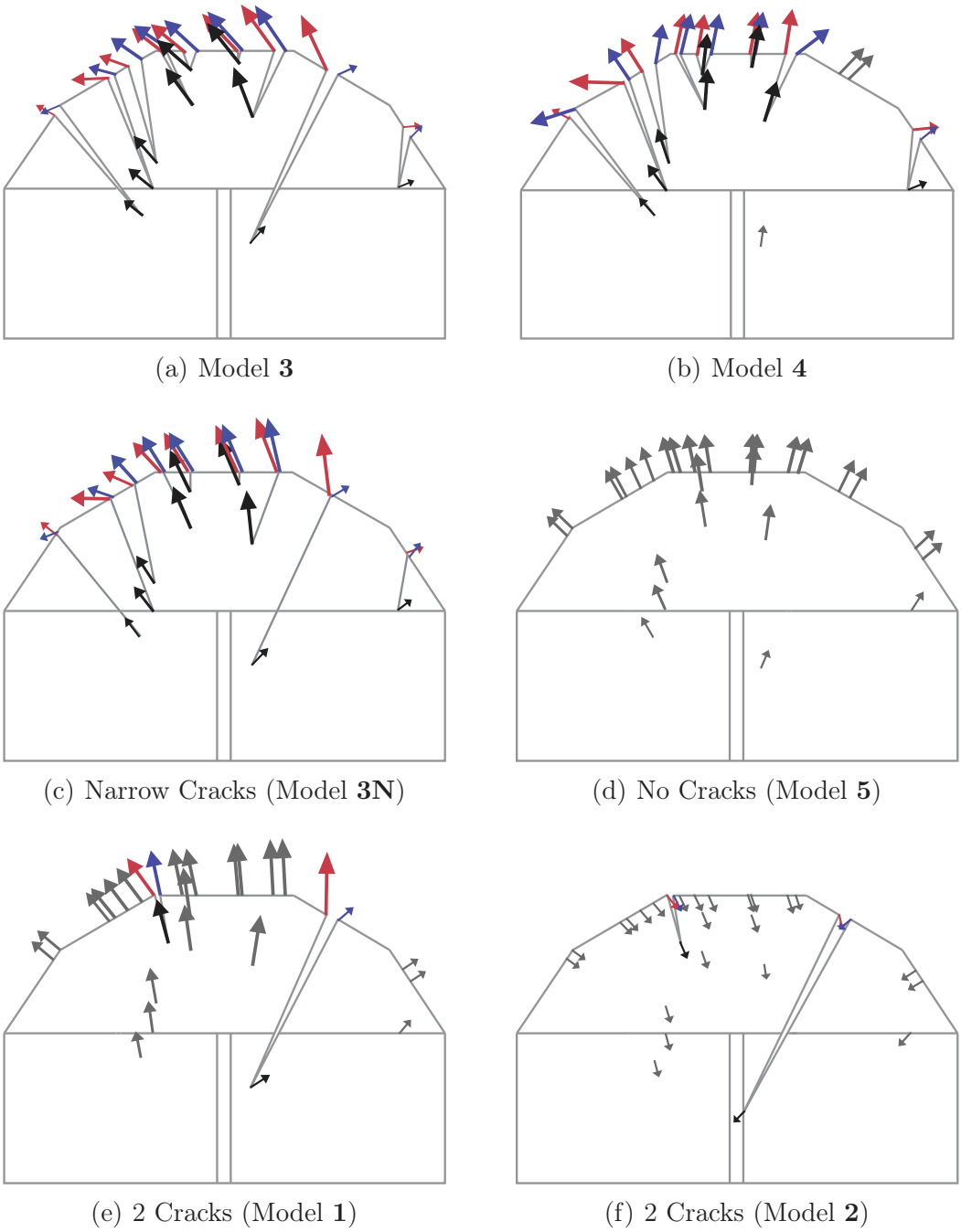

(a) Model **3**

(b) Model **4**

(c) Narrow Cracks (Model **3N**)

(d) No Cracks (Model **5**)

(e) 2 Cracks (Model **1**)

(f) 2 Cracks (Model **2**)

Figure 7.17: Arrows illustrating the magnitude and direction of displacement relative to the starting displacement for the cracks. Magnitudes across all models range between $4 - 528$ mm. The left, right and end points of each crack are coloured red, blue and black, respectively. Grey arrows represent the displacement change at the arrow locations when the cracks are not present in that particular model.

widening in response to the pressurisation. Model **2** shows dramatically different behaviour from all the other five models. Although all the arrows show very small magnitudes (mm rather than cm as in the other models), they all point inwards,

showing deflation of the dome rather than expansion. This would seem counter-intuitive. However, as shown in the previous section, Crack *2* intersecting with the conduit readily permits gas present within the conduit to escape. Furthermore, the high permeability conduit acts to draw gas from the surrounding wall-rocks and dome to exit via this crack, consequently resulting in depressurisation and deflation. In all the models, the greatest displacement occurs directly above the conduit, with the lower flanks of the dome showing decreasing displacement change in response to the pressurisation. Therefore, in response to an event, some cracks would open, whilst others close. This would be observed as a change in fumarolic activity with widening cracks potentially permitting a greater gas emission, provided they are in proximity to a region of gas storage. In contrast, gas emissions may cease in other regions of the dome. Therefore, by using both surface displacement and surface gas emissions, the type of event, the location of its source and the properties of the cracks can be inferred.

7.3 Summary

The initial state of the volcano, and subsequent changes, are strongly dependent upon the presence or creation of cracks. Each crack plays a role in determining this behaviour, and removing even one single crack may result in a dramatic change in the response of the pressurisation, gas storage, gas loss and surface displacement. If all the surface cracks and other surface features are known, mapped (in a very high resolution DEM) and monitored, the cracks and their behaviour (crack narrowing/widening and the volume of gas lost) could be used to infer the interior conditions. For example, the widening of many cracks implies pressurisation and gas storage. Whereas if the cracks show narrowing, this may suggest depressurisation. However, the situation is made more complex by the cracks interacting. One crack widening in response to pressurisation, inevitably results in the closure of another. Using this behaviour and the crack's location, it may be possible to infer the depth of the surface features and the location of the pressurisation source.

This model may be used to simulate changes in the behaviour of crack dimensions with respect to changes to the internal pressurisation of the volcano. If a high resolution topographic profile or thermal images could be obtained for a volcano, containing the characteristics of cracks (and other features) present, the changes in behaviour of those cracks could be modelled using this method.

Cracks which are "filled" by a permeability show only expansion because this method models the domains as connected, rather than as separate entities, which interact but also act independently.

The main purpose of the models to this point has been to demonstrate the use of the method and its viability as a technique to aid our understanding of volcanic phenomena. In subsequent chapters, the modelling is taken further to look at particular volcanoes in three dimensions in an attempt to appreciate some of the observations seen, such as gas volumes released and where, and surface displacement measurements.

Chapter 8

Gas Storage and Release in 3D

Models created in 3D provide a means of directly comparing the interior conditions of the volcano with the surface expression in terms of gas loss and displacement change. In turn these surface results may be compared with real gas emission and displacement measurements at active volcanoes. Creating models in 3D rather than 2D axi-symmetric removes the necessity for the model to exhibit rotational symmetry. Consequently, analysis of real volcanoes with their innate irregularities of shape is possible. Realistic 3D models of volcanoes are made possible by topographic research such as that by Wadge et al. (2009) providing high resolution DEM's (Digital Elevation Models).

This model looks at sealing within the dome of a 3D volcanic edifice and the development of a localised fracture zone within that sealed region. Such sealing may be the result of processes such as melt crystallisation, degassing, hydrothermal mineralisation and subsidence (e.g. Sparks and Pinkerton, 1978, Matthews et al., 1997, Cashman and Blundy, 2000) which result in a decrease in the permeability within the region. Fracturing may subsequently occur due to pressurisation, erosion, cooling and contraction, shear zones and local tectonics (e.g. Heiken et al., 1988, Sparks, 1997, Giammanco et al., 1998, Edmonds et al., 2003a, Sparks, 2003a). This is a useful starting model for coupling fluid flow and the resulting displacement in three-dimensions and investigating the role of permeability.

8.1 Model Setup

The geometry (Figure 8.1) is created using two sets of topographic data from Wadge et al. (2009). The data for 1 August 2005 (the start of the 2005-2006 dome growth) is used to approximate the topography of the crater and surrounding country rock whilst the data for 12 July 2003 (the end of the 1999-2003 dome growth) is used for the surface of the dome. Furthermore, the dome surface is modified to approximate

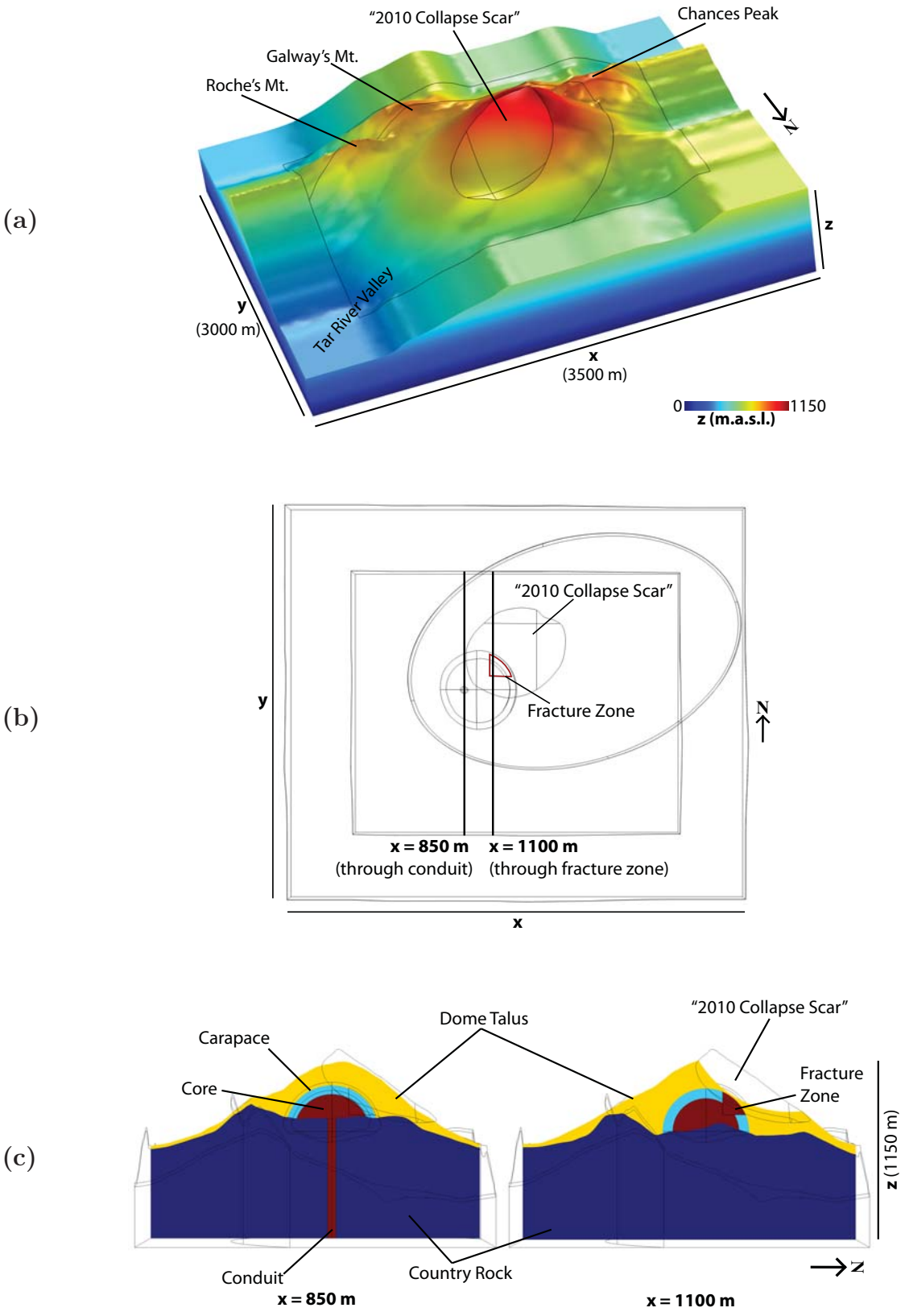

Figure 8.1: The model setup showing (a) 3D representation with important locations on Soufrière Hills marked. (b) Plan view illustrating the location and orientation of the two cross sections used to display the results and the position of the imposed 2010 collapse scar. (c) Examples of cross sections through the conduit (left) and through the FZ (right), indicating the domains modelled.

the scar that was created during the partial collapse event of 11 February 2010. Into this geometry is added a cylinder of radius 25 m to represent the conduit. For simplicity, a spine is not included and the dome is crudely sealed through the insertion of a hemispherical shell with radius 250 m and shell thickness 50 m. The portion of dome inside this shell is denoted as the "core", whilst the low permeability shell is referred to as the "carapace". This is consistent with the dome morphology suggested by Herd et al. (2005) (via photographic images during dome growth) and modelled by Hale (2008), Hale et al. (2009a,b) for the dome structure of Soufrière Hills in 2005-06. They assumed the core was intact and malleable, surrounded by a carapace of degassed material. The remaining dome is referred to as the "dome talus".

In order to trigger a degassing event, there is a localised increase in permeability within a region of the carapace. This "fracture zone" (FZ) is intended to represent a fracture density increase, rather than a single fracture and is imposed over a time period of 20 minutes. It measures 11880 m^2 on the core expanding to 30750 m^2 at the surface of the carapace. This is a large region to fail, however in Section 9.1 the results for smaller FZ are analysed. The FZ is restricted to the region of the carapace and therefore does not reach the surface, rather, it is capped by the overlying dome talus material.

This model combines an approximation of the current topography of Soufrière Hills volcano with the interior conditions as envisioned by Herd et al. (2005) for 2005-06. However, more realistic models for the state of the volcano in 2005-06 and 2012 are presented in Chapters 9.3 and 10.2, respectively.

8.2 Permeability variation and implications

This model provides a good platform for investigating how changes to the permeability of the volcano influences the outcome. To that end, a systematic parameter variation is run for the permeability values listed in Table 8.1. Through the inclusion of three different FZ permeabilities, this generates a catalogue of 72 starting (pre-fracturing) and 216 end-equilibrium (post-fracturing) solutions. The conduit and core are modelled as regions of most gas and highest permeability, whilst the carapace is simulated as a "sealed" region. Therefore the permeability must be less than or equal to that of the conduit and core. Two values are chosen for the country rock - to represent an "open" and "closed" state. A similar choice was made for the dome talus. However, a higher permeability of 10^{-14} m^2 was chosen to show a higher permeability than the country rock where the permeability may be limited due to the effects of compaction.

Domain	**Permeability (m^2)**
Conduit	$10^{-10}, 10^{-12}, 10^{-14}$
Carapace	$10^{-14}, 10^{-16}$
Country rock	$10^{-12}, 10^{-16}$
Core	$10^{-10}, 10^{-12}, 10^{-14}$
Dome talus	$10^{-12}, 10^{-14}$
Fracture zone (FZ)	$10^{-10}, 10^{-12}, 10^{-14}$

Table 8.1: Permeability values chosen for each domain in the model. See Figure 8.1 for the location of each domain listed.

8.2.1 Pressure

There are great variations in the initial pressurisation of each domain dependent upon the permeabilities chosen, not only for a particular domain, but also of the surrounding domains (Figure 8.2). However, for the 72 variations modelled, the conduit, core and carapace show similar patterns, as do the country rock and dome talus. This suggests changes in the permeability conditions affect the domains in the same way. Important points of note from Figure 8.2 are labelled and summarised in Table 8.2. Eight example models are also marked which will be discussed in detail in Section 8.4.

The conduit is always the region of highest gas pressure due to its location and permeability relative to its surroundings. The greatest conduit pressure occurs for high conduit permeabilities, but low surrounding permeabilities (**C** and **G**) because the gas is confined to the conduit and has no escape route, thus increasing its pressure. Consequently, these models also show low dome talus and country rock average pressures, because these domains are essentially devoid of gas. Furthermore, if the core is also highly permeable (10^{-10} or 10^{-12} m^2), the core and carapace pressures also increase with increasing conduit permeability, because the conduit supplies the core with gas which is subsequently sealed by the low permeability of the carapace. However, if the conduit is more permeable than the core, the core itself acts like a seal resulting in pressurisation of the conduit, but conversely, a decreased pressure within the core itself (e.g. **21** - **24**, **29**, **30**). This is because gas penetration into the core is limited, so there may be gas present at the base of the core, but absent from the remaining domain resulting in a decreased overall pressure. This sealing effect of the core increases with increasing permeability difference between the core and conduit. Furthermore, the less gas present within the core, due to a decreasing permeability, the lower the carapace average pressure (**23**, **24**). An average core pressure which is very close to that of the conduit shows a highly

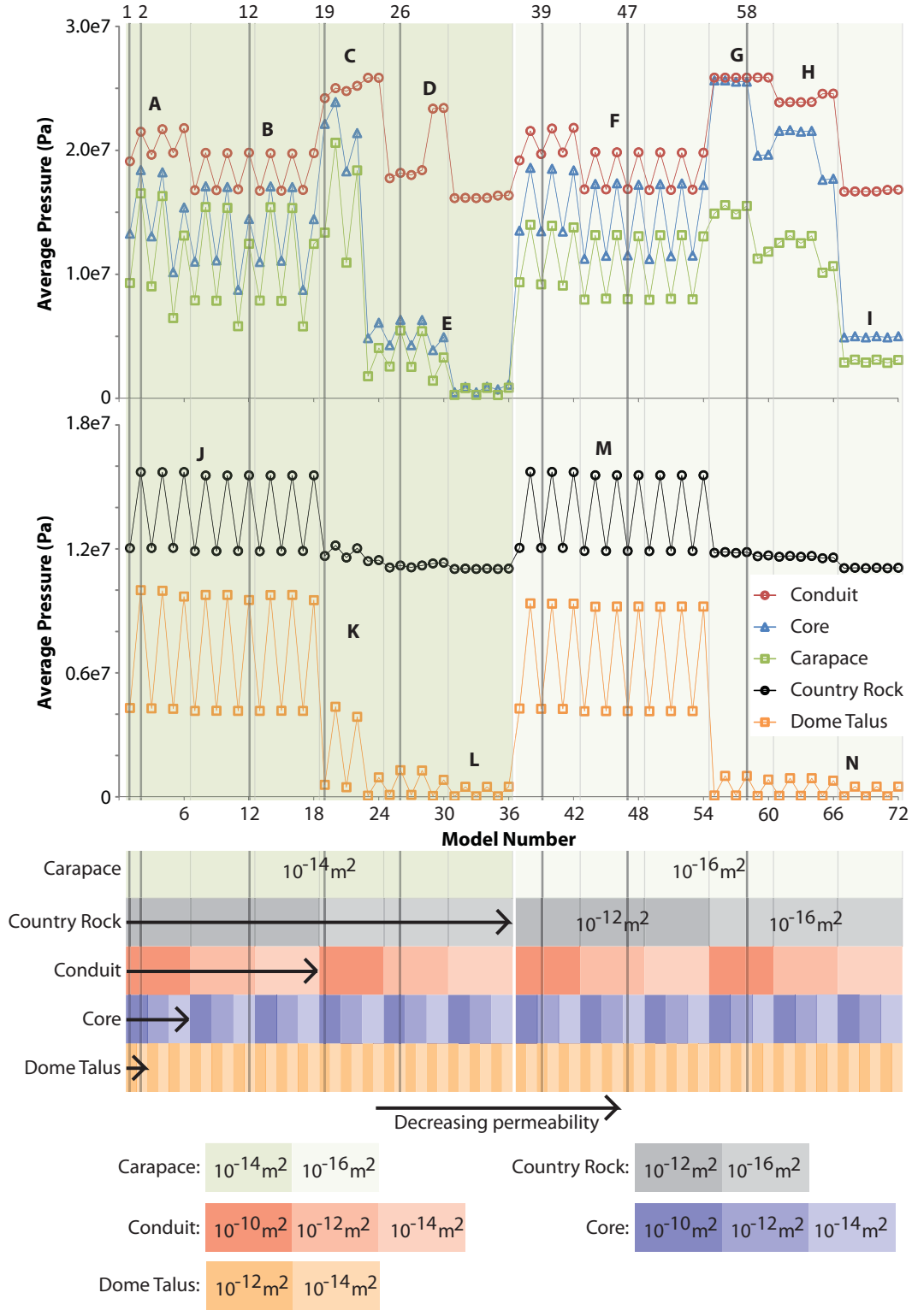

Figure 8.2: The average gas pressure within each domain for the initial state of the models. The permeability for each domain decreases from left to right (dark to light), with the values as listed in Table 8.2. Letters **A**-**N** are described in Table 8.2. The labelled models (**1**, **2**, **12**, **19**, **26**, **39**, **47**, **58**) are example models which are described in detail in Section 8.4. Arrows indicate the direction of decreasing permeability.

	Label	Detail
Conduit, **Core** and **Carapace**	**A**	High conduit k results in higher conduit pressure. Core and carapace pressures decrease with decreasing core k, but this does not significantly increase the conduit pressure because the gas can escape the conduit via the permeable country rock.
	B	Pressure in all three domains is lower than **A** due to the decreased conduit k.
	C	High conduit k is confined by a low country rock k. Increase in pressure with decreasing core k. The average core and carapace pressures decrease dramatically with decreasing core k.
	D	Moderate conduit k only showing significant pressurisation once the conduit is more permeable than the core (**29**, **30**).
	E	Low core and carapace pressures due to decreased conduit k. As the conduit k decreases, it contains less gas, and so the core pressure drops. Lower pressure than **B** because the lower country rock k does not supply additional gas.
	F	Similar conduit pressure to **A** and **B** but decreasing the core k does not significantly affect the core and carapace pressurisation.
	G	High conduit pressure is not altered by decreasing the core k, but a very low core permeability decreases the core and carapace pressures.
	H	Similar conduit pressurisation behaviour as **D**, but increased due to lower carapace k. Simultaneous decrease of the core and carapace pressures due to the decreased core k.
	I	Higher core and carapace pressures than **E** due to decreased carapace k.
Dome Talus and **Country Rock**	**J**	High country rock and dome talus pressurisation. Large decrease in pressure for high dome talus k.
	K	Dramatic decrease in pressure due to decreased country rock k containing less gas. Slight increase in pressure for a high conduit k.
	M	Similar pattern to **J**, although the country rock pressure is higher (up to 10^4 Pa), whilst the dome talus pressure is lower (up to 6×10^5 Pa) due to decreased carapace k.
	N	Similar low pressures as **L**, due to the low permeabilities in the carapace and country rock preventing gas penetrating the country rock and dome talus.

Table 8.2: Explanation for the main points of interest in Figure 8.2, where k is the permeability.

pressurised volcanic interior due to a higher permeability in these two domains coupled with a low country rock and carapace permeability (**55** - **58**).

The lowest pressure in all domains occurs when the country rock and conduit are at their least permeable, whilst the carapace is its most permeable (**31** - **36**). The low permeabilities in the country rock and conduit suggest there is little volcanic gas and any gas present is not confined by the equal permeability in the carapace. Decreasing the carapace permeability similarly gives very low pressures in each domain (**67** - **72**), but they are higher than in **31** - **36**. This variation occurs because the less permeable the carapace, relative to the underlying material, the more strongly any gas present is confined to the interior, but because the rest of the volcanic interior also has low permeabilities, there is little gas to confine.

Whilst the greatest conduit pressure occurs with the highest conduit permeability, coupled with the lowest carapace and country rock permeabilities (**55** - **60**), the highest core average pressure occurs in **55** - **58**. **59** and **60** have lower core pressures than **55** - **58** because they have a lower core permeability and thus contain less gas to be confined by the less permeable carapace. Decreasing the dome talus permeability also increases the conduit and core average pressures. This is further amplified for high country rock permeabilities (even numbered models between **2** - **18** and **38** - **54**). Whilst a high country rock permeability permits gas to escape laterally from the conduit, a low dome talus acts to confine this gas charged country rock, resulting in pressurisation. In contrast, decreasing the carapace permeability has a greater confining influence on the conduit and core if the country rock permeability is low. An impermeable country rock prevents lateral gas escape, which combined with the lack of a vertical degassing route, results in pressurisation of the interior domains (**25** - **28** are less pressurised than **61** - **64**).

For a high country rock permeability, decreasing the carapace permeability has little impact on the conduit pressure because gas can still escape to the country rock. However, the core pressure increases, because the core is surrounded by the carapace (core pressure is higher in **42** than **6**).

The average pressurisation of the country rock and dome talus are both most strongly controlled by their own combined permeabilities. When the country rock has the higher permeability of 10^{-12} m^2, the dome talus permeability has an influence, such that the greater the dome talus permeability, the lower the gas pressure (**1** is less pressurised than **2**). For the lower country rock permeability, this influence of the dome talus is still present, but far less prominent. A permeable country rock permits gas to escape from the interior conduit, which is confined by a low permeability dome talus which restricts gas escape to the atmosphere. However, for a low country rock permeability, if the conduit and carapace are their most perme-

able (10^{-10} and 10^{-14} m^2, respectively), there is an increase in the dome talus and country rock pressures (**19**, **21** have higher pressures than **55**, **57**). This is because the high interior pressure forces gas to "leak" through the carapace into the dome talus, thus increasing its average gas pressure.

8.2.2 Pressure change

The end equilibrium pressure change for each domain in the model is shown in Figure 8.3 and the main features are summarised in Table 8.3. The pressure change is similar in the core, carapace, conduit and country rock and all show depressurisation. In contrast, whilst some models also show depressurisation in the dome talus, many show pressurisation. In all models, the more permeable the FZ, the greater the pressure change. Furthermore, the lowest FZ permeability (10^{-14} m^2) only has an effect when the carapace and country rock have the lowest permeability of 10^{-16} m^2. The greatest depressurisation occurs in models **19**, **55**, **57**, **61 - 64**. These models all have a high permeability within the conduit and core, but low permeabilities within the country rock. Initially, as shown previously, this resulted in high interior pressurisation within the conduit, core and carapace. Consequently, the generation of the FZ has permitted the stored gas to escape, resulting in a decrease in pressure. In these models, the core and carapace show the greatest pressure loss, with the conduit showing less. Therefore, the core has lost a large volume of gas due to its proximity to the FZ. However, the conduit has lost less gas due to its depth and distance from the FZ and also because it continues to receive additional gas from depth. The country rock shows the least depressurisation because it also showed the least average pressure initially, as its low permeability could not accommodate significant volumes of gas. However, it is important to note that not all models which initially showed high pressures result in significant depressurisation. Some models retain their stored gas despite the increased permeability of the FZ (**23**, **24**, **29**, **30**), whilst others only show minor pressure decreases (**56**, **58**). Those models retaining their gas have a high permeability conduit, but a low permeability core. This core acts to restrict the gas to the conduit, which is also confined laterally due to the low country rock permeability. Consequently, the FZ within the carapace fails to provide a degassing route for the gas trapped within the conduit. Furthermore, despite having a high permeability within the conduit and core, some models (**20**, **22**, **56**, **58**) only partially decrease in pressure due to the low permeability within the dome talus which acts to restrict the motion of gas.

The pressure change in the dome talus is significantly different to that of the other domains, with some models showing pressurisation. This is particularly noticeable in models **55 - 58**, but also present to a lesser degree in models with a high permeability

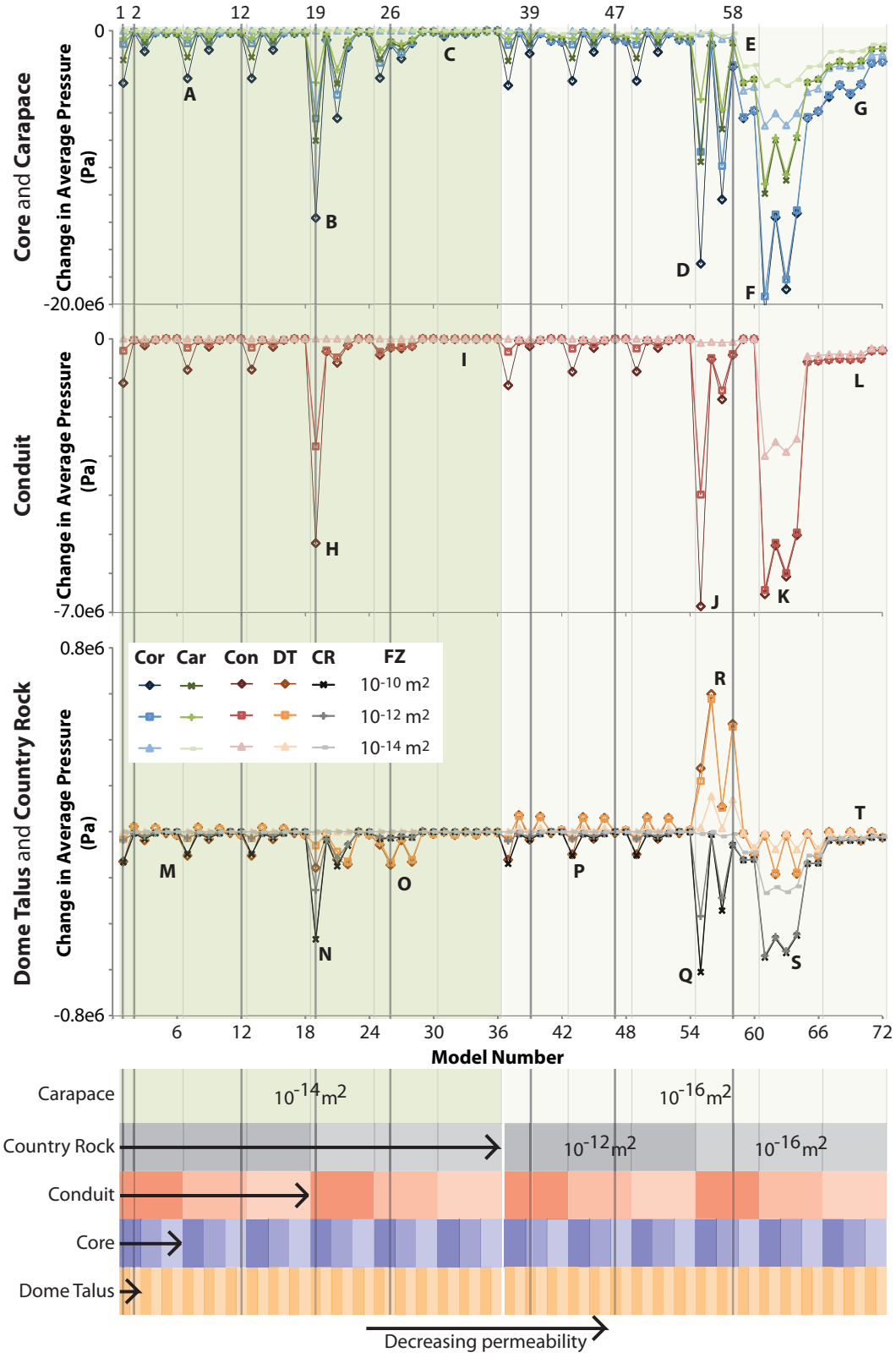

Figure 8.3: The difference between the end and start gas pressure results for each model for the different FZ permeabilities (10^{-10}, 10^{-12} and 10^{-14} m^2). Arrows indicate the direction of decreasing permeability. For Core (Cor), Carapace (Car), Conduit (Con), Dome Talus (DT) and Country Rock (CR). See Figure 8.2 for the legend on the different domain permeabilities.

	Label	Detail
Core and **Carapace**	**A**	Small change in pressure because carapace and country rock k are at their highest. Decreases with decreasing core, but little change with decreasing conduit k.
	B	Large pressure decrease because a low country rock and carapace k is combined with a high interior k.
	C	Very small depressurisation due to the lowest country rock and conduit k.
	D	Large depressurisation due to high conduit, and core k confined by a low country rock k. A high dome k aids gas escape.
	E	An FZ of 10^{-14}m^2 only has a significant effect on the pressurisation when the carapace and country rock are both 10^{-16} m^2.
	F	The largest depressurisation of the two domains. This is seen for the conduit k of 10^{-12} m^2, a high core k (10^{-10} and 10^{-12} m^2) and low dome talus and country rock k. A moderate conduit k would add to the initial pressurisation but also act to confine the gas within the core slightly.
	G	Decreasing levels of depressurisation due to lowest conduit and decreasing core k.
Conduit	**H**	Similar depressurisation as **B**, but much less.
	I	No appreciable depressurisation due to a low conduit and country rock k.
	J	Greatest depressurisation seen in the conduit (different model to the maximum core depressurisation **F**). Occurs with the highest conduit, core and dome talus k, when all other domains are lowest.
	K	Similar to **F**, but changing the dome talus k has less impact.
	L	Greater than **I** due to lower carapace k, confining the interior.
Dome Talus and **Country Rock**	**M**	Small change in pressure due to high k exterior.
	N	Large decrease in country rock pressurisation, similar to **B** and **H**.
	O	Decrease in dome talus pressure with low dome talus k due to high conduit and core k with low country rock k.
	P	Similar country rock behaviour as **M**. Increase in dome talus pressure due to high country rock and low carapace k.
	Q	Greatest decrease in country rock pressure, due to high conduit, and low country rock and carapace, but high dome talus k.
	R	Greatest increase in dome talus pressure, due to high conduit, and low country rock, carapace and dome talus k. Pressure change decreases with decreasing core permeability.
	S	Decrease in pressurisation in both domains, similar to **F** and **K**.
	T	Little change in pressure in both domains due to low k in conduit, country rock and carapace.

Table 8.3: Explanation for the main features of interest in the pressure change results relating to Figure 8.3

country rock, but low permeability dome talus (**2**, **4**, **8**, **10**, **14**, **16**, **38**, **40**, **44**, **46**, **50**, **52**). This pressure increase suggests the dome talus is restricting the motion of gas which has been lost by other domains. Models **55** - **58** show the greatest initial interior pressure, but the lowest dome talus pressure. Consequently, these volcanic systems consist of a highly gas-charged interior, but a largely degassed dome talus slope. The low permeability of the country rock and carapace prevents gas from escaping until the FZ develops. Once this new degassing route is created, some gas escapes from the pressurised interior, providing gas to the dome talus, thus increasing its average gas pressure.

8.2.3 Gas velocity

Initially, the strongest controllers determining the maximum surface gas velocity are the country rock and dome talus permeabilities (Figure 8.4, Table 8.4). The more permeable the country rock and dome talus, the greater the surface gas velocity (e.g. **1** and **37**). This is because at the start of each model, the conduit and core are capped by the lower carapace permeability. Consequently, gas must move laterally through the country rock in order to escape. Furthermore, a high dome talus permeability is required to permit this gas to then readily escape to the atmosphere. Moreover, the greater the conduit permeability, the greater the surface gas velocity, because the higher permeability generates a greater gas pressure gradient pushing the gas outwards. In general, the core permeability has little noticeable impact upon the initial surface gas velocity due to the surrounding low permeability of the carapace. However, when the country rock has a low permeability, and the conduit, carapace and dome talus are at their most permeable (10^{-10}, 10^{-14} and 10^{-12} m^2, respectively), the gas velocity does increase with increasing core permeability because the gas is forced vertically (**19** and **21**).

The maximum increase in gas velocity at the end equilibrium is dependent upon the initial pressure and the pressure change in response to the FZ, which in turn, is dependent upon the permeability conditions. Therefore, this end equilibrium surface gas velocity increase reflects, not only the internal pressurisation, but also the ease and efficiency with which stored gas is lost. Models which were previously more pressurised can result in a lower end equilibrium velocity because more gas has been lost, and therefore, their end pressurisation is lower (e.g. Model **1** is initially less pressurised than **19**, but results in a higher end equilibrium gas velocity). The gas velocity would be higher immediately after the formation of the FZ, when the pressure gradient is highest, but steadily reduces as gas is lost. There is only a significant increase in the gas velocity if the dome talus has the higher permeability of 10^{-12} m^2. Consequently, models with a lower dome talus permeability remain

internally pressurised and do not lose significant volumes of gas. The end surface gas velocity also increases with increasing conduit and core permeabilities, because high internal permeabilities provide efficient gas storage which can subsequently be tapped once the FZ provides an outlet for gas.

8.2.4 Displacement

The initial maximum surface displacement for each model (Figure 8.5, Table 8.5) follows a pattern very similar to that of the initial gas pressure in the country rock and dome talus (Figure 8.2). Consequently, the surface displacement is highly dependent upon the permeability of these two domains such that the greater the country rock and the lower the dome talus permeability, the greater the surface displacement in response to the presence of volcanic gas. Due to their relative size and location, the conduit and core domains play a secondary role, resulting in small increases to the maximum surface displacement with increasing permeability.
Figure 8.5 also shows the change in surface displacement for each model run, defined as the maximum change in surface uplift and the maximum surface deflation. All models are dominated by either deflation or inflation in response to the FZ. The dominance of deflation or inflation is strongly dependent upon the dome talus permeability. For the higher dome talus permeability (odd numbered models) deflation is dominant. In contrast, for a low dome talus permeability, inflation usually dominates. The exception to this rule is when the carapace and country rock both have the low permeability of 10^{-16} m^2. In which case, these models (**59** - **72**) show deflation which is relative to the depressurisation in response to the FZ. In turn this is dependent upon the difference between the interior (conduit and core) and exterior (country rock and dome) permeabilities: the more permeable the interior and dome talus, and the more impermeable the country rock, the greater the deflation.

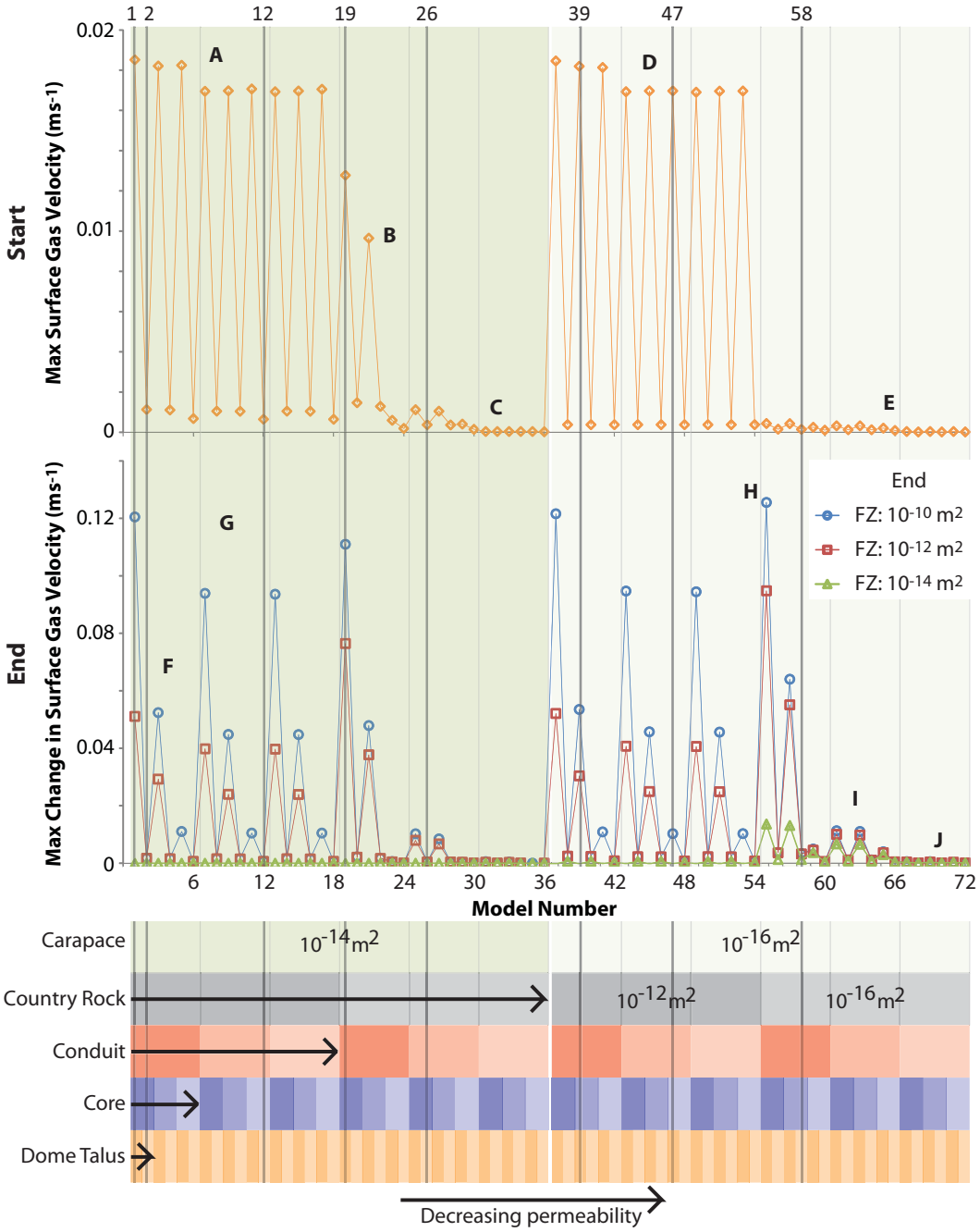

Figure 8.4: Maximum surface gas velocity at the start and surface gas velocity change at the end for each model with the three different FZ permeabilities. See Figure 8.2 for the legend.

	Label	Detail
Initial Surface Gas Velocity	**A**	High gas velocity due to high country rock k. Slightly higher for the highest conduit k.
	B	Decreasing initial gas velocity due to low country rock k and decreasing conduit and core k.
	C	Very low gas velocities for low conduit and country rock k.
	D	Similar gas velocities to **A**. Decreased carapace k has limited influence because gas escapes from the conduit laterally via the more permeable country rock.
	E	Similar to **C** with very small decreases in velocity with decreasing conduit k.
End Change in Surface Gas Velocity	**F**	Decreasing change in gas velocity with decreasing core k.
	G	Decreasing change in gas velocity with decreasing conduit k.
	H	Greatest increase in gas velocity corresponds with the the greatest conduit depressurisation (Figure 8.3) in response to the FZ (Model **55**).
	I	Only a small change in end gas velocity due to models having the greatest core depressurisation (Figure 8.3). The gas velocity increase is less than in **H** due to the lower conduit k, which resulted in a lower initial pressurisation (Figure 8.2).
	J	Little change in gas velocity due to the low k throughout.

Table 8.4: Explanation for points labelled in Figure 8.4 regarding the surface gas velocity at the start and end of each model.

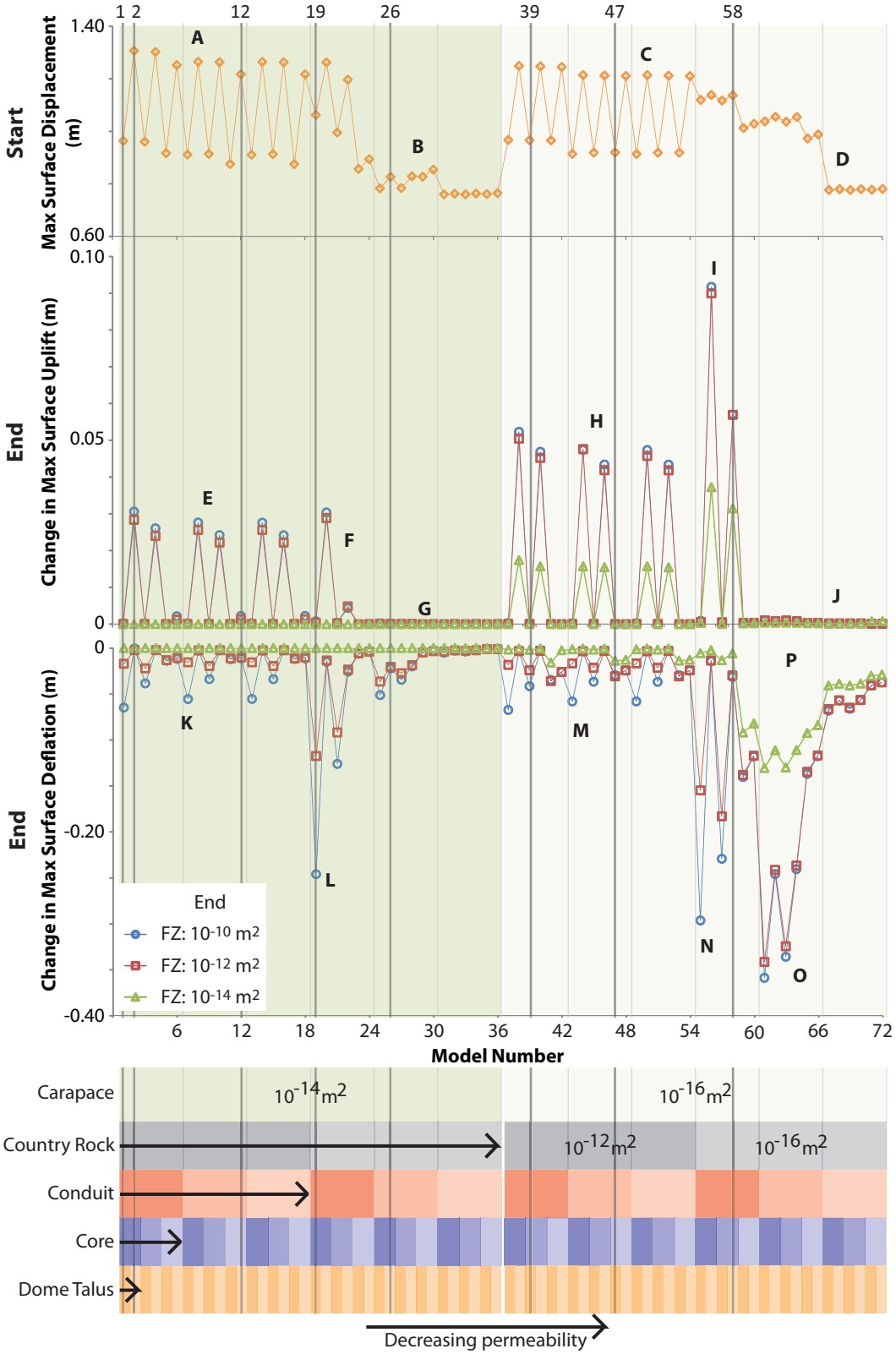

Figure 8.5: The maximum initial surface displacement and the displacement change in terms of uplift and subsidence for each model at the three FZ permeabilities. Labels are explained in Table 8.5. See Figure 8.2 for the legend.

	Label	Detail
Initial Max Surface Displacement	**A**	High surface displacement, decreasing greatly due to dome talus k. Slight decrease for decreasing conduit or core k.
	B	Decreasing surface displacement due to low country rock k and decreasing k in all other domains.
	C	Similar surface displacement to **A**, but core permeability has less influence.
	D	Similar to **B**, but higher surface displacement due to lower carapace k.
Change in Max Surface Uplift	**E**	Uplift with a low dome talus k. Uplift decreases with core k, but little change with conduit k.
	F	Decreasing surface uplift with decreasing core k. Models also show deflation.
	G	No appreciable uplift. Corresponds with the models showing the least change in pressure (Figure 8.3).
	H	Similar to **E**, but uplift is greater due to the high interior k and the low dome talus k.
	I	Highest surface uplift due to the highest conduit and core k surrounded by low k. When the FZ occurs, the stored gas is released into the FZ but remains confined due to the low dome k.
	J	Very low uplift due to large depressurisations.
Change in Max Surface Deflation	**K**	Deflation decreases with decreasing core k.
	L	Large deflation due to a corresponding high depressurisation. Stored gas is released.
	M	Similar to **K**. The higher country rock k prevents initial pressurisation, so there is less stored gas to release.
	N	Large subsidence due to large conduit and core depressurisation.
	O	Largest deflation corresponds with models showing the largest core depressurisation.
	P	All models with a carapace and country rock k of 10^{-16} m^2 show subsidence. The degree of which is dependent upon the depressurisation in response to the FZ.

Table 8.5: Explanation for features shown in Figure 8.5 for the initial surface displacement and final displacement change.

8.3 Groups with similar displacement behaviour

By analysing the graphs and the model results[1] there are large variations dependent upon the permeability conditions. Chapter 3 showed pressurisation is strongly controlled by the interior permeabilities and this model behaves in a similar way. There is a strong relationship between pressure change and displacement change. Consequently, the 72 models may be subdivided into groups of similar behaviour in response to the FZ. This is illustrated and described in Figure 8.6 and Table 8.6, respectively. Whilst inspection of the model images indicates some groups show similar starting pressures (`1`, `2B`, `3`, `4B`, `4C`), there are large variations in the initial pressure in other groups (`2A`, `4A`, `4D`). Consequently, it is the response which determines the group, rather than the initial conditions. However, some common factors must exist before these models can respond in a similar way. The groupings are based entirely upon patterns, rather than magnitude.

Group `1` is characterised by a small, localised uplift with a subsidence to the NE. Groups `2A` and `2B` are very similar with a localised (relative) uplift with a large subsidence to the SW. However, they are separated due to the relative magnitudes between the positive and negative displacement. The large subsidence is located over the core/carapace and represents the volume of gas which has been lost from the core. Group `3` comprises two models (**56** and **58**), and shows comparable degrees of uplift (NE) and subsidence (SW). Groups `4A - 4D` are all similar as they are dominated by subsidence, although the size and character of this deflation is what categorises them into separate groups. Group `4A` shows the smallest subsidence which is due to limited gas loss from the low permeability of the core. Group `4B` shows a larger subsidence, as more gas is lost from a larger volume of core. Group `4C` is very similar to `2A`, but has been separated due to the greater deflation relative to the inflation (Figure 8.7). Finally, Group `4D` shows the most extensive deflation with little evidence for uplift in the final equilibrium result (Figure 8.7).

8.4 Example Models

Eight models are chosen to illustrate the pressure and displacement response which characterises the groups in Figure 8.6 and Table 8.6. The permeability conditions for these models are shown in Figure 8.8, with the models ordered by group rather than model number. The initial permeability conditions are shown through two cross sections: through the conduit ($x = 850$ m), and through the FZ ($x = 1100$ m)

[1] Cross sections showing the pressure and the change in pressure along with surface plots showing the change in displacement, for the 72 models with a FZ permeability of 10^{-10} m^2, are contained within the accompanying DVD.

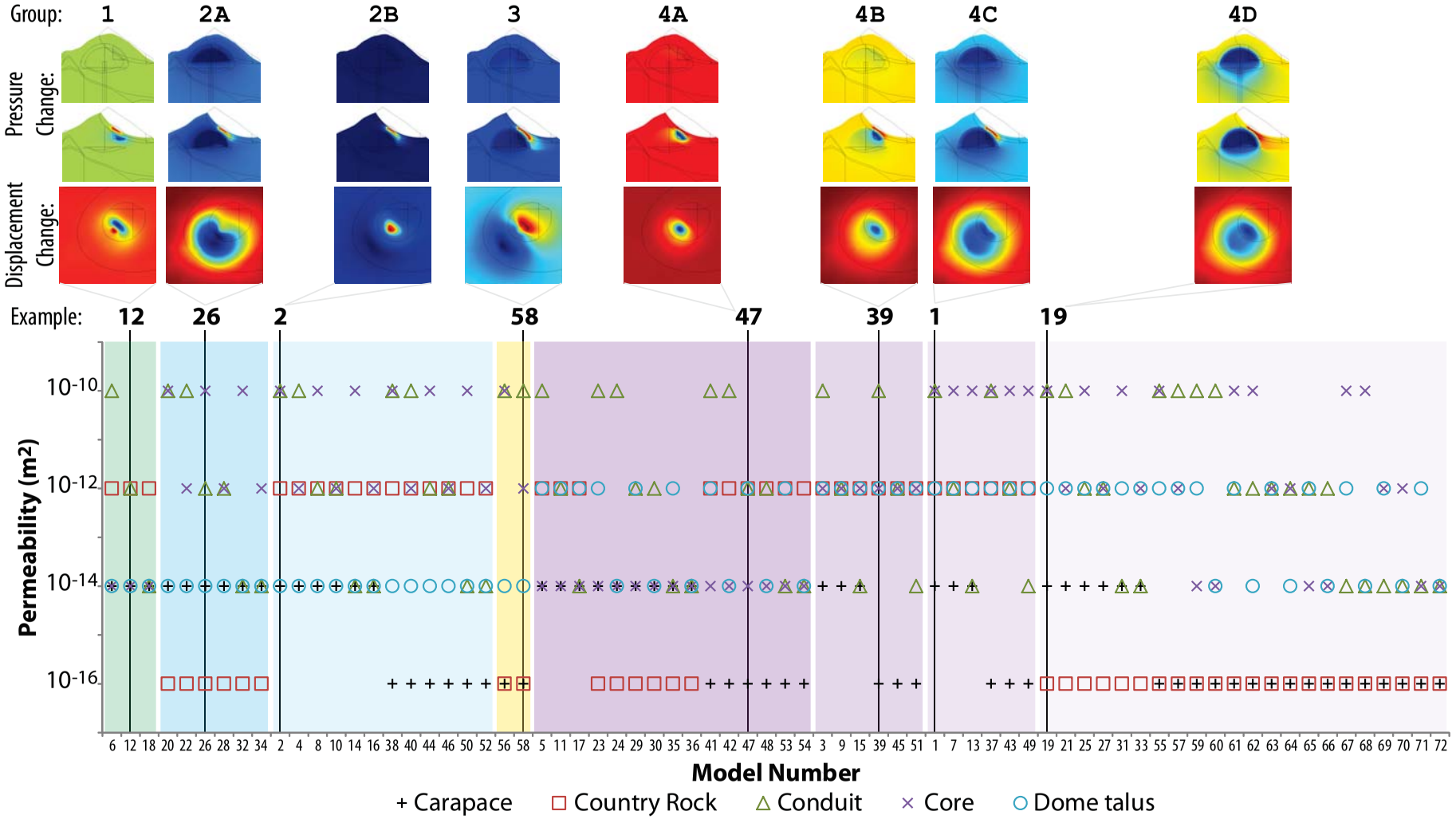

Figure 8.6: Permeability criteria determining which model displays which displacement behaviour due to the FZ. See Table 8.6. Scales are not included as the pressure change and displacement change examples show the general pattern rather than actual behaviour of each model in the specific group, however, the change is on a linear scale from blue (negative) to red (positive).

	Relative permeability	**Domains unchanged**
1	Carapace = core = dome talus = 10^{-14} m^2, AND country rock = 10^{-12} m^2.	Carapace, country rock, core, dome talus
	Country rock is more permeable than the bulk dome.	
2A	Carapace = dome talus = 10^{-14} m^2, AND country rock = 10^{-16} m^2, AND core = 10^{-10} OR 10^{-12} m^2.	Carapace, country rock, dome talus
2B	Country rock = 10^{-12} m^2, AND dome talus = 10^{-14} m^2, AND core = 10^{-10} or 10^{-12} m^2.	Country rock, dome talus
	More permeable conduit and core confined by less permeable dome.	
3	Carapace = country rock = 10^{-16} m^2, AND dome talus = 10^{-14} m^2, AND conduit = 10^{-10} m^2.	Carapace, country rock, conduit, dome talus
	Conduit and core are significantly more permeable than the surroundings.	
4A	Carapace = core = 10^{-14} m^2 AND country rock = dome talus = 10^{-12} m^2, OR Carapace = core = 10^{-14} m^2 AND country rock = 10^{-16} m^2, OR Carapace = 10^{-16} m^2 AND country rock = 10^{-12} m^2 AND core = 10^{-14} m^2.	Core
4B	Country rock = core = dome talus = 10^{-12} m^2.	Country rock, core, dome talus
4C	Country rock = dome talus = 10^{-12} m^2 AND core = 10^{-10} m^2.	Country rock, core, dome talus
4D	Carapace = 10^{-14} m^2 AND Country rock = 10^{-16} m^2 AND dome talus = 10^{-12} m^2 AND core = 10^{-10} OR 10^{-12} m^2, OR Carapace = Country rock = 10^{-16} m^2 AND IF conduit = 10^{-10} m^2 AND dome talus = 10^{-14} m^2 THEN core = 10^{-14} m^2	Country rock
	Lower permeability surroundings confining a more permeable interior.	

Table 8.6: Permeability criteria determining which model displays which displacement behaviour due to the FZ. See Figure 8.6.

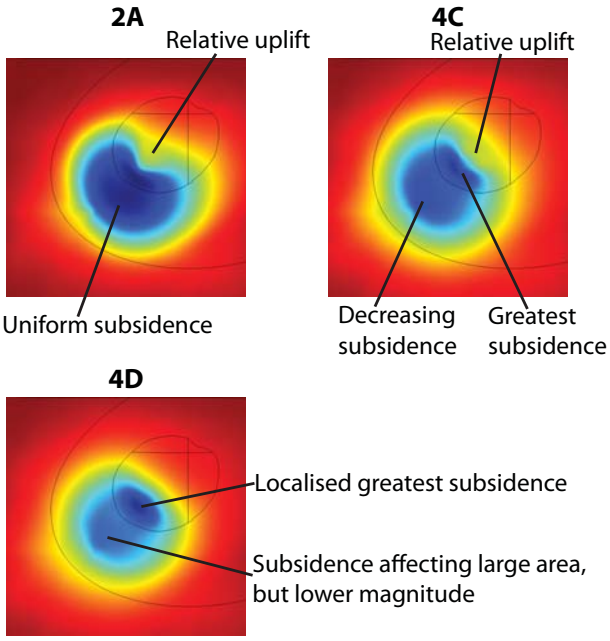

Figure 8.7: The differences between Groups `2A`, `4C` and `4D` are subtle, but are due to the relative distributions of subsidence and uplift.

(Figure 8.8). However, only the end permeabilities through the FZ are shown because there is no change in the cross section through the conduit. The models chosen show a good variation in permeability conditions across each of the five domains. The FZ is the same, at 10^{-10} m^2, in each case to ensure the maximum response. The permeability relationships described here are unique to the example models chosen, and not necessarily representative of the group as a whole.

8.4.1 Example Models: Pressure

The initial gas pressure and pressure change at the end are shown in Figures 8.9 and 8.10, respectively. Whilst the initial pressurisation is not representative of the group as a whole, it is included to show how the pressure relates to the permeability conditions set. Models **58** and **19** show the greatest initial pressurisation within the conduit and core due to the low country rock and carapace permeabilities. This low country rock permeability prevents gas escaping laterally from the conduit. In Model **12**, the three domains of the dome have the same permeability, which is lower than that in the underlying country rock and conduit, which are also equal. This configuration permits free sharing of gas between the conduit and country rock, but this gas is restricted from exiting due to the low overall dome permeability. In Models **26** and **2**, the carapace and the dome talus permeabilities are equal, and consequently, the dome talus itself acts to pressurise the system. Model **47**

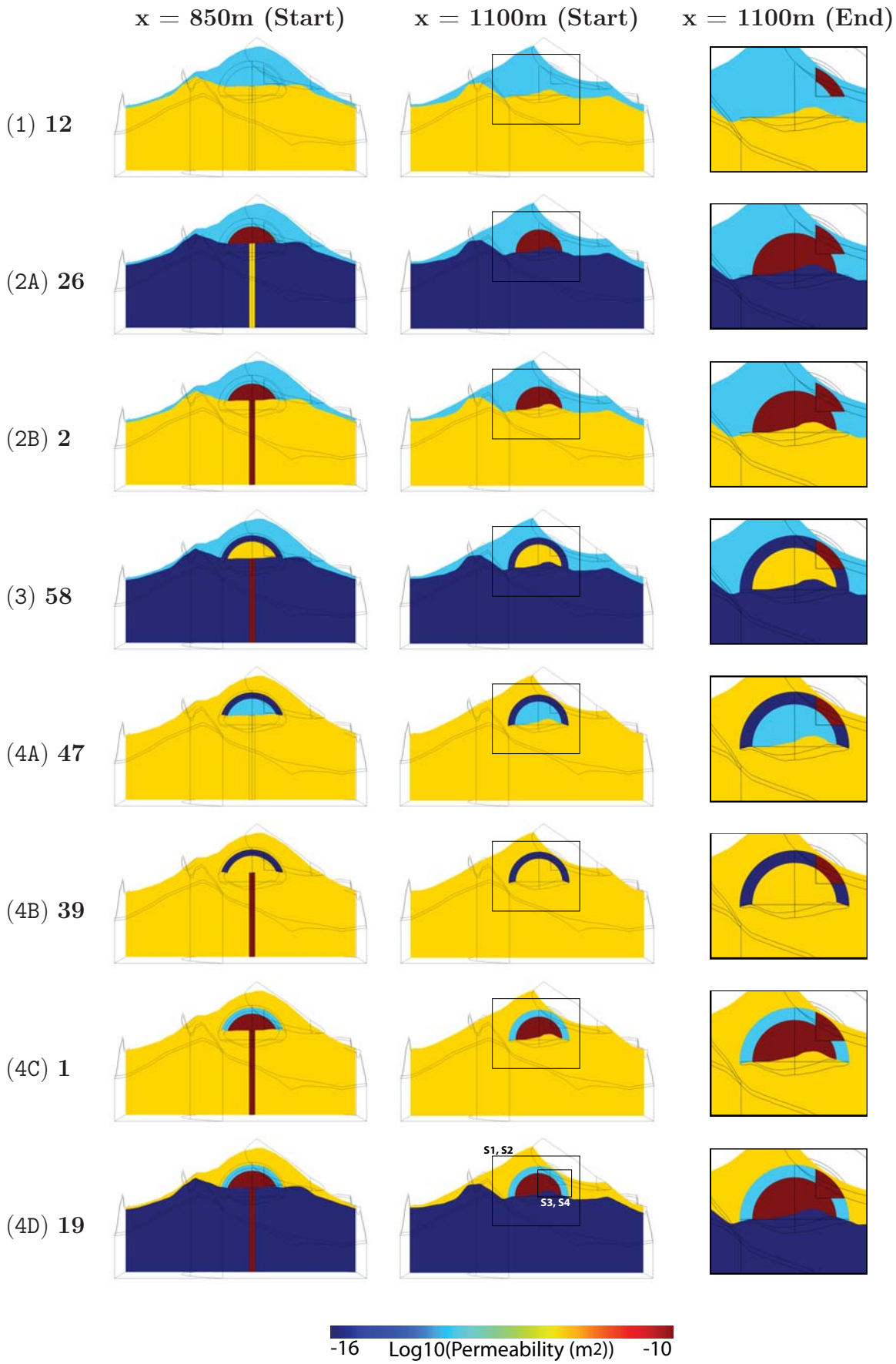

Figure 8.8: Permeability conditions for the two cross sections at the start, and through the failure at the end (x = 1100m). The models are listed according to group number (in brackets).

has equal permeability in all the domains of the conduit, country rock and dome talus, however a lower permeability within the core, which is "sealed" by a more impermeable carapace. Therefore, the gas pressure is low in the majority of the conduit and country rock, because the gas can freely escape via the dome. However, any gas present within the core is restricted, leading to pressurisation. Models **39** and **1** are very similar to this, but due to the more permeable conduit and core, more gas is contained within the interior leading to a greater pressurisation, not only in the core, but also in the vicinity of the conduit.

Based upon the initial pressure results (Figure 8.9), many of the systems modelled would be prone to failure within the core and carapace regions of the dome. Models **2**, **47**, **39** and **1** all experience gas overpressures of at least 10 MPa in the region of the core. Whilst, Models **58** and **19** have gas overpressures in excess of 20 MPa. In all these cases, such high overpressures exceeds the yield strength of 5 MPa estimated by Sparks (1997).

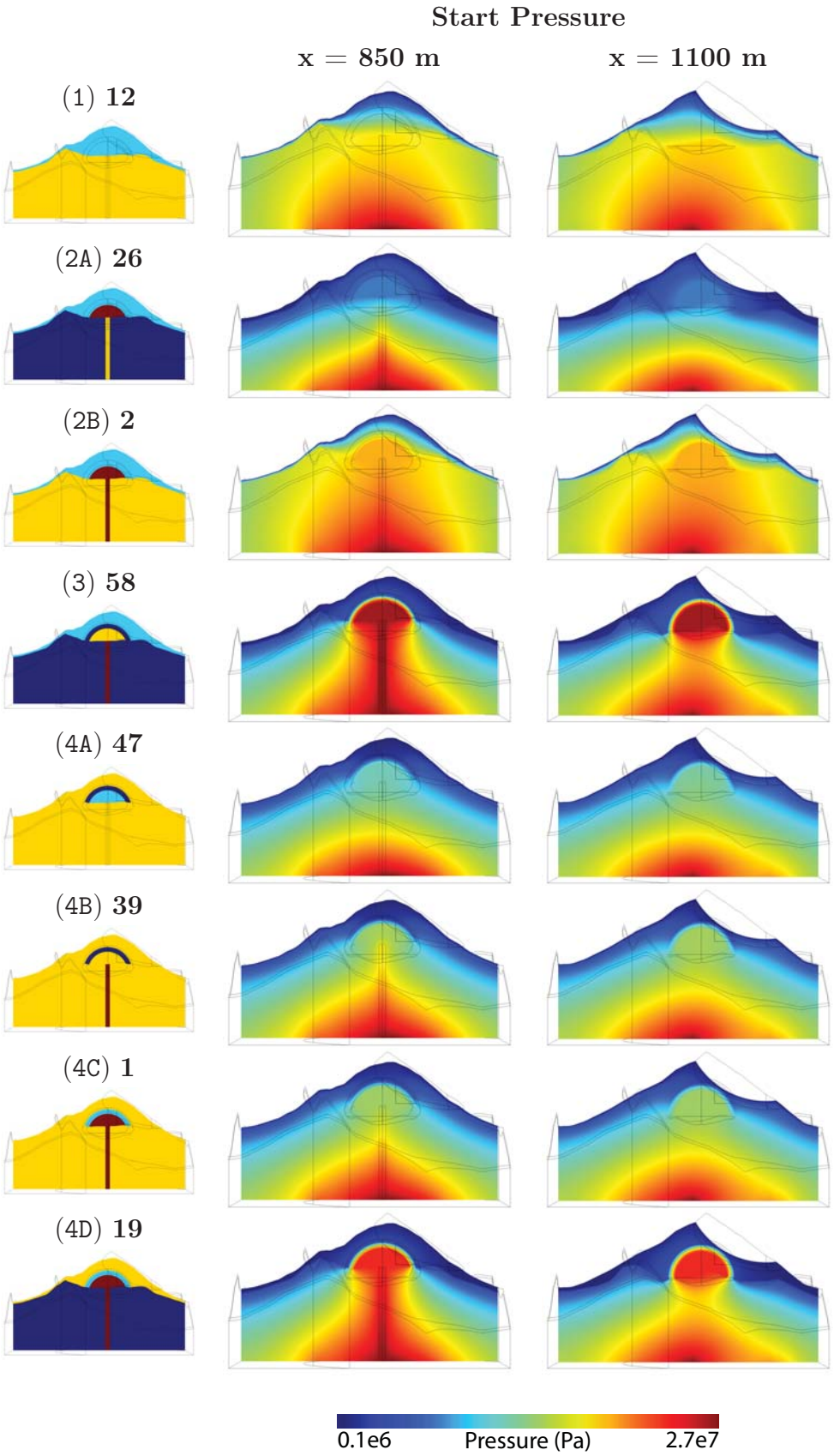

Figure 8.9: The initial gas pressure, with the permeability conditions from Figure 8.8 shown for reference.

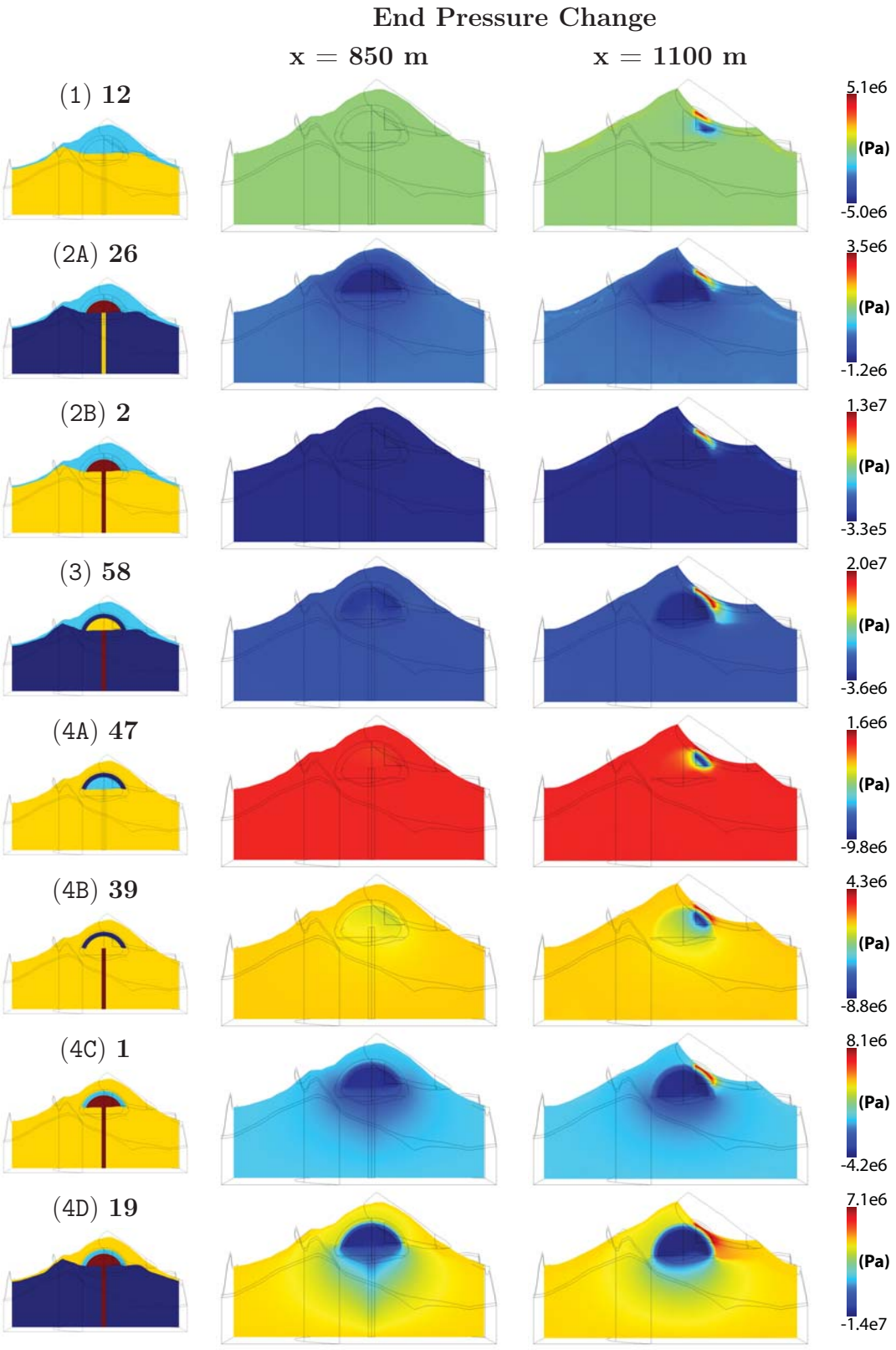

Figure 8.10: The end pressure change relative to the initial pressurisation shown in Figure 8.9. All models show a pressure change in the vicinity of the FZ. 2A, 3, 4C and 4D also show a significant decrease in pressure within the core.

8.4.2 Example Models: Pressure Change

All models show both pressurisation and depressurisation in response to the FZ (Figure 8.10). The pressurisation is because the high permeability of the imposed FZ is still overlain by the lower permeability of the dome talus. However, the size, location and magnitude of the depressurisation is related to the interior permeability conditions. A more permeable core allows more gas to exit from the volcano resulting in greater depressurisation (**26**, **1**). This is further enhanced if the conduit is also permeable, but the country rock is not (**19**). However, a low core permeability means gas is only lost from the region immediately adjacent to the FZ (**12**, **47**).

The change in average pressure in each domain in response to the FZ shows it takes considerable time to adapt to the FZ (Figures 8.11 and 8.12). In all models, except **1** and **19**, the region of the FZ shows the greatest pressure change, due to the change in permeability. In the case of **1** and **19**, the depressurisation is greatest in the core due to the high initial pressurisation and the efficiency with which the stored gas is subsequently lost. Models **58**, **2** and **26** all show pressurisation which is retained due to the FZ becoming a viable gas storage region due to the less permeable dome talus. **39** and **47** show similar patterns of deflation because the FZ provides an exit route for the stored gas due to the permeable dome talus. However, models **19** and **1** show very different behaviour from the other six models, as the FZ initially pressurises, reaching a peak approximately 500 seconds post FZ, due to the time taken for the FZ permeability to reach a similar magnitude to that of the core. The average pressure then gradually decreases as gas is lost to the atmosphere.

The core average gas pressure decreases in all the example models, although the magnitude varies widely. Some models also show depressurisation within the carapace (**12**, **47**, **1** and **19**), due to the decreased volume of stored gas exerting less pressure upon the sealed carapace. **2** shows a very rapid initial decrease in the core average pressure, although this is only by 0.175 MPa, reaching a peak at approximately 300 s post initiation of the FZ. This pressure then gradually increases to a new level 0.1 MPa lower than the initial. Furthermore, the carapace average pressure increases in this model.

In models **1** and **19**, the conduit also experiences depressurisation, although of a lower magnitude to that of the core. This shows gas is being lost from the conduit, but with a constant gas supply, it cannot fully depressurise.

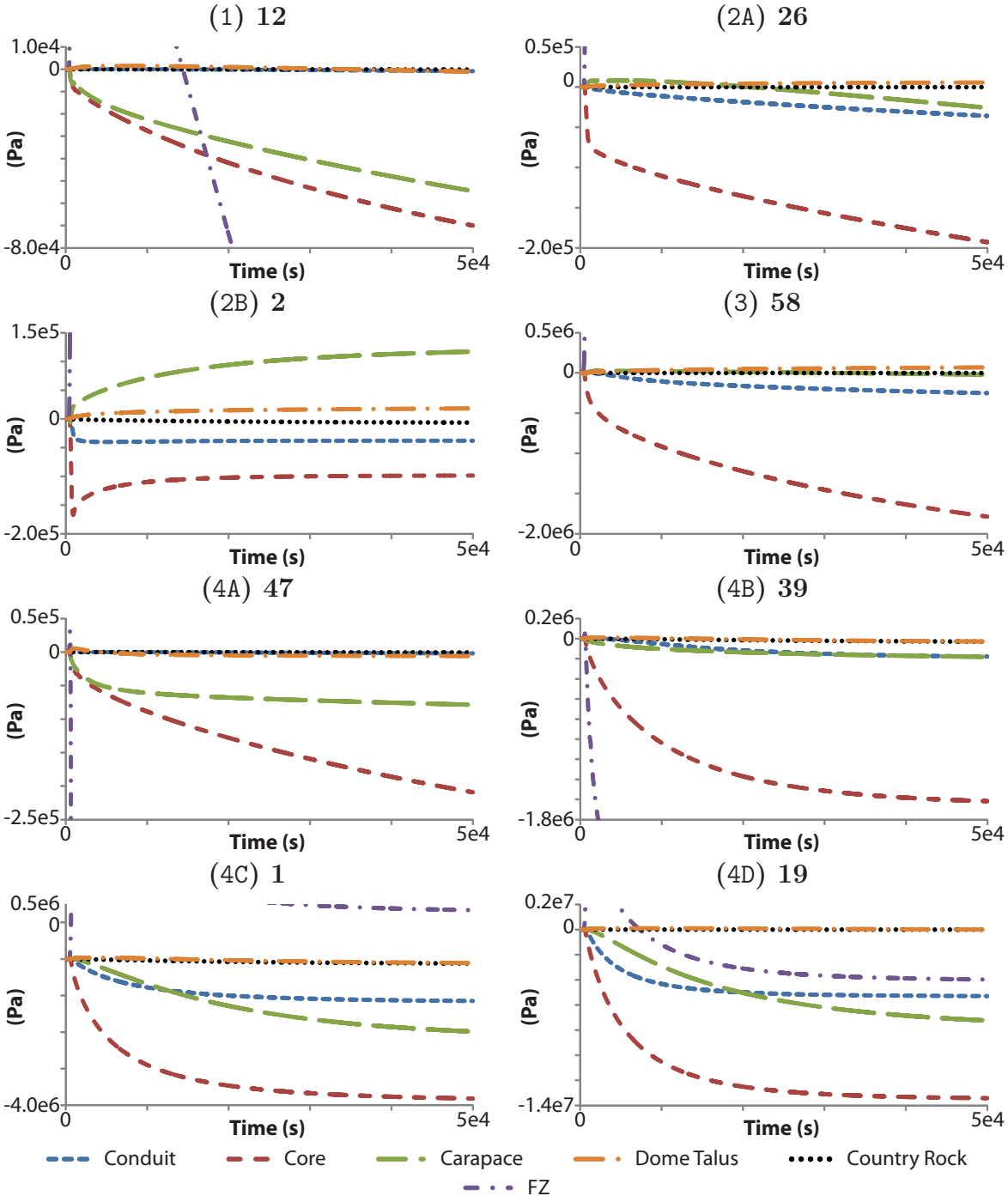

Figure 8.11: The average pressure change within each domain for all the example models. The pressure change in the FZ is shown in Figure 8.12.

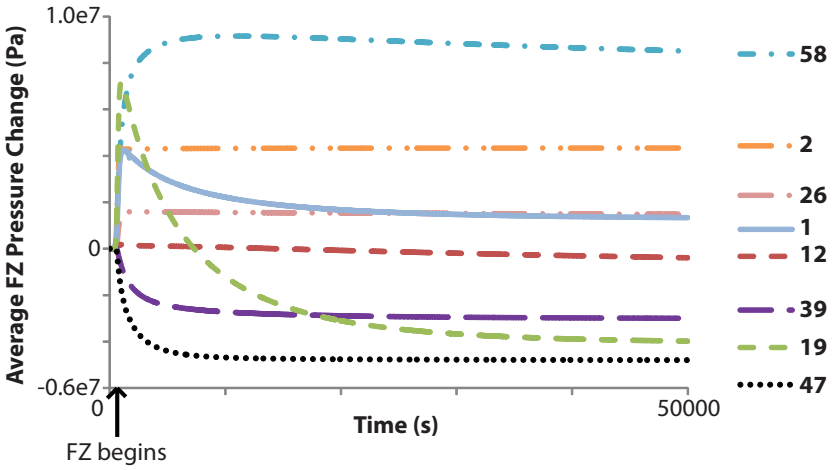

Figure 8.12: Pressure change in the FZ for each example model.

8.4.3 Example Models: Surface gas emissions

The surface gas velocity is shown in Figure 8.13 for the start and end equilibrium situations. The most striking observation is all the models with a high permeability country rock result in extensive gas emissions on the volcano flanks (**12**, **2**, **47**, **39** and **1**). Despite the sealing by the carapace, gas can escape laterally via the country rock to exit from the dome talus, particularly where the dome talus is thin. However, when the country rock has a very low permeability (**26**, **58**, **19**), these peripheral gas emissions are not present.

The three models where the carapace and dome talus have the same permeability (**12**, **26**, **2**) already show a localised gas emission above the FZ at the start. Due to the presence of the scar in this region, the dome talus is modelled as very thin, and thus the core is very close to the surface. Consequently, the pressure gradient is such that a localised gas emission occurs, although with very slow velocities. Following the FZ, all models show this localised gas emission (or it is increased). However, the gas velocities vary between the models due to the interior permeability conditions and resulting pressure gradient.

All models reach a maximum gas emission velocity shortly after the FZ, because this is when the interior pressurisation is greatest (Figure 8.14). However, the gas velocity gradually decreases as the interior pressurisation decreases. This decrease occurs most rapidly in Model **47** because the change in pressure in this model is localised to the region of the FZ.

Figure 8.15 gives an estimate for the gas lost from the conduit and core, and also an approximate rate of gas emission from the surface fumarole. In all models, the greatest gas loss is from the core. The contribution from the conduit varies between the models dependent upon the pressurisation of the conduit and the permeability of

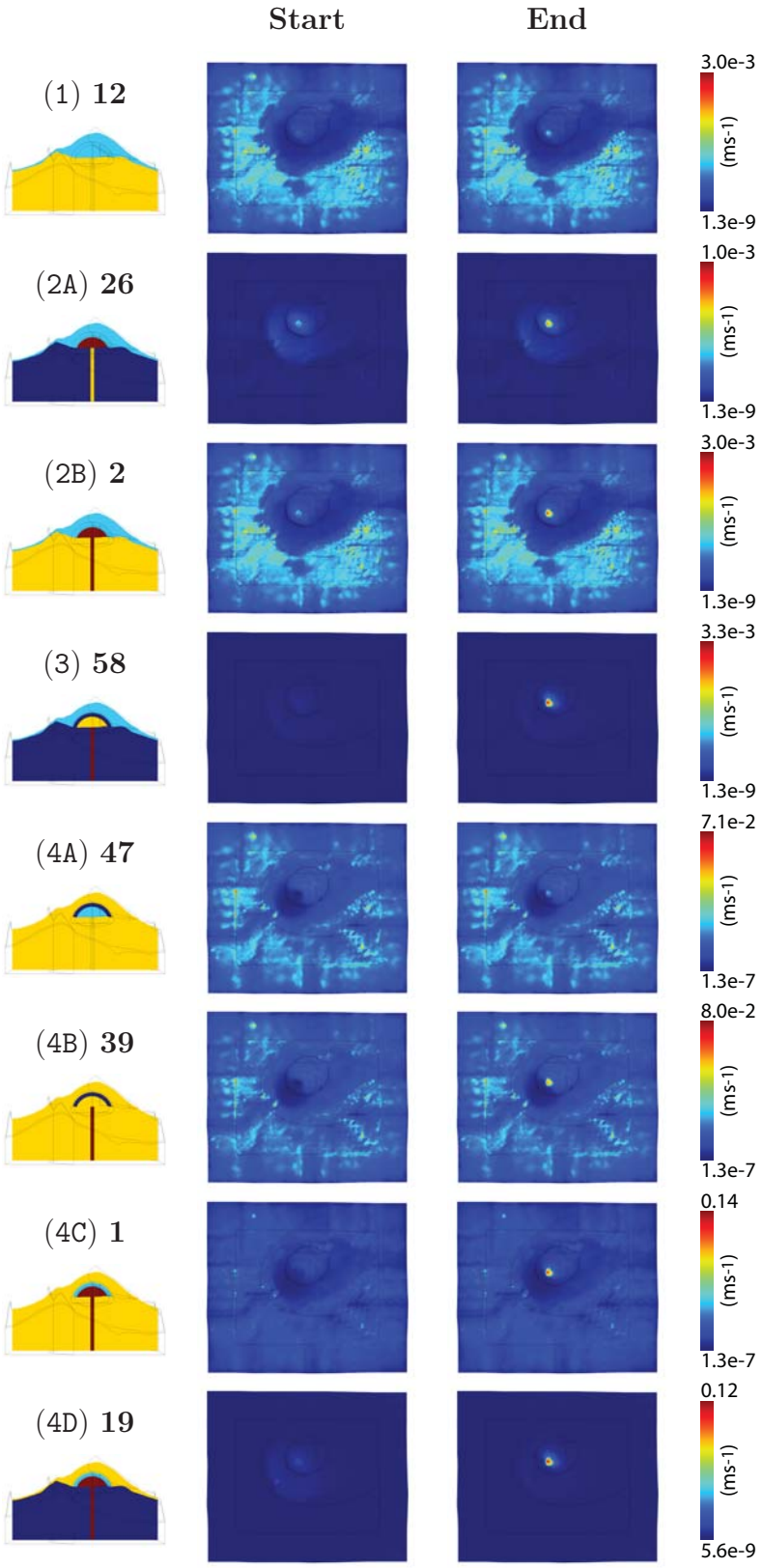

Figure 8.13: Surface gas velocity at the start and end. A high permeability country rock permits gas to escape laterally to be emitted from the dome around the core. Models **12**, **2**, **47**, **39** and **1** show slower gas loss around the periphery of the dome due to the high country rock permeability. There are small scale variations in this peripheral gas loss due to the topography.

the core. The conduit needs to have sufficient gas stored to result in pressurisation, and the core sufficiently permeable to allow the gas to escape. The contribution from the conduit is most significant in Model **19**.

Models **12**, **26**, **2**, and **58** have the slowest surface emission rate, whilst the surface emission for Models **47**, **39**, **1** and **19** is more rapid. Surface emissions of H_2O have been estimated at between 2 - 100 ktd^{-1} during dome building phases for Soufrière Hills volcano, with an average emission of 9 - 24 ktd^{-1} (Edmonds et al., 2002). Therefore, the estimates for gas emissions (100 td^{-1} - 50 ktd^{-1}) from some models may seem low. However the model neglects many features which would enhance gas loss, for example, the upward motion of magma during dome building, which adds to the gas velocity, the effects of additional exsolution due to the pressure change, structural changes such as the redistribution of fractures and other degassing pathways in response to the loss of mass. Furthermore, the surface gas emission is calculated solely on the localised fumarole, and neglects any emissions from the surrounding area. However, it may also suggest that certain permeability combinations are unrealistic or unsustainable for any length of time without a change occurring, either an increase in the permeability allowing gas to ascend from deeper levels (e.g. **12**) or significant failure, including dome collapse, releasing the stored gas (e.g. **58**).

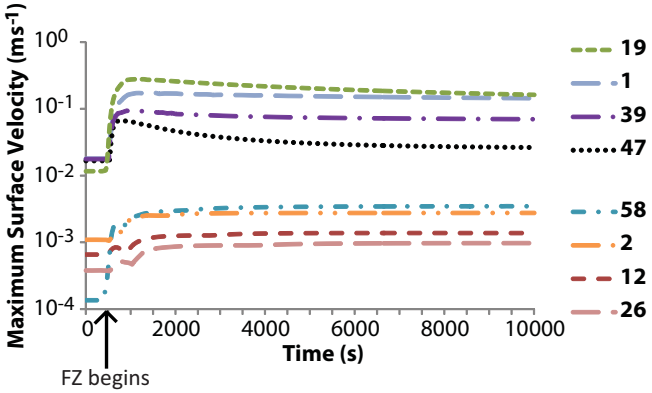

Figure 8.14: Graph showing the maximum surface gas velocity within the scar. All eight example models show an increase in surface gas velocity in this location after the FZ event has begun, although to different magnitudes.

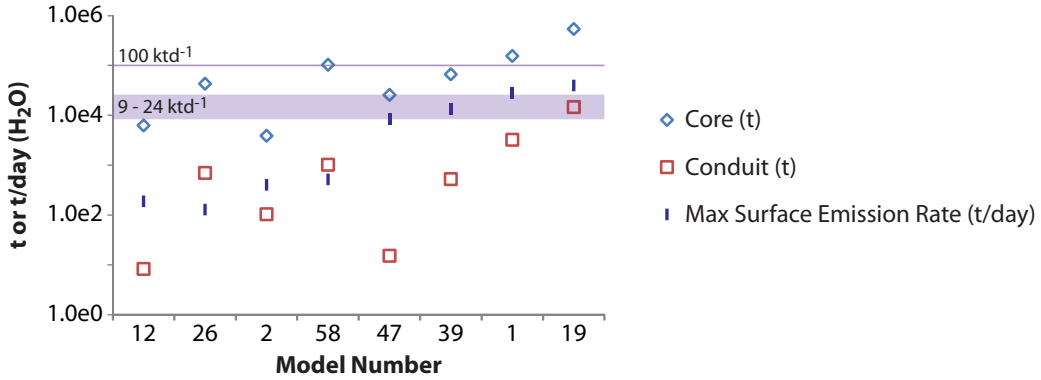

Figure 8.15: Gas loss estimates for the conduit and core domains in metric tonnes (t). Approximate gas loss rates (t/day) from the surface are also indicated. However, the gas loss from the conduit is only calculated for the shallow section modelled, and therefore neglects any contribution from the conduit at deeper depths. Gas loss from the domains is calculated as a product of the domain volume and the gas density ($(\rho_E - \rho_S)\, V$). Surface gas loss is calculated as a product of the gas velocity, gas density and surface area of the emission ($\rho_A A \boldsymbol{u}$). The gas velocity is taken at the time of maximum gas velocity for each model. Therefore, the actual gas loss and emission rate for a particular volcanic system would decline as the the pressure reduces and the volume of stored gas decreases. However, all measurements for the gas emission rate are less than the maximum (100 ktd^{-1}) estimated by Edmonds et al. (2002) for dome building events at Soufrière Hills volcano. The average range of $9 - 24$ ktd^{-1} estimated by Edmonds et al. (2002) is also marked.

8.4.4 Example Models: Surface displacement

The average surface displacement increases with the average pressure across all domains (Figures 8.16 and 8.17). Models **12** and **2** show the greatest maximum and average initial surface displacement. This implies a large area of the volcanic dome is affected by the underlying widespread pressurisation. In contrast, **26** and **19** show the lowest average surface displacement, but **19** shows a much higher maximum. This shows that the high internal pressurisation in **58** and **19** only affects a small region of the volcanic dome, resulting in a high maximum, but a low average initial surface displacement. This average pressure across all domains is related to the total gas present within the volcano, including that within the country rock. Consequently, because **12** has the same high permeability in both the conduit and country rock, and this is capped by a less permeable dome, it can accommodate larger volumes of gas which result in a greater surface displacement affecting a larger region of the volcanic edifice and surrounding area. In contrast, the low country rock permeability surrounding a highly permeable conduit and core (**19**), restricts the gas to the central regions of the volcano. This highly permeable interior can store a large volume of gas, but because the conduit and core volume is small compared to that of the surrounding edifice, it results in a very localised surface displacement signal

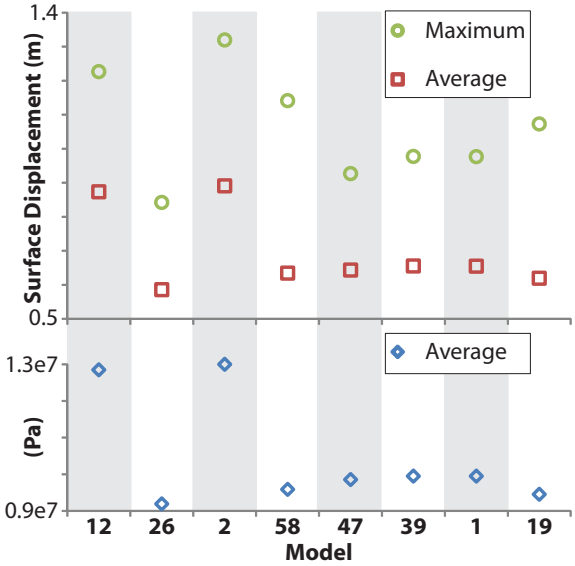

Figure 8.16: Comparison between the initial surface displacement (top) and the average pressure across all domains in the eight example models (bottom). The greater the average pressure, the greater the average surface displacement. For the eight example models, the maximum surface displacement (inflation) also follows this pattern, except **58** and **19**, which show a higher maximum, due to the high interior pressure.

(Figure 8.17).

In the model, the conduit and country rock are connected, however in reality, these regions may be "de-coupled" as evidenced by the presence of shear fractures (e.g. Melnik and Sparks, 2002, Tuffen et al., 2003, Neuberg et al., 2006, Gaunt et al., 2011, 2012). This de-coupling could locally enhance the surface displacement in response to the localised pressurisation of the conduit in scenarios such as those in **58** and **19**, if the gas remains trapped and is not subsequently released by these fractures. For reference, a discussion on the potential impacts of this de-coupling is presented in Appendix D.

As shown previously, the change in displacement in response to the FZ is dependent largely on the relative permeability conditions of the interior domains (Figure 8.5). Consequently, some models result in uplift, others subsidence. Furthermore, the change shortly after the FZ can be considerably different to the end equilibrium behaviour (Figure 8.18). After the formation of the FZ, all eight models are initially dominated by a very localised inflation (Figure 8.18, time 1000s), even though the displacement change at the end is dominated by deflation (**26**, **47**, **39**, **1**, **19**). These models begin to show deflation, which may override the inflation, as large volumes of gas are lost from the interior. In contrast, **12**, **2** and **58** maintain the inflation even up to equilibrium.

From Figure 8.18, there is a wide range in the magnitude of deflation and uplift (< 1 mm $-$ 25 cm) dependent upon the permeability conditions of the model. For example, Model **19** shows the greatest deflation of 25 cm, but a very low uplift of only 0.79 mm. In contrast, the greatest uplift occurs in Model **58** at 5.7 cm. **58** shows a comparable level of subsidence of 3.1 cm. These levels of surface displacement are consistent with those measured for real volcanoes which are generally in the range of mm $-$ several cm (Lu et al., 2000, Norton et al., 2002, Hautmann et al., 2013) (Section 1.3.2).

The progressive change in displacement in terms of the inflation, deflation and average at the surface is shown in Figure 8.19. They reinforce the results from Figure 8.18 showing the models which lose the most gas, initially show inflation which subsides as the gas from the interior is released (e.g. **1** and **19**), whilst in others, the inflation reaches a level and is sustained (e.g. **58**). However, it should be noted that the location of the maximum inflation and deflation is transient, and each time step plotted may represent a completely different portion of the dome or edifice. Furthermore, whilst the extremes of the surface displacement may be large (several cm), the average across the entire surface as modelled, is very small (mm) (Figure 8.20).

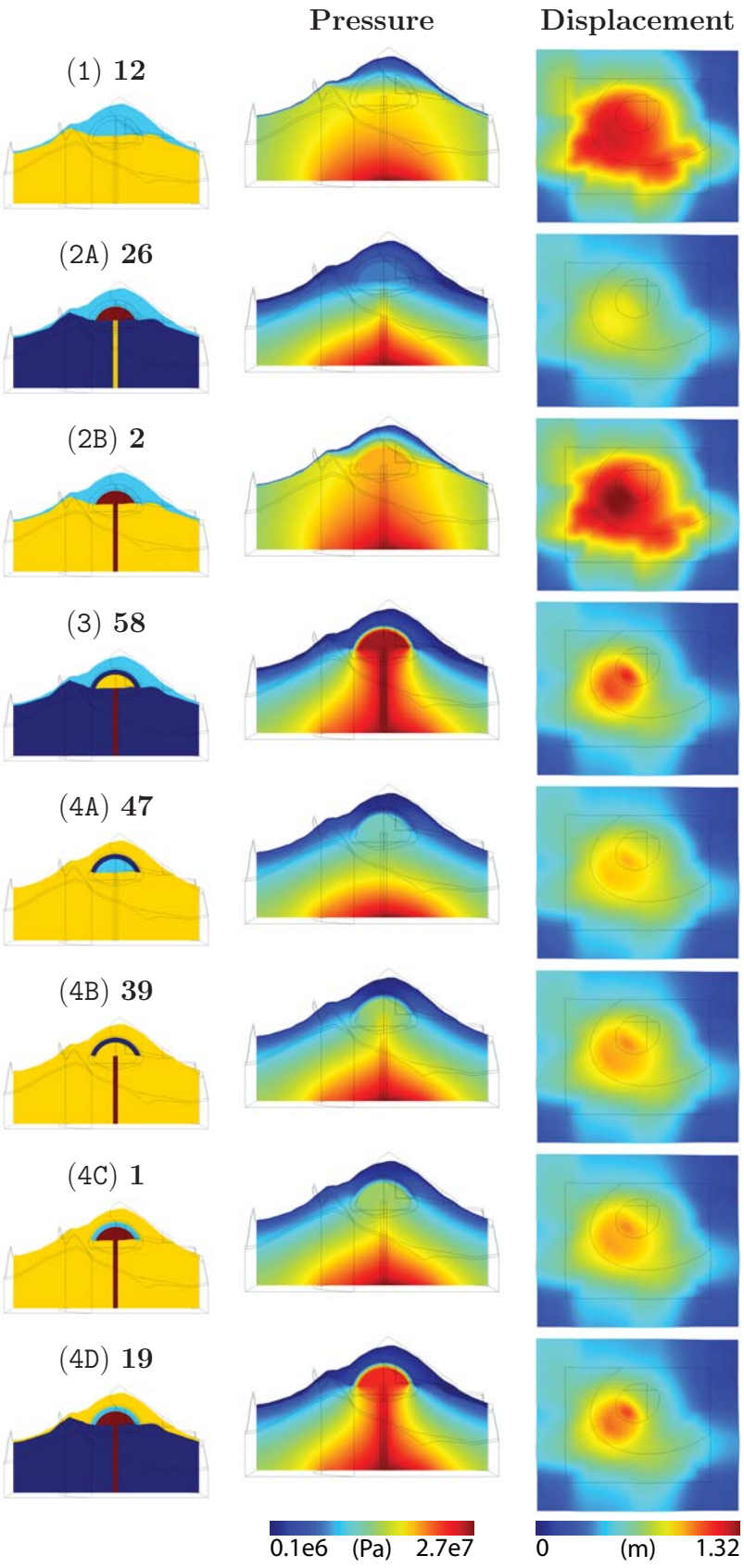

Figure 8.17: The pressure (at x = 850m) and the total surface displacement at the start for the eight example models. The average pressure across all domains, rather than localised extremes, is more important in determining the magnitude of the initial surface displacement.

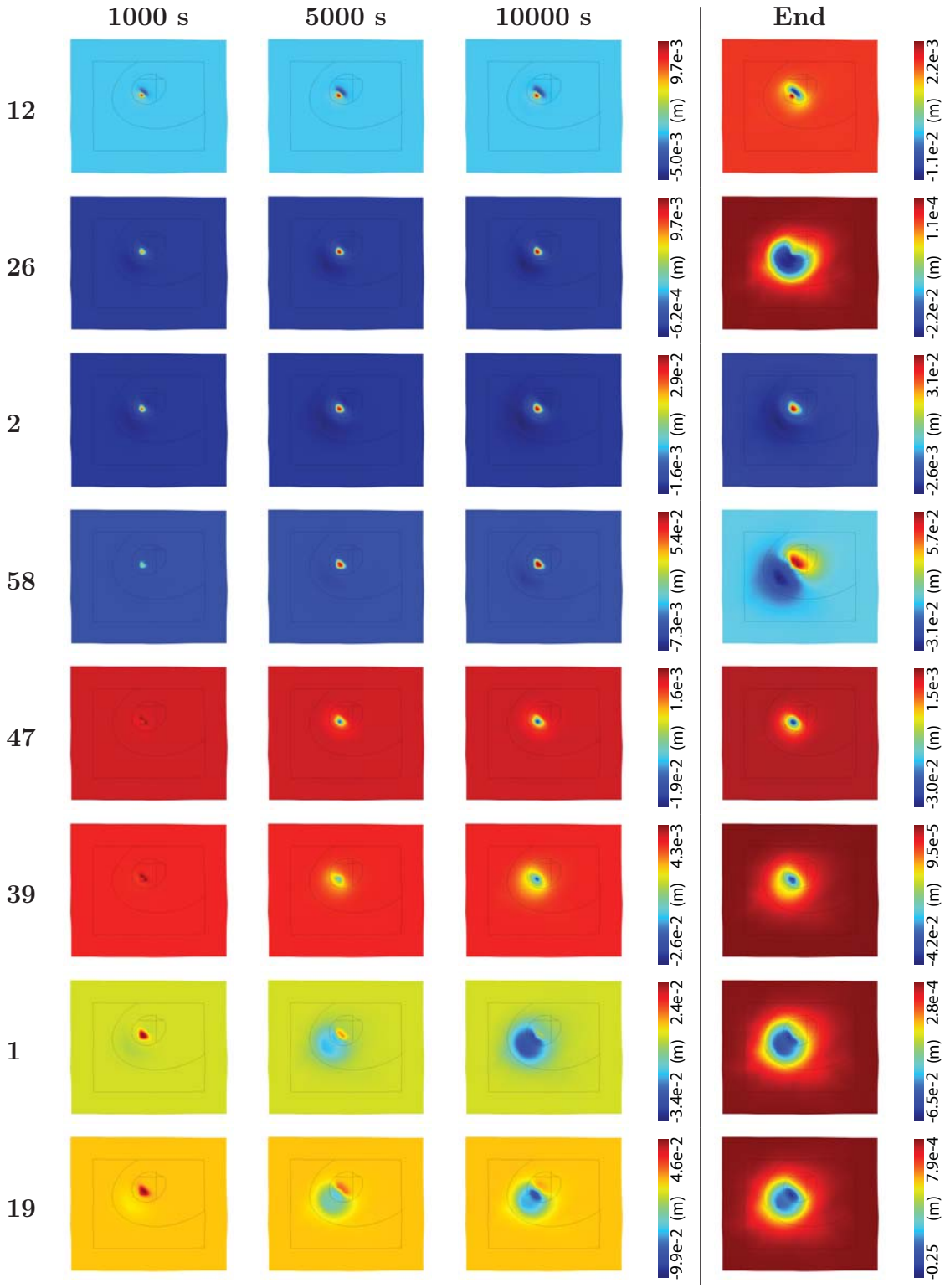

Figure 8.18: Displacement change at three time-steps and the final equilibrium displacement change for each example model.

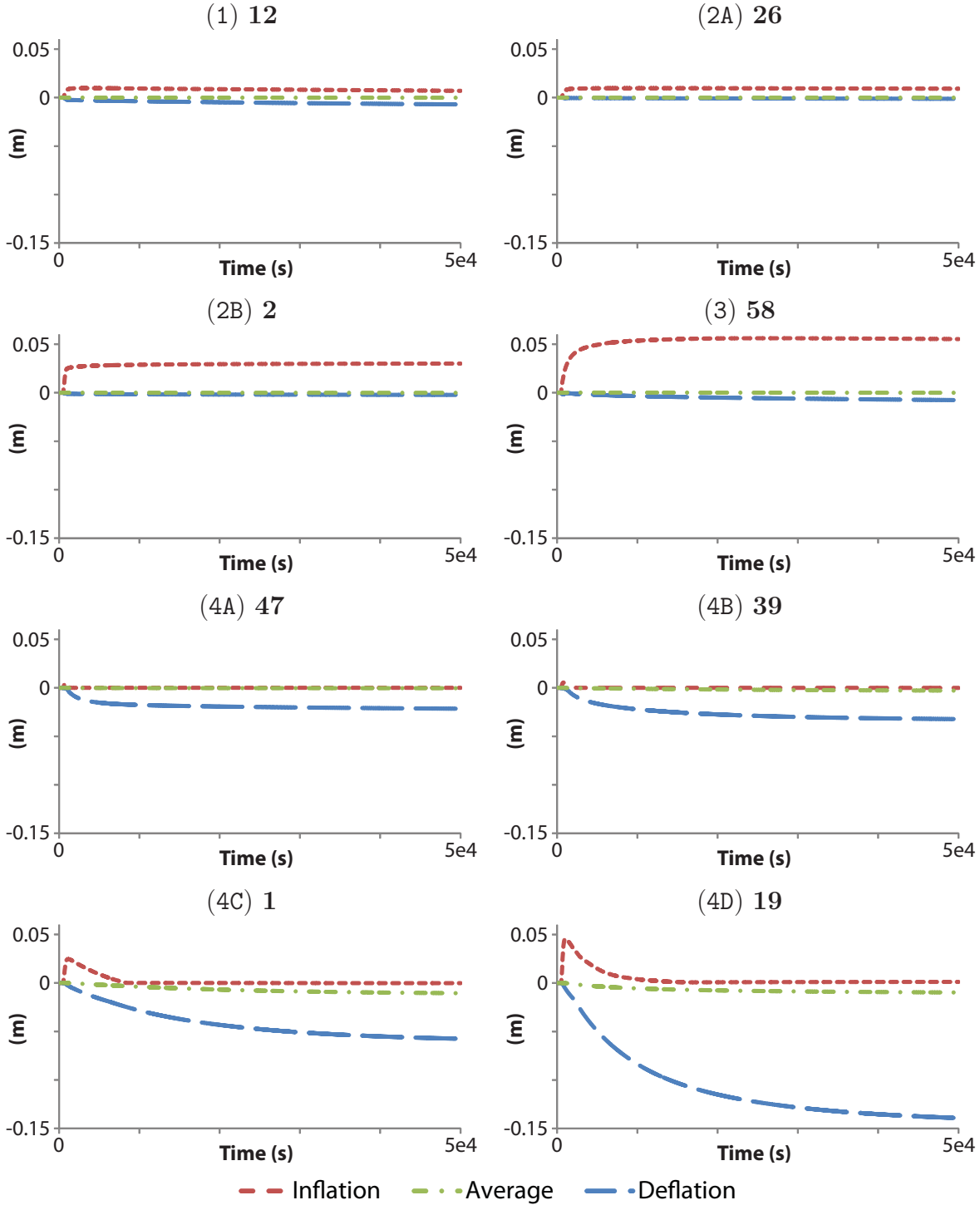

Figure 8.19: The displacement change for the maximum inflation, maximum deflation and average surface displacement for each example model. Group numbers are given in brackets.

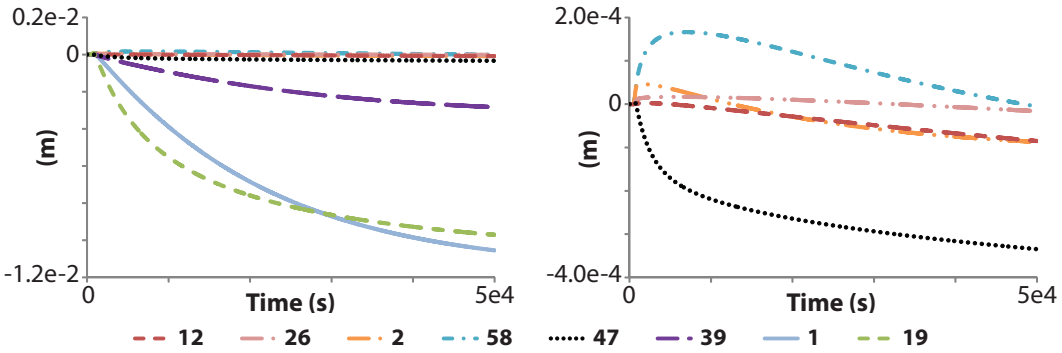

Figure 8.20: Average change in surface displacement for all the models (left) and for models **58**, **2**, **26**, **12** and **47** only (right).

8.5 Summary

There are large variations in the results dependent upon the permeability conditions of the domains. A high interior permeability coupled with low surrounding permeabilities generates the greatest initial localised pressurisation. However, a high permeability within the country rock in addition to a highly permeable conduit, capped by a dome talus with lower permeability results in the greatest overall average pressurisation.

The pressure change which occurs in each domain in response to the FZ is highly dependent upon the permeability conditions and the initial pressurisation state. However, despite these variations, there are similarities between models with widely different interior conditions. This can make it difficult to predict precisely the interior conditions based upon the surface changes observed. However, the model results presented in this chapter were split into different groups according to their response to the FZ development. Consequently, it is possible to predict general permeability relationships from surface observations.

The permeability conditions determining the initial pressurisation have a big impact upon the surface displacement. The larger the region of high permeability, surrounded or overlain by low permeability, the greater the surface displacement and the more extensive the region affected. This suggests volcanoes with a more permeable country rock (in addition to a permeable conduit) can accommodate more gas, resulting in greater surface displacement. In contrast, volcanoes with a permeable interior surrounded by a low permeability country rock may accommodate a large volume of gas within the conduit and dome interior, resulting in a more localised surface displacement pattern, and less or no peripheral degassing. Consequently, the surface displacement pattern, in conjunction with subsequent changes, could be used to infer the interior permeability conditions and the location and extent of

regions of stored gas. For example, in these models, the location and size of the gas storage region was indicated by the displacement change pattern in response to the FZ development. A large subsidence (e.g. **19**) indicated gas was stored within the core of the dome which was released, whilst subsidence and inflation (e.g. **58**) showed gas was removed from one storage region (the core) and migrated to another (the dome talus).

The resulting surface displacement change in response to the FZ is related to the location of the FZ, the location (including to the proximity to the FZ) and volume of stored gas, and the availability of degassing pathways. Consistent with near-field displacement measured at volcanic sites (e.g. Jackson et al., 1998, Voight et al., 1998, Wadge et al., 2006), those presented here cover a relatively small portion of the volcanic edifice and surrounding region. Consequently, in practice, they may be missed by GPS measurements, but may be detectable from InSAR. However, the signal related to stored gas may be masked by other processes such as magma motion and local tectonics which are not considered here. The low peripheral displacement change in the models suggests there is no evidence for larger far-field displacement changes in response to the FZ. This supports the theory that extensive displacement is reliant on changes at greater depths than are modelled here (Wadge et al., 2006).

Many volcanic systems are highly dynamic and therefore it is reasonable to expect permeabilities particularly in the conduit, dome and immediate vicinity to change over both short and long time-scales. However, this model is particularly applicable to volcanoes such as Soufrière Hills which continues to degas from the dome without active magma extrusion, suggesting the system has reached an equilibrium state.

In these models, the dome core is massively simplified. In reality, photographic monitoring during dome growth showed the core to be highly irregular in shape and punctuated by multiple spines, lobes and fractures, related to the conflicting styles of endogenous and exogenous dome growth (Herd et al., 2005, Hale, 2008, Hale et al., 2009a,b). These additional features create even more complexity for the degassing behaviour of volcanic domes, particularly as they present potential degassing routes preventing gas storage.

In Chapter 9, additional structural and permeability variations to this model setup are investigated to determine their effect on the pressurisation and surface results.

Chapter 9

Further Model Variations of Gas Storage and Release in 3D

The previous chapter illustrated there was much variation in the pressurisation, gas velocity and displacement change in response to a localised permeability increase (Fracture zone (FZ)) within a volcanic system. This chapter aims to build on this by investigating further changes to the volcanic structure and consequently, has been subdivided into three parts: variation in FZ size, conduit permeability and topographical changes.

All 72 starting and 216 end models from Chapter 8 are used to show the variability due to altering the dome topography (Section 9.3). However, Model **19** (Table 9.1) is used to show how changes to the size of the FZ (Section 9.1) and the permeability structure of the conduit (Section 9.2) affect the results. This model is chosen because it represents the group which shows the most surface change in response to the FZ. Furthermore, the models for FZ size and permeability variability are repeated

Domain	**Permeability (m^2)**
Conduit	10^{-10}
Carapace	10^{-14}
Country Rock	10^{-16}
Core	10^{-10}
Dome Talus	10^{-12}
Fracture Zone (FZ)	10^{-10}

Table 9.1: Permeability conditions for model **19**, which is used to compare the consequences of altering the size of FZ and changing the permeability conditions within the conduit.

for a more permeable country rock (10^{-12} m^2). This is because, if vertical degassing through the dome above the conduit is restricted, due to the low permeability carapace, a more permeable country rock provides an alternative degassing route which dramatically affects the results.

9.1 Altering the fracture zone

In the models in Chapter 8, the FZ, located within the carapace, had a surface area of 11880 m^2 on the core expanding to 30750 m^2. This is a very large area and consequently, the results from this model are compared with three others, each with a different FZ size.

Figure 9.1 shows the initial and end permeability conditions for the model and, graphically, the FZ sizes. The only change imposed in this section is the size of the FZ, therefore the starting permeability conditions are the same for each model. The FZ sizes cover a wide range as quantified in Table 9.2. Models **S1** (Original Model **19** from Chapter 9.1) and **S2** have a FZ which expands through the carapace. In contrast, models **S3** and **S4** are modelled as cylinders and as such, the surface area of these FZs is the same on both core and carapace top surfaces.

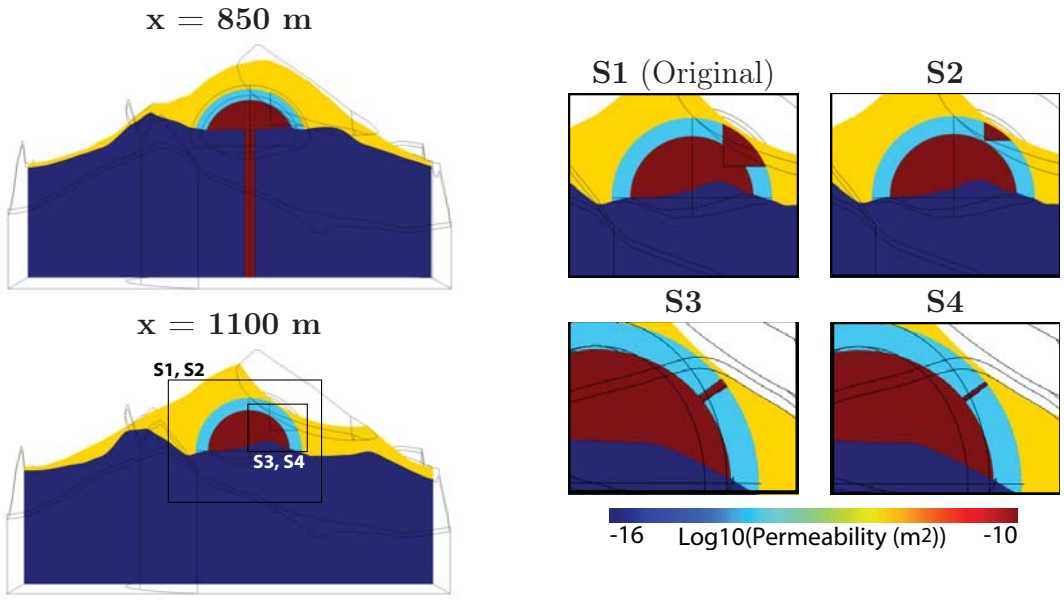

Figure 9.1: The initial permeability conditions (left) and zoomed images of the different end FZ sizes. The sizes of the FZ are presented in Table 9.2. The FZs in **S1** and **S2** are formed as a tetrahedron removed from the carapace, whilst in **S3** and **S4**, the FZs are cylindrical. A closer view of **S3** and **S4** is shown to show the form of the FZ more clearly.

	S1	**S2**	**S3**	**S4**
Area on core (m^2)	11880	849	307	71
Area on carapace (m^2)	30750	10820	307	71
Total volume (m^3)	1029000	28370	15340	3553

Table 9.2: Quantification of the FZ sizes in the four models. These are shown graphically in Figure 9.1.

The initial pressure, as derived for Model **19** in Chapter 8, is shown in Figure 9.2 in addition to the end pressure change for the four models. Due to the variation in pressure change results, they are presented on different scales. Whilst all four models show both pressurisation and depressurisation within their structure, the degree and extent varies greatly between them due to the size of FZ. Models **S1** and **S2** both show significant depressurisation of the core in addition to the upper conduit and surrounding country rock. Furthermore, both show pressurisation of the dome talus immediately adjacent to the FZ. This is most extensive in **S1**, but the magnitude is greater in **S2**. The larger FZ in **S1** suggests the gas may access a larger region of dome, whilst the smaller FZ in **S2** forces more gas into a smaller region of the dome talus leading to a greater pressurisation. Models **S3** and **S4** show significantly less depressurisation within the core and the pressurisation of the dome talus adjacent to the FZ is far more localised and greater in magnitude than either **S1** or **S2**.

The gas velocity results are presented in Figure 9.3. All four models have the same initial gas velocity pattern. However, the change in gas velocity behaviour in response to the FZ is different in each model. Models **S1** and **S2** show there is a large increase in the gas velocity up the conduit, particularly at the top of the conduit where it meets the core. Furthermore, the area around the FZ shows increased gas velocity values, particularly within the FZ, but also in the surrounding core and dome talus. Conversely, these models (**S1** and **S2**) show a decrease in the gas velocity along the country rock boundary with the conduit. This suggests that whilst the carapace was sealed, the pressurisation may have forced some gas to penetrate the country rock margin, despite the low permeability. However, once the FZ opens, this gas has a more viable exit route vertically.

S3 and **S4** show very little change in gas velocity behaviour, with increased velocities restricted to the region of the FZ, with little evidence for input from the conduit or core. Figure 9.3 also highlights the extent of the surface gas emission is directly related to the size of FZ - the larger the FZ, the larger the gas exit route and the larger the region of dome talus emitting gas.

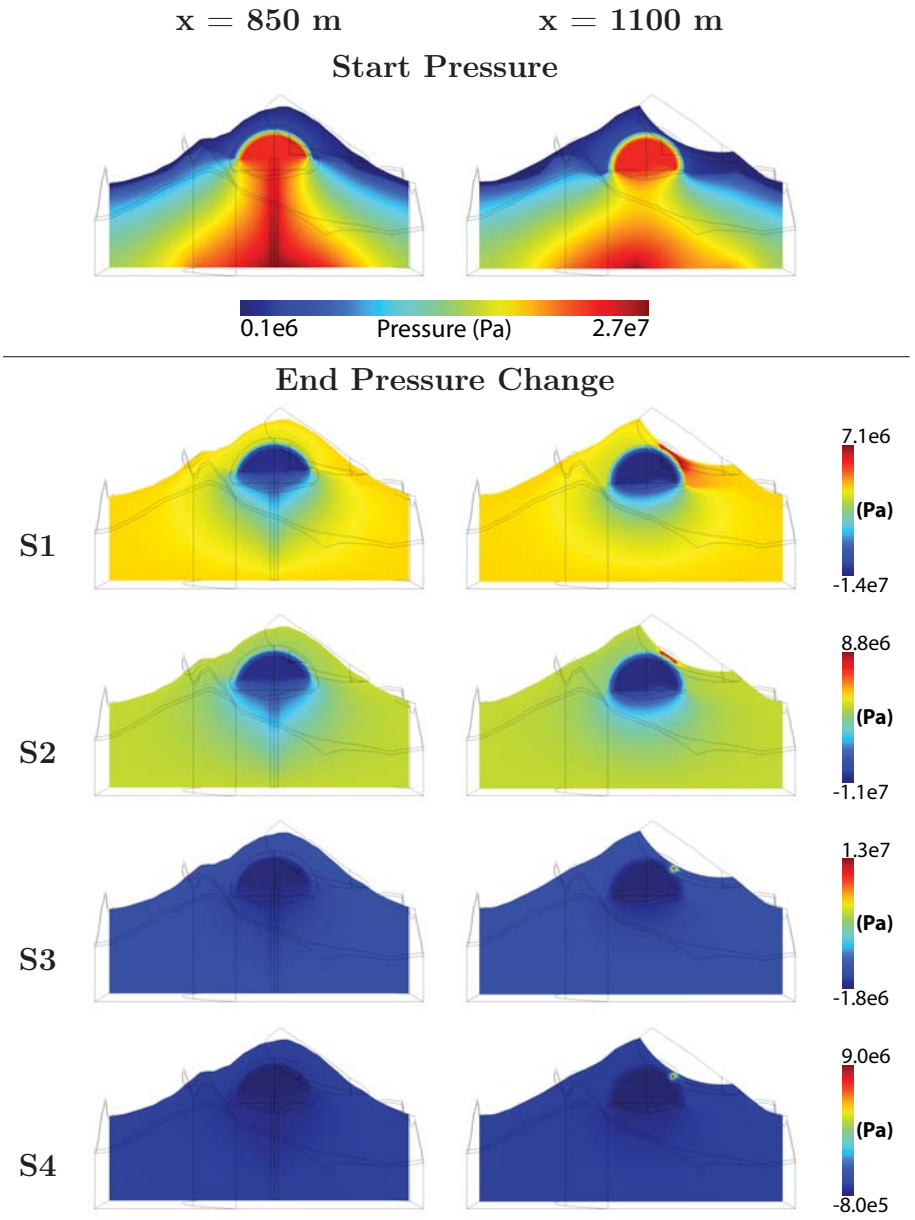

Figure 9.2: The start pressure (top) and the pressure change results for the four model runs. The pressure change in response to the FZ is strongly linked to the size of the gas escape route - the greater the size of the FZ, the greater the degree of depressurisation.

The approximate gas loss from the domains of the conduit and core is indicated in Figure 9.4. An estimate of the surface gas emission rate is also shown. The greater the size of the FZ in the model, the greater the volume of gas emitted. This does not necessarily imply a greater degassing speed, rather the surface area is sufficiently larger to emit more gas in any time period.

Figure 9.5 shows the initial surface displacement, displacement change at different time-steps and the end equilibrium surface displacement change for each model

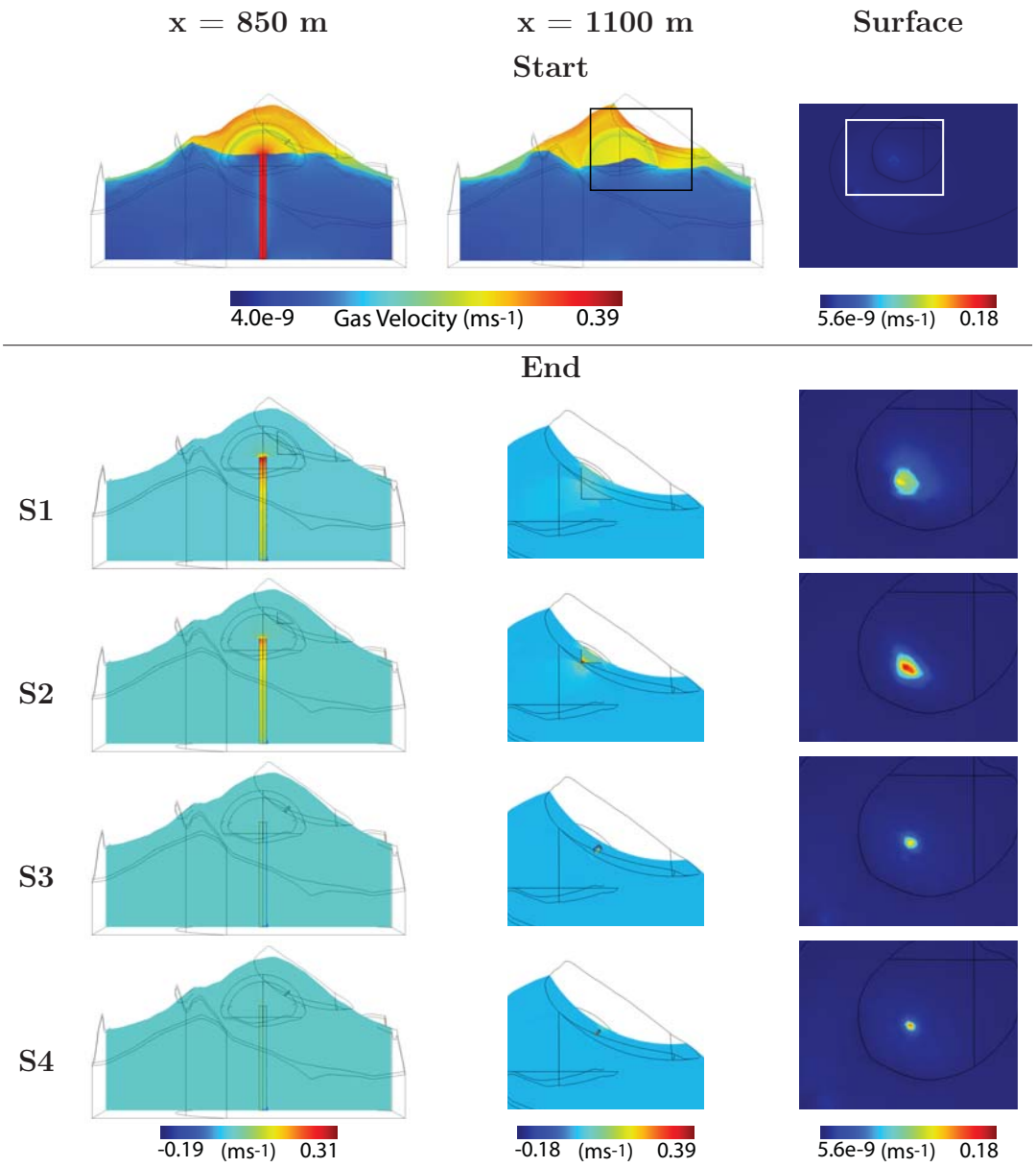

Figure 9.3: The initial gas velocity and the associated surface gas velocity (top). Also, cross-sections for the end gas velocity increase and the end surface gas velocity (bottom). The location of the end surface gas emission plots is indicated in the start surface plot. There is a marked increase in gas emission size with FZ size. Furthermore, the region of dome affected by the FZ also increases. In Model **S4**, only the area immediately surrounding the FZ is directly affected.

run. All four models result in the same basic surface displacement change pattern, beginning with a very localised uplift above the FZ, decreasing with decreasing FZ size. Furthermore, subsidence over the core begins and becomes progressively more dominant. In models **S1** and **S2**, there is no evidence of the uplift present in the end equilibrium result, due to the large volumes of gas which have been lost from the

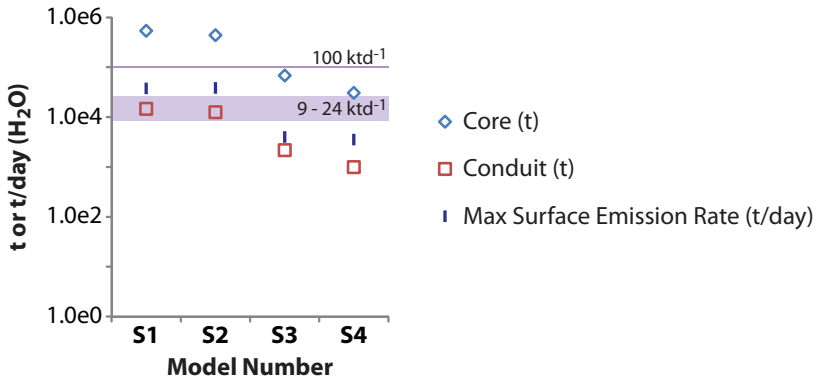

Figure 9.4: Approximate gas loss (t) from the domains of the conduit and core. More gas is lost from the core than the conduit in response to the FZ. An estimate of the maximum surface emission rate (t/day) is also indicated. Gas loss from each domain is calculated using the change in density and domain volume: $(\rho_E - \rho_S)V$. Whilst the surface emission rate is calculated using: $\rho_A A \boldsymbol{u}$. For ρ_S, ρ_E and ρ_A, the gas densities at the start, end and surface, respectively. The maximum (100 ktd^{-1}) and average ($9 - 24$ ktd^{-1}) emission rates as estimated by Edmonds et al. (2002) for dome building eruptions are Soufrière Hills volcano are indicated for reference.

volcanic interior. In contrast, **S3** and **S4** maintain this uplift signal, although it has diminished, particularly in **S3** with the slightly larger FZ size. However, this uplift is so localised and small in magnitude (<1mm), it would not be recordable on a volcanic dome surface, particularly one which is continuously changing. The region of the surface affected by subsidence is the same in each model and is determined by the size of the core. However, the magnitude of subsidence varies greatly between the models, highlighting the larger volumes of gas which have been lost through the larger FZ sizes.

The change in average pressure, surface gas velocity and displacement are summarised in Figure 9.6. Each model has been replicated for a more permeable country rock of 10^{-12} m^2, which compares the models to Model **1**, the example from Group **4C** (Chapter 8). Compared to **19**, Model **1** was characterised by a less pressurised interior and a surface displacement pattern which retained an uplift to the NE. The results are also duplicated for three different conduit permeabilities (10^{-10} m^2 (as already discussed), 10^{-12} and 10^{-14} m^2).

The initial pressure, gas velocity and displacement values are the same for the models with the same permeability conditions regardless of the FZ size. However, as noted previously in this section, there are large differences in the response of the models due to the varied FZ size. The average pressure in the conduit, core and carapace all decrease in response to the FZ, although the magnitude increases with increasing FZ size. A more permeable country rock also decreases the change in pressure, because

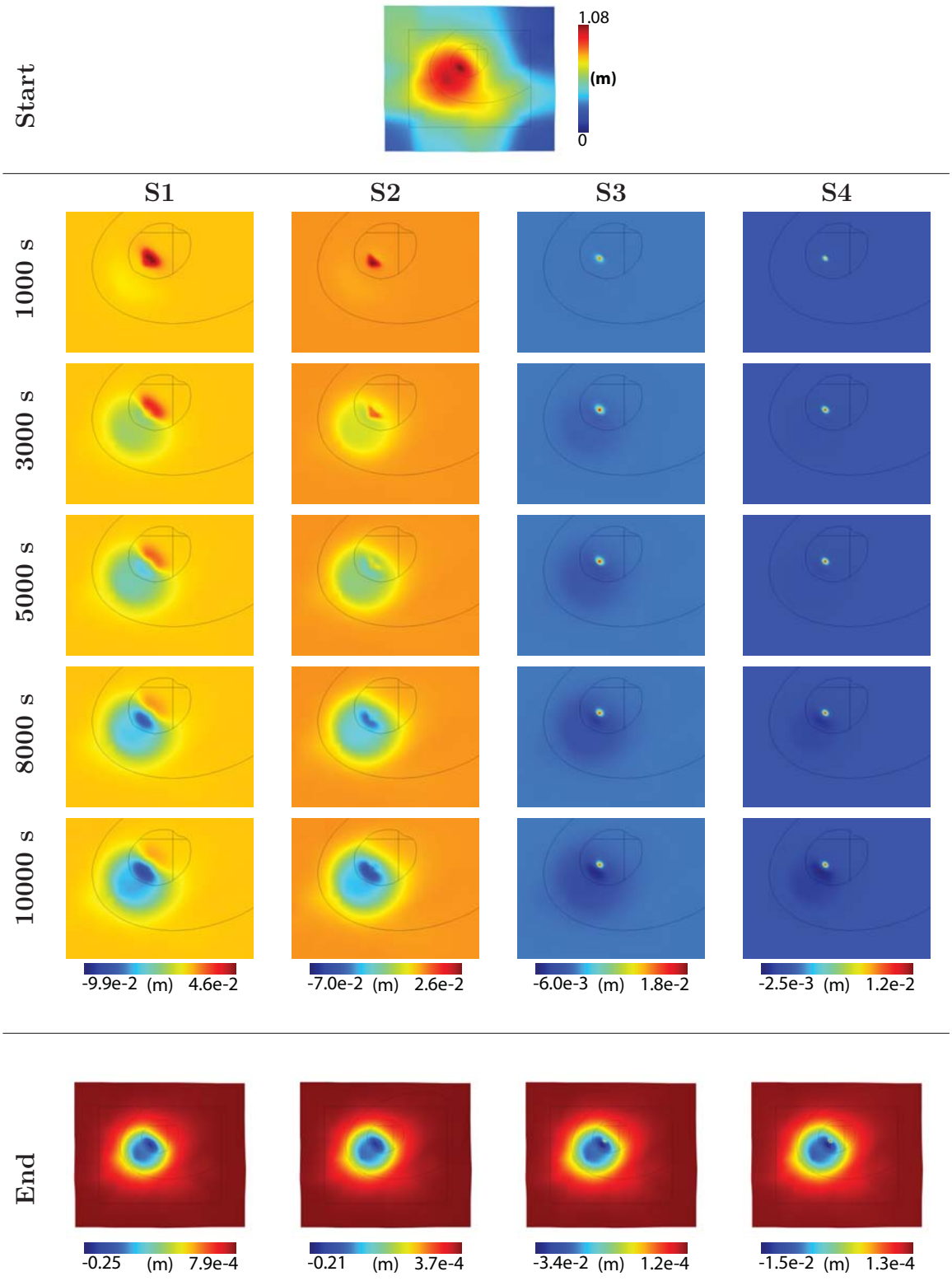

Figure 9.5: The displacement change at different times and the end equilibrium displacement change. Different scales were chosen for each model due to the wide range. The end equilibrium of each model results in a large deflation surrounded by a very small (< 1mm) inflation.

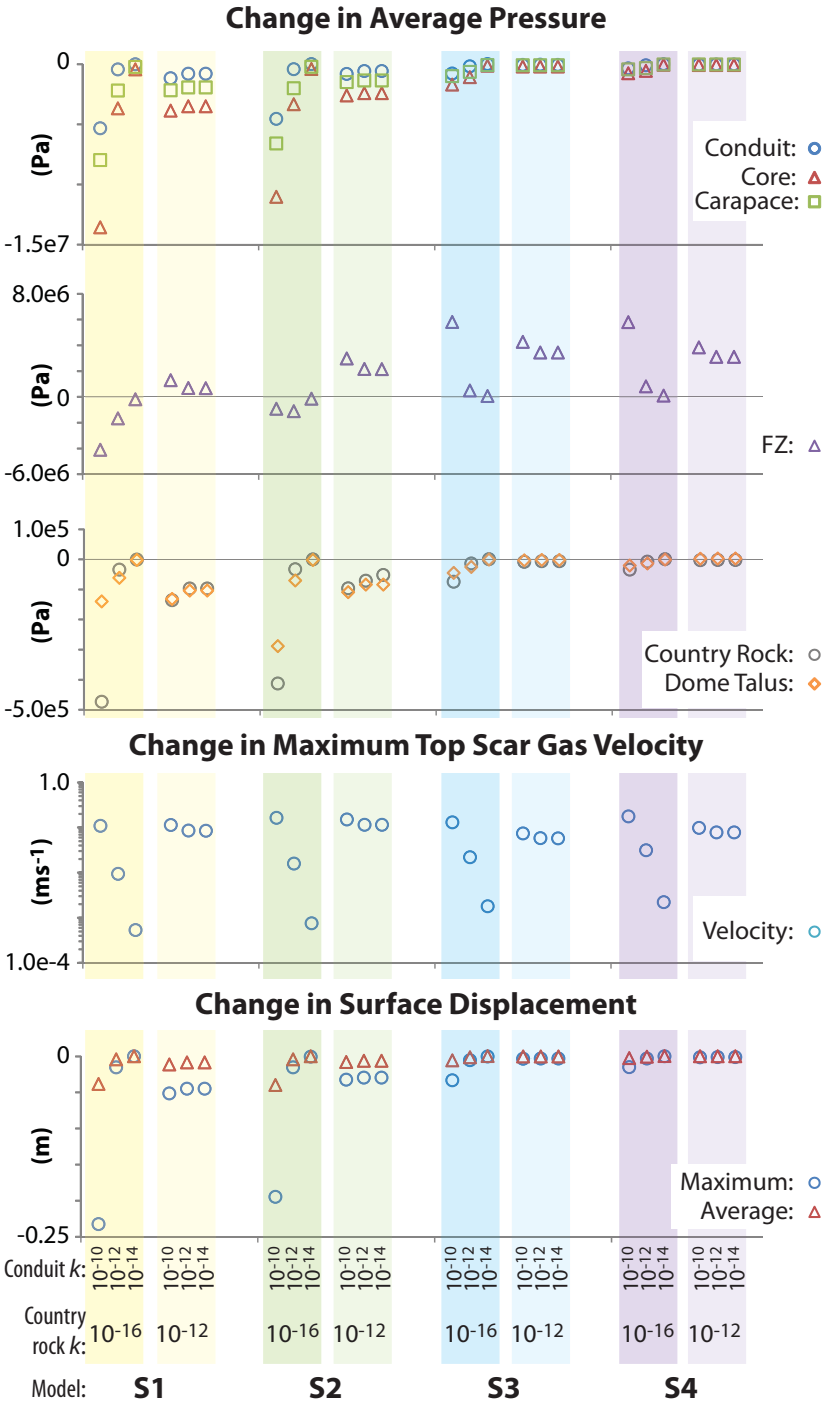

Figure 9.6: Change in average pressures, maximum surface gas velocity and maximum and average surface displacement for each model. Each model was run for three conduit permeabilities (10^{-10}, 10^{-12} and 10^{-14} m^2) and two country rock permeabilities (10^{-16} and 10^{-12} m^2). The difference between the models (of the same permeability) is the size of the FZ, therefore, the starting position of each model is the same, except for the average carapace and FZ pressures which are dependent upon the FZ size, shape and location. However, the combined carapace and FZ average pressure is always the same.

the high permeability prevents gas concentrating in the inner domains of the conduit and core. For a low permeability country rock, **S1** and **S2** both show a decrease in the FZ pressure, however in all other models, the region shows pressurisation. This is because in these models, the region becomes a location for potential gas storage, rather than gas loss.

There are significant increases in surface gas velocity with increasing conduit permeability, regardless of the model when the country rock permeability is low. However, with a high country rock permeability, the change is much smaller due to the lower pressure gradient. With the less permeable country rock, the smaller the size of the FZ, the greater the end surface gas velocity (shown as the greatest gas velocity change). However this does not mean more gas is lost because the region emitting gas is very small.

The change in maximum surface displacement is greatest in **S1** and **S2** with a subsidence of >20 cm for a highly permeable conduit. However, the change in maximum surface displacement drops dramatically with decreasing conduit permeability. Furthermore, the change in average displacement is much smaller than that of the maximum, showing that whilst localised regions may experience a large subsidence, the subsidence over the larger area is much smaller (<5 cm). When the country rock has a high permeability, the change in surface displacement is very similar regardless of the conduit permeability (although the initial displacement is higher for a more permeable conduit). This is because much of the gas stored within the conduit has been lost to the country rock, and therefore the FZ within the carapace has little effect upon the gas contained within the conduit, and only affects the gas in the core.

9.1.1 Implications of fracture zone size

The size of the FZ has a profound impact on all the results in the model, particularly if there is a large volume of gas available due to a high permeability conduit but low permeability country rock. A large FZ has the potential to remove more gas from the volcanic interior, whilst a smaller FZ may only affect the immediate vicinity. A smaller FZ results in greater gas velocities, which are maintained for longer periods of time, because the FZ is too small to efficiently remove the gas, consequently the pressure remains high. Therefore, the magnitude of the pressurisation of the region surrounding a small FZ suggests a small fracture may easily develop into a much larger FZ.

9.2 Permeability Variation

As shown in Chapter 8, the permeability conditions within the entire volcano have a dramatic effect on the resulting pressurisation, gas flow and surface displacement. Many studies have derived anisotropic permeabilities for volcanic eruption products (e.g. Tait et al., 1998, Wright et al., 2006a, 2009, Bernard et al., 2007, Bouvet de Maisonneuve et al., 2009). Furthermore, the effects of compaction, exsolution, degassing and crystallisation may result in the development of permeability gradients (e.g. Blower, 2001, Sparks, 2003a, Massol and Jaupart, 2009). Consequently, the aim of this section is to investigate what effect permeability variations in the conduit, including anisotropy and gradients, have on the results and whether these variations can be discernible from surface observations.

In order to investigate the conduit permeability further, a number of model variations are run based on Model **19** from Chapter 8 (Figure 9.7). The models are separated into three groups: Uniform (**U**), Anisotropic (**A**) and Gradient (**G**) representing the different conduit permeability types considered. In reality, the conduit permeability (and the permeability in other domains) is likely to be a combination of all three permeability characteristics; with graduated regions due to varied gas exsolution versus degassing, coupled with different fracture densities and anisotropic regions due to alignment of sealed regions and strain induced bubble elongation. However, for simplicity, each permeability variation type is explored separately. The models are run with two different country rock permeabilities; firstly a low permeability country rock (10^{-16} m^2) as was present in Model **19**, and secondly a higher permeability of 10^{-12} m^2 (Model **1**) to explore the impact of the country rock on the results.

9.2.1 Model description

Model **U1** is identical to Model **19** from Chapter 8 with a conduit and core permeability equal at 10^{-10} m^2. A second model, **U2** explores the effects of a conduit which is less permeable than the core. This is equivalent to Model **25** from Chapter 8 and in this scenario, the core becomes the region of greatest gas storage.

Two Anisotropic models are shown to investigate the effects of the permeability being greater in one orientation. Firstly, **Az** has a vertical (parallel to the conduit flow direction) permeability greater than the horizontal, simulating shear-induced bubble elongation. In contrast, **Ax** is the reverse situation with the vertical permeability less than the horizontal, simulating the horizontal alignment of bubbles (Llewellin, 2007).

Four different Gradient models are also shown. In **Gz_**, the permeability in the con-

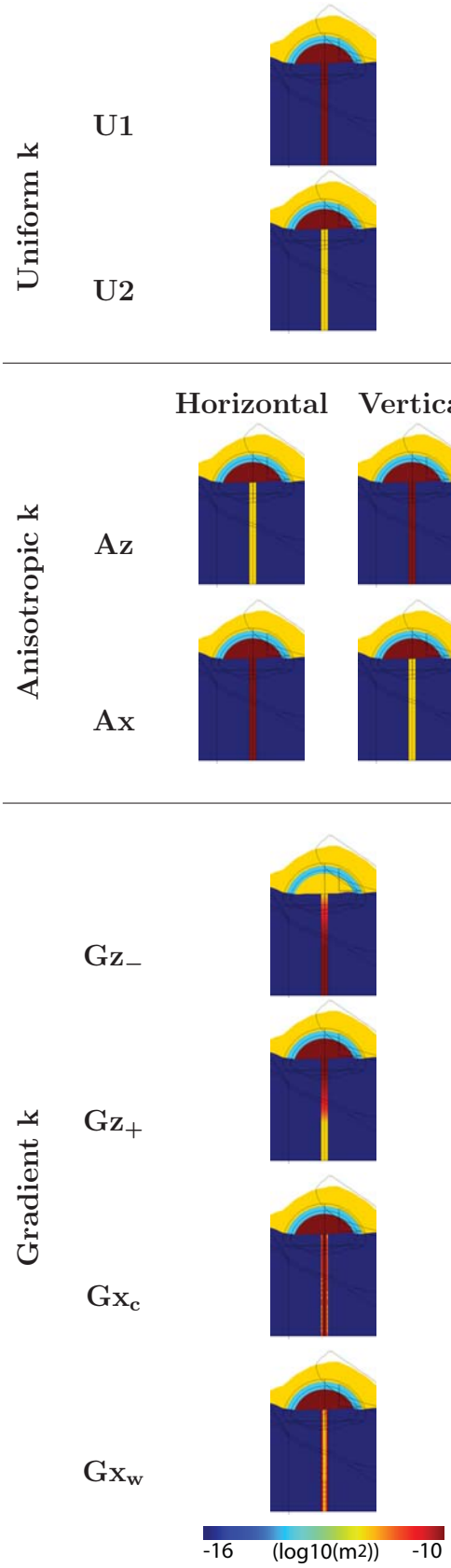

Figure 9.7: The initial permeability conditions for the different permeability variations. Only the central region in the vicinity of the conduit and dome core is shown.

duit and core increases with depth, simulating progressively degassed or mineralised magma towards the surface. In $\mathbf{Gz_+}$, the permeability within these two domains decreases with depth, exploring the effects of increased permeability perhaps due to increased exsolution or fracturing near the surface or closed-system degassing at depth, becoming open-system degassing towards the surface (e.g. Edmonds et al., 2008). $\mathbf{Gx_c}$ and $\mathbf{Gx_w}$ have horizontal gradients within the conduit, with the permeability increasing and decreasing towards the conduit centre, respectively. $\mathbf{Gx_c}$ may represent a volcanic system where the conduit-wall margin is becoming sealed, whilst $\mathbf{Gx_w}$ may show the increase in permeability derived by shear fractures and/or bubble elongation.

9.2.2 Pressure

Figure 9.8 shows the pressure results at the start and the end pressure change for each model. As discussed previously, the high interior permeability in **U1**, surrounded by less permeable material, results in internal pressurisation which decreases once the FZ occurs, resulting in a strong deflation signal and fumarolic gas emission. Decreasing the conduit permeability to 10^{-12} m^2 (**U2**) dramatically reduces the internal pressurisation. For example, the average conduit gas pressure is 6.4 MPa lower than in **U1**. Consequently, because the lower permeability can accommodate less gas, this results in decreased depressurisation with the conduit average gas pressure decreasing by 0.2 MPa, compared to 1.2 MPa in **U1**. The change in pressure within the core is greater than that in the conduit, but still much less than that in **U1**.

Model **Az**, where the conduit permeability is highest in the vertical direction, shows a pressure pattern which is very similar to that of **U1**. This is because the low country rock permeability prevents horizontal gas escape, so decreasing the horizontal permeability has little effect. In contrast, the model with the greater horizontal permeability, **Ax**, results in behaviour similar to that of **U2**. Consequently, this scenario results in a markedly reduced depressurisation signal and slower gas emission. This decreased initial pressure is because the lower vertical permeability restricts the flow of gas upwards through the conduit. Consequently, there is less gas present within the conduit.

For the graduated permeability models, both instances where the permeability varies vertically result in markedly different pressurisation patterns compared to the original model (**U1**). When the permeability decreases towards the surface ($\mathbf{Gz_-}$), the gas within the conduit is pressurised, whilst that in the core is under lower pressure. The higher conduit pressure is maintained due to the less permeable surroundings (including the core). Depressurisation in this model is restricted to the core domain,

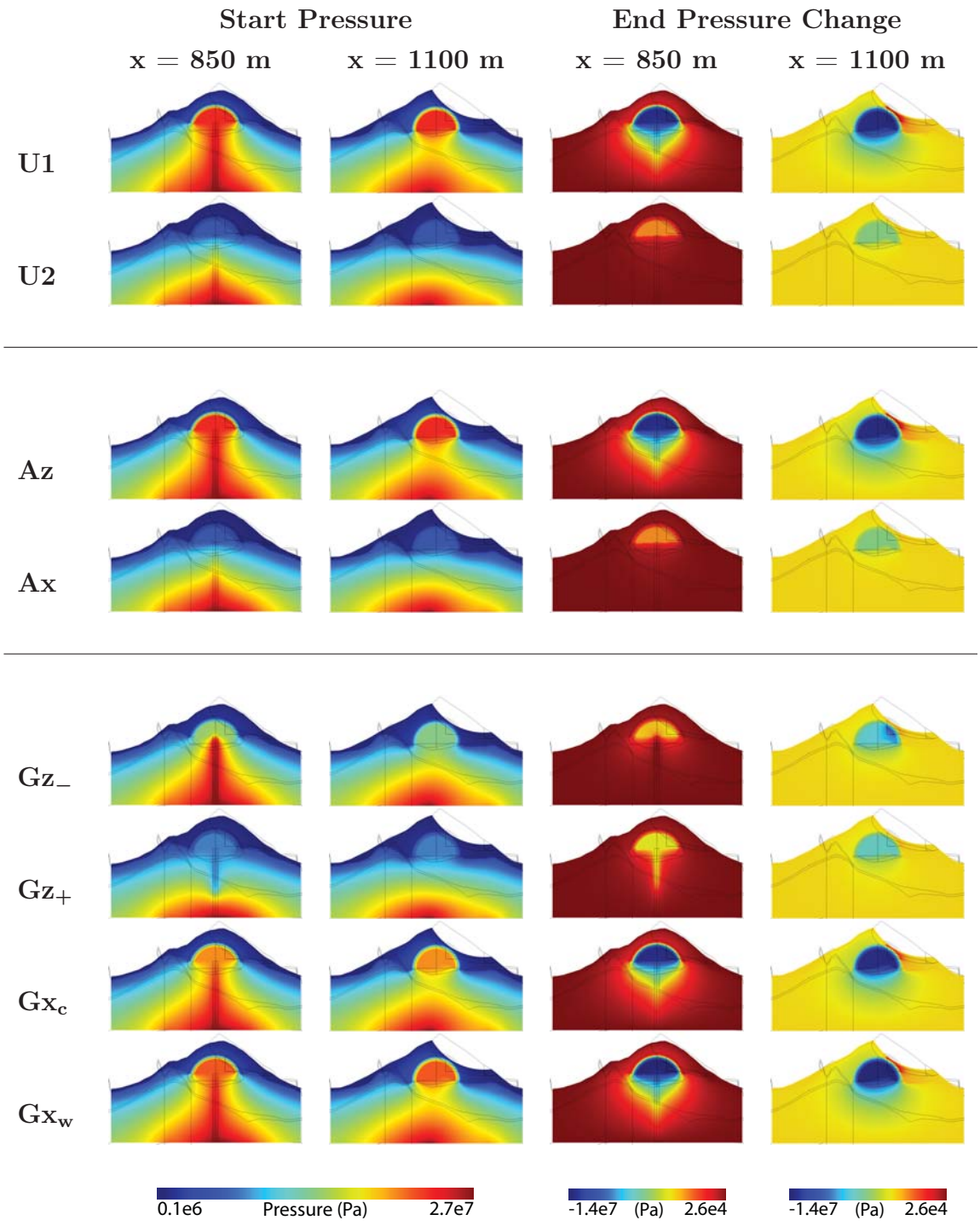

Figure 9.8: Start pressure and the end pressure change for two cross sections through the model: one through the conduit, the other through the FZ. The country rock permeability is 10^{-16} m^2.

and is biased towards the region immediately adjacent to the FZ. In contrast, when the permeability increases towards the surface (**Gz$_+$**), the entire conduit and core have less pressurisation, due to the decreased volume of stored gas and the shallower

depths at which it is stored. However, once the FZ occurs, the higher permeability of the upper conduit permits gas to escape, resulting in depressurisation throughout the upper conduit. The depth of this depressurisation is determined by the conduit permeability gradient.

With a horizontal permeability gradient within the conduit ($\mathbf{Gx_c}$ and $\mathbf{Gx_w}$), the differences are less obvious. Both models are very similar to **U1**, although the pressurisation in all domains is lower. Furthermore, decreasing the permeability towards the conduit-wall boundary ($\mathbf{Gx_c}$) results in a lower pressurisation within all domains compared to $\mathbf{Gx_w}$. For example, the core pressure is 1.5 MPa lower than when the conduit permeability increases towards the boundary ($\mathbf{Gx_w}$). Similarly, the conduit and carapace pressures are also lower by 0.6 MPa and 1 MPa, respectively. Consequently, increasing the conduit permeability towards the boundary ($\mathbf{Gx_w}$) results in greater pressurisation. The high permeability at the conduit-wall boundary is confined by the low permeability of the country rock and also partially by the lower permeability of the conduit centre. In response to the FZ both $\mathbf{Gx_c}$ and $\mathbf{Gx_w}$ show very similar depressurisation patterns to that in **U1**.

Figure 9.9 shows the pressure plots for the initial pressurisation and the end pressure change for the same models, but for a more permeable country rock (10^{-12} m^2). Compared to the less permeable country rock (Figure 9.8), the majority of the models show a lower initial pressure with the more permeable country rock. The exceptions to this are models **U2**, **Ax** and $\mathbf{Gz_+}$. These three models showed the least internal pressurisation for the less permeable country rock (Figure 9.8) and they show similar behaviour due to their comparable permeability conditions. In each of these three models, the conduit permeability (or vertical conduit permeability) is less than that of the core. Whilst **U2** and **Ax** show a lower conduit pressure, the core has a higher pressure than with the less permeable country rock. In contrast $\mathbf{Gz_+}$ shows increased pressurisation in both the upper conduit and the core. An increased internal pressurisation with an increase in the "confining permeability" seems counter-intuitive. However, in **U2**, the increased country rock permeability equals that of the conduit and, therefore, this increases the volume of gas available. When the country rock has a low permeability, the core may only be supplied with gas from the conduit. However, if the conduit and country rock permeabilities are equal, the gas source region is significantly larger. In **Ax**, the horizontal conduit permeability is greater than the vertical. Consequently, when the country rock permeability is low, the gas is unable to utilise this and must transfer vertically. However, opening the country rock to gas transfer allows viable horizontal degassing. Therefore, similar to **U2**, gas may be transferred between the conduit and country rock. Gas within the country rock may originate from the magma body at deeper

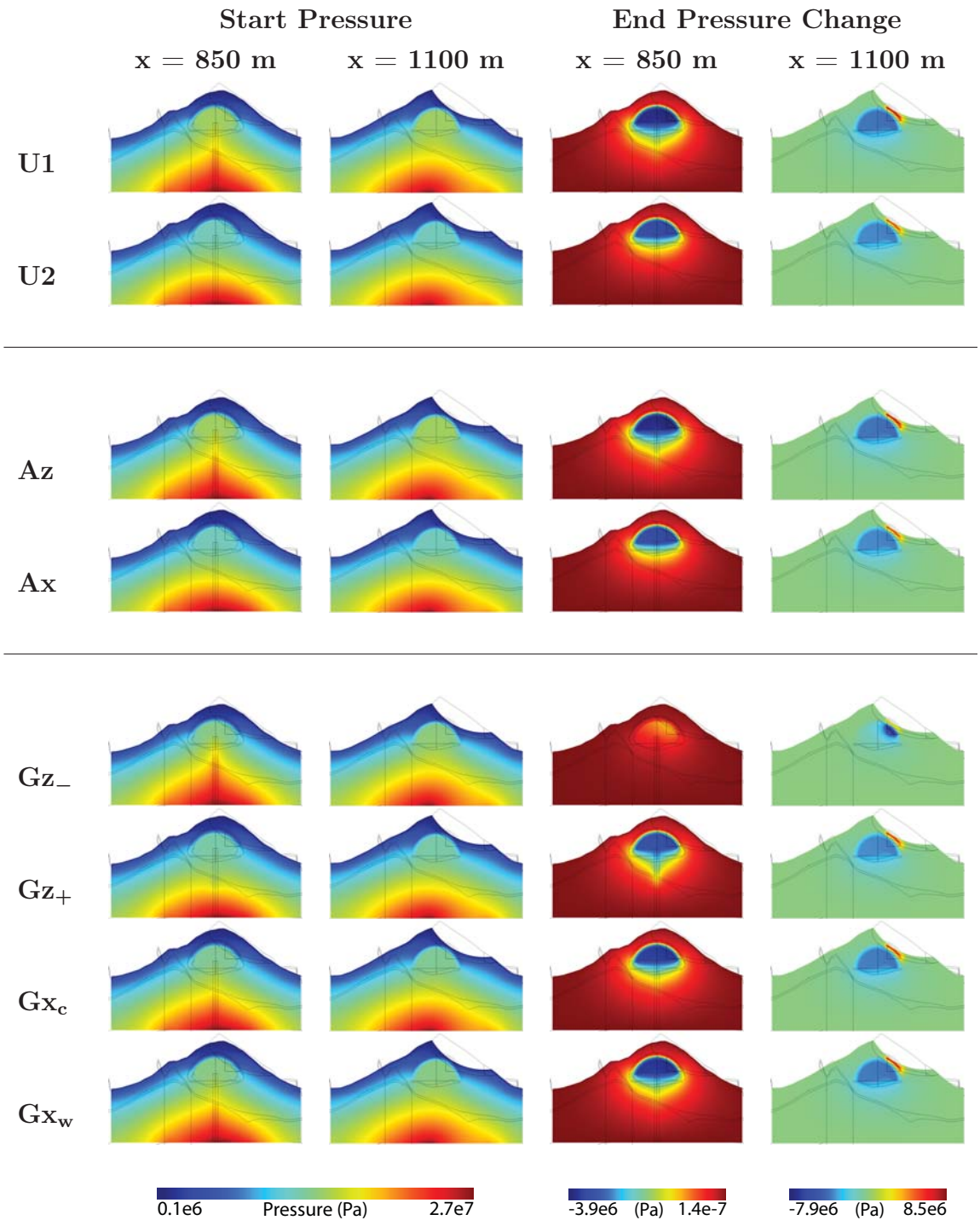

Figure 9.9: Start pressure and end pressure change for the models when the country rock has the higher permeability of 10^{-12} m^2.

levels, the conduit, or geothermal fluids. This sharing of the gas between the conduit and country rock results in a decrease in the conduit gas pressure (because the gas is lost to the country rock), but an increase in the country rock pressure as it receives gas from the conduit and other source regions. In the case of Model $\mathbf{Gz_+}$, the

permeability increases with decreasing depth within the conduit and core. Hence, the volume of gas stored in the upper regions is limited by the permeability and available gas below. However, with a more permeable country rock, there is the potential for gas to transfer from the country rock to the upper regions of the conduit and core, thus increasing the conduit gas pressure. Increasing the country rock permeability in this model increases the pressurisation of every domain in the volcano.

The depth to which the conduit depressurises in response to the FZ is also influenced by the country rock permeability. For a low country rock permeability (Figure 9.8), large regions of the conduit beneath the dome are depressurised. This is because the gas was confined to the conduit and therefore, readily takes advantage of the new vertical degassing route. In contrast, the higher country rock permeability provides a viable exit route for the gas, so the FZ has less effect on the conduit, because there is less gas available for removal. Surprisingly, the model which shows the greatest magnitude of depressurisation is Model **Gz_**, although this is extremely localised to the region of the FZ and the core immediately juxtaposed. The country rock and dome talus average pressures are always greater when the country rock is more permeable. The dome talus pressure is greater because the higher country rock permeability permits gas storage within the country rock which subsequently may migrate to the dome talus.

9.2.3 Displacement and gas velocity

Figure 9.10 shows the surface response to the permeability conditions for model **U1** and **Gz_**, for country rock permeabilities of 10^{-16} m^2 and 10^{-12} m^2. For the two country rock permeabilities, all the models, except **Gz_**, show the initial surface displacement, end surface displacement change and gas velocity patterns as shown for **U1**, with magnitude being the only difference between them. The greater the initial surface displacement, the greater the change in response to the FZ. This is because the initial displacement pattern is generated by the stored gas. The greater the volume of stored gas and related pressurisation, the greater the volume of gas may be lost, resulting in depressurisation and deflation. The models which show the greatest surface displacement are **U1**, **Az**, $\mathbf{Gx_c}$ and $\mathbf{Gx_w}$. These models have the greatest average conduit permeability or the highest conduit permeability is in the vertical. Furthermore, those models with the greatest surface displacement and end surface displacement change also show the greatest surface gas velocity.

However, Model **Gz_** shows a displacement change pattern which is markedly different. This is particularly evident when the country rock is more permeable (10^{-12}m^2). The displacement pattern includes a very localised deflation, and less of the sur-

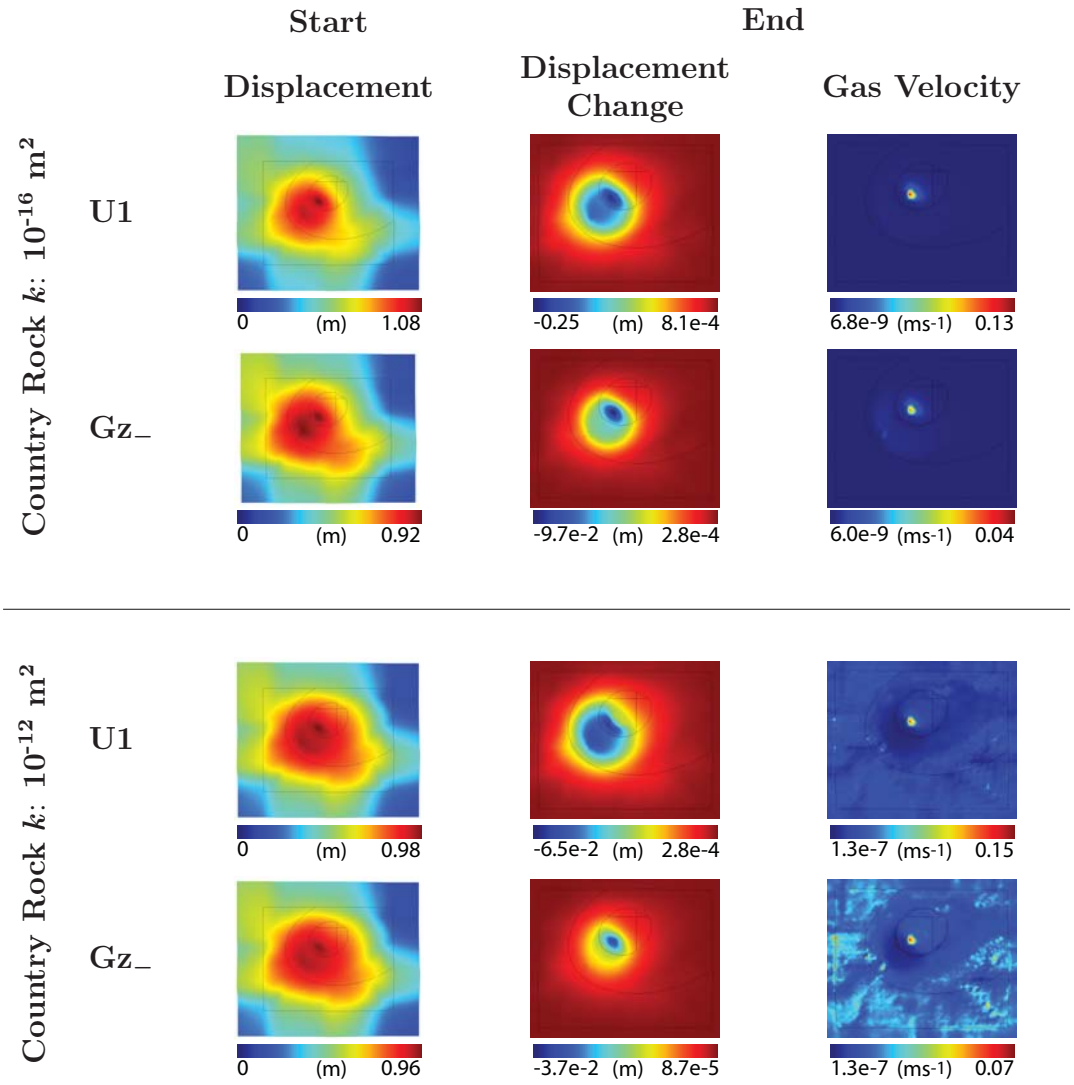

Figure 9.10: Start surface displacement, end surface displacement change and the end surface gas velocity for models **U1** and **Gz_** for the two different country rock permeabilities. Despite the variations in conduit permeability, all models except **Gz_** show the same basic start and end displacement and gas velocity patterns as **U1**. The only difference between the model runs is the magnitude.

rounding region is affected. The reason for this is the localised depressurisation pattern. Whereas in the other models the entire core is affected by the FZ within the carapace, in Model **Gz_**, only the region immediately adjacent is affected.

All models show the same basic gas emission pattern - a localised fumarole above the FZ. The only difference between the models is the magnitude. However, with a more permeable country rock, there is more widespread degassing evident which may be visible on the flanks of the volcano (or further afield) as either smaller, less prolific fumaroles or diffuse degassing. Figure 9.11 shows estimates for the gas lost from the core and conduit, and the maximum surface emission rate for each model.

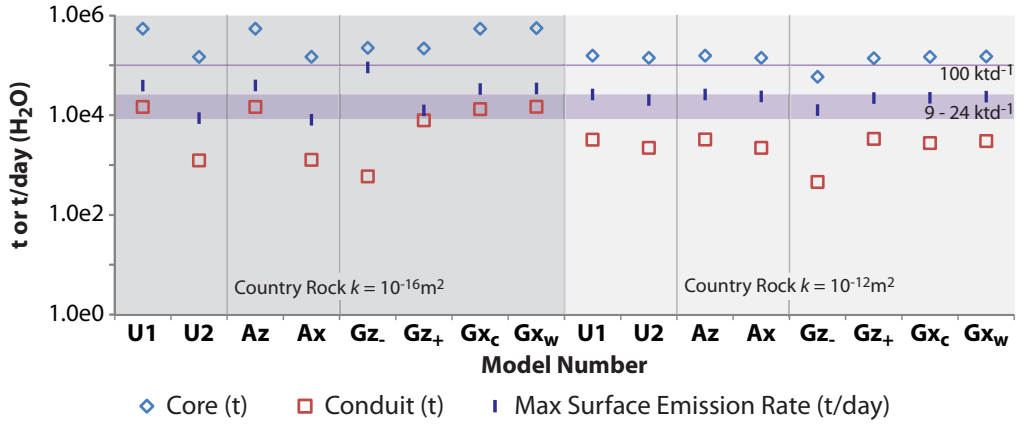

Figure 9.11: Estimates for the gas lost (t) from each of the conduit and core domains and the maximum surface gas emission rate (t/day) for the models with the different country rock permeabilities. The maximum (100 ktd^{-1}) and average ($9-24$ ktd^{-1}) emission rates as estimated by Edmonds et al. (2002) for dome building eruptions are Soufrière Hills volcano are indicated for reference.

Increasing the country rock permeability leads to less gas lost from the core because there is less gas available within this domain. However, the gas lost from the conduit is more complex due to the variations in the permeability conditions modelled. For the less permeable country rock, **U1**, **Az**, $\mathbf{Gx_c}$ and $\mathbf{Gx_w}$ show similar levels of gas loss from the conduit and core domains, and also a similar rate of surface gas loss. This is due to the similarity in their initial pressure patterns and the manner in which they respond to the FZ with extensive depressurisation within the core, and upper conduit (Figure 9.8). Furthermore, **U2** and **Ax** also show comparable levels of gas loss and degassing rate, although this is lower than **U1**, **Az**, $\mathbf{Gx_c}$ and $\mathbf{Gx_w}$. In conjunction with the pressure and displacement patterns, the degassing behaviour of **Gz_** is different. This model shows a large volume lost from the core, but markedly less from the conduit. Furthermore, this model also shows the greatest surface gas emission rate. This is due to the high velocity generated by the localised pressure increase in the core adjacent to the FZ.

For a more permeable country rock, the degassing behaviours of all models are very similar, except in **Gz_**. The similarity between the other models is due to the sharing of gas between the conduit and country rock which limits the effect of the permeability variations. **Gz_** shows a decreased gas loss and emission rate because the lower permeability in the core contains less gas to be lost. Furthermore, the higher country rock permeability prevents pressurisation within the conduit and therefore, a large pressure gradient is not generated which would force more gas from the system.

9.2.4 Changing the minimum conduit permeability

To further investigate the effects of permeability variation within the conduit, the models are repeated for different minimum conduit permeabilities as shown in Table 9.3. The maximum conduit permeability is kept constant at 10^{-10} m^2. The initial results and the response to the FZ for each of these model runs are summarised in Figures 9.12 and 9.13, respectively.

Uniform conduit permeability

The first runs of the two Uniform models have the same permeability conditions in both the conduit and core. In both Models, **U1** and **U2**, changing the conduit permeability has a big impact upon the pressurisation of each domain, the surface gas velocity and the surface displacement. However, the difference between the results of the two models, particularly for the lower country rock permeability, is limited suggesting the permeability of the core, has little impact. For example,

	Uniform					
	U1			**U2**		
	1	2	3	1	2	3
Conduit k (m^2)	10^{-10}	10^{-12}	10^{-14}	**10^{-10}**	**10^{-12}**	**10^{-14}**
Core k (m^2)	10^{-10}	10^{-12}	10^{-14}	10^{-10}	10^{-10}	10^{-10}
	Anisotropic					
	Az			**Ax**		
	1	2	3	1	2	3
Vertical Conduit k (m^2)	10^{-10}	10^{-10}	10^{-10}	**10^{-12}**	**10^{-14}**	**10^{-16}**
Horizontal Conduit k (m^2)	**10^{-12}**	**10^{-14}**	**10^{-16}**	10^{-10}	10^{-10}	10^{-10}
Core k (m^2)	10^{-10}	10^{-10}	10^{-10}	10^{-10}	10^{-10}	10^{-10}
	Gradient					
	Gz$_-$			**Gz$_+$**		
	1	2	3	1	2	3
Base Conduit k (m^2)	10^{-10}	10^{-10}	10^{-10}	**10^{-12}**	**10^{-14}**	**10^{-16}**
Top Core k (m^2)	**10^{-12}**	**10^{-14}**	**10^{-16}**	10^{-10}	10^{-10}	10^{-10}
	Gx$_c$			**Gx$_w$**		
	1	2	3	1	2	3
Centre Conduit k (m^2)	10^{-10}	10^{-10}	10^{-10}	**10^{-12}**	**10^{-14}**	**10^{-16}**
Conduit wall k (m^2)	**10^{-12}**	**10^{-14}**	**10^{-16}**	10^{-10}	10^{-10}	10^{-10}
Core k (m^2)	10^{-10}	10^{-10}	10^{-10}	10^{-10}	10^{-10}	10^{-10}

Table 9.3: Permeability conditions for the models with each conduit permeability variation type. Each model is run three times for a different lowest permeability (shown in bold). In **U1** the conduit and core always have the same permeability, whilst in **U2** the conduit permeability is either equal to or less than the core, where the core always has a permeability of 10^{-10} m^2.

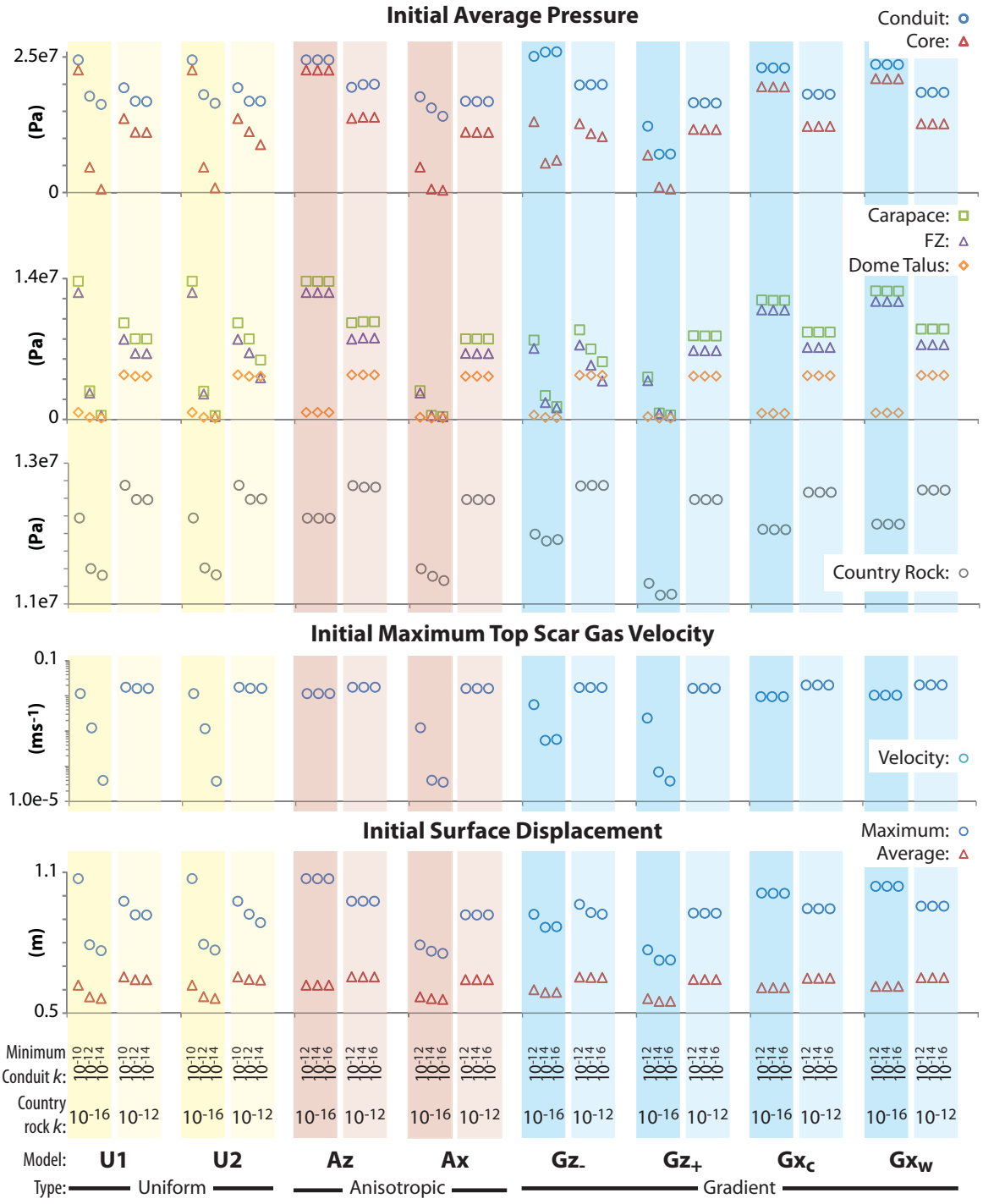

Figure 9.12: The initial results for the three model runs for the eight models. For each model and country rock permeability, the minimum conduit permeability decreases from left to right.

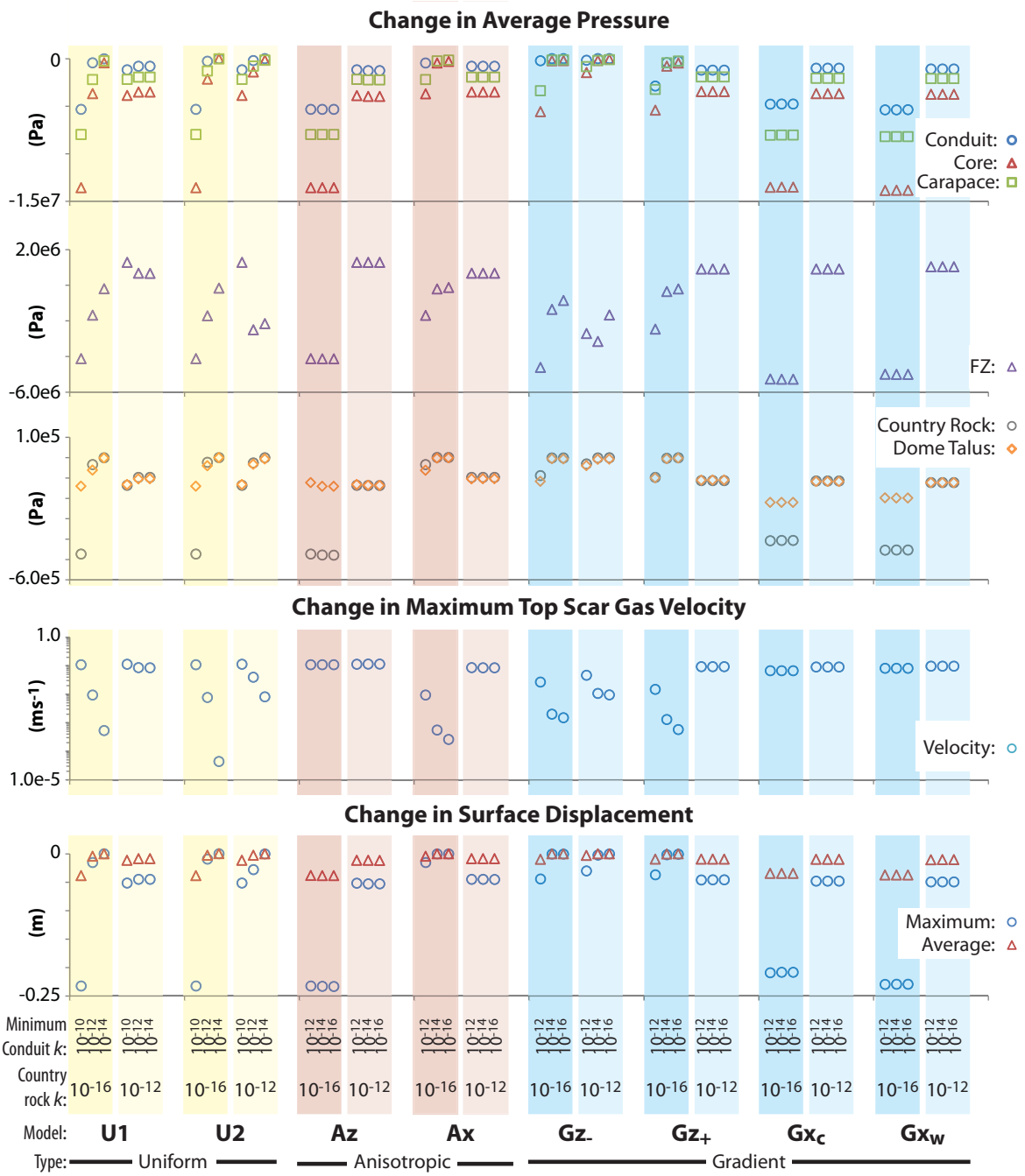

Figure 9.13: The change in average pressure for each domain, maximum gas velocity in the top of the scar and maximum and average surface displacement for each model in response to FZ. Each model is run three times for different minimum conduit permeabilities. This is then duplicated for the more permeable country rock of 10^{-12} m^2. For each property, the start and end value is plotted. The first model of **U1** and **U2** is the same with a conduit and core permeability of 10^{-10} m^2 (this is the original model **19**). This permits easy comparison of the different model runs to determine the effects of changing the permeability conditions within the conduit. The average pressure graphs are grouped differently from Figure 9.12 due to the variation in scale.

in the third run of **U2**, despite a core permeability of 10^{-10} m^2, and a conduit permeability of 10^{-14} m^2, there is only a small difference compared to when both domains have the same permeability of 10^{-14} m^2 (third run of **U1**). This may be explained by the decreased volume of stored gas - the smaller the region containing gas, the lower the pressurisation and consequently the decreased change in surface observations. A greater difference between the initial and end behaviour of the two models occurs when the country rock has the higher permeability (10^{-12} m^2). In this case, decreasing the minimum permeability (conduit) in **U2** has a greater effect than in **U1** (conduit and core), for both the initial results (Figure 9.12) and in response to the FZ (Figure 9.13).

Anisotropic conduit permeability

In **Az**, the permeability is greater in the vertical (parallel to the conduit), whilst in **Ax**, the permeability is greater in the horizontal direction, suggesting bubble elongation or horizontal bubble alignment, respectively. For both models, the conduit is the only domain with an anisotropic permeability, all others are set to a uniform value. For the low permeability country rock, there is very little variation in the results for decreasing the horizontal permeability in **Az**. This is because, the permeability of the country rock is too low to permit efficient lateral degassing. Consequently, even with a high horizontal permeability, the gas continues to be lost vertically. However, with an increased country rock permeability, there is a small increase in the initial average country rock pressure of 0.1 MPa (Figure 9.12) when the horizontal conduit permeability is increased from 10^{-16} to 10^{-12} m^2, illustrating some gas is being lost horizontally.

For **Ax** (where the horizontal permeability is greater than the vertical), there is greater variation in the results when the country rock has a low permeability, such that as the vertical permeability is decreased, the pressure in all domains decreases (Figure 9.12). Furthermore, the pressure within the carapace, FZ and dome talus are all very low. This is because gas is preferentially lost laterally through the country rock rather than vertically through the bulk of the dome. However, the core experiences greater initial pressurisation when the country rock is most permeable. A higher country rock permeability permits gas to escape from the conduit laterally, thereby increasing the pressurisation of the country rock. This gas may then escape in all directions through the country rock, including vertically towards the core. For a high country rock permeability, there is little change in the pressurisation, gas velocity and surface displacement in response to the FZ for decreasing the vertical conduit permeability (Figure 9.13).

In the modelled scenario, the greater pressurisation occurs when the permeability is

greater in the vertical rather than the horizontal direction (**Az** is more pressurised than **Ax**). This is echoed by a greater degree of surface displacement. Consequently the domains in **Az** experience greater depressurisation than **Ax** when the country rock permeability is low because there is more gas available to be lost. However, for a high country rock permeability, the change in pressure, gas velocity and surface displacement is very similar, indicating similar volumes of gas are lost from both scenarios, despite the greater initial pressurisation of **Az**.

Gradient conduit permeability

Four models investigate gradient permeability within the conduit - two vertical (**Gz**$_-$, **Gz**$_+$), and two horizontal (**Gx**$_\mathbf{c}$, **Gx**$_\mathbf{w}$). Decreasing the conduit permeability vertically towards the surface (**Gz**$_-$) results in a higher average conduit pressurisation compared to **U1**. Furthermore, in contrast with all the other models, when the country rock has the lowest permeability, decreasing the minimum conduit permeability in **Gz**$_-$(upper conduit and core) results in increased pressurisation of the conduit (by 1 MPa between 10^{-12} and 10^{-16} m^2) (Figure 9.12). This increase results from the lower permeability of the upper conduit and core having an increased sealing capacity over the underlying, more permeable conduit. Furthermore, decreasing the permeability closer to the surface results in less pressure change in response to the FZ because the gas is prevented from reaching this degassing outlet (Figure 9.13).

Increasing the conduit permeability towards the surface (**Gz**$_+$), results in decreased pressurisation within the conduit and core, when the country rock is less permeable, which further decreases with decreasing permeability at depth. As this deeper (minimum conduit) permeability decreases, it permits less gas to reach the upper conduit and core. Consequently, as this same permeability decreases, the pressure change in response to the FZ also decreases (Figure 9.13). However, for a more permeable country rock, the pressure change is very similar between all model runs of **Gz**$_+$, because the core can still receive gas from the surrounding country rock which is subsequently lost through the FZ.

In **Gx**$_\mathbf{c}$, the permeability decreases towards the wall-rock, whilst in **Gx**$_\mathbf{w}$, the permeability increases. There are only small variations in the results between these two models. The only difference is a small increase in the pressurisation in **Gx**$_\mathbf{w}$ which results in a higher maximum surface displacement (Figure 9.12) and a slightly greater displacement change in response to the FZ (Figure 9.13).

All models

Increasing the country rock permeability, in these models, always increases the country rock average pressure (Figure 9.12). This is because the greater permeability permits the gas to escape from the interior of the volcanic conduit horizontally into the country rock. Hence there is a greater volume available for gas storage. This is shown at the surface by a greater average surface displacement, although not always the greater maximum (Figure 9.12). The greatest maximum surface displacement is reserved for those models which are able to maintain the highest localised pressurisation, resulting in a localised maximum, but with less displacement elsewhere resulting in a lower average (Figure 9.12). For all models, there is always a decrease in the average pressurisation in the conduit, core, carapace and country rock in response to the FZ (Figure 9.13)

For the high country rock permeability, the initial maximum gas velocity (Figure 9.12) is very similar between the model runs, because the gas is emitted above the country rock, rather than over the conduit due to the imposed sealing from the carapace. However, for a less permeable country rock, the maximum initial surface gas velocity increases with increasing minimum conduit permeability, except in models **Az**, $\mathbf{Gx_c}$ and $\mathbf{Gx_w}$ where there is little change between the model runs (Figure 9.12). The higher vertical conduit permeability in **Az** continues to move gas upwards regardless of the decreasing horizontal permeability. In $\mathbf{Gx_c}$ and $\mathbf{Gx_w}$ changing the minimum permeability has little effect because the more permeable portion of the conduit, albeit at the conduit centre or margin, still permits vertical gas motion.

9.2.5 Implications of permeability variability

In this section, permeability gradients and anisotropy were applied to the conduit. The results show that changing the conduit permeability in this manner adds additional complexity to the behaviour of the gas and the resulting pressurisation and surface displacement. In particular, anisotropy and gradients exert more control over the direction of gas motion. The gas may be forced preferentially vertically towards the dome, or laterally into the country rock. The situation is made more complex by the country rock permeability. A more permeable country rock allows gas to be lost laterally, whilst a less permeable country rock confines the gas to the volcanic interior.

Permeability gradients and anisotropy were investigated independently and only for the conduit domain. However, in reality, such permeability variations will co-exist in all regions of the volcano and will vary with depth. For example, fracturing may

be more prolific closer to the surface. With exsolution increasing on depressurisation, the volumes of gas available for storage and migration will also increase with decreasing depth. Sealing mechanisms and magma motions will also generate their own permeability changes. If the different gradient and anisotropic permeability variations were modelled as co-existing within the same system, this has the potential to make the system even more complex and generate different results dependent upon which variation was dominant. For example, if the permeability within the conduit increases both towards the country rock and the surface, the volume of gas lost horizontally would increase towards the surface. Furthermore, setting permeability variations to different parts of the volcanic system can further complicate the situation. For example, vertical anisotropy at the conduit-wall boundary generated by shear can provide an effective degassing route. However, if the permeability within the conduit interior decreases towards the boundary, gas may be unable to reach and utilise the degassing pathway.

Permeability gradients and/or anisotropy add complexity to a volcanic system and can enhance or limit the migration of gas to the surface. A lower permeability near the surface, due to sealing, implies gas can become trapped at deeper levels and is not released by fracturing at shallow levels within the dome.

9.3 Effects of Topography

Here, the model from Chapter 8 is continued, to investigate the effects of changing the topography. In the original model configuration, a scar was introduced to simulate that formed on Soufrière Hills during the February 2010 partial collapse event. For comparison, results are presented here for the same model, but without the scar (Figure 9.14). With the scar, the modelled dome volume is 0.33 km^3, whilst without it is 0.42 km^3. This added mass increases the dome talus volume by 11% and increases the maximum lithostatic pressure by 2%.

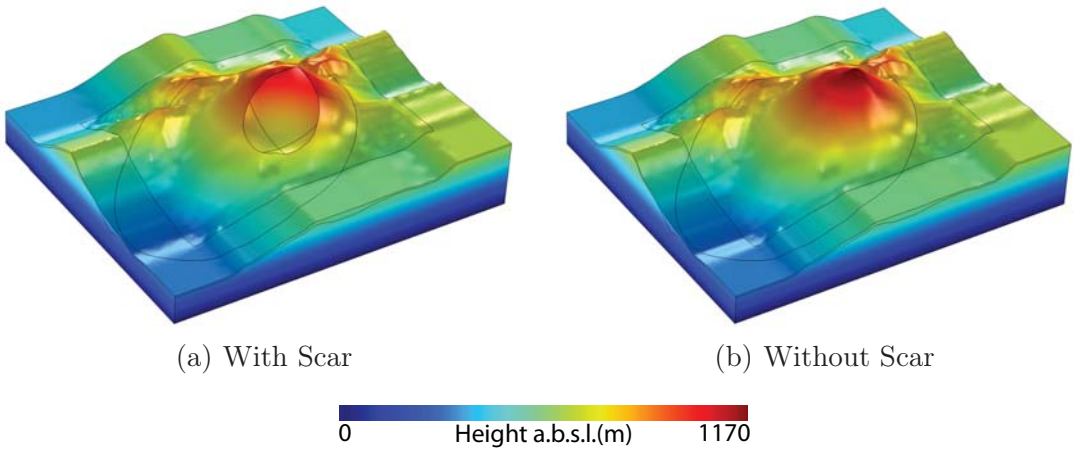

(a) With Scar (b) Without Scar

Figure 9.14: The topography for the two model configurations (a) the original model from Chapter 8 with the scar, and (b) the model without the scar.

This section refers to models both with the scar (from Chapter 8) and without. In order to distinguish between them, single models without the scar are prefixed with **t** and model groups with `T`.

9.3.1 Pressure

The initial average pressure (Figure 9.15) in each domain follows a pattern very similar to that of the examples with the imposed scar (Figure 8.2, Page 119). This shows the dominant controller of the average pressure is not the actual topography, but the permeability relationships. However, plotting the difference between the two sets of models, as a percentage, shows there are differences (Figure 9.16). In particular, the average dome talus pressure varies by up to 50%, with the most notable increase in **t19**, **t21**, and **t25 - t28**. However, the greatest percentage increase occurs in the models which had the lowest dome talus average pressure in the original models. Therefore, an increase of 50% is not as significant as it appears. The carapace and core domains also show an increase in average pressure compared

to the original models, although this is less than 20%, with the greatest increase occurring in models **t26**, **t28**, **t32**, **t34** and **t36**. In terms of actual values of increase, **t20**, **t22**, **t26** and **t28** experience the greatest change in dome talus pressure (0.5 - 1 MPa). Whilst the greatest increase in the core and carapace domains occurs in models **t6**, **t12**, **t18**, **t22**, **t26** and **t28** (Core: 0.7 - 1 MPa, Carapace: 1 - 1.1 MPa). **t20** also shows a large pressure increase in the carapace (0.9 MPa), but not the core. All these models have the lowest dome talus permeability which is the same as that in the carapace (10^{-14} m^2). Consequently, the interior of these models is confined by a combination of the carapace and the dome talus.
The increase in average pressure is greatest within the dome talus due to the increased dome talus volume. The core and carapace also experience pressure increases due to the proximity of the extra dome talus load. The influence of actual topographic features (rather than the influence of an overburden "mass") decreases with depth and distance from the features. Consequently, the change in pressure within the conduit and country rock are significantly less at $< 2.5\%$ (< 0.4 MPa) and $< 2.0\%$ (< 0.2 MPa), respectively.

9.3.2 Pressure change

The end pressurisation of these volcanic systems is, in some cases, significantly higher than in the original models. In particular, the differences in the end pressure of the dome talus, core and carapace have extremes of 350 %, 150 % and 90 %, respectively. However, the change in end pressure in the conduit and country rock is much smaller at less than 8 % and 2.5 %, respectively. These percentages are markedly higher than that for the difference in initial pressurisation. Consequently, these alterations are more significant than can be explained by the extra mass alone, and indicates the additional dome volume affects the manner in which gas behaves within the volcano in response to the FZ.
The pattern of the change in average pressure (Figure 9.17) in response to the FZ is also very similar to that of the original models with the scar (Figure 8.3). However, there are significant differences, particularly in the magnitude of the pressure change in certain models, whilst in others the pressure change is the same. Furthermore, whilst **55** showed the greatest pressure change in the conduit with the scar present, in these results (without the scar), the greatest conduit pressure change occurs in **t61**. **t61** also shows the greatest pressure change in the core and carapace, in concurrence with **61**. In the original set of models, some showed depressurisation in the dome talus, however, with the changed topography, all models which previously showed the greatest pressure change now show pressurisation.
Plotting the difference in end pressure change (Figure 9.18) between the two sets

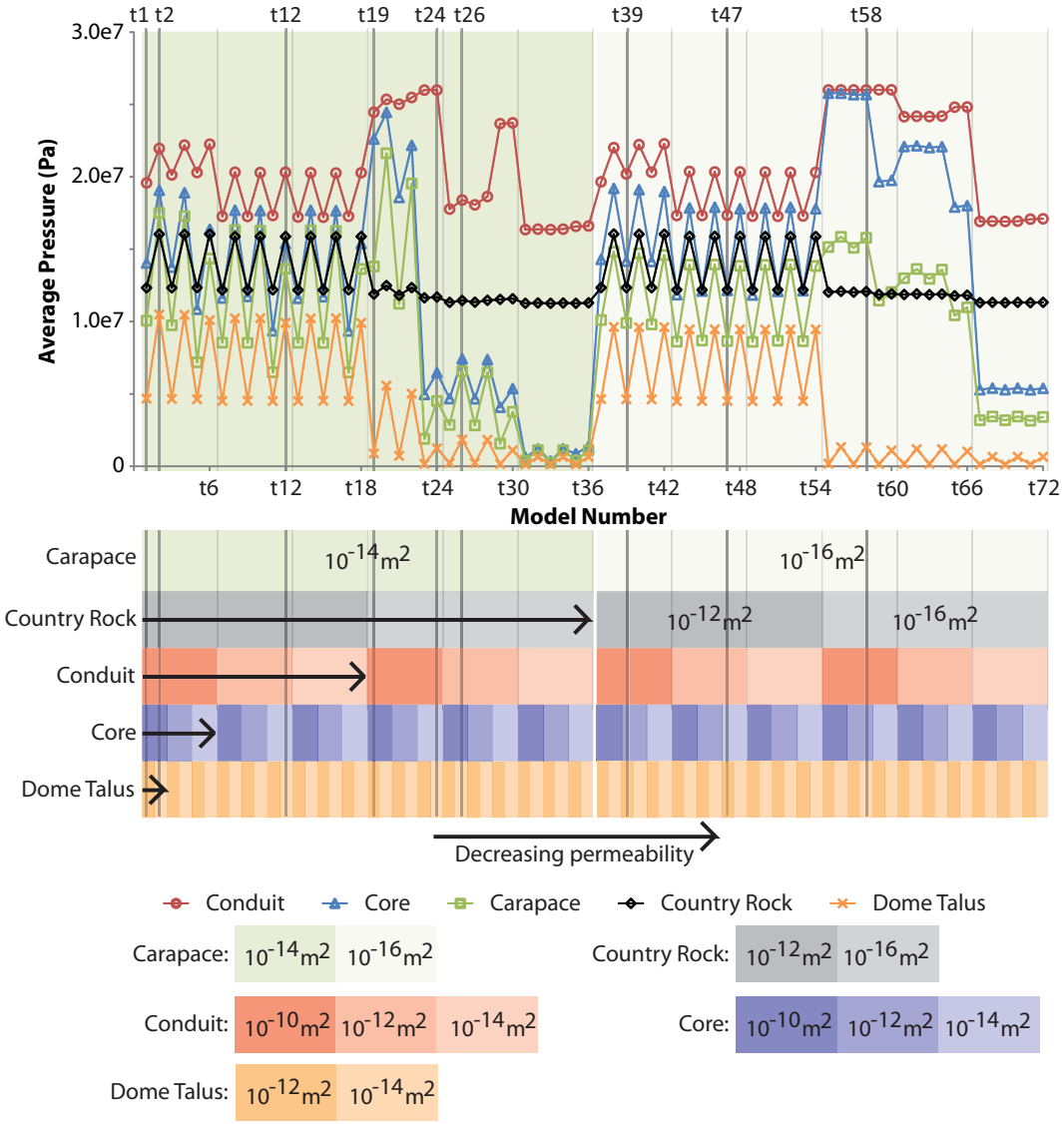

Figure 9.15: The average pressure in each domain at the start. The pattern is very similar to that for the original models with the scar (compare with Figure 8.2, Page 119).

of models highlights more readily the changes to the results due to the impact of the differing topography. In this plot, a positive difference means less depressurisation, whilst a negative difference shows greater depressurisation, compared to the original models. In general, the greater the original pressure change in the core and carapace due to the FZ, the greater the increase in end pressure for the changed topography. The greatest difference in pressure change of the core, carapace and conduit occurs in models **t19**, **t55**, **t62**, **t64**. These models show considerable depressurisation in response to the FZ. However, this large positive difference between the models indicates the increased dome talus mass prevents these volcanic systems from depressurising to the same extent. However, other models (**t21**, **t57**, **t61** and

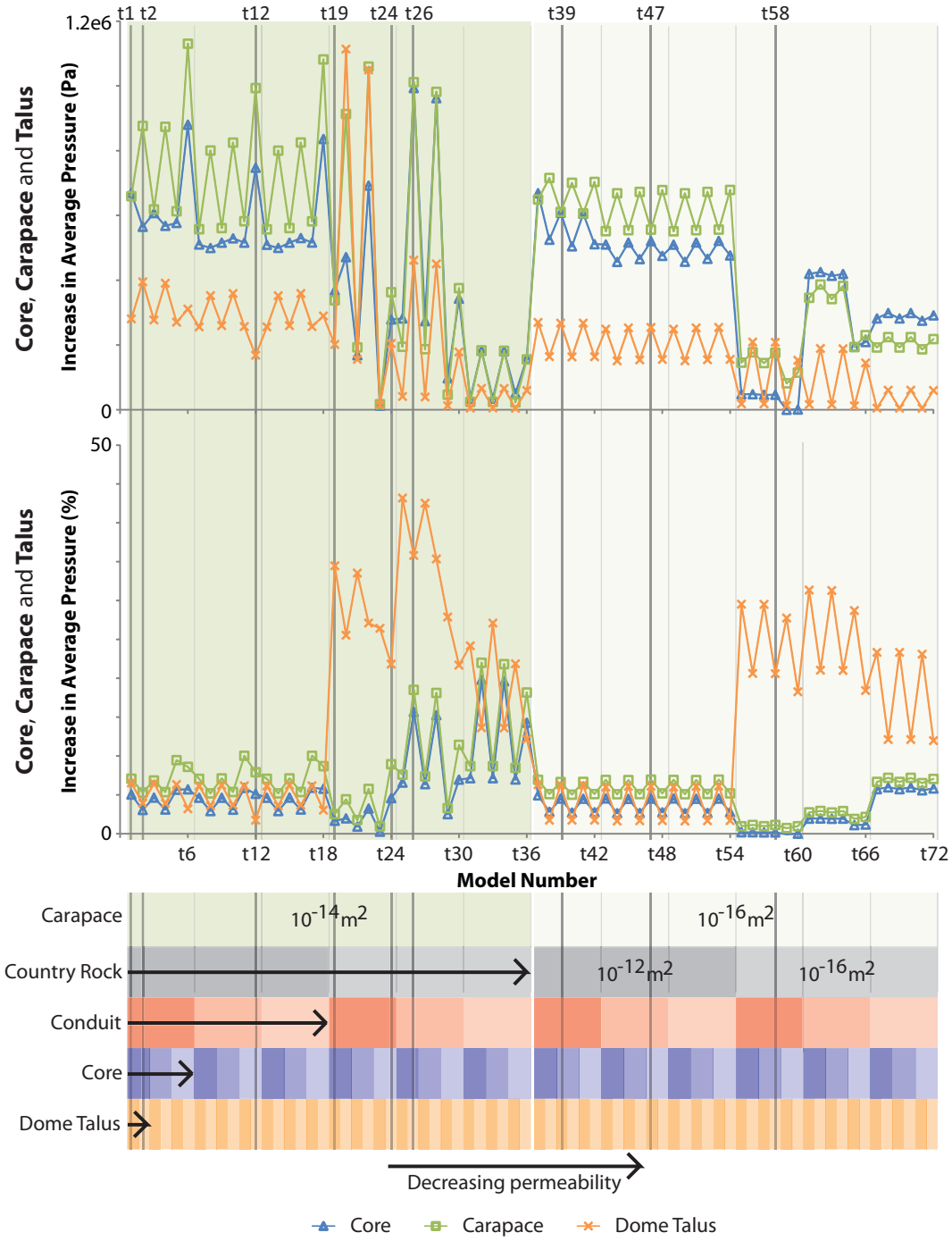

Figure 9.16: The difference in initial average pressure for the models without and with a scar, plotted in pascals and as a percentage. All domains show an increased average pressure when the scar is omitted. The conduit and country rock have not been included as the percentage increase is relatively minor compared to the three domains shown (Conduit: < 2.5 %, Country rock: < 2.0 %). Only the difference with a FZ of 10^{-10} m^2 is shown. See Figure 9.15 for the legend for the domain permeabilities.

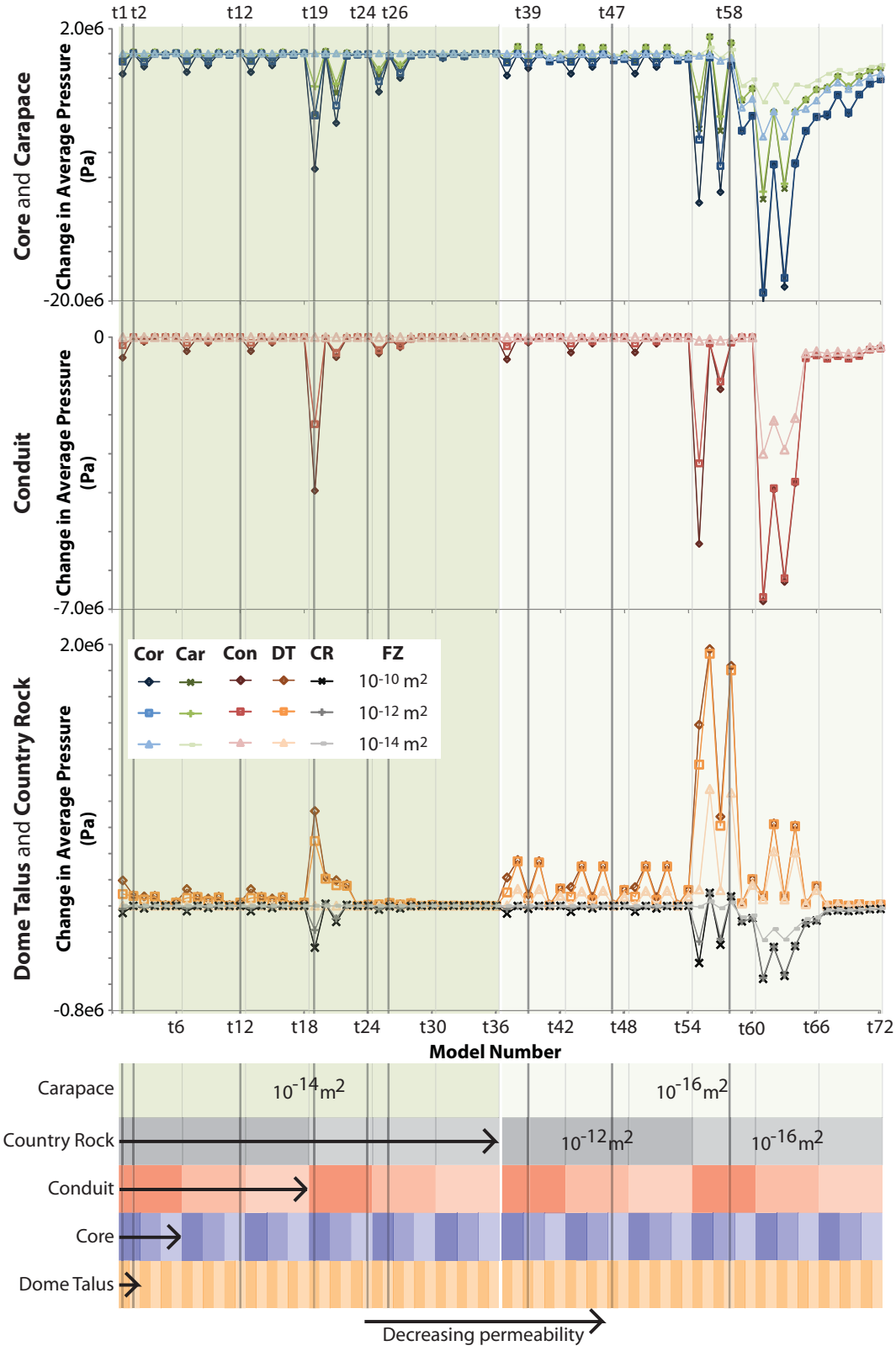

Figure 9.17: Change in average pressure at the end of each model without the scar. The pattern is similar to that for the original models, however, the dome talus average pressure is very different. Compare with Figure 8.3, Page 123. For Core (Cor), Carapace (Car), Conduit (Con), Dome Talus (DT) and Country Rock (CR). See Figure 9.15 for the legend for the domain permeabilities.

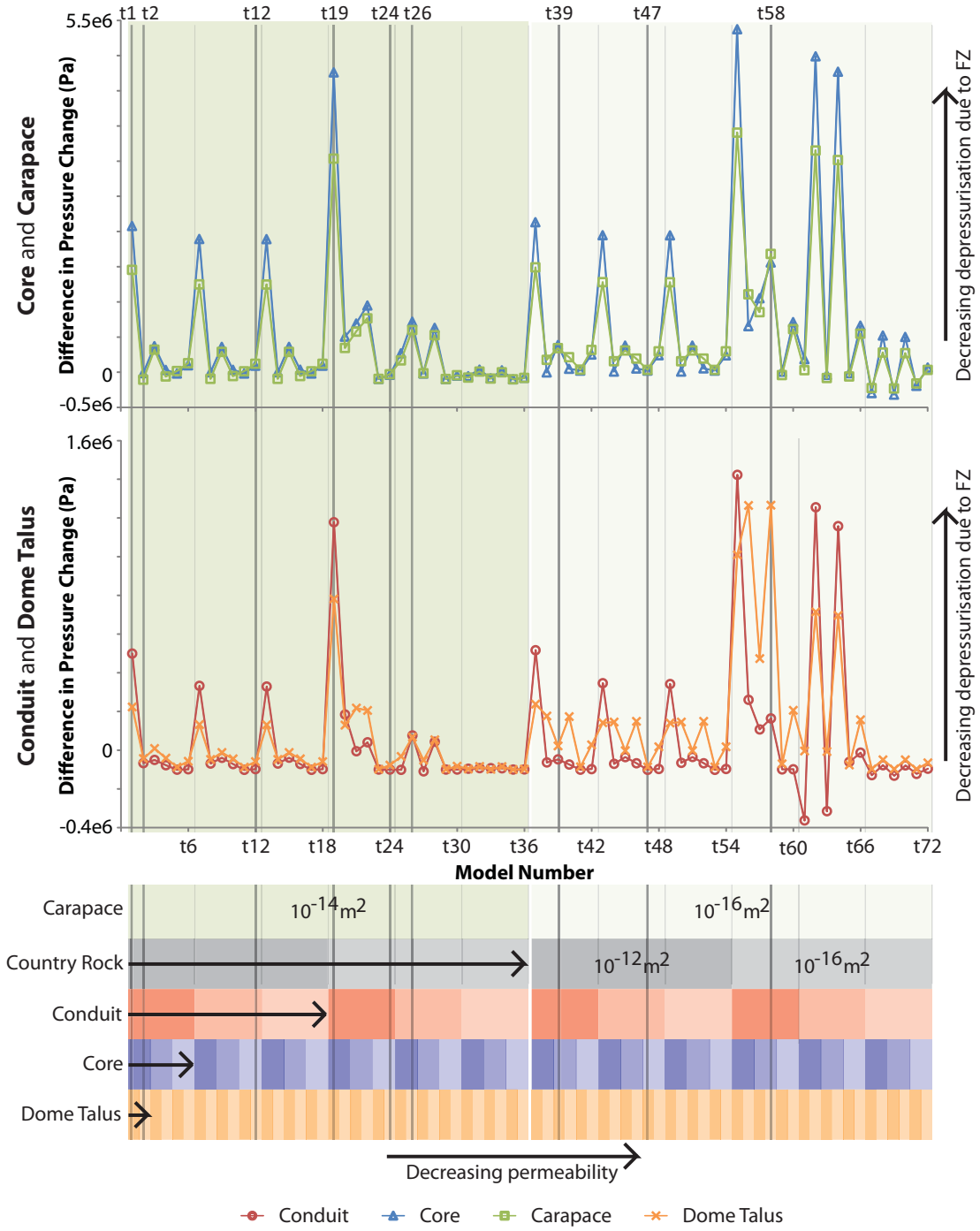

Figure 9.18: Difference in end pressure change between the models without the scar compared to the original models (subtracting the change in pressure with the scar from the change in pressure without the scar). Most models show an increase in the pressure change, which because the original values were negative, means less depressurisation and therefore less gas loss. See Figure 9.15 for the legend for the domain permeabilities.

t63) which depressurise in response to the FZ show little or no difference with the changed topography. This indicates these volcanic systems are still able to depressurise significantly (almost to the same extent) despite the changed topography. In **t21** and **t57**, the change in pressure is less than **t19** and **t55** due to a decreased core permeability. Consequently, it should be expected that the difference in pressure change would be comparatively less. However, **t61** and **t63** show considerably less difference in the pressure change compared to **t62** and **t64** due to the differences in dome talus permeability. In the former, the dome talus has the high permeability of 10^{-12} m^2, which in combination with the high interior pressure gradient (due to low carapace and country rock permeabilities), permits the gas to readily escape. In contrast, the lower dome talus permeability in **t62** and **t64** acts as a seal and prevents the gas from escaping as it did previously due the increased volume of material the gas must pass through. Models **t67**, **t69** and **t71** show a negative difference in pressure change indicating a larger depressurisation of the core and carapace. However, at less than 0.3 MPa, this is small and is due to the increased initial pressure. Similarly **t61** and **t63** show a negative difference in pressure change within the conduit of 0.3 MPa. The increased initial pressure indicates the presence of more gas, which is subsequently lost post-FZ, resulting in greater apparent depressurisation of these domains.

The greatest difference in dome talus pressure change occurs in models **t19**, **t55**, **t56**, **t58**, **t62**, **t64**. These models are amongst those with the most pressurisation at the start and result in the greatest pressure change post-FZ. Consequently, the greater the initial pressurisation, and resulting pressure change of the interior domains, the greater the increase in pressure change within the dome talus.

Increased pressure at the end within the core, carapace and conduit indicates less gas is being lost from the volcanic interior in response to the FZ. However, increased pressure within the dome talus suggests gas is being stored or restricted within the dome talus itself.

9.3.3 Displacement

In concurrence with the initial pressure and the pressure change at the end, the initial displacement and the resulting displacement change follow the same pattern as the original models, regardless of the changed topography (Figure 9.19). However, the magnitudes of the displacement change, both inflation and deflation are lower. In general, the greater the initial maximum surface displacement, the greater the difference between the two sets of models (Figure 9.20), such that a model showing a high initial surface displacement, also shows a greater difference from its counterpart in Chapter 8. However, **t19**, **t55** - **t64** are notable in showing a lower initial

maximum surface displacement than their counterparts. The low country rock permeability, coupled with the more permeable interiors and low carapace permeability (**t55** - **t64**) shows these models would initially have a highly pressurised conduit and surrounding region, but much less pressurisation within the country rock. Consequently, the localised nature of this pressurisation results in less displacement at the surface, which is further minimised by the greater distance to the surface due to the larger dome talus bulk.

The greater the deflation in Figure 9.19, the greater the difference in deflation between the two model sets (Figure 9.20). This shows the changed topography is retaining more gas and restricting its loss to the atmosphere. Furthermore, for many models, particularly those with the more permeable carapace of 10^{-14} m^2, the difference in inflation follows a similar pattern to that of the deflation (Figure 9.20). Many models are experiencing less deflation because the gas is being redistributed through the volcanic structure and its loss restricted rather than the gas simply escaping to the atmosphere.

t2, **t4**, **t8**, **t10**, **t14** and **t16** are very notable in showing less inflation (1 - 1.5 cm) in response to the FZ with the changed topography (Figure 9.20). These six models have the same carapace (10^{-14} m^2), country rock (10^{-12} m^2) and dome talus (10^{-14} m^2) permeabilities. In the models with the imposed scar, these models resulted in a very localised inflation due to gas being partially sealed by the low permeability of the dome talus, and because the internal pressure gradient was too low, this gas could not readily escape. However, with the increased dome talus bulk, the gas may penetrate further into the dome talus structure thereby reducing the maximum surface inflation, but resulting in a greater region experiencing inflation. The models with the greatest surface deflation (**t61** and **t63**) (Figure 9.19) show small changes to the inflation (Figure 9.20). Similarly, the models with the greatest surface uplift (**t56** and **t58**) show small changes to the deflation.

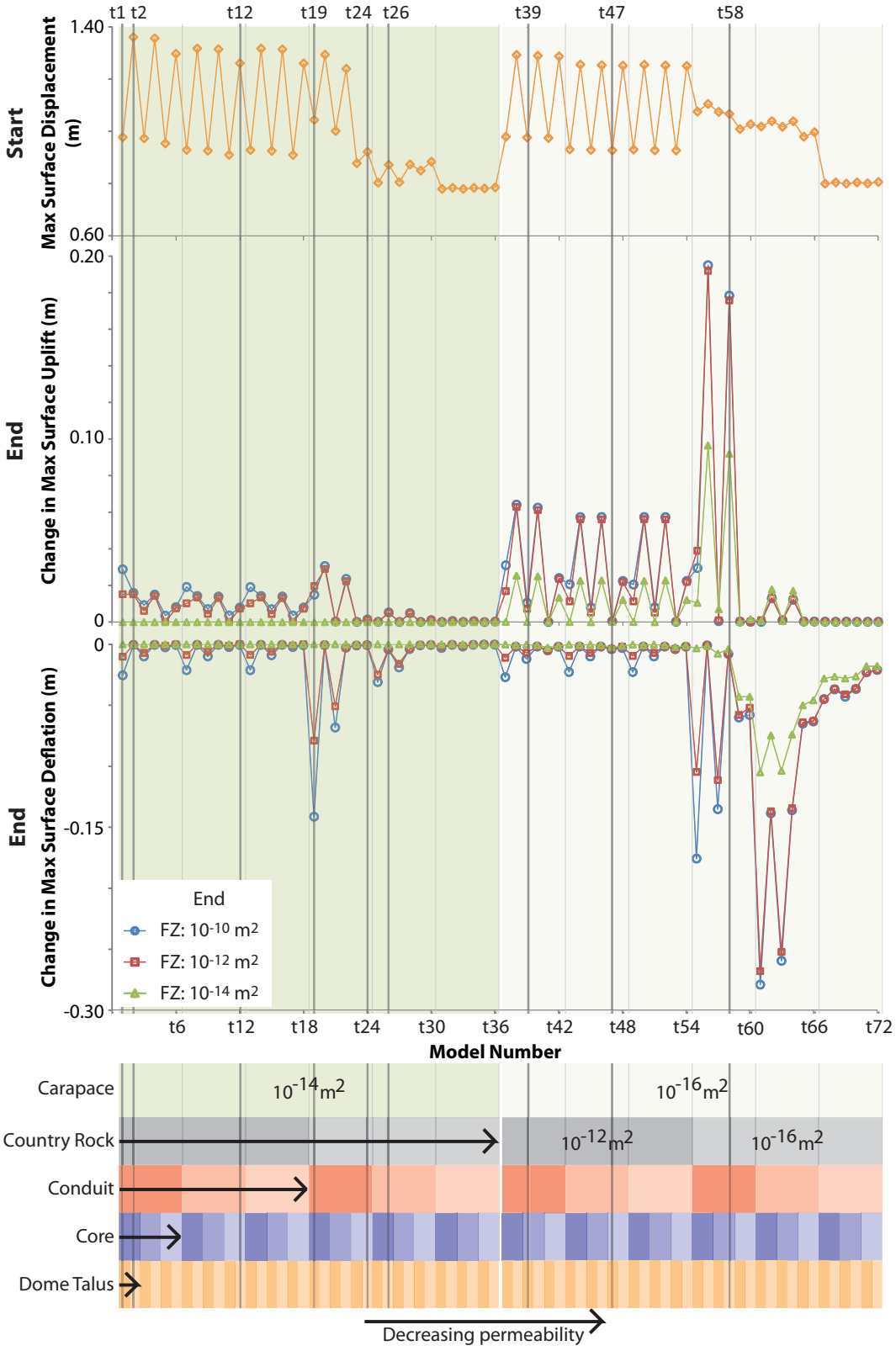

Figure 9.19: Initial maximum surface displacement and change, for the models without the scar, in response to the FZ. Compare with Figure 8.5 (Page 129). See Figure 9.15 for the legend for the domain permeabilities.

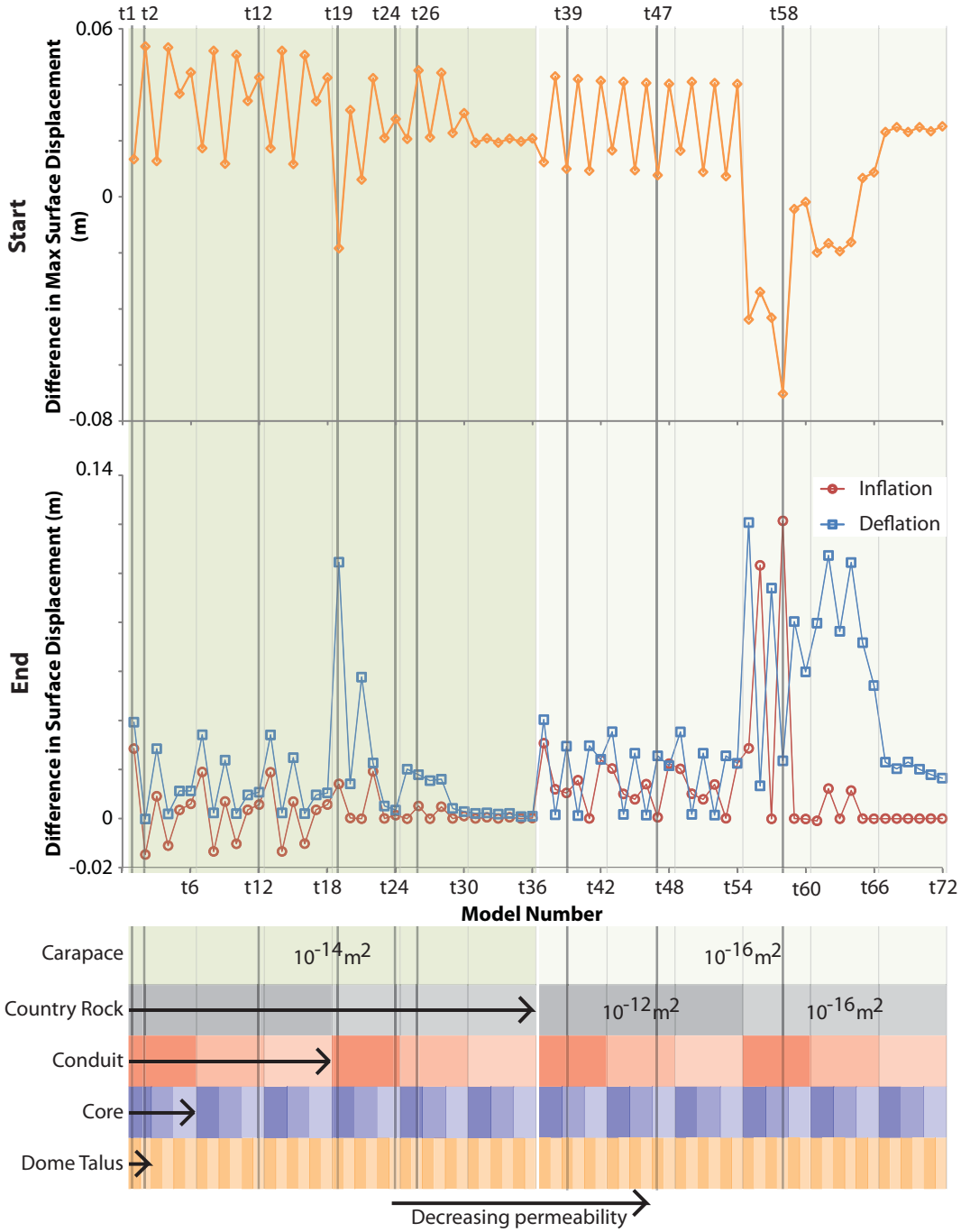

Figure 9.20: Difference in initial maximum surface displacement, and displacement change in response to the FZ, in terms of inflation and deflation, between the two sets of models (subtracting the change in pressure with the scar from the change in pressure without the scar). Only the difference with a FZ of 10^{-10} m^2 is shown. A positive change in inflation means greater inflation, whilst a positive change in deflation means less deflation for the changed topography in comparison to the original models. Many models show decreased deflation or increased inflation with the changed topography. See Figure 9.15 for the legend for the domain permeabilities.

9.3.4 Groups

Whilst there is little change in the initial pressure, subtle changes to the pressure change response has resulted in differences in the displacement change with the different topography. Not only has the response changed, but some models in the groups with the scar no longer fit into the same groups (Figure 9.21). Whilst Groups 1 (T2[1]) and 4D (T8) still contain the same models, all other groups have changed. Group T1 is characterised by a ring of deflation centred around the FZ, with the strongest subsidence to the NE. Above the FZ there is a very minor inflation. This displacement pattern is due to a small volume of gas exiting the core into the dome talus. This results in pressurisation within the dome talus, but the loss of gas from the core adjacent to the FZ causes the subsidence. This group (T1) contains all the members of Group 4A which have a dome talus permeability of 10^{-12} m^2, plus Model **t36**. Model **t36** is an exception in this group with a lower dome talus permeability of 10^{-14} m^2. However, it behaves in the manner of T1, rather than as T7 due to the low conduit permeability (10^{-14} m^2). All other models from Group 4A, which have a dome talus permeability of 10^{-14} m^2 (**t24**, **t30**, **t42**, **t48**, and **t54**) have moved to Groups T3 and T7. Group T2 contains the same members as Group 1, but the displacement has changed to being dominantly inflation, with a minor deflation to the NE. This is similar to the pattern seen in T1, but the deflation is less extensive due to the low core permeability. Group T3 contains all the models from 2B in addition to models **t42**, **t48** and **t54** from 4A. These two original groups showed opposite behaviour (2B: dominant inflation, 4A: dominant deflation). However, they all now show dominant inflation above the FZ, with minor deflation to the SW. Group T4 contains just four models and is very similar to T3 except the inflation is more extensive due to the lower country rock permeability, confining the gas to the interior, which is then released into the dome talus post FZ. The remaining members of 2A move to group T5 which shows a similar displacement pattern to T3 and T4, except there is more surface deflation. The dome talus and carapace permeabilities are the same in these models, and consequently, when the FZ occurs, the dome talus becomes the new "seal" and, gas may move from the core into the FZ. This results in deflation over the core, but inflation above the FZ. Group T6 is essentially the opposite to T1 with inflation surrounded by deflation, and the greatest subsidence to the SW. This is different to Group T5 due to the ring-shaped subsidence around the inflation. The high dome talus permeability implies post-FZ, gas may transfer from the core into the dome talus. However, the dome talus still restricts gas motion, resulting in inflation, but because of the loss of gas from the core, there is also

[1] T1 - T8 are used to distinguish the models in this section from those in Chapter 8 with the imposed scar.

subsidence. Two models from Group 4A comprise T7 (**t24** and **t30**). In these two models, the entire dome structure has the same permeability (10^{-14} m^2) which is higher than that of the country rock (10^{-16} m^2). Therefore, the FZ becomes a region of very high permeability, surrounded by low permeability material. Consequently, gas may migrate from the core immediately juxtaposed into the FZ itself, resulting in pressurisation. Both subsidence and deflation signals in these models are very low at < 1 mm. Group T8 contains all the models from 4D and displays the most extensive deflation observed. However, there is an associated inflation to the NE, although this is always of a lower magnitude to the deflation. All these models have a very low country rock permeability which confines the gas to the more permeable conduit and core. Furthermore, the carapace is always less permeable than the core and dome talus slope. Consequently, the FZ releases the gas which was confined to the volcanic interior. This gas transfers to the dome talus where it may be partially restricted prior to emission at the surface. The large volumes of gas which may be lost from the volcanic interior in this scenario results in the large deflation.

Groups T1 and T2 are similar in that they have the inflation point over the FZ with a subsidence to the NW. All other models show the displacement to the SW, over the core. When the topography is modelled with the scar, all models show a deflation signal, which is usually dominant (except in 2B and 3). However, without the scar, most models are dominated by inflation (except in T1 and T8).

The key to the resultant displacement is the location and volume of gas which is originally stored, and where this gas migrates to once the FZ occurs, including if it moves to a new storage location or is emitted to the atmosphere.

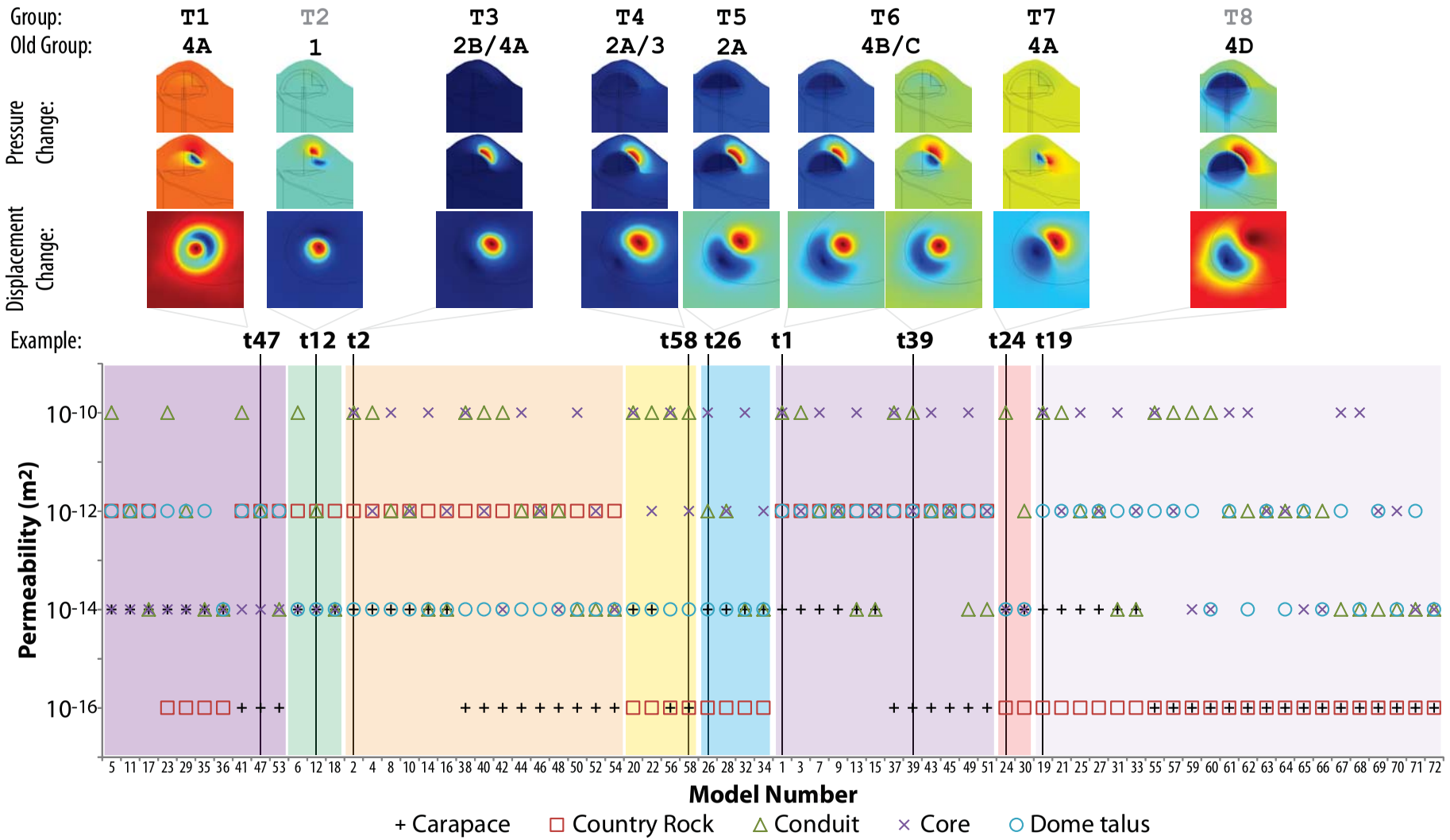

Figure 9.21: Permeability criteria determining which model displays which displacement behaviour due to the FZ. See Table 9.4. Groups T2 and T8 have not changed from their counterparts (1 and 4D, respectively). The differences between groups T2 - T4 and T5 - T6 are shown in more detail in Figure 9.22.

	Relative permeability	**Domains unchanged**
T1	Core $k = 10^{-14}$ m^2, AND dome talus $k = 10^{-12}$ m^2 (except model **t36**).	Core
	Low permeability core prevents gas loss from underlying conduit and country rock.	
T2	Same as group 1. Carapace k = core k = dome talus $k = 10^{-14}$ m^2, AND country rock $k = 10^{-12}$ m^2.	Carapace, country rock, core, dome talus
	Permeable country rock overlain by less permeable dome structure.	
T3	Country rock $k = 10^{-12}$ m^2, AND dome talus $k = 10^{-14}$ m^2, AND core $k >$ carapace k.	Country rock, dome talus
	Permeable country rock overlain by less permeable dome, but core is sealed by carapace.	
T4	Country rock $k = 10^{-16}$ m^2, AND dome talus $k = 10^{-14}$ m^2, AND conduit $k = 10^{-10}$ m^2.	Country rock, conduit, dome talus
	Low permeability country rock, carapace and dome talus with a more permeable conduit and core.	
T5	Carapace k = dome talus $k = 10^{-14}$ m^2, AND country rock $k = 10^{-16}$ m^2, AND conduit $k = 10^{-12}$ or 10^{-14} m^2.	Carapace, country rock, dome talus
	Low permeability country rock, carapace and dome talus with a more permeable core.	
T6	Country rock k = dome talus $k = 10^{-12}$ m^2, AND core $k = 10^{-10}$ or 10^{-12} m^2.	Country rock, dome talus
	Permeable country rock and dome talus with less permeable carapace.	
T7	Country rock $k = 10^{-16}$ m^2, AND carapace k = core k = dome talus $k = 10^{-14}$ m^2, AND conduit $k = 10^{-10}$ or 10^{-12} m^2.	Carapace, country rock, core, dome talus
	Conduit is more permeable than surrounding country rock and bulk dome.	
T8	Same as 4D. Carapace = 10^{-14} m^2 AND country rock = 10^{-16} m^2 AND dome talus = 10^{-12} m^2 AND core = 10^{-10} OR 10^{-12} m^2, OR Carapace = country rock = 10^{-16} m^2 AND IF conduit = 10^{-10} m^2 AND dome talus = 10^{-14} m^2 THEN core = 10^{-14} m^2	Country rock
	Conduit and core surrounded by less permeable country rock and carapace.	

Table 9.4: Permeability criteria determining which model displays which displacement behaviour due to the FZ. See Figure 9.21.

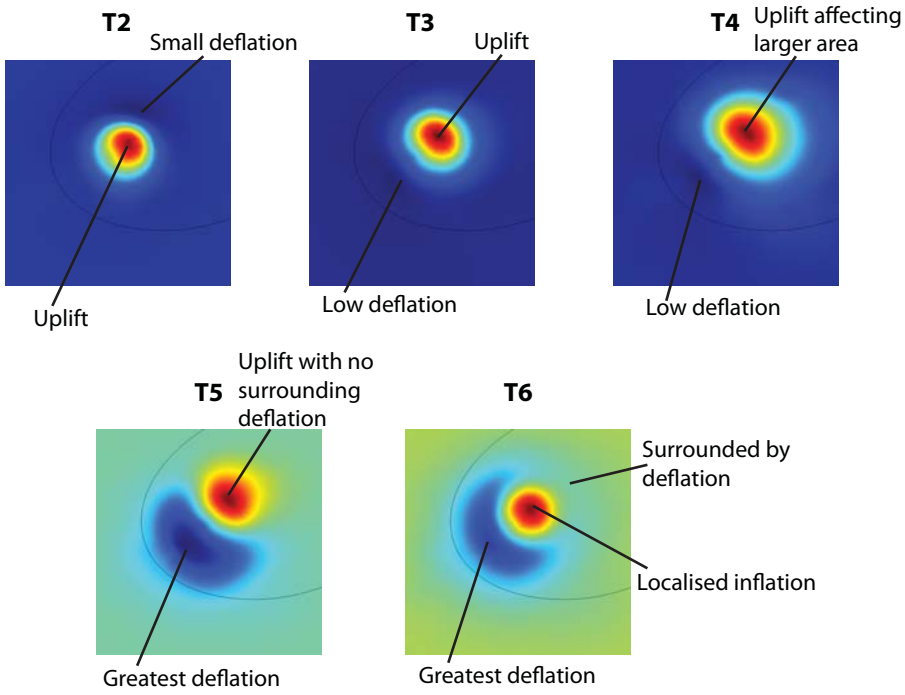

Figure 9.22: The differences between groups T2, T3 and T4 showing dominant inflation, and groups T5 and T6 with both deflation and inflation.

9.3.5 Example Models

As in Chapter 8, example models are shown and described forthwith to illustrate the pressure change and displacement change characterising each group. For continuity, the same models used before are described here, despite the redistribution of the groupings. Consequently, **t1** and **t39** are both described for T6. Furthermore, **t24** is also included as a representative of T7. **24** was a member of 4A and displayed behaviour in accordance with **47** (the example model for 4A). However, it will be shown here that the changed topography results in a dramatically different behaviour in response to the FZ.

Example Models: Pressure

Due to the similarity in the initial pressure results to those in Chapter 8, the initial pressure for the changed topography is not shown. However, the end change in pressure is shown in Figure 9.23, and Figure 8.10 is repeated and reordered for reference (Figure 9.24). The pressure change within all domains, except the dome talus, is essentially the same regardless of topography, although of different magnitude, as discussed earlier. The difference between the models, and the reason they become subdivided into different groups, is the gas behaviour within the dome talus. In all models, the gas penetrates into the dome talus structure thus increasing its pressure.

Whilst the interior pressure remains high, gas may be forced through the dome talus to escape. However, once the pressure drops too low, the volume of gas leaving the dome talus is matched by that entering from below, due to the continuous supply of gas.

Example Models: Velocity

Of the example models, **t47**, **t1**, **t39** and **t19** show the most prominent change in the surface gas velocity in response to the FZ (Figure 9.25). The surface area of these gas emissions is more extensive than that in the original models with the scar. In each of these four models, the gas emission is approximately elliptical giving a surface area of $0.10 - 0.25$ km^2, which is significantly larger than the localised fumaroles from the original configuration[2]. The increased dome mass above the FZ permits the gas to penetrate further into its structure and therefore the surface emission is larger. In contrast, when the scar is imposed, the distance between the top of the FZ and the surface is less and therefore, the gas escapes to the surface without migrating extensively into the dome structure.
By taking the average velocity across this area, the increase in surface gas loss may be estimated (Figure 9.26). Estimates for the volume of gas lost from the conduit and core are also presented in Figure 9.26. As seen previously, the core loses the greatest volume of gas. Despite models **t2**, **t58**, **t26** and **t24** losing significant volumes of gas from both the core and conduit, the surface gas emission rates are negligible. Instead of rapid loss from the surface of the dome talus, this gas is retained by the enlarged dome talus, which retards the gas velocity and dramatically decreases its exit velocity. Model **t12** is different in that its core gains more gas than it loses. It gains approximately 1000 t H_2O which may be derived from the other domains such as the conduit or country rock, which both have the same permeability.

Example Models: Displacement

Figure 9.27 shows the total initial displacement and the final displacement change (with respect to the initial) for both the original example models, and the examples without the scar. Whilst the initial total surface displacement patterns are very similar, there are striking differences between the displacement change results. The most obvious difference is the dominant deflation present in many of the original model results, has been replaced by a combination of deflation and inflation. Of the nine example models, seven (**t2**, **t58**, **t26**, **t1**, **t39**, **t24** and **t19**) show very similar

[2]Assuming an elliptical shape, measuring the length (l) and width (w), and using the formula: $\frac{1}{4}\pi lw$.

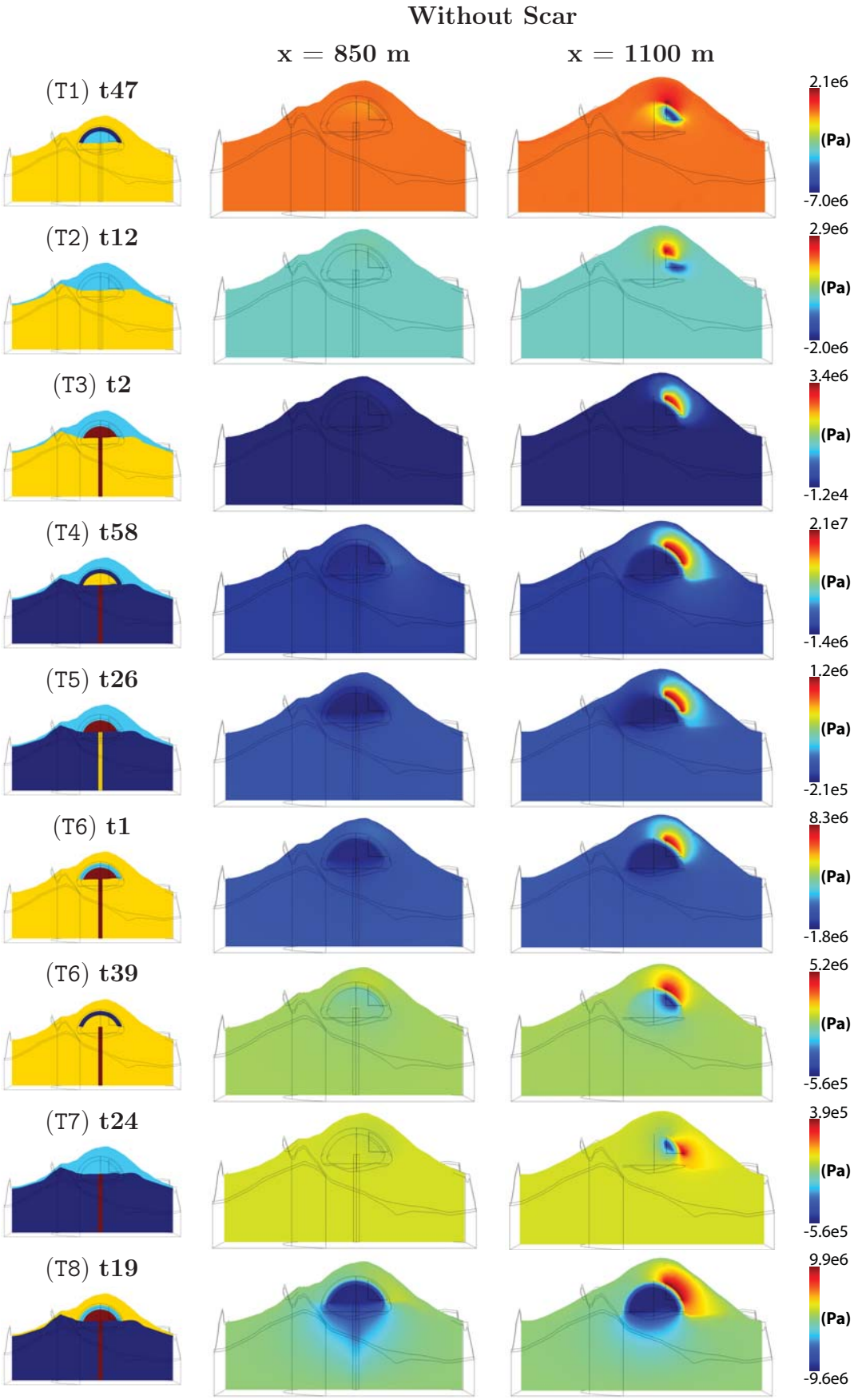

Figure 9.23: End pressure change for the example models without the scar, through the conduit (left) and through the FZ (right). The permeability conditions for each example model are shown for reference. Compare with the original models, from Chapter 8, in Figure 9.24.

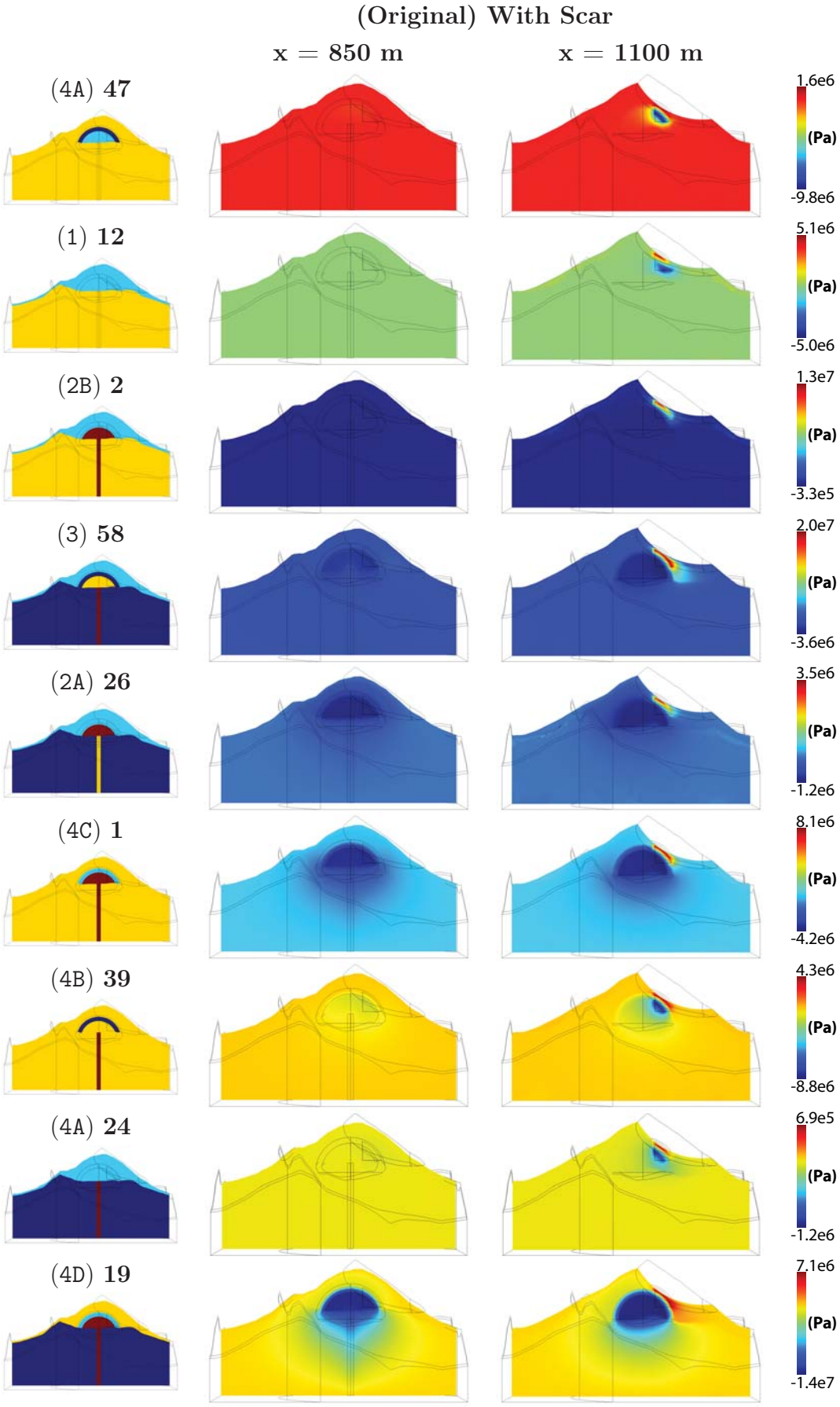

Figure 9.24: The end pressure change, for the models with the scar, relative to the initial pressurisation as shown in Figure 8.9. All models show a pressure change in the vicinity of the FZ. 2A, 3, 4C and 4D also show a significant decrease in pressure within the core.

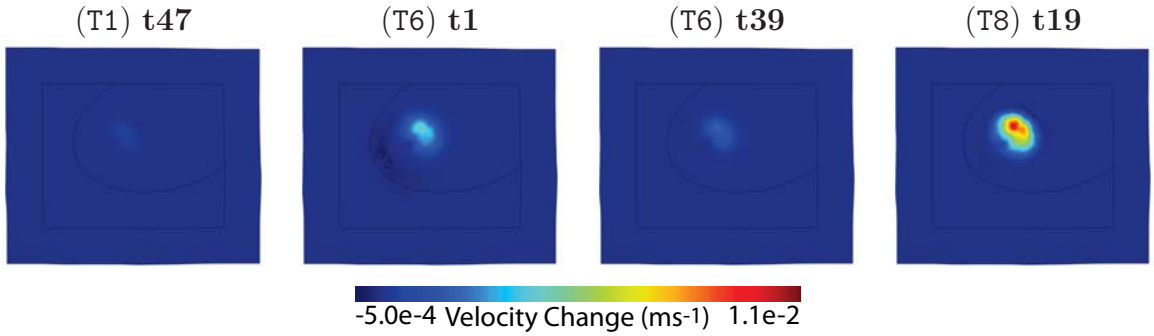

Figure 9.25: Gas velocity change at time 10000 seconds with respect to the initial, for models **t47**, **t1**, **t39** and **t19**. Of the eight example models, these four show the greatest increase in gas velocity on the surface in response to the imposed FZ.

displacement change behaviour. Namely a strong inflation over the FZ "surrounded" by deflation which is most intense towards the SW (over the dome core). This pattern indicates a migration of the stored gas, which was once confined to the interior by the "sealed" carapace, into the surrounding dome talus. However, due to the increased dome thickness above the FZ, the gas is restricted by the dome talus, with only limited degassing to the surface possible. In contrast, the other example models (**t12** and **t47**) show different behaviour. The uplift has a similar position, but the deflation is most intense to the NE. In both models, the core has a low permeability of 10^{-14} m^2, providing an inefficient environment for gas storage and

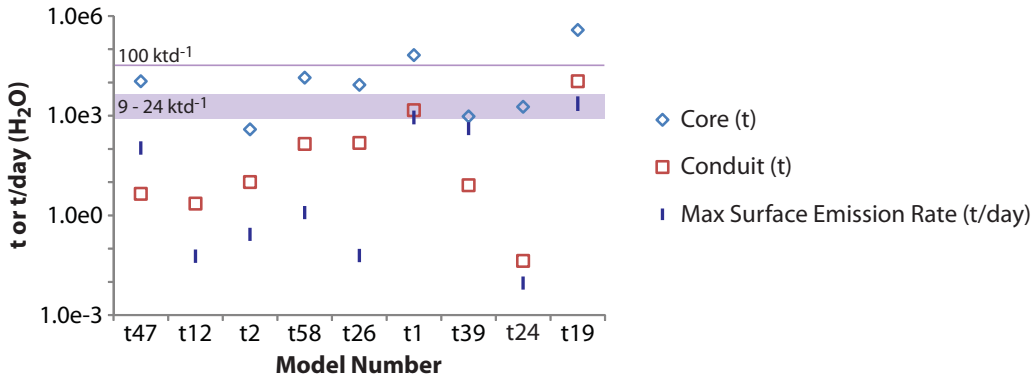

Figure 9.26: There are large uncertainties in the calculation of the maximum surface gas emission due to the large surface area the emissions cover. Estimates put the surface area between 10,000 to 25,000 m^2. In models **t12**, **t2**, **t58**, **t26** and **t24** the gas velocity at the surface is very small resulting in very low surface emissions rates (t/day). The estimated gas loss (t) for the core in model **12** is not plotted because it gains more gas than it loses. The maximum (100 ktd^{-1}) and average ($9-24$ ktd^{-1}) emission rates as estimated by Edmonds et al. (2002) for dome building eruptions are Soufrière Hills volcano are indicated for reference.

hence the effect of the FZ is limited. Consequently, the FZ itself becomes the source of the gas, such that the gas moves from the base of the FZ (causing subsidence) to the top of the FZ (causing inflation). The overall displacement change patterns tend to be larger in the models without the scar. This is related to the depth of the FZ compared to the top surface of the dome. The dome structure is larger and so has a greater capacity to restrict the motion of the gas.

The change in displacement pattern for each model at three time-steps (1000 s, 5000 s and 10000 s), and the end equilibrium, is shown in Figure 9.28. All the example models illustrate very similar behaviour at these times, with inflation above the FZ at 1000 s coupled with subsidence as gas is transferred from the volcanic interior into the dome talus structure. The differences between the models shows as differing proportions of uplift vs subsidence and the relative locations of these features. In turn, these are related to whether the gas originates adjacent to the FZ, within the core and/or the dome talus.

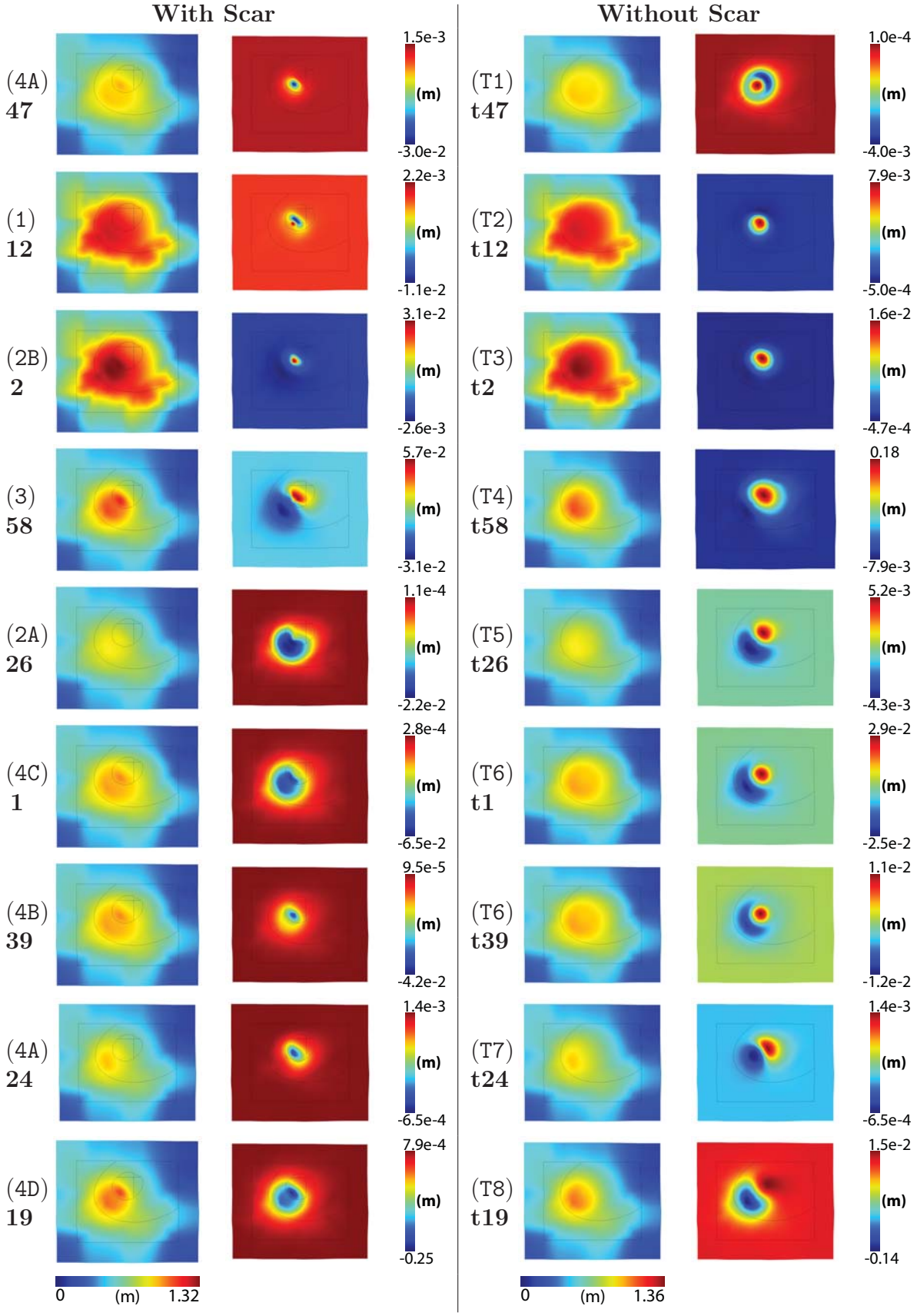

Figure 9.27: The initial total surface displacement and the end displacement change patterns for the models with and without the scar. There are no significant differences in the initial surface displacement between the two sets of models, but the response due to the FZ is markedly different.

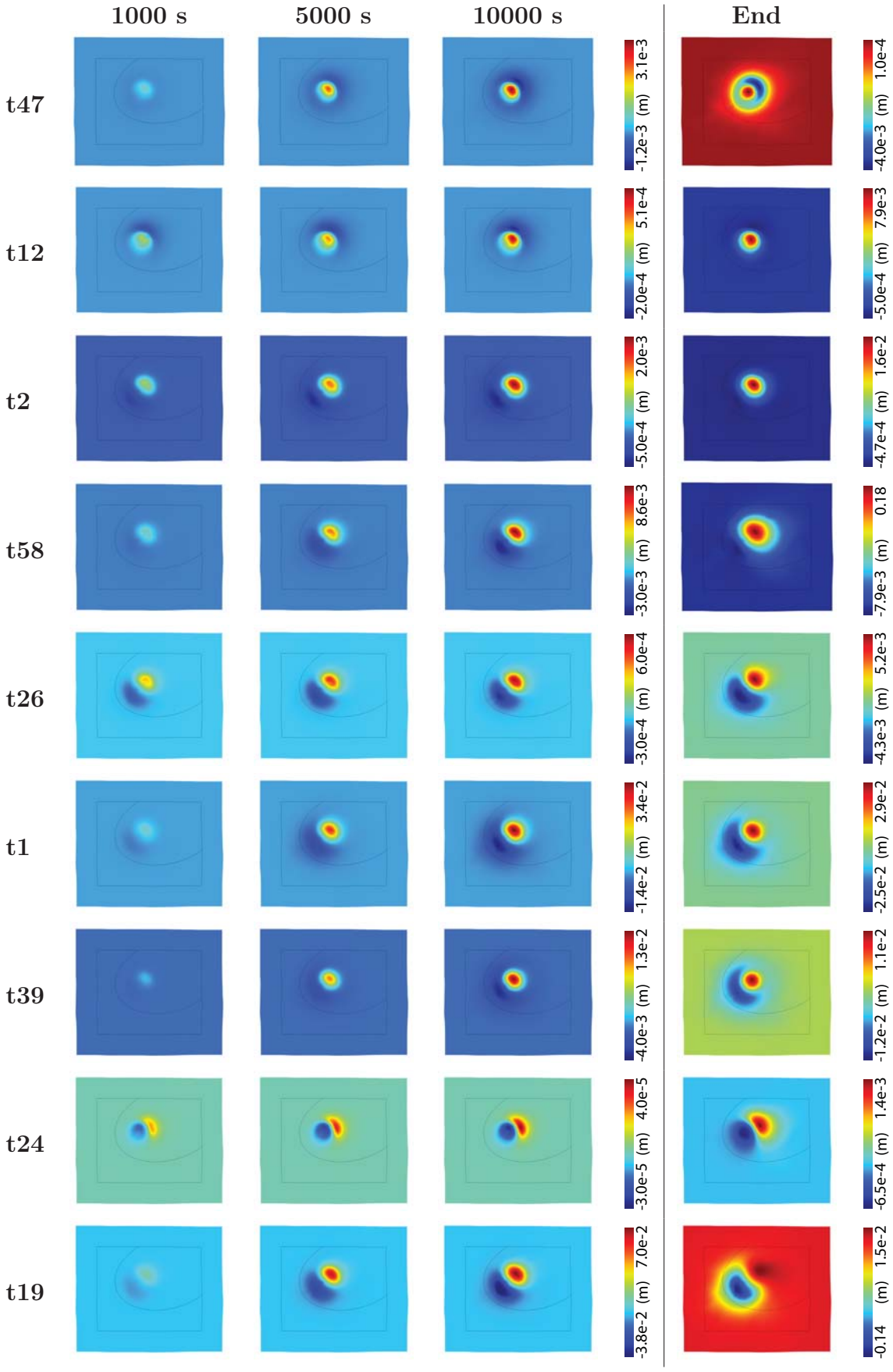

Figure 9.28: Displacement change at three time-steps and the final equilibrium displacement change.

9.3.6 Model 19 comparison

Model **19** (Figure 9.29) and, its counterpart, **t19** (Figure 9.30) are used to show how the pressure changes over the first 10000 s inside the volcano have a bearing on the resultant surface observations. For each time-step of the two models, the pressure change through the conduit and FZ are plotted along with the surface displacement change and the change in gas velocity. As noted previously, the pressure change of the interior is very similar between the two models, with both losing gas (depressurising) from the core and conduit. The degree of this depressurisation and gas loss increases with increasing time from the FZ formation. However, there are large differences at the surface. When the scar is imposed on the topography (**19**), there is a strong, localised inflation by 750 s which increases in magnitude up to 5 cm before decreasing. By 10000 s, this inflation is barely discernible and it is completely lost by the end equilibrium position, replaced by a large depressurisation caused by the volume of gas lost from the core and conduit. The initial inflation is accompanied by a highly localised gas emission (fumarole). The maximum gas emission rate is reached by 1000 s, and the rate gradually decreases as the internal pressurisation decreases. In contrast, **t19** shows a larger region of inflation above the FZ and surrounding dome talus, and deflation above the core. The magnitude of both increase with time, although at the end equilibrium, deflation is dominant due to the volume of gas which has been lost from the interior. However, gas is present within the dome talus structure, as evidenced by both the pressurisation and inflation. The first signs of gas emission at the surface do not occur until 5000 s, over 1 hr after **19**. Furthermore, contrary to the localised fumarole of **19**, the gas emission from **t19** covers a significantly larger area, although the gas velocity is much less.

9.3.7 Implications of topography

The topography does not alter the general patterns of pressure and displacement, indicating the interior permeability is the controlling factor. However, the increased dome talus mass does affect the manner in which volcanoes respond to changes within the system, which permits gas to be released into the dome talus. The added mass impedes the motion of gas towards the surface resulting in less depressurisation and consequently, less deflation in response to the FZ. Furthermore, the movement of gas from interior regions into the dome structure results in deflation over the original site and inflation over the new catchment area. This suggests it may be possible to use the changing displacement patterns to track movements of large volumes of gas within a volcanic system.

Unlike those with the scar, many models here predict ephemeral gas emission. The

gas emission at the surface is dependent upon the interior pressure. Once this pressure drops too low, gas emission ceases. In reality, this may indicate the size and depth of a gas storage region.

The dome talus slope is modelled as less permeable than the FZ and so acts as a partial seal. Furthermore, because the permeability of the dome talus is still high enough to transmit the gas, gas may still pass through. However, the lower permeability decreases the gas velocity forcing gas to accumulate (potentially temporarily) within the dome structure. Visible gas emissions would only persist whilst the pressure gradient is high enough.

Altering the topography in this manner has dramatically altered the pressure change and displacement change results in response to the FZ and redistributed many models into separate groups. Models which previously showed similar behaviour now show a widely differing response. The main reason is the effect of the additional dome talus bulk. A greater internal pressure gradient is now required to force the gas through this dome talus material. Once the internal pressure gradient deteriorates due to loss of gas, the pressure is no longer sufficient to force gas from the system, and it resides within the dome structure itself to be released at a much lower rate, similar to that of diffuse degassing.

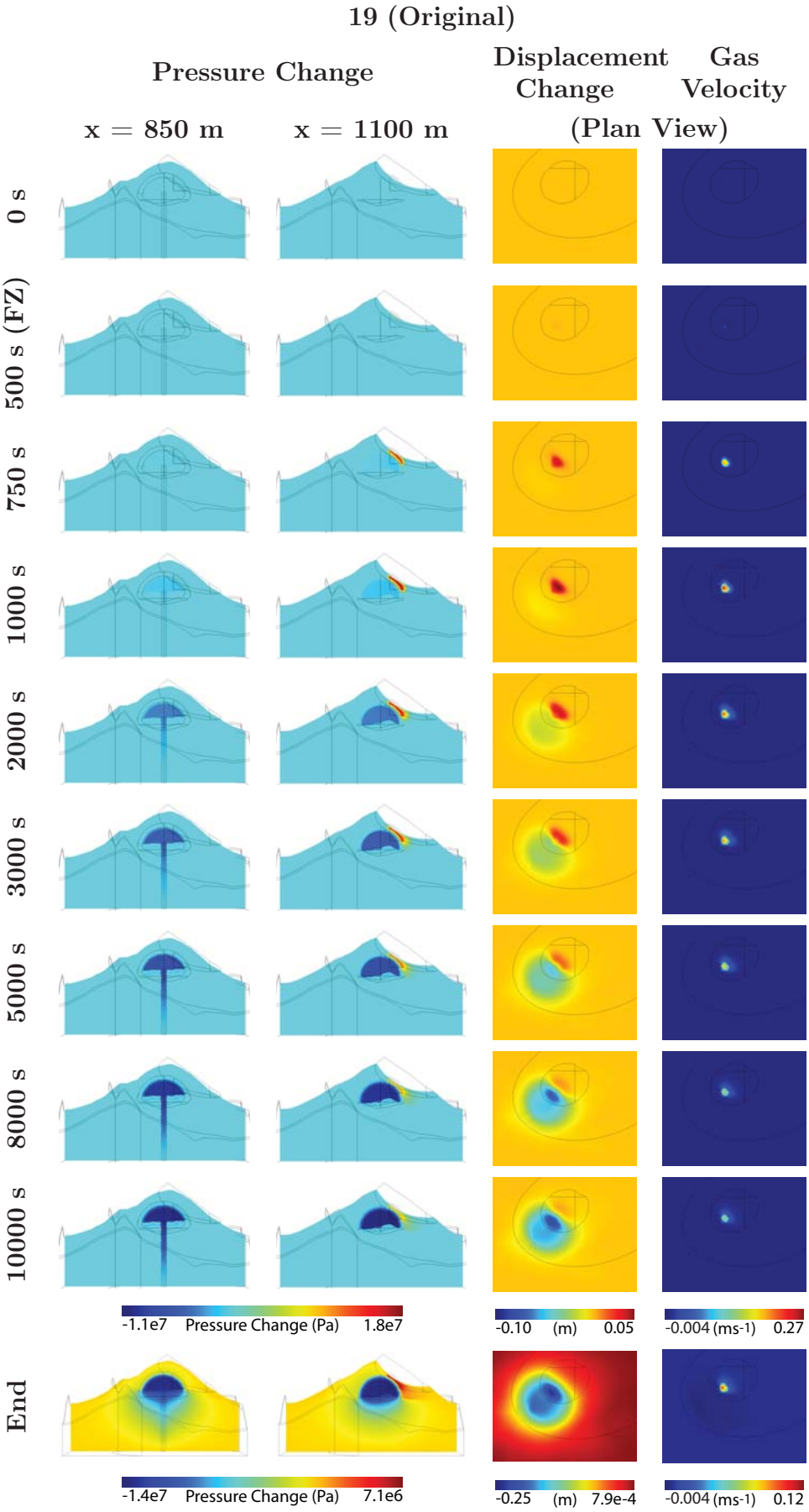

Figure 9.29: Progression showing the relationship between the changing pressure, displacement and gas velocity for the original Model **19** with the imposed scar.

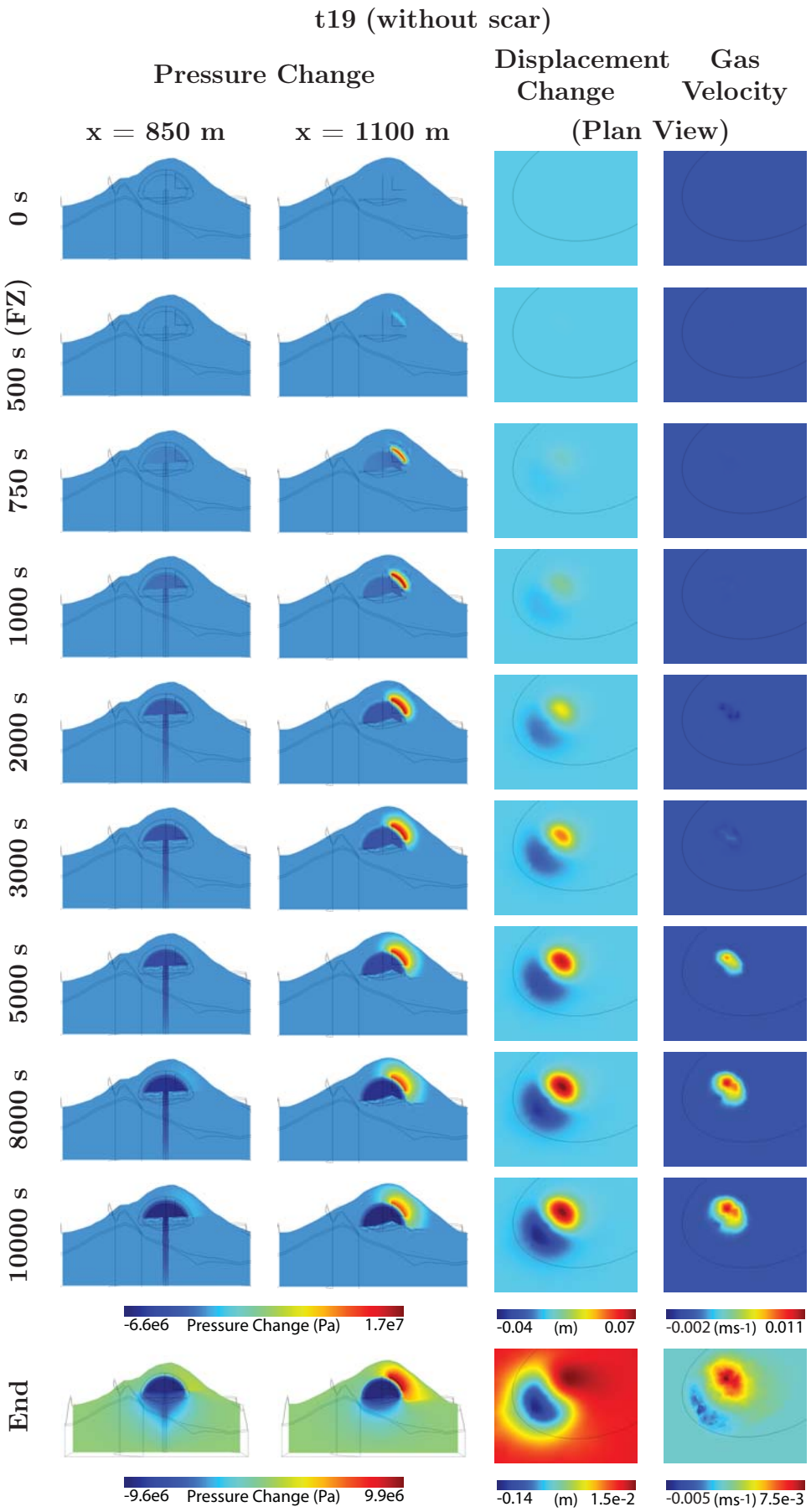

Figure 9.30: Progression showing the relationship between the changing pressure, displacement and gas velocity for Model **t19** without the scar.

9.4 Summary

In order to accurately model the degassing behaviour and displacement patterns due to the presence of gas not only are the permeability conditions required, but an accurate representation of the volcanic structure is also necessary. This includes both the surface topography and the internal structure of the volcano.

Whilst the conduit plays an important role, the country rocks and dome structure are also vitally important because the gas must pass through these zones before emission to the atmosphere.

As has been shown in this chapter, simply changing the surface topography does not affect the initial pressure and displacement patterns, showing permeability is the dominant controller in this scenario. However, the topography has a dramatic effect on the way in which the volcanic gas behaves in response to the FZ. Increasing the dome volume implies a greater capacity for gas storage, but also a higher pressure gradient is required to result in visual gas loss from the surface. It is possible that the movement of large volumes of gas within the structure by means of fracture development may be monitored due to the change in displacement pattern (assuming there is no active magma contribution).

The results from this chapter have suggested that whilst permeability variations within the conduit are evident from the modelled surface results, the differences between models are so small, it is unlikely the permeability conditions could be inferred from surface results. The surface response is largely dependent upon the average permeability relationships rather than the finer scale features.

The model developed over the last two Chapters (8 and 9) is extremely versatile, adaptable and especially relevant because it is based on a real volcano. Further potential adaptations which could be explored include altering the size of the core, and considering the malleable nature of the core, as suggested by Hale (2008), Hale et al. (2009a,b), or the addition of spines. Altering the size of the core would change the size of the gas storage region. A smaller core, would accommodate less gas and less pressurisation. However, a smaller core, situated further from the surface, would have implications for the effect of the modelled FZ. Increasing the distance between the gas source and the surface means the dome structure will play a greater role in hampering the release of gas and a higher overpressure would be required to force the gas towards the surface (Section 9.3). A ductile, malleable core has the potential to limit the effects of surface displacement - if the stress imposed is absorbed by the reorganisation of the dome structure. Consequently, this could result in a less extensive displacement pattern, potentially transforming a Group `4D` model to one with a displacement pattern similar to Group `4B`. Finally, the intrusion of spines into

the dome core and carapace structure would potentially limit the storage capacity of the core, because gas may be able to escape via the margin between the spine and the surrounding dome (Chapters 5 and 6). Furthermore, less overpressure would be accommodated because the pressure will force the spines to extrude (Chapter 10.3). In the next chapter the assumptions laid out in Chapter 2 are revisited and assessed before the model is used to investigate specific events on real volcanoes including Soufrière Hills and Santiaguito.

Chapter 10

Case Studies

In Chapters 3 - 9, a variety of models have been created, using the method presented in Chapter 2, to investigate different volcanological phenomena. The method is based upon the use of Darcy's law to calculate the pressure and gas velocity, and the momentum equation to derive the associated surface displacement. In Chapter 2, this method was described and a number of assumptions itemized. Here, these assumptions on the modelling approach are revisited and their impact assessed, before the method is applied to two specific case studies.

10.1 Model framework

10.1.1 Boundary conditions

This modelling looks at the state of the volcano at shallow levels. By necessity, the model extent is finite, therefore the state at deeper depths must be approximated by the specific constraints (boundary conditions). In this modelling framework, lithostatic pressure was calculated, using a constant density of 2500 kgm^{-3}, and used throughout and the overpressure corresponding to the permeability conditions and the contained gas was calculated accordingly, rather than directly imposed. The consistency of this method approach has its advantages because it allows easy comparison between different systems, in terms of the impact of altering the permeability. However, it is less realistic because it does not take into account changes in the gas supply or the density.

10.1.2 Permeability

The main aim of the modelling is to determine the impact the permeability has on the pressurisation, gas velocity and resulting surface displacement. The assumption is this can then lead to discussions regarding the storage, migration and loss of

gas from the system. The choice of permeability values is extremely complicated. Figures 1.1 (page 9) and 1.2 (page 10) in Chapter 1 highlighted the large variation in permeability values which have been measured for various quenched volcanic eruption products and experimental materials. However, these can only give an approximation of the actual values within the volcano due to the processes occurring syn- and post-eruption, for example flow-induced deformation (Polacci et al., 2003, Wright and Cashman, 2013) or foam collapse (Westrich and Eichelberger, 1994, Saar and Manga, 1999). Consequently, throughout this modelling a variety of permeability values have been chosen and models run with small changes to those permeabilities in order to appreciate how these small changes can impact upon the volcano's behaviour (Chapters 3, 8 and 9). By necessity, permeability values have been set to large domains as an average for that region, for example, the country rock, conduit and dome. The reality is likely one of pockets of high and low permeability in a state of constant flux dependent upon all the other processes occurring within the volcano. Attempts have been made to isolate specific zones, such as conduit margins (Chapter 5), sealed layers (Chapter 6) and dome cracks (Chapter 7) and set the permeability conditions accordingly. The modelling results have shown different permeability combinations may be grouped according to similar resulting behaviour (Chapters 3, 8 and 9.3). Consequently, it is the relative, rather than the actual permeability conditions which control the general behaviour. Hence, although the actual nature of the interior permeabilities in real-time for the active volcano is unknown, the relationships may be surmised based upon the surface observations.
A particular omission from the modelling as it stands is a lack of consideration for how the permeability within the degassing pathways will change through time. In the simulations, the most significant degassing pathways (fractures and cracks) are created as an increase in the permeability (Chapters 5, 7, 8 and 9). Once created, these pathways are static and remain open for the duration of the model. In reality, the emitting gas will generate significant changes to the entire system, including these pathways. For example, as stored gas is released, this will decrease the interior pressure, resulting in subsidence (e.g. Lu et al., 2000). In turn, this can result in the closure of the pathways (Bluth and Rose, 2004, Holland et al., 2011). Secondly, viability of a degassing pathway can be reduced in time by vapour-phase crystallisation (Baxter et al., 1999).

10.1.3 Porosity

The porosity describes the actual voids within a material which could be occupied by the gas, whilst the permeability defines the connectivity of the pore spaces which facilitates the migration and loss of gas. Although the relationship between them

is not clear (Figure 1.1), the porosity and permeability are intimately linked. For example it has been shown previously that increasing the porosity from $2 - 90$ % can result in a permeability increase of up to four orders of magnitude (Takeuchi et al., 2008). However, compared to the permeability, porosity is given far less emphasis in this modelling. This is because, from the method outline in Chapter 2, the porosity does not alter the equilibrium result of a model, it only affects the duration over which a change occurs when a permeability change is imposed. Consequently, porosity values are set to isotropic constants which remain unchanged through time. However, attempts are made to choose a porosity value appropriate to the domains permeability. Consequently, regions of higher permeability are set to higher porosities and *vice versa*.

Due to the limited contribution from porosity in this work, it is not included in the discussions relating to gas storage and migration. Utilising permeable degassing pathways is a more efficient mechanism for gas migration, compared to gas buoyancy. All discussions in the text are related to the changes in permeability, because the permeability determines if gas is permanently stored, or if it can migrate and escape from the system. Once a viable degassing pathway is established, a high permeability within the storage region is required for efficient gas loss. If the gas is stored in unconnected porosity, gas loss would be much slower.

The lack of inclusion of porosity in the density of rock has consequences - a rock containing 80 % porosity will be significantly less dense than one with 10 %. However, in the calculation for pressure and gas velocity, the rock density is only used in the boundary conditions to indicate the gas pressure exerted from depth. If porosity was included, the overall pressure, and consequently the gas overpressure would be reduced. This would have a greater impact at shallower depths where porosity is likely to be more significant due to continued exsolution and bubble expansion, and the creation of fractures. However, using a constant rock density of 2500 kgm^{-3}, will yield the greatest pressure for a given scenario.

10.1.4 Volcanic gas

The volatile content in the model is assumed to be 100 % H_2O and the model assumes all the available pore spaces are filled with gas. The model neglects the processes of exsolution, and consequently, the interactions which occur in a multi-volatile system (Holloway, 1976, Papale, 1999), (except in Chapter 4 where exsolution is included as an additional source of gas during an unloading event). Furthermore, the supply of gas from the boundary conditions is infinite, and does not take into account any changes in the amount of gas available. Changing the permeability due to sealing or crack development would likely alter the supply rate of gas. This continuous

supply of gas inevitably forces the system to continuously lose gas, however, in reality, the supply of gas is finite. Consequently, the pressurisation as modelled is likely to be higher than that in real volcanoes. Continuous gas loss would lead to more significant, and earlier development of deflation and subsidence. A particularly relevant example where high gas velocities are maintained is Model **2** from Chapter 7. In this model, a crack is simulated as an increase in permeability within a narrow zone extending from the dome surface to the conduit. The model suggests a high gas flow, which would be accurate at the start of the model, where stored gas is released. However, as this stored gas is released and the internal pressure decreases, the gas emission rate in a real volcano would decrease as the gas supply wanes. Furthermore, the decreased pressure accompanying the gas loss should result in subsidence (Lu et al., 2000), which in turn would force the crack to close (Bluth and Rose, 2004, Holland et al., 2011). This may lead to re-pressurisation, as the gas supply is gradually replenished from depth, returning the system to a state whereby gas can again accumulate. Such behaviour results in volcanoes exhibiting cyclic behaviour (e.g. Sparks, 1997, Voight et al., 1999, 2010b).

Gas density

The gas density of H_2O is calculated according to the ideal gas law, using a constant temperature of 850 °C. The difference between this "ideal" gas density and the true behaviour of water at high temperatures and pressures is investigated in Appendix C. The results show, that although the real density of water is less than that calculated by the ideal gas law, the difference is fairly insignificant at the temperature of 850 °C. Furthermore, the effect of temperature on the density is also explored in Appendix C. In the context of the current model framework and the magnitude of the pressure modelled, changing the temperature or introducing a temperature gradient has little impact on the pressurisation results. However, temperature is important when considering the rheology of volcanic rocks (Section 10.1.5).

A similar discussion is presented regarding the gas viscosity (Appendix C). From the method in Chapter 2, the gas viscosity only impacts on the gas velocity. The value of 1.5×10^{-5} Pas was chosen based upon conduit models (e.g. Melnik and Sparks, 1999, Collombet, 2009, de' Michieli Vitturi et al., 2010, Schneider et al., 2012). However, this deviates from the true viscosity of water at high temperatures and pressures. Altering the gas viscosity to more accurate values (e.g. 4.2×10^{-5} Pas (850 °C)) does impact upon the gas velocities modelled, however they are of the same magnitude as those derived using the value of 1.5×10^{-5} Pas.

Laminar or turbulent flow

Throughout the modelling, Darcy's law was used to describe the pressure and gas velocity. However, Darcy's law is only valid for laminar flow. Appendix B compares the gas velocity results for Darcy's law to those derived from the Forchheimer equation for turbulent flow. The results show Darcy's law will always predict a higher gas velocity. The difference between the two equations decreases with decreasing Darcian permeability or increasing inertial permeability. The consideration as to whether Darcy's law is applicable is particularly pertinent to the unloading model (Chapter 4) and the cracked dome models (Chapter 7). In both cases, the velocity of the gas exiting the high permeability regions ($\approx$ 100 ms^{-1}) would be too high for laminar flow to be applicable. However, Darcy's law is useful because, it does not require an inertial permeability, of which there are only a few measurements (e.g. Rust and Cashman, 2004, Takeuchi et al., 2008, 2009, Wright et al., 2006a,b, Yokoyama and Takeuchi, 2009) and it provides the upper limit to the gas velocity possible.

10.1.5 Rheology

The magma is assumed to be static, and therefore, in addition to lacking the supplementary velocity contribution for the gas, this also impacts upon the surface displacement patterns modelled. For example, the model cannot describe the magma extrusion which is an additional consequence of pressurisation.

The manner in which a rock deforms is strongly related to the magma composition, temperature, pressure, gas content and crystallisation (Sparks, 1997, Cashman and Blundy, 2000, Cashman and Sparks, 2013, de' Michieli Vitturi et al., 2010, Schneider et al., 2012). The viscosity is a measure of the resistance to rock deformation in response to an imposed stress. Viscosity increases with crystallisation (Spera, 2000, Cashman and Sparks, 2013), but decreases with temperature (Spera, 2000, Llewellin et al., 2002). The effect of exsolution is dependent upon the nature of the bubbles - small bubbles at low strain rates increases the viscosity, whilst large bubbles at higher strain rates decreases the viscosity of the magma (Llewellin and Manga, 2005, Cashman and Sparks, 2013). All the factors combined, generate significant heterogeneity within volcanic systems. For example, the drop in temperature, and increased crystallisation close to the surface increases the viscosity. Consequently, rocks close to the surface are more likely to deform in a brittle, rather than ductile, manner. Sparks (1997) suggest brittle failure of rocks at the magma chamber depths occurs when the overpressure exceeds 20 MPa. However, for rocks at shallow depths, this failure is suggested by Sparks (1997) to occur when the overpressure is greater

than 5 MPa.

Constant values are used for both Young's modulus and Poisson's ratio of 10 GPa and 0.25, respectively. These values were chosen such that the impact of the permeability on the surface displacement could be ascertained. From Section 2.4.5, as either value increases, the surface displacement decreases. Therefore, the effect of changing either value for the entire model is intuitive. However, as discussed by Wadge et al. (2006), the value can change significantly throughout the volcanic structure, due to for example, temperature, depth and composition. Furthermore, the value of either variable can alter as deformation proceeds (Heap et al., 2009). For example, increased fracturing may decrease Young's modulus (Heap et al., 2009). Decreasing the Young's modulus would make rocks more prone to deformation, therefore, the surface displacement effects would increase.

Coupled or de-coupled

In all the models which investigate the surface displacement, the domains are coupled. This means that the deformation of each domain is dependent upon those surrounding it. However, in reality, it is possible for certain domains to be decoupled. For example, this may occur along the conduit-wall margin due to brittle failure (Tuffen et al., 2003, Neuberg et al., 2006, Lavallée et al., 2008, 2011). Decoupling domains can result in more extreme surface displacement patterns than are modelled here (Appendix D). This limitation is particularly pertinent to the models in Chapter 5, 8 and 9, but also in the forthcoming case studies.

10.1.6 Topography

Models created in Chapters 8 and 9 utilised real topographic data from Soufrière Hills volcano (Wadge et al., 2009). For the majority of models (Chapters 8, 9.1, 9.2), this surface of the dome was modified to simulate the existence of the 11 February 2010 collapse scar. However, in Chapter 9.3, this collapse scar was not present. Therefore, comparing the models from Chapters 8 and 9.3, provides some indication as to the dependency of the results on the topography. Varying the topographic surface affects the results in two main ways: firstly, a different topography will exert a different pressure in terms of lithostatic load; secondly, changing the topography will alter the distance between the surface and important features simulated inside the volcano (for example, the core and carapace structure within the dome in Chapters 8 and 9). In the case of the models with the scar (Chapter 8), the modelled FZ event resulted in dominant deflation of the surface, whilst the same event without the scar showed dominant inflation (Chapter 9). A simple comparison of the models in

Chapter 7.2 shows that even altering the location of cracks can have a significant impact upon the displacement patterns observed.
The results suggest that to provide an accurate representation of the deformation patterns for a particular volcano, the general form of the topography is required. Unfortunately, this does imply that model results are not always directly transferable between volcanoes, particularly if their topographic surfaces are significantly different, for example Soufrière Hills volcano *versus* Santiaguito or Colima. However, this does not take into considerations any alterations to the interior. For example, a different dome topography will likely be composed of a different dome structure.

10.1.7 Summary of results

As shown in Chapters 3, 8 and 9, the results are strongly related to the permeability configurations applied (Chapters 3, 8 and 9). In order to reach significant internal pressurisations, a high contrast in the interior permeabilities is required (Chapter 3). The overpressure derived can range from $\approx$ 3 MPa for a less pressurised system to 25 MPa when the gas is confined to the high permeability conduit (e.g. Chapter 3). Consequently, some models represent systems where the yield strength of the rocks would be exceeded (magma chamber: $\approx$ 20 MPa, near-surface: $\approx$ 5 MPa (Sparks, 1997)). Therefore, these system will likely result in brittle failure, either along the conduit-wall margin or through explosive eruption.
Gas velocities are measured for all the models, and gas emission rates are calculated for models in Chapters 8 and 9. In some cases, the gas velocities exceed the limitations of Darcy's law (Appendix B), most notably the unloading model from Chapter 4 and the cracked dome models (Chapter 7). The maximum emission rates calculated (100 td^{-1} to 50 ktd^{-1}) for the models in Chapters 8 and 9 lie in the range of those estimated for Soufrière Hills volcano during dome building phases (Edmonds et al., 2002). These rates gradually decline as the internal pressure decreases due to the release of gas.
The modelled surface displacement measurements in response to a simulated change are more extreme in the two-dimensional systems (Chapters 5 - 7), with localised uplift of up to 50 cm in the cracked dome models (Chapter 7). This is due to the lack of lateral extent as is present in three-dimensions. In Chapters 8 and 9, all models predict mm displacement, with notable exceptions being Models **19**, **t19**, **t58**, with subsidence of 25 cm (**19**) and 14 cm (**t19**) and uplift of 18 cm (**t58**). However, these models are the most pressurised with gas overpressures exceeding 20 MPa, which is significantly higher than the yield strength of rocks ($\approx$ 5 MPa (Sparks, 1997)). Therefore, it is likely these systems would undergo failure before reaching such high gas overpressures.

10.1.8 Implications

The model as it stands provides pressure, gas velocity and displacement results, which generally lie in the range observed at real volcanoes. However, the effect of the assumptions applied must be considered when interpreting the results. These assumptions, in particular omission of inertial effects, ideality, saturation and an infinite supply of gas, all act to ensure the model provides the extreme solution to any particular scenario. Through setting bulk permeabilities, porosities and elastic moduli, the model neglects the finer detail and concentrates on the larger scale features.

Acknowledging the consequences of these limitations, the method may be applied to two case studies. Firstly, an ash-venting event at Soufrière Hills volcano after a prolonged period of no magma extrusion, and secondly, ring-shaped degassing at Santiaguito. For each event, details about the volcano and the observations are outlined before a model scenario is presented and the results analysed. The aim is to apply the method to these scenarios in an attempt to understand the permeability relationships required during each event.

10.2 Ash-Venting at Soufrière Hills volcano

Soufrière Hills volcano is located on the southern half of Montserrat, West Indies (Figure 10.1). The current eruption began in 1995 and has been typified by five episodes of dome growth punctuated by dome collapses, vulcanian explosions, degassing and ash venting (e.g. Edmonds et al., 2001, 2002, Watts et al., 2002, Carn et al., 2004, Carn and Prata, 2010, Hautmann et al., 2014, Nicholson et al., 2013). The last extrusion event recorded at the volcano occurred on 11 February 2010

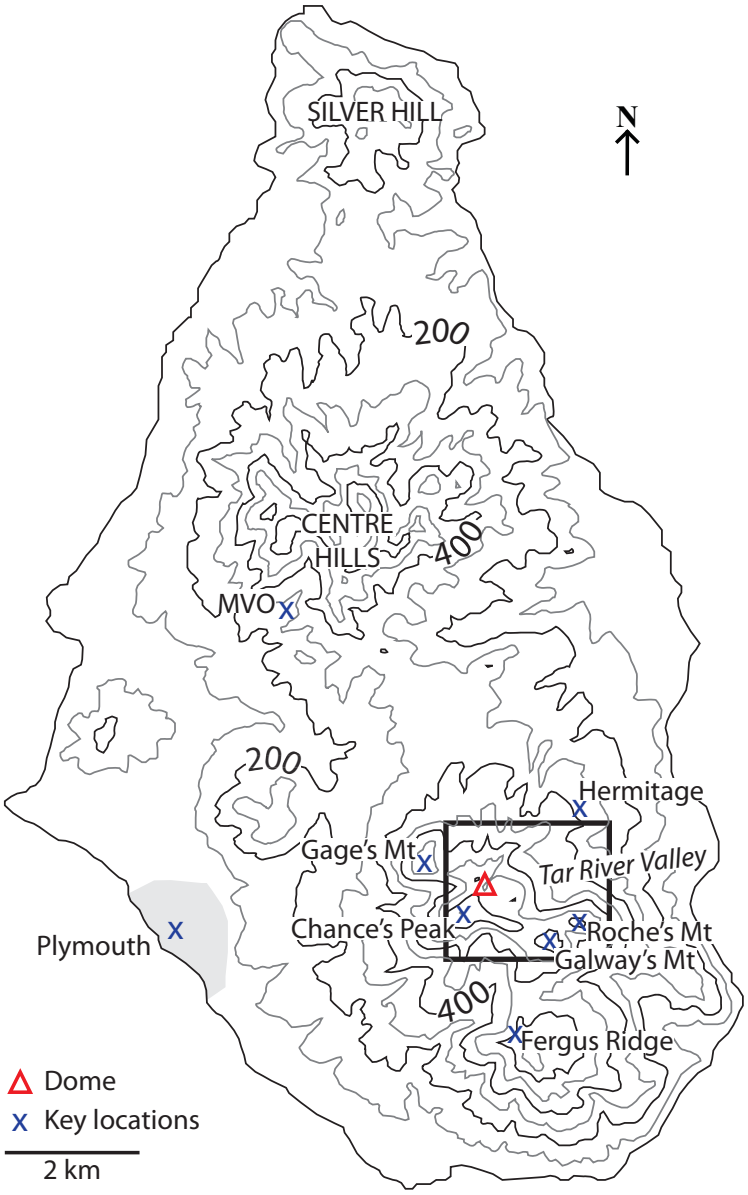

Figure 10.1: Map of Montserrat showing key locations, adapted from MVO (2012a). The coverage of the DEM used is indicated by the box over the Soufrière Hills volcano.

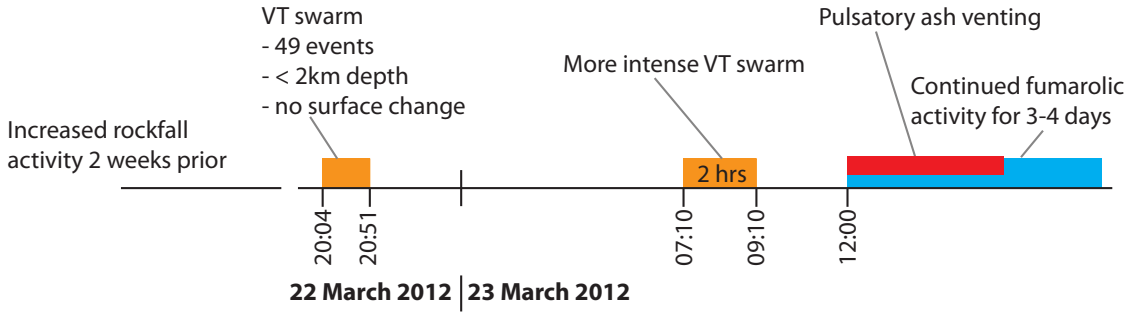

Figure 10.2: Timeline for the March 2012 degassing event. All times are UTC. From MVO (2012b,c).

(MVO, 2013a) and coincided with the partial collapse of the northern section of the dome (MVO, 2010a,b).

Prior to the event of 22-23 March 2012, activity at the volcano had been low with no active extrusion. A Volcano-tectonic (VT) swarm began at 20:00 and lasted approximately one hour (MVO, 2012b) (Figure 10.2). The majority of these events were located less than 2 km below the surface of the dome. A second VT swarm occurred 11 hours later on 23 March at 07:10. However, the first visible activity did not begin until 12:00, at which point gas emissions were observed from two new vents (Figure 10.3). The first, the site of ash venting, was located within the 11 February 2010 collapse scar, whilst the second, emitting steam, was located outside the scar, between Gage's Mountain and the dome (MVO, 2012b,d). The ash venting from the first vent was short-lived and none was observed after 23 March. By the 28 March, the vent behaviour was fumarolic (MVO, 2012c). Elevated SO_2 emissions continued to be measured between 23 and 27 March with a peak of 5200 t/d on 24 March (MVO, 2012d,b). For comparison, the average SO_2 emission rate for the volcano before and after the event is estimated at between $200-400$ t/d (MVO, 2012c, 2013b). An outward radial displacement of 1-2 cm was recorded by GPS at Hermitage and Fergus Ridge (stations closest to the dome (Figure 10.1) on 23 March (MVO, 2012d) which has been interpreted as caused by changes to the magma chambers (Hautmann et al., 2014). Alternatively, it could be the result of pressurisation, as gas exsolves and ascends from within the volcano, triggered by the VT events. Similar events also occurred on 7-8 August 2012 and 3-6 February 2013, however they were not as intense as that on 22-23 March 2012 (MVO, 2012c, 2013b).

The location of the new vent within the collapse scar suggests fracturing occurred in close proximity to the conduit. Shear fractures generated by the upward motion of magma within the conduit represent potential degassing pathways. Even when magma motion has ceased, they may still represent lines of weakness which may be

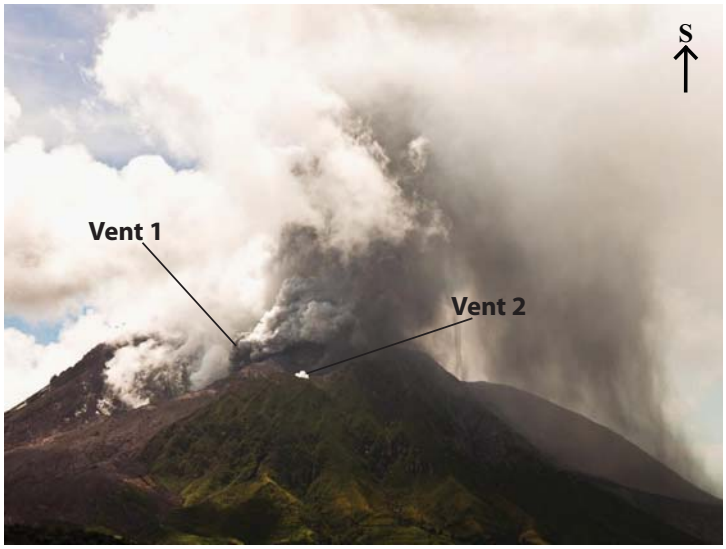

(a) Eruption event

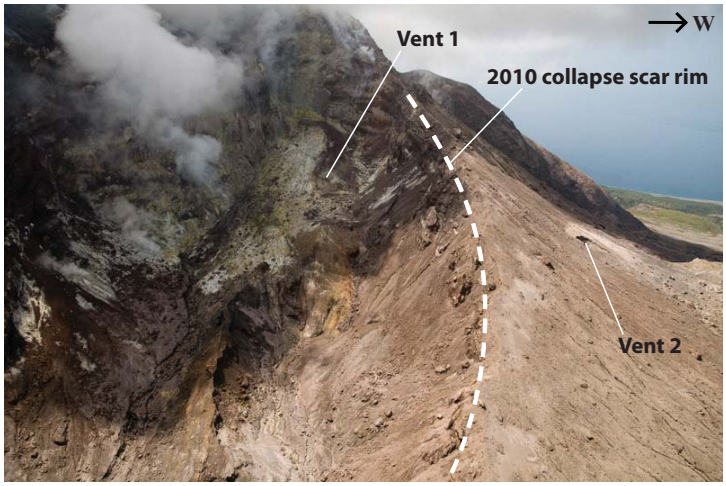

(b) Location of vents

(c) Detail of vent within collapse scar (6 September 2012)

Figure 10.3: The eruption event and the location of vents relative to the dome and its collapse scar, (a) from MVO (2012b), (b) and (c) from MVO, October 2012.

exploited later by escaping volatiles, particularly if these fractures have been weakened by seismicity. Here, the hypothesis is tested that the VT swarms reactivated these shear fractures leading to an increase in permeability and the development of viable degassing pathways. Furthermore, in addition to providing a degassing pathway for gas at depth, this may also permit gas stored within the dome structure to escape via the newly created vent. The time lag between the seismicity and the first visible signs of gas emission suggests gas was stored at depth and its release was triggered by the seismic activity. If this gas had been stored at shallow levels, as suggested for the major dome collapses of July 2003 and May 2006 (Herd et al., 2005), gas emission would have been expected soon after the onset of seismicity. Furthermore, the 11 February 2010 collapse scar potentially represents a region of weakness due to the decreased distance between the conduit and surface, providing a strong pressure gradient which volatiles can follow.

10.2.1 Model scenario

Following Chapter 8, topographic data from Wadge et al. (2009) are used for the separate surfaces of the country rock and dome where the dome topography is modified to approximate the February 2010 collapse scar. In addition, the geometry is sliced to create internal domains representing the conduit, the crystallised magma plug ('spine'), and the location of the new vent within the scar (Figures 10.4 and 10.5). A relatively deep spine is simulated due to the continued degassing activity, and the long duration since active extrusion ceased. A permeability increase is imposed (Table 10.1), through time, up the margin between the conduit and walls in order to simulate a reactivation of shear fractures (in response to the seismic activity). As these fractures propagate towards the surface, the creation of the vent is also simulated with surface expression located within the collapse scar. Two different models with different fracture extents are run. Following the depth of the seismic activity MVO (2012b), the fractures begin at 2500 s at a depth of 2 km below the surface of the dome. For shorter fractures, resealing commences 250 s later, whilst for longer fractures, resealing begins with a 2500 s delay.

10.2.2 Results: Pressure

The initial pressure distribution (Figure 10.6) shows elevated levels at deeper depths within the volcano, due to a more permeable conduit surrounded by a less permeable country rock and spine.

The pressure change results for the two models are shown in Figures 10.7 and 10.8. In both cases, depressurisation occurs within the conduit when the fractures extend

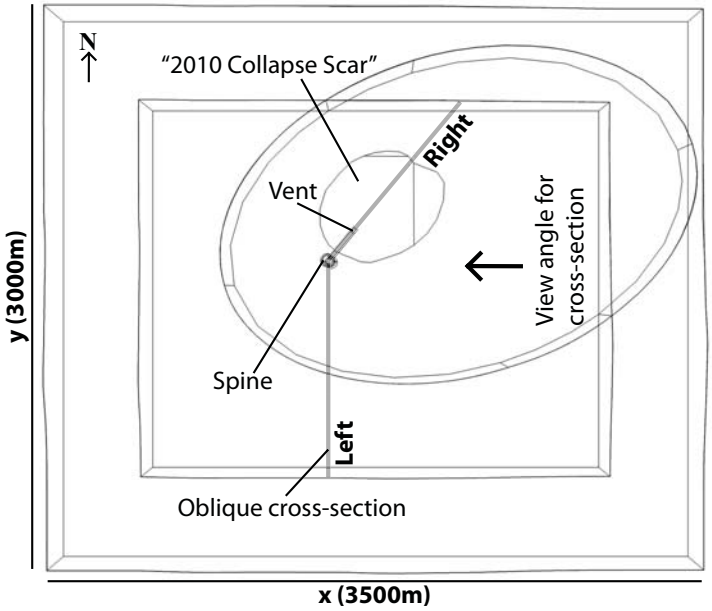

Figure 10.4: Plan view showing the location of the imposed "2010 collapse scar" and the new vent. The location and orientation of the cross-section (Figure 10.5) used for the results is also indicated.

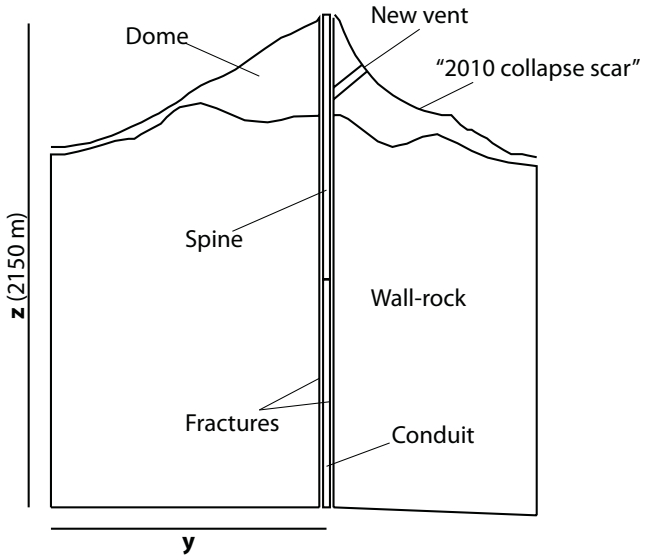

Figure 10.5: Cross-section through the model showing the different domains.

past the base of the spine. However, pressurisation occurs within the spine itself. This suggests that whilst the conduit loses gas, the spine may gain more gas than it loses. When the fractures reach the base of the dome ($\approx$ 5880 s), pressurisation continues and extends into the dome itself, as gas is forced into the dome structure. However, once the vent opens (6000 s), depressurisation occurs, both within the dome and the spine, but in the case of the longer fractures (Figure 10.8) also

Domain	Permeability (m^2)		Porosity
	t_1	t_2	
Conduit	10^{-12}	-	0.5
Country Rock	10^{-16}	-	0.1
Spine	10^{-14}	-	0.1
Dome	10^{-13}	-	0.4
Fracture Zones	10^{-15}	10^{-10}	0.8
Vent	10^{-13}	10^{-8}	0.8

Table 10.1: Permeability conditions for the ash-venting event at Soufrière Hills model. Due to the extended period of time with no active magma extrusion, the conduit and spine are set to relatively low permeabilities to reflect the effects of conduit cooling and the resulting crystallisation. Furthermore, the country rock has a low permeability to prevent any gas loss and ensure gas can be stored and then released during the degassing event. The fracture zones and the vent are set to different end permeabilities. This is because the fracture zones are likely to still contain significant material which will hamper the gas loss. In contrast, the vent is simulated with a much higher permeability of 10^{-8} m^2 due to the occurrence of ash-venting (MVO, 2012b,d) which may have aided in the removal of material.

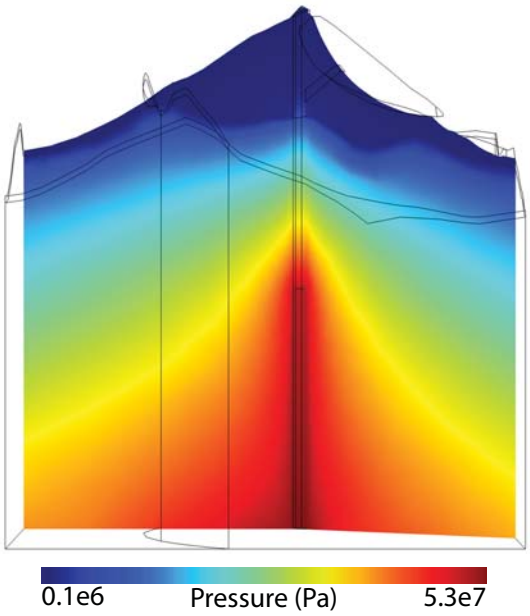

Figure 10.6: Pressure at the start of the model.

continues within the conduit.

The change in pressure with time for different depths within the conduit and fracture zones provides insights into where gas migrates from (Figure 10.9). When the

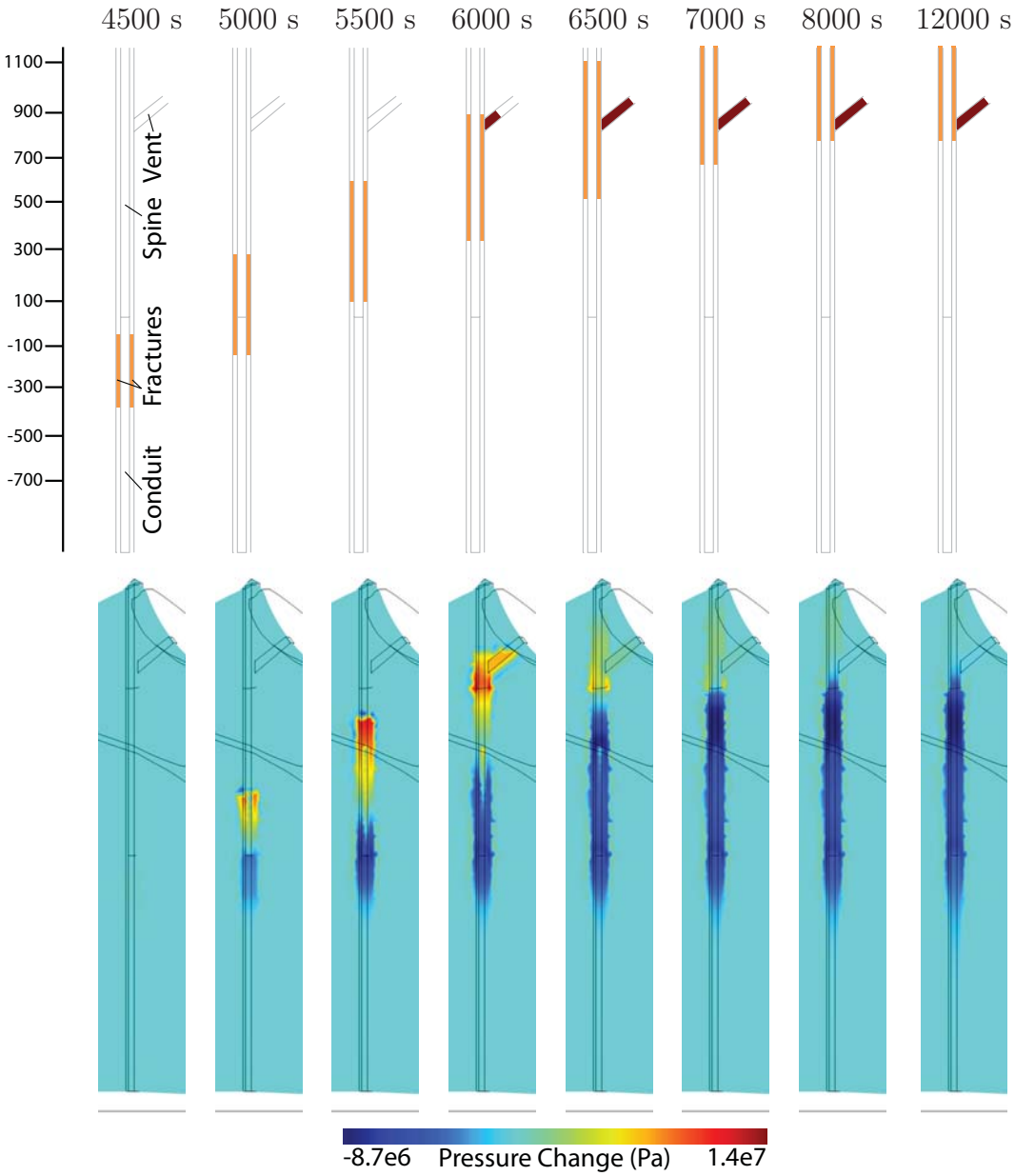

Figure 10.7: The pressure change with time. The location and extent of the fracture zones are indicated, although the fracture zones are not to scale.

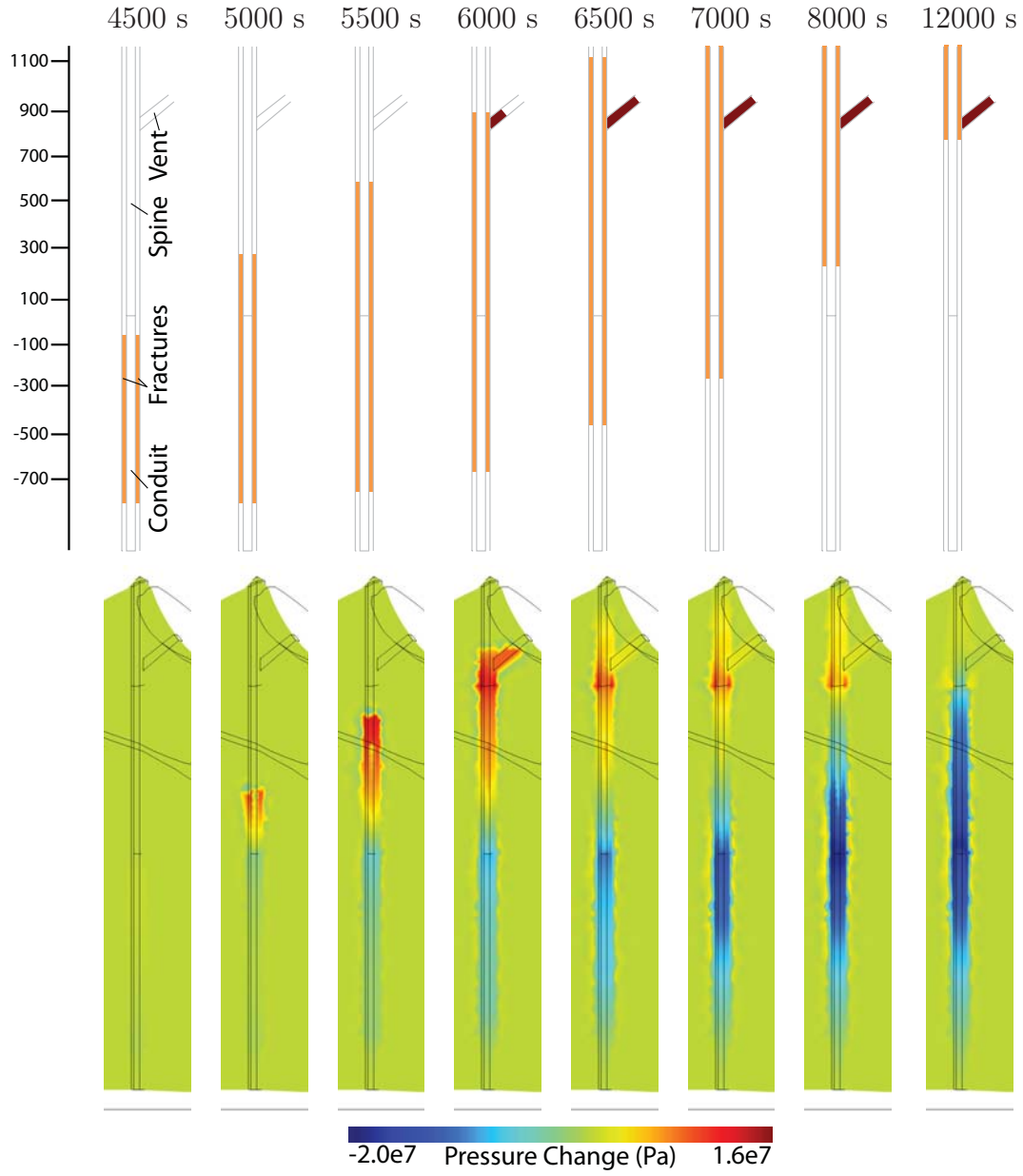

Figure 10.8: Pressure change with time for longer fracture zones. The location and extent of the fracture zones is also indicated, although the fracture zones are not to scale.

fracture zones extend to just below a particular depth, there is depressurisation at that depth. However, this then turns to pressurisation as the fractures extend to that depth and the gas becomes trapped by the overlying un-fractured material. Once the fractures extend above this depth, depressurisation occurs as the gas is lost vertically. In both models, the greatest pressurisation is at 700 m, which corresponds to the margin between the wall-rock and dome, and therefore a change in permeability.

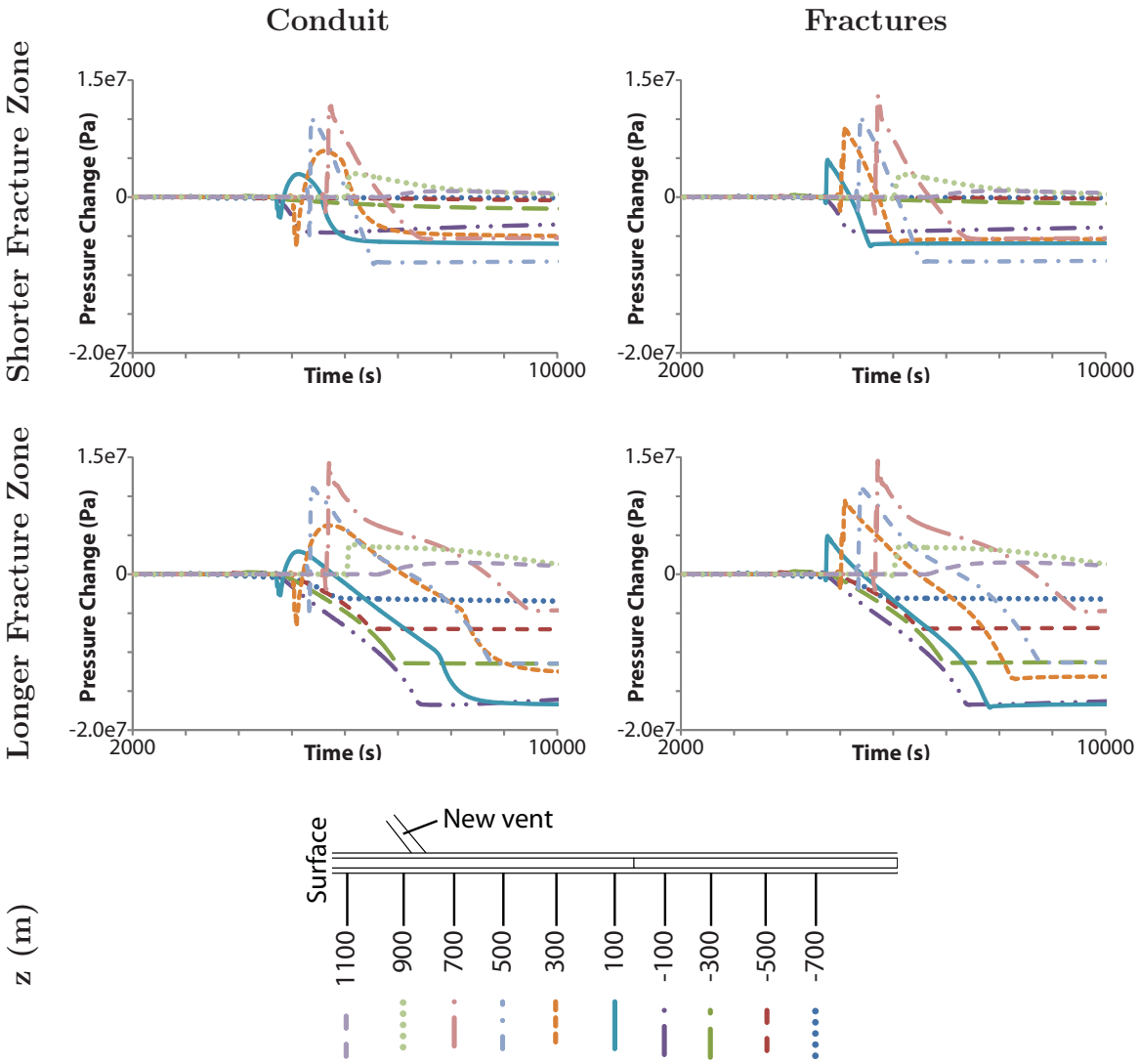

Figure 10.9: Pressure change at different depths with time for the conduit and fractures. The pressure change, especially depressurisation, is more extreme for longer fractures. The new vent results in depressurisation below, but pressure loss above the vent is minimal.

10.2.3 Results: Surface gas emissions

The gas velocity once the new vent has opened and the fractures have reached the surface is shown in Figure 10.10. The velocity is much higher from the new vent due to the increased permeability and the proximity to the high pressure region. The dome immediately surrounding shows a lower gas velocity. Gas is preferentially lost from the higher permeability regions and areas where the dome thickness is less. The vent displays a rapid increase in gas velocity immediately as it is created (Figure 10.11). This gas velocity then rapidly subsides, as the internal pressure decreases, due to the loss of the stored gas. The high gas velocities at the onset follow the nature of the ash venting which turns to fumarolic activity without ash. Even once the shear fractures have resealed, the new vent can continue to emit gas, albeit less intense, whilst there remains trapped gas within the structure of the dome and underlying country rock in proximity to the new vent.

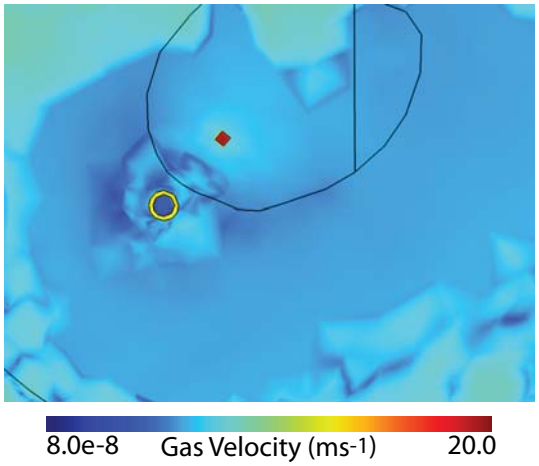

Figure 10.10: Detail of the dome region showing the gas velocity, on a logarithmic scale, for the new vent and the top of the dome when the fractures have reached the surface (after 7000 seconds).

A fracture zone permeability of 10^{-10} m^2 allows a maximum gas ascent velocity of $\approx 0.1 - 0.3$ ms^{-1}. Under the modelled pressure conditions, and provided the gas already had direct access to the fracture zones, this would allow the gas to ascend from 1 km depth in $\approx 1 - 3$ hrs.

Assuming a vent permeability of 10^{-8} m^2, the model predicts a maximum emission rate of H_2O of 5000 kg/s ($\approx$ 450 kt/d) immediately after the vent opens. The emission rate subsides to less than 200 kg/s ($\approx$ 17 kt/d) $\approx$ 1 hr after the vent opens. However, this assumes complete saturation of the available porosity which, given the preceding activity at the volcano, is unlikely, so the actual emission rate of H_2O would be less. Furthermore, decreasing the vent permeability also decreases

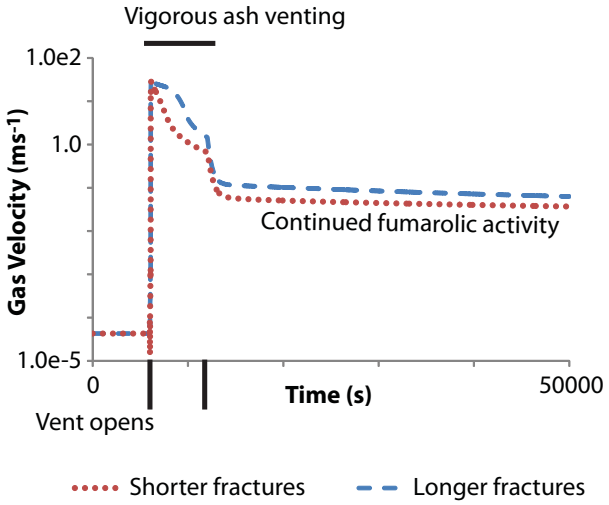

Figure 10.11: Average velocity for the vent in the 2010 scar for the two different fracture lengths modelled. However, this is strongly dependent upon the vent permeability. Decreasing the vent permeability to 10^{-9} m^2 decreases the average vent velocity to 7 m/s whist a vent permeability of 10^{-10} m^2 yields a maximum average vent velocity of 1 m/s.

the rate of gas loss. A lower vent permeability of 10^{-9} m^2 results in a maximum emission rate of 1200 kg/s ($\approx$ 104 kt/d).

Using the average emission rate of SO_2 of 400 t/d as measured by Young et al. (1998) for the 1995-1997 dome growth period, Hammouya et al. (1998) estimated the coincident emission rate of H_2O at 25 kt/d (for an initial magma H_2O content of $3.5 - 3.0$ wt.% (Barclay et al., 1998)). This gives a rough estimate of 345 kt/d H_2O simultaneously with the measured SO_2 peak of 5200 t/d using a H_2O : SO_2 ratio of 62.5. However it should be noted, this has a very large margin for error for a number of reasons: the duration since the measurements were taken, the volcanic activity has changed, the gas content may have changed as well, especially as the volcano has gone several years without active magma extrusion, the SO_2 value used to derive the ratio is only an average, the excess sulphur problem which may or may not still be applicable to the volcano can dramatically change the ratio. Using ratios of 50 and 70 would yield a range 260 kt/d $-$ 364 kt/d H_2O. Furthermore, this is an estimate for the H_2O derived from magmatic sources, and does not include any contribution from groundwater.

An additional portion of gas emitted may be geothermal in origin through the interaction of the rising gas and associated heat with the extensive hydrothermal system (Boudon et al., 1998). Furthermore, the localised nature of the emission and the creation of the new vent, suggests permeability in the country rock surrounding the conduit is low and lateral escape via the fracture zone is limited.

10.2.4 Results: Surface displacement

As the fracture zones propagate upwards, permitting gas stored at depth to ascend and leading to pressurisation, there is uplift of the dome region, particularly over the scar, due to the decreased loading at this part of the dome (Figure 10.12). Once the vent opens and the gas is released, there is subsidence. There is a second peak in the maximum surface uplift after the opening of the vent due to the continued propagation of the shear fractures towards the surface. The surface then continues to subside as the internal stored gas is released. Figure 10.13 shows the displacement change in more detail for the model with the shorter fractures. The surface uplift is particularly noticeable once the fractures have extended above the base of the spine and reach a peak just prior to the creation of the new vent (10.13c). There is then a ring of subsidence centred around the conduit (10.13d) and the location of maximum uplift has changed to above the conduit due to the gas rising with the opening of the shear fractures towards the surface. Subsidence of the dome then continues whilst more gas is lost.

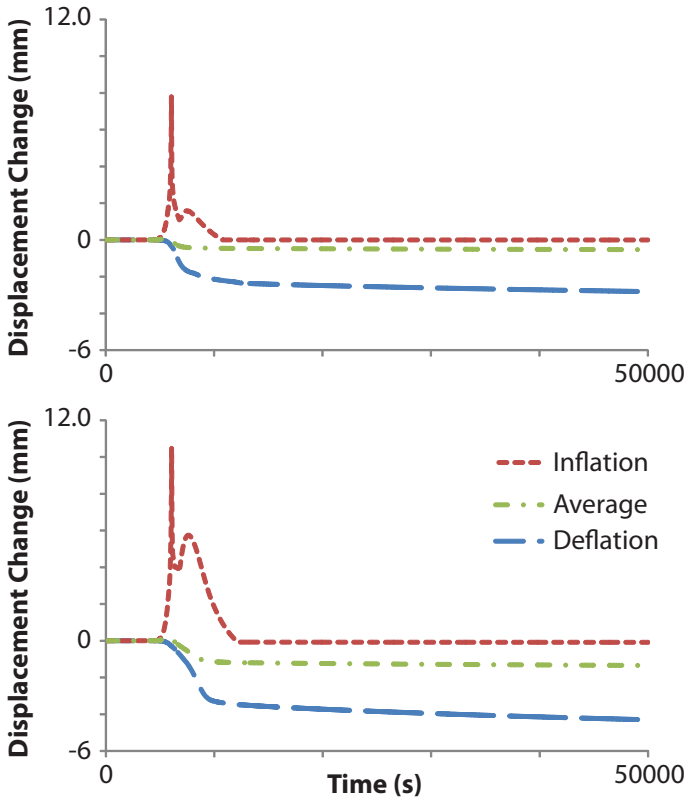

Figure 10.12: Displacement change for the shorter (top) and longer (bottom) length fractures. Shown are the maximum inflation and deflation in addition to the average surface displacement across the entire dome.

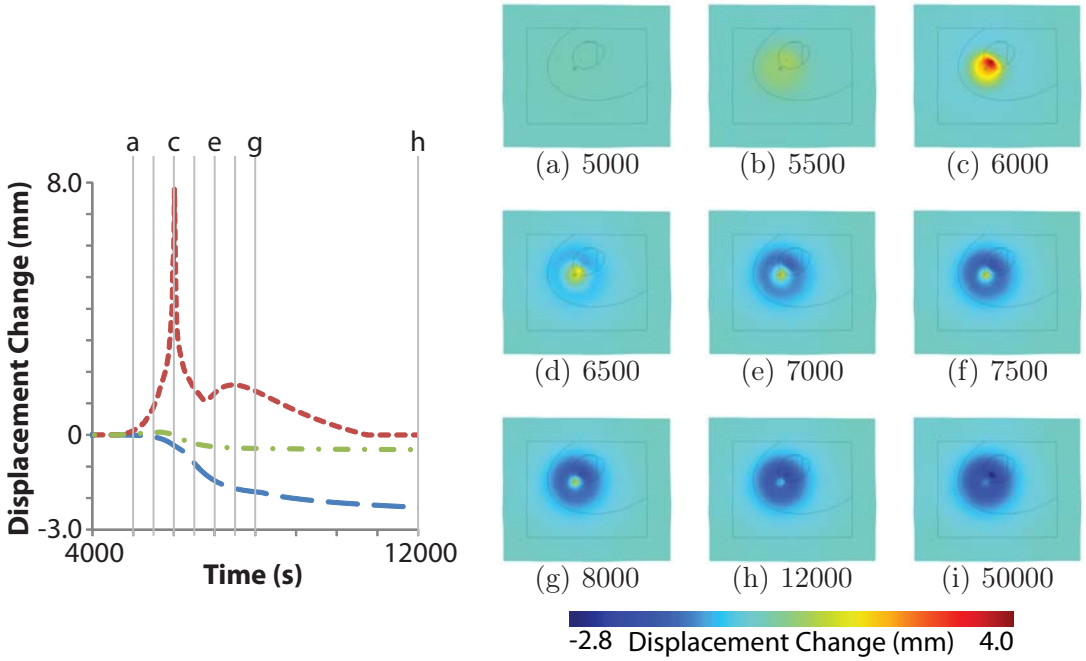

Figure 10.13: Displacement change images for the shorter length fractures. The locations of images (a) - (h) (5000 - 12000 s) are marked.

10.2.5 Summary of the March 2012 ash-venting event

Since there was no magma extrusion, the gas must have ascended through permeable networks without amplification from magma motion. This explains the delay between the seismic activity and the first visible signs of emission. However, the longevity of the event, suggests the fracture zone development may have presented a viable degassing route for isolated pockets of gas present within the volcanic interior. The lack of recent magma extrusion suggests the upper portions of the conduit may have become a stiffened, degassed spine, potentially with a relatively low permeability.

This modelling attempt has concentrated on the hypothesis that the gas migrated up from depth via the reactivation of shear fractures and the delay was due to the time taken to ascend from the storage region. However, an additional source of gas may be magmatic volatiles stored within the dome structure which were consequently re-mobilised due to propagating fractures or ongoing crystallisation.

Figure 10.14 summarises the processes occurring during the event whilst, Figure 10.15 outlines the suggested permeability relationships.

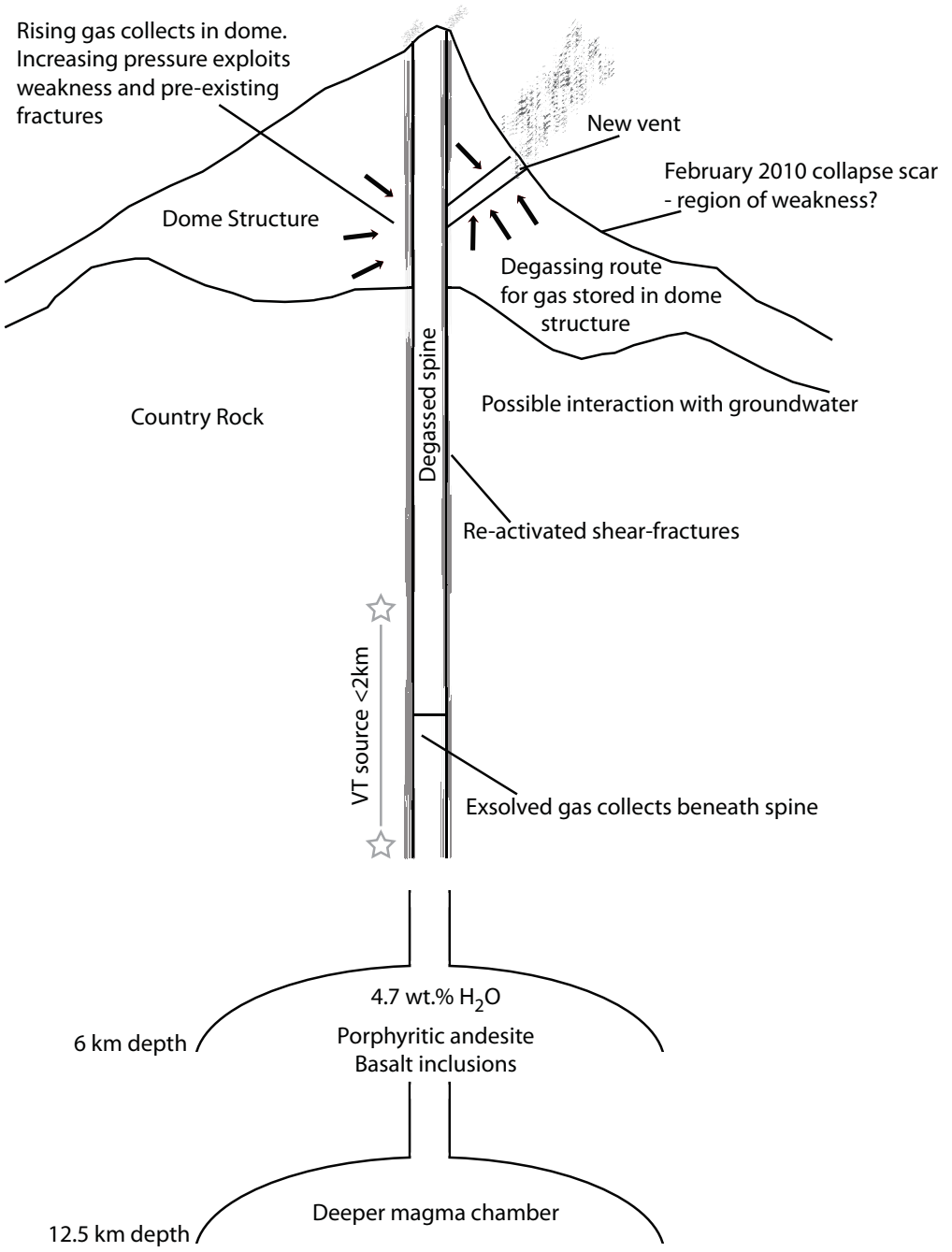

Figure 10.14: The hypothesis is the VT seismicity triggered the reactivation of shear fractures along the margin between the conduit and country rock. This provided a temporary escape route for gas stored at the top of the spine. At shallow depths, gas stored in the structure of the country rock and dome in the vicinity of the new vent and shear fractures can degas through the newly created high permeability. No magma extrusion accompanies the event. Water content and magma chamber configuration from Barclay et al. (1998), Hautmann et al. (2014).

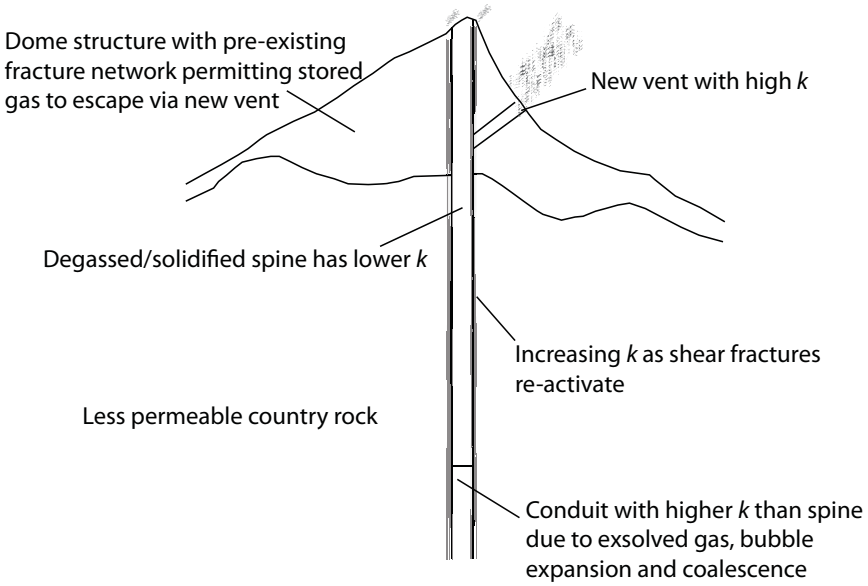

Figure 10.15: Suggested permeability relationships for the event at Soufrière Hills volcano in March 2012.

10.3 Ring-shaped degassing at Santiaguito

Santiaguito is a dome complex extruded into the eruption crater of the the catastrophic 1902 plinian eruption of its parent stratovolcano, Santa Maria (Guatemala) (Rose, 1972) (Figure 10.16). The complex consists of four vents: El Caliente, La Mitad, El Monje and El Brujo (Figure 10.17), but volcanic activity since 1977 has been focussed solely on the El Caliente vent (Rose, 1987, Ball et al., 2013). Activity at this vent has been typified by andesitic-dacitic block lava flow extrusion and frequent weak ash-and-gas vulcanian-type eruptions (Harris et al., 2003, Bluth and Rose, 2004, Johnson et al., 2004, Sahetapy-Engel et al., 2004, 2008, Sahetapy-Engel and Harris, 2009a,b, Johnson et al., 2008, Avard and Whittington, 2012). Approximately 50 % of these ash-and-gas eruptions are ring shaped with emissions originating from a series of fractures before gas emission from the rest of the dome. Other eruptions occur crater-wide without an initial ring (Bluth and Rose, 2004). The diameter of the ring-shaped emission varies through time, and increased from

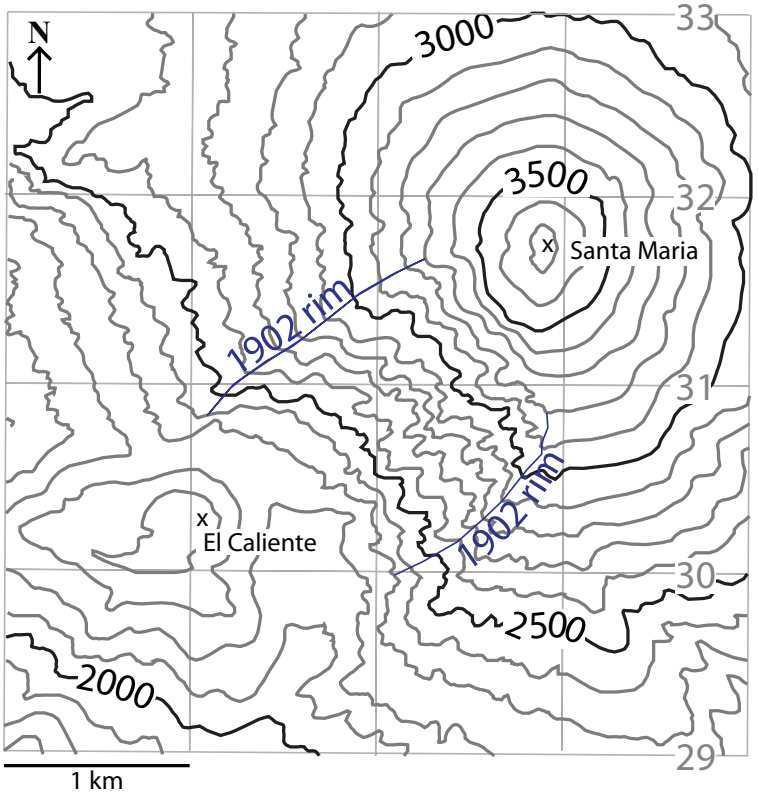

Figure 10.16: Topographic map for Santa Maria Volcano and Santiaguito. The approximate location of the 1902 Santa Maria eruption crater rim is marked. Adapted from: Colomba, Guatemala [map], Series E754, Sheet 1860 II, 1:50,000, U.S. Central Intelligence Agency 1991. El Caliente and the 1902 rim are marked according to Scott (2013).

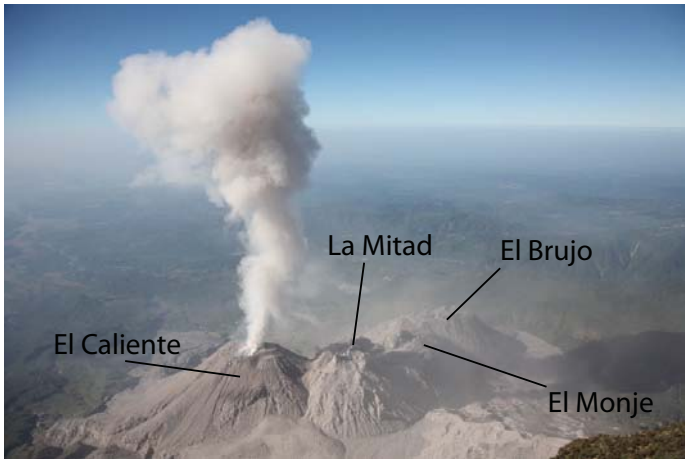

(a)

(b)

Figure 10.17: (a) View of Santiaguito from Santa Maria volcano showing the four dome complexes comprising Santiaguito. El Caliente is the site of the active vent. Adapted from source: (Roscoe, 2014). (b) Ring shaped gas emission from El Caliente (Roscoe, 2014).

70 m in 2003 to 120 m in 2004 (Bluth and Rose, 2004). Eruptions consist of an initial vigorous emission lasting $30-60$ s, followed by less intense continued gas loss which lasts up to 20 minutes and with short repose times of between 5 minutes to 2 hours (Bluth and Rose, 2004, Johnson et al., 2004, 2008).

In addition to these vulcanian events, continuous degassing from fumaroles is observed from the dome between eruptions (Bluth and Rose, 2004). The location of these fumaroles is spatially and temporally variable and they can open and close over time periods as little as 10 minutes (Bluth and Rose, 2004, Holland et al., 2011). Furthermore, continuous degassing is observed on the flanks of El Caliente, which are unaffected by the more vigorous dome emissions (Bluth and Rose, 2004).

Coincident with the crater eruptions, are seismic and acoustic signals (Jones and Johnson, 2011, Johnson et al., 2009, Sanderson et al., 2010) (Figure 10.18). The seismic signals have been attributed to fluid flow, brittle rock fracture, shear frac-

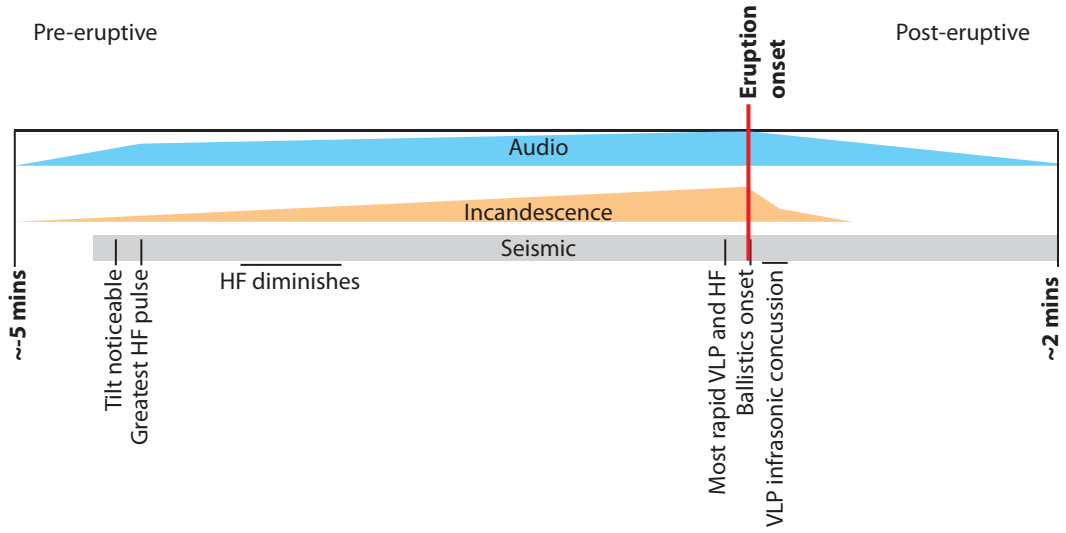

Figure 10.18: Visible, audio and seismic signals associated with an event as described by Johnson et al. (2009). Signals for this event preceded the eruption by approximately 5 minutes. Johnson et al. (2009) attributes HF (High Frequency) seismicity to rock fall, and VLP (Very Long Period) to magma motion. All signals gradually increase and peak at the eruption onset before diminishing.

turing and rockfall (Sahetapy-Engel et al., 2008, Johnson et al., 2009, Sanderson et al., 2010). The source location for the eruptions has been estimated at between $100 - 620$ m with the depth varying by up to 340 m between successive eruptions (Sahetapy-Engel et al., 2008). Furthermore, from petrological evidence, the dacitic magma is believed to have a solidification depth between $200 - 600$ m (Scott et al., 2012) suggesting a potential link to the seismic and acoustic source. This rigid magma is thought to be degassed and act as a stiffened plug (Bluth and Rose, 2004, Johnson et al., 2004, Sahetapy-Engel et al., 2008). However Scott et al. (2008) suggest progressive decay of the matrix glass occurs at depths up to 200 m which could explain the block lava flow rather than the creation of spines. Spines are useful in providing dimensions for the conduit. Unfortunately, due to the block lava flow, the conduit diameter is unknown. However, from thermal observations and conduits at other volcanoes, it has been estimated at $36 - 50$ m (Bluth and Rose, 2004, Sahetapy-Engel and Harris, 2009b, Holland et al., 2011).

10.3.1 Trigger mechanism

A number of hypotheses have been proposed for the eruptive behaviour at Santiaguito and the repetitive nature of the ring-shaped degassing. At El Caliente, Johnson et al. (2008) suggest the cycles are related to the accumulation of gas beneath a thin ($20 - 80$ m thick) viscoelastic lava dome which is released by the décollement of the

dome. However, this requires the base of this dome to rapidly and repetitively seal to gas escape between successive eruptions. A source depth of $100 - 620$ m with variability of up to 340 m sheds doubt on gas accumulation at such shallow levels (Sahetapy-Engel et al., 2008). Furthermore, the continuous degassing observed from the dome between eruptions indicates the presence of fractures. The emissions are highly temporally and spatially variable suggesting the sealing capacity of the domain is limited (Holland et al., 2011).
An alternative hypothesis proposed by Bluth and Rose (2004) is shear induced fragmentation due to the stick-slip upward motion of the dacitic plug, which would generate permeable degassing routes. Bluth and Rose (2004) further suggest the presence of a conical widening towards the surface to account for the large and variable ring diameter. The repetitive nature of the explosions together with seismic and acoustic signals supports the hypothesis of shear fractures (Holland et al., 2011).

10.3.2 Model scenario

In order to generate such a distinctive ring-shaped degassing emission, there must exist a cylindrical region of higher permeability and a corresponding pressure gradient which forces the gas to the periphery. In accordance with conclusions drawn by Bluth and Rose (2004) and supported by Holland et al. (2011), such a high permeability may be derived through slip-stick shear between the conduit and surrounding edifice, resulting in the opening of a series of surface concentric fractures. An adequate pressure gradient may be derived by the interaction between the differing permeabilities of a gas-rich magma below a rubbly degassed plug and/or dome. If the conduit and plug/dome have the same permeability, there is no mechanism for gas storage at shallow levels. Consequently, gas may migrate through the conduit and plug unhindered. Furthermore, the characteristics of the gas rings, i.e. intermittent visible bursts of ring-shaped emissions suggests the gas must first be stored before being released to the atmosphere. Consequently, a question to be considered is whether the fracture zones are active continuously and the gas is stored at deeper depths by some other mechanism, or if the fractures are ephemeral and reactivated by pressurisation, which reaches a critical pressure before the gas is released. However, the temporal similarity between the seismicity and gas emissions and the duration of the emissions suggests the gas must be sourced from a shallow depth.
There are two main requirements for the release of gas to the atmosphere: gas content and degassing pathways. The duration of emissions and their repetitive nature suggests that between each emission the system much recharge: either re-saturate a storage zone with gas, or recreate degassing pathways (increase the permeability). The repetition of the events, since 1977 (Sahetapy-Engel et al., 2008, Holland et al.,

2011), implies the same mechanism is required and that it is non-destructive. Furthermore, lava dome extrusion occurs coincident with the small vulcanian explosions (Bluth and Rose, 2004), suggesting the extrusion is directly linked. Such stick-slip motion of the dacitic plug would promote bubble elongation within the magma, and brittle fractures above the solidification depth, both of which would locally enhance the permeability along the conduit-wall margin and may subsequently reseal as the system relaxes (dependent upon magma viscosity) and recharges between events. Furthermore, gas accumulation beneath the plug, including continued processes of exsolution, bubble growth (by decompression and coalescence) and crystallisation would enhance the permeability in the upper regions of the conduit (beneath the plug) such that once the shear fractures are generated, this accumulated gas is released. Furthermore, the observation of continued degassing from discrete, but transient fumaroles within the crater itself (Bluth and Rose, 2004) suggests the plug is still permeable to gas flow, although with a relatively low permeability permitting both gas transmission and storage. The ephemeral nature shows the high variability of the degassing pathways and consequently, the gas supply.

The presence of fumaroles on the flanks of El Caliente suggest the edifice/country rock permeability is high in these regions, or highly fractured. Furthermore, the continued emissions, which are unaffected by the eruptions (Bluth and Rose, 2004), suggests the conduit is sealed to horizontal degassing at shallow depths and the source is different, perhaps with gas being transferred from the conduit to the country rock at depths below that which directly sources the summit emissions. Consequently, these emissions are assumed to be unrelated and are neglected from the model.

The scenario is simulated using a simple 3D model of the conduit, plug and dome surrounded by the edifice (Figure 10.19). Following Chapter 5, shear fractures are imposed as an increase in permeability up the conduit-wall margin (Table 10.2). These fractures are then progressively resealed, by decreasing the permeability. Due to the repetitive nature of the gas emissions with short repose times, seven ring-shaped emissions are simulated. This number of events is sufficient to discern any trends within the results whilst still being computationally viable. Each event is identical, with the same eruption duration and repose time. The volcano is simulated with a 40 m diameter conduit surrounded by a fracture zone of width 5 m (in concurrence with the shear-induced damage zone at Mount St. Helens (Gaunt et al., 2011, 2012)). The conduit region is widened in the top 50 m to generate a ring of diameter 120 m.

Here, the event is defined as the time when the fractures are active at the surface and gas would be emitted, simulating the vulcanian explosions. Each event is preceded

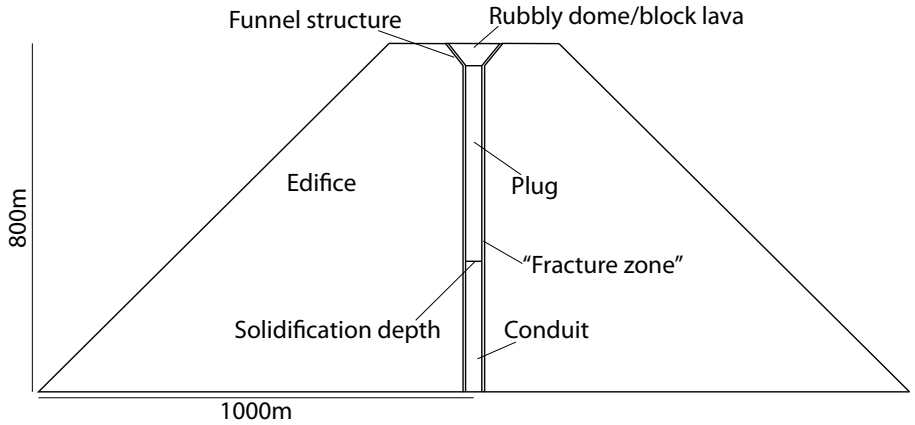

Figure 10.19: Cross section through the 3D model geometry showing the separate regions. The geometry is subdivided into five main domains to which permeabilities are set: conduit, plug, dome, edifice and fracture zones.

Domain	**Permeability (m^2)**		**Porosity**
	t_1	t_2	
Conduit (constant)	10^{-10}	-	0.5
Conduit (gradient)	10^{-12} to 10^{-10}	-	0.5
Edifice	10^{-14}	-	0.3
Plug	10^{-14}	-	0.5
Dome	10^{-12}	-	0.5
Fractures	10^{-14}	10^{-10}	0.5

Table 10.2: Permeability and porosity values for the ring-shaped degassing model. A high conduit permeability is chosen to aid the replenishment of gas between eruptions. The edifice and plug are set to a lower permeability is order to act as a partial seal preventing rapid gas loss from the conduit and permitting gas storage between eruptions. Finally, the dome has a higher permeability than the plug due to the existence of continued fumarolic activity between events (Bluth and Rose, 2004), suggesting the presence of fractures.

by shear fracture development which is inferred to correspond with the seismic activity, and followed by a repose period during which the system reseals, recharges and pressurises at depth as gas is accumulated and stored.

The model was run for seven events (Figure 10.20) with an eruption time of 16 minutes and repose period of 2 hours. This is in accordance with the maximum repose time reported (Bluth and Rose, 2004, Johnson et al., 2004, 2008). The interior pressure, surface gas velocity and displacement change results are presented forthwith. Results are given for the whole time period, but also specifically for

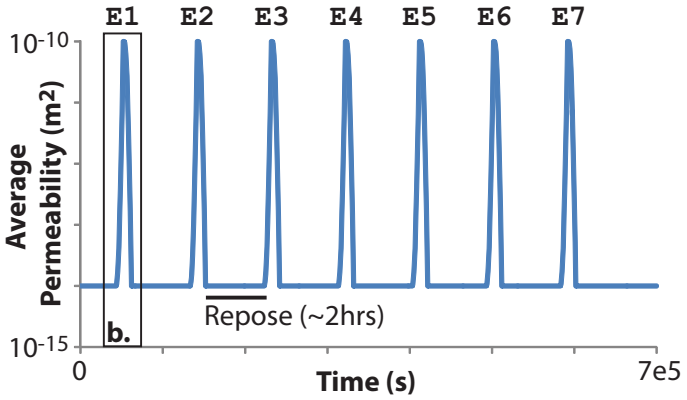

(a)

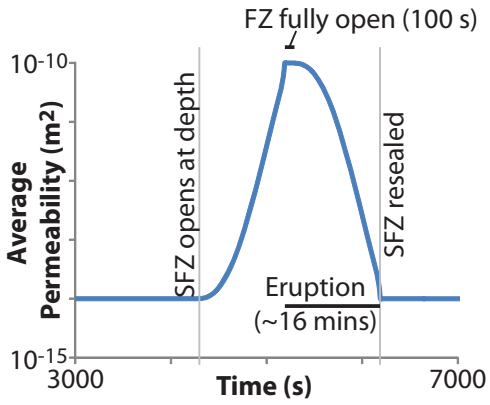

(b)

Figure 10.20: (a) Average permeability in the fracture zones with time for the seven events. (b) Detail for event 1 showing the duration and repose period.

events `E1` and `E4` to show graphically how the scenario develops.

10.3.3 Results: Pressure

The initial pressure is shown in Figure 10.21. The highest initial pressure is within the conduit due to the lower permeabilities within the surrounding edifice and plug. The conduit supplies the gas and its average pressure drops by 1.2 MPa during each eruption event (Figure 10.22). However, it resumes its original average pressure of 20 MPa during the repose between each event. The three domains of the fractures, plug and dome all increase in average pressure which accumulates with each successive eruption, particularly in the plug. This suggests the gas is being redistributed by the fractures from the conduit to the plug. Whilst much of the gas is lost to the surface, some must be retained within the less permeable structure of the plug. The pressure does not accumulate in this manner within the dome implying the higher permeability is unable to retain the gas and it is gradually lost between eruptions.

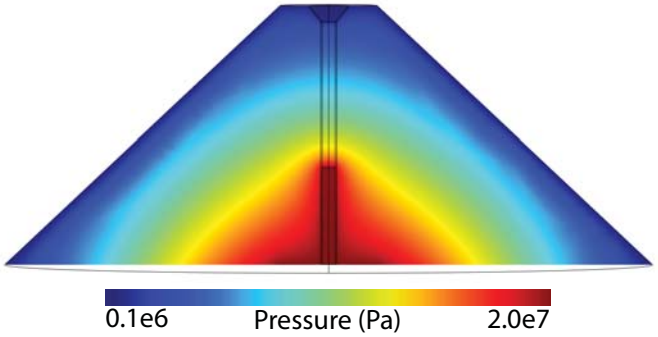

Figure 10.21: The initial pressure for the model prior to any vulcanian emissions. The more permeable conduit surrounded by the less permeable plug and edifice results in pressurisation and gas storage.

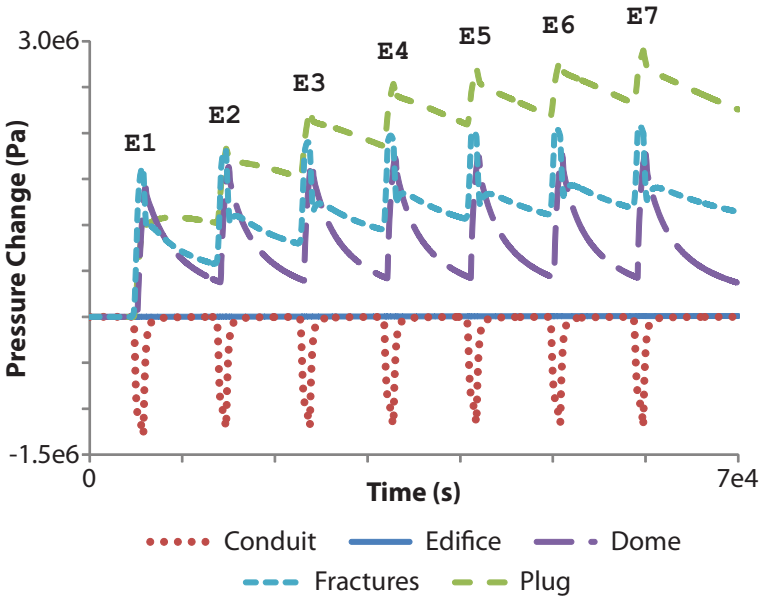

Figure 10.22: Average pressure change for the five domains in the model. The conduit shows a large depressurisation, whilst all other domains increase in pressure to varying degrees.

In contrast, the average pressure within the edifice is largely uniform, increasing by only 0.01 MPa between events `E1` and `E4`. This shows the bulk of the edifice is unaffected by the degassing events. However, gas is being forced into the country rock immediately adjacent to the conduit region.

Figure 10.23 shows the pressure change at different depths within the conduit, fractures and edifice margin for events `E1` and `E4`. For both the conduit and the fractures, depths of 700, 600 and 500 m show depressurisation in response to the fractures extending past the base of the plug, before re-pressurising to equilibrium once the fractures have sealed up to the base of the plug. In contrast, all depths shallower

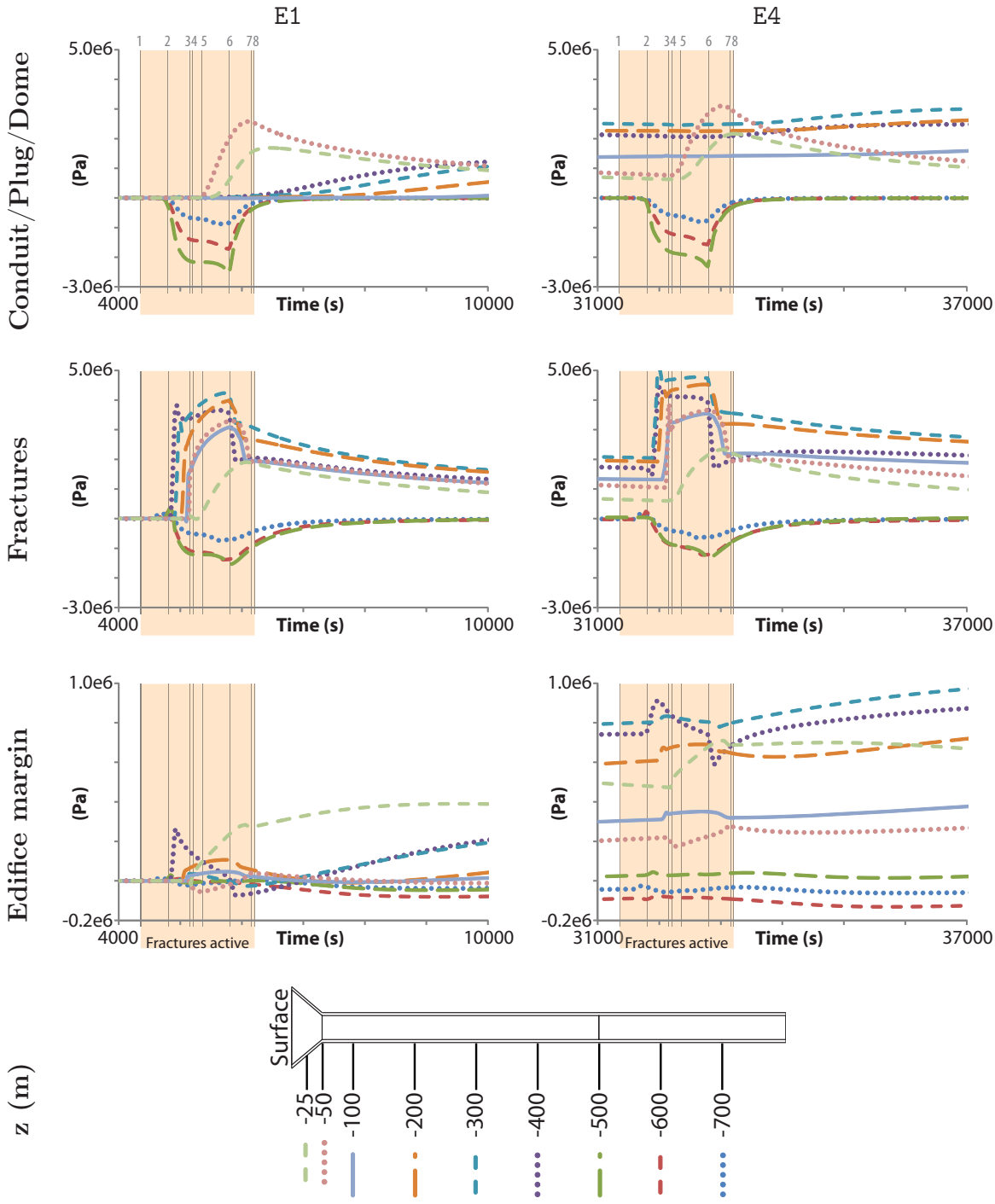

Figure 10.23: Pressure change at different depths within the conduit/plug ($x = 0$ m), fractures ($x = 23$ m) and edifice margin ($x = 50$ m) for events `E1` and `E4`. The values for the edifice margin are taken 25 m distant from the fracture zone. Important fracture progressions are marked in time as follows, 1: fractures begin, 2: at base of plug, 3: at base of dome, 4: at surface, 5: fractures start to reseal, 6: sealed to base of plug, 7: sealed to base of dome, 8: fracture completely resealed.

than 500 m show pressurisation in the fractures as the gas ascends through the opening fractures, but is confined by the unfractured material above. This turns to depressurisation once the fractures have sealed to the base of the plug and continued gas supply from the conduit has stopped. As the fractures reseal, gas is forced out from the fracture region, shown as a decrease in pressure, and forced into the surroundings. During event `E1`, gas is lost from the edifice margin below the base of the plug, and it is not regained by event `E4`. In contrast, all other depths within the edifice margin show pressurisation, indicating gas is being transported vertically and becomes trapped within the edifice margin as the fractures are resealed. However, the edifice margin is significantly less affected compared to the central regions of the conduit, plug and dome. Given time, and a sufficiently permeable network of fractures, it is possible this gas within the edifice could be transmitted to the surface and lost diffusively. This is unlikely to be the source of the observed flank fumaroles due to the lack of change observed in response to the vulcanian explosive events.
Figure 10.24 shows graphically the change in pressure for the two events at different fracture zone extents. Whilst the depressurisation within the conduit is very similar between the two events, there is significant pressurisation already present within the plug structure and edifice margin at the start of `E4`, which builds further during this eruption event. The pressure increase within the fractures, relative to the start of the model, is also much larger in `E4` compared to `E1`, by 1.5 MPa. This is due to the gas already present within the edifice margin and plug, which can be remobilised during the fracturing. In both events, once the fractures have reached the surface, gas from the fractures is transferred directly to the dome and accumulates at the base of the funnel structure. Due to the higher permeability of this dome, the gas then migrates vertically. However, the dome pressure is still high once the fractures have resealed, so whilst much of this gas is lost during the eruption event itself, some gas continues to escape during the repose period.

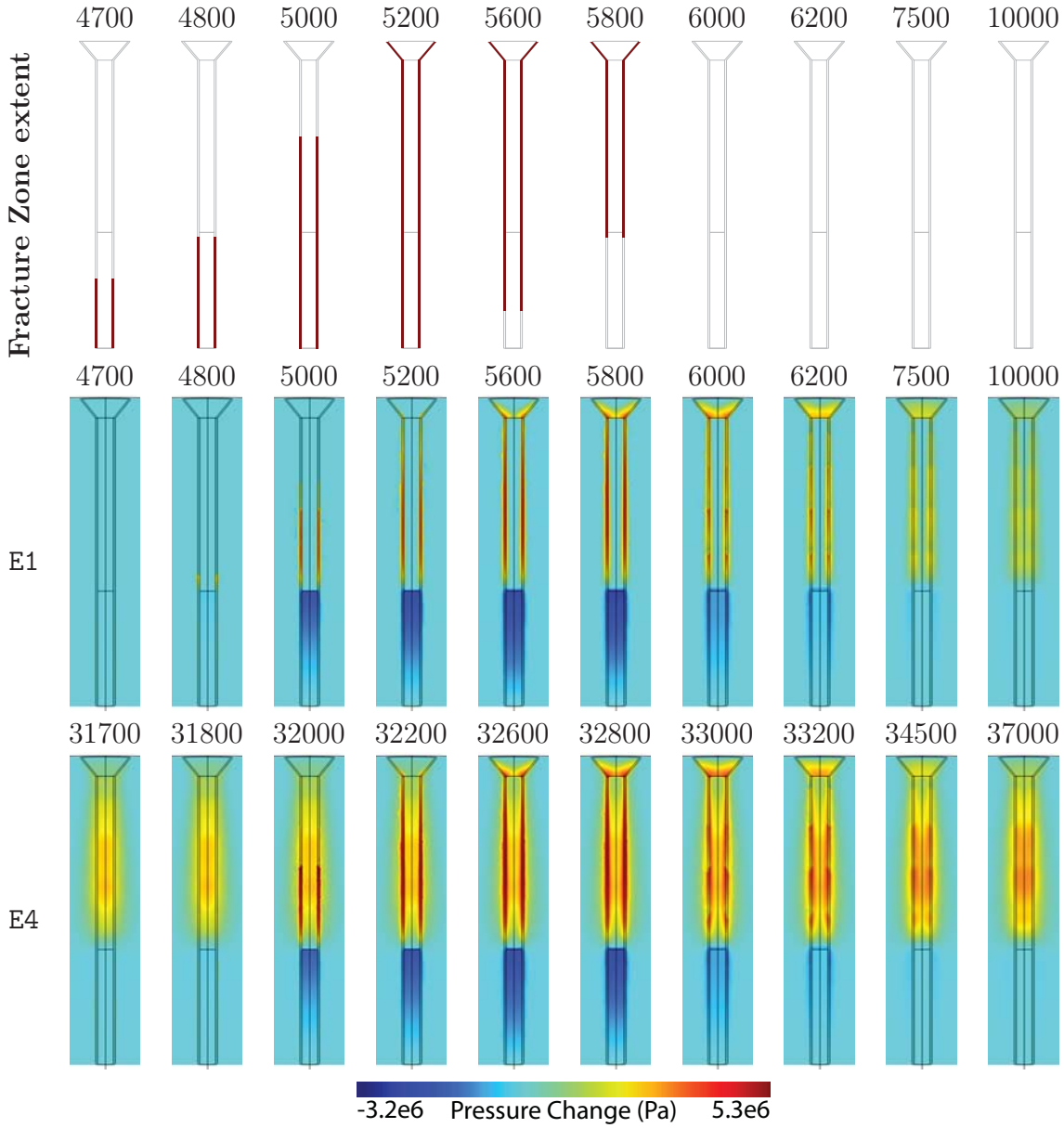

Figure 10.24: Pressure change at different times (s) for events `E1` and `E4`. Due to the short repose time of 2 hours (Bluth and Rose, 2004, Johnson et al., 2004, 2008), the model cannot attain equilibrium before the next degassing event. Consequently, during each successive event, gas accumulates within the less permeable plug and dome, thus increasing their pressure. During the repose between events, this gas continues to degas from the surface.

10.3.4 Results: Surface gas emissions

Gas emissions from the ring structure are short-lived and occur only as long as the fractures have a high permeability (Figure 10.25). Furthermore, the gas velocity increases with each event in the model sequence due to the contribution from the stored gas at shallow depths. In contrast, gas emissions from the dome gradually increase once the fractures reach the surface, but don't reach a peak in `E4` until 900 s after the peak ring emission.

The surface gas emissions (Figure 10.26) show the distinctive ring-shaped degassing pattern, but also a delayed velocity increase from the interior dome which gradually migrates towards the dome centre (Figure 10.27). The initial dome velocity for event `E4` is higher than that for `E1` due to the increased pressure and gas storage and migration within the plug and dome. This temporary gas storage provides a viable explanation for the transient fumaroles observed between events. Furthermore, fol-

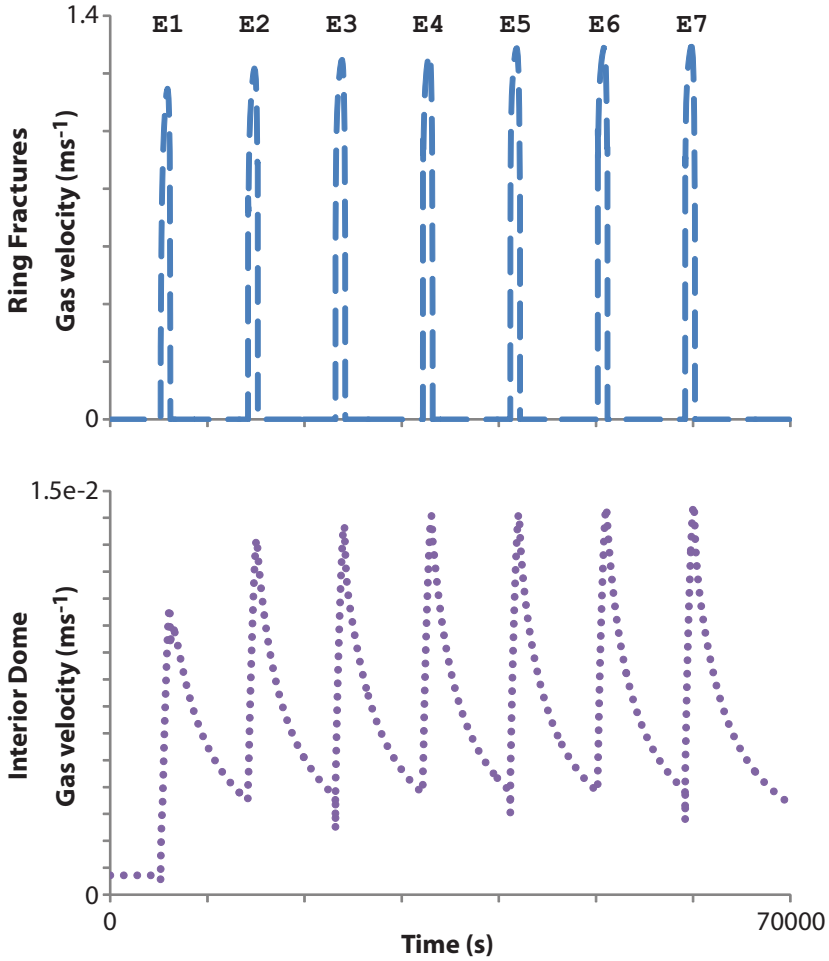

Figure 10.25: Average surface gas velocity in the ring fractures and the interior dome in response to the seven ring-shaped degassing events.

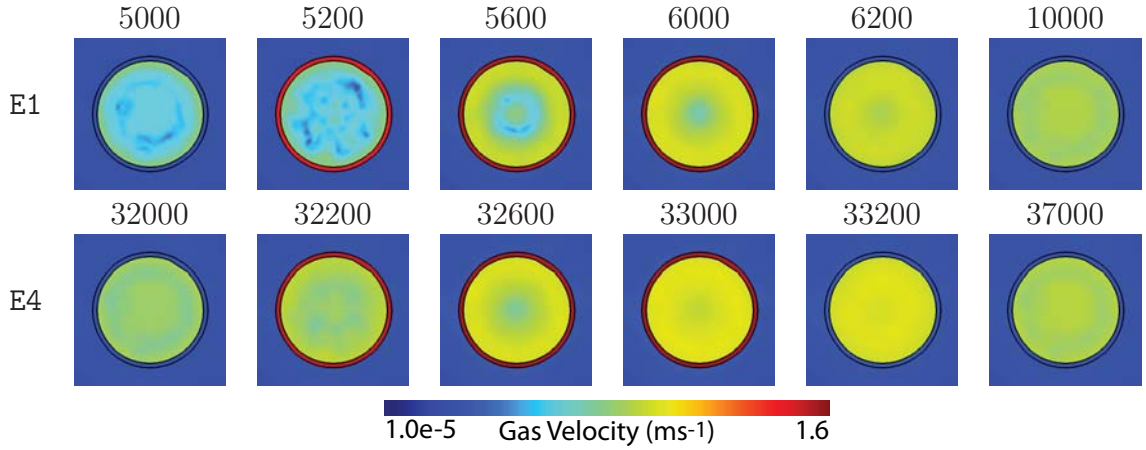

Figure 10.26: Gas velocity at different times (s) on a logarithmic scale for events `E1` and `E4`, showing the gas ring and the progressive gas velocity increase within the interior dome.

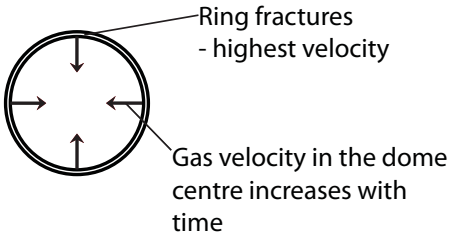

Figure 10.27: After the development of the ring, the region of the dome emitting increased gas propagates inwards. Therefore, the gas velocity in the dome centre increases with time.

lowing the results from Chapter 7, once a fracture has transmitted its gas load, the localised region would deflate, permitting the opening of other fractures elsewhere on the dome.

Gas emission data is documented for SO_2, with an average emission of 395 kg (Holland et al., 2011). From this and an SO_2 mass fraction of $1.35 - 2.97$ %, Holland et al. (2011) have inferred a total mass of gas emitted for an average event at $13,000 - 29,000$ kg over a time period of $5 - 10$ mins. However, for an extreme of 1270 kg SO_2 (Holland et al., 2011), this range increases to $43,000 - 94,000$ kg. In this study, all the gas is assumed to be magmatic H_2O.

In the modelling, the degassing event itself lasts 16 minutes and emits $370,000$ kg (`E1`) and $460,000$ kg (`E4`) of H_2O. This is significantly higher than those estimated by Holland et al. (2011). However, they represent an upper limit for the scenario with the volcano initially completely saturated with gas and a continual supply of gas for the duration of the event. Observations by (Bluth and Rose, 2004) indicate the most intense gas emissions have a duration of $30 - 60$ s followed by less vigorous

emissions lasting several minutes. Using this, event `E1` emits 9000 kg in the first 60 s, whilst `E4` emits 22000 kg. The majority of the gas is emitted from the fractures, with only $2-7$ % from the interior dome. During the repose, the gas is emitted from the interior dome with a modelled emission rate of 11 kgs^{-1} for the entire dome surface. Holland et al. (2011) indicate an average repose emission rate of $0.28-1.01$ $\text{kgs}^{-1}(SO_2)$ $(9-74$ kgs^{-1} (total gas)).
The average SO_2 emission rate during eruptions is $2-3$ kgs^{-1} with an extreme of 6.25 kgs^{-1} (Holland et al., 2011). From a mass fraction of $1.35-2.97$ % (Holland et al., 2011), this suggests a total gas emission rate of $67-222$ kgs^{-1} with an extreme between $210-463$ kgs^{-1}. The model predicts a maximum emission rate of 455 kgs^{-1} during the eruption, and a repose of 11 kgs^{-1} from the dome in good agreement with the observations.

10.3.5 Results: Surface displacement

The maximum inflation and average surface displacement for the region of the dome increases sharply at the onset of each event, due to the rising gas increasing the pressure at shallow depths (Figure 10.28). As this gas is released, the surface subsides, although, due to the short repose period, the surface does not attain its original equilibrium position, but remains elevated. Consequently, with each additional event, the surface displacement increases. During event `E1`, the surface rises a maximum of 5 mm and decreases to 3 mm prior to event `E2`. Whereas the surface rises to a maximum of 10 mm by event `E4` and only subsides down to 6 mm. The difference in maximum surface elevation decreases between events, such that the difference

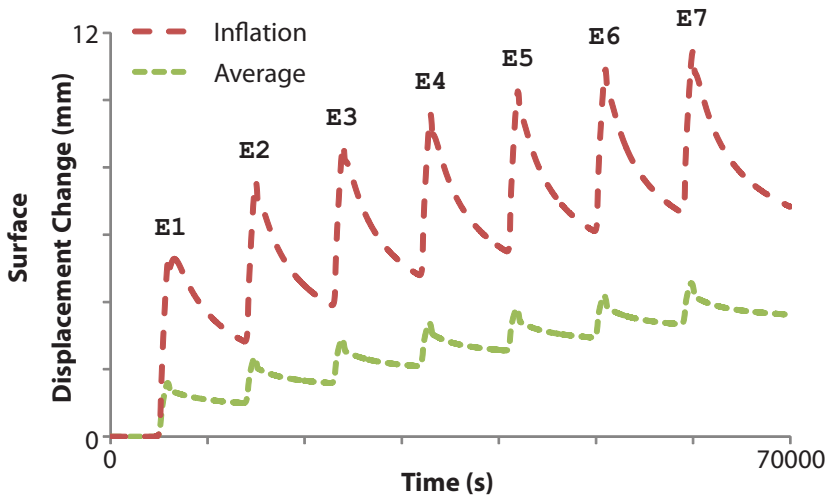

Figure 10.28: Maximum and average dome surface displacement in response to 7 ring-shaped degassing events.

between events E1 and E2 is 2 mm, whilst between E6 and E7, the difference is just 1 mm. This suggests with such repetitive activity, the surface displacement due to the gas pressure would eventually reach an equilibrium. Furthermore, the surface displacement is significantly lower than that measured by Johnson et al. (2008) at $20 - 50$ cm. However, Johnson et al. (2008) attributes the upward displacement to piston flow of the plug in response to the gas-induced pressurisation. Here, only the permeability change is modelled which is a secondary effect to that of the plug motion.

Figure 10.29 shows the displacement pattern during events E1 and E4 relative to time 0 s. The greatest surface displacement occurs in the centre of the dome, directly overlying the conduit. The area affected is limited, although it increases with subsequent events, with the exterior flank experiencing 0.1 mm uplift at a height of 400 m below the summit.

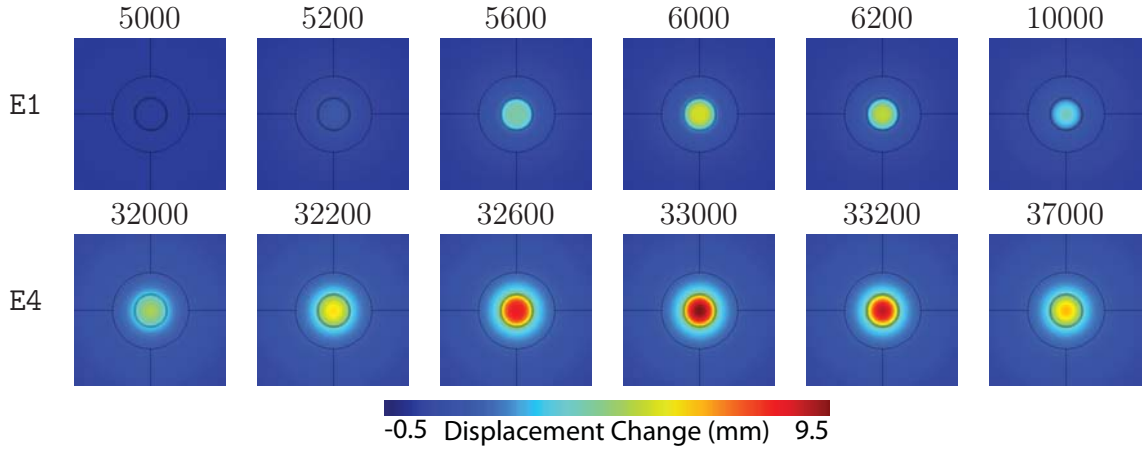

Figure 10.29: Displacement change at different times (s) for events E1 and E4.

10.3.6 Conduit permeability gradient

Two additional models are run to investigate the effects of a permeability gradient in the conduit which increases with decreasing depth. This simulates the local increase in permeability due to bubble expansion and coalescence in response to the greater volume of stored gas immediately below the plug, as suggested by Johnson et al. (2008). Furthermore, two different plug extents are simulated, one at 600 m depth, following the original model, and the second at 200 m depth (Figure 10.30). Both models show elevated pressure within the conduit beneath the base of the plug due to the higher permeability surrounded by lower permeabilities. This pressurisation indicates the presence of stored gas.

The pressure change results for events `E1` and `E4` are shown in Figures 10.31 and 10.32 for the deeper and shallower plugs, respectively. In both cases, the results are very similar to that of the original model (Figure 10.24) with depressurisation in the conduit, but pressurisation within the fractures, plug and dome as the gas is redistributed by the fractures to shallower depths. However, the conduit depressurisation is significantly less for a shallower plug due to the decreased initial pressure, which accommodates less gas. Furthermore, particularly evident for the shallow plug, is pressurisation of the conduit as the fractures ascend, before they reach the base of the plug. This indicates the higher permeability of the fractures aids the vertical

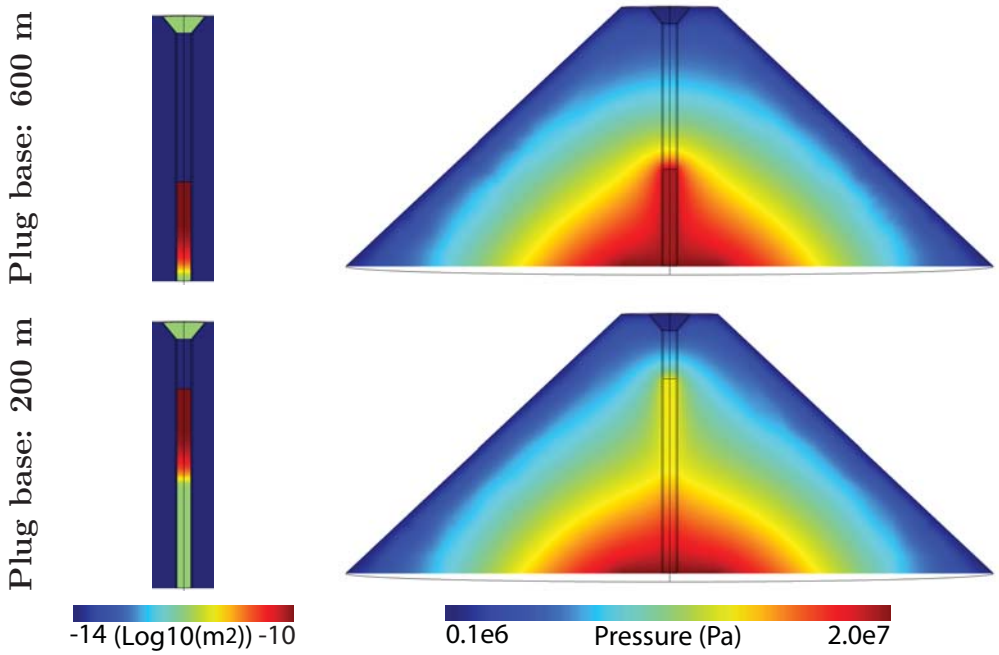

Figure 10.30: The conduit permeability (left) and the initial pressure before any vulcanian explosions. The more permeable conduit surrounded by the less permeable plug and edifice results in pressurisation and gas storage.

transport of gas from depth to the increased conduit permeability immediately below the plug. This pressurisation is retained by the less permeable region of the conduit until the fractures are resealed and upward flow of gas from deeper depths has ceased. This excess gas aids the resupply of the storage region directly beneath the plug. In contrast with the original model, neither model with a conduit permeability gradient attains their original conduit pressure. This suggests the permeability gradient decreases the ability for the storage zone to recharge, due to the lower gas capacity and gas transfer speed of the less permeable conduit at depth.

There is little appreciable difference between these models and the original with regards to the surface gas velocity pattern. Both models exhibit the same behaviour with the greatest repose velocity occurring from the bulk of the dome. During the vulcanian eruptions, the highest velocity occurs from the ring structure, with a velocity increase propagating towards the centre of the dome as the event proceeds.

Whilst the surface displacement patterns of the dome region are very similar to that of the original model, these two models also show significant displacement changes along the flank, although of lower magnitude compared to the dome. The maximum inflation of the dome region is 8.5 mm for `E4` for the deeper plug, but only 7 mm for the same event with the shallower plug. Figure 10.33 shows the temporal variation in the displacement change for a line down the surface of the flank according to Figure 10.34. The surface line extends from the edge of the summit to the base of the flank as modelled. It does not include the surface displacement of the central regions of the dome due to large differences in scale. In response to the fracturing, the flank inflates due to the gas rising vertically. However, once the fractures reach the surface and depressurisation occurs, deflation of the flank is evident. Of particular interest is the location of this deflation is related to the depth at which the gas is stored. With the plug at 600 m depth, the deflation is lower and occurs between $\approx 225 - 425$ m depth on the flank. In contrast, for a shallower plug, the deflation is more intense and occurs between $\approx 25 - 125$ m. This flank displacement was not evident on the original model due to the constant conduit permeability. The permeability gradient within the conduit has such a dramatic effect on the results because the lower permeability at depth has a much lower maximum gas capacity, in addition to a lower gas velocity. Consequently, it takes a longer time to replenish the higher permeability storage region above and allow it to resume its original equilibrium position. However, as indicated in Figures 10.31 and 10.32 the repose time modelled does not provide sufficient time for the gas to be resupplied. Therefore, a conduit permeability gradient, and its variability, may have a key influence on the size of eruption and the repose time between events.

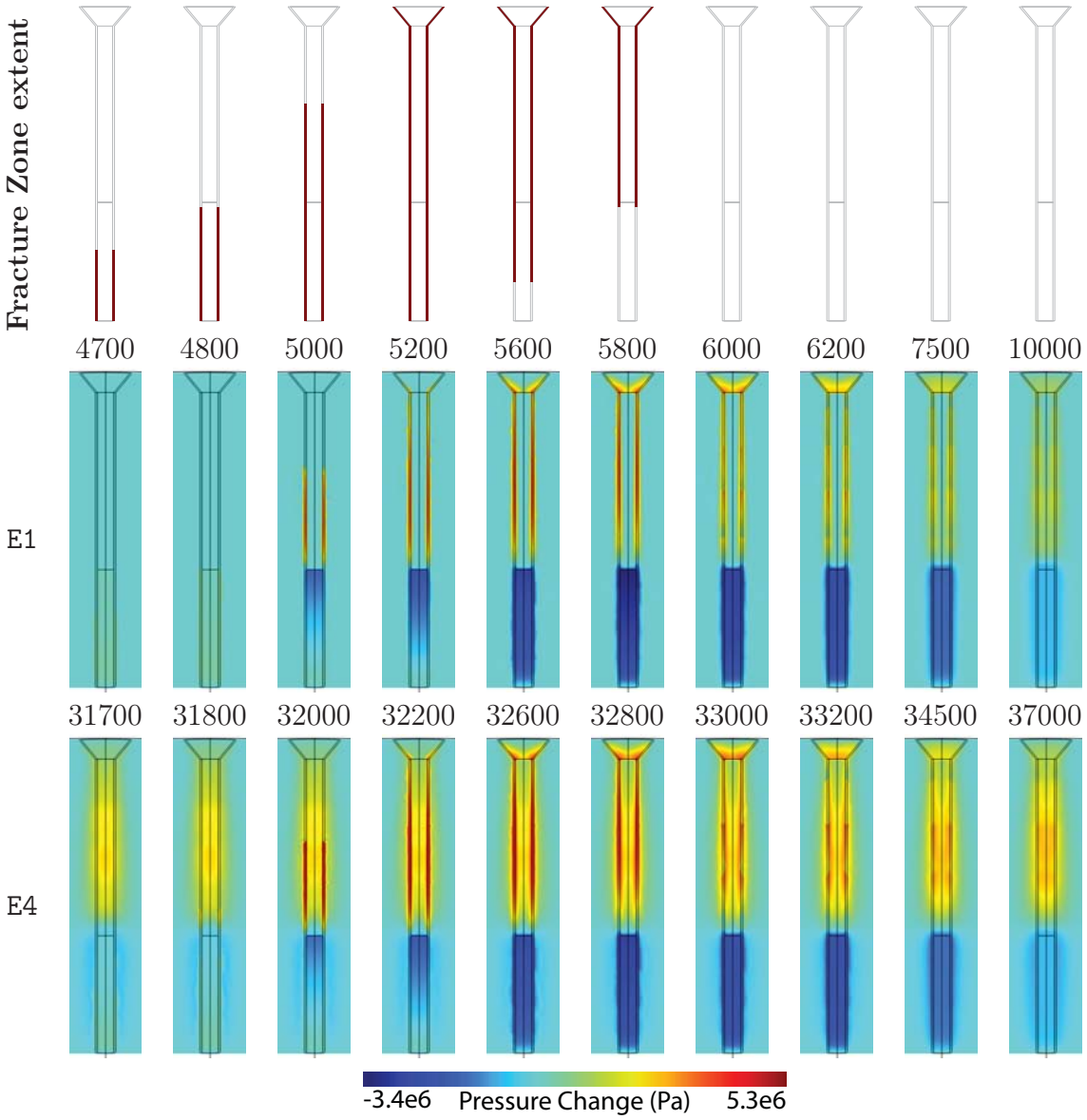

Figure 10.31: Pressure change at different times (s) for events `E1` and `E4` for a gradient permeability in the conduit and deeper plug. Due to the short repose time, the model cannot attain equilibrium before the next degassing event. Consequently, during each successive event, gas accumulates within the less permeable plug and dome, thus increasing their pressure. During the repose between events, this gas continues to degas from the surface.

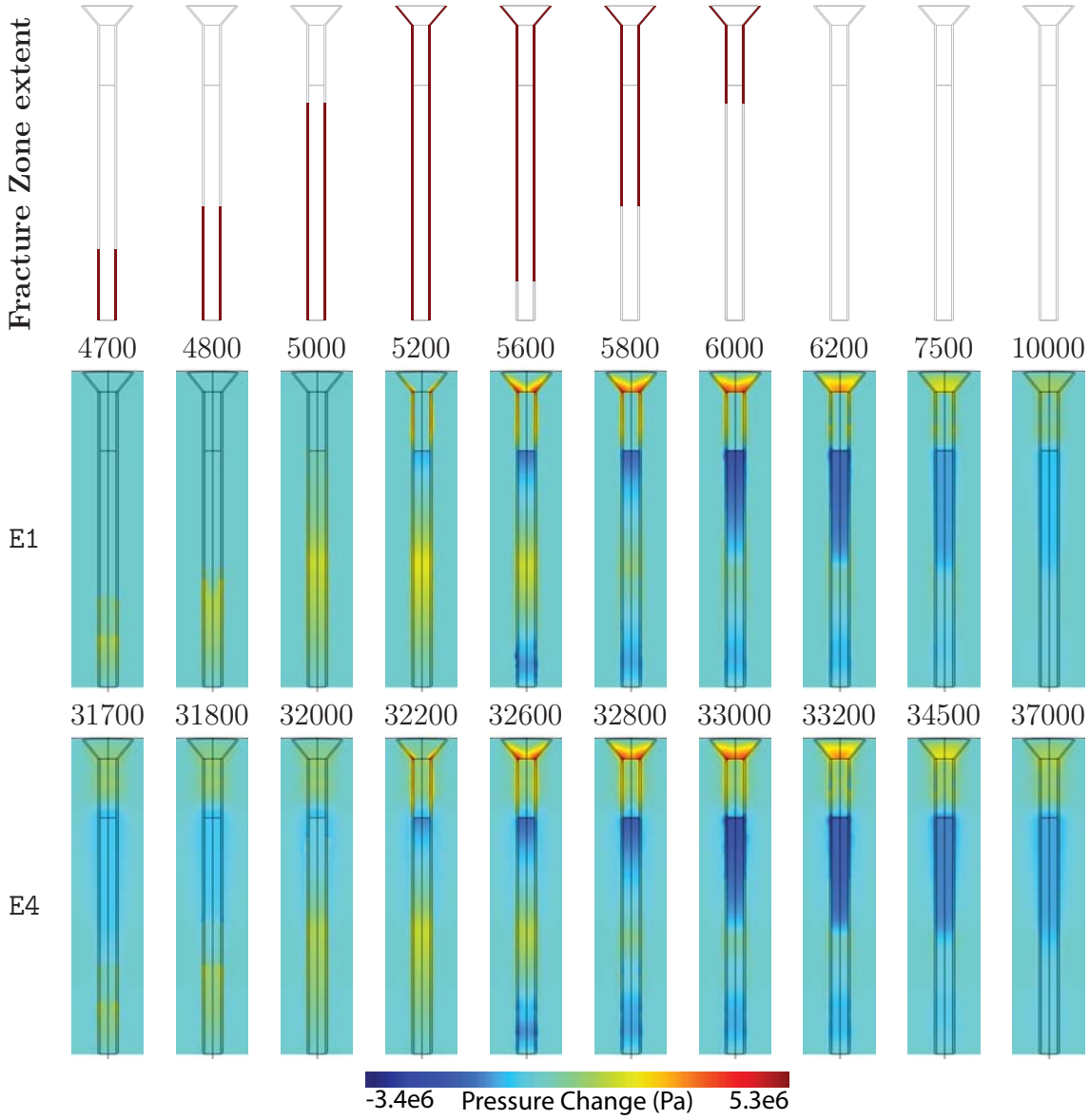

Figure 10.32: Pressure change at different times (s) for events `E1` and `E4` for a gradient permeability in the conduit and shallow plug.

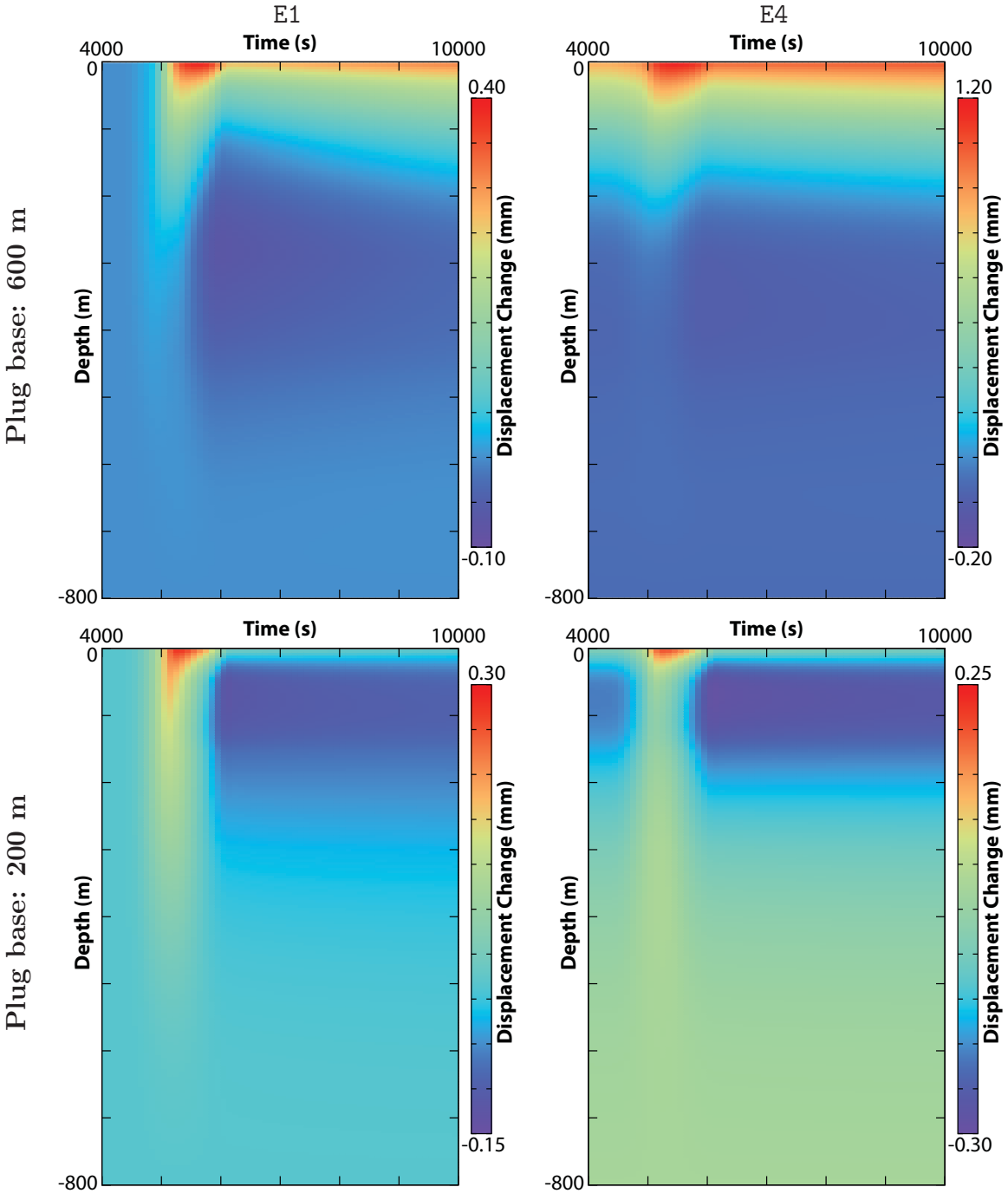

Figure 10.33: Surface displacement change for the volcano flank with depth (z) for events E1 and E4 for two different plug extents.

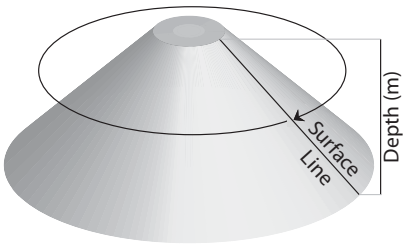

Figure 10.34: For Figure 10.33, the surface displacement change is taken for a line along the surface of the flank. Due to the rotational symmetry of the model structure, the surface displacement change for any section of the flank can be predicted. The surface displacement for the dome is not included in Figure 10.33. Depth corresponds to depth below the surface and not length along the line.

10.3.7 Summary of ring-shaped degassing at Santiaguito

Here, ring-shaped degassing at Santiaguito is modelled via the generation of shear fractures during upward plug flow. This increase in permeability generates a viable degassing pathway for gas which collects beneath the solidification zone between eruptions. This permeability increase is inferred to be highest, and allow the greatest gas loss, during magma motion. Between events, the permeability of the fracture zone decreases, due to sealing processes such as compaction and forces exsolving gas to accumulate in the underlying conduit. With repeated events, if the form of the eruption and interval is the same, gas accumulates within the plug and dome. This may represent a source for continued inter-eruption degassing events through ephemeral fractures on the dome surface. The dome is inferred to overlie the solidified magma and have a high permeability due to abundant fractures. This higher permeability permits gas to be lost progressively towards the dome centre, although the greatest gas loss occurs from the peripheral fractures. There is a delay between the initial ring emission and the subsequent emissions from the dome. The modelled events echo the repose times for actual events and does not permit sufficient time for the volcano to attain equilibrium in between. Consequently, pressure and gas velocity progressively increase with events. The accumulation of gas may be such that it contributes more significantly in the eruptions where the gas venting occurs dome-wide rather than dominated by the fractures.

In this model, a repose time of 2 hours was chosen. This is the upper end of the durations quoted by Bluth and Rose (2004) and Johnson et al. (2004, 2008). If a shorter repose period was chosen, this would imply the pressure would accumulate more with successive events if the gas supply was the same. However, if the repose time is too short to permit full recharge of the conduit before eruption, the pressure would be less, and less gas would be transported vertically. Conversely, a longer

repose period would permit the system to get closer to an equilibrium state and in particular, more of the stored gas within the plug and dome would be lost. Furthermore, the greater repose duration would permit greater recharge of the conduit and lead to greater pressurisation.

The processes and suggested permeability relationships are summarised in Figures 10.35 and 10.36, respectively.

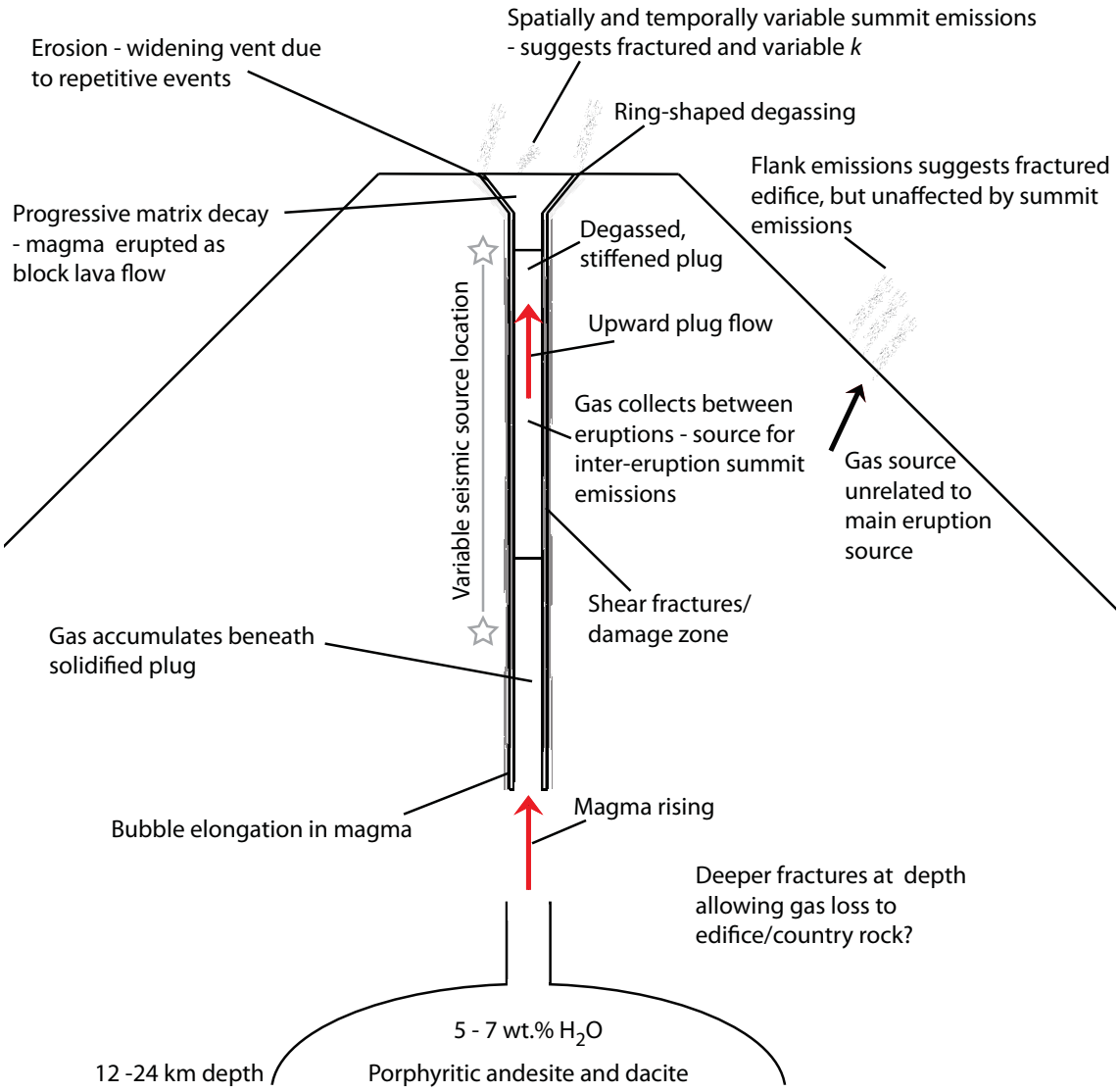

Figure 10.35: Details of the processes hypothesised to occur to generate ring-shaped degassing at Santiaguito. The seismic source location may vary due to changing conduit properties and varied sealing of the fractures, for example, if the fractures persist at depth, but seal near the surface. Gas content and magma composition from Scott et al. (2012).

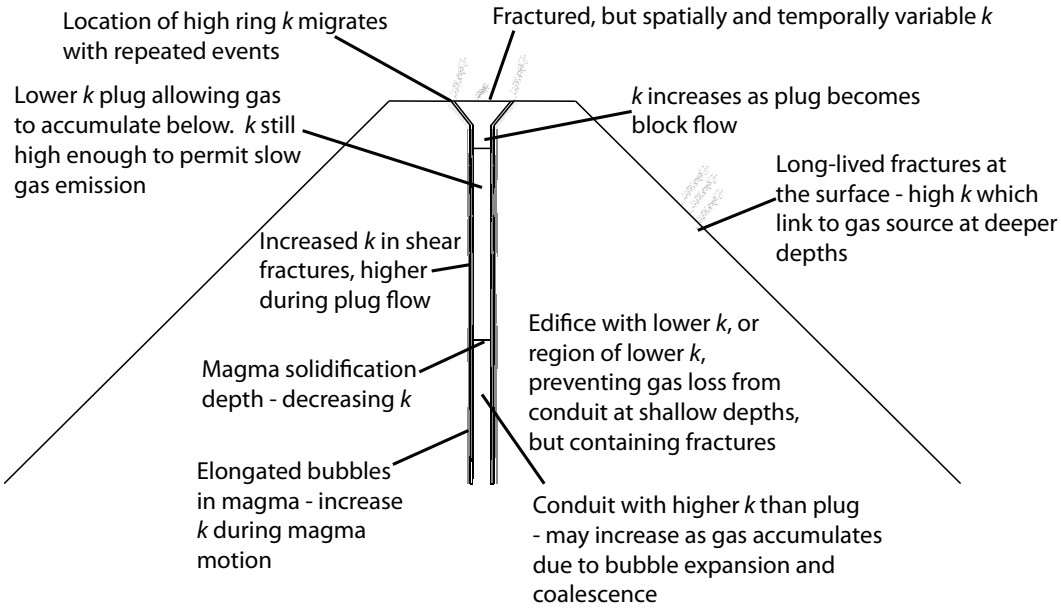

Figure 10.36: The suggested permeability relationships for the gas ring events at Santiaguito.

10.4 Summary

In this chapter, two specific events have been investigated and potential scenarios modelled. The models proposed for each scenario are remarkably similar. However, there are key differences between them. Specifically, at Santiaguito, the degassing event is proposed to occur simultaneously with magma extrusion, whilst at Soufrière Hills, the event involved no magma extrusion and fractures were reactivated due to the occurrence of seismicity. Furthermore, the gas source for the two events is thought to be very different. At Santiaguito, gas is collected at shallow depths in high volumes, whilst the delay between the seismicity and first gas emission at Soufrière Hills suggests gas was stored and transported from much deeper depths. Santiaguito is a volcano which is currently highly active with a very high gas content. In contrast Soufrière Hills has been quiescent for an extended period with no active magma extrusion. Consequently, the gas content is likely to be less, and continued processes of crystallisation may be decreasing permeabilities. Finally, the dome structure of the two volcanoes is very different, from a thin, flat "pancake" dome at Santiaguito, to the well developed spine and lobe structure of Soufrière Hills. This has significant implications for gas storage and transport within the volcanoes. A thin, pancake dome has limited capacity for gas storage and so the gas is not retained for prolonged periods. In contrast, the size and extent of the dome structure at Soufrière Hills provides plentiful possibilities for gas to become trapped and stored, to be released during further fracturing events.

In the following chapter, the results from the previous eight chapters are reviewed and discussed.

Chapter 11

Discussion and Conclusions

In this study, a modelling approach was adopted to investigate the interaction between pressure and gas velocity in a volcanic system of variable permeability. Furthermore, displacement modelling was used to infer the surface effects of this pressurisation and gas content. This constitutes a poroelasticity, numerical experiment whereby Darcy's law describes the gas velocity after the pressure distribution has been determined as a function of permeability. The momentum equation takes the pressure distribution into account and infers the surface displacement that results from the storage or loss of the volcanic gas. Combined monitoring of the degassing and surface deformation, provide comprehensive constraints when using this model framework.

11.1 Implications from the modelling

11.1.1 Sealing the volcano

Impermeable layers within a volcano (Chapter 6) imply not only a barrier to gas transfer, but also a lack of a sufficiently high quantity of gas which may create degassing pathways in magma, due to bubble expansion and coalescence. However, if a region of very high permeability is enclosed in such a material, the impermeable layers act to confine the gas, thus increasing the pressure at shallow depths. This process will also increase the magma pressure, increasing the volume of gas dissolved in the melt. Therefore, this permits the storage of high volumes of gas close to the surface, which may then be released during a decompressional event such as a dome collapse, vulcanian explosions or tapped by cracks within the dome structure (Edmonds et al., 2003b,a, Sparks, 2003a, Green and Neuberg, 2005, Herd et al., 2005, Jousset et al., 2013). Consequently, a low permeability region is necessary to confine volcanic volatiles; however, high pressure and high permeability are also

required for effective gas transport and storage.
Sealed layers within the wall-rocks and dome can result in the gas being deflected and released at the boundaries between regions of different permeability, for example, the margin between fresh dome material and the talus slope, or around the spine (Chapter 6). Concentrating the gas in this way may lead to weakening associated with hydrothermal alteration. If this occurs at a mechanically critical point within the structure, the associated pressurisation could trigger a dome collapse (Stix et al., 1993). Once the gas enters the wall-rocks or dome, and a viable exit route exists, loss to the atmosphere may occur via a variety of outlets, such as cracks within the dome.

11.1.2 Dome cracks and fracturing

Sealing alone is not the only way to increase the permeability contrast within the volcano and trigger a switch in volcanic behaviour. A similar response could be achieved through seismically induced fracturing or brittle failure of the conduit-wall margin resulting in the development of shear fractures during magma movement and spine extrusion, resulting in a permeability increase (Chapter 5). The comparison between the two directions in which fracture zones develop (cracks vs shear fractures) show a very different behaviour (Chapter 5). Ascending magma that triggers shear fracture propagation upwards towards the surface, leads to pressurisation of the magma conduit and gas storage prior to explosive release. In contrast, downwards propagation of the fracture zones promotes depressurisation, gas exsolution and gentle degassing through the edifice.
Dome crack development and fracturing down the conduit margin act to draw gas from the system and invoke decompression (which could affect dome stability) (Chapters 5 and 7). Whether this occurs passively or explosively would depend upon the volume of gas stored, where it is located and the confining pressure. In turn, this is strongly determined by the relative permeabilities within the volcano (Chapter 3).
Widening of cracks does not necessarily suggest increased gas loss, as it depends upon the other properties of that crack: its length, depth and location relative to a gas storage zone and the availability of permeable pathways between the two (Chapter 7). Furthermore, opening and closing cracks may also indicate settling behaviour after an eruption, such as at Santiaguito (Chapter 10.3), where continued degassing from the dome continues during the repose between vulcanian explosions (Bluth and Rose, 2004). This may be due to the postulated presence of shear fractures (Bluth and Rose, 2004, Holland et al., 2011) aiding the upwards transportation of gas, which due to the pressures involved, may be forced into the plug or dome structure.

11.1.3 Permeability variations

Permeability values are known for volcanic rocks, but only for quenched samples at the surface, post-eruption (e.g. Eichelberger et al., 1986, Melnik and Sparks, 2002, Rust and Cashman, 2004, Figures 1.1, 1.2 and B.2). This can provide some idea about the textures, processes and characteristics of the portion of volcano through which they have travelled. For example, glass implies open-system degassing, because the rock has formed in an environment with little gas. This therefore suggests there simultaneously existed a region of very high permeability which allowed this gas to escape, or conversely was surrounded by sealing which shielded the magma from gas input during its formation. Pumice, however, suggests closed-system degassing because the rock has formed in an environment with a plentiful supply of gas.

Syn- and post-eruption processes may have significantly altered the permeabilities and porosities. Volcanic systems are in constant flux, and so are the permeabilities that can derive particular events. In conjunction with gas emissions and surface displacement measurements this can be narrowed down further. For example, if a dome collapse event releases an excessively large volume of gas, this implies there must have existed a storage body large enough to supply that gas, whether it contained exsolved bubbles, or volatiles in solution until they were decompressed.

Chapters 3 and 8 highlighted how even seemingly small changes to permeability can have a dramatic effect upon the volcanic behaviour resulting in different gas loss and surface displacement patterns. In contrast, other permeability variations result in no change at all to the general behaviour. Furthermore, models with very different permeability conditions could be grouped showing a similar response to a fracturing event (Chapter 8). However, changing the topography results in a dramatic alteration to those groupings because it alters the size of the dome which in turn alters the volume through which gas must transfer and may become stored (Chapter 9.3).

In terms of pressurisation, it is the relative permeability contrasts that are more important rather than actual values (Chapter 3). So for example, a conduit of permeability 10^{-10} m^2 with a surrounding permeability of 10^{-14} m^2 would experience the same pressurisation pattern as a conduit of 10^{-14} m^2 surrounded by 10^{-18} m^2. This is because the gas contained within the conduit is dependent upon the porosity and permeability.

Gradient and anisotropic permeabilities

Permeability gradients and/or anisotropy can add complexity to a volcanic system and can enhance or retard the migration of gas to the surface (Chapter 9.2). A decreasing permeability near the surface may be due to crystallisation and gas loss, but can limit the ability for gas at deeper depths to reach the surface. Similarly, an increasing permeability towards the surface may limit the flow of exsolved gas towards the surface due to the lower gas transport capacity of a decreased permeability at depth. Furthermore, an increasing permeability towards the surface could limit the depth to which gas may be released in response to the formation of cracks or an eruption event. This limit may show as deflation on the surface which could be used to infer the depth and size of the gas storage region.

Gradient and anisotropic permeabilities within the conduit can have a large impact upon the pressurisation of the volcano. This is because differing permeability characteristics alter the path through which gas is transferred and the location to which it may be stored. A high vertical permeability implies there is less impact from the surrounding country rock because if the dome is not sealed, gas will be preferentially lost vertically. In contrast, a high horizontal permeability will aid the transport of gas from the centre of the conduit to the conduit-wall margin. This may be a more effective method of gas loss as gas can then utilise the potential presence of bubble elongation or shear fractures at the margin which enhance the permeability vertically.

11.1.4 Country rock and dome

The gas behaviour within a volcanic system is not simply controlled by the conduit; the surrounding country rock and dome also play a role (e.g. Chapters 8 and 9). This is because both regions can either hinder or aid degassing processes dependent upon their permeabilities. A low country rock permeability restricts the gas to the conduit region by preventing lateral gas loss. A decreased permeability in the country rock also reduces the size of the potential gas storage region. If the country rock has a relatively high permeability, gas can migrate between the conduit and country rock, thereby enlarging the volume through which gas may move or become stored. If gas is permitted to enter into the country rock structure, it can result in significantly larger regions exhibiting surface displacement and degassing. In contrast, confining gas to the central regions of the conduit suggests a more localised inflation signal and less extensive degassing. Similarly, a low permeability within the dome, traps gas below, not only in the conduit, but also the surrounding country rock. A higher dome permeability allows gas to escape the system and, whilst the driving pressure

is high enough, high velocity fumaroles may be seen. However, once the internal pressurisation drops, gas velocity would decrease. This in itself can aid the sealing processes through the redistribution and deposition of minerals. The importance of the country rock as a viable degassing route has already been considered before, due to the observation of diffuse degassing (e.g. Allard et al., 1991, Giammanco et al., 1998, Delmelle and Stix, 2000, Williams-Jones et al., 2000, Bonforte et al., 2013).
Chapter 9 showed that the topography had a large impact upon the gas storage and transport through a volcano in response to a change. The effects of the topography are directly related to the form of the dome. A dome structure such as Santiaguito has less capacity to influence gas motion compared to that of Soufrière Hills. Not only does a large dome increase the lithostatic load, it also increases the volume through which volcanic gas must travel to exit the dome, and therefore also increases the likelihood that pockets of gas will become trapped (Chapter 8 and 9.3. Furthermore, a model needs to link the rock type, eruption behaviour and endogenous/exogenous dome growth. Endogenous dome growth could result in gas becoming trapped within the structure, whilst exogenous dome growth with the extrusion of spines or lobes permits the development of potentially viable degassing routes along the spine/edifice boundary.
The motion of gas from one region of the volcano to another, for example, in response to fracturing within the dome structure (Chapter 9.3), can result in surface deflation over the original site, but inflation over the new catchment area. This suggests it may be possible to track the movement of large volumes of gas based upon the changing surface displacement patterns. With the increasing availability of high resolution deformation images through InSAR or ground based radar as observational constraints, this possibility is within reach.
When a dome is present, the ability for gas to be continually lost is dependent upon the internal pressurisation. Once a large proportion of the stored gas has been lost and the pressure drops too low, significant degassing may cease.
The complex relationships between regions of different permeabilities, as shown throughout this study (especially Chapters 3, 8 and 9), illustrates the conduit cannot be considered in isolation when studying the behaviour of volcanic gas. All regions of the conduit, country rock and dome have the potential to dramatically affect gas storage and transport.

11.1.5 Switches in volcanic behaviour

The modelling suggested a permeability decrease of only two orders of magnitude could switch between effusive and explosive volcanic behaviour (Chapter 3). This change in permeability would be observable from the surface as a reduction in the

gas loss from existing fumaroles and surface uplift, due to the pressurisation caused by confining the volatiles. Conversely, this change in surface displacement could also lead to the creation or re-opening of fumaroles fed by fractures. Moore et al. (1994) performed experiments on the sealing of granite at different temperatures in response to the precipitation of silica by hydrothermal fluids through cracks and porosity during cooling. From these experiments, Edmonds et al. (2003b) extrapolated that at 700 °C, a permeability reduction of three orders of magnitude is possible over as little as 2 - 6 days. Conversely, at the much lower temperature of 400 °C, the same process can take 1 - 2 years (Edmonds et al., 2003b). Both extremes carry their own complications when predicting volcanic activity. For example, 2 - 6 days does not provide much warning and evacuation time, whilst if the change occurs over a time scale of years, the decreased gas loss and increased surface uplift could occur too slowly to be readily observable. Furthermore, time scales of years provide ample time for additional processes to occur, for example within the conduit, which could reduce the effectiveness of sealing in triggering a switch in behaviour. Permeabilities are in constant flux and if the conduit is permitted to continue degassing, even at a steadily reducing rate, continued crystallisation of the conduit will occur. Long-term permeability decreases have been measured for the Mt. St Helens dome between December 2004 and December 2005 (Gaunt et al., 2011, 2012) and have been suggested for the activity at Soufrière Hills between July 1998 and November 1999, which showed decreasing SO_2 emissions (Edmonds et al., 2003b). Similar permeability decreases may be continuing during the current phase of the eruption at this volcano. In contrast, rapid permeability changes have been suggested for Soufrière Hills between April and June 1999 during a period of repeated explosive ash venting (Edmonds et al., 2003b). Similar rapid permeability changes may also be involved in the current eruptive activity of Santiaguito.
The region of sealing does not need to be extensive, just continuous and strategically placed, such as at the margin between the conduit and wall, or within the dome structure, to make a big difference.

11.1.6 Event equilibrium times and cyclicity

Equilibrium times have been provided for many models, representing the time taken for all domains to resume an equilibrium state whereby no further changes in response to the imposed event occurs. However, in a dynamic volcanic system, the event modelled is unlikely to occur in isolation, therefore, the volcano is unlikely to reach the end equilibrium point if the required time is considerable, or the repose time between events is short. Repetitive events modelled for Santiaguito in Chapter 10.3 indicated that the creation of shear fractures allows gas stored within

the conduit to escape vertically, but suggests some of this gas may become trapped within the structure of the plug and the dome due to the elevated pressures. Consequently, because of the short repose times between events, this gas accumulates, resulting in increased pressures and surface displacement. Furthermore, the degree of accumulation would depend upon the repose and eruption durations.

11.2 Suggestions for further work

Volcanic systems and their behaviour are governed by a very large number of variables which are constantly in flux and dependent upon any given circumstance. If they were all fully known and understood, there would be no need for modelling as the behaviour of volcanoes would be intuitive and predictable. Unfortunately, this is not the case and models such as these provide a best guess at a very specific scenario which, when applied to real volcanoes, may provide important insights into the processes occurring. The method as it stands is capable of increasing understanding of gas behaviour within a volcanic edifice, but it is currently not suitable as a diagnostic tool. However, there are a number of improvements and adaptations which could be developed to improve its accuracy and usefulness in the future.

11.2.1 Reynolds number and applicability of Darcy's law

Darcy's law determines the transfer of a fluid which exhibits laminar behaviour. It is therefore not applicable to turbulent flow. The transition from laminar to turbulent flow is often defined by the Reynolds number (Re) (Jaupart and Allègre, 1991, Rust and Cashman, 2004) which is defined according to Equation 11.1

$$Re = \frac{\rho \boldsymbol{u} d_p}{\mu} \tag{11.1}$$

for ρ the fluid density, $\boldsymbol{u}$ the velocity, d_P the particle size and μ the fluid dynamic viscosity (Appendix B.1).

Darcy's law is applicable to the majority of the models where the permeability conditions are sufficient such that low gas velocity results. However, in order to accurately model the gas behaviour in high permeability environments, such as cracks where high gas velocities might occur, consideration of turbulent flow is required. Forcheimer's equation (Equation 11.2) is a potential adaptation to account for the inertial effects associated with turbulent flow

$$\nabla P = -\frac{\mu}{k}\boldsymbol{u} - \frac{\rho}{k_f}\boldsymbol{u}^2 \tag{11.2}$$

where P_2, and P_1 represent the highest and lowest pressures the sample experiences, and P_0 is the pressure present during which the gas volume flux (v_0) is measured (approximately atmospheric pressure). L is the length of the sample, μ_a the viscosity, ρ_a the density of air, and k_1 and k_2 are the Darcian (viscous) and non-Darcian (inertial) permeabilities respectively (Takeuchi et al., 2009). A preliminary discussion on the differences between the results from Darcy's law and Forchheimer's equation is presented in Appendix B.2.

11.2.2 Gas species

A further adaptation should be a more realistic quantification of the volume of gas actually present within the volcano, rather than assuming all pore spaces are filled, following Darcy's law, and the ideal gas law. In connection with this, the model can account for the behaviour of all the dominant species of volcanic gas, especially those currently measured and used to infer volcanic processes, including HCl (as a proxy for magma extrusion rate) and SO_2 (potentially influenced by degassing pathways within the edifice and conduit and intrusion of mafic magma) (e.g. Edmonds et al., 2001).

11.2.3 Crystallisation

Crystallisation is directly linked to the exsolution process, but it also greatly impacts upon the permeability by restricting the region which may be occupied by exsolved gas (Sparks and Pinkerton, 1978, Sparks, 1997, Cashman and Blundy, 2000). Furthermore, continued crystallisation at shallow depths has an impact, due to the creation of sealing layers.

11.2.4 Permeability

The variability of permeability in space and time is enormously important and is dependent upon numerous factors. Superficially, permeability is dependent upon the pore spaces within a material, whether it be fractures or gas bubbles. However, delving deeper, the permeability is directly and indirectly related to a large number of factors within the volcanic plumbing system and its surrounding edifice, dome and country rock. In order to fully appreciate the role of permeability in volcanic systems, the permeability and any temporal variations in its value need to be calculated dependent upon the various conditions determining the volcano's state. Through experiments, the permeability has been found to be directly affected by pressure and temperature (Gaunt et al., 2011, 2012), stress and strain (Kendrick

et al., 2013). Pressure affects the permeability by altering the volume of gas which may be kept in solution, altering the permeability increase through bubble growth and connectivity. Furthermore, increased pressure helps to keep fractures closed at depth thereby reducing the permeability. The strength of the rock within the conduit and country rock must also be considered. Rocks deforming in a brittle manner may fracture, thereby increasing the permeability, whereas ductile deformation may also permit the alignment of minerals or pores, also enhancing the permeability, particularly in one direction. Further knowledge of these processes suggests the permeability changes due to shear at the conduit-wall boundary could be modelled rather than explicitly set.
The ideal model would be one in which the permeability is calculated throughout dependent upon the properties (stress/strain, gas content, crystallinity, composition, pressure, temperature, compaction) rather than being explicitly imposed.

11.2.5 Geological structure

As already discussed, the country rock and dome play an important role in affecting the behaviour of volcanic volatiles. The modelling currently assumes uniform permeabilities within the country rock with only simple subdivisions within the dome. However, different rock types within the country rock could also be significant, not only in the way they interact with the volcanic plumbing system through contact metamorphism (e.g. release of additional volatiles (Yallup et al., 2013)) but also how their respective rock properties can affect the gas transport and storage capacity laterally from the conduit. The location and extent of different rock types, the presence of aquifers, faults and fractures can all affect the permeability and consequently the flow laterally through the country rock. Furthermore, to more accurately model the displacement in response to features such as cracks and shear fractures, the different domains should be decoupled such that they can deform together or independently dependent upon the processes occurring.

11.2.6 An optimal model

An optimum model to simulate volcanic degassing, based upon current volcanological knowledge, is shown in Figures 11.1 and 11.2. The most important observation is that many of the processes listed on these figures either influence or depend upon the permeability. To create such a comprehensive model would require input from a wide variety of areas, including, but not limited to:

- permeability and porosity studies and in particular how they vary with time under changing conditions (e.g. Gaunt et al., 2012, Kendrick et al., 2013);

- geochemistry and petrology to determine the magma composition and its variation with time and depth, in addition to the use of trace elements which may provide another constraint on interior permeabilities (e.g. Berlo et al., 2006);
- gas emission studies to develop more accurate and reliable real-time observations of gas emission volumes and compositions (e.g. Shinohara, 2005, Edmonds and Herd, 2007);
- dome morphology such as Herd et al. (2005) to infer the internal structure;
- conduit morphology studies using fossil volcanoes such as Mule Creek (Stasiuk et al., 1996) and spine profiles (Gaunt et al., 2011, 2012);
- seismicity and the relationship between seismic events and changing conditions at depth including if this is related to fracturing or changing conduit geometry (e.g. Neuberg et al., 2006, Thomas and Neuberg, 2012);
- structural geology to determine the structure and properties of the country rock (e.g. Pallister et al., 2013);
- experimental studies to help constrain the models.

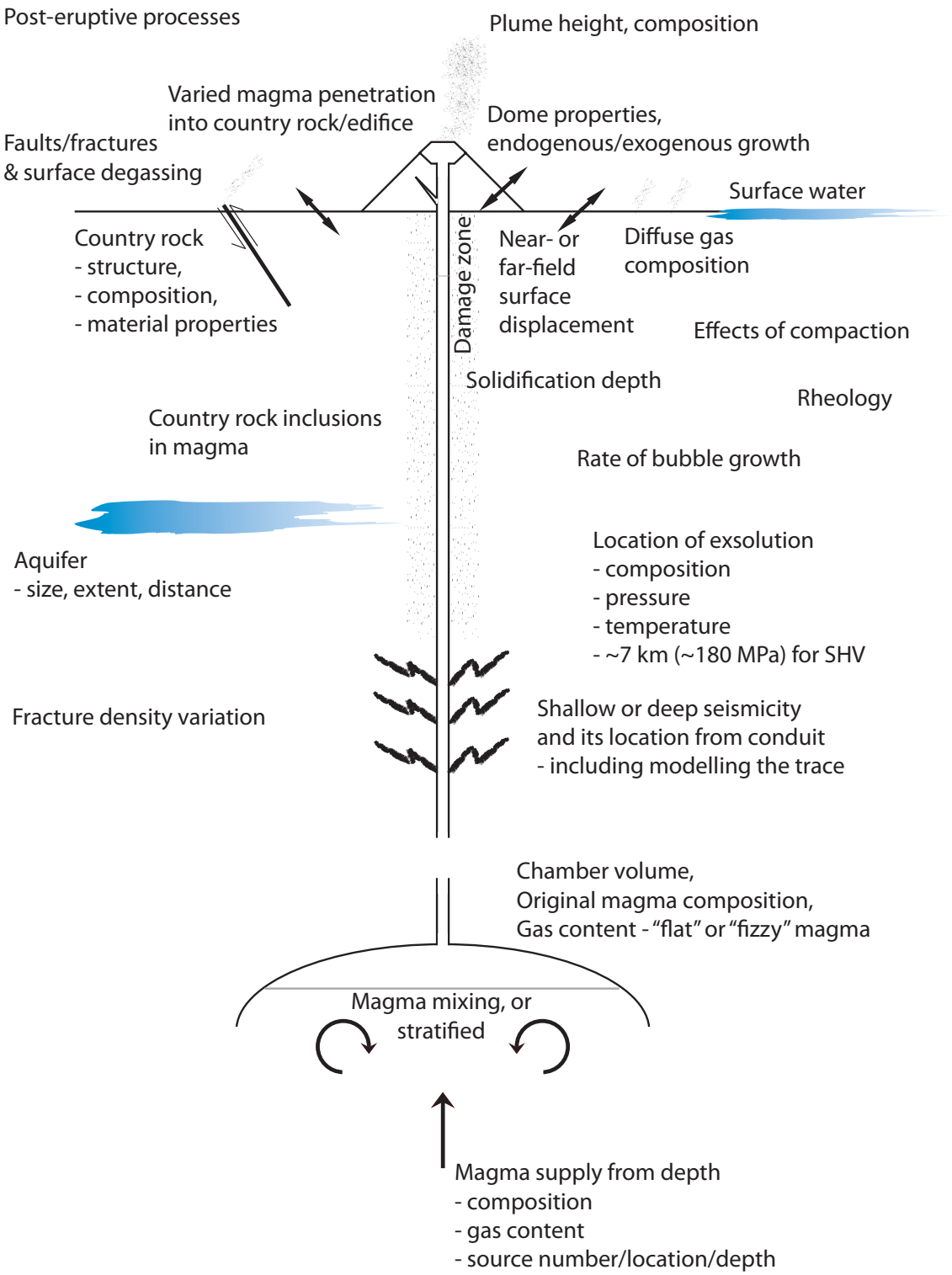

Figure 11.1: An optimal degassing model (not to scale) incorporating the most important processes occurring inside volcanic systems. The optimal degassing model would need to consider all processes between the magma source and the surface, including the country rock and dome. A striking observation is that the permeability is tied to many of the processes listed. Suggestions for processes within the conduit are illustrated in Figure 11.2. The exsolution depth for Soufrière Hills (SHV) is from Edmonds et al. (2002).

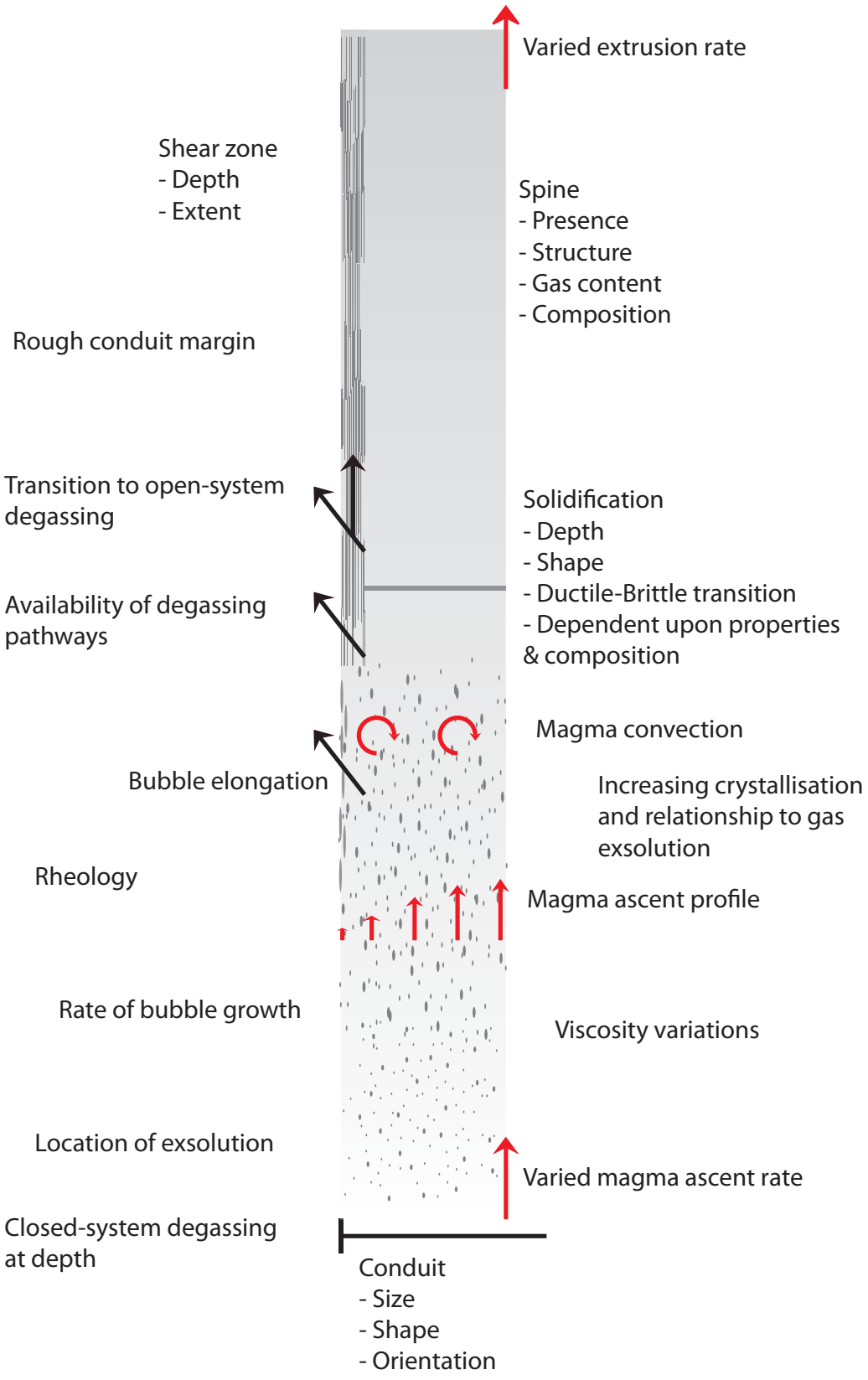

Figure 11.2: An optimal half-conduit model, to be incorporated with Figure 11.1.

11.3 Conclusions

This is an innovative method which provides insights into the effects of permeability variation on the behaviour of volcanic volatiles and the resulting pressurisation and surface displacement. It is a flexible approach because it is possible to experiment with different setups to investigate a particular scenario by changing the interior structure or permeability conditions. The model framework can be further expanded to include additional physics. Furthermore, models can be created in three-dimensions with time dependency to investigate how the results change through time. This is particularly effective because the surface results of gas emissions and displacement can be directly compared to observations from real volcanoes. The main conclusions from this study are:

- These models provide a valuable insight into how gas moves through a volcano - how and where it may be stored and where it escapes from the surface.
- These models provide an understanding of the time-dependent response of the system to pressure changes induced by sealing (Chapter 6 and the formation of cracks and fractures (Chapters 5, 7, 8, 9 and 10.
- These simulations are capable of modelling volcanic conditions in three-dimensions allowing the prediction of surface gas loss and displacement in time (Chapters 8, 9 and 10.
- Small changes to permeability conditions can result in profound changes in behaviour. A reduction of just two orders of magnitude in the surrounding permeability could switch between effusive and explosive behaviour.
- A high-permeability region surrounded by low-permeability leads to pressurisation which permits greater gas storage at shallow levels.
- In this study, a higher conduit permeability is a dominant controller on the gas velocity, whilst the permeability within the surrounding edifice plays a secondary role (Chapter 3).
- Cracks in the dome structure can be efficient at degassing and depressurising the dome, but their influence is limited, dependent upon their location and depth (Chapter 7). A partial decompression of the dome could affect the stability of the dome.
- Upwards propagation of shear fractures leads to pressurisation and gas storage prior to explosive release whilst downward propagation promotes depressurisation, gas exsolution and gentle degassing (Chapter 5).
- Ring shaped degassing at volcanoes such as Santiaguito may be simulated by the presence of fractures around the periphery of the dome and a pressure gradient induced by a more permeable conduit below the dome (Chapter 10.3).

- The degree of surface displacement seen is dependent upon the pressurisation and the location of that pressurisation. Consequently, tracking of large volumes of gas may be possible (Chapters 8 and 9).
- A volcano can take a long time to respond to a change in permeability. Therefore, repeated events with a short repose time can change the manner in which the volcano responds compared to a single, isolated event (Chapter 10).
- The dome and edifice contribute significantly to the results and must be considered in further work to fully understand the behaviour of volatiles in volcanic systems (Chapters 8, 9 and 10).
- The model framework developed here provides several quantitative outputs: timing, gas velocity and related deformation. By using observations such as gas emissions and deformation rates as constraints, the model can be used in day-to-day monitoring programs, to obtain a better insight into general volcanic behaviour.

Chapter 12

References

Aiuppa, A., S. Inguaggiato, A. J. S. McGonigle, M. O'Dwyer, C. Oppenheimer, M. J. Padgett, D. Rouwet, and M. Valenza (2005), H_2S fluxes from Mt. Etna, Stromboli and Vulcano (Italy) and implications for the sulfur budget at volcanoes, *Geochimica et Cosmochimica Acta*, *69*(7), 1861–1871, doi:10.1016/j.gca.2004.09.018.

Aiuppa, A., C. Federico, G. Giudice, S. Gurrieri, M. Liuzzo, H. Shinohara, R. Favara, and M. Valenza (2006), Rates of carbon dioxide plume degassing from Mount Etna volcano, *Journal of Geophysical Research*, *111*(B9), B09207, doi:10.1029/2006JB004307.

Aiuppa, A., A. Bertagnini, N. Métrich, R. Moretti, A. Di Muro, M. Liuzzo, and G. Tamburello (2010), A model of degassing for Stromboli volcano, *Earth and Planetary Science Letters*, *295*(1–2), 195–204, doi:10.1016/j.epsl.2010.03.040.

Aiuppa, A., G. Giudice, M. Liuzzo, G. Tamburello, P. Allard, S. Calabrese, I. Chaplygin, A. J. S. McGonigle, and Y. Taran (2012), First volatile inventory for Gorely volcano, Kamchatka, *Geophysical Research Letters*, *39*(6), L06307, doi:10.1029/2012GL051177.

Alean, J. (2007), Stromboli online, `http://www.swisseduc.ch/stromboli/glossary/fumarole-en.html`, accessed 08-10-2013.

Alidibirov, M., and D. B. Dingwell (1996), Magma fragmentation by rapid decompression, *Nature*, *380*, 146–148.

Allard, P., J. Carbonnelle, D. Dajlevic, J. Le Bronet, P. Morel, M. C. Robe, J. M. Maurenas, R. Faivre-Pierret, D. Martin, J. C. Sabroux, and P. Zettwoog (1991), Eruptive and diffuse emissions of CO_2 from Mount Etna, *Letters to Nature*, *351*, 387–391, doi:10.1038/351387a0.

Avard, G., and A. G. Whittington (2012), Rheology of arc dacite lavas: experimental determination at low strain rates, *Bulletin of Volcanology*, *74*(5), 1039–1056, doi:10.1007/s00445-012-0584-2.

Ball, J. L., E. S. Calder, B. E. Hubbard, and M. L. Bernstein (2013), An assessment of hydrothermal alteration in the Santiaguito lava dome complex, Guatemala: implications for dome collapse hazards, *Bulletin of Volcanology*, *75*(676), doi:10.1007/s00445-012-0676-z.

Barclay, J., M. J. Rutherford, M. R. Carroll, M. D. Murphy, J. D. Devine, J. Gardner, and R. S. J. Sparks (1998), Experimental phase equilibria constraints on pre-eruptive storage conditions of the Soufrière Hills magma, *Geophysical Research Letters*, *25*(18), 3437–3440, doi:10.1029/98GL00856.

Baxter, P. J., C. Bonadonna, R. Dupree, V. L. Hards, S. C. Kohn, M. D. Murphy, A. Nichols, R. A. Nicholson, G. Norton, A. Searl, R. S. J. Sparks, and B. P. Vickers (1999), Cristobalite in Volcanic Ash of the Soufriere Hills Volcano, Montserrat, British West Indies, *Science*, *283*, 1142–1145.

Benson, P. M., M. J. Heap, Y. Lavallée, A. Flaws, K. U. Hess, A. P. S. Selvadurai, D. B. Dingwell, and B. Schillinger (2012), Laboratory simulations of tensile fracture development in a volcanic conduit via cyclic magma pressurisation, *Earth and Planetary Science Letters*, *349–350*, 231–239, doi:10.1016/j.epsl.2012.07.003.

Berlo, K., S. Turner, J. Blundy, S. Black, and C. Hawkesworth (2006), Tracing pre-eruptive magma degassing using (^{210}Pb/^{226}Ra) disequilibria in the volcanic deposits of the 1980-1986 eruption of Mount St Helens, *Earth and Planetary Science Letters*, *249*(3–4), 337–349, doi:10.1016/j.epsl.2006.07.018.

Berlo, K., H. Tuffen, V. Smith, J. M. Castro, D. M. Pyle, T. A. Mather, and K. Geraki (2013), Element variations in rhyolitic magma resulting from gas transport, *Geochimica et Cosmochimica Acta*, *121*, 436–451, doi:10.1016/j.gca.2013.07.032.

Bernard, M. L., M. Zamora, Y. Géraud, and G. Boudon (2007), Transport properties of pyroclastic rocks from Montagne Pelée volcano (Martinique, Lesser Antilles), *Journal of Geophysical Research*, *112*(B5), B05205, doi:10.1029/2006JB004385.

Blower, J. D. (2001), Factors controlling permeability-porosity relationships in magma, *Bulletin of Volcanology*, *63*(7), 497–504, doi:10.1007/s004450100172.

Bluth, G. J. S., and W. I. Rose (2004), Observations of eruptive activity at Santiaguito volcano, Guatemala, *Journal of Volcanology and Geothermal Research*, *136*(3–4), 297–302, doi:10.1016/j.jvolgeores.2004.06.001.

Bobrowski, N., G. Hönninger, F. Lohberger, and U. Platt (2006), IDOAS: A new monitoring technique to study the 2D distribution of volcanic gas emissions, *Journal of Volcanology and Geothermal Research*, *150*(4), 329–338, doi:10.1016/j.jvolgeores.2005.05.004.

Bonforte, A., F. Guglielmino, M. Coltelli, A. Ferretti, and G. Puglisi (2011), Structural assessment of Mount Etna volcano from Permanent Scatterers analysis, *Geochemistry, Geophysics, Geosystems*, *12*(2), Q02002, doi:10.1029/2010GC003213.

Bonforte, A., C. Federico, S. Giammanco, F. Guglielmino, M. Liuzzo, and M. Neri (2013), Soil gases and SAR measurements reveal hidden faults on the sliding flank of Mt. Etna (Italy), *Journal of Volcanology and Geothermal Research*, *251*, 27–40, doi:10.1016/j.jvolgeores.2012.08.010.

Boudon, G., B. Villemant, J.-C. Komorowski, P. Ildefonse, and M. P. Semet (1998), The hydrothermal system at Soufriere Hills Volcano, Montserrat (West Indies): Characterization and role in the on-going eruption, *Geophysical Research Letters*, *25*(19), 3693–3696, doi:10.1029/98GL00985.

Bouvet de Maisonneuve, C., O. Bachmann, and A. Burgisser (2009), Characterization of juvenile pyroclasts from the Kos Plateau Tuff (Aegean Arc): insights into the eruptive dynamics of a large rhyolitic eruption, *Bulletin of Volcanology*, *71*(6), 643–658, doi:10.1007/s00445-008-0250-x.

Burnham, C. W. (1975), Water and magmas; a mixing model, *Geochimica et Cosmochimica Acta*, *39*(8), 1077–1084, doi:10.1016/0016-7037(75)90050-2.

Caltabiano, T., R. Romano, and G. Budetta (1994), SO_2 flux measurements at Mount Etna (Sicily), *Journal of Geophysical Research*, *99*(D6), 12,809–12,819, doi:10.1029/94JD00224.

Candela, P. A. (1991), Physics of aqueous phase evolution in plutonic environments, *American Mineralogist*, *76*, 1081–1091.

Carn, S. A., and F. J. Prata (2010), Satellite-based constraints on explosive SO_2 release from Soufrière Hills Volcano, Montserrat, *Geophysical Research Letters*, *37*(19), L00E22, doi:10.1029/2010GL044971.

Carn, S. A., R. B. Watts, G. Thompson, and G. E. Norton (2004), Anatomy of a lava dome collapse: the 20 March 2000 event at Soufrière Hills Volcano, Montserrat, *Journal of Volcanology and Geothermal Research*, *131*(3–4), 241–264, doi:10.1016/S0377-0273(03)00364-0.

Casadevall, T. J., W. I. Rose Jr., W. H. Fuller, W. H. Hunt, M. A. Hart, J. L. Moyers, D. C. Woods, R. L. Chuan, and J. P. Friend (1984), Sulfur Dioxide and particles in Quiescent Volcanic Plumes from Poás, Arenal, and Colima Volcanos, Costa Rica and Mexico, *Journal of Geophysical Research*, *89*(D6), 9633–9641, doi:10.1029/JD089iD06p09633.

Cashman, K., and J. Blundy (2000), Degassing and crystallization of ascending andesite and dacite, *Philosophical Transactions of the Royal Society, London, A.*, *358*(1770), 1487–1513, doi:10.1098/rsta.2000.0600.

Cashman, K., and R. S. J. Sparks (2013), How volcanoes work: A 25 year perspective, *Geological Society of America Bulletin*, *125*(5–6), 664–690, doi:10.1130/B30720.1.

Castro, J. M., B. Cordonnier, H. Tuffen, M. J. Tobin, L. Puskar, M. C. Martin, and H. A. Bechtel (2012), The role of melt-fracture degassing in defusing explosive rhyolite eruptions at volcán Chaitén, *Earth and Planetary Science Letters*, *333–334*, 63–69, doi:10.1016/j.epsl.2012.04.024.

Chadwick, W. (1981), USGS/Cascades Volcano Observatory, `http://vulcan.wr.usgs.gov/Glossary/Emissions/description_gases_fumaroles.html`, accessed: 08-10-2013.

Chardot, L., B. Voight, R. Foroozan, S. Sacks, A. Linde, R. Stewart, D. Hidayat, A. Clarke, D. Elsworth, N. Fournier, J. C. Komorowski, G. Mattioli, R. S. J. Sparks, and C. Widiwijayanti (2010), Explosion dynamics from strainmeter and microbarometer observations, Soufrière Hills Volcano, Montserrat: 2008-2009, *Geophysical Research Letters*, *37*(19), L00E24, doi:10.1029/2010GL044661.

Chouet, B. (1986), Dynamics of a fluid-driven crack in three dimensions by the finite difference method, *Journal of Geophysical Research*, *91*(B14), 13,967–13,992, doi:10.1029/JB091iB14p13967.

Chouet, B. (1988), Resonance of a fluid-driven crack: Radiation properties and implications for the source of long-period events and harmonic tremor, *Journal of Geophysical Research*, *93*(B5), 4375–4400, doi:10.1029/JB093iB05p04375.

Chouet, B. A. (1996), Long-period volcano seismicity: its source and use in eruption forecasting, *Nature*, *380*, 309–316, doi:10.1038/380309a0.

Christopher, T., M. Edmonds, M. C. S. Humphreys, and R. A. Herd (2010), Volcanic gas emissions from Soufrière Hills Volcano, Montserrat 1995-2009, with implications for mafic magma supply and degassing, *Geophysical Research Letters*, *37*(19), L00E04, doi:10.1029/2009GL041325.

Clarke, A. B., S. Stephens, R. Teasdale, R. S. J. Sparks, and K. Diller (2007), Petrological constraints on the decompression history of magma prior to Vulcanian explosions at the Soufrière Hills volcano, Montserrat, *Journal of Volcanology and Geothermal Research*, *161*(4), 261–274, doi:10.1016/j.jvolgeores.2006.11.007.

Collier, L., and J. Neuberg (2006), Incorporating seismic observations into 2D conduit flow modeling, *Journal of Volcanology and Geothermal Research*, *152*(3–4), 331–346, doi:10.1016/j.jvolgeores.2005.11.009.

Collier, L., J. W. Neuberg, N. Lensky, V. Lyakhovsky, and O. Navon (2006), Attentuation in gas-charged magma, *Journal of Volcanology and Geothermal Research*, *153*(1–2), 21–36, doi:10.1016/j.jvolgeores.2005.08.009.

Collinson, A. S. D., and J. W. Neuberg (2012), Gas storage, transport and pressure changes in an evolving permeable volcanic edifice, *Journal of Volcanology and Geothermal Research*, *243–244*, 1–13, doi:10.1016/j.jvolgeores.2012.06.027.

Collinson, A. S. D., and J. W. Neuberg (in prep.), Modelling gas transfer, storage and resulting displacement in a 3D permeable volcanic edifice.

Collombet, M. (2009), Two-dimensional gas loss for silicic magma flows: Toward more realistic numerical models, *Geophysical Journal International*, *177*(1), 309–318, doi:10.1111/j.1365-246x.2008.04086.x.

Costa, A., O. Melnik, R. S. J. Sparks, and B. Voight (2007), Control of magma flow in dykes on cyclic lava dome extrusion, *Geophysical Research Letters*, *34*, L02303, doi:10.1029/2006GL027466.

Daines, M. J. (2000), Migration of Melt, in *Encyclopedia of Volcanoes*, edited by H. Sigurdsson, B. Houghton, S. Mcnutt, H. Rymer, and J. Stix, pp. 69–88, Academic Press.

de' Michieli Vitturi, M., A. B. Clarke, A. Neri, and B. Voight (2010), Transient effects of magma ascent dynamics along a geometrically variable dome-feeding conduit, *Earth and Planetary Science Letters*, *295*(3–4), 541–553, doi:10.1016/j.epsl.2010.04.029.

de' Michieli Vitturi, M., A. B. Clarke, A. Neri, and B. Voight (2013), Extrusion cycles during dome-building eruptions, *Earth and Planetary Science Letters*, *371–372*, 37–48, doi:10.1016/j.epsl.2013.03.037.

Delgado-Granados, H., L. Cárdenas González, and N. Piedad Sánchez (2001), Sulfur dioxide emissions from Popocatépetl volcano (Mexico): case study of a high-emission rate, passively degassing erupting volcano, *Journal of Volcanology and Geothermal Research*, *108*(1–4), 107–120, doi:10.1016/s0377-0273(00)00280-8.

Delmelle, P., and J. Stix (2000), Volcanic Gases, in *Encyclopedia of Volcanoes*, edited by H. Sigurdsson, B. Houghton, S. Mcnutt, H. Rymer, and J. Stix, pp. 803–815, Academic Press.

Denlinger, R. P., and R. P. Hoblitt (1999), Cyclic eruption behaviour of silicic volcanoes, *Geology*, *27*, 459–462, doi:10.1130/0091-7613(1999)027<0459:CEBOSV>2.3.CO;2.

Devine, J. D., H. Sigurdsson, A. N. Davis, and S. Self (1984), Estimates of sulfur and chlorine yield to the atmosphere from volcanic eruptions and potential climatic effects, *Journal of Geophysical Research*, *89*(B7), 6309–6325, doi:10.1029/JB089iB07p06309.

Di Muro, A., J. Pallister, B. Villemant, C. Newhall, M. Semet, M. Martinez, and C. Mariet (2008), Pre-1991 sulfur transfer between mafic injections and dacite magma in the Mt. Pinatubo reservoir, *Journal of Volcanology and Geothermal Research*, *175*(4), 517–540, doi:10.1016/j.jvolgeores.2008.02.025.

Dingwell, D. B. (1998), Recent experimental progress in the physical description of silicic magma relevant to explosive volcanism, in *The Physics of Explosive Volcanic Eruptions*, vol. 145, edited by J. S. Gilbert and R. S. J. Sparks, pp. 9–26, Geological Society, London, Special Publications.

Dixon, J. E., E. M. Stolper, and J. R. Holloway (1995), An Experimental Study of Water and Carbon Dioxide Solubilities in Mid-Ocean Ridge Basaltic Liquids. Part I: Calibration and Solubility Models, *Journal of Petrology*, *36*(6), 1607–1631.

Edmonds, M. (2008), New geochemical insights into volcanic degassing, *Philosophical Transactions of the Royal Society A*, *366*(1885), 4559–4579, doi:10.1098/rsta.2008.0185.

Edmonds, M., and R. A. Herd (2005), Inland-directed base surge generated by the explosive interaction of pyroclastic flows and seawater at Soufrière Hills volcano, Montserrat, *Geology*, *33*(4), 245–248, doi:10.1130/G21166.1.

Edmonds, M., and R. A. Herd (2007), A volcanic degassing event at the explosive-effusive transition, *Geophysical Research Letters*, *34*, L21310, doi:10.1029/2007GL031379.

Edmonds, M., D. Pyle, and C. Oppenheimer (2001), A model for degassing at Soufrière Hills Volcano, Montserrat, West Indies, based on geochemical data, *Earth and Planetary Science Letters*, *186*(2), 159–173, doi:10.1016/s0012-821x(01)00242-4.

Edmonds, M., D. Pyle, and C. Oppenheimer (2002), HCl emissions at Soufrière Hills Volcano, Montserrat, West Indies, during a second phase of dome building: November 1999 to October 2000, *Bulletin of Volcanology*, *64*(1), 21–30, doi:10.1007/s00445-001-0175-0.

Edmonds, M., R. A. Herd, B. Galle, and C. M. Oppenheimer (2003a), Automated, high time-resolution measurements of SO_2 flux at Soufrière Hills Volcano, Montserrat, *Bulletin of Volcanology*, *65*(8), 578–586, doi:10.1007/s00445-003-0286-x.

Edmonds, M., C. Oppenheimer, D. M. Pyle, R. A. Herd, and G. Thompson (2003b), SO_2 emissions from Soufrière Hills Volcano and their relationship to conduit permeability, hydrothermal interaction and degassing regime, *Journal of Volcanology and Geothermal Research*, *124*(1–2), 23–43, doi:10.1016/s0377-0273(03)00041-6.

Edmonds, M., R. A. Herd, and M. H. Strutt (2006), Tephra deposits associated with a large lava dome collapse, Soufrière Hills Volcano, Montserrat, 12-15 July 2003, *Journal of Volcanology and Geothermal Research*, *153*(3–4), 313–330, doi:10.1016/j.jvolgeores.2005.12.008.

Edmonds, M., K. A. McGee, and M. Doukas (2008), Chlorine degassing during the lava dome-building eruption of Mount St. Helens, 2004-2005, in *A Volcano Rekindled: The Renewed Eruption of Mount St. Helens, 2004-2006*, vol. 1750, edited by D. R. Sherrod, W. E. Scott, and P. H. Stauffer, pp. 573–589, U.S. Geological Survey Professional Paper.

Edmonds, M., A. Aiuppa, M. Humphreys, R. Moretti, G. Giudice, R. S. Martin, R. A. Herd, and T. Christopher (2010), Excess volatiles supplied by mingling of mafic magma at an andesite arc volcano, *Geochemistry, Geophysics, Geosystems*, *11*(4), Q04005, doi:10.1029/2009GC002781.

Eichelberger, J. C., C. R. Carrigan, H. R. Westrich, and R. H. Price (1986), Non-explosive silicic volcanism, *Nature*, *323*, 598–602, doi:10.1038/323598a0.

Ferrazzini, V., and K. Aki (1987), Slow waves trapped in a fluid-filled infinite crack: Implication for volcanic tremor, *Journal of Geophysical Research*, *92*(B9), 9215–9223, doi:10.1029/JB092iB09p09215.

Fink, J. H., S. W. Anderson, and C. R. Manley (1992), Textural constraints on effusive silicic volcanism: Beyond the permeable foam model, *Journal of Geothermal Research*, *97*(B6), 9073–9083, doi:10.1029/92JB00416.

Fowler, A. C., B. Scheu, W. T. Lee, and M. J. McGuinness (2010), A theoretical model of the explosive fragmentation of vesicular magma, *Proceedings of the Royal Society A*, *466*(2115), 731–752, doi:10.1098/rspa.2009.0382.

Friedman, I. (1989), Are extrusive rhyolites produced from permeable foam eruptions?, *Bulletin of Volcanology*, *51*(1), 69–71, doi:10.1007/BF01086762.

Garboczi, E. J., K. A. Snyder, J. F. Douglas, and M. F. Thorpe (1995), Geometric percolation threshold of overlapping ellipsoids, *Physical Review E*, *52*(1), 819–828, doi:10.1103/PhysRevE.52.819.

Gardner, C. A., and R. A. White (2002), Seismicity, gas emission and deformation from 18 July to 25 September 1995 during the initial phreatic phase of the eruption of Soufrière Hills Volcano, Montserrat, in *The Eruption of Soufrière Hills Volcano, Montserrat, from 1995 to 1999*, vol. 21, edited by T. H. Druitt and B. P. Kokelaar, pp. 567–581, Geological Society, London, Memoirs, doi:10.1144/GSL.MEM.2002.021.01.26.

Gaunt, E., P. Sammonds, R. Smith, P. Meredith, and C. Kilburn (2011), Volcanic dome stability: Permeability and fluid pressurisation of the Mount St Helens 2004-2008 lava dome complex, EGU General Assembly Poster, A38, EGU2011-10209.

Gaunt, E., P. Sammonds, P. Meredith, C. Kilburn, and R. Smith (2012), Fluid flow and degassing in high temperature magma, EGU General Assembly Poster.

Gerlach, T. M., H. Delgado, K. A. McGee, M. P. Doukas, J. J. Venegas, and L. Cárdenas (1997), Application of the LI-COR CO_2 analyzer to volcanic plumes: A case study, volcán Popocatépetl, Mexico, June 7 and 10, 1995, *Journal of Geophysical Research*, *102*(B4), 8005–8019, doi:10.1029/96JB03887.

Giachetti, T., and H. M. Gonnerman (2013), Water in volcanic pyroclast: Rehydration or incomplete degassing?, *Earth and Planetary Science Letters*, *369-370*, 317–332, doi:10.1016/j.epsl.2013.03.041.

Giammanco, S., S. Gurrieri, and M. Valenza (1998), Anomalous soil CO_2 degassing in relation to faults and eruptive fissures on Mount Etna (Sicily, Italy), *Bulletin of Volcanology*, *60*(4), 252–259, doi:10.1007/s004450050231.

Giggenbach, W. F. (1975), A simple method for the collection and analysis of volcanic gas samples, *Bulletin of Volcanology*, *39*(1), 132–145, doi:10.1007/BF02596953.

Gil Cruz, F., and B. A. Chouet (1997), Long-period events, the most characteristic seismicity accompanying the emplacement and extrusion of a lava dome in Galeras Volcano, Colombia, in 1991, *Journal of Volcanology and Geothermal Research*, *77*(1–4), 121–158, doi:10.1016/s0377-0273(96)00091-1.

Gonnermann, H. M., and M. Manga (2005), Nonequilibrium magma degassing: Results from modeling of the ca. 1340 A.D. eruption of Mono Craters, California., *Earth and Planetary Science Letters*, *238*(1–2), 1–16, doi:10.1016/j.epsl.2005.07.021.

Gonnermann, H. M., and M. Manga (2007), The Fluid Mechanics Inside a Volcano, *Annual Review of Fluid Mechanics*, *39*, 321–356, doi:10.1146/annurev.fluid.39.050905.110207.

Green, D. N., and J. Neuberg (2005), Seismic and infrasonic signals associated with an unusual collapse event at the Soufrière Hills volcano, Montserrat, *Geophysical Research Letters*, *32*(7), L07308, doi:10.1029/2004GL022265.

Hale, A. J. (2008), Lava dome growth and evolution with an independently deformable talus, *Geophysical Journal Internation*, *174*(1), 391–417, doi:10.1111/j.1365-246X.2008.03806.x.

Hale, A. J., E. S. Calder, G. Wadge, S. C. Loughlin, and G. A. Ryan (2009a), Modelling the lava dome extruded at Soufrière Hills Volcano, Montserrat, August 2005 - May 2006, Part I: Dome shape and internal structure, *Journal of Volcanology and Geothermal Research*, *187*(1–2), 53–68, doi:10.1016/j.jvolgeores.2009.08.023.

Hale, A. J., E. S. Calder, S. C. Loughlin, G. Wadge, and G. A. Ryan (2009b), Modelling the lava dome extruded at Soufrière Hills Volcano, Montserrat, August 2005 - May 2006: Part II: Rockfall activity and talus deformation, *Journal of Volcanology and Geothermal Research*, *187*(1–2), 69–84, doi:10.1016/j.jvolgeores.2009.08.014.

Hammouya, G., P. Allard, P. Jean-Baptiste, F. Parello, M. P. Semet, and S. R. Young (1998), Pre- and syn-eruptive geochemistry of volcanic gases from Soufriere Hills of Montserrat, West Indies, *Geophysical Research Letters*, *25*(19), 3685–3688, doi:10.1029/98GL02321.

Harris, A., S. Alparone, A. Bonforte, J. Dehn, S. Gambino, L. Lodato, and L. Spampinato (2012), Vent temperature trends at the Vulcano Fossa fumarole field: the role of permeability, *Bulletin of Volcanology*, *74*(6), 1293–1311, doi:10.1007/s00445-012-0593-1.

Harris, A. J., W. I. Rose, and L. P. Flynn (2003), Temporal trends in lava dome extrusion at Santiaguito 1922-2000, *Bulletin of Volcanology*, *65*(2–3), 77–89, doi:10.1007/s00445-002-0243-0.

Hautmann, S., D. Hidayat, N. Fournier, A. T. Linde, I. S. Sacks, and C. P. Williams (2013), Pressure changes in the magmatic system during the December 2008/January 2009 extrusion event at Soufrière Hills Volcano, Montserrat (W.I.), derived from strain data analysis, *Journal of Volcanology and Geothermal Research*, *250*, 34–41, doi:10.1016/j.jvolgeores.2012.10.006.

Hautmann, S., F. Witham, T. Christopher, P. Cole, A. T. Linde, I. S. Sacks, and R. S. J. Sparks (2014), Strain field analysis on Montserrat (W.I.) as tool for assessing permeable flow paths in the magmatic system of Soufrière Hills Volcano, *Geochemistry, Geophysics, Geosystems*, *15*(3), doi:10.1002/2013GC005087.

Heap, M. J., S. Vinciguerra, and P. G. Meredith (2009), The evolution of elastic moduli with increasing crack damage during cyclic stressing of a basalt from Mt. Etna volcano, *Tectonophysics*, *471*, 153–160, doi:10.1016/j.tecto.2008.10.004.

Heiken, G., K. Wohletz, and J. Eichelberger (1988), Fracture fillings and intrusive pyroclasts, Inyo Domes, California, *Journal of Geophysical Research*, *93*(B5), 4335–4350, doi:10.1029/JB093iB05p04335.

Heiligmann, M., J. Stix, G. Williams-Jones, B. Sherwood Lollar, and V. G. Garzón (1997), Distal degassing of radon and carbon dioxide on Galeras volcano, Colombia, *Journal of Volcanology and Geothermal Research*, *77*(1–4), 267–283, doi:10.1016/s0377-0273(96)00099-6.

Heilprin, A. (1903), *Mont Pelée and The Tragedy of Martinique: A study of the great catastrophies of 1902, with observations and experiences in the field*, Philadelphia and London, J.B. Lippincott Company.

Herd, R. A., M. Edmonds, and V. A. Bass (2005), Catastrophic lava dome failure at Soufrière Hills Volcano, Montserrat, 12–13 July 2003, *Journal of Volcanology and Geothermal Research*, *148*(3–4), 234–252, doi:10.1016/j.jvolgeores.2005.05.003.

Hicks, P. D., A. J. Matthews, and M. J. Cooker (2009), Thermal structure of a gas-permeable lava dome and timescale separation in its response to perturbation, *Journal of Geophysical Research*, *114*(B7), B07201, doi:10.1029/2008JB006198.

Hobbs, P. V., L. F. Radke, J. H. Lyons, R. J. Ferek, D. J. Coffman, and T. J. Casadevall (1991), Airborne measurements of particle and gas emissions from the 1990 volcanic eruptions of Mount Redoubt, *Journal of Geophysical Research*, *96*(D10), 18,735–18,752, doi:10.1029/91JD01635.

Holland, A. S. P., I. M. Watson, J. C. Phillips, L. Caricchi, and M. P. Dalton (2011), Degassing processes during lava dome growth: Insights from Santiaguito lava dome, Guatemala, *Journal of Volcanology and Geothermal Research*, *202*(1–2), 153–166, doi:10.1016/j.jvolgeores.2011.02.004.

Holloway, J. R. (1976), Fluids in the evolution of granitic magmas: Consequences of finite CO_2 solubility, *Geological Society of America Bulletin*, *87*(10), 1513–1518, doi:10.1130/0016-7606(1976)87<1513:FITEOG>2.0.CO;2.

Horwell, C. J., B. J. Williamson, E. W. Llewellin, D. E. Damby, and J. S. Le Blond (2013), The nature and formation of cristobalite at the Soufrière Hills volcano, Montserrat: implications for the petrology and stability of silicic lava domes, *Bulletin of Volcanology*, *75*(3), 1–19, doi:10.1007/s00445-013-0696-3.

Hutton, D. V. (2004), *Fundamentals of finite element analysis*, McGraw-Hill.

Ida, Y. (2007), Driving force of lateral permeable gas flow in magma and the criterion of explosive and effusive eruptions, *Journal of Volcanology and Geothermal Research*, *162*(3–4), 172–184, doi:10.1016/j.jvolgeores.2007.03.005.

Jackson, P., J. B. Shepherd, R. E. A. Robertson, and G. Skerritt (1998), Ground deformation studies at Soufriere Hills Volcano, Montserrat I: Electronic distance meter studies, *Geophysical Research Letters*, *25*(18), 3409–3412, doi:10.1029/98GL01656.

Jaggar, T. A. (1956), *My Experiments with Volcanoes*, Hawaiian Volcano Research Association, Honolulu.

Jaupart, C., and C. Allègre (1991), Gas content, eruption rate and instabilities of eruption regime in silicic volcanoes, *Earth and Planetary Science Letters*, *102*(3–4), 413–429, doi:10.1016/0012-821x(91)90032-D.

Jellinek, A. M., and D. Bercovici (2011), Seismic tremors and magma wagging during explsoive volcanism, *Nature*, *470*, 522–525, doi:10.1038/nature09828.

Ji, K. H., and T. A. Herring (2011), Transient signal detection using GPS measurements: Transient inflation at Akutan volcano, Alaska, during early 2008, *Geophysical Research Letters*, *38*, L06307, doi:10.1029/2011GL046904.

Johnson, J. B., A. J. L. Harris, S. T. M. Sahetapy-Engel, R. Wolf, and W. I. Rose (2004), Explosion dynamics of pyroclastic eruptions at Santiaguito Volcano, *Geophysical Research Letters*, *31*(6), L06610, doi:10.1029/2003GL019079.

Johnson, J. B., J. M. Lees, A. Gerst, D. Sahagian, and N. Varley (2008), Long-period earthquakes and co-eruptive dome inflation seen with particle image velocimetry, *Nature*, *456*, 377–381, doi:10.1038/nature07429.

Johnson, J. B., R. Sanderson, J. Lyons, R. Escobar-Wolf, G. Waite, and J. M. Lees (2009), Dissection of a composite volcanic earthquake at Santiaguito, Guatemala, *Geophysical Research Letters*, *36*(16), L16308, doi:10.1029/2009GL039370.

Jones, K. R., and J. B. Johnson (2011), Mapping complex vent eruptive activity at Santiaguito, Guatemala using network infrasound semblance, *Journal of Volcanology and Geothermal Research*, *199*(1–2), 15–24, doi:10.1016/j.jvolgeores.2010.08.006.

Jouniaux, L., M. L. Bernard, M. Zamora, and J. P. Pozzi (2000), Streaming potential in volcanic rocks from Mount Pelée, *Journal of Geophysical Research*, *105*(B4), 8391–8401, doi:10.1029/1999JB900435.

Jousset, P., A. Budi-Santoso, A. D. Jolly, M. Boichu, Surono, S. Dwiyono, S. Sumarti, S. Hidayati, and P. Thierry (2013), Signs of magma ascent in LP and VLP seismic events and link to degassing: An example from the 2010 explosive eruption at Merapi volcano, Indonesia, *Journal of Volcanology and Geothermal Research*, *261*, 171–192, doi:10.1016/j.jvolgeores.2013.03.014.

Kayzar, T. M., K. M. Cooper, M. K. Reagan, and A. J. R. Kent (2009), Gas transport model for the magmatic system at Mount Pinatubo, Philippines: Insights from (^{210}Pb)/(^{226}Ra), *Journal of Volcanology and Geothermal Research*, *181*(1–2), 124–140, doi:10.1016/j.jvolgeores.2009.01.006.

Kendrick, J. E., Y. Lavallée, K. U. Hess, M. J. Heap, H. E. Gaunt, P. G. Meredith, and D. B. Dingwell (2013), Tracking the permeable porous network during strain-dependent magmatic flow, *Journal of Volcanology and Geothermal Research*, *260*, 117–126, doi:10.1016/j.jvolgeores.2013.05.012.

Kilburn, C. R. J. (2000), Lava flows and flow fields, in *Encyclopedia of Volcanoes*, edited by H. Sigurdsson, B. Houghton, S. Mcnutt, H. Rymer, and J. Stix, pp. 291–305, Academic Press.

Klug, C., and K. V. Cashman (1996), Permeability development in vesiculating magmas: implications for fragmentation, *Bulletin of Volcanology*, *58*(2–3), 87–100, doi:10.1007/s004450050128.

Kolzenburg, S., and J. K. Russell (2014), Welding of pyroclastic conduit infill: A mechanism for cyclic explosive eruptions, *Journal of Geophysical Research*, *119*, 5305 – 5323, doi:10.1002/2013JB010931.

Kolzenburg, S., M. J. Heap, Y. Lavallée, J. K. Russell, P. G. Meredith, and D. B. Dingwell (2012), Strength and permeability recovery of tuffisite-bearing andesite, *Solid Earth*, *3*, 191–198, doi:10.5194/se-3-191-2012.

Kozono, T., and T. Koyaguchi (2010), A simple formula for calculating porosity of magma in volcanic conduits during dome-forming eruptions, *Earth, Planets and Space*, *62*(5), 483–488, doi:10.5047/eps.2010.02.005.

Lahr, J. C., B. A. Chouet, C. D. Stephens, J. A. Power, and R. A. Page (1994), Earthquake classification, location, and error analysis in a volcanic environment: implications for the magmatic system of the 1989-1990 eruptions at redoubt volcano, Alaska, *Journal of Volcanology and Geothermal Research*, *62*(1–4), 137–151, doi:10.1016/0377-0273(94)90031-0.

Lavallée, Y., K. U. Hess, B. Cordonnier, and D. B. Dingwell (2007), Non-Newtonian rheological law for highly crystalline dome lavas, *Geology*, *35*, 843–846, doi:10.1130/G23594A.1.

Lavallée, Y., P. G. Meredith, D. B. Dingwell, K. U. Hess, J. Wassermann, B. Cordonnier, A. Gerik, and J. H. Kruhl (2008), Seismogenic lavas and explosive eruption forcasting, *Nature*, *453*, 507–510, doi:10.1038/nature06980.

Lavallée, Y., N. R. Varley, M. A. Alatorre-Ibargüengoitia, K. U. Hess, U. Kueppers, S. Mueller, D. Richard, B. Scheu, O. Spieler, and D. B. Dingwell (2011), Magmatic architecture of dome-building eruptions at Volcán de Colima, Mexico, *Bulletin of Volcanology*, *74*(1), 249–260, doi:10.1007/s00445-011-0518-4.

Lensky, N. G., R. S. J. Sparks, O. Navon, and V. Lyakhovsky (2008), Cyclic activity at Soufrière Hills Volcano, Montserrat: degassing-induced pressurization and stick-slip extrusion, in *Fluid motions in volcanic conduits: a source of seismic and acoustic signals*, vol. 307, edited by S. Lane and R. Sparks, pp. 169–188, Geological Society of London, doi:10.1144/SP307.10.

Linde, A. T., S. Sacks, D. Hidayat, B. Voight, A. Clarke, D. Elsworth, G. Mattioli, P. Malin, E. Shalev, S. Sparks, and C. Widiwijayanti (2010), Vulcanian explosion at Soufrière Hills Volcano, Montserrat on March 2004 as revealed by strain data, *Geophysical Research Letters*, *37*(19), L00E07, doi:10.1029/2009GL041988.

Liu, Y., Y. Zhang, and H. Behrens (2005), Solubility of H_2O in rhyolitic melts at low pressures and a new empirical model for mixed $H_2O - CO_2$ solubility in rhyolitic melts, *Journal of Volcanology and Geothermal Research*, *143*(1–3), 219–235, doi:10.1016/j.jvolgeores.2004.09.019.

Llewellin, E. W. (2007), Development of anisotropy of permeability in expanding vesicular magma, `https://community.dur.ac.uk/ed.llewellin/papers/Llewellin_anisotropy_pre.pdf`, [online; accessed 21-May-2013].

Llewellin, E. W., and M. Manga (2005), Bubble suspension rheology and implications for conduit flow, *Journal of Volcanology and Geothermal Research*, *143*, 205–217, doi:10.1016/j.jvolgeores.2004.09.018.

Llewellin, E. W., H. M. Mader, and S. D. R. Wilson (2002), The rheology of a bubbly liquid, *Proceedings of the Royal Society A*, *458*, 987–1016, doi:10.1098/rspa.2001.0924.

Loughlin, S. C., R. Luckett, G. Ryan, T. Christopher, V. Hards, S. De Angelis, L. Jones, and M. Strutt (2010), An overview of lava dome evolution, dome collapse and cyclicity at Soufrière Hills Volcano, Montserrat, 2005-2007, *Geophysical Research Letters*, *37*(19), L00E16, doi:10.1029/2010GL042547.

Lu, Z., C. Wicks, J. A. Power, and D. Dzurisin (2000), Ground deformation associated with the March 1996 earthquake swarm at Akutan volcano, Alaska, revealed by satellite radar interferometry, *Journal of Geophysical Research*, *105*(B9), 21,483–21,495, doi:10.1029/2000JB900200.

Mader, H. M., E. W. Llewellin, and S. P. Mueller (2013), The rheology of two-phase magmas: A review and analysis, *Journal of Volcanology and Geothermal Research*, *257*, 135–158, doi:10.1016/j.jvolgeores.2013.02.014.

Massol, H., and C. Jaupart (2009), Dynamics of magma flow near the vent: Implications for dome eruptions, *Earth and Planetary Science Letters*, *279*(3–4), 185–196, doi:10.1016/j.epsl.2008.12.041.

Matsushima, N. (2011), Estimation of permeability and degassing depth of Iwodake volcano at Satsuma-Iwojima, Japan, by thermal observation and numerical simulation, *Journal of Volcanology and Geothermal Research*, *202*(1–2), 167–177, doi:10.1016/j.jvolgeores.2011.02.005.

Matthews, S. J., M. C. Gardeweg, and R. S. J. Sparks (1997), The 1984 to 1996 cyclic activity of Lascar Volcano, northern Chile: cycles of dome growth, dome subsidence, degassing and explosive eruptions., *Bulletin of Volcanology*, *59*(1), 72–82, doi:10.1007/s004450050176.

Mattioli, G. S., T. H. Dixon, F. Farina, E. S. Howell, P. E. Jansma, and A. L. Smith (1998), GPS measurement of surface deformation around Soufriere Hills Volcano, Montserrat from October 1995 to July 1996, *Geophysical Research Letters*, *25*(18), 3417–3420, doi:10.1029/98GL00931.

Mattioli, G. S., S. R. Young, B. Voight, R. S. J. Sparks, E. Shalev, S. Sacks, P. Malin, A. Linde, W. Johnston, D. Hidayat, D. Elsworth, P. Dunkley, R. Herd, J. Neuberg, G. Norton, and C. Widiwijayanti (2004), Prototype PBO instrumentation of CALIPSO project captures world-record lava dome collapse on Montserrat Volcano, *Eos, Transactions American Geophysical Union*, *85*(34), 317–325, doi:10.1029/2004EO340001.

Melnik, O., and R. S. J. Sparks (1999), Nonlinear dynamics of lava dome extrusion, *Nature*, *402*, 37–41, doi:10.1038/46950.

Melnik, O., and R. S. J. Sparks (2002), Dynamics of magma ascent and lava extrusion at Soufrière Hills Volcano, Montserrat, in *The Eruption of Soufrière Hills Volcano, Montserrat, from 1995 to 1999*, vol. 21, edited by T. H. Druitt and B. P. Kokelaar, pp. 153–171, Geological Society, London, Memoirs, doi:10.1144/GSL.MEM.2002.021.01.07.

Moore, D. E., D. A. Lockner, and J. D. Byerlee (1994), Reduction of Permeability in Granite at Elevated Temperatures, *Science*, *265*(5178), 1558–1561, doi:10.1126/science.265.5178.1558.

Moretti, R., I. Arienzo, L. Civetta, G. Orsi, and P. Papale (2013), Multiple magma degassing sources at an explosive volcano, *Earth and Planetary Science Letters*, *367*, 95–104, doi:10.1016/j.epsl.2013.02.013.

Mueller, S., O. Melnik, O. Spieler, B. Scheu, and D. B. Dingwell (2005), Permeability and degassing of dome lavas undergoing rapid decompression: An experimental determination, *Bulletin of Volcanology*, *67*(6), 526–638, doi:10.1007/s00445-004-0392-4.

Mueller, S., B. Scheu, O. Spieler, and D. B. Dingwell (2008), Permeability control on magma fragmentation, *Geology*, *36*(5), 399–402, doi:10.1130/G24605A.1.

Murphy, M. D., R. S. J. Sparks, J. Barclay, M. R. Carroll, and T. S. Brewer (2000), Remobilization of Andesite Magma by Intrusion of Mafic Magma at the Soufriere Hills Volcano, Montserrat, West Indies, *Journal of Petrology*, *41*(1), 21–42, doi:10.1093/petrology/41.1.21.

MVO (2006), Assessment of the hazards and risks associated with the Soufriere Hills Volcano, Montserrat. Seventh Report of the Scientific Advisory Committeee on Montserrat Volcanic Activity, Part II: Technical Report, [Available at: `http://www.mvo.ms`].

MVO (2010a), Assessment of the hazards and risks associated with the Soufriere Hills Volcano, Montserrat. Fourteenth Report of the Scientific Advisory Committeee on Montserrat Volcanic Activity, Part I: Main Report, [Available at: `http://www.mvo.ms`].

MVO (2010b), Assessment of the hazards and risks associated with the Soufriere Hills Volcano, Montserrat. Fifteenth Report of the Scientific Advisory Committeee on Montserrat Volcanic Activity, Part I: Main Report, [Available at: `http://www.mvo.ms`].

MVO (2012a), Scientific Report for Volcanic Activity between 1 May 2012 and 12 October 2012. Open File Report OFR 12-02, [Available at: `http://www.mvo.ms`].

MVO (2012b), Scientific report for volcanic activity between 1 November 2011 and 30 April 2012. Open File Report OFR 12-01, [Available at: `http://www.mvo.ms`].

MVO (2012c), MVO Activity Reports, Open File Report 13-01, [Available at: `http://www.mvo.ms`].

MVO (2012d), Assessment of the hazards and risks associated with the Soufriere Hills Volcano, Montserrat. Seventeenth Report of the Scientific Advisory Committeee on Montserrat Volcanic Activity, Part II: Full Report, [Available at: `http://www.mvo.ms`].

MVO (2013a), Assessment of the hazards and risks associated with the Soufriere Hills Volcano, Montserrat. Eighteenth Report of the Scientific Advisory Committeee on Montserrat Volcanic Activity, Part II: Full Report, [Available at: `http://www.mvo.ms`].

MVO (2013b), MVO Activity Reports, Open File Report 14-01, [Available at: `http://www.mvo.ms`].

Nabovati, A., E. W. Llewellin, and A. C. M. Souse (2009), A general model for the permeability of fibrous porous media based on fluid flow simulations using the lattice boltzmann method, *Composites: Part A*, *40*, 860–869, doi:10.1016/j.compositesa.2009.04.009.

Navon, O., and V. Lyakhovsky (1998), Vesiculation processes in silicic magmas, in *The Physics of Explosive Volcanic Eruptions*, vol. 145, edited by J. S. Gilbert and R. S. J. Sparks, pp. 27–50, Geological Society, London, Special Publications.

Neuberg, J. (2000), Characteristics and causes of shallow seismicity in andesite volcanoes., *Philosophical Transactions of the Royal Society. Mathematical, Physical and Engineering Sciences*, *358*(1770), 1533–1546, doi:10.1098/rsta.2000.0602.

Neuberg, J., and C. O'Gorman (2002), A model of the seismic wavefiled in gas-charged magma: application to Soufrière Hills Volcano, Montserrat, in *The Eruption of Soufrière Hills Volcano, Montserrat, from 1995 to 1999*, vol. 21, edited by T. H. Druitt and B. P. Kokelaar, pp. 603–609, Geological Society, London, Memoirs, doi:10.1144/GSL.MEM.2002.021.01.29.

Neuberg, J. W., H. Tuffen, L. Collier, D. Green, T. Powell, and D. Dingwell (2006), The trigger mechanism of low-frequency earthquakes on Montserrat, *Journal of Volcanology and Geothermal Research*, *153*(1–2), 37–50, doi:10.1016/j.jvolgeores.2005.08.008.

Newman, S., and J. B. Lowenstern (2002), VolatileCalc: a silicate melt-$H_2O - CO_2$ solution model written in Visual Basic for excel, *Computers & Geosciences*, *28*(5), 597–604, doi:10.1016/s0098-3004(01)00081-4.

Newman, S., S. Epstein, and E. Stolper (1988), Water, carbon dioxide and hydrogen isotopes in glasses from the ca. 1340 A.D. eruption of Mono Craters, California: Constraints on degassing phenomena and initial volatile content, *Journal of Volcanology and Geothermal Research*, *35*(1–2), 75–96, doi:10.1016/0377-0273(88)90007-8.

Nicholson, E. J., T. A. Mather, D. M. Pyle, H. M. Odbert, and T. Christopher (2013), Cyclic patterns in volcanic degassing revealed by SO_2 flux timeseries analysis: An application to Soufrière Hills Volcano, Montserrat, *Earth and Planetary Science Letters*, *375*, 209–221, doi:10.1016/j.epsl.2013.05.032.

Noguchi, S., A. Toramaru, and S. Nakada (2008), Groundmass crystallization in dacite dykes taken in Unzen Scientific Drilling Project (USDP-4), *Journal of Volcanology and Geothermal Research*, *175*(1–2), 71–81, doi:10.1016/j.jvolgeores.2008.03.037.

Norton, G. E., R. B. Watts, B. Voight, G. S. Mattioli, R. A. Herd, S. R. Young, G. E. Devine, W. P. Aspinnall, C. Bonadonna, B. J. Baptie, M. Edmonds, A. D. Jolly, S. C. Loughlin, R. Luckett, and R. S. J. Sparks (2002), Pyroclastic flow and explosive activity at Soufrière Hills Volcano, Montserrat, during a period of virtually no magma extrusion (March 1998 to November 1999), in *The Eruption of Soufrière Hills Volcano, Montserrat, from 1995 to 1999*, vol. 21, edited by T. H. Druitt and B. P. Kokelaar, pp. 467–481, Geological Society, London, Memoirs, doi:10.1144/GSL.MEM.2002.021.01.21.

Odbert, H. M., R. C. Stewart, and G. Wadge (2014), Cyclic phenomena at the Soufrière Hills Volcano, Montserrat, in *The Eruption of Soufrière Hills Volcano, Montserrat, from 2000 to 2010*, vol. 39, edited by G. Wadge, R. E. A. Robertson, and B. Voight, pp. 41–60, Geological Society, London, Memoirs, doi:10.1144/M39.2.

Okumura, S., M. Nakamura, S. Takeuchi, A. Tsuchiyama, T. Nakano, and K. Uesugi (2009), Magma deformation may induce non-explosive volcanism via degassing through bubble networks, *Earth and Planetary Science Letters*, *281*(3–4), 267–274, doi:10.1016/j.epsl.2009.02.036.

Okumura, S., M. Nakamura, T. Nakano, K. Uesugi, and A. Tsuchiyama (2012), Experimental constraints on permeable gas transport in crystalline silicic magmas, *Contributions to Mineralogy and Petrology*, *164*(3), 493–504, doi:10.1007/s00410-012-0750-8.

Okumura, S., M. Nakamura, K. Uesugi, T. Nakano, and T. Fujioka (2013), Coupled effect of magma degassing and rheology on silicic volcanism, *Earth and Planetary Science Letters*, *362*, 163–170, doi:10.1016/j.epsl.2012.11.056.

Oppenheimer, C., P. W. Francis, D. A. Rothery, and R. W. T. Carlton (1993), Infrared Image Analysis of Volcanic Thermal Features: Láscar Volcano, Chile, 1984-1992, *Journal of Geophysical Research*, *98*(B3), 4269–4286, doi:10.1029/92JB02134.

Oppenheimer, C., M. Edmonds, P. Francis, and M. Burton (2002), Variation in HCl/SO_2 gas ratios observed by Fourier transform spectroscopy at Soufrière Hills Volcano, Montserrat, in *The Eruption of Soufrière Hills Volcano, Montserrat, from 1995 to 1999*, vol. 21, edited by T. Druitt and B. Kokelaar, pp. 621–639, Geological Society, London, Memoirs, doi:10.1144/GSL.MEM.2002.021.01.31.

Palano, M., E. Guarrera, and M. Mattia (2012), GPS ground deformation patterns at Mount St. Helens (Washington, USA) from 2004 to 2010, *Terra Nova*, *24*(2), 148–155, doi:10.1111/j.1365-3121.2011.01049.x.

Pallister, J. S., K. V. Cashman, J. T. Hagstrum, N. M. Beeler, S. C. Moran, and R. P. Denlinger (2013), Faulting within the Mount St. Helens conduit and implications for volcanic earthquakes, *GSA Bulletin*, *125*(3/4), 359–376, doi:10.1130/B30716.1.

Papale, P. (1999), Modeling of the solubility of a two-component $H_2O + CO_2$ fluid in silicate liquids, *American Mineralogist*, *84*, 477–492.

Parfitt, E. A., and L. Wilson (2008), *Fundamentals of Physical Volcanology*, 65 pp., Blackwell Publishing.

Peiró, J., and S. Sherwin (2005), Finite Difference, Finite Element and Finite Volume Methods for Partial Differential Equations.

Platz, T., S. J. Cronin, K. V. Cashman, R. B. Stewart, and I. E. M. Smith (2007), Transition from effusive to explosive phases in andesite eruptions - A case-study from the AD1655 eruption of Mt. Taranaki, New Zealand, *Journal of Volcanology and Geothermal Research*, *161*(1–2), 15–34, doi:10.1016/j.jvolgeores.2006.11.005.

Polacci, M., L. Pioli, and M. Rosi (2003), The Plinian phase of the Campanian Ignimbrite eruption (Phlegrean Fields, Italy): evidence from density measurements and textural characterization of pumice, *Bulletin of Volcanology*, *65*, 418–432, doi:10.1007/s00445-002-0268-4.

Polacci, M., C. Bouvet de Maisonneuve, D. Giordano, M. Piochi, L. Mancini, W. Degruyter, and O. Bachmann (2014), Permeability measurements of Campi Flegrei pyroclastic products: An example from the Campanian Ignimbrite and Monte Nuovo eruptions, *Journal of Volcanology and Geothermal Research*, *272*, 16–22, doi:10.1016/j.jvolgeores.2013.12.002.

Quane, S. L., J. K. Russel, and E. A. Friedlander (2009), Time scales of compaction in volcanic systems, *Geology*, *37*(5), 471–474, doi:10.1130/G25625A.

Ramírez-Ruiz, J. J., H. Santiago-Jiménez, E. Alatorre-Chávez, and M. Bretón-González (2002), EDM deformation monitoring of the 1997-2000 activity at Volcán de Colima, *Journal of Volcanology and Geothermal Research*, *117*(1–2), 61–67, doi:10.1016/s0377-0273(02)00235-4.

Ratté, J. C. (2004), A guide to the Mule Creek Volcanic Vent, the rhyolite of Potholes Country, and obsidian ledges, Gila National Forest, southwestern New Mexico., *New Mexico Geology*, *26*(4), 111–122.

Read, C. (2006), Alaska volcano observatory (usgs), `http://www.avo.alaska.edu/images/image.php?id=11205`, accessed: 08-10-2013.

Roberge, J., H. Delgado-Granados, and P. J. Wallace (2009), Mafic magma recharge supplies high CO_2 and SO_2 gas fluxes from Popocatépetl volcano, Mexico, *Geology*, *37*(2), 107–110, doi:10.1130/G25242A.1.

Roscoe, R. (2014), PhotoVolcanica, `http://www.photovolcanica.com/VolcanoInfo/Santiaguito/Santiaguito.html`, accessed: 10-03-2014.

Rose, W. I. (1972), Santiaguito Volcanic Dome, Guatemala, *Geological Society of America Bulletin*, *83*(5), 1413–1434, doi:10.1130/0016-7606(1972)83[1413:SVDG]2.0.CO;2.

Rose, W. I. (1987), Volcanic activity at Santiaguito volcano, 1976-1984, *Geological Society of America Special Papers*, *212*, 17–28, doi:10.1130/SPE212-p17.

Rose, W. I., R. E. Stoiber, and L. L. Malinconico (1982), Eruptive gas compositions and fluxes of explosive volcanoes: Budget of S and Cl emitted from Fuego volcano, Guatemala, in *Andesites: Orogenic Andesites and Related Rocks*, edited by R. Thorpe, pp. 669–676, Wiley.

Rust, A. C., and K. V. Cashman (2004), Permeability of vesicular silicic magma: inertial and hysteresis effects, *Earth and Planetary Science Letters*, *228*(1–2), 93–107, doi:10.1016/j.epsl.2004.09.025.

Rust, A. C., and K. V. Cashman (2011), Permeability controls on expansion and size distributions of pyroclasts, *Journal of Geophysical Research*, *116*(B11), B11202, doi:10.1029/2011JB008494.

Rust, A. C., K. V. Cashman, and P. J. Wallace (2004), Magma degassing buffered by vapor flow through brecciated conduit margins, *Geology*, *32*(4), 349–352, doi:10.1130/G20388.2.

Saar, M. O., and M. Manga (1999), Permeability-porosity relationship in vesicular basalts, *Geophysical Research Letters*, *26*(1), 111–114, doi:10.1029/1998GL900256.

Sahetapy-Engel, S. T., and A. J. L. Harris (2009a), Thermal-image-derived dynamics of vertical ash plumes at Santiaguito volcano, Guatemala, *Bulletin of Volcanology*, *71*(7), 827–830, doi:10.1007/s00445-009-0284-8.

Sahetapy-Engel, S. T., and A. J. L. Harris (2009b), Thermal structure and heat loss at the summit crater of an active lava dome, *Bulletin of Volcanology*, *71*(1), 15–28, doi:10.1007/s00445-008-0204-3.

Sahetapy-Engel, S. T., A. J. L. Harris, and E. Marchetti (2008), Thermal, seismic and infrasound observations of persistent explosive activity and conduit dynamics at Santiaguito lava dome, Guatemala, *Journal of Volcanology and Geothermal Research*, *173*(1–2), 1–14, doi:10.1016/j.jvolgeores.2007.11.026.

Sahetapy-Engel, S. T. M., L. P. Flynn, A. J. L. Harris, G. J. Bluth, W. I. Rose, and O. Matias (2004), Surface temperature and spectral measurements at Santiaguito lava dome, Guatemala, *Geophysical Research Letters*, *31*(19), L19610, doi:10.1029/2004GL020683.

Sahimi, M. (1994), *Applications of percolation theory*, Taylor & Francis Ltd.

Sanderson, R. W., J. B. Johnson, and J. M. Lees (2010), Ultra-long period seismic signals and cyclic deflation coincident with eruptions at Santiaguito volcano, Guatemala, *Journal of Volcanology and Geothermal Research*, *198*(1–2), 35–44, doi:10.1016/j.jvolgeores.2010.08.007.

Savov, I. P., J. F. Luhr, and C. Navarro-Ochoa (2008), Petrology and geochemistry of lava and ash erupted from Volcán Colima, Mexico, during 1998-2005, *Journal of Volcanology and Geothermal Research*, *174*(4), 241–256, doi:10.1016/j.jvolgeores.2008.02.007.

Scharff, L., M. Hort, and A. Gerst (2014), The dynamics of the dome at Santiaguito volcano, Guatemala, *Geophysical Journal International*, *197*(2), 926–942, doi:10.1093/gji/ggu069.

Schneider, A., A. W. Rempel, and K. V. Cashman (2012), Conduit degassing and thermal controls on eruption styles at Mount St. Helens, *Earth and Planetary Science Letters*, *357–358*, 347–354, doi:10.1016/j.epsl.2012.09.045.

Scott, J. A. J. (2013), *The Santiaguito volcanic dome complex, Guatemala*, University of Oxford.

Scott, J. A. J., T. A. Mather, D. M. Pyle, W. I. Rose, and G. Chigna (2012), The magmatic plumbing system beneath Santiaguito Volcano, Guatemala, *Journal of Volcanology and Geothermal Research*, *237-238*, 54–68, doi:10.1016/j.jvolgeores.2012.05.014.

Scott, W. E., D. R. Sherrod, and C. A. Gardner (2008), Overview of the 2004 to 2006, and Continuing, Eruption of Mount St. Helens, Washington, in *A Volcano Rekindled: The Renewed Eruption of Mount St. Helens, 2004-2006*, vol. 1750, edited by D. R. Sherrod, W. E. Scott, and P. H. Stauffer, pp. 3–22, U.S. Geological Survey Professional Paper.

Sharma, K., S. Blake, S. Self, and A. J. Krueger (2004), SO_2 emissions from basaltic eruptions, and the excess sulfur issue, *Geophysical Research Letters*, *31*, L13612, doi:10.1029/2004GL019688.

Shepherd, J. B., R. A. Herd, P. Jackson, and R. Watts (1998), Ground deformation measurements at the Soufriere Hills Volcano, Montserrat: II: Rapid static GPS measurements June 1996–June 1997, *Geophysical Research Letters*, *25*(18), 3413–3416, doi:10.1029/98GL01655.

Shinohara, H. (2005), A new technique to estimate volcanic gas composition: plume measurements with a portable multi-sensor system, *Journal of Volcanology and Geothermal Research*, *143*(4), 319–333, doi:10.1016/j.jvolgeores.2004.12.004.

Sparks, R. S. J. (1978), The dynamics of bubble formation and growth in magmas: A review and analysis, *Journal of Volcanology and Geothermal Research*, *3*(1–2), 1–37, doi:10.1016/0377-0273(78)90002-1.

Sparks, R. S. J. (1997), Causes and consequences of pressurisation in lava dome eruptions., *Earth and Planetary Science Letters*, *150*(3–4), 177–189, doi:10.1016/s0012-821x(97)00109-x.

Sparks, R. S. J. (2003a), Dynamics of magma degassing, in *Volcanic Degassing*, vol. 213, edited by C. Oppenheimer, D. M. Pyle, and J. Barclay, pp. 5–22, Geological Society, Special Publications, doi:10.1144/GSL.SP.2003.213.01.02.

Sparks, R. S. J. (2003b), Forecasting volcanic eruptions, *Earth and Planetary Science Letters*, *210*, 1–5, doi:10.1016/S0012-821X(03)00124-9.

Sparks, R. S. J., and H. Pinkerton (1978), Effects of degassing on rheology of basaltic lava, *Nature*, *276*, 385–386, doi:10.1038/276385a0.

Sparks, R. S. J., M. D. Murphy, A. M. Lejeune, R. B. Watts, J. Barclay, and S. R. Young (2000), Control on the emplacement of the andesite lava dome of the Soufriere Hills volcano, Montserrat by degassing-induced crystallization, *Terra Nova*, *12*(1), 14–20, doi:10.1046/j.1365-3121.2000.00267.x.

Sparks, R. S. J., J. Biggs, and J. W. Neuberg (2012), Monitoring Volcanoes, *Science*, *335*(6074), 1310–1311, doi:10.1126/science.1219485.

Sparks, R. S. J., W. P. Aspinall, H. S. Crosweller, and T. K. Hincks (2013), Risk and uncertainty assessment of volcanic hazards, in *Risk and Uncertainty Assessment for Natural Hazards*, pp. 364–397, Cambridge University Press.

Spera, F. J. (2000), Physical properties of magma, in *Encyclopedia of Volcanoes*, edited by H. Sigurdsson, B. Houghton, S. Mcnutt, H. Rymer, and J. Stix, pp. 171–190, Academic Press.

Stasiuk, M. V., J. Barclay, M. R. Carroll, C. Jaupart, J. C. Ratté, R. S. J. Sparks, and S. R. Tait (1996), Degassing during magma ascent in the Mule Creek vent (USA), *Bulletin of Volcanology*, *58*(2–3), 117–130, doi:10.1007/s004450050130.

Stinton, A. J., P. D. Cole, H. M. Odbert, T. Christopher, G. Avard, and M. Bernstein (2014), Dome growth and valley fill during Phase 5 (8 October 2009-11 February 2010) at the Soufrière Hills Volcano, Montserrat, in *The Eruption of Soufrière Hills Volcano, Montserrat, from 2000 to 2010*, vol. 39, edited by G. Wadge, R. E. A. Robertson, and B. Voight, pp. 113–131, Geological Society, London, Memoirs, doi:10.1144/M39.6.

Stix, J., and H. Gaonac'h (2000), Gas, Plume and Thermal Monitoring, in *Encyclopedia of Volcanoes*, edited by H. Sigurdsson, pp. 1141–1163, Academic Press.

Stix, J., J. A. G. Zapata, M. V. Calvache, G. P. J. Cortés, T. P. Fischer, D. M. Gómez, L. M. Narvaez, M. V. Ordoñez, A. E. Ortega, R. C. Torres, and S. N. Williams (1993), A model of degassing at Galeras Volcano, Columbia, 1988-1993, *Geology*, *21*(11), 963–967.

Stoiber, R. E., and A. Jepsen (1973), Sulfur Dioxide Contributions to the Atmosphere by Volcanoes, *Science*, *182*(4112), 577–578, doi:10.1126/science.182.4112.577.

Surono, P. Jousset, J. Pallister, M. Boichu, M. F. Buongiorno, A. Budisantoso, F. Costa, S. Andreastuti, F. Prata, D. Schneider, L. Clarisse, H. Humaida, S. Sumarti, C. Bignami, J. Griswold, S. Carn, C. Oppenheimer, and F. Lavigne (2012), The 2010 explosive eruption of Java's Merapi volcano - A '100-year' event, *Journal of Volcanology and Geothermal Research*, *241–242*, 121–135, doi:10.1016/j.jvolgeores.2012.06.018.

Tait, S., R. Thomas, J. Gardner, and C. Jaupart (1998), Constraints on cooling rates and permeabilities of pumice in an explosive eruption jet from colour and magnetic mineralogy, *Journal of Volcanology and Geothermal Research*, *86*(1–4), 79–91, doi:10.1016/s0377-0273(98)00075-4.

Takeuchi, S., S. Nakashima, A. Tomiya, and H. Shinohara (2005), Experimental constraints on the low gas permeability of vesicular magma during decompression, *Geophysical Research Letters*, *32*(10), L10312, doi:10.1029/2005GL022491.

Takeuchi, S., S. Nakashima, and A. Tomiya (2008), Permeability measurements of natural and experimental volcanic materials with a simple permeameter: Toward an understanding of magmatic degassing processes, *Journal of Volcanology and Geothermal Research*, *177*(2), 329–339, doi:10.1016/j.jvolgeores.2008.05.010.

Takeuchi, S., A. Tomiya, and H. Shinohara (2009), Degassing conditions for permeable silicic magmas: Implications from decompression experiments with constant rates, *Earth and Planetary Science Letters*, *283*(1–4), 101–110, doi:10.1016/j.epsl.2009.04.001.

Taran, Y., J. C. Gavilanes, and A. Cortés (2002), Chemical and isotopic composition of fumarolic gases and the SO_2 flux from Volcán de Colima, México, between the 1994 and 1998 eruptions, *Journal of Volcanology and Geothermal Research*, *117*(1–2), 105–119, doi:10.1016/s0377-0273(02)00239-1.

Taran, Y. A., N. R. Varley, S. Inguaggiato, and E. Cienfuegos (2010), Geochemistry of H_2- and CH_4-enriched hydrothermal fluids of Socorro Island, Revillagigedo Archipelago, Mexico. Evidence for serpentinization and abiogenic methane, *Geofluids*, *10*(4), 542–555, doi:10.1111/j.1468-8123.2010.00314.x.

Taylor, B. E., J. C. Eichelberger, and H. R. Westrich (1983), Hydrogen isotopic evidence of rhyolitic magma degassing during shallow intrusion and eruption, *Nature*, *306*, 541–545, doi:10.1038/306541a0.

Thomas, M. E., and J. Neuberg (2012), What makes a volcano tick - A first explanation of deep multiple seismic sources in ascending magma, *Geology*, *40*(4), 351–354, doi:10.1130/G32868.1.

Tilling, R. I. (1989), Volcanic hazards and their mitigation: Progress and problems, *Reviews of Geophysics*, *27*(2), 237–269, doi:10.1029/RG027i002p00237.

Trofimovs, J., C. Foster, R. S. J. Sparks, S. Loughlin, A. Le Friant, C. Deplus, L. Porritt, T. Christopher, R. Luckett, P. J. Talling, M. R. Palmer, and T. Le Bas (2012), Submarine pyroclastic deposits formed during the 20th May 2006 dome collapse of the Soufrière Hills Volcano, Montserrat, *Bulletin of Volcanology*, *74*(2), 391–405, doi:10.1007/s00445-011-0533-5.

Tuffen, H., D. B. Dingwell, and H. Pinkerton (2003), Repeated fracture and healing of silicic magma generate flow banding and earthquakes?, *Geology*, *31*(12), 1089–1092, doi:10.1130/G19777.1.

Vallance, J. W., D. J. Schneider, and S. P. Schilling (2008), Growth of the 2004-2006 Lava-Dome Complex at Mount St. Helens, Washington, in *A Volcano Rekindled: The Renewed Eruption of Mount St. Helens, 2004-2006*, vol. 1750, edited by D. R. Sherrod, W. E. Scott, and P. H. Stauffer, pp. 169–208, U.S. Geological Survey Professional Paper.

Versteeg, H. K., and W. Malalasekera (2007), *An Introduction to Computational Fluid Dynamics: The Finite Volume Method*, 2 ed., 511 pp., Pearson Education Limited.

Voight, B. (1990), The 1985 Nevado del Ruiz volcano catastrophe: anatomy and retrospection, *Journal of Volcanology and Geothermal research*, *44*(3–4), 349–386, doi:10.1016/0377-0273(90)90027-D.

Voight, B., and D. Elsworth (2000), Instability and collapse of hazardous gas-pressurized lava domes, *Geophysical Research Letters*, *27*(1), 1–4, doi:10.1029/1999GL008389.

Voight, B., R. P. Hoblitt, A. B. Clarke, A. B. Lockhart, A. D. Miller, L. Lynch, and J. McMahon (1998), Remarkable cyclic ground deformation monitored in real-time on Montserrat, and its use in eruption forecasting, *Geophysical Research Letters*, *25*(18), 3405–3408, doi:10.1029/98GL01160.

Voight, B., R. S. J. Sparks, A. D. Miller, R. C. Stewart, R. P. Hoblitt, A. Clarke, J. Ewart, W. P. Aspinall, B. Baptie, E. S. Calder, P. Cole, T. H. Druitt, C. Hartford, R. A. Herd, P. Jackson, A. M. Lejeune, A. B. Lockhart, S. C. Loughlin, R. Luckett, L. Lynch, G. E. Norton, R. Robertson, I. M. Watson, R. Watts, and S. R. Young (1999), Magma Flow Instability and Cyclic Activity at Soufriere Hills Volcano, Montserrat, British West Indies, *Science*, *283*(5405), 1138–1142, doi:10.1126/science.283.5405.1138.

Voight, B., A. T. Linde, I. S. Sacks, G. S. Mattioli, R. S. J. Sparks, D. Elsworth, D. Hidayat, P. E. Malin, E. Shalev, C. Widiwijayanti, S. R. Young, V. Bass, A. Clarke, P. Dunkley, W. Johnston, N. McWhorter, J. Neuberg, and P. Williams (2006), Unprecedented pressure increase in deep magma reservoir triggered by lava-dome collapse, *Geophysical Research Letters*, *33*(3), L03312, doi:10.1029/2005GL024870.

Voight, B., D. Hidayat, S. Sacks, A. Linde, L. Chardot, A. Clarke, D. Elsworth, R. Foroozan, P. Malin, G. Mattioli, N. McWhorter, E. Shalev, R. S. J. Sparks, C. Widiwijayanti, and S. R. Young (2010a), Unique strainmeter obervations of Vulcanian explosions, Soufrière Hills Volcano, Montserrat, July 2003, *Geophysical Research Letters*, *37*(19), L00E18, doi:10.1029/2010GL042551.

Voight, B., C. Widiwijayanti, G. Mattioli, D. Elsworth, D. Hidayat, and M. Strutt (2010b), Magma-sponge hypothesis and stratovolcanoes: Case for a compressible reservoir and quasi-steady deep influx at Soufrière Hills Volcano, Montserrat, *Geophysical Research Letters*, *37*, L00E05, doi:10.1029/2009GL041732.

Wadge, G., G. S. Mattioli, and R. A. Herd (2006), Ground deformation at Soufrière Hills Volcano, Montserrat during 1998-2000 measured by radar interferometry and GPS, *Journal of Volcanology and Geothermal Research*, *152*(1–2), 157–173, doi:10.1016/j.jvolgeores.2005.11.007.

Wadge, G., G. Ryan, and E. S. Calder (2009), Clastic and core lava components of a silicic lava dome, *Geology*, *37*(6), 551–554, doi:10.1130/G25747A.1.

Wadge, G., B. Voight, R. S. J. Sparks, P. D. Cole, S. C. Loughlin, and R. E. A. Robertson (2014), An overview of the eruption of Soufrière Hills Volcano, Montserrat from 2000 to 2010, in *The Eruption of Soufrière Hills Volcano, Montserrat, from 2000 to 2010*, vol. 39, edited by G. Wadge, R. E. A. Robertson, and B. Voight, pp. 1–39, Geological Society, London, Memoirs, doi:10.1144/M39.1.

Wallace, P. J. (2001), Volcanic SO_2 emissions and the abundance and distribution of exsolved gas in magma bodies, *Journal of Volcanology and Geothermal Research*, *108*(1–4), 85–106, doi:10.1016/s0377-0273(00)00279-1.

Wallace, P. J., and T. M. Gerlach (1994), Magmatic Vapor Source for Sulfur Dioxide Released During Volcanic Eruptions: Evidence from Mount Pinatubo, *Science*, *265*(5171), 497–499, doi:10.1126/science.265.5171.497.

Walsh, S. D. C., and M. O. Saar (2008), Magma yield stress and permeability: Insights from multiphase percolation theory, *Journal of Volcanology and Geothermal Research*, *177*(4), 1011–1019, doi:10.1016/j.jvolgeores.2008.07.009.

Watson, I. M., C. Oppenheimer, B. Voight, P. W. Francis, A. Clarke, J. Stix, A. Miller, D. M. Pyle, M. R. Burton, S. R. Young, G. Norton, S. Loughlin, B. Darroux, and MVO Staff (2000), The relationship between degassing and ground deformation at Soufriere Hills Volcano, Montserrat, *Journal of Volcanology and Geothermal Research*, *98*(1–4), 117–126, doi:10.1016/s0377-0273(99)00187-0.

Watts, R. B., R. A. Herd, R. S. J. Sparks, and S. R. Young (2002), Growth patterns and emplacement of the andesitic lava dome at Soufrière Hills Volcano, Montserrat, in *The Eruption of Soufrière Hills Volcano, Montserrat, from 1995 to 1999*, vol. 21, edited by T. H. Druitt and B. P. Kokelaar, pp. 115–152, Geological Society, London, Memoirs.

Westrich, H. R., and J. C. Eichelberger (1994), Gas transport and bubble collapse in rhyolitic magma: an experimental approach, *Bulletin of Volcanology*, *56*(6–7), 447–458, doi:10.1007/BF00302826.

Williams-Jones, G., J. Stix, M. Heiligmann, A. Charland, B. Sherwood Lollar, N. Arner, G. V. Garzón, J. Barquero, and E. Fernandez (2000), A model of diffuse degassing at three subduction-related volcanoes, *Bulletin of Volcanology*, *62*(2), 130–142, doi:10.1007/s004450000075.

Williamson, B. J., A. Di Muro, C. J. Horwell, O. Spieler, and E. W. Llewellin (2010), Injection of vesicular magma into an andesitic dome at the effusive-explosive transition, *Earth and Planetary Science Letters*, *295*, 83–90, doi:10.1016/j.epsl.2010.03.027.

Woods, A. W. (1995), The dynamics of explosive volcanic eruptions, *Reviews of Geophysics*, *33*(4), 495–530, doi:10.1029/95RG02096.

Woods, A. W., and T. Koyaguchi (1994), Transitions between explosive and effusive eruptions of silicic magmas, *Letters to Nature*, *370*, 641–644, doi:10.1038/370641a0.

Wright, H. M., and K. V. Cashman (2013), Compaction and gas loss in welded pyroclastic deposits as revealed by porosity, permeability, and electrical conductivity measurements of the Shevlin Park Tuff, *Geological Society of America Bulletin*, *126*(1-2), 234–247, doi:10.1130/B30668.1.

Wright, H. M. N., J. J. Roberts, and K. V. Cashman (2006a), Permeability of anisotropic tube pumice: Model calculations and measurements, *Geophysical Research Letters*, *33*(17), L17316, doi:10.1029/2006GL027224.

Wright, H. M. N., K. V. Cashman, M. Rosi, and R. Cioni (2006b), Breadcrust bombs as indicators of Vulcanian eruption dynamics at Guagua Pichincha volcano, Ecuador, *Bulletin of Volcanology*, *69*(3), 281–300, doi:10.1007/s00445-006-0073-6.

Wright, H. M. N., K. V. Cashman, E. H. Gottesfeld, and J. J. Roberts (2009), Pore structure of volcanic clasts: Measurements of permeability and electrical conductivity, *Earth and Planetary Science Letters*, *280*(1–4), 93–104, doi:10.1016/j.epsl.2009.01.023.

Yallup, C., M. Edmonds, and A. V. Turchyn (2013), Sulfur degassing due to contact metamorphism during flood basalt eruptions, *Geochimica et Cosmochimica Acta*, *120*, 263–279, doi:10.1016/j.gca.2013.06.025.

Yokoyama, T., and S. Takeuchi (2009), Porosimetry of vesicular volcanic products by a water-expulsion method and the relationship of pore characteristics to permeability, *Journal of Geophysical Research*, *114*(B2), B02201, doi:10.1029/2008JB005758.

Young, S. R., P. W. Francis, J. Barclay, T. J. Casadevall, C. A. Gardner, B. Darroux, M. A. Davies, P. Delmelle, G. E. Norton, A. J. H. Maciejewski, C. M. M. Oppenheimer, J. Stix, and I. M. Watson (1998), Monitoring SO_2 emission at the Soufriere Hills Volcano: Implications for changes in eruptive conditions, *Geophysical Research Letters*, *25*(19), 3681–3684, doi:10.1029/98GL01406.

Young, S. R., B. Voight, and H. J. Duffell (2003), Magma extrusion dynamics revealed by high-frequency gas monitoring at Soufrière Hills volcano, Montserrat, in *Volcanic Degassing*, vol. 213, edited by C. Oppenheimer, D. Pyle, and J. Barclay, pp. 219–230, Geological Society, London, Special Publications, doi:10.1144/GSL.SP.2003.213.01.13.

Zelenski, M. E., T. P. Fischer, J. M. de Moor, B. Marty, L. Zimmermann, D. Ayalew, A. N. Nekrasov, and V. K. Karandashev (2013), Trace elements in the gas emissions from the Erte Ale volcano, Afar, Ethiopia, *Chemical Geology*, *357*, 95–116, doi:10.1016/j.chemgeo.2013.08.022.

Appendix A

Analytical Solutions

In contrast to the approximate solutions yielded from the finite element method (FEM), analytical solutions are a way to define the actual solution to a problem through the use of common mathematical operations and functions. Unfortunately, analytical solutions to problems are only possible for basic scenarios with simple geometries. However, deriving analytical solutions for these simplistic scenarios and comparing the results to those provided using FEM lends credence to the FEM results for more complex situations.
Analytical solutions are presented here for simple one-, two- and three-dimensional problems using Darcy's law. For each problem the analytical method is documented before the results are compared to the numerical solution using Comsol Multiphysics®.

A.1 1D homogeneous model

The first example is the most simplistic problem of one-dimensional flow within a homogeneous medium (Figure A.1). In this scenario, the pressure gradient is calculated according to $\nabla P = \frac{\Delta P}{L}$, where L is the length over which the pressure drops (ΔP). Consequently, the pressure may be derived according to:

$$P = P_0 - \frac{\Delta P}{L} x \tag{A.1}$$

where x is the location within the domain. Finally, the gas velocity is calculated from Darcy's law:

$$\boldsymbol{u} = -\frac{k}{\mu} \nabla P \tag{A.2}$$

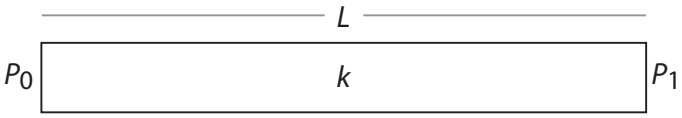

Figure A.1: Model setup for a one-dimensional homogeneous system. Pressure is applied to two boundaries as P_0 (inlet) and P_1 (outlet), and the permeability is set as k. The length of the domain is specified by L. For every point, x inside the domain, there is a pressure (P), pressure gradient (∇P) and a gas velocity ($\boldsymbol{u}$).

A.1.1 Analysis of Results

An example of this problem, with inlet pressure (P_0) 10 MPa, outlet pressure (P_1) 0 Pa, length (L) 1000 m and permeability (k) 10^{-12} m^2, is shown in Figure A.2. The analytical solution is plotted in addition to the numerical solution for 3 different meshes. The numerical results for both the pressure and gas velocity show a very good correlation with the analytical solution.

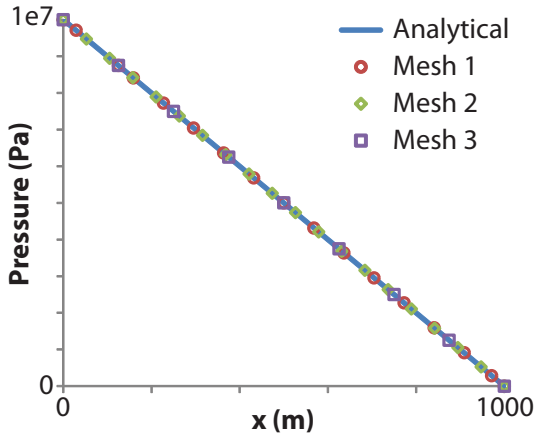

Figure A.2: Comparison between the analytical and numerical solutions for 3 different meshes. Mesh 1: 32, Mesh 2: 19, Mesh 3: 4. All results agree with a gas velocity of 6.67×10^{-4} ms^{-1}.

A.2 1D layered model

The previous homogeneous model may be adapted to investigate a layered system (Figure A.3). The method presented here provides a general method for calculating the solution for any layered 1D problem.

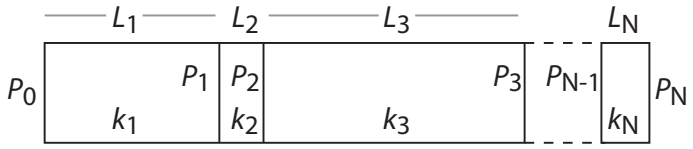

Figure A.3: Model setup showing a one-dimensional system with N layers. Pressure is applied to two boundaries as P_0 and P_N, and permeabilities are set to each layer as k_N. The length of each domain is specified by L_N, and the pressure gradient within each layer as ∇P_N.

The problem is a one-dimensional incompressible system, and therefore, the gas velocity is constant across the entire length. To account for the variations in permeability across the system, the average permeability ($\overline{k}$) is included in Darcy's law and the pressure gradient is rewritten as $\dfrac{\Delta P}{L}$:

$$u = -\frac{\overline{k}}{\mu}\left(\frac{\Delta P}{L}\right) \tag{A.3}$$

Consequently, by accounting for each permeability (k_N) and layer length (L_N), the gas velocity throughout the system is calculated according to:

$$u = \frac{-\dfrac{(P_N - P_0)}{\mu}}{\left(\dfrac{L_1}{k_1} + \dfrac{L_2}{k_2} + ... + \dfrac{L_N}{k_N}\right)} \tag{A.4}$$

Once the gas velocity is known, the interface pressure (P_N) between each layer may be calculated, relative to the previous interface (or inlet) pressure (P_{N-1}):

$$P_N = P_{N-1} - u\mu\left(\frac{L_N}{k_N}\right) \tag{A.5}$$

Determining the pressure at each interface then allows the pressure gradient across each layer to be determined, and therefore the pressure at any point (x) within a layer may be calculated:

$$P = P_{N-1} - \nabla P(x - x_{N-1}) \tag{A.6}$$

where P_{N-1} is the previous interface (or inlet) pressure, x is the location and x_{N-1} is the location of the previous interface.

A.2.1 Analysis of Results

The results for this problem are calculated for 4 different models with different layer thickness's and permeabilities (Table A.1). Each analytical solution (Figure A.4) is compared to the numerical results for 3 different meshes (Table A.2). As with the homogeneous scenario, all the layered models show a good correlation between the pressure and gas velocity results regardless of the number of mesh elements used.

Model	**Domain**	**Thickness (m)**	**Permeability (m^2)**
1	1	700	10^{-10}
	2	300	10^{-12}
2	1	700	10^{-12}
	2	300	10^{-10}
3	1	250	10^{-16}
	2	300	10^{-12}
	3	450	10^{-15}
4	1	250	10^{-12}
	2	100	10^{-10}
	3	200	10^{-12}
	4	150	10^{-10}
	5	300	10^{-12}

Table A.1: The thickness and permeability for the layers in each of the four models.

Model	**Mesh 1**	**Mesh 2**	**Mesh 3**	**Velocity (ms^{-1})**
1	40	20	4	2.17×10^{-3}
2	40	20	4	9.48×10^{-4}
3	40	20	4	2.26×10^{-7}
4	54	20	5	8.86×10^{-4}

Table A.2: The number of mesh elements used and the gas velocity through the one-dimensional layered system. Model **4** has more elements than the other models due to the large number of layers. For each model, all three mesh configurations show a good agreement with the velocity derived analytically.

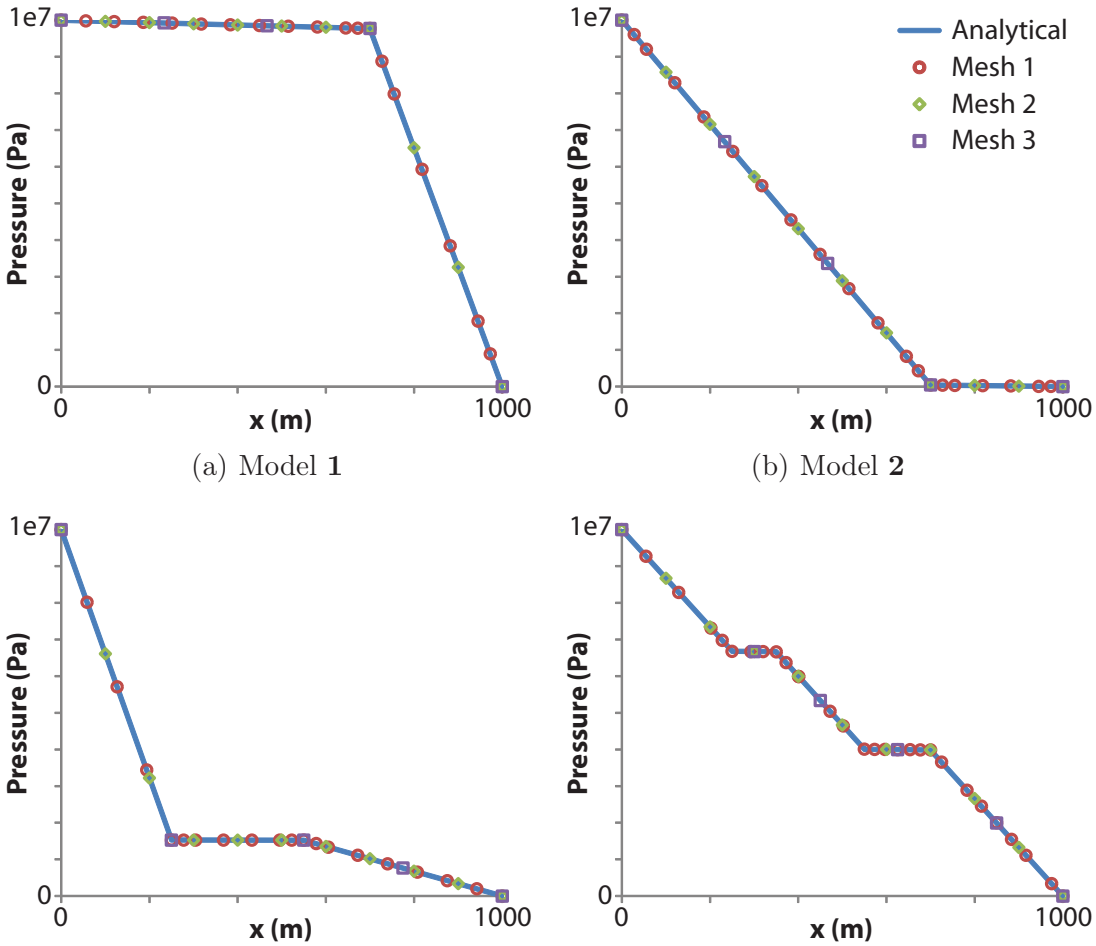

(a) Model **1**

(b) Model **2**

(c) Model **3**

(d) Model **4**

Figure A.4: The analytical and numerical pressure results for each model run. There is a very good agreement between the analytical and numerical results, even for the coarsest mesh.

A.3 2D circular flow

The first two-dimensional scenario investigates circular flow (Figure A.5). This setup could represent flow around an impermeable object.

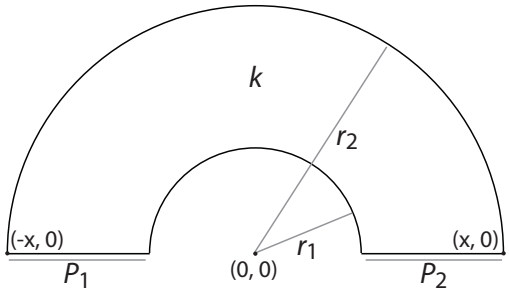

Figure A.5: Setup for two-dimensional circular flow. The gas flows from the inlet (P_1) to the outlet at P_2. The two circles have their centre at the origin $(0, 0)$ and the extremes of the outer circle are located at $(-x, 0)$ and $(x, 0)$.

The problem may be described analytically by an infinite number of circles, centred about the origin $(0, 0)$ of the form:

$$x^2 + y^2 = r^2 \tag{A.7}$$

where $r = \sqrt{x^2 + y^2}$. For each circle, the same angle of rotation clockwise has the same pressure. Therefore, the pressure for any point (x, y) may be derived from:

$$P = P_1 - \frac{\Delta P}{\pi}\left(\pi - \cos^{-1}\left(\frac{x}{r}\right)\right) \tag{A.8}$$

and the pressure gradient according to:

$$\nabla P = \frac{\Delta P}{\pi r} \tag{A.9}$$

where πr is the arc length for each semi-circle. The velocity is calculated according to Darcy's law in the usual form:

$$\boldsymbol{u} = -\frac{k}{\mu}\nabla P \tag{A.10}$$

The flow of gas follows the path of each circle and therefore its direction may be defined as the tangent of the circle at any point.

A.3.1 Analysis of results

Figure A.6 shows the results for 2D circular flow in a homogeneous space with a permeability of 10^{-12} m^2. The inner (r_1) and outer (r_2) radii are located at 25 m and 150 m, respectively. A comparison between the analytical and numerical results is also shown for three different mesh densities. For this scenario, there is good agreement between the two sets of results for both the pressure and gas velocity.

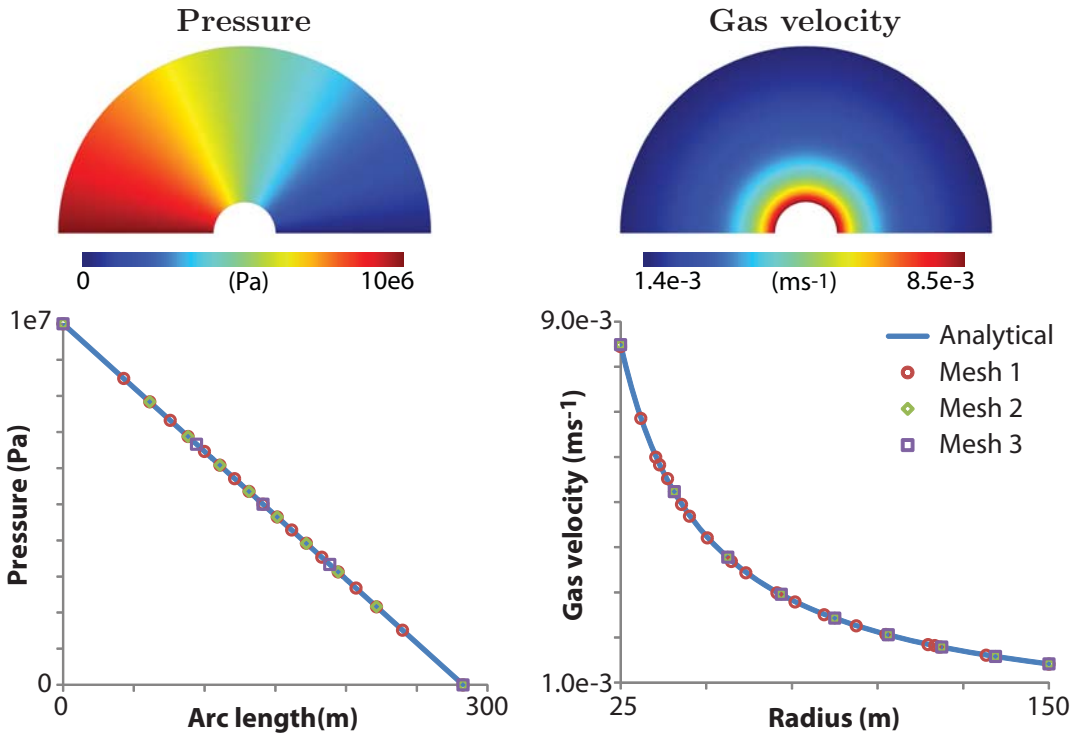

Figure A.6: Pressure along the circle with radius 90 m and the velocity at $y = 0$. Mesh 1: 400, Mesh 2: 240, Mesh 3: 12.

A.3.2 Layered circular flow

This method may be extend for a hemispherical model containing multiple domains, each boundary is drawn perpendicular to the circles. The coordinates where the boundary between domains intersects the circles is calculated according to:

$$x = rcos\left(\frac{a}{b}\pi\right)$$
$$y = \sqrt{r^2 - x^2}$$

where $\frac{a}{b}\pi$ is the sector angle. Consequently, the velocity may be calculated according to:

$$\boldsymbol{u} = -\frac{\frac{\Delta P}{\mu}}{\left(\frac{a_1\pi r}{b_1 k_1} + \frac{a_2\pi r}{b_2 k_2} + ... + \frac{a_N\pi r}{b_N k_N}\right)} \tag{A.11}$$

From the velocity, the interface pressure may be calculated from:

$$P_N = P_{N-1} - \boldsymbol{u}\mu\left(\frac{a_N\pi r}{b_N k_N}\right) \tag{A.12}$$

and the pressure gradient in each domain:

$$\nabla P_N = \frac{(P_N - P_{N-1})(b_N k_N)}{a_N\pi r} \tag{A.13}$$

or more generally, from the velocity as:

$$\nabla P = -\frac{\boldsymbol{u}\mu}{k} \tag{A.14}$$

A.3.3 Analysis of results

Layered circular flow in two dimensions is simulated in two models (Table A.3). In Model **1**, there are two layers, whilst Model **2** has five layers. The layer extent is determined by the sector angle. Consequently, the thickness of each layer increases outwards with the radius. The two models are run for three different mesh densities (Table A.4). The pressure and gas velocity results along with a comparison between the analytical and numerical solutions are shown in Figures A.7 and A.8 for Model **1** and **2**, respectively. The measurement for the pressure is taken along the circle with a radius of 90 m, whilst the gas velocity is measured along the line $x = 0$ (vertically upwards through the centre). The numerical results show a very good agreement with the analytical solution, even for the lowest mesh density.

Model	Domain	Sector angle	Permeability (m^2)
1	1	$\frac{1}{2}\pi$	10^{-10}
	2	$\frac{1}{2}\pi$	10^{-12}
2	1	$\frac{1}{4}\pi$	10^{-12}
	2	$\frac{1}{10}\pi$	10^{-10}
	3	$\frac{1}{5}\pi$	10^{-12}
	4	$\frac{3}{20}\pi$	10^{-10}
	5	$\frac{3}{10}\pi$	10^{-12}

Table A.3: The sector angle and permeability for the layers in the two circular models. The sector angle represents the portion of the model taken up by each layer.

Model	Mesh 1	Mesh 2	Mesh 3
1	482	192	12
2	488	242	16

Table A.4: The number of elements in each mesh used in the two models for circular flow.

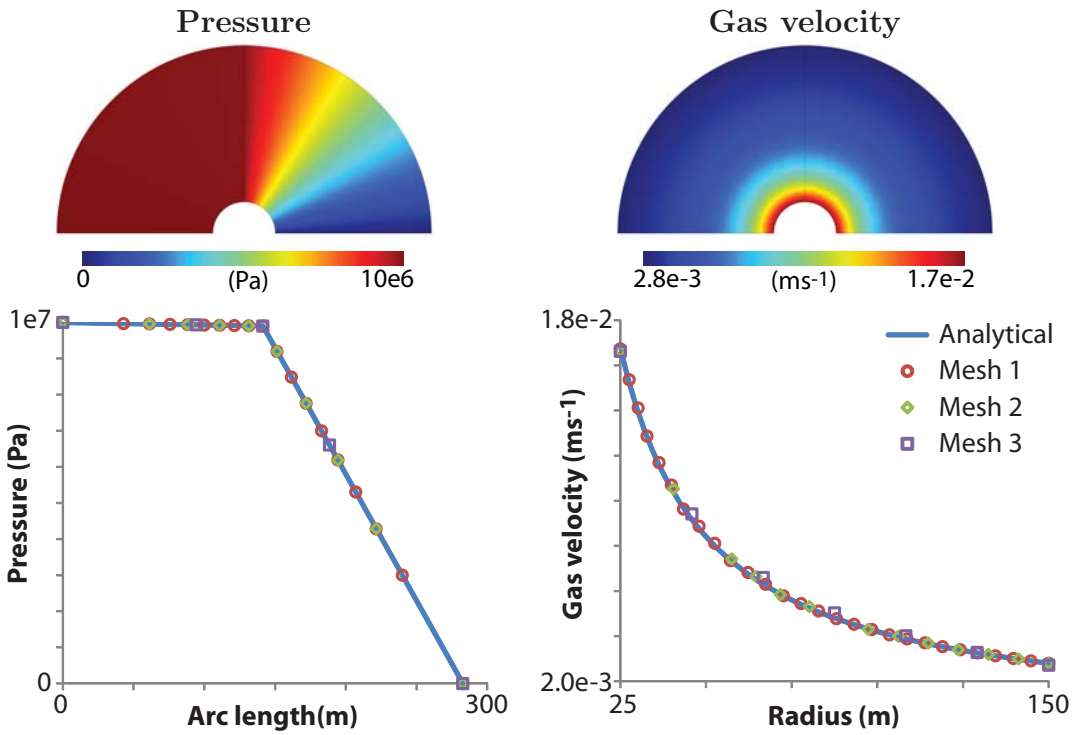

Figure A.7: Pressure along the circle with radius 90 m and gas velocity at $x = 0$ for Model **1** with 2 layers.

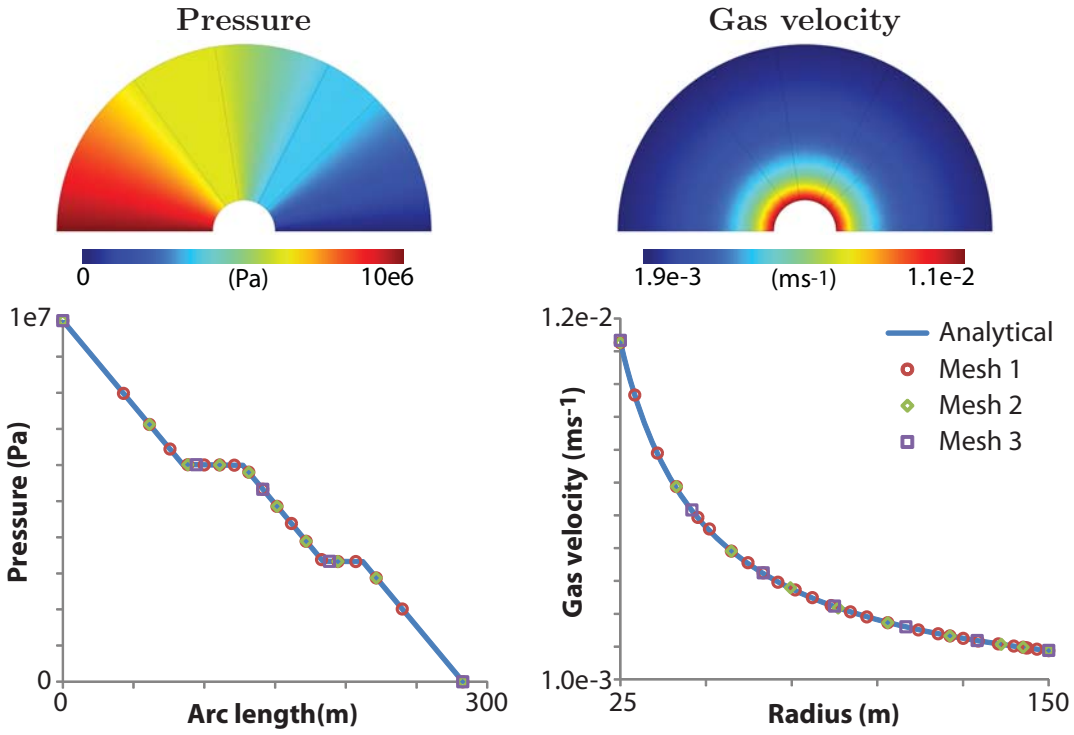

Figure A.8: Pressure along the circle with radius 90 m and gas velocity at $x = 0$ for Model **2** with 5 layers.

A.4 Radial flow

Radial flow describes the flow of the gas outwards, for example from the conduit into the surrounding wall-rock. The scenario modelled here is depicted in Figure A.9 showing the flow from an inner, smaller, semi-circle outwards, to exit from the surface of a larger semi-circle.

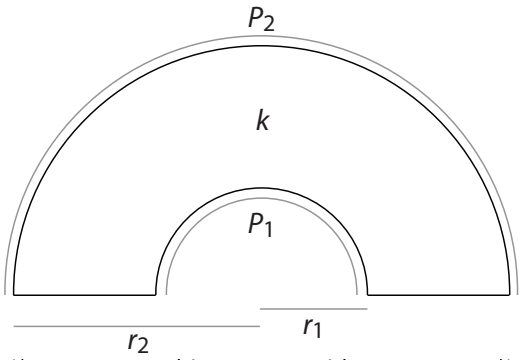

Figure A.9: Scenario modelling radial gas flow. Gas enters along the boundary with radius, r_1, and pressure, $P = P_1$, and exits the system from the surface of a circle with radius, $r = r_2$, and pressure, $P = P_2$.

The flow of fluid in this scenario may be described by the Laplace equation:

$$\nabla^2 P = 0 \tag{A.15}$$

which written in cylindrical coordinates ($r_1 < r < r_2, 0 \leq \theta < \pi, -\infty < z < \infty$) is:

$$\frac{1}{r}\frac{\partial}{\partial r}\left(r\frac{\partial P}{\partial r}\right) + \frac{1}{r^2}\frac{\partial^2 P}{\partial \theta^2} + \frac{\partial^2 P}{\partial z^2} = 0 \tag{A.16}$$

However, because the problem is cylindrical and the pressure at each point will be determined solely by r (the terms in θ and z are 0) this equation can be simplified to:

$$\frac{1}{r}\frac{d}{dr}\left(r\frac{dP}{dr}\right) = 0 \tag{A.17}$$

$r \neq 0$, therefore:

$$\frac{d}{dr}\left(r\frac{dP}{dr}\right) = 0 \tag{A.18}$$

Integrating once with respect to r, gives:

$$r\frac{dP}{dr} = C \tag{A.19}$$

$$\frac{dP}{dr} = \frac{C}{r} \tag{A.20}$$

Integrating again gives:

$$P = C \ln r + D \tag{A.21}$$

where C and D are constants. Applying the boundary conditions at $r = r_1$ and $r = r_2$:

$$D + C \ln(r_1) = P_1 \tag{A.22}$$

$$D + C \ln(r_2) = P_2 \tag{A.23}$$

and solving:

$$C = \frac{P_2}{\ln(r_2)} - \left(\frac{P_2 \ln(r1) - P_1 \ln(r2)}{\ln(r_2) \ln\left(\frac{r_1}{r_2}\right)} \right) \tag{A.24}$$

$$D = \frac{P_2 \ln(r_1) - P_1 \ln(r_2)}{\ln\left(\frac{r_1}{r_2}\right)} \tag{A.25}$$

Therefore, by substituting the Equations for C and D into Equation A.21, the pressure, at any radius (r), may be calculated by:

$$P = \frac{P_2}{\ln(r_2)} - \left(\frac{P_2 \ln(r_1) - P_1 \ln(r_2)}{\ln\left(\frac{r_1}{r_2}\right)} \right) \left(\frac{\ln(r)}{\ln(r_2)} - 1 \right) \tag{A.26}$$

If the outlet pressure is $P_2 = 0$, Equation A.26 reduces to:

$$P = \frac{P_1 \ln\left(\frac{r}{r_2}\right)}{\ln\left(\frac{r_1}{r_2}\right)} \tag{A.27}$$

Differentiating Equation A.26, with respect to r, gives the pressure gradient:

$$\nabla P = -\frac{P_2 \ln(r_1) - P_1 \ln(r_2)}{\ln\left(\frac{r_1}{r_2}\right) \ln(r_2) r} \tag{A.28}$$

Finally, the gas velocity:

$$\boldsymbol{u} = -\frac{k}{\mu} \left(-\frac{P_2 \ln(r_1) - P_1 \ln(r_2)}{\ln\left(\frac{r_1}{r_2}\right) \ln(r_2) r} \right) \tag{A.29}$$

The gas flows through the system with direction perpendicular to the surface of the circles.

A.4.1 Analysis of results

This model is run for three different scenarios as itemized in Table A.5. The models are run for the same permeability ($k = 10^{-12}$ m^2) and inner radius ($r_1 = 25$ m), but different external radii. Furthermore, each scenario was run for three different mesh densities. The pressure and gas velocity results for Model **2** are shown in Figure A.10, whilst Figure A.11 shows a comparison between the analytical and numerical results. The pressure results generally show a good agreement with the analytical solution, with only the lowest quality mesh (mesh 3) deviating slightly. However, in the velocity results, there are significant differences between the analytical and numerical solutions for the lowest quality mesh.

Model	r_1	r_2	Mesh 1	Mesh 2	Mesh 3
1	25	50	226	22	6
2	25	150	400	42	12
3	25	250	454	50	12

Table A.5: The inner (r_1) and outer (r_2) radii for each radial flow model. The number of elements in each mesh used is also shown.

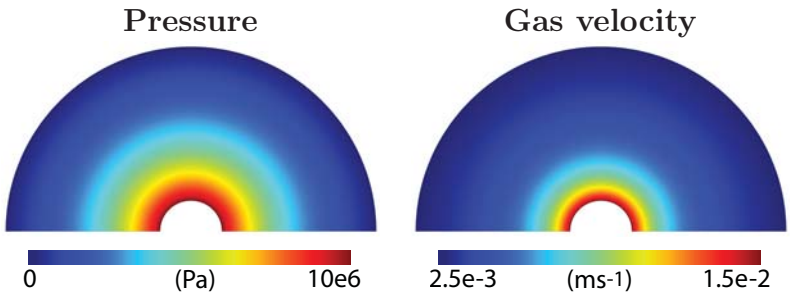

Figure A.10: Pressure and gas velocity for the radial flow scenario, Model **2**.

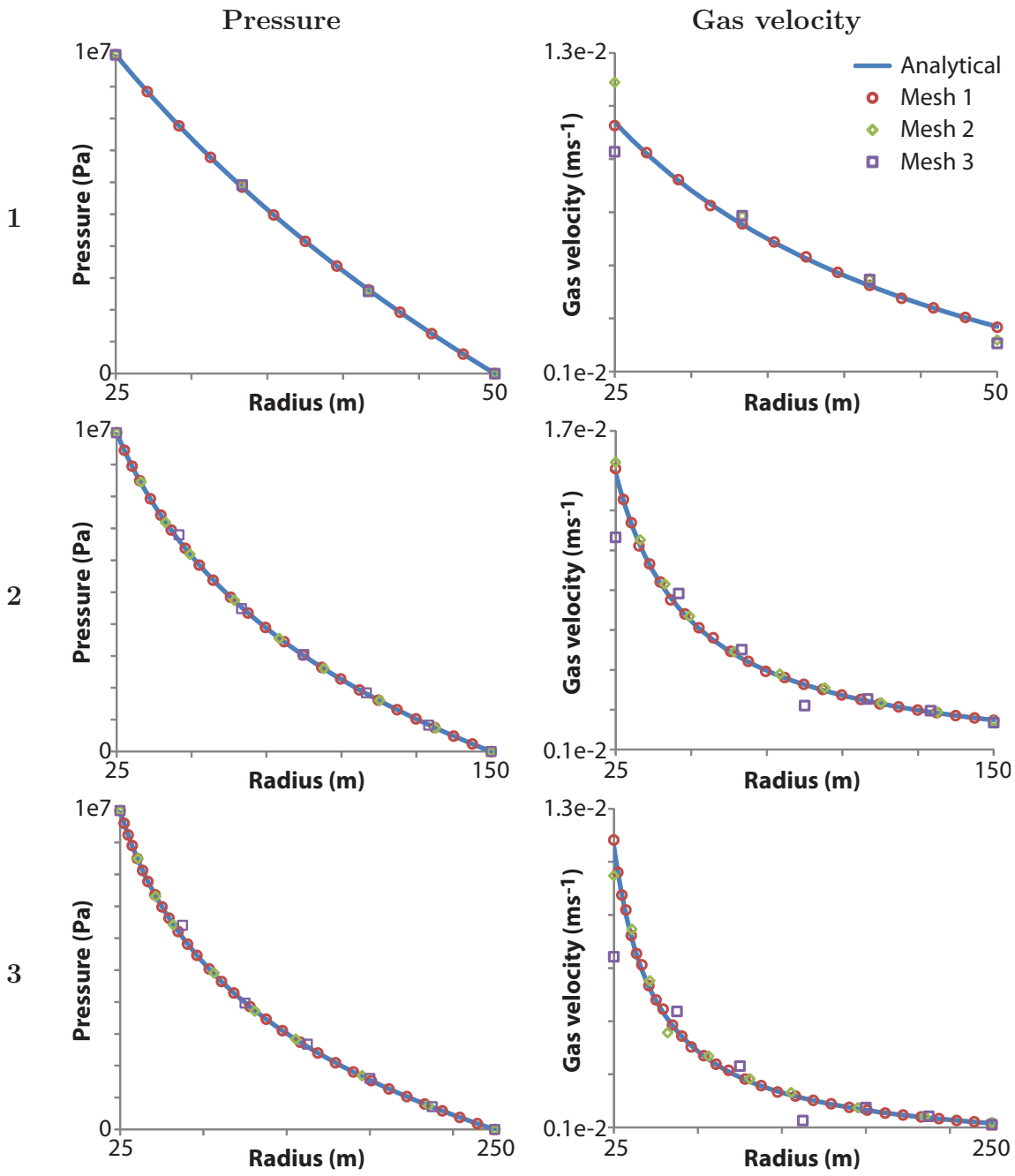

Figure A.11: Comparison between the analytical and numerical results for three different meshes.

A.5 Spherical flow

Spherical flow is similar to radial flow, but it echoes the form of the dome core modelled in Chapters 8 and 9. As with radial flow, spherical flow may be described using the Laplace Equation:

$$\nabla^2 P = 0 \tag{A.30}$$

However, in spherical polar coordinates ($r_1 < r < r_2, 0 \leq \theta < \pi, 0 \leq \phi < 2\pi$), the form is:

$$\frac{1}{r^2}\frac{\partial}{\partial r}\left(r^2\frac{\partial P}{\partial r}\right) + \frac{1}{r^2\sin\theta}\frac{\partial}{\partial\theta}\left(\sin\theta\frac{\partial P}{\partial\theta}\right) + \frac{1}{r^2\sin^2\theta}\frac{\partial^2 P}{\partial\phi^2} = 0 \tag{A.31}$$

which for this problem, because the terms in θ and ϕ have no influence, reduces to the ordinary differential equation:

$$\frac{1}{r^2}\frac{d}{dr}\left(r^2\frac{dP}{dr}\right) = 0 \tag{A.32}$$

$r^2 \neq 0$, therefore:

$$\frac{d}{dr}\left(r^2\frac{dP}{dr}\right) = 0 \tag{A.33}$$

Integrating with respect to r, gives:

$$r^2\frac{dP}{dr} = C \tag{A.34}$$

$$\frac{dP}{dr} = \frac{C}{r^2} \tag{A.35}$$

Integrating a second time yields:

$$P = D - \frac{C}{r} \tag{A.36}$$

where C and D are constants. Applying the boundary conditions at $r = r_1$ and $r = r_2$:

$$D - \frac{C}{r_1} = P_1 \tag{A.37}$$

$$D - \frac{C}{r_2} = P_2 \tag{A.38}$$

and solving:

$$C = \frac{(P_2 - P_1)r_1 r_2}{(r_2 - r_1)} \tag{A.39}$$

$$D = P_1 + \frac{(P_2 - P_1)r_1 r_2}{(r_2 - r_1)r_1} \tag{A.40}$$

Therefore, by substituting the Equations for C and D into Equation A.36, the pressure, at any radius (r), may be calculated according to:

$$P = P_1 + \frac{(P_2 - P_1)r_2}{(r_2 - r_1)}\left(1 - \frac{r_1}{r}\right) \tag{A.41}$$

If the outlet pressure is $P_2 = 0$, Equation A.41 reduces to:

$$P = P_1 \frac{r_1}{r_2 - r_1}\left(\frac{r_2}{r} - 1\right) \tag{A.42}$$

Differentiating Equation A.41 provides the equation for the pressure gradient:

$$\nabla P = \frac{(P_2 - P_1)r_1 r_2}{(r_2 - r_1)r^2} \tag{A.43}$$

Finally, the gas velocity:

$$\boldsymbol{u} = -\frac{k}{\mu}\left(\frac{(P_2 - P_1)r_1 r_2}{(r_2 - r_1)r^2}\right) \tag{A.44}$$

The flow of the gas is perpendicular to the surface of each sphere.

A.5.1 Analysis of results

As with the radial example, spherical flow is modelled for three scenarios (Table A.6). Each model has the same permeability ($k = 10^{-12}$ m^2) and inner radius ($r_1 = 25$ m), but different external radii. Each scenario is also run for three different mesh densities. Spherical flow is modelled in 3D and therefore, the meshes contain significantly more elements than their 2D radial flow counterparts. The three scenarios are compared to the analytical solutions in Figure A.12, whilst the pressure and gas velocity results for Model **2** are shown in Figure A.13. There is good agreement between the analytical and numerical

Model	$\mathbf{r_1}$	$\mathbf{r_2}$	**Mesh 1**	**Mesh 2**	**Mesh 3**
1	25	50	22661	3557	129
2	25	150	26984	4368	257
3	25	250	16200	4710	116

Table A.6: The inner (r_1) and outer (r_2) radii for each spherical flow model. The number of elements in each mesh used is also shown.

solutions, although the lowest quality mesh (Mesh 3) does noticeably deviate from the analytical solution for both pressure and gas velocity. This is particularly evident for the largest models, with the greater r_2.

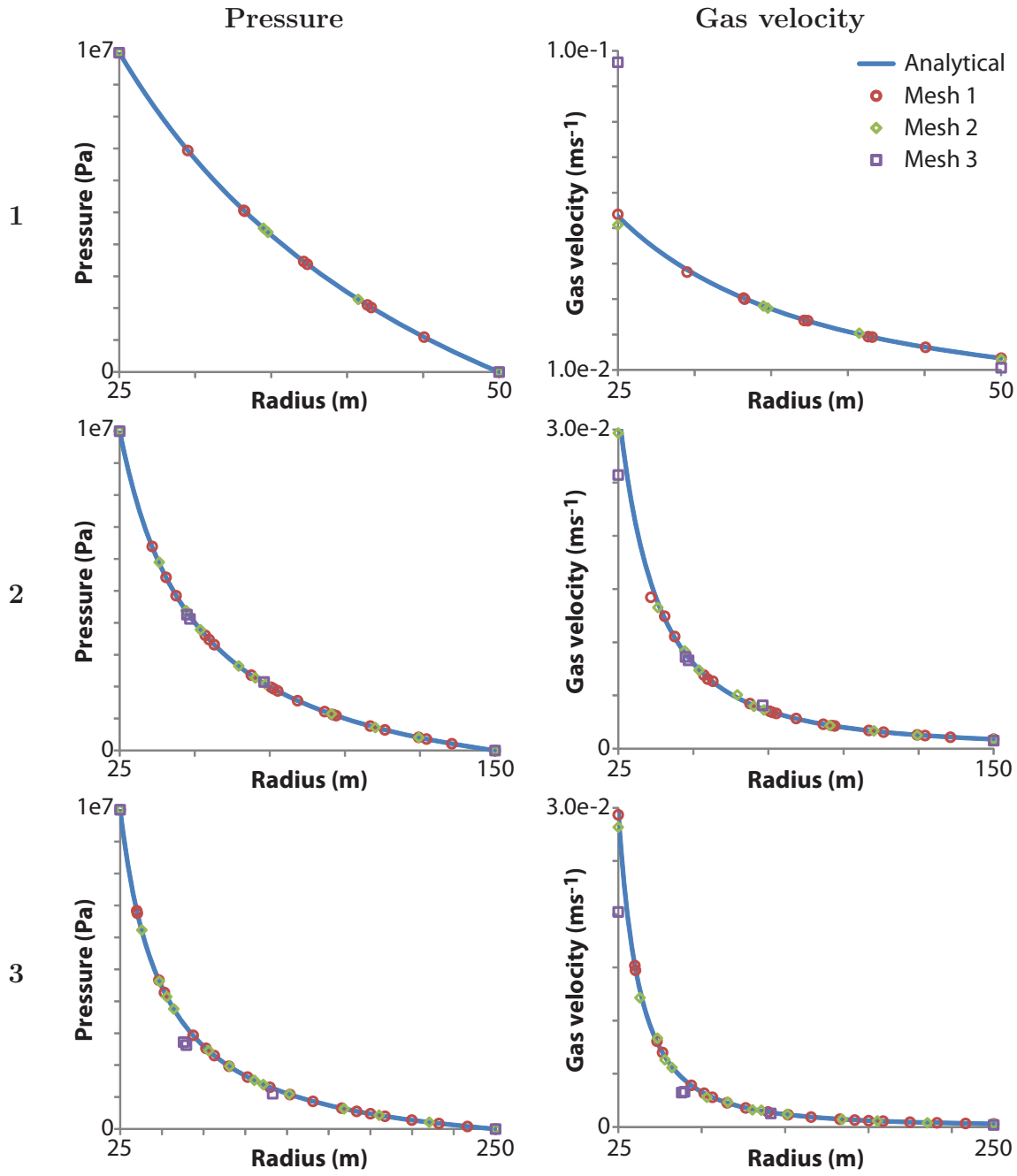

Figure A.12: Comparison between the analytical and numerical results for spherical model with three different meshes. Both pressure and gas velocity measurements are taken along the line between $(r_1, 0, 0)$ and $(r_2, 0, 0)$.

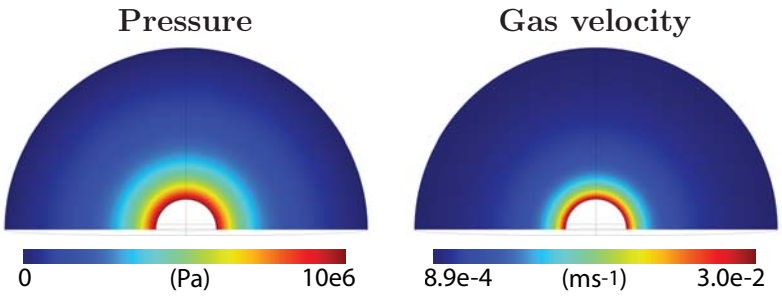

Figure A.13: Pressure and gas velocity for the 3D radial flow model, Scenario **2**.

A.6 Implications for the modelling

Comsol Multiphysics® gives a very good solution compared to the analytical solutions for the scenarios provided. However, in the more complex radial models, a mesh which is too coarse results in errors, particularly with the gas velocity. Therefore, provided a mesh with a suitable resolution is used, Comsol Multiphysics® should provide a very good solution and this lends credence to the results from more complex models.

Appendix B

The validity of Darcy's law

Darcy's law has been utilised in numerous volcanic studies, to model the migration of volatiles (e.g. Eichelberger et al., 1986, Klug and Cashman, 1996, Melnik and Sparks, 1999, Scharff et al., 2014). However, one limitation is that it is formulated for laminar flow. Consequently, it cannot accurately predict the flow of gas at high velocities which exhibit turbulence.

In laminar (viscous) flow, the particles of the fluid travel parallel to the direction of the pathway through which it is flowing. Whilst in turbulent (inertial) flow, the fluid travels in a chaotic manner. The transition between the two flow regimes is determined by the fluid viscosity, the size of the pathway and the velocity of the fluid. Therefore, at low viscosities, large pathways and high velocities, flow would be turbulent.

Here, the transition from laminar flow to turbulent flow is investigated using the Reynolds number, before the Forchheimer equation (a modified form of Darcy's law specifically for modelling turbulence) is discussed.

B.1 Reynolds number

The Reynolds number (Re) is a dimensionless ratio between the inertial and viscous forces acting on a flow according to Equation B.1:

$$Re = \frac{\text{inertial forces}}{\text{viscous forces}} = \frac{\rho \boldsymbol{u} d_p}{\mu} \tag{B.1}$$

for the gas density (ρ), gas velocity ($\boldsymbol{u}$) and the pathway diameter (d_p).

Darcy's law is valid for laminar flow which is defined as flow with a Reynolds number of less than 1 (Nabovati et al., 2009). For Reynolds numbers greater than 2000 (Jaupart and Allègre, 1991, Bouvet de Maisonneuve et al., 2009), inertial forces become important and flow becomes turbulent. This transition is dependent upon the gas viscosity, velocity and the pathway size through which it travels. In this modelling, the gas viscosity is set to the constant value of 1.5×10^{-5} Pas (e.g. Melnik and Sparks, 1999, Costa et al., 2007, Collombet, 2009, de' Michieli Vitturi et al., 2010). Furthermore, the velocity is

determined by Darcy's law based upon the pressurisation and the permeability. However, the size of degassing pathway is particularly important in controlling whether the resultant flow at a given velocity is laminar or turbulent (Figure B.1). The value of the degassing pathway (d_p) is largely dependent upon its location within the volcanic system, the form of the degassing pathway and the volcanic state. In the magma conduit where gas bubbles are continually exsolving and growing by decompression and coalescence, the degassing pathway is the connectivity of the gas bubbles themselves (Eichelberger et al., 1986). In this case, the pathway size is therefore determined by the bubble diameter which is thought to be μm scale (Navon and Lyakhovsky, 1998, Klug and Cashman, 1996). However, along the conduit-wall margin, tuffisites are an example of a potential degassing route. Tuffisites are generally on the cm scale (Tuffen et al., 2003, Castro et al., 2012, Kolzenburg et al., 2012, Berlo et al., 2013). In contrast, surface cracks could be much larger, and during large eruptions, the degassing pathway effectively becomes the entire width of the conduit (10's of m).

Figure B.1 plots the Reynolds numbers for different pathway widths and gas velocities. For very small degassing pathways, high velocities are permissible whilst still satisfying the requirements for laminar flow. However, as the pathway size increases, the velocity needs to decrease for Darcy's law to still be applicable. Therefore, gas flow by bubble connectivity within the conduit should be accurately modelled by Darcy's law. However, gas flow from surface cracks is likely to be turbulent, even for small velocities, and therefore Darcy's law cannot accurately predict flow.

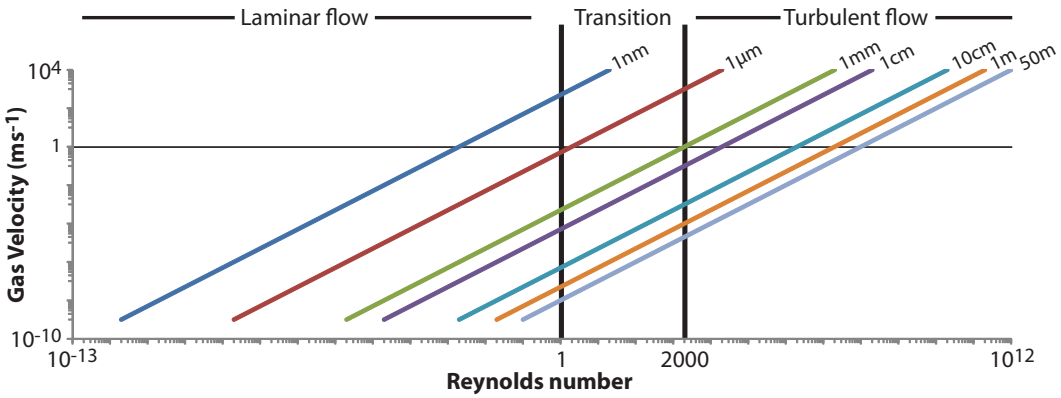

Figure B.1: The Reynolds number for different gas velocities and pathway sizes. Creeping flow has a Reynolds number less than 1 (Nabovati et al., 2009) whilst turbulent flow has a Reynolds number greater than 2000 (Jaupart and Allègre, 1991, Bouvet de Maisonneuve et al., 2009).

B.2 Darcy's law versus Forchheimer equation

The majority of permeability measurements for volcanic products (Figure 1.2) represent the Darcian permeability. However, the inertial permeability is increasingly being measured (Figure B.2). The permeability is usually measured using a permeameter which measures the flow rate at different applied pressures (e.g. (Rust and Cashman, 2004, Takeuchi et al., 2008, Kolzenburg and Russell, 2014)). Using this, the Darcian permeability may be derived from Darcy's law, or both permeabilities are calculated using the Forchheimer equation. A low Darcian permeability means a high resistance to flow due to viscous effects (Rust and Cashman, 2004). Similarly, a low Inertial permeability suggests flow is strongly restricted by inertial effects (Rust and Cashman, 2004).

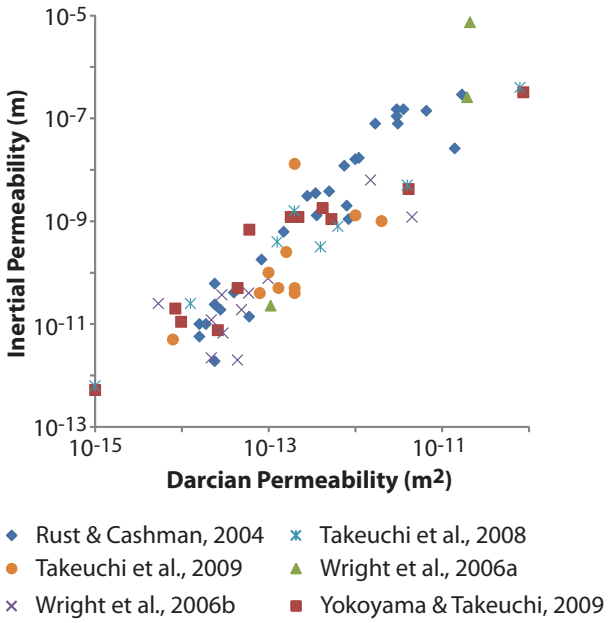

Figure B.2: A comparison between Inertial and Darcian permeabilities for volcanic rocks. Compared to Darcian permeability measurements, there are significantly fewer measurements for the inertial permeability (74 inertial permeabilities, compared to 565 Darcian permeabilities in Figure 1.1). There is a general trend of increasing inertial permeability with increasing Darcian permeability. However, the same Darcian permeability can show a difference of two orders of magnitude in the inertial permeability.

Here, the velocity measured by Darcy's law (Equation B.2) is compared to that derived from the Forchheimer equation.

$$\boldsymbol{u} = -\frac{k}{\mu}(\nabla P) \tag{B.2}$$

The Forchheimer equation is usually expressed as:

$$\nabla P = -\frac{\mu}{k}\boldsymbol{u} - \frac{\rho}{k_f}\boldsymbol{u}^2 \tag{B.3}$$

However, for easy comparison with Darcy's law, it is rearranged in terms of $\boldsymbol{u}$, by taking the positive root from the quadratic formula:

$$\boldsymbol{u} = \frac{k_f}{2\rho}\left(-\frac{\mu}{k} + \sqrt{\left(\frac{\mu}{k}\right)^2 - 4\left(\frac{\rho}{k_f}\right)\nabla P}\right) \tag{B.4}$$

For very low velocities, or very high inertial permeabilities, the Forchheimer equation reduces to Darcy's law. In Darcy's law, the gas density does not directly affect the velocity - it influences the pressure distribution which alters the velocity. However, in the Forchheimer equation, the density changes the velocity directly.

B.2.1 Analysis of results

Figures B.3 and B.4 compare the velocities from the two equations at different pressure gradients for gas densities of 0.19 and 96.39, respectively. These gas densities correspond to atmospheric pressure and a pressure of 50 MPa ($\approx$ 2 km). The pressure gradients in both plots range from 0 to 1 MPam^{-1}. For reference, in the basic cracked dome model (**1** - Chapter 7) at the start, the bulk of the pressure gradients are $\approx 2 \times 10^4$ Pam^{-1}. With only the very surface regions experiencing higher gradients of up to 0.3 MPam^{-1}. Once the cracks open, the highest pressure gradient is at the crack tips (with a maximum of 2 MPam^{-1} and along the surface (with a maximum of 0.5 MPam^{-1}) The highest pressure gradients are restricted to the less permeable domains of the wall-rocks and dome (10^{-14} m^2).

In both Figures B.3 and B.4, the greatest deviation between the two equations occurs at the highest Darcian permeability ($k = 10^{-8}$ m^2) and lowest inertial permeability ($k_f = 10^{-10}$ m). However, this difference also increases with the gas density.

At high Darcian permeabilities, the gas velocity is dominated by the inertial permeability, whilst at low Darcian permeabilities, the gas velocity is dominated by the Darcian permeability and the inertial permeability has little effect. In the case of Figure B.3 with a gas density of 0.19 kg/m^3, this means the gas velocity results for Darcy's law are acceptable for permeabilities of less than 10^{-12} m^2, and may still be acceptable for high inertial permeabilities. However, for the highest Darcian permeability investigated (10^{-8} m^2), the inertial term is significant and all gas velocities derived from Darcy's law will be much higher than is realistic. For Figure B.4 with a gas density of 96.39 kg/m^3, Darcy's law

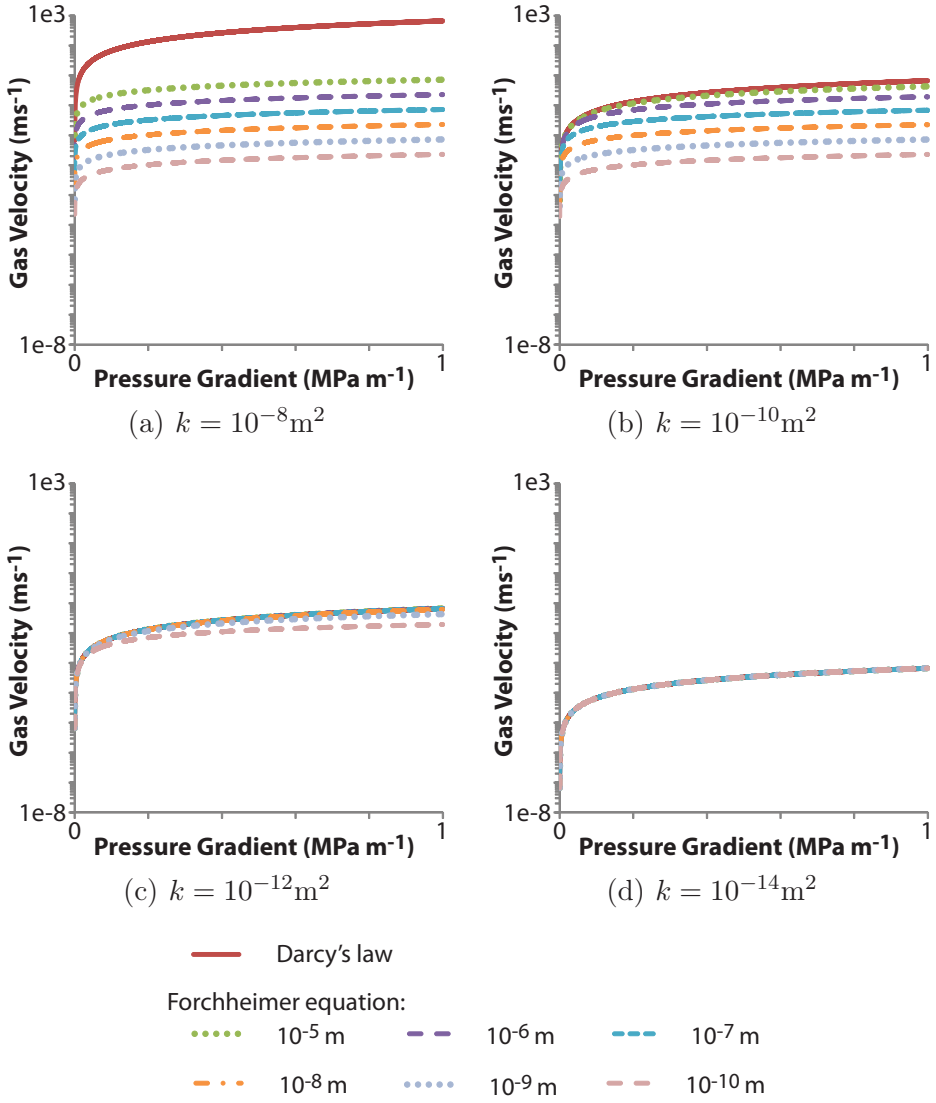

(a) $k = 10^{-8}\text{m}^2$ (b) $k = 10^{-10}\text{m}^2$

(c) $k = 10^{-12}\text{m}^2$ (d) $k = 10^{-14}\text{m}^2$

Figure B.3: A comparison between Darcy's law and the Forchheimer equation for different Darcian permeabilities (k) and a gas density of 0.19 kg/m^3. The difference between the two equations is greater for larger Darcian permeabilities. Furthermore, the lower the inertial permeability, the slower the gas velocity in comparison to using Darcy's law.

and Forchheimer agree for a permeability of 10^{-14} m^2 and also 10^{-12} m^2, if the inertial permeability is high.

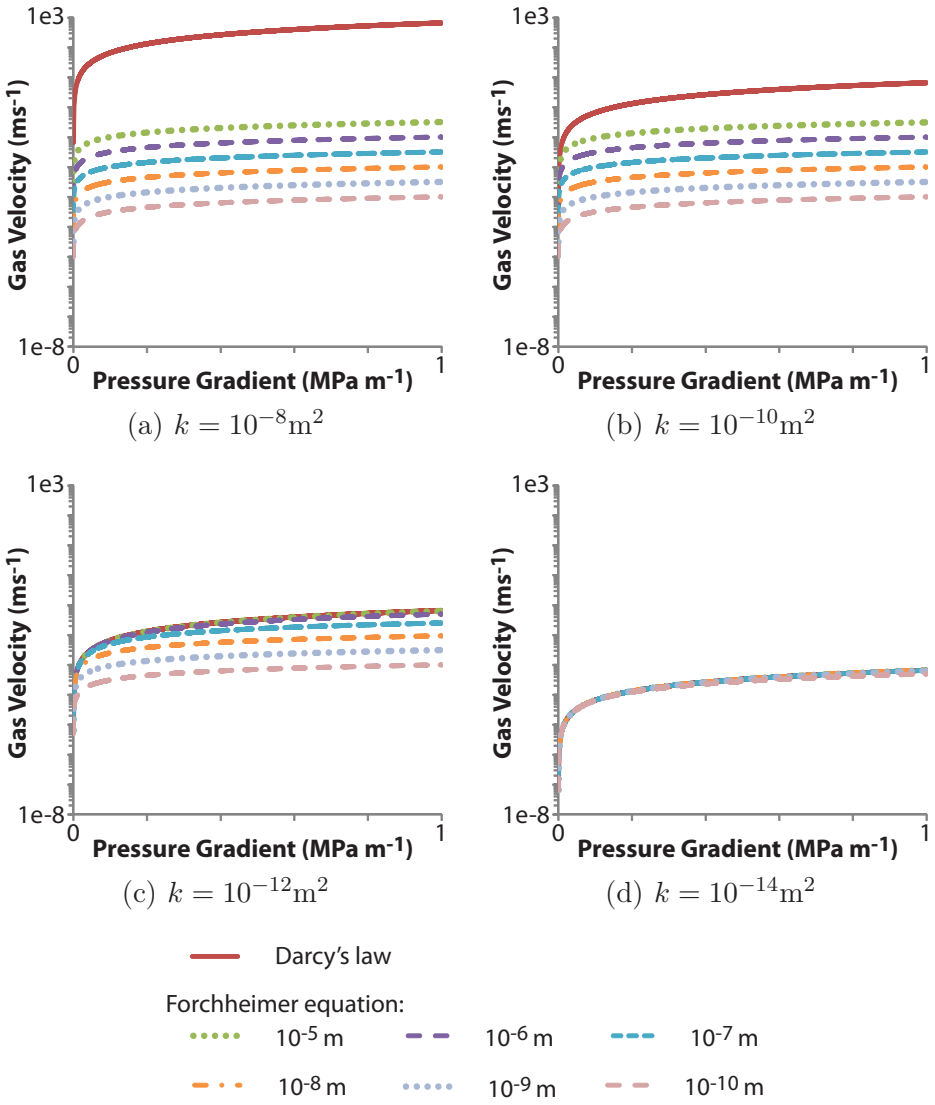

(a) $k = 10^{-8}\text{m}^2$ (b) $k = 10^{-10}\text{m}^2$

(c) $k = 10^{-12}\text{m}^2$ (d) $k = 10^{-14}\text{m}^2$

Figure B.4: A comparison between Darcy's law and the Forchheimer equation for different Darcian permeabilities (k) and a gas density of 96.39kg/m^3.

B.3 Implications for the modelling

The investigations presented here are simplistic and the equations are not compared for an actual model. However, the results serve to show that the Reynolds number and Forchheimer's equation both indicate that if the actual flow is turbulent, Darcy's law will predict a higher velocity. Darcy's law is applicable to many of the models presented, however in the domains with very high permeability regions, such as the dome collapse (Chapter 4), fracture zones (Chapter 5) and dome cracks (Chapter 7), the Forchheimer equation may give a more accurate result. Darcy's law is applicable for this work because it provides the upper limit, so the maximum gas velocities and the maximum gas storage and loss. However, the results here highlight that inertial effects must be investigated further to create a more realistic model.

Appendix C

Gas density and viscosity

In the modelling, the gas density is calculated from the ideal gas law using a temperature of 850 °C:

$$\rho = \frac{M}{RT}P \tag{C.1}$$

for the mean molar mass ($M = 0.018\,\mathrm{kgmol^{-1}}$), ideal gas constant ($R = 8.314\,\mathrm{PaK^{-1}mol^{-1}}$), temperature ($T$) and the pressure ($P$). The gas viscosity is set to a constant value of 1.5×10^{-5} Pas. Here, the effect of these assumptions is investigated.

C.1 Gas density

The discussion on gas density is two-fold. Firstly, the impact of the temperature is explored, and secondly, the assumption of ideality is investigated.

C.1.1 Temperature

The eruption temperature of magma depends on its composition and ranges from $\approx 700 - 1200$ °C, with silicic magmas erupting at lower temperatures than basalt (Kilburn, 2000). The temperature of the andesitic magma at Soufrière Hills has been estimated at 850 °C (Murphy et al., 2000), and conduit-flow models often use this value (e.g. (Melnik and Sparks, 1999, de' Michieli Vitturi et al., 2010)). However, the temperature decreases away from the conduit, both laterally into the country rock, and within the dome structure. Measurements of dome surfaces suggest temperatures of $200 - 400$ °C (Oppenheimer et al., 1993, Stinton et al., 2014), rapidly climbing to > 650 °C at 1 m depth (Sparks et al., 2000). From the method in Chapter 2, temperature is used to derive the gas density according to the ideal gas law (Equation C.1). Throughout the modelling, a uniform value of 850°C (1123 K) is used. However, here the effect of different temperatures is investigated before two examples with temperature gradients are described.

Uniform temperature

The effect of different temperatures and pressures on the gas density as calculated according to the ideal gas law is shown in Figure C.1. Following simple inspection of the equation, the gas density increases with pressure, but decreases with temperature. The graph shows there are significant differences in the gas density with changing temperature at high pressures. However, the greatest change in temperature in the region of the volcano modelled would be the surface regions of the dome, with lower pressures.

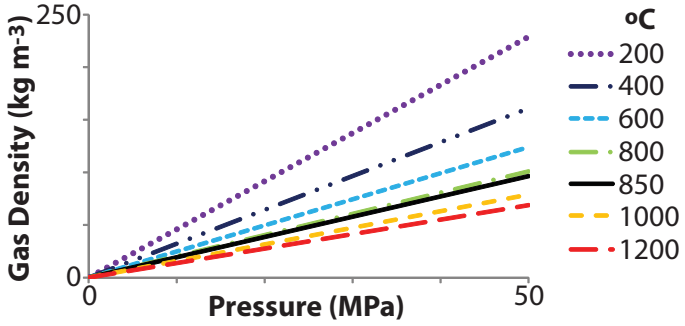

Figure C.1: Gas densities at different temperatures (°C) and pressures (MPa) according to the ideal gas law.

In order to investigate the impact this has on the model results, the six example models from Chapter 3 (Figure 3.3) are re-run for different temperatures (Figure C.2). The influence of the temperature is dependent upon the pressurisation of the model - the greater the

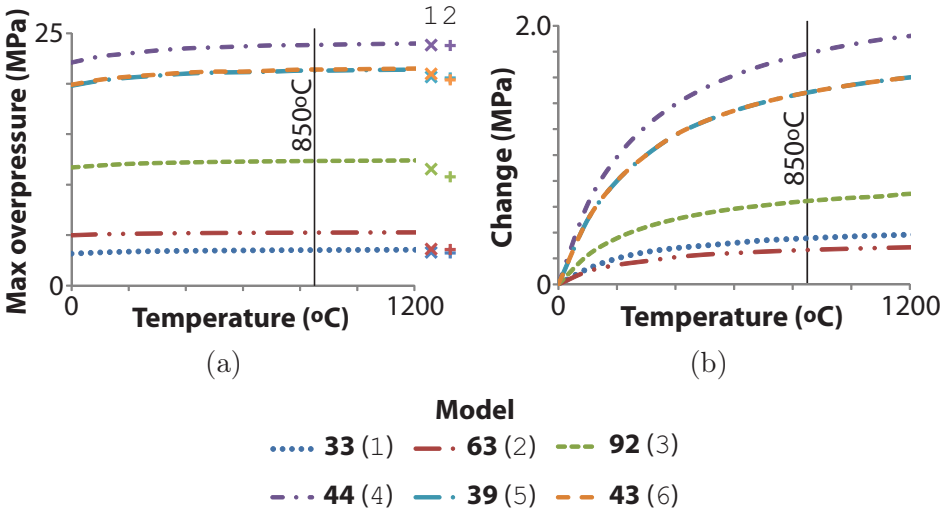

Figure C.2: (a) The maximum overpressure at different constant temperatures for the six example models from Chapter 3 (Figure 3.3). Crosses indicate the maximum overpressure for the two gradient temperature examples shown in Figure C.3. (b) The change relative to a temperature of 0°C. The temperature used in the modelling (850°C) is marked.

pressurisation, the greater the change in maximum overpressure. Consequently Models **44**, **39** and **43** are more affected by the change in temperature than **33**, **63** and **92**. However, the difference within the range of temperatures measured at volcanoes ($\approx 200 - 1200$°C) is relatively insignificant compared to the actual overpressure, at < 1 MPa. Therefore, a value of 850°C gives a good approximation when the temperature throughout the simulation is uniform.

Gradient temperature

In order to simulate the effects of cooling with increasing distance from the magma conduit, two gradient temperatures are imposed according to Figure C.3. In gradient `1`, the temperature decreases outwards from the magma conduit (850°C) with a temperature at the overburden surface of 200 °C. In gradient `2`, the temperature decreases outwards from the magma conduit with a temperature on the lateral exterior boundaries and the overburden surface of 200 °C. Using these two temperature distributions, the six example models from Chapter 3 are re-run.

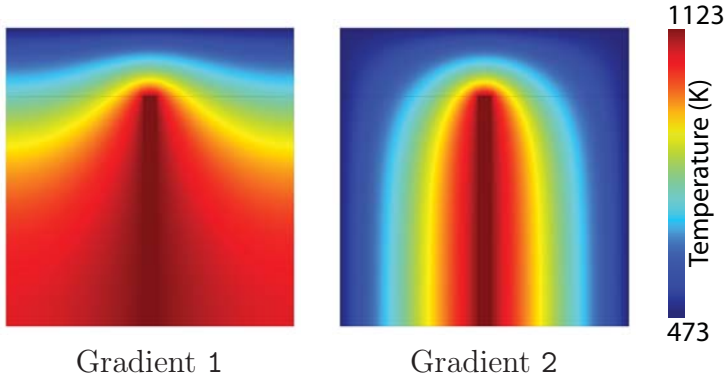

Figure C.3: Temperature distribution with a conduit temperature of 850 °C decreasing to 200 °C at the overburden surface (`1`) or at all exterior boundaries (`2`).

The maximum overpressure for each model is shown as crosses in Figure C.2a. The overpressure is less than that calculated using a uniform temperature of 850°C and is related to the difference between the highest and lowest temperatures modelled. The greater the temperature difference between the conduit and surface, the lower the maximum overpressure.

The gas overpressure for the two temperature distributions follows the same pattern as Figure 3.4 (Chapter 3). The differences between the uniform (850°C) and gradient temperature distributions are shown in Figures C.4 and C.5. For both temperature gradients, the gas overpressure calculated is lower than that for the uniform temperature. Gradient `2` has a lower pressure, and the deviation from the uniform temperature examples is more extensive due to the greater temperature variation. The greater the pressurisation within the model, the greater the difference between the gas overpressure results.

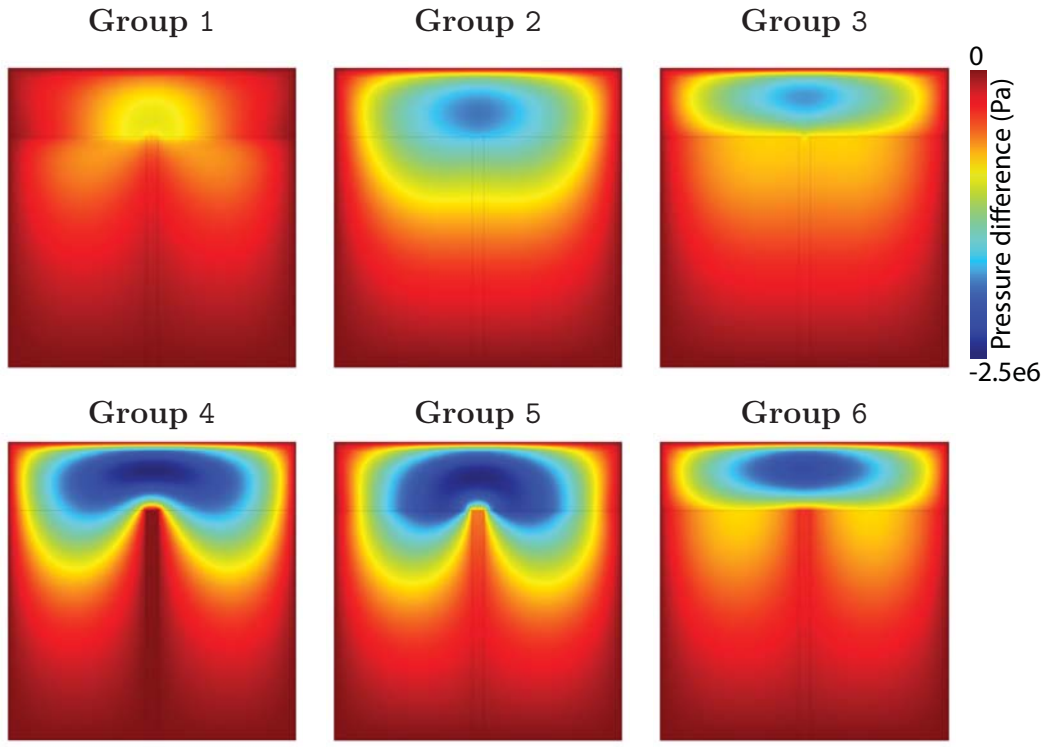

Figure C.4: The difference between the results for the Gradient 1 compared to a constant temperature. Models **33**, **63**, **92**, **44**, **39** and **43**, respectively (Chapter 3).

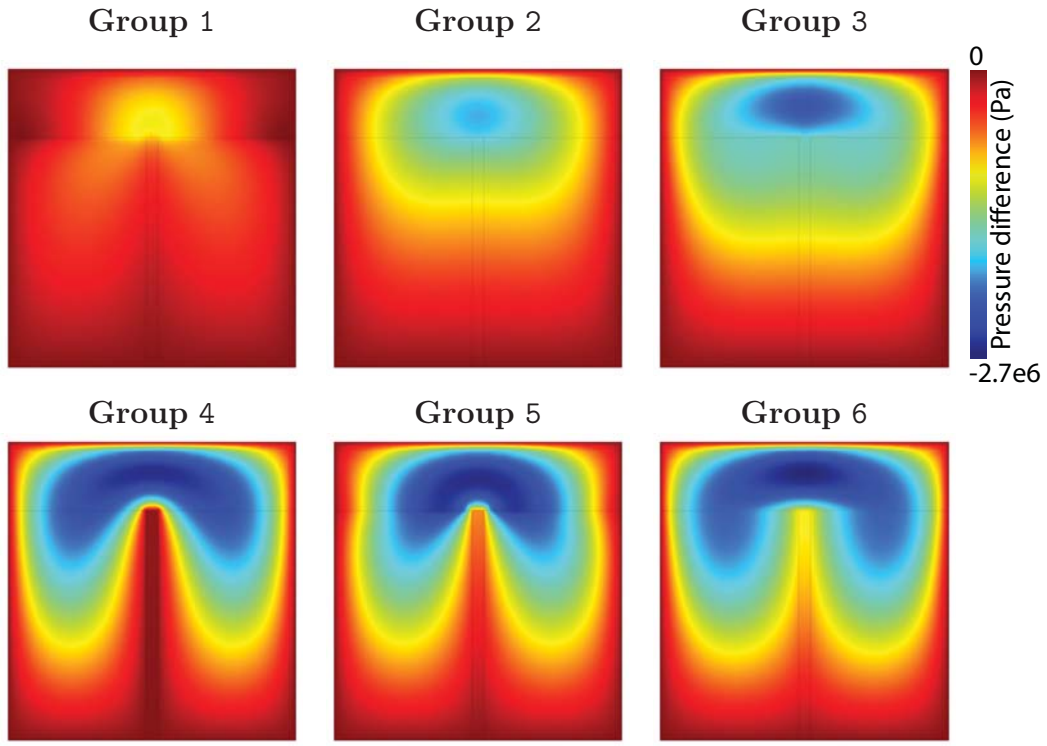

Figure C.5: The difference between the results for Gradient 2 compared to a constant temperature. Models **33**, **63**, **92**, **44**, **39** and **43**, respectively (Chapter 3).

C.1.2 Ideality

Throughout the modelling, ideality is assumed, and consequently, the gas density (ρ) is calculated according to the ideal gas law (Equation C.1). However, ideality is known to deviate from the true behaviour of water. Therefore, the density from the ideal gas law is compared to that derived from steam tables (Figure C.6). For the three temperatures plotted, the ideal gas law always calculates a higher density. However, the difference between the two calculations decreases with increasing temperature. In order to assess the impact of this on the results, the six example models from Chapter 3 are re-run for the true density of water for a temperature of 850 °C (Figure C.7). When using an accurate representation of the gas density, the calculated pressure for the example models is lower than when the density is calculated using the ideal gas law. The greatest difference occurs in the regions of lowest pressure, and is largest in Group 1. However, the difference is very small at $< 1.7 \times 10^5$ Pa (just above atmospheric pressure).

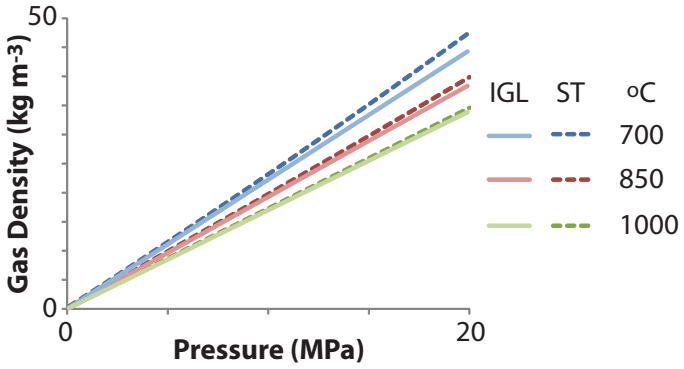

Figure C.6: A comparison between the gas density as calculated by the ideal gas law (IGL) and from steam tables (ST) (e.g. `http://www.spiraxsarco.com/esc/SH_Properties.aspx`).

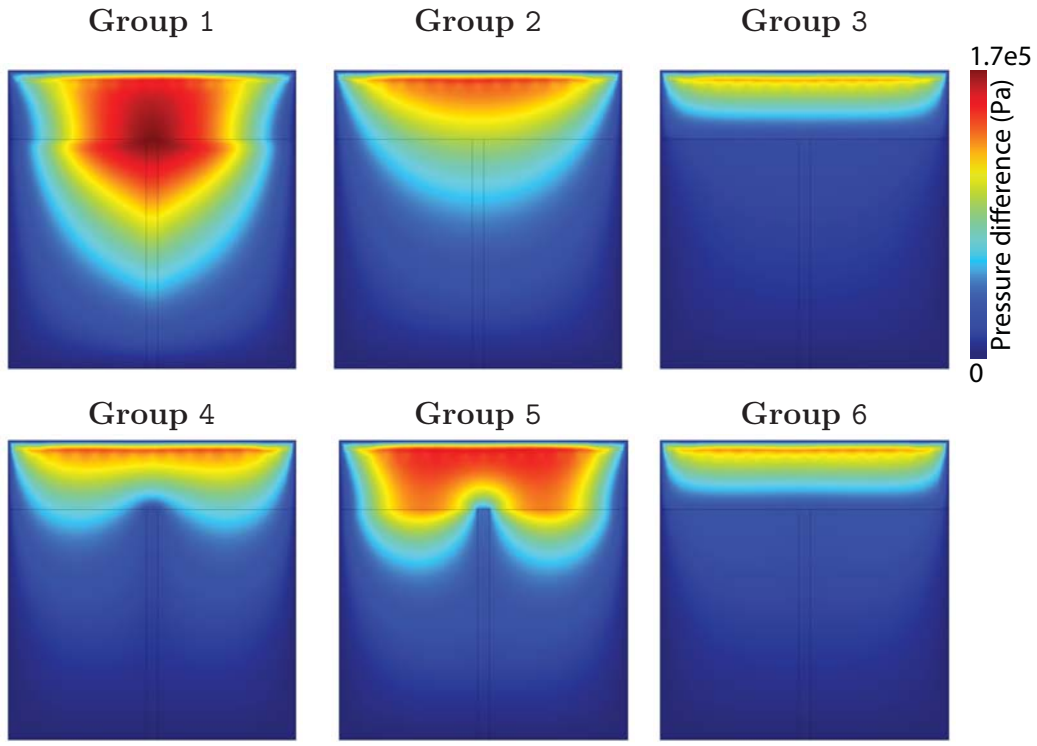

Figure C.7: The difference between the pressure when the density is calculated by the ideal gas law to that from steam tables with a temperature of 850 °C. Models **33**, **63**, **92**, **44**, **39** and **43**, respectively (Chapter 3).

C.2 Gas viscosity

The value for the gas viscosity ($\mu = 1.5 \times 10^{-5}$ Pas) used follows the values used in conduit flow models (e.g. Melnik and Sparks, 1999, Collombet, 2009, de' Michieli Vitturi et al., 2010, Schneider et al., 2012). However, this does deviate from the true viscosity of water. In the modelling, the viscosity is used in the calculation of the gas velocity (Darcy's law). Hence, changing the viscosity only affects the gas velocity and does not alter the pressure distribution.

Figure C.8 plots the gas velocity for different viscosities and permeabilities. The viscosities chosen represent the viscosity of the gas for three temperatures (700, 850 and 1000 °C, respectively). Unsurprisingly, the gas velocity increases with the permeability, but decreases with increasing gas viscosity. However, for different permeabilities, the gas velocity with the quoted gas viscosities will be of the same order of magnitude. No additional models are run for this comparison because the gas velocity is so dependent upon the permeability. Hence, due to the range of permeability settings for the models in each group from Chapter 3, the example models would not be representative of the group as a whole.

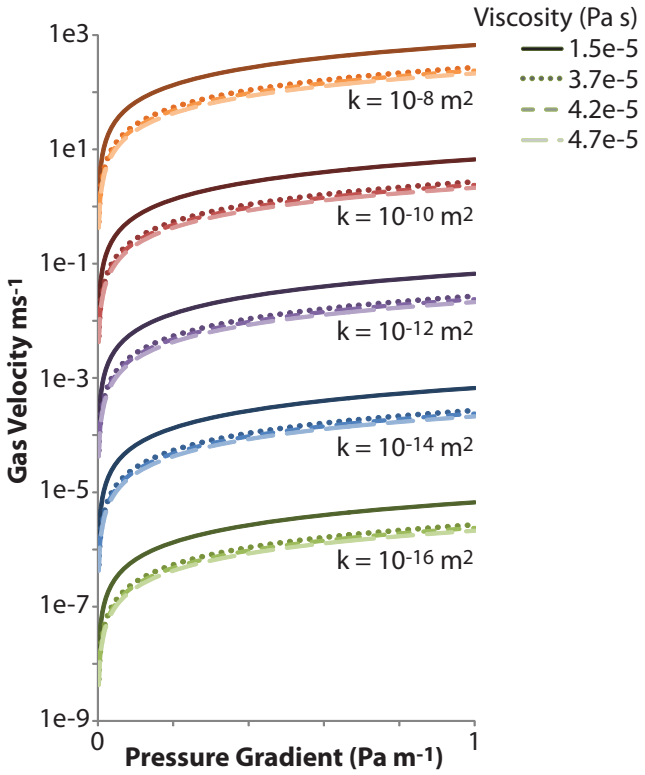

Figure C.8: The velocity at different permeabilities and viscosities against the pressure gradient. The value of the gas viscosity used in the modelling is $\mu = 1.5 \times 10^{-5}$ Pas. The other three values plotted represent the gas viscosity (3.7×10^{-5}, 4.2×10^{-5} and 4.8×10^{-5} Pas) calculated for different temperatures (700, 850 and 1000 °C, respectively) from steam tables (e.g. `http://www.spiraxsarco.com/esc/SH_Properties.aspx`).

C.3 Implications for the modelling

The results from the simplistic experiments show despite variations in the temperature, the pressurisation patterns are the same as derived from using the uniform temperature of 850°C. There are differences in the overpressures reached, however given the total pressurisation of the systems, the deviation is small. The gas would be expected to follow the behaviour as modelled. Therefore, within the scope of this study and the assumptions made, the temperature has little impact. However, it is worth considering the larger role that temperature plays in volcanoes, for example rheology. The manner in which rocks behave to an imposed stress is related to the temperature, such that rocks at higher temperatures will deform in a ductile manner, whilst colder rocks, such as those in the dome are more likely to fracture and experience brittle deformation. Therefore, temperature must be included in any further work, particularly if the processes related to rheology are included.

From Figure C.7, the true density of water at high temperature and pressure is only slightly less than that calculated from the ideal gas law. Therefore, this only has a very limited

impact upon the pressure results for the modelling.
A difference would be expected in the gas velocity results when using the true viscosity of water. However, Figure C.8 showed that although using the true gas viscosity would decrease the gas velocity, it would still be of the same order of magnitude for a particular permeability. The gas viscosity does not change the pressure distribution, so the pattern of behaviour of the gas would be the same.

Appendix D

De-coupling along the conduit-wall margin

De-coupled domains allows them to deform independently rather than together. Consequently, if the conduit is de-coupled from the surrounding wall-rocks a spine may be extruded. However, if the domains remain coupled, bulging of the entire region (conduit and wall-rocks) may result. In order for de-coupling to occur the exerted stress must exceed the strength of the rocks resulting in brittle failure (Tuffen et al., 2003, Neuberg et al., 2006, Lavallée et al., 2008, 2011). Therefore, in real volcanoes, both scenarios are likely to occur dependent upon the stress regime at any particular point in space and time. The transition between regimes is highly complex. However, comparing the results between a coupled and a de-coupled system can provide important insights into the impacts of each on the displacement behaviour.

D.1 Modelling de-coupling

Here, the effect of de-coupling the conduit region from the surrounding volcanic edifice or country rock is investigated. This may be applicable to the models for brittle failure along the margin between the conduit and country rock (Chapters 5 and 10). Furthermore, the ability for the conduit domain, and other domains, to de-couple from the surroundings, may also have implications for the variable pressurisation results in Chapters 8 and 9.

Although an accurate model for de-coupling is complex and beyond the scope of this research, it is crudely simulated through comparison of two model setups (Figure D.1). **1** represents the coupled scenario with a central conduit, overlain by a spine and surrounded by two wall-rocks. Following the method in Chapter 2, the exterior boundaries in **1** are all set to lithostatic pressure. This first model is compared to a de-coupled scenario (**2**) where only the conduit and spine are directly modelled, and the presence of the wall-rocks is inferred by setting the lateral exterior boundaries to the conduit-wall boundary pressure as calculated in **1**. The top and bottom exterior boundaries in **2** are set to lithostatic

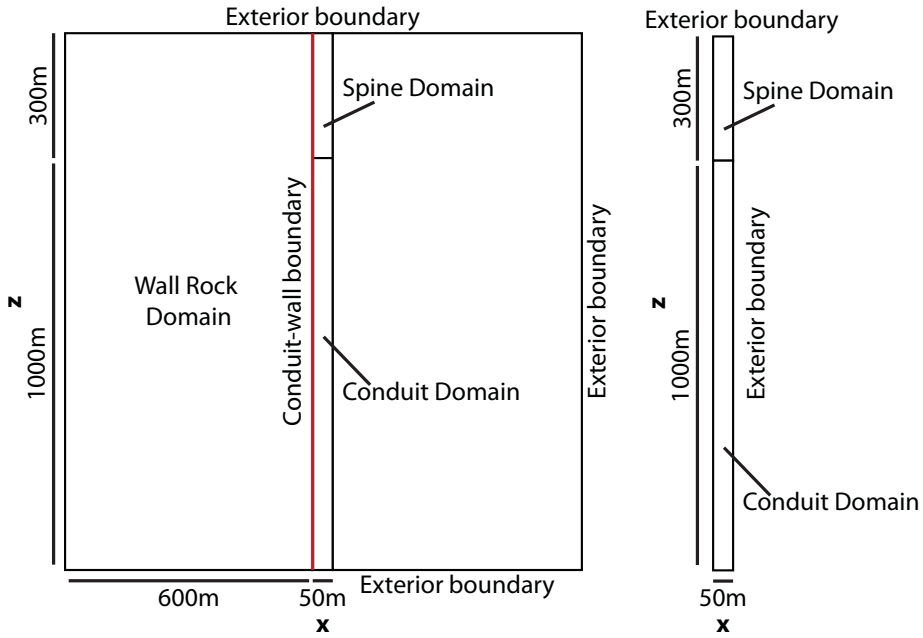

(**1**) Coupled (**2**) De-coupled

Figure D.1: The two models used to investigate de-coupling the conduit region from the surrounding wall-rocks. In **1** all exterior boundaries are set to lithostatic pressure. Whilst in **2** the top and bottom boundaries are lithostatic pressure, but the lateral exterior boundaries are set to the conduit-wall boundary pressure derived from **1**, thereby implicitly suggesting the presence of the wall-rocks. This ensures the conduit-spine pressure distribution is the same in each scenario.

pressure. Consequently, the pressure distribution for the conduit and spine are exactly the same in each scenario. These two stationary scenarios are run and the results compared for 125 different permeability combinations.

The average pressure in each domain and the maximum surface displacement above the conduit/spine for each model in the two scenarios is shown in Figure D.2. The average pressure results follow those from Chapter 3 (Figure 3.2), with any differences due to the differing model configuration (e.g. a spine instead of an overburden).

The maximum surface displacement above the spine follows the pressurisation results such that models with high average pressures result in the greatest surface displacement. Consequently, the coupled and de-coupled results both follow the same pattern. However, the de-coupled models show more extreme surface displacement. For high pressure systems, de-coupling results in greater surface displacement. For low pressure systems, the surface displacement is less. When the conduit/spine are coupled to the wall-rocks, the surface displacement is determined by the pressurisation, whether this is in the conduit/spine region or within the wall-rocks. Conversely, when the domains are de-coupled, the surface displacement above the spine is determined by the conduit/spine pressurisation without being dragged up or down by the wall-rock.

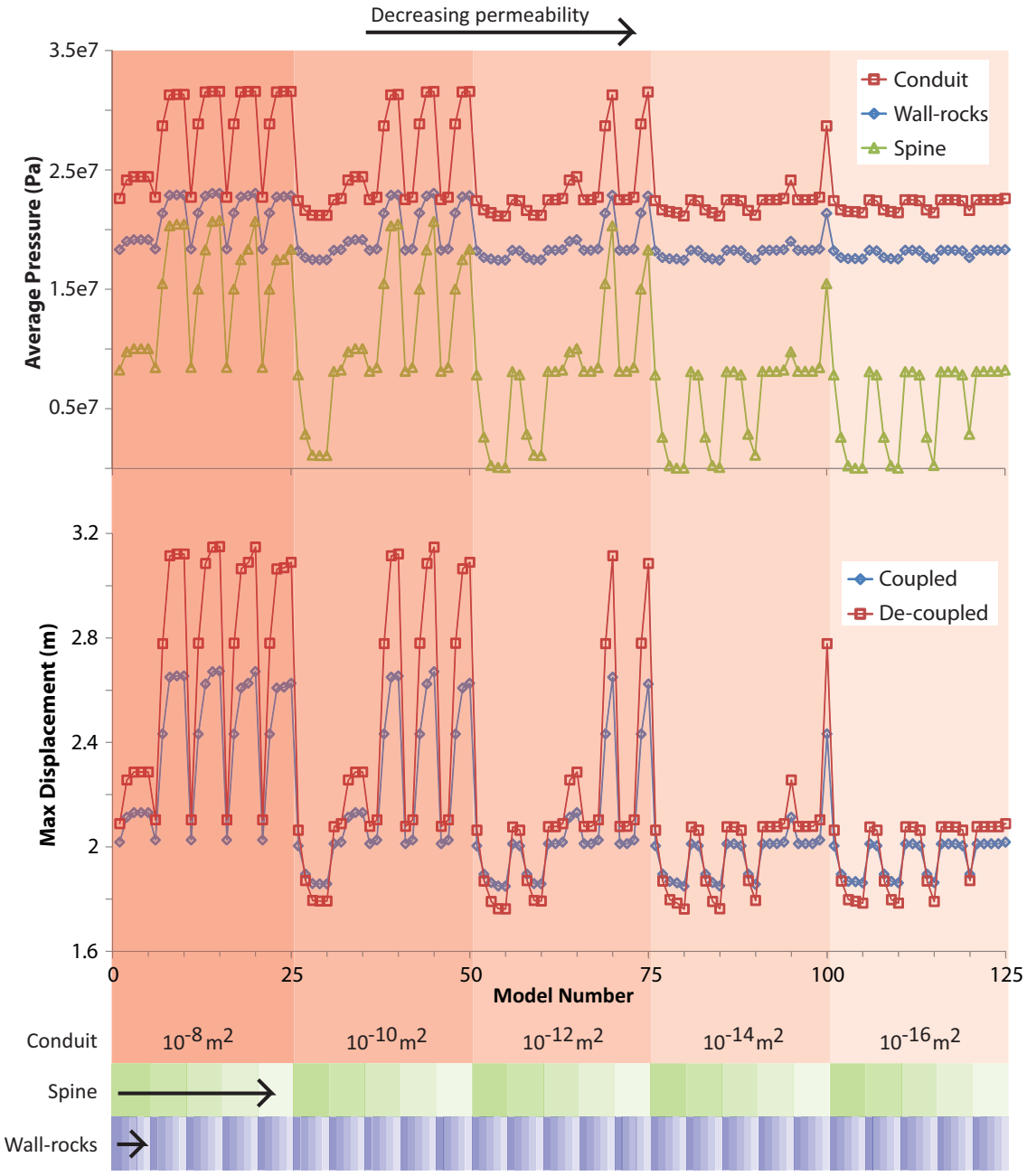

Figure D.2: The average pressure for each domain and the maximum surface displacement above the spine for the coupled and de-coupled scenarios. For each conduit permeability, there are five spine permeabilities and for each spine permeability, there are five wall-rock permeabilities. All permeabilities decrease from left to right by 10^2 decrements from 10^{-8} to 10^{-16}m^2.

D.2 Implications for the modelling

The two scenarios modelled here are extreme and represent end-members. The de-coupled scenario assumes complete separation of the conduit/spine region from the wall-rocks, therefore simulating a smooth piston-like behaviour. However, in reality, the conduit-wall margin would be rough, therefore promoting friction-controlled slip (Collier and Neuberg, 2006) rather than free motion, as modelled here. Furthermore, the situation in a real volcano may be a combination of both coupled and de-coupled, dependent upon the rock properties and the stress-regime. However, the modelling has highlighted some important implications for the results of other models. For example, the brittle failure models in Chapter 5 and 10 would likely respond to the high pressure by greater surface uplift above the conduit/spine, and less surface displacement above the wall-rocks. Similarly, in Chapter 8, groups `3` and `4D` with pressurisation localised to the conduit region, would result in greater displacement above the conduit than is measured in the coupled configuration.

Finally, thank you to Oscar for standing on the keyboard and lying on the mouse, and deleting whole passages of text...

...thank you also to whomever invented "undo".